

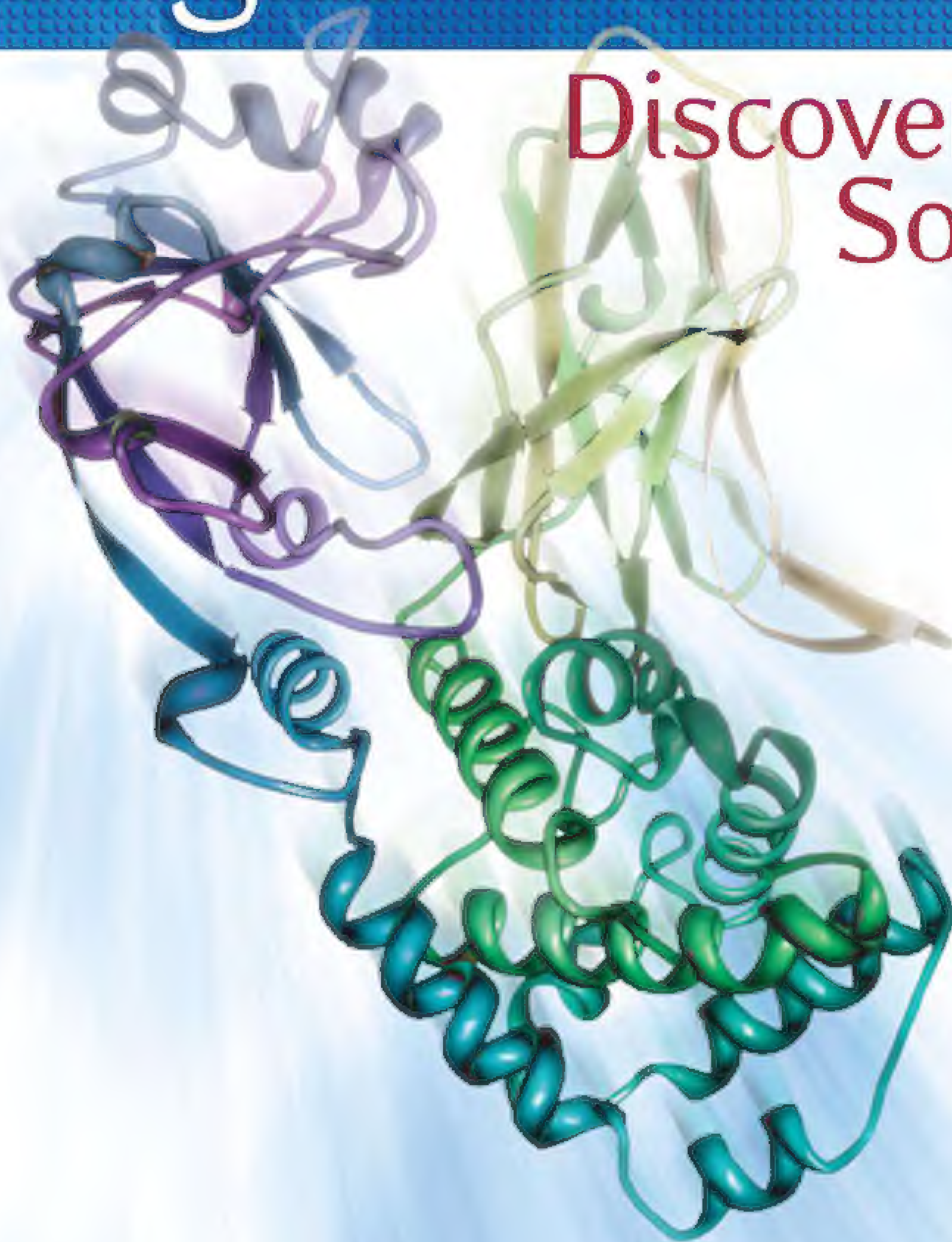
11 May 2012 | S10

Science

Dawn at Vesta

Reagent Proteins

Discover the
Source



Reagent Proteins is the source

With over 5,000 recombinant proteins available, *Reagent Proteins* provides seamless access to the highest quality reagent, pre-clinical and cGMP grade proteins for research purposes.





WEBINAR

Detecting Disease in Blood

What miRNA Biomarkers Can Tell Us

May 30, 2012

12 noon ET, 9 a.m. PT, 4 p.m. GMT, 5 p.m. UK

microRNAs (miRNAs) are becoming increasingly recognized as powerful biomarkers for human disease. The information potential held by miRNAs, combined with the fact that they are stable in serum and plasma, has led to a rapidly growing interest in using miRNAs in blood as diagnostic and prognostic biomarkers. This webinar will present the latest advances that are allowing researchers to move miRNA biomarker research from discovery in the lab to application in the clinic.

During the webinar, our expert panel of researchers will discuss:

- Strategies and technologies for successful cancer biomarker discovery through robust detection and analysis of miRNAs in biofluids
- Research into analytic and biological variables that impact miRNA measurements in serum and plasma from the clinical pathologist's point of view
- The novel application of miRNAs in serum as biomarkers of aging and chronic disease
- The answers to questions submitted by the live, online viewers.

SPEAKERS

Colin C. Pritchard, M.D., Ph.D.
University of Washington
Seattle, WA

Monty Montano, Ph.D.
Boston University School of Medicine
Boston, MA

Adam Baker, Ph.D.
Exiqon
Vedbaek, Denmark

REGISTER NOW!
webinar.sciencemag.org

Brought to you by
the *Science*/AAAS
Custom Publishing Office



Webinar sponsored by

EXIQON
Seek Find Verify



Mix it up.

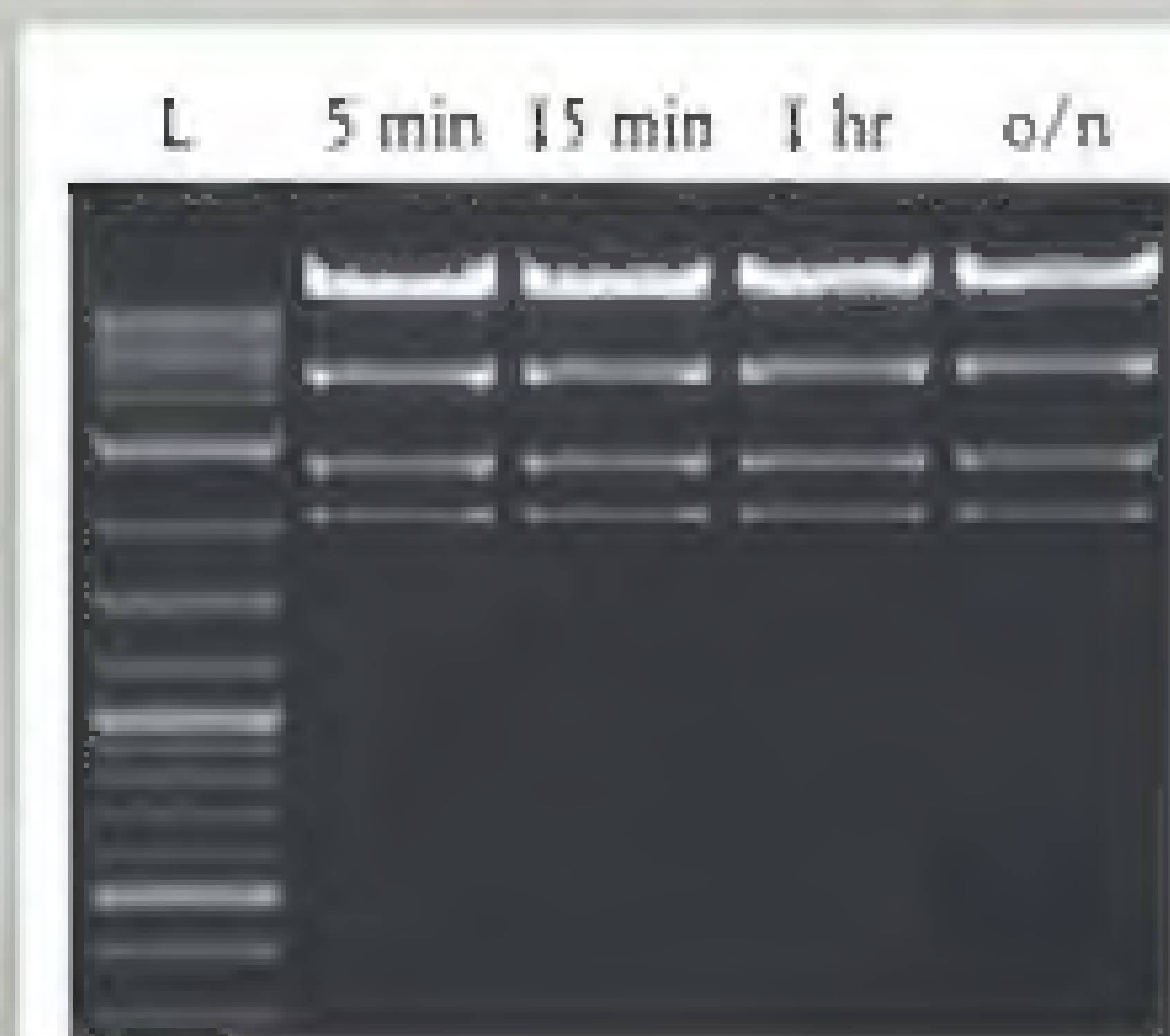
RE-Mix™ Restriction Enzyme Master Mixes

Restriction enzyme digests are now even easier! The same high quality restriction enzymes that you have come to trust from New England Biolabs are now available in master mix format, including enzyme, buffer and loading dye; simply add your DNA and digest.

With RE-Mix Master Mixes take advantage of:

- Simplified and shortened protocols
- Fast digestion in 15 minutes (Time-Saver qualified)
- High product quality with reproducible results

RE-Mix Master Mixes — just add your DNA and mix



pXba DNA was digested with EcoRV-HF™ RE-Mix™ according to the recommended protocol. Lane L is the TriDye™ 2-Log DNA Ladder (NEB #N3270). The same results are obtained whether incubated for 5–15 minutes, 1 hour or overnight.

GTAGCCT
TCUTGAT
AGTITC
TTOUTT
GTTACG

To experience the new restriction enzyme challenge from NEB, visit www.NEBcutitout.com

For more information, visit
www.NEBREMIX.com

EDITORIAL

- 647 Tackling Human Fungal Infections
Gordon D. Brown et al.
>> *Science Podcast*

NEWS OF THE WEEK

- 654 A roundup of the week's top stories

NEWS & ANALYSIS

- 658 Europe Picks Jupiter Probe; Runners-Up Vow to Press On
659 Death of California Researcher Spurs Investigation
660 Venus's Rare Sun Crossing May Aid Search for Exoplanets
661 Reprise of First Experiment Casts Doubt on Supersolid Helium

NEWS FOCUS

- 662 Primeval Land Rises From the Ashes
>> *Science Podcast*
664 Researchers Set Course to Blockade Ballast Invaders
A Foul Problem
666 With Novel Paint, Chemist Aims to Vanquish the *Vinchuca*

LETTERS

- 668 Conservation Concerns in the Deep
A. C. Hartmann and L. A. Levin
Presumed Guilt in the Anthrax Case
J. Guillemin
Response
D. A. Relman
668 NextGenVOICES
670 CORRECTIONS AND CLARIFICATIONS

BOOKS ET AL.

- 671 How We Remember
M. E. Hasselmo, reviewed by L. L. Colgin
672 Harvest the Wind
P. Warburg, reviewed by D. Reicher

POLICY FORUM

- 673 ELSI 2.0 for Genomics and Society
J. Kaye et al.

PERSPECTIVES

- 675 FGF21 Takes a Fat Bite
C. Cantó and J. Auwerx
676 Understanding Earthquakes
P. Segall
>> *Report p. 707*
678 PARP-1 Activation—Bringing the Pieces Together
J.-P. Gagné et al.
>> *Report p. 728*
679 Intertwining Electron Tunneling with Light
M. H. Szymańska
>> *Report p. 704*
681 RNA Plays Meiotic Matchmaker
A. F. Dernburg
>> *Report p. 732*
682 The Ice Age Carbon Puzzle
E. Brook
>> *Report p. 711*

CONTENTS continued >>



page 662



page 671



COVER

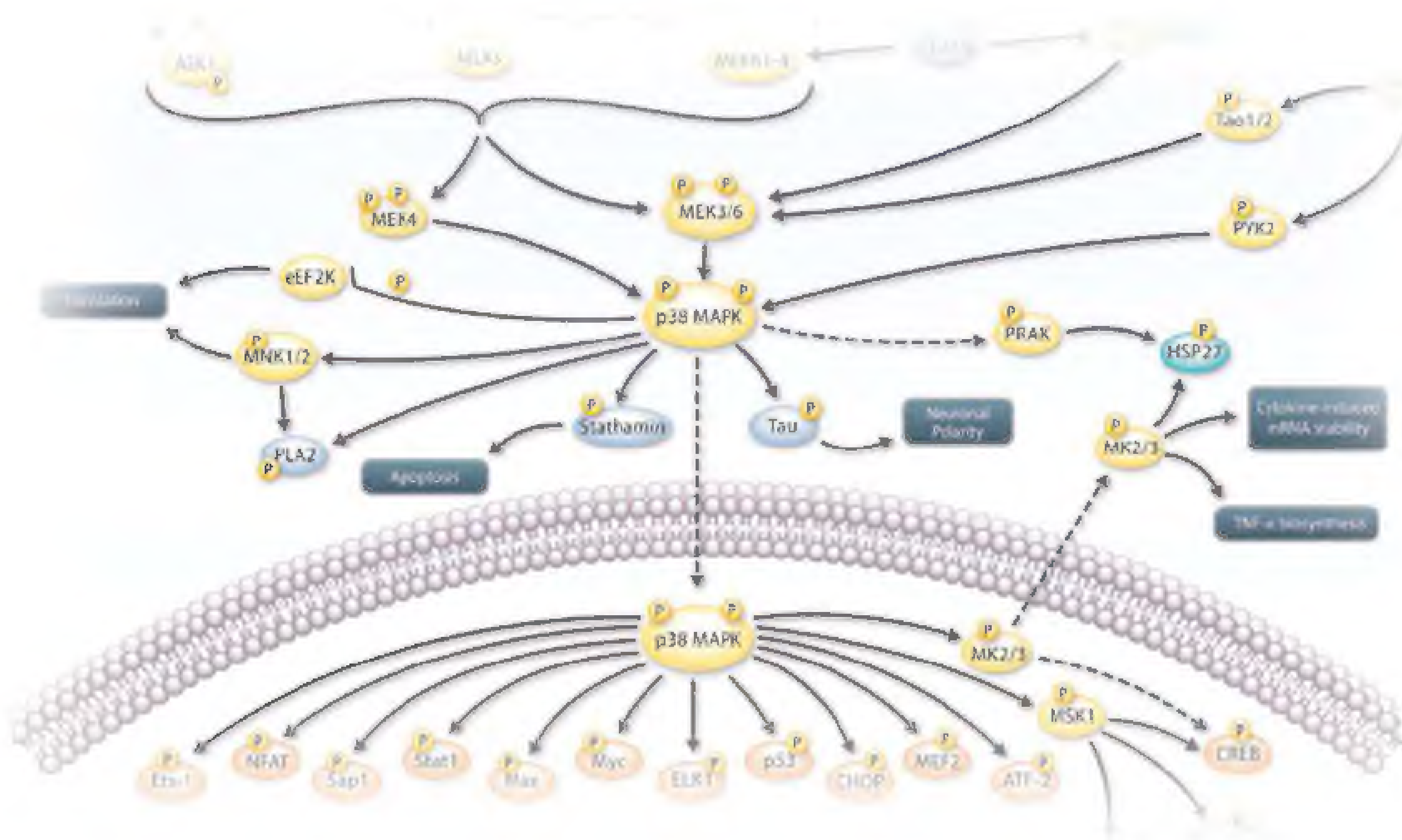
Enhanced-color view of the "Snowman" craters (Marcia, Calpurnia, and Minucia) on the asteroid Vesta generated by combining imaging and topography data from NASA's Dawn spacecraft. The 60-kilometer-wide Marcia crater (at bottom) is one of the youngest large craters on Vesta with a small central peak, as well as light and dark streaks on its walls. See the series of six Reports beginning on page 684.

Image generated using Dawn Framing Camera images: Lucille Le Corre (MPS), David O'Brien (PSI), Vishnu Reddy (MPS/UND); PI of Dawn mission: Christopher T. Russell (UCLA); Dawn Framing Camera leader: Andreas Nathues (MPS), significant contributions from Ralf Jaumann (DLR)

DEPARTMENTS

- 643 This Week in *Science*
649 Editors' Choice
652 Science Staff
751 New Products
752 Science Careers

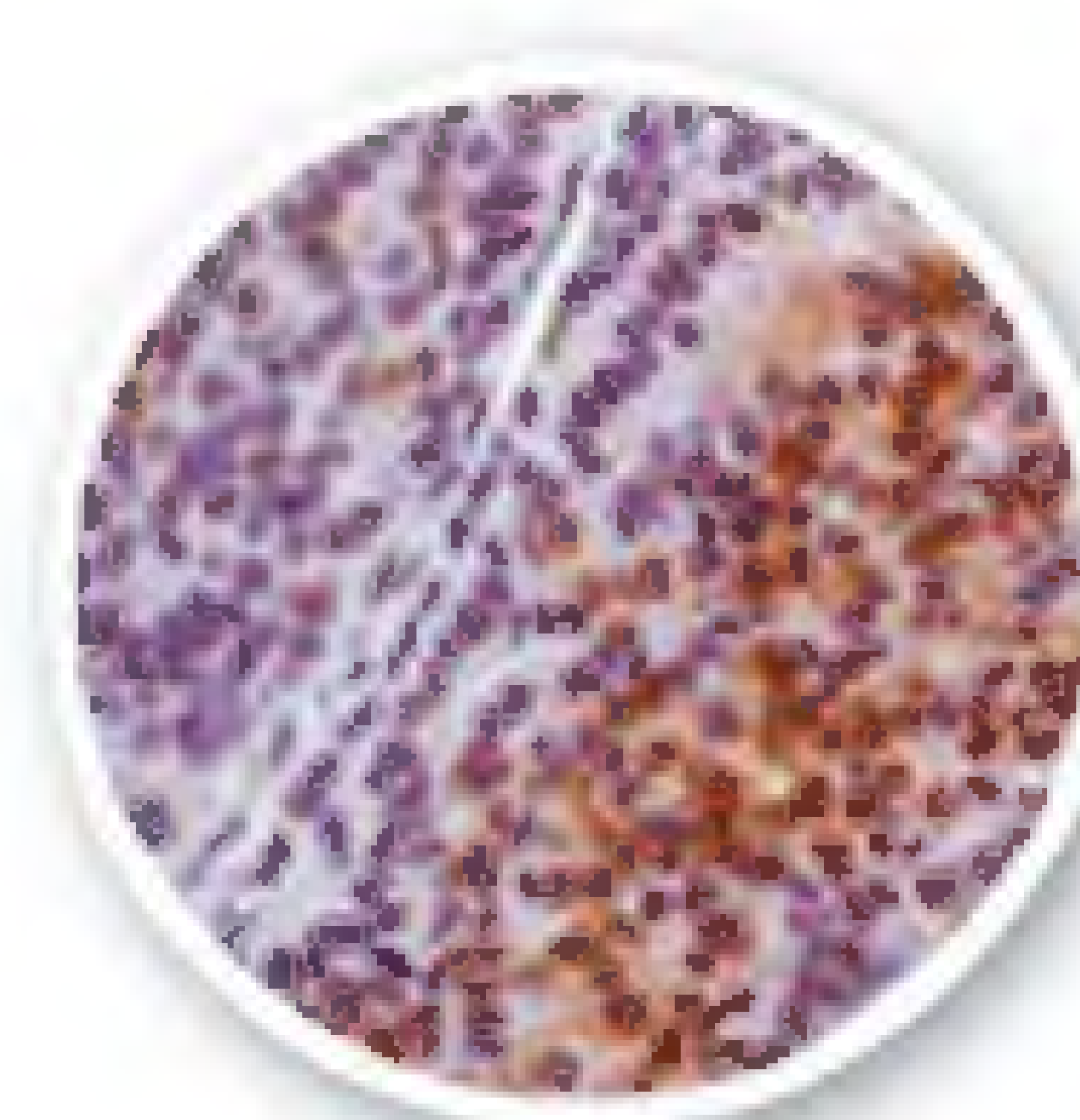
Antibodies for **MAP Kinase** Pathways



- High quality antibodies to MEKK, JNK, ERK and More
- Validated in WB, IHC, IF, IP and FACS
- Over 7000 antibodies and counting

At Epitomics, we provide a wide range of high quality antibodies to MAP Kinase pathways (MAPK-ERK, MAPK-ERK, MAPK-p38). Using our patented Rabbit Monoclonal Antibody (RabMAb®) technology, we have developed a collection of high quality MAP Kinase pathway specific antibodies. Each RabMAb offers superior antigen recognition of the rabbit immune system and the specificity of a monoclonal antibody.

Learn more @ www.epitomics.com/MAPK



Erk1 (pT202) / Erk2 (pT185)

Immunohistochemical analysis of paraffin-embedded human thyroid gland cancer using anti-ERK1(pT202) / ERK2 (pT185) RabMAb (cat. # 1481-1)



MEK1 (pS298)

Immunofluorescent staining of HeLa cells using Phospho-specific anti-MEK1 (pS298) RabMAb (cat. # 2711-1).



Antibody Satisfaction Guarantee

www.epitomics.com

US & Canada | 1-877-772-2622
Outside NA | 650-583-6688
info@epitomics.com

REPORTS

- 684 **Dawn at Vesta: Testing the Protoplanetary Paradigm**
C. T. Russell et al.
>> *Science Podcast*
- 687 **Vesta's Shape and Morphology**
R. Jaumann et al.
- 690 **The Violent Collisional History of Asteroid Vesta**
S. Marchi et al.
- 694 **The Geologically Recent Giant Impact Basins at Vesta's South Pole**
P. Schenk et al.
- 697 **Spectroscopic Characterization of Mineralogy and Its Diversity Across Vesta**
M. C. De Sanctis et al.
- 700 **Color and Albedo Heterogeneity of Vesta from Dawn**
V. Reddy et al.
Spacecraft data provide a detailed characterization of the second most massive asteroid in the solar system.
- 704 **Coupling Quantum Tunneling with Cavity Photons**
P. Cristofolini et al.
Optical coupling is used to control the tunneling of electrons between a pair of quantum wells.
>> *Perspective p. 679*
- 707 **Under the Hood of the Earthquake Machine: Toward Predictive Modeling of the Seismic Cycle**
S. Barbot et al.
Computational models predict the long-term recurrence of earthquakes along a segment of the San Andreas Fault.
>> *Perspective p. 676*
- 711 **Carbon Isotope Constraints on the Deglacial CO₂ Rise from Ice Cores**
J. Schmitt et al.
The stable isotopic composition of the carbon in carbon dioxide over the last 24,000 years illuminates past carbon cycle behavior.
>> *Perspective p. 682*
- 714 **Ancient Maya Astronomical Tables from Xultun, Guatemala**
W. A. Saturno et al.
Wall paintings in a Mayan temple dating to the 9th century C.E. show calculations of Moon and, perhaps, planetary motion.
>> *Science Podcast*

- 717 **A Stem Cell-Based Approach to Cartilage Repair**
K. Johnson et al.
A chemical screen using mesenchymal stem cells identifies a small molecule, kartogenin, that can promote chondrogenesis.
- 721 **Differential Diffusivity of Nodal and Lefty Underlies a Reaction-Diffusion Patterning System**
P. Müller et al.
The inhibitor Lefty diffuses more widely than the activator Nodal.
- 724 **Mechanical Control of Morphogenesis by Fat/Dachsous/Four-Jointed Planar Cell Polarity Pathway**
F. Bosveld et al.
Polarized proto-cadherin and myosin induce an anisotropic tension at cell junctions and thereby shape epithelial tissue.
- 728 **Structural Basis for DNA Damage-Dependent Poly(ADP-ribosylation) by Human PARP-1**
M.-F. Langelier et al.
An enzyme that binds to damaged DNA undergoes a structural reorganization that enhances its catalytic activity.
>> *Perspective p. 678*
- 732 **Meiosis-Specific Noncoding RNA Mediates Robust Pairing of Homologous Chromosomes in Meiosis**
D.-Q. Ding et al.
An RNA transcript helps to bring together homologous chromosomes during cell division.
>> *Perspective p. 681*
- 736 **Epigenomic Enhancer Profiling Defines a Signature of Colon Cancer**
B. Akhtar-Zaidi et al.
Methylation tags at long-distance gene regulatory elements provide a signature specific to cancer cells.
- 740 **Recent Explosive Human Population Growth Has Resulted in an Excess of Rare Genetic Variants**
A. Keinan and A. G. Clark
Genetic models that incorporate recent human population growth can better identify mutations in large samples.
- 744 **Transcription-Independent Function of Polycomb Group Protein PSC in Cell Cycle Control**
A. Mahd-Sarip et al.
A Polycomb group protein regulates the cell cycle by promoting cyclin B ubiquitylation and degradation.

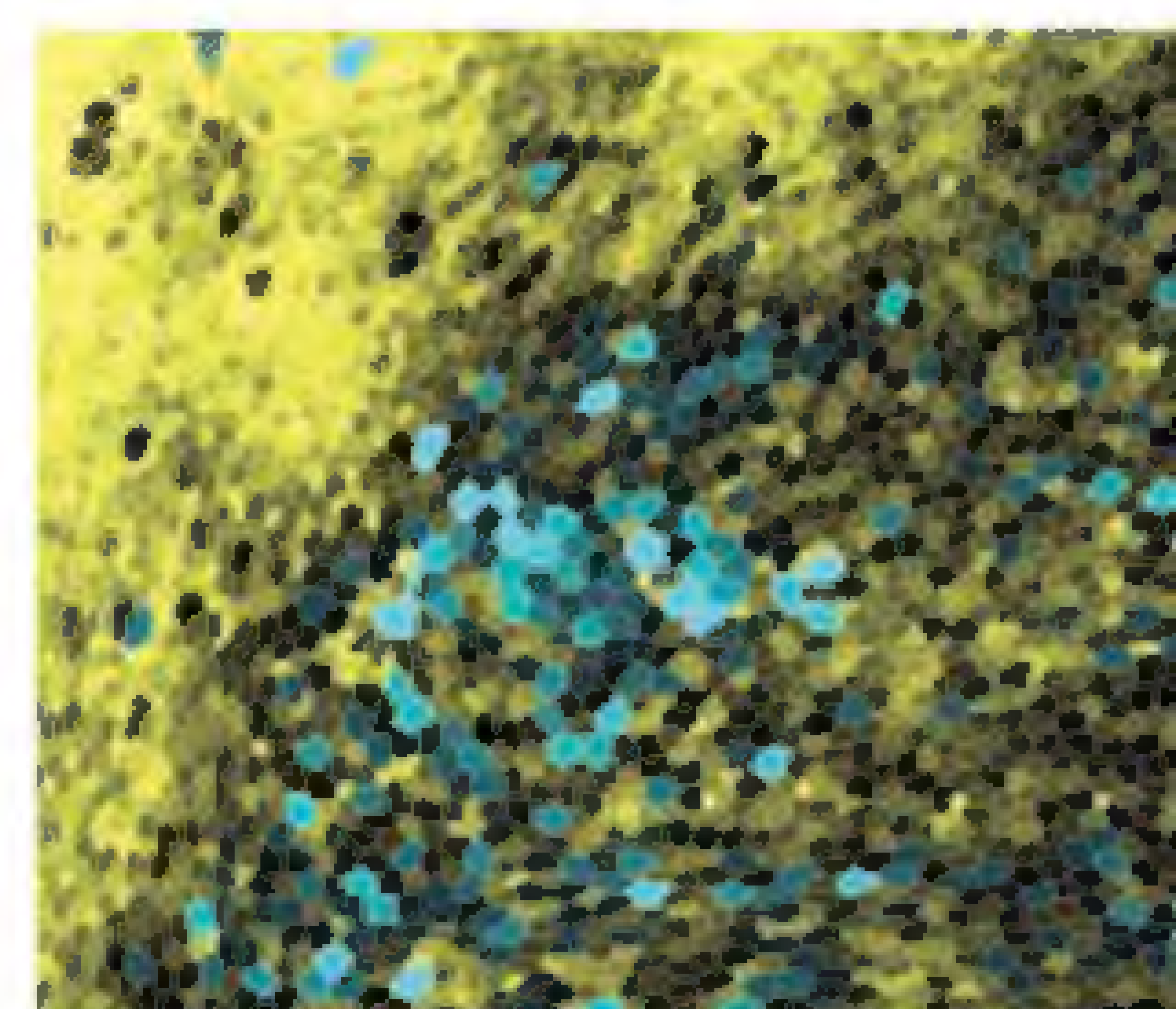
CONTENTS continued >>



page 675



page 714



page 724

Congratulations to the AAAS Student Poster Competition Winners

The 2012 Student Poster Competition took place at the AAAS Annual Meeting in Vancouver, BC, 16-20 February. The students' work in a variety of fields displayed originality and understanding that set them apart from their peers. First-place winners receive cash prizes thanks to the generous support of Subaru of America, Inc.

BRAIN AND BEHAVIOR

Winner: Nicholas D. Olivas, University of California, Irvine

Laminar Circuit Organization and Inhibitory Neuronal Control of Primary Visual Cortex

Honorable Mention: Evan Ardiel and Andrew Giles, University of British Columbia
Optogenetic Stimulation Uncovers a Role for Neuropeptide Signalling in Habituation of a C. elegans Avoidance Response

CELLULAR AND MOLECULAR BIOLOGY

Winner (tie): Diana Hunter, Jessica Inskip, Mario Cruz Cabrera, and Nima Alan, University of British Columbia
A Very Large Organelle in Sympathetic Neurons

Winner (tie): Johnny Rodríguez, University of California, Irvine
Rewiring the Genetic Code for Global Protein Footprinting

Honorable Mention: Ben Paylor, University of British Columbia
Cardiac-Resident PDGFRA+SCA1+ Mesenchymal Progenitors Regulate the Development of Fibrosis in the Heart

DEVELOPMENTAL BIOLOGY, PHYSIOLOGY, AND IMMUNOLOGY

Winner: Cymone Gates, Emory University
Drosophila-Derived Commensal Bacteria Stimulate ROS-Dependent Anti-Oxidant Pathway

Honorable Mention: Alex C.Y. Chang, Victoria Garside, Megan Fuller, Audi Setiadi, and Justin Smrz, University of British Columbia

Notch Initiates Endothelial Mesenchymal-Transition in the Developing Atrioventricular Canal Through Autocrine Activation of Soluble Guanylyl Cyclase

ENVIRONMENT AND ECOLOGY

Winner: Benjamin Sandkam and Corey Watson, Simon Fraser University
Impacts of Genomic and Lighting Environments on Guppy Color Vision

Honorable Mention: Christopher Avis, University of Victoria
Evolution of Northern Wetlands in Response to Permafrost Thaw

MATH, TECHNOLOGY, AND ENGINEERING

Winner: Kelly Paton, University of British Columbia
The Appearance of Reentrant Arrhythmias in Undamaged Cardiac Tissue

Honorable Mention: D. Leland Taylor, Davidson College
PHAST: Phage Assembly Suite and Tutorial

MEDICINE AND PUBLIC HEALTH

Winner: Alexander Sorum, Augsburg College
Effects of Airway Epithelial Secretions on Pseudomonas aeruginosa Biofilm Formation

Honorable Mention: Nathan Gamarra, University of California, Irvine

Rapid Detection of Antibiotics by Nanowire-Assisted Laser Desorption Ionization (NALDI) Mass Spectrometry

PHYSICAL SCIENCES

Winner: Laleh Samii, Simon Fraser University
Motor Properties of Molecular Spiders

SCIENCE IN SOCIETY

Winner: Sheldon Turner, Michigan State University
The Effectiveness of Visualizations in Communicating Natural Resource Issues

Honorable Mention: Bridgette Kelly, University of St. Thomas, Minnesota
Waste(less): A Psychological Approach Toward Reducing Food Waste

SOCIAL SCIENCES

Winner: Stefani Crabtree, Washington State University, and Lydia Smith, University of California, Berkeley
Trophic Interconnectedness in Southwestern Colorado: An Archaeological Food-Webs Study of Ancestral Puebloans

Honorable Mention: Audrey Groleau, Université Laval
Pre-Service Elementary Teachers' Relationships to Physics and Physics Teaching

View full abstracts:
www.aaas.org/meetings

Sign up at www.aaas.org/meetings to receive announcements about the 2013 AAAS Annual Meeting 14-18 February in Boston, MA.

The 2013 poster entry site opens on 14 May 2012. The AAAS Student Poster Competition recognizes the individual research efforts of students who are actively working toward an undergraduate, graduate, or doctoral degree. Posters are judged at the meeting. Winners in each category receive a cash award, certificate, and recognition in the journal *Science*. Individuals holding doctoral degrees are not eligible and are invited to review the criteria for participating in the General Poster session.



ADVANCING SCIENCE. SERVING SOCIETY



SCIENCEONLINE

SCIENCEEXPRESS

www.scienceexpress.org

A Rogue Earthquake Off Sumatra

J. J. McGuire and G. C. Beroza

10.1126/science.1223983

The Heliosphere's Interstellar Interaction:
No Bow Shock

D. J. McComas et al.

Observations from the Interstellar Boundary Explorer are not consistent with a bow shock ahead of the heliosphere.

10.1126/science.1221054

The Detection and Characterization
of a Nontransiting Planet by Transit
Timing Variations

D. Nesvorný et al.

Analysis of the deviations in the orbit of a transiting exoplanet revealed an outer planet in the same planetary system.

10.1126/science.1221141

Evidence of Things Not Seen

N. W. Murray

10.1126/science.1222590

Regulated Virulence Controls the Ability of a
Pathogen to Compete with the Gut Microbiota

N. Kamada et al.

Virulence genes and nutritional requirements determine the course of a gastroenteric bacterial infection in mice.

10.1126/science.1222195

Virulence or Competition?

V. Sperandio

10.1126/science.1223303

Secreted Kinase Phosphorylates Extracellular
Proteins That Regulate Biomineralization

V. S. Tagliabracci et al.

The elusive enzyme that modifies proteins involved in building bone and teeth has now been identified.

10.1126/science.1217817

Vitamin K₂ Is a Mitochondrial Electron Carrier
That Rescues Pink1 Deficiency

M. Vos et al.

Adding vitamin K rescues fruit flies bearing a mutation in a Parkinson's disease gene homolog.

10.1126/science.1218632

SCIENCENOW

www.sciencenow.org

Highlights From Our Daily News Coverage

Dogs Feel Your Pain

Canines yawn when they hear people yawn, suggesting cross-species empathy.

http://scim.ag/Dogs_Pain

Infants' Flexible Heads Stretch Back
Millions of Years

'Soft skulls' were present in human ancestors.

<http://scim.ag/Flexible-Heads>

The Great Outdoors Is Good for Allergies

Teens living in more rural environments harbor more anti-inflammatory microbes on their skin.

http://scim.ag/Outdoors_Allergies

SCENCESIGNALING

www.sciencesignaling.org

The Signal Transduction Knowledge Environment

8 May issue: <http://scim.ag/ss050812>

EDITORIAL GUIDE: Focus Issue—

Series on Structural Biology

W. Wong

Research and commentary highlight the use of structural analysis to understand signaling molecules and events.

RESEARCH ARTICLE: An ATP-Site On-Off Switch
That Restricts Phosphatase Accessibility of Akt

K. Lin et al.

PERSPECTIVE: Uncaging Akt

S. J. Humphrey and D. E. James

ATP and ADP regulate a conformational switch that determines the kinase activity of Akt.

RESEARCH ARTICLE: Syndecan 4 Regulates
FGFR1 Signaling in Endothelial Cells
by Directing Macropinocytosis

A. Effenbein et al.

The FGF2 co-receptor syndecan 4 shapes endothelial signaling initiated by a fibroblast growth factor receptor.

PODCAST

M. T. Nelson and A. M. VanHook

Maximal blood vessel dilation can be induced by calcium influx through a just few channel molecules in vascular endothelial cells.

SCIENCETRANSLATIONAL MEDICINE

www.sciencetranslationalmedicine.org

Integrating Medicine and Science

9 May Issue: <http://scim.ag/stm050912>

RESEARCH ARTICLE: Mixed Chimerism and
Growth Factors Augment β Cell Regeneration
and Reverse Late-Stage Type 1 Diabetes

M. Wang et al.

FOCUS: Three Strikes and You're Cured

A. S. Chang and G. I. Bell

Glucose tolerance can be restored in a mouse model of type 1 diabetes.

RESEARCH ARTICLE: The Predictive Capacity
of Personal Genome Sequencing

N. J. Roberts et al.

FOCUS: What's a Genome Worth?

I. S. Kohane and J. Shendure

Analysis of data from monozygotic twins assesses how well whole-genome sequencing can predict disease risk in the general population.

RESEARCH ARTICLE: Survivin Is a Therapeutic
Target in Merkel Cell Carcinoma

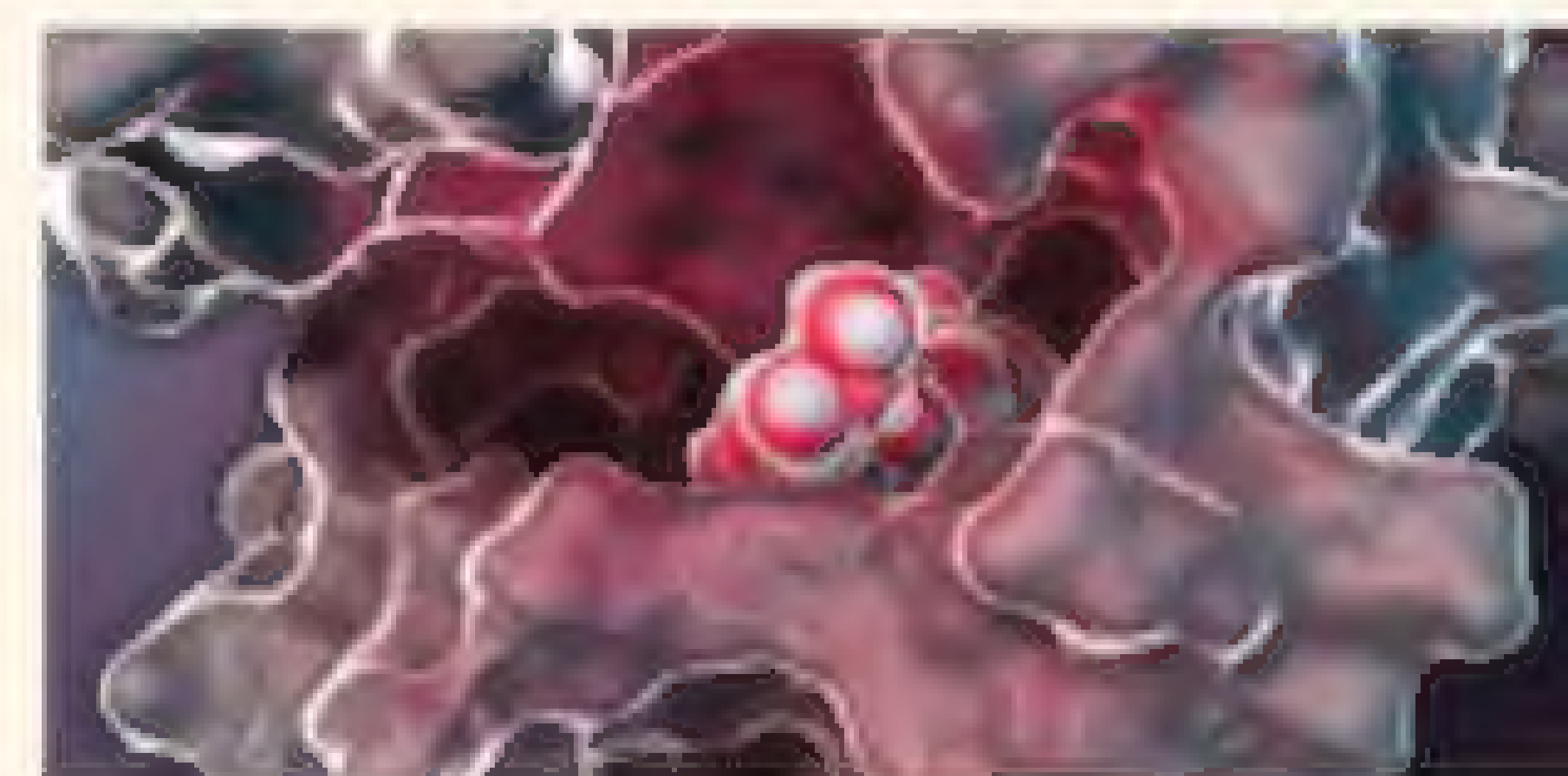
R. Arora et al.

A targeted therapy for a virus-induced cancer involves blockade of the cellular oncoprotein survivin.

RESEARCH ARTICLE: Extended Survival
of Glioblastoma Patients After Chemoprotective
HSC Gene Therapy

J. E. Adair et al.

Gene therapy using P140K-modified hematopoietic progenitor cells is chemoprotective, enabling glioblastoma patients to withstand myelotoxic doses of chemotherapy.



SCENCESIGNALING
Kinase and inhibitor.

SCIENCECAREERS

www.sciencereers.org/career_magazine

Free Career Resources for Scientists

Career Q&A: A Career Without Credentials

E. Pain

Paleontologist Jack Horner overcame dyslexia and the lack of a traditional education to become a world leader in his field.

http://scim.ag/QA_JackHorner

Submitting Your Best Possible R01 Application

S. Webb

At a meeting on Long Island, some neuroscientists got tips on how to win an R01 in lean times.

<http://scim.ag/BestR01>

Perspective: Real Data on Career Preferences

J. Austin

When it comes to careers, graduate students in the sciences are flexible, a new study shows.

<http://scim.ag/PreferencesData>

SCIENCEPODCAST

www.sciencemag.org/multimedia/podcast

Free Weekly Show

On the 11 May Science Podcast: Mayan astronomical tables from the 9th century, cosmic insights from Vesta, a fossilized forest in China, and more.

SCIENCEINSIDER

news.sciencemag.org/scienceinsider


Science Policy News and Analysis

SCIENCE (ISSN 0036-8075) is published weekly on Friday, except the last week in December, by the American Association for the Advancement of Science, 1200 New York Avenue, NW, Washington, DC 20005. Periodicals Mail postage (publication No. 484460) paid at Washington, DC, and additional mailing offices. Copyright © 2012 by the American Association for the Advancement of Science. The title SCIENCE is a registered trademark of the AAAS. Domestic individual membership and subscription (51 issues): \$149 (\$74 allocated to subscription). Domestic institutional subscription (51 issues): \$990; Foreign postage extra; Mexico, Caribbean (surface mail) \$55; other countries (air assist delivery) \$85. First class, airmail, student, and emeritus rates on request. Canadian rates with GST available upon request, GST #1254 88122. Publications Mail Agreement Number 1069624. Printed in the U.S.A.

Change of address: Allow 4 weeks, giving old and new addresses and 8-digit account number. Postmaster: Send change of address to AAAS, P.O. Box 96178, Washington, DC 20090-6178. Single-copy sales: \$10.00 current issue, \$15.00 back issue prepaid (includes surface postage); bulk rates on request. Authorization to photocopy material for internal or personal use under circumstances not falling within the fair use provisions of the Copyright Act is granted by AAAS to libraries and other users registered with the Copyright Clearance Center (CCC) Transactional Reporting Service, provided that \$30.00 per article is paid directly to CCC, 222 Rosewood Drive, Danvers, MA 01923. The identification code for Science is 0036-8075. Science is indexed in the Reader's Guide to Periodical Literature and in several specialized indexes.



ADVANCING SCIENCE. SERVING SOCIETY



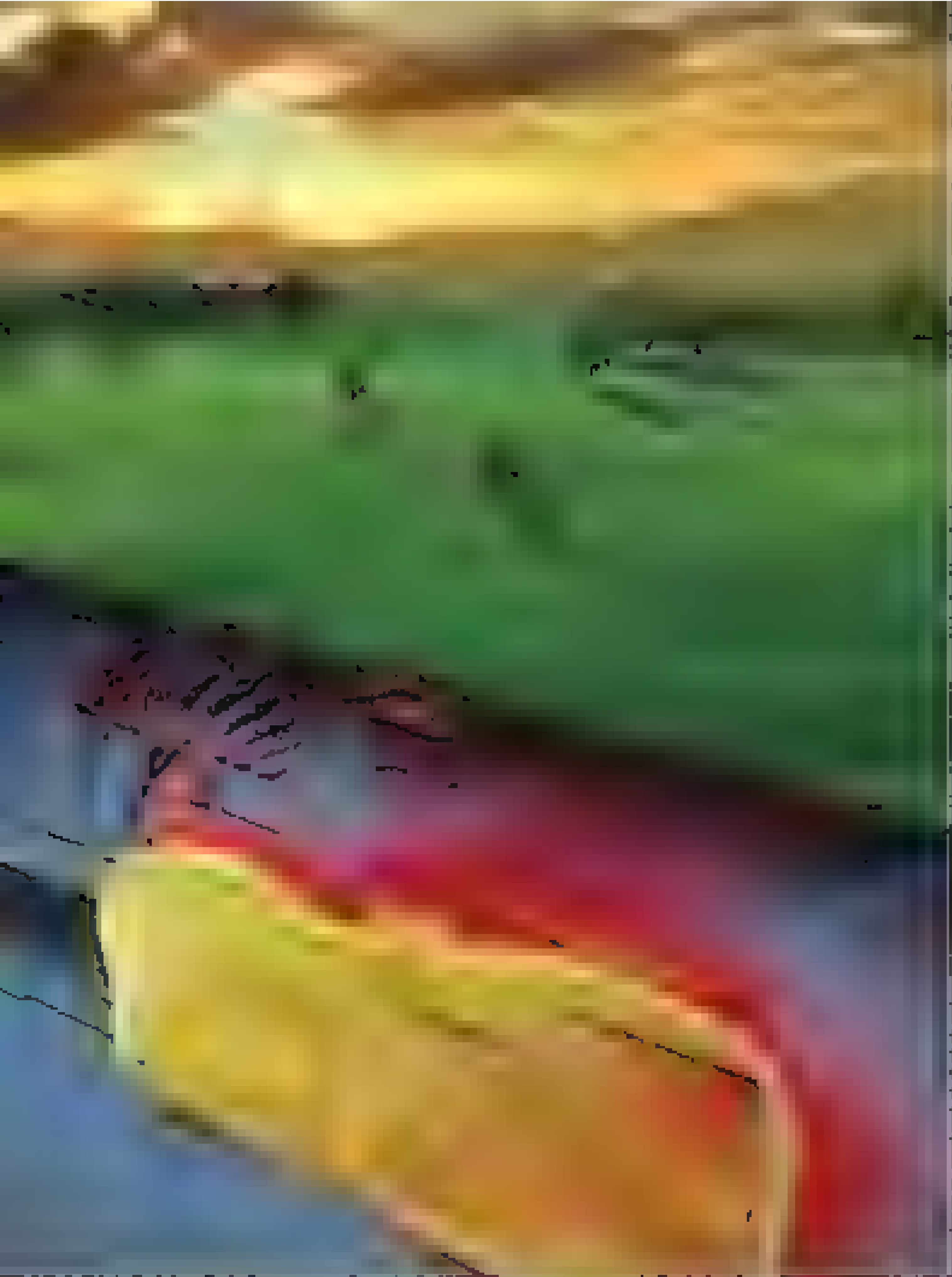
I seek the future.

MiSeq. Next-generation sequencing for all you seek.

You want amazing accuracy and performance on your benchtop. Illumina delivers—yet again. The MiSeq Personal Sequencer is the only fully integrated, truly end-to-end benchtop solution around. It's just one more example of why Illumina solutions generate a remarkable 90% of all the world's sequencing data. Discover what's possible.

illumina.com/miseq

illumina®



Earthquake Model Shakedown

The Parkfield segment of the San Andreas Fault in California experiences Magnitude 6.0 earthquakes at a surprisingly regular interval—roughly every 22 years. This area is one of the most well studied fault segments in the world, yet computational models often struggle to integrate the wealth of observational data with theoretical predictions. Barbot *et al.* (p. 707; see the Perspective by Segall) constructed a dynamic model of a fault segment which, when integrated with previous observations, reproduces the behavior of the Parkfield segment over the entire earthquake cycle. Because the model is based on realistic fault physics, it not only explains the distribution of small earthquakes but also the recurrence interval of large earthquakes and the amount of geodetic strain accumulated postseismically. It also reveals how smaller earthquakes can influence this region's semiregular earthquake cycle.

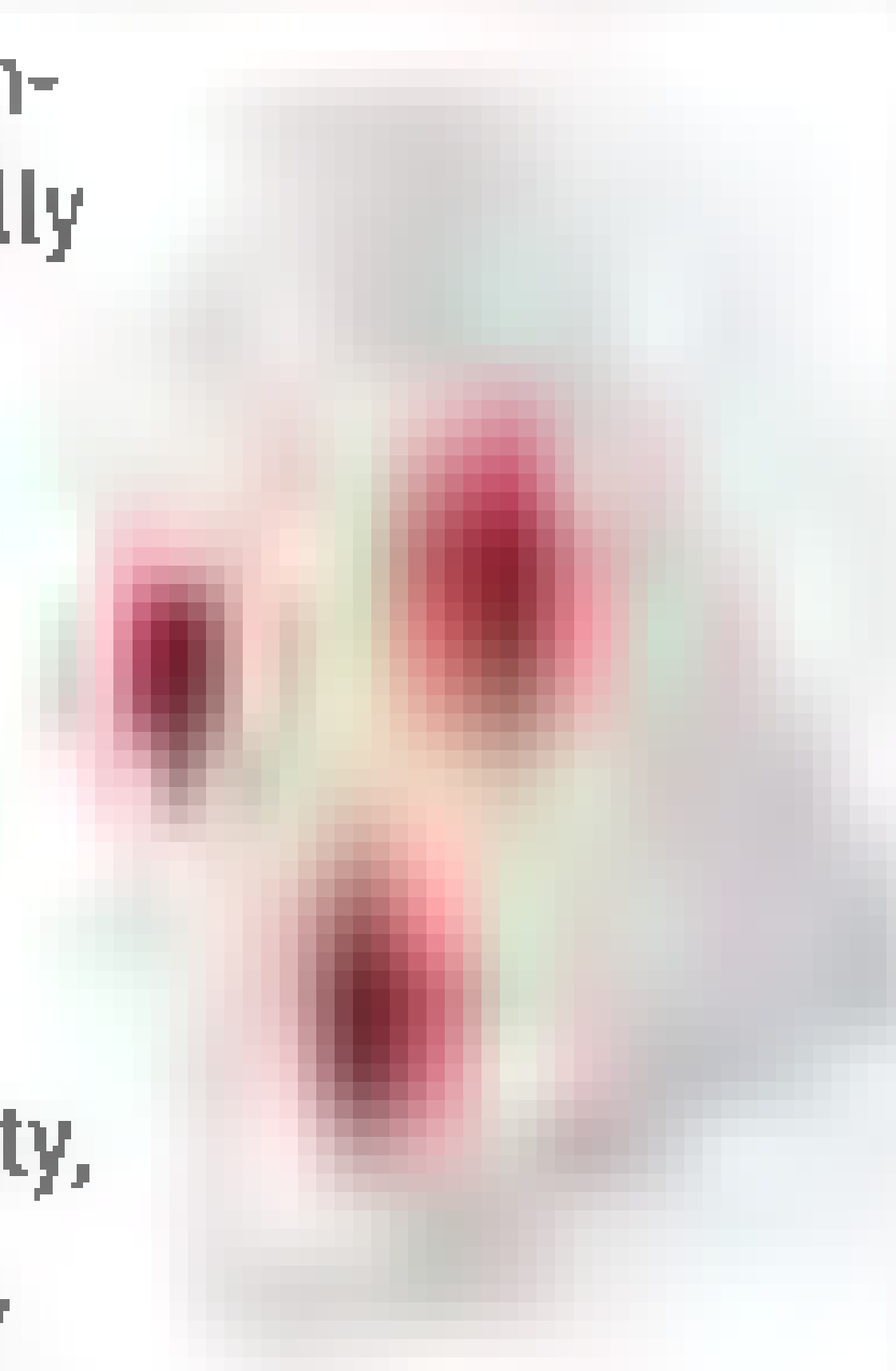
A New Dawn

Since 17 July 2011, NASA's spacecraft Dawn has been orbiting the asteroid Vesta—the second most massive and the third largest asteroid in the solar system (see the cover). Russell *et al.* (p. 684) use Dawn's observations to confirm that Vesta is a small differentiated planetary body with an inner core, and represents a surviving proto-planet from the earliest epoch of solar system formation; Vesta is also confirmed as the source of the howardite-eucrite-diogenite (HED) meteorites. Jaumann *et al.* (p. 687) report on

the asteroid's overall geometry and topography, based on global surface mapping. Vesta's surface is dominated by numerous impact craters and large troughs around the equatorial region. Marchi *et al.* (p. 690) report on Vesta's complex cratering history and constrain the age of some of its major regions based on crater counts. Schenk *et al.* (p. 694) describe two giant impact basins located at the asteroid's south pole. Both basins are young and excavated enough amounts of material to form the Vestoids—a group of asteroids with a composition similar to that of Vesta—and HED meteorites. De Sanctis *et al.* (p. 697) present the mineralogical characterization of Vesta, based on data obtained by Dawn's visual and infrared spectrometer, revealing that this asteroid underwent a complex magmatic evolution that led to a differentiated crust and mantle. The global color variations detailed by Reddy *et al.* (p. 700) are unlike those of any other asteroid observed so far and are also indicative of a preserved, differentiated proto-planet.

Tunneling Through with a Light Touch

Quantum tunneling underpins a host of essential techniques, such as scanning tunneling microscopy and quantum cascade lasers, as well as chemical reactions. The tunneling particles are normally electrons, and control of the tunneling process has generally been by electric fields. By coupling tunneling electrons with cavity photons trapped inside a semiconductor microcavity, Cristofolini *et al.* (p. 704, published online 5 April; see the Perspective by Szymańska) produced mixed states that then allowed direct optical control of the tunneling process. Such an optical-based approach to manipulating and controlling the tunneling process may find applications in quantum information science.



By the Numbers

As carbon dioxide is exchanged between the atmosphere, the oceans, and the terrestrial biosphere, its carbon isotopic composition is modified by various processes involved in its transfer between the different reservoirs. The carbon isotopic composition of the carbon dioxide contained in bubbles of air trapped in ice cores thus provides a record of the processes that

regulated the composition of the atmosphere in the past. Using data from three Antarctic ice cores, Schmitt *et al.* (p. 711, published online 29 March; see the Perspective by Brook) present a record of the carbon isotopic makeup of atmospheric CO₂ for the past 24,000 years. The findings reveal the dominant role of the oceans during the early part of the deglaciation and the effects of the regrowth of the terrestrial biosphere later in the deglacial transition. Before the deglaciation, during the Last Glacial Maximum, the carbon cycle was essentially at equilibrium.

Mayan Astronomy

Mayan Codices are books written on bark in the few centuries before Columbus landed. Several records detailed hieroglyphic calculations of lunar and planetary motions and their relation to the Mayan calendar. Their predecessors have been unclear. Saturno *et al.* (p. 714) now describe a room in a Mayan complex in Guatemala dating to several centuries before the Codices that seems to have similar calculations on two of its walls. The east wall contains lunar calculations; the calculations on the north wall are more enigmatic, but may relate to Mars, Mercury, and/or Venus.

Osteoarthritis and Kartogenin

Osteoarthritis is characterized by progressive breakdown of articular cartilage and affects over 25 million people in the United States. Mesenchymal stem cells (MSCs), which reside in healthy and diseased joints, are multipotent adult stem cells that are able to differentiate into a variety of cell types. Johnson *et al.* (p. 717, published online 5 April) identified a small molecule, kartogenin, which was able to induce MSCs to differentiate into chondrocytes *in vitro*. When administered locally, kartogenin was efficacious in two animal models of osteoarthritis.

The Right Move

During development, epithelial tissues deform to give rise to functional tissues and organs. How gene expression controls local cell mechanical properties to drive tissue deformation remains poorly understood. Bosveld *et al.* (p. 724, published online 12 April) have uncovered how the conserved Fat/Dachsous/Four-jointed signaling pathway controls local mechanical cell properties to generate global tissue contraction in *Drosophila* epithelial tissue.

Continued on page 645

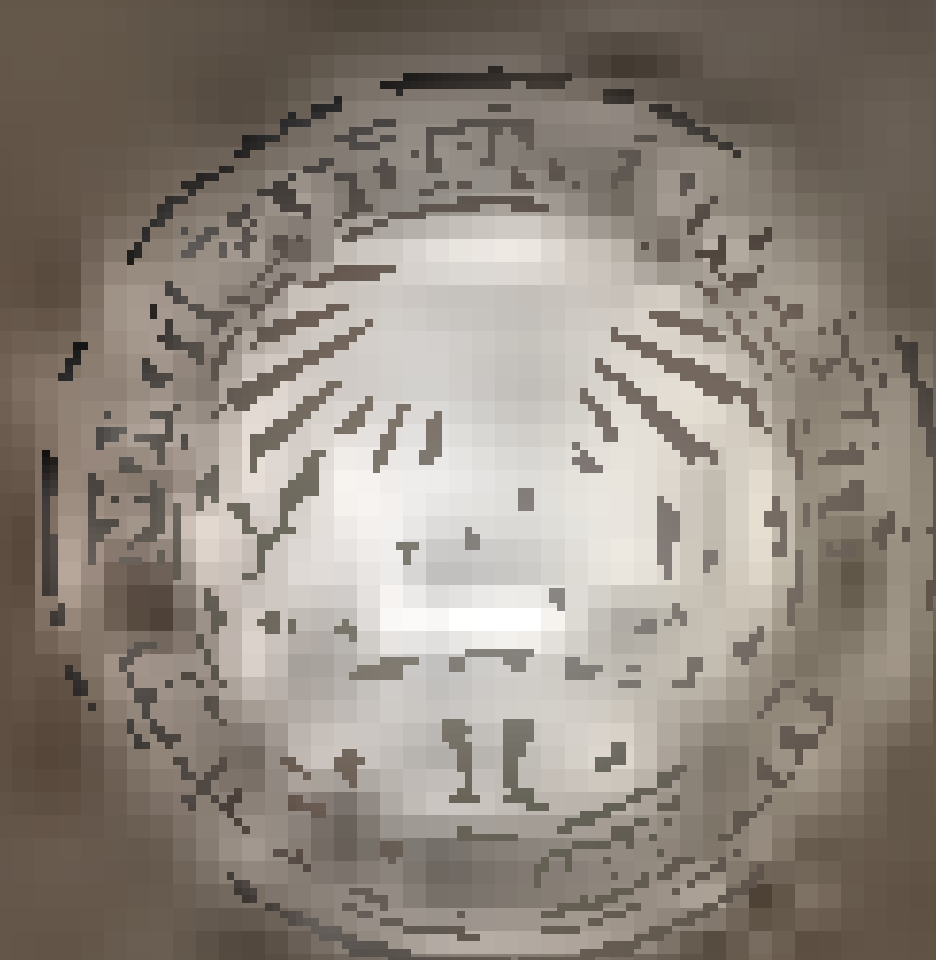


Making gasoline power history

Northeastern University researchers are seeking to make fossil fuels go the way of the dinosaur. In collaboration with partners such as BASF, Los Alamos National Laboratory, Nissan, and the U.S. Department of Energy, we're developing a less costly, more efficient fuel-cell catalyst. The goal: to bring a new generation of more affordable all-electric cars to market by 2019.

Our broad range of interdisciplinary research turns discoveries into solutions, with a focus on global challenges in health, security, and sustainability.

northeastern.edu



Northeastern University

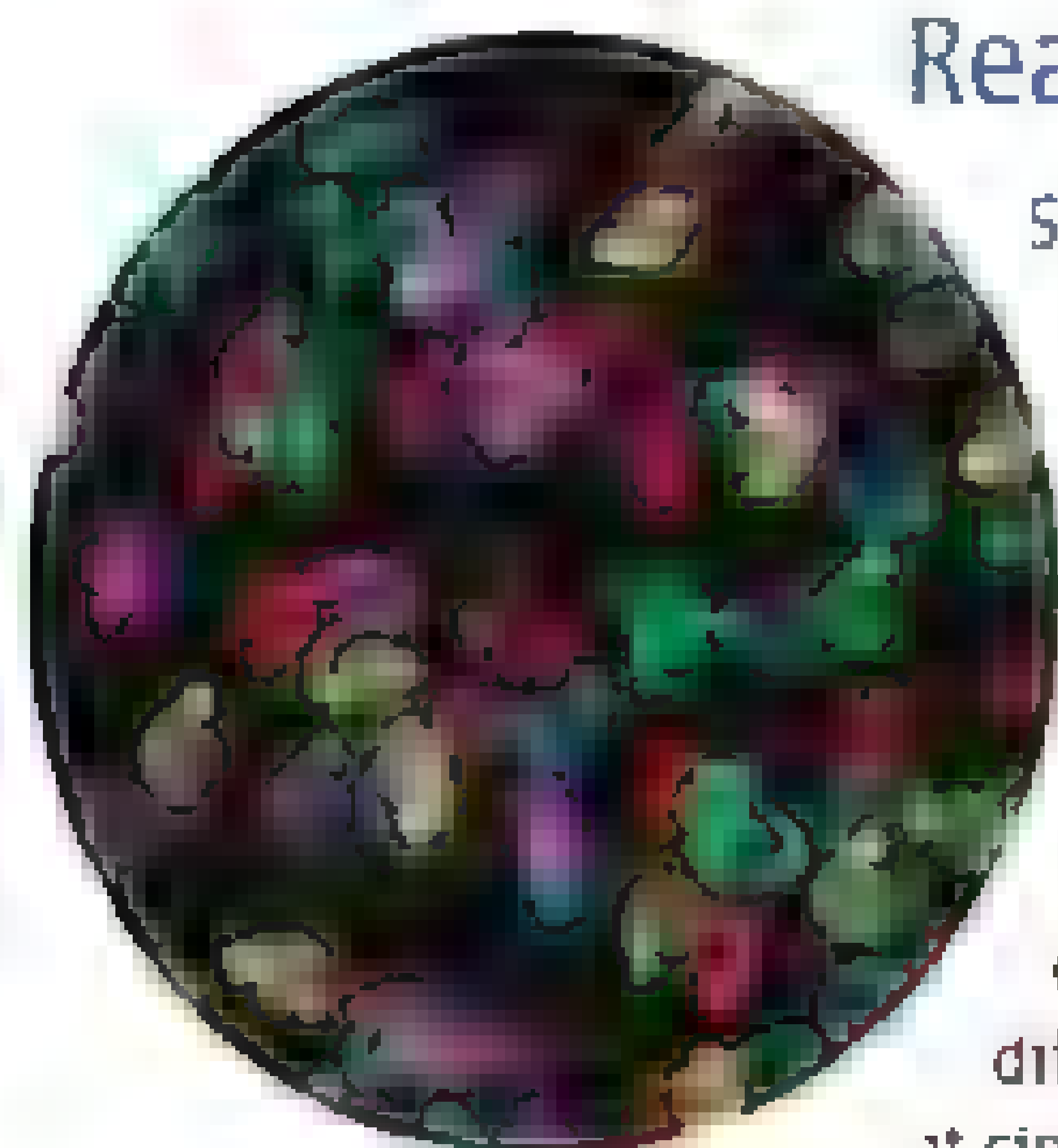
Continued from page 643

Dissecting DNA Repair

Covalent modification of proteins can be a crucial regulatory event. Poly(ADP-ribose) polymerase 1 (PARP-1) (ADP, adenosine diphosphate) synthesizes poly(ADP-ribose), which is attached to and regulates proteins involved in DNA repair. **Langelier *et al.*** (p. 728; see the Perspective by **Gagné *et al.***) use x-ray crystallography and biochemical analysis to demonstrate how PARP-1 detects DNA damage and how the interaction with DNA is coupled to poly(ADP-ribosylation) activity.

Find Your Partner

Gametes generally have haploid genomes, so that when they fuse during fertilization, they reconstitute a diploid organism. Meiosis is required to make haploid gametes, which involves a reduction division where two homologous chromosomes first pair and are then segregated away from each other. Working in the fission yeast *Schizosaccharomyces pombe*, **Ding *et al.*** (p. 732; see the Perspective by **Dernburg**) explored how homologous chromosomes recognized each other and found that a non-coding RNA locus, *smeZ*, helps to drive the pairing of homologous chromosomes.



Reaction-Diffusion Patterning

Six decades ago, Alan Turing proposed the reaction-diffusion model to explain how complex patterns emerge during morphogenesis. In this model, an activator activates both itself and an inhibitor (the "reaction"), with the activator being less mobile than the inhibitor ("diffusion"). Many activator/inhibitor pairs have been described, but the role of differential mobility versus differential clearance of activators and inhibitors is often unclear. Now, **Müller *et al.*** (p. 721, published online 12 April) show that during zebrafish embryogenesis, the activator Nodal has lower diffusivity than the inhibitor Lefty, while both molecules are cleared at similar rates, which supports the idea that Nodal and Lefty form a classical reaction-diffusion system.

Colorectal Cancer Signature

The mutations and genome aberrations that characterize cancer result in often dramatically altered gene and protein expression patterns. It is these altered expression patterns that directly and indirectly drive progression of the disease. In human primary colorectal cancer cells, **Akhtar-Zaidi *et al.*** (p. 736, published online 12 April) analyzed the pattern of epigenetically modified chromatin at "enhancer" sequences that are known to be critical in the control of gene expression. An epigenetic enhancer signature was defined that was specifically associated with colorectal cancer cells.

Exponential Growth Effects

Humans are an extraordinarily successful species, as measured by our large population size—approximately 7 billion—much of which can be put down to recent explosive growth. Leveraging human genomic data, **Keinan and Clark** (p. 740) examined the effects of population growth on our ability to detect rare genetic variants, those hypothesized to be most likely associated with disease. It appears that rapid recent growth increases the load of rare variants and is likely to play an important role in the individual genetic burden of complex disease risk.

Silence, Please

Polycomb group (PcG) proteins play pivotal roles in epigenetic gene control, development, and disease. PcG proteins can control cell cycle progression, but the underlying mechanisms remain unclear. PcG proteins are thought to silence transcription of target genes through modulating chromatin structure. **Mohd-Sarip *et al.*** (p. 744, published online 5 April) uncovered an unanticipated transcription-independent function for the canonical PcG protein "Posterior sex combs" in cell cycle control, through its direct regulation of cyclin B destruction.



What — You *Don't* Dip and Read?!

Do less and get more from your ELISAs

- Quantitate 96 protein samples in 15 minutes, not hours
- Take advantage of a 4-log dynamic range and dilute less
- Run automated assays without wash steps or overnight incubations
- Analyze crude samples with less prep
- Get information-rich direct binding data, not end-point results
- Develop new assays in a few hours, not weeks



The Octet® Platform

Octet Systems with Dip and Read assays.
No hassle, label-free ELISAs.

fortéBIO

A Division of Pall Life Sciences

PALL Life Sciences

fortebio.com • 1-888-OCTET-75

Be the
next
winner!

2011 Winner
Dr. Tiago Branco
Postdoctoral
Research Fellow
University College
London



Get recognized!
US\$ 25,000 Prize

Deadline for entries
June 15, 2012

It's easy to apply! Learn more at:
www.eppendorf.com/prize



Eppendorf & Science Prize for Neurobiology

Congratulations to Dr. Tiago Branco on winning the 2011 Eppendorf & Science Prize for his studies on how dendrites discriminate temporal input sequences and apply different integration rules depending on input location. The results of Dr. Branco's research provide insight on how the brain performs computations, and suggest that even single neurons can solve complex computational tasks.

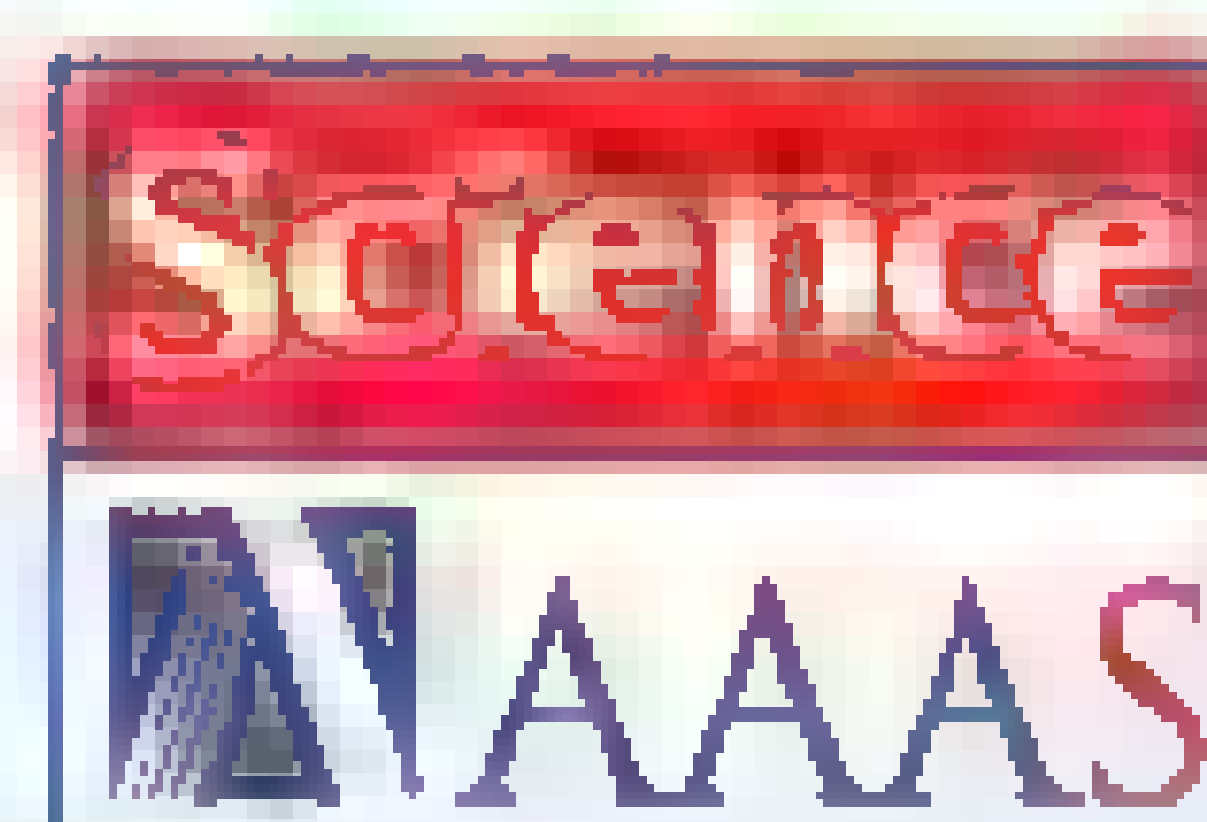
You could be the 11th winner of this award.

The annual Eppendorf & Science Prize for Neurobiology honors young scientists for their outstanding contributions to neurobiological research based on methods of molecular and cell biology. The winner and finalists are selected by a committee of independent scientists, chaired by *Science's* Senior Editor, Dr. Peter Stern.

To be eligible, you must be 35 years of age or younger. If you're selected as this year's winner, you will receive US\$ 25,000, have your work published in *Science* and be invited to visit Eppendorf in Hamburg, Germany. Past winners and finalists have come from as far a field as China, Chile, India and New Zealand.

Yes, it can happen to you. Enter your research now!

eppendorf
In touch with life



Gordon D. Brown is a professor at the Aberdeen Fungal Group, Institute of Medical Sciences, University of Aberdeen, AB25 2ZD, UK. E-mail: gordon.brown@abdn.ac.uk.

David W. Denning is a professor at the University of Manchester and director of the National Aspergillosis Centre, University Hospital of South Manchester, Manchester, M23 9LT, UK. E-mail: david.denning@manchester.ac.uk

Stuart M. Levitz is a professor in the Department of Medicine, University of Massachusetts Medical School, Worcester, MA 01605, USA. E-mail: stuart.levitz@umassmed.edu

Tackling Human Fungal Infections

FUNGI INFECT BILLIONS OF PEOPLE EVERY YEAR, YET THEIR CONTRIBUTION TO THE GLOBAL BURDEN of disease is largely unrecognized. Most are “relatively” minor infections, but millions contract diseases that kill at least as many people as tuberculosis or malaria. Although true mortality rates are unknown because of a lack of good epidemiological data, the incidence of invasive fungal infections is rising as a result of modern medical interventions and immunosuppressive diseases, such as AIDS. Despite the high mortality rates of invasive fungal infections, they remain understudied and underdiagnosed as compared with other infectious diseases. What can be done to remedy this unfortunate situation?

Most important is to raise the general awareness of the problem. Over 600 different fungi have been reported to infect humans, ranging from common to fatal infections, including those of the mucosa, skin, hair, and nails, and other ailments including allergies. Even influential international organizations, such as the World Health Organization and the Bill & Melinda Gates Foundation, appear not to fully appreciate the burden imposed by infection with fungi.

Three issues require immediate attention. Robust, rapid, simple, and cheap diagnostics are needed to allow quicker implementation of antifungal therapeutics. Most diagnostics still suffer from long assay times and poor specificity and/or sensitivity. These problems, combined with subtle clinical presentations, often result in missed or delayed diagnosis and compromise clinical care. Appropriate diagnostics would immediately affect mortality and reduce morbidity.

Safer and more effective antifungal drugs are also needed. Although several classes of antifungal drugs are clinically available, they have had only modest success in reducing the high mortality rates of invasive mycoses such as candidiasis and cryptococcosis. Although this is due in large part to delays in disease diagnosis and fungal identification, antifungal drugs also suffer from restrictions in route of administration, toxicity, a

narrow spectrum of activity, detrimental drug interactions, the development of drug resistance, and bioavailability in target tissues. These factors, and the high cost of many antifungal therapies, exacerbate the problem in resource-limited settings, where mortality rates are consequently much higher. Although combinations of existing drugs may yet prove to be more efficacious, new and cheaper drugs are needed that are rapidly fungicidal and overcome the various deficiencies listed above. Only a few drugs are currently in preclinical development, and it

will be years before any of them reach the clinic (if they do). We also need a better understanding of who is at risk of infection, to facilitate targeted preventative measures.

Finally, fungal vaccines must be developed for clinical use. There are currently no approved human vaccines for any fungal pathogen, despite the advances in our understanding of antifungal immunity. Although effective in animal models, few vaccines have reached clinical trials, which is due in part to a lack of commercial interest. In addition to preventing invasive infections, an effective vaccine could also benefit those with fungal-related allergies and mucocutaneous infections, such as vulvovaginal candidiasis.

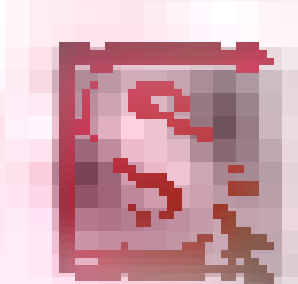
Accurate data on fungal disease burdens and their economic impact are needed to raise scientific interest and increase global investments. The major U.S. and UK funding agencies currently invest only about 2% of their infectious disease budgets in fungal research. More private funding can be generated through partnerships with academia and public health institutions. The population at risk for life-threatening fungal infections is growing worldwide, and tackling the challenges of these pathogens should become a much higher priority.*

— Gordon D. Brown, David W. Denning, Stuart M. Levitz

10.1126/science.1222236

Online

sciencemag.org



Podcast interview
(http://scim.ag/ed_6082) with author
Gordon D. Brown.



*Neil Gow, Mihai Netea, and Theodore White contributed equally to this editorial.



Absolute Certainty!

Get peace of mind with Eppendorf

Experience peace of mind with Eppendorf
guaranteed quality and order your free sample
on www.eppendorf.com/consumables

Don't leave your results to chance –
count on Eppendorf consumables

- Unique features to make every day routines faster and easier
- Minimized risk of chemical leaching from our consumables
- Purity grades tailored to even the highest requirements

eppendorf
In touch with life



GENETICS

The Evolution of X and Y

Although most flowering plants are hermaphroditic, having male and female function within a single flower, a few have shifted sexual function into separate male and female individuals, a condition known as dioecy. White campion (*Silene latifolia*) is a dioecious plant with XY chromosomes that determine the plant's sex; however, whether they arose through a similar evolutionary process as the mammalian XY system is unclear. Muyle *et al.* sequenced the transcriptome of *S. latifolia* and found that genes on the Y chromosome show significantly less gene expression than those from the X. Examination of sex-linked transcripts from male and female plants indicated that *S. latifolia* is in the process of evolving dosage compensation for the X chromosome because of the degeneration of the Y, analogous to that of many animals, including humans. Furthermore, given the evolutionary youthfulness of this system (<10 million years compared to 150 million years for mammals), these findings suggest that dosage compensation is a relatively early process in the evolution of sex chromosomes. — LMZ

PLoS Biol. 10, e1001308 (2012)

BIOMEDICINE

Mediating Metabolism

Heart disease is a common complication of obesity-associated metabolic disorders such as type 2 diabetes, but the molecular mechanisms underlying this link are not fully understood. Much research has focused on the notion that specific metabolic aberrations such as lipid accumulation compromise the heart's structure and function. A new study suggests that the situation is more complex: Rather than simply being an organ targeted by metabolic dysfunction, the heart itself may regulate whole-body metabolism. Grueter *et al.* observed improved metabolic features in transgenic mice with cardiac-specific overexpression of MED13, a regulatory subunit of Mediator (a protein complex bridging transcription factors and RNA polymerase). These mice were resistant to diet-induced obesity and metabolic syndrome because of an

increase in energy expenditure, and they showed altered expression of genes controlled by the thyroid hormone receptor. Interestingly, cardiac expression of MED13 is negatively regulated by miR-208a, a microRNA encoded by an intron of a cardiac-specific myosin gene. Pharmacological inhibition of miR-208a in wild-type mice on a high-fat diet slowed both weight gain and the development of glucose intolerance. — PAK

Cell 149, 671 (2012)

HYDROLOGY

Groundwater Maps for Africa

Access to safe drinking water and to water resources for agriculture is essential for African development; water use on the continent is likely to

increase substantially in the next few decades. Groundwater responds more slowly to climate variability than surface water and is therefore important, for example, in the event of drought. Yet information about groundwater resources on the African continent is woefully incomplete. MacDonald *et al.* report quantitative maps of groundwater storage and potential groundwater yields in Africa. To do so, they collated and reviewed existing hydrogeological maps, aquifer studies, and borehole data from across the continent. The estimated overall volume of groundwater, 0.66 million km³, far exceeds that of the annual renewable freshwater resources and of lake waters. However, groundwater distribution is uneven across the continent. Most of the large groundwater stores that would be able to accommodate high-yielding boreholes are located in northern Africa and are often far away from population centers. The authors also caution that groundwater resources must be managed carefully to avoid degradation and depletion. — JFU

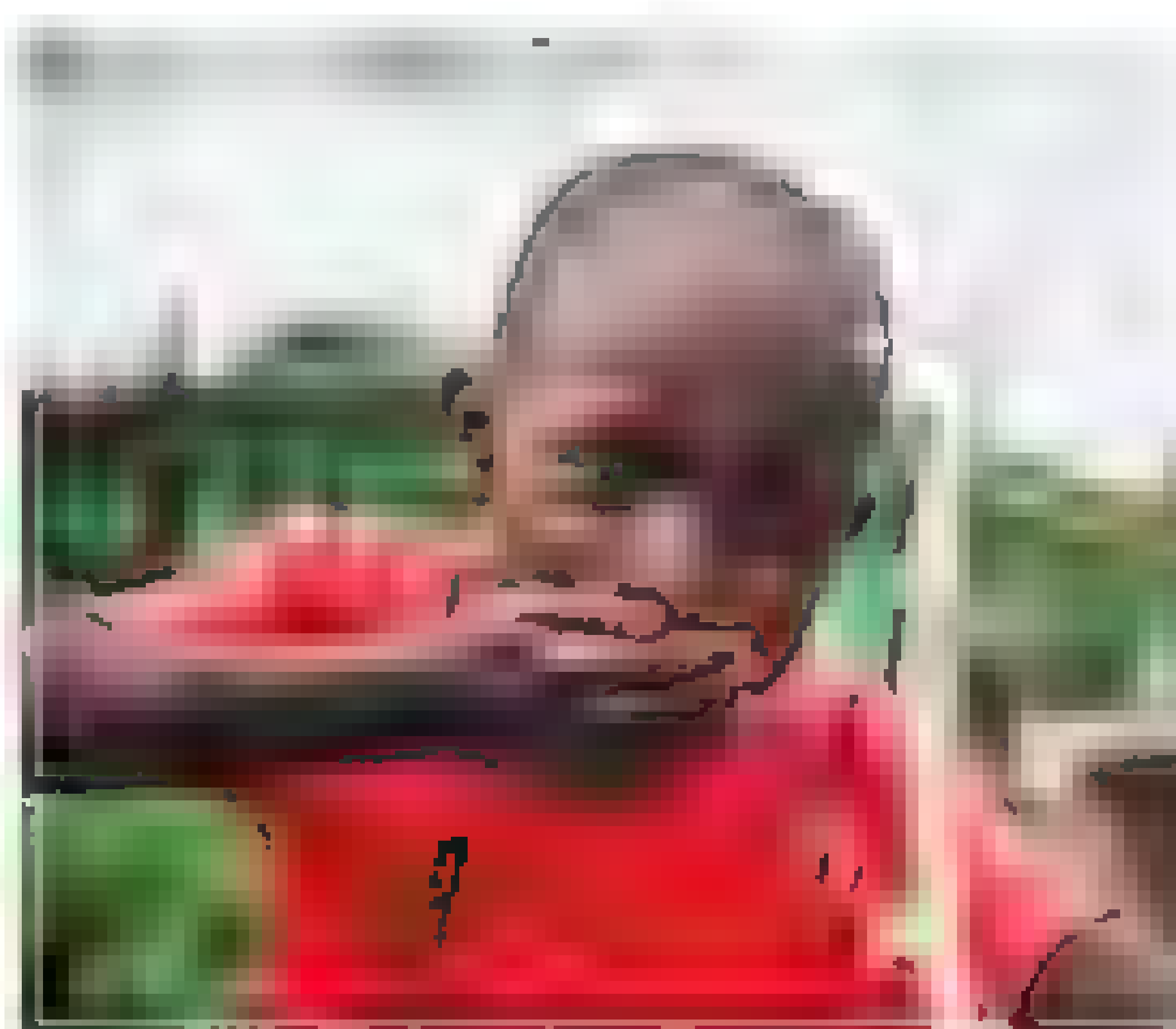
Environ. Res. Lett. 7, 024009 (2012)

BIOCHEMISTRY

A (PEP)py Response

Phosphoenolpyruvate (PEP), the final intermediate of glycolysis, is a central cellular metabolite. Besides its conversion to pyruvate by pyruvate kinase during glycolysis, in prokaryotes it is also the substrate for glucose phosphorylation (required for the import of glucose), and in some bacteria it is also converted to oxaloacetate by PEP carboxylase—an anapleurotic reaction that replenishes an intermediate in the tricarboxylic acid (TCA) cycle. Xu *et al.* found that as expected, depriving *Escherichia coli* of glucose resulted in a decrease in early glycolysis intermediates such as fructose-1,6-bisphosphate (FBP), but also observed the remarkable finding seen by others, that PEP increased at least 10-fold. A metabolic flux analysis showed that this was likely due to almost complete inhibition of PEP carboxylase. Although FBP is a known PEP carboxylase activator, on the basis of previously

measured effects, the change in FBP concentration would not explain the reduction in PEP carboxylase activity. Rather, acetyl-CoA and aspartate enhanced the effect of FBP on PEP carboxylase

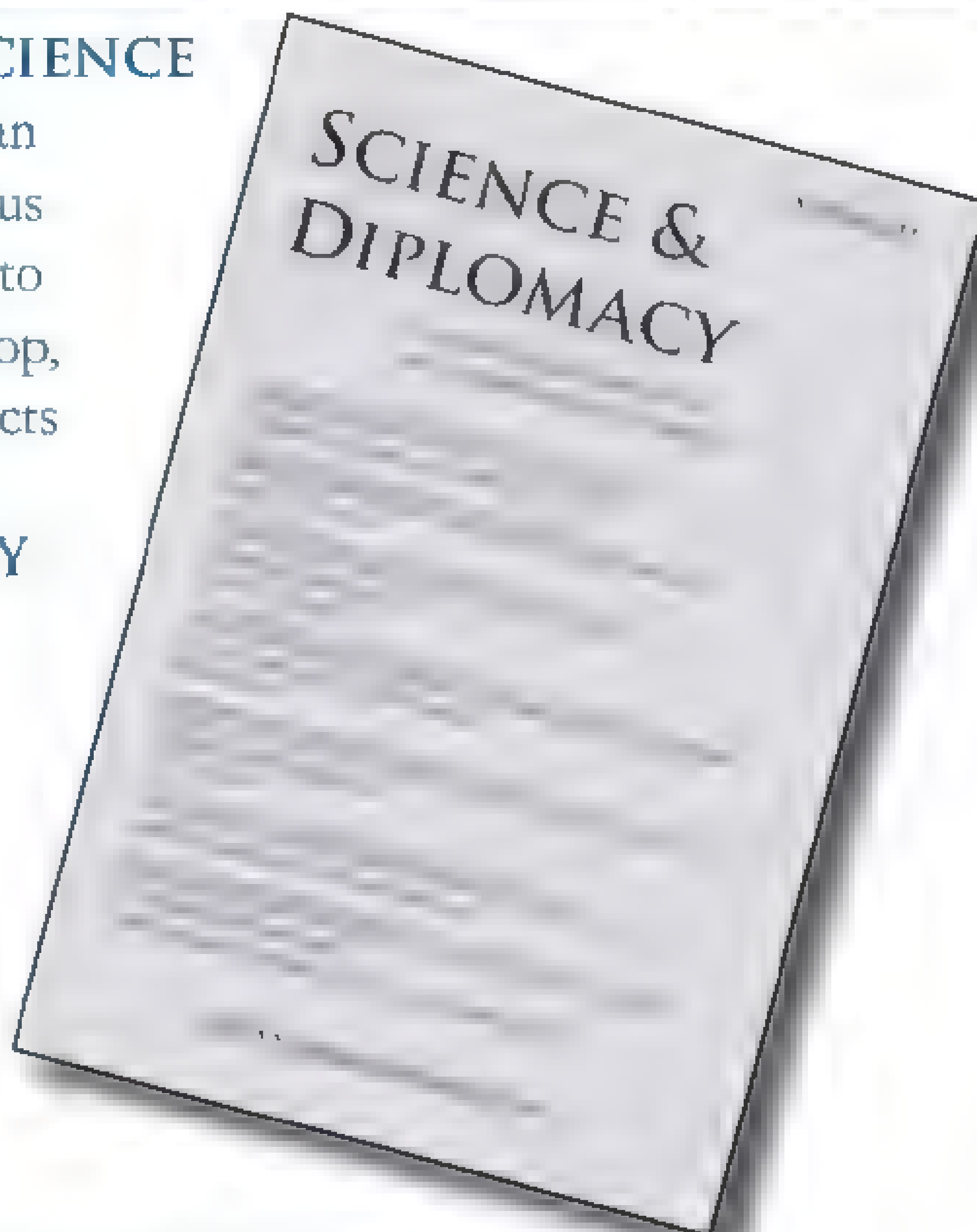


Continued on page 651

SCIENCE & DIPLOMACY

A quarterly publication from the AAAS Center for Science Diplomacy

Launched in March 2012, **SCIENCE & DIPLOMACY** provides an open access forum for rigorous thought, analysis, and insight to serve stakeholders who develop, implement, and teach all aspects of science and diplomacy. **SCIENCE & DIPLOMACY** features a mix of original perspectives and research articles by leading science and diplomacy practitioners and thinkers. Learn more about the latest ideas in science diplomacy and receive regular updates by registering for free at www.sciencediplomacy.org/user/register.



WWW.SCIENCEDIPLOMACY.ORG

Senior Advisory Board

Norman P. Neureiter (Chair), AAAS

Peter C. Agre, Johns Hopkins

Nicholas Burns, Harvard

David C. Clary, Oxford and UK FCO

Paula J. Dobriansky, Harvard

Nina V. Fedoroff, Penn State and KAUST

Richard N. Foster, Yale

David A. Hamburg, AAAS

Mohamed Hassan, IAP

Neal F. Lane, Rice

Science & Diplomacy is published by the Center for Science Diplomacy of the American Association for the Advancement of Science (AAAS), the world's largest general scientific society.

AAAS
ADVANCING SCIENCE SERVING SOCIETY

Continued from page 619

activity, and modeling showed that this could explain the observed PEP accumulation. Metabolic data obtained with an FBP-insensitive mutant suggested that PEP accumulation is required for normal resumption of growth upon reexposure to glucose. Thus, the anaplerotic reaction is switched on and off through sensitive allosteric regulation of PEP carboxylase, enabling bacteria to rapidly adapt to changing environmental conditions. — VV

Nat. Chem. Biol. **8**, 10.1038/nchembio.941 (2012)

EDUCATION

All in Our Heads?

Math anxiety is a familiar ailment to many adults; however, little is known regarding its neurodevelopmental basis. To investigate this, Young *et al.* used a scale for evaluating math anxiety in adults to assess math anxiety in 7- to 9-year-old children. In a separate session, functional MRI data were obtained from these children while they determined whether



addition and subtraction problems were done correctly. Math anxiety was found to associate with hyperactivity in the amygdala, a region of the brain involved in processing negative emotions, and with reduced activity in prefrontal cortex regions implicated in mathematical reasoning. Furthermore, connectivity between the amygdala and prefrontal cortex regions involved in emotional regulation was elevated in children experiencing math anxiety. These findings confirm math anxiety as a legitimate type of stimulus- and situation-specific anxiety. Future studies should investigate whether it is possible to design treatment strategies based on successful therapies for other phobias that result from aberrant activity in the amygdala. Future work should also focus on whether studies like these can provide information on how problem-solving and reasoning are influenced by math anxiety. — MM

Psychol. Sci. **23**, 10.1177/0956797611429134 (2012)

APPLIED PHYSICS

Optical Origami

The Japanese art of origami, in which paper is meticulously folded into a wide range of intricate three-dimensional shapes, also lends itself to myriad applications in engineering; examples include the possibility of efficient flat pack transportation of "pop-up" accommodation buildings in disaster-struck areas, and the preparation of expandable stents that allow for minimally invasive keyhole surgery. The folding itself can be induced by a number of stimuli depending on the materials involved, with electrical, magnetic, chemical, or mechanical stimuli having been demonstrated. Ryu *et al.* now show that light can also be used to fold photoresponsive polymers into intricate shapes. The light absorbed in the polymer film induces a photochemical reaction that relaxes the stress. By using a pattern of photomasks, they could localise the regions of stress relaxation to form hinges that then allowed the film to fold into a prescribed shape. The authors discuss the flexibility of blending in other molecules into the polymer that would provide the structure with advanced functionality. — ISO

Appl. Phys. Lett. **100**, 161908 (2012)

CLIMATE SCIENCE

The Climate of the Apes

The middle Miocene, around 15 million years ago, was a crucial time in the evolution of apes and eventually humans. Apes had recently evolved, and as climate warmed, their range expanded greatly, across most of Eurasia, leading to further diversification. One view is that some of these Eurasian apes eventually recolonized Africa as climate later cooled, although the fossil record remains sparse from this period. Hamon *et al.* explored the climatic conditions that led to this period of warmth in the Miocene and particularly that were favorable for the expansion of subtropical forests that the apes depended on. Using a global climate model, they concluded that the range of forests would be greatest when atmospheric CO₂ levels were between about 560 and 700 ppmv. The East Antarctica Ice Sheet, which is thought to have begun to form by the middle Miocene as the overall Cenozoic climate was cooling, but not uniformly, was about 25% of its modern extent. Both conditions are needed to increase precipitation in Europe at that time. Further decreases in atmospheric CO₂ levels and the expansion of ice led to the reduction of forests later in the Miocene. — BH

Geology **10.1130/G32990.1** (2012)

22

minutes and
58 seconds
of video
on accelerated
mass loss
from Antarctica's
ice shelves.

One more data point on why
you should spend more time
at membercentral.aaas.org.
There you can enjoy
evidence-based videos,
webinars, downloads,
blogs, and discounts geared
for people who live for all
things empirical.

AAAS
MEMBERCENTRAL

membercentral.aaas.org

Science Mobile App Now Available for Android Phones



They say you never know when inspiration will strike. Download the *Science* mobile app for Android devices and be ready the next time you're inspired to read the latest news, research, and career advice from *Science* on your mobile phone.

To download the *Science* mobile app for Android visit content.aaas.org/mobile, visit the Android Market on your phone, or just scan this barcode.



Features include:

- Summaries and abstracts from *Science*, *Science Translational Medicine*, and *Science Signaling*.
- Ability to e-mail full-text links.
- The latest news from *ScienceNOW*.
- Career advice articles from *Science Careers*.
- Access to the *Science* weekly podcast and other multimedia.
- Content caching for reading without wi-fi access.



AROUND THE WORLD



San Diego, California 1

A Battle Over Bones

In the latest round of an unusual custody battle for two of the oldest human skeletons ever found in the Americas, attorneys for three University of California professors were in federal court in San Francisco this week to prevent the University of California, San Diego (UCSD), from handing over 9000-year-old bones to American Indians in San Diego County. The professors obtained a temporary restraining order on 27 April



Meanwhile, in anticipation of the professors' lawsuit, members of the Kumeyaay Native American tribes filed their own lawsuit in federal court in San Diego demanding the transfer of the skeletons under the auspices of the controversial Native American Graves Protection and Repatriation Act. It requires museums to transfer remains or artifacts if they can be traced to a modern tribe or reservation.

The bones were discovered in 1976 dur-

ing an excavation at University House in San Diego. The Kumeyaay have been seeking the remains for reburial, claiming that they were found on traditional aboriginal lands. However, both a UCSD scientific advisory committee and a separate system-wide UC research committee found that the remains have no cultural or biological affinity with the Kumeyaay or any living Native American. <http://scim.ag/ucsdskeltons>

Bethesda, Maryland 2

Continuing Crossfire Over Flu Papers

A senior U.S. health official has disputed charges that the government tried to prearrange an advisory panel's recommendation to publish two controversial studies that describe how to make the H5N1 avian influenza virus transmissible in mammals. In late March, the National Science Advisory Board for Biosecurity (NSABB) said the two studies should see the light of day, essentially reversing an earlier decision (*Science*, 4 May, p. 529).

But in a 12 April letter to Amy Patterson, the associate director for science policy at the National Institutes of Health, NSABB member Michael Osterholm, an influenza expert at the University of Minnesota, Twin Cities, detailed a number of complaints about the process. A classified briefing to the panel was "useless," he wrote, and officials had prepared a "one-sided" agenda for the meeting that "was designed to produce the outcome that occurred."

Patterson fired back point-by-point in a letter dated 25 April and released last week. "You are of course entitled to your opinion," she wrote, but "the agenda was not designed to produce any specific outcome other than a rigorous scientific discussion."



Manila 3

Philippine Scientists Defend Transgenic Crops

The Philippines National Academy of Science and Technology (NAST) last week blasted Greenpeace for trying to stop field trials of a genetically modified eggplant. Two weeks ago, the environmental group petitioned the country's supreme court claiming that crops modified with a gene from *Bacillus thuringiensis* (Bt) are dangerous for humans and the environment and that approval procedures are flawed. NAST hit back on 2 May, calling the allegations "baseless" and the petition "not in the public interest."

NAST President Emil Javier, a plant scientist and former president of the University of the Philippines, says the country has 10 years of experience growing Bt corn without any documented adverse effects. Greenpeace campaigns with farmers and consumers are "not making headway, so they are trying something else," Javier says. A year ago, Greenpeace activists uprooted a trial plot of Bt eggplant. To answer the petition, the scientists conducting the trials and several governmental departments will file briefs explaining the "stringent" precautions being taken to ensure safety.

Bethesda, Maryland 4

NIH Unveils Plan to Rescue Old Drugs

The National Institutes of Health (NIH) has launched a pilot project with three major pharmaceutical companies to share aban-



CREDITS (TOP TO BOTTOM): © VEE-JAY VILAFRANCA FOR GREENPEACE PHILIPPINES; JAN AUST/N/SANTA MONICA COLLEGE; N.H.S.

doned drugs with academic researchers so that they can look for new uses

Pfizer, AstraZeneca, and Eli Lilly will provide 24 compounds that passed through safety studies but were later shelved either because they didn't work for a specific disease or because a business decision sidelined them. The new program will allow academics to "crowdsource" ways to use them, said NIH Director Francis Collins.

It is the first major initiative from NIH's 4-month-old National Center for Advancing Translational Sciences. NCATS plans to put \$20 million of its 2013 budget into grants to study the drugs. Researchers will be able to browse basic information on the drugs online. Those receiving a grant will be given access to the compounds and detailed data. If the drug shows promise in animal models, they may receive funding for early clinical trials. The companies will retain ownership of the compound, but researchers will have rights to new intellectual property that they discover and can publish their results.

<http://scim.ag/olddrugs>

Friedrichshafen, Germany 5

PEGASOS Prepares to Take Flight

The European Union's Pan-European Gas-Aerosols-Climate Interaction Study (PEGASOS), intended to study links between atmospheric chemistry and climate change, officially kicked off on 4 May. From an airship, which can hover 1 to 2 kilometers above the ground and ascend and descend vertically, the PEGASOS team plans to collect atmospheric chemistry data, including measurements of hydroxyl radicals and aerosols, across Europe during three flights over 20 weeks. The first flight is scheduled to launch 14 May from Friedrichshafen and travel to the Netherlands through 27 May. A June flight will collect data over Italy and France; an April 2013 flight will collect data over northern Europe.

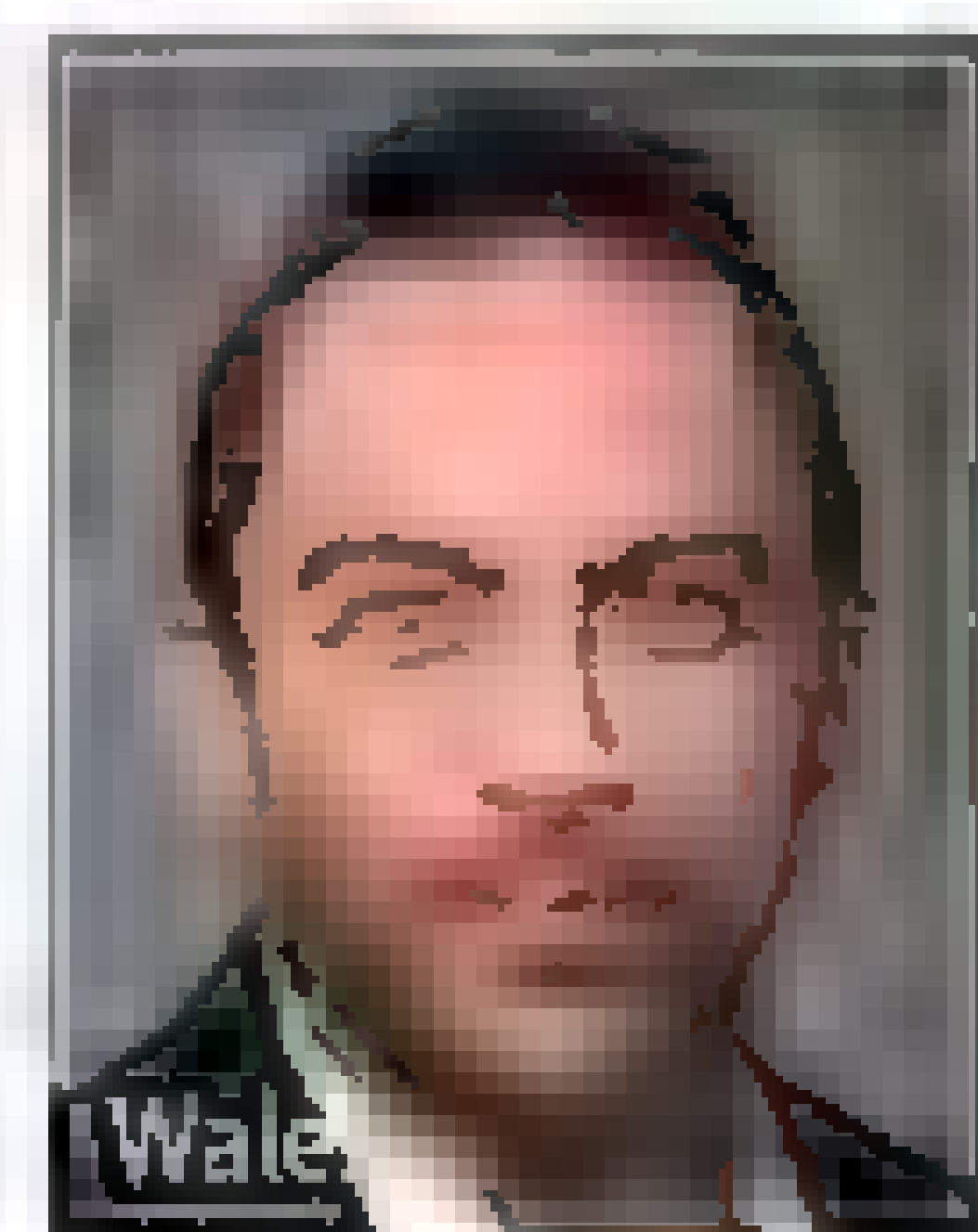
PEGASOS, which is funded by the European Commission under the auspices of the Seventh Framework Programme for Research, involves 26 partners from 15 countries and investigates the relationship between atmospheric chemistry and climate change.

"According to the European Environment Agency, the health and environmental cost of air pollutants released every year in Europe exceeds €100 billion," said European Commissioner for Research, Innova-

tion, and Science Máire Geoghegan-Quinn in a press release. Data from PEGASOS, she said, will likely contribute to a review of E.U. air policies due in 2013.

London 6

U.K. Enlists Wikipedia Founder For Open-Access Policy



The British government has enlisted the help of Wikipedia founder Jimmy Wales, a vocal supporter of open access to information on the Web, to figure out how to make research information more easily accessible. U.K. science minister David Willetts announced Wales's role as an unpaid adviser 2 May in a speech at the annual meeting of the Publishers Association in London.

Wales will initially advise the government on how to set up a new £2 million "Gateway to Research" portal, a database of British researchers that links to their funding sources, information about their findings, and publications. The database should offer entrepreneurs and others the opportunity to

find information and even seek collaboration with scientists, Willetts said today.

Later, Wales will also advise on the next generation of open-access publication systems, which would include improved peer review and tools to give postpublication feedback. <http://scim.ag/Walesadvising>

Beijing 7

Tobacco Research Project Out of National Competition

A tobacco research project nominated for a prestigious Chinese science prize (*Science*, 20 April, p. 280) has been withdrawn from further consideration, according to a 4 May story in *Science and Technology Daily*. The Chinese newspaper reported that during a 40-day public comment period, the office managing this year's National Science and Technology Progress Award competition received 58 objections to the 19 candidate projects—33 objections of which were lodged against the tobacco project, which claims to have improved the quality and marketability and boosted sales of Chinese cigarettes. After the office forwarded the objections to the nominating agencies for their responses, the State Tobacco Monopoly Administration withdrew its candidate.



Students See the Light

Students from five schools in rural Montana captured \$15,000 in prize money in the inaugural America's Home Education Energy Challenge, sponsored by the U.S. Department of Energy and administered by the National Science Teachers Association. Some 120,000 students in grades 3 through 8 participated in a 3-month effort to become smarter consumers. Sixth grader Kennedy Tooke (second from left) gained a measure of notoriety for calculating the savings from pulling the plug on her grandmother's Christmas tree lights.

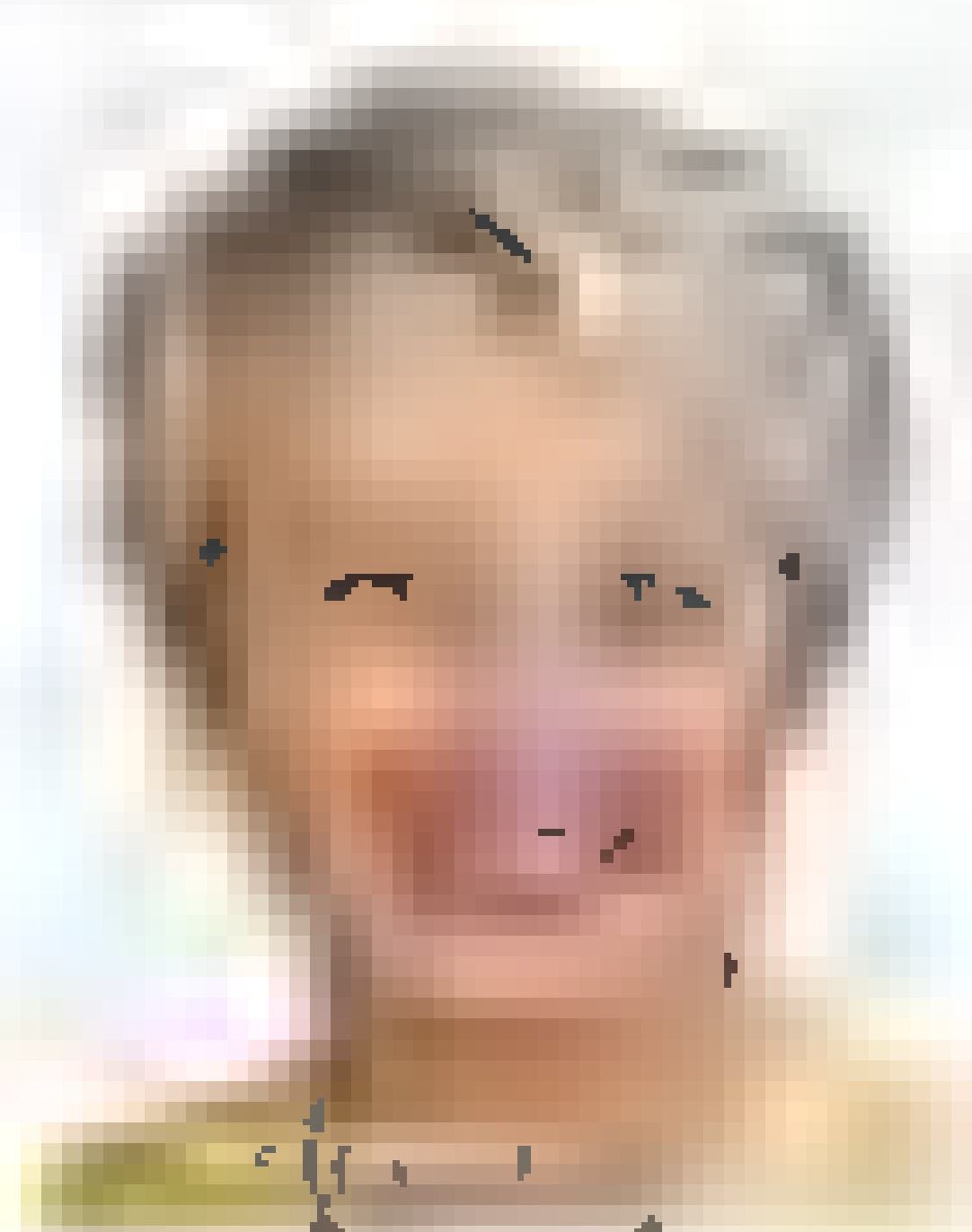
NEWSMAKERS

German Research Minister Faces Plagiarism Allegations

German Education and Research Minister **Annette Schavan** is facing allegations that she plagiarized parts of her dissertation, published in 1980. A Web site called *schavanplag* has listed 56 incidents in

which the anonymous accuser says Schavan copied phrasing from improperly cited sources.

Schavan, 56, received her doctorate in educational science in 1980 from the University of Düsseldorf; her dissertation was entitled "Person and conscience: Studies



on conditions, need and requirements of today's consciences."

"The dissertation was written 32 years ago, and I will be happy to give my account to those who are looking into the work; but it is difficult to deal with anonymous allegations," Schavan said at a press conference on 2 May. A ministry spokesperson told the German press agency dpa that the University of Düsseldorf will look into the allegations at Schavan's request.

Schavan's case is the latest in a string of similar accusations against German politicians. Defense Minister Karl-Theodor zu Guttenberg resigned last year after a blogger turned up evidence of extensive plagiarism in his dissertation. Since then, six other German politicians have had their Ph.D.s revoked because of similar offenses. <http://scim.ag/Schavan>

Random Sample

That Age-Old Question: What to Wear on Mars?

Deep inside a mountain cave in Dachstein, Austria, on 28 April, an international team of researchers sought to answer this question, showing off a new suit that simulates the challenges that await human visitors to Mars.

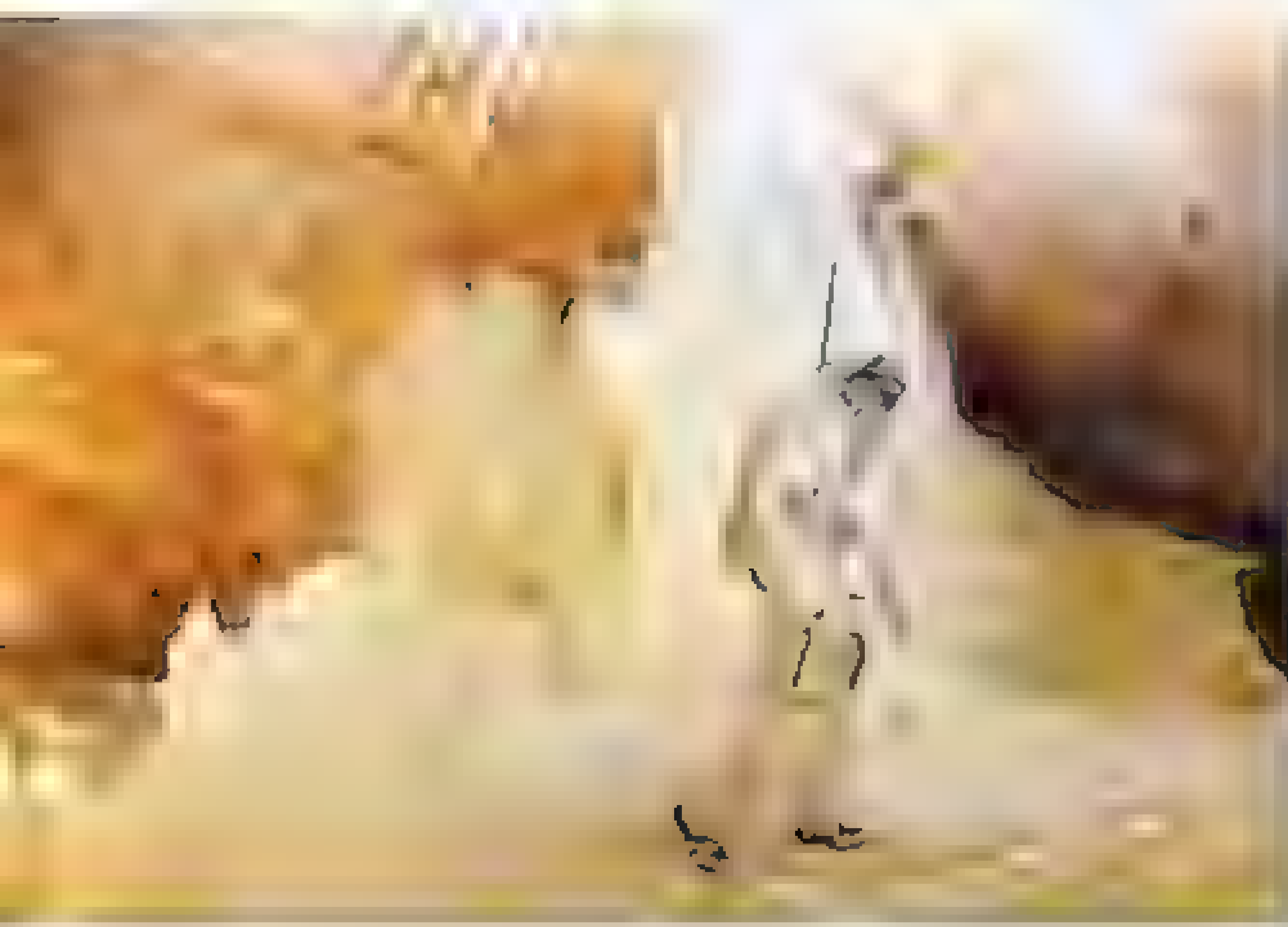
Most Mars simulations have taken place in rocky deserts or Antarctica to mimic the planet's cold, arid surface. But martian life could also exist in caves that formed long ago through volcanic activity. "[Caves] provide excellent shielding from cosmic radiation," says Gernot Grömer, Austrian Space Forum (ASF) president and head of the design team, and they also allow for a higher atmospheric water content and a more stable temperature regime. "So if life ever arose on Mars, these would be a natural retreat."

The sartorial challenges of the Red Planet are serious. The atmosphere is a near vacuum, and moving the limbs of a pressurized suit requires constant exertion. A Mars astronaut may need to both eat and use the bathroom inside the suit. And, as radio waves take up to 1 hour roundtrip between Earth and Mars, the suit should be able to provide real-time information on the wearer's health and environment.

To help prepare for these challenges, ASF offers the

Aouda.X, its Mars space suit simulator. The 45-kilogram garment includes a computer that monitors the wearer's vital signs and a weighty exoskeleton to mimic the exhausting martian environment. "You really feel like a turtle in a high-tech shell," says Grömer. The suit can also be sterilized and cleaned well enough to not contaminate Martian samples with Earthly biomolecules. "We'd like to break the spell that humans are too dirty for Mars," Grömer says.

The next test of Aouda.X is a field mission in a desert in Morocco in February 2013.



CERN Physicist Gets 5 Years For Plotting Terror

On 4 May, more than a month after his brief, 2-day trial, Franco-Algerian particle physicist **Adlène Hicheur** received a 5-year prison sentence on terrorism charges. But Hicheur, 35, may be released before the end of June, says his lawyer, Patrick Baudouin, because of possible sentence reductions and

the time he has already spent in custody.

Hicheur, a former CERN researcher, has been held in "preventive detention" in a high-security jail near Paris since October 2009. The court ruled that Hicheur was guilty of "participation in a criminal organiza-

tion whose goal was to plan terrorist acts." During the trial, Hicheur acknowledged exchanging e-mails with Mustafa Debeli, an alleged member of al-Qaida in the Islamic Maghreb, and discussing future terrorist actions. Baudouin admitted that words used by Hicheur in the e-mails were "disturbing" but argued that his client never took any concrete steps toward a terrorist act.



Hicheur

BY THE NUMBERS

10,000 Number of signatures a group called Forecast the Facts gathered to protest the Discovery Channel's self-censorship of climate change issues in their *Frozen Planet* series.

25% Percentage of current Earth-observing capacity that the United States will have by 2020 if aging satellites continue to be replaced by new satellites at the current rate, according to a National Research Council report released 2 May.

12% Rate of premature births in the United States, according to a new World Health Organization report. Most European countries, Canada, and Australia are in the 7% to 9% range.

Hicheur won't return to CERN; he was on a 4-year, nonrenewable contract that ended a few months after his arrest, says Aurelio Bay, the head of the particle physics laboratory at the Federal Polytechnic School of Lausanne in Switzerland <http://scim.ag/Hicheurtrial>

FINDINGS

Infants' Flexible Heads Go Back Millions of Years

A human infant's skull changes shape as it squeezes through the birth canal because its cranial bones don't entirely fuse together for at least 2 years after birth. A study online this week in the *Proceedings of the National Academy of Sciences (PNAS)* shows that

early humans who lived nearly 3 million years ago also experienced this delayed fusion. One possible explanation is that bipedalism, which constrains the shape of the

human pelvis, created obstetrical challenges even for smaller-brained human ancestors.

A team led by anthropologist Dean Falk of the School for Advanced Research in Santa Fe, New Mexico, looked at the metopic suture (MS), the joint between the cranium's two frontal bones, in a large number of fossil early humans, modern humans, chimpanzees, and bonobos. The MS of chimps and bonobos, they found, fuses very shortly after birth, whereas the MS of early and later hominins tends to fuse at 2 years of age or later.

But Robert Martin, an anthropologist at the Field Museum in Chicago, Illinois, cautions that the age of MS closure is "notoriously variable" in modern humans. A more reliable indicator of overall skull fusion, he suggests, would be the closure of the anterior fontanelle "soft spot." <http://scim.ag/skullflex>

Late-Stage Grad Students Want Nonacademic Careers

The further students progress through science graduate programs, the less likely they are to want a career in academic research, according to a survey of 4109 grad students from 39 top-tier research universities. Across all disciplines, the average number of students who rated academic jobs as "attractive" or "extremely attractive" dropped from 74% to 62% between

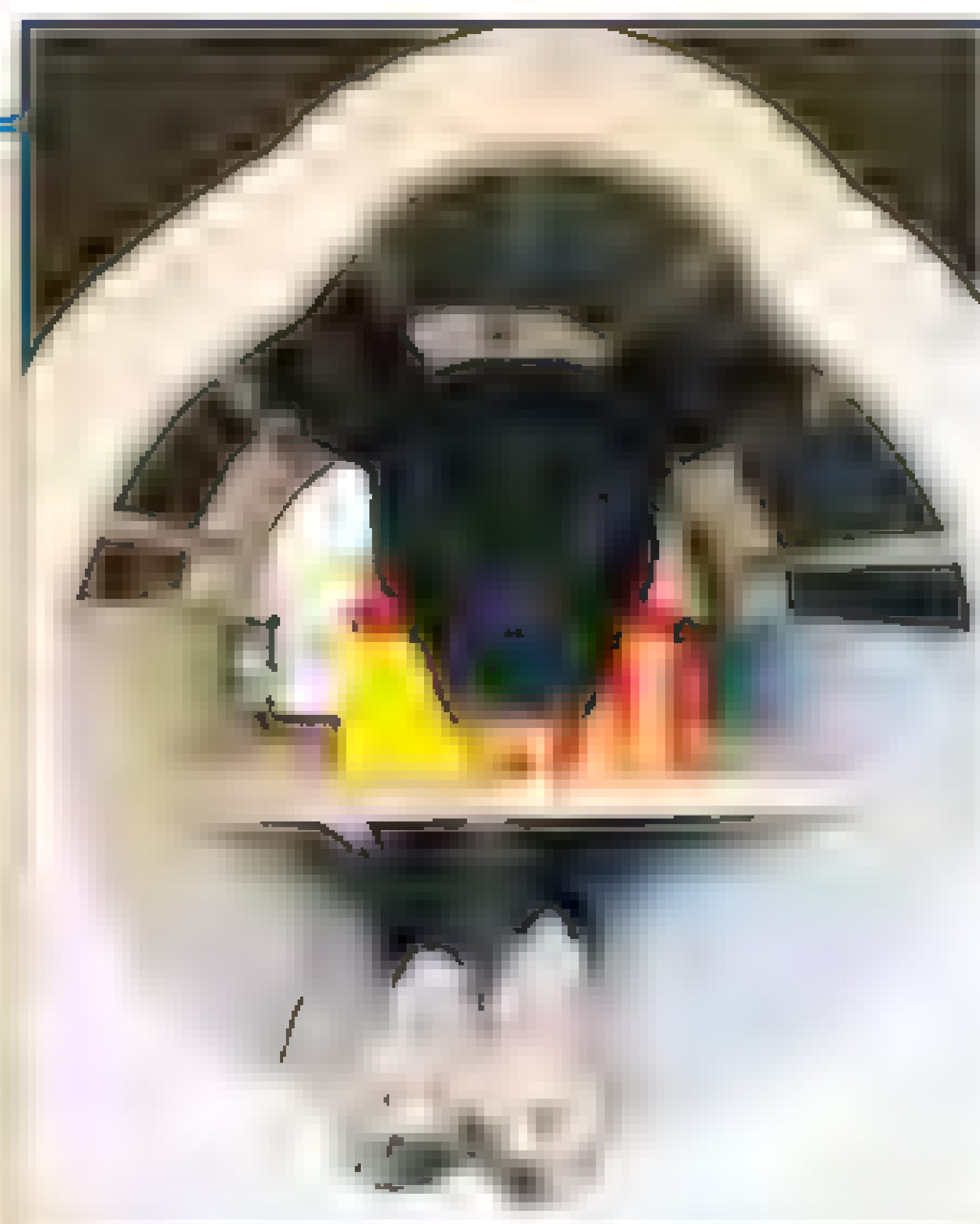
What's on a Dog's Mind

Dogs may appear to be pleading for a bit of steak, but what are they really thinking? A team at Emory University is starting to crack that nut by taking brain scans of two nonsedated dogs using functional magnetic resonance imaging (fMRI).

Training the dogs—a 3-year-old border collie named McKenzie and a 2-year-old mutt named Callie (pictured practicing)—to stay still within an fMRI scanner was the first step. The team then studied the dogs' neural responses to different hand gestures that indicated whether a treat was forthcoming.

The dogs did have rewards on their minds: An area of the brain associated with reward pathways, the ventral caudate, activated when the pooches anticipated a treat, the researchers confirmed in a paper in press at *PLoS ONE*.

Now that they've shown canine fMRIs are possible, the authors noted, scientists can also begin to explore how dogs process human language, how they distinguish between different people, and how they represent human facial cues and gestures.



the early and later stages of grad school. Careers in industry and startup companies either jumped up slightly or stayed about the same. Government jobs saw the biggest spike in relative attractiveness.

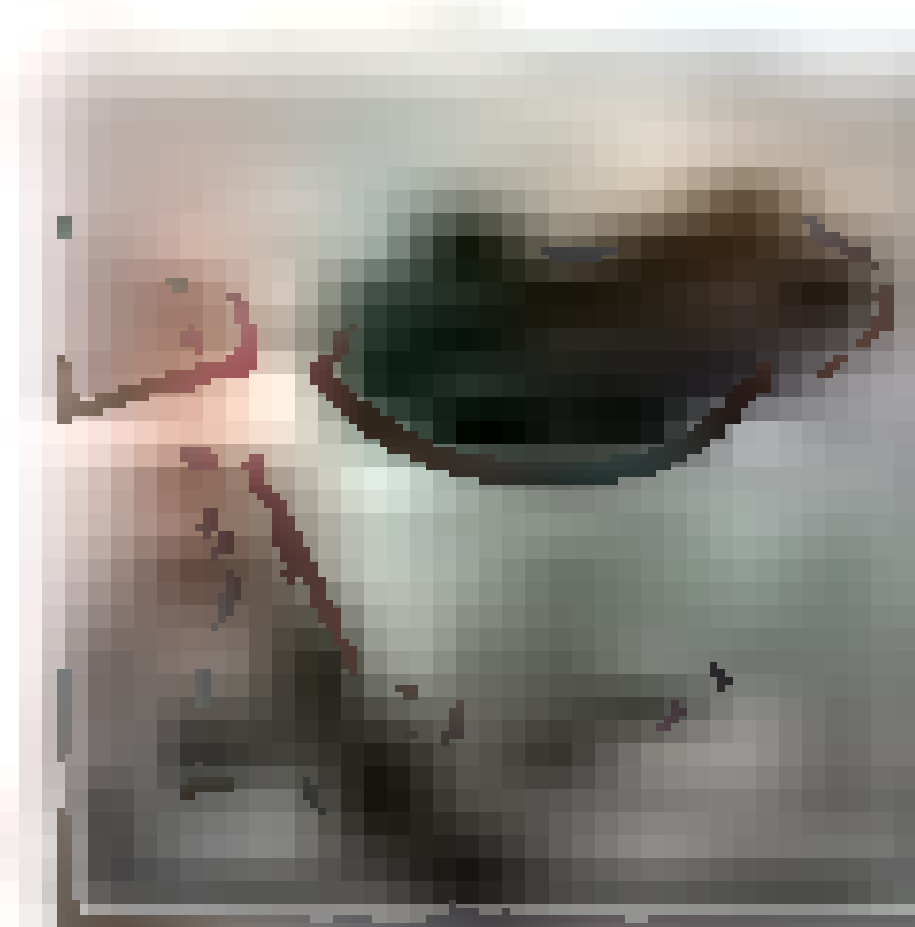
Students in the life sciences in particular became disillusioned with academia: 78% of them rated faculty research positions as attractive early in grad school, and only 67% did so in later stages.

The study, which appeared online 2 May in *PLoS ONE*, is among the first to look empirically at how students' career preferences change over time. The authors say it's difficult to tell what's discouraging students from faculty research jobs, but possibilities include the weak job market and seeing their advisers stress over tenure decisions and grants. <http://scim.ag/PreferencesData>

The Fluid Mechanics Of Walking With Coffee

Fret no more, overburdened conference attendees. Scientists have learned how to avoid a common research pitfall: spilled coffee.

Rouslan Krechetnikov, a mechanical engineer at the University of California, Santa Barbara, and graduate student Hans Mayer studied the problem, which involves



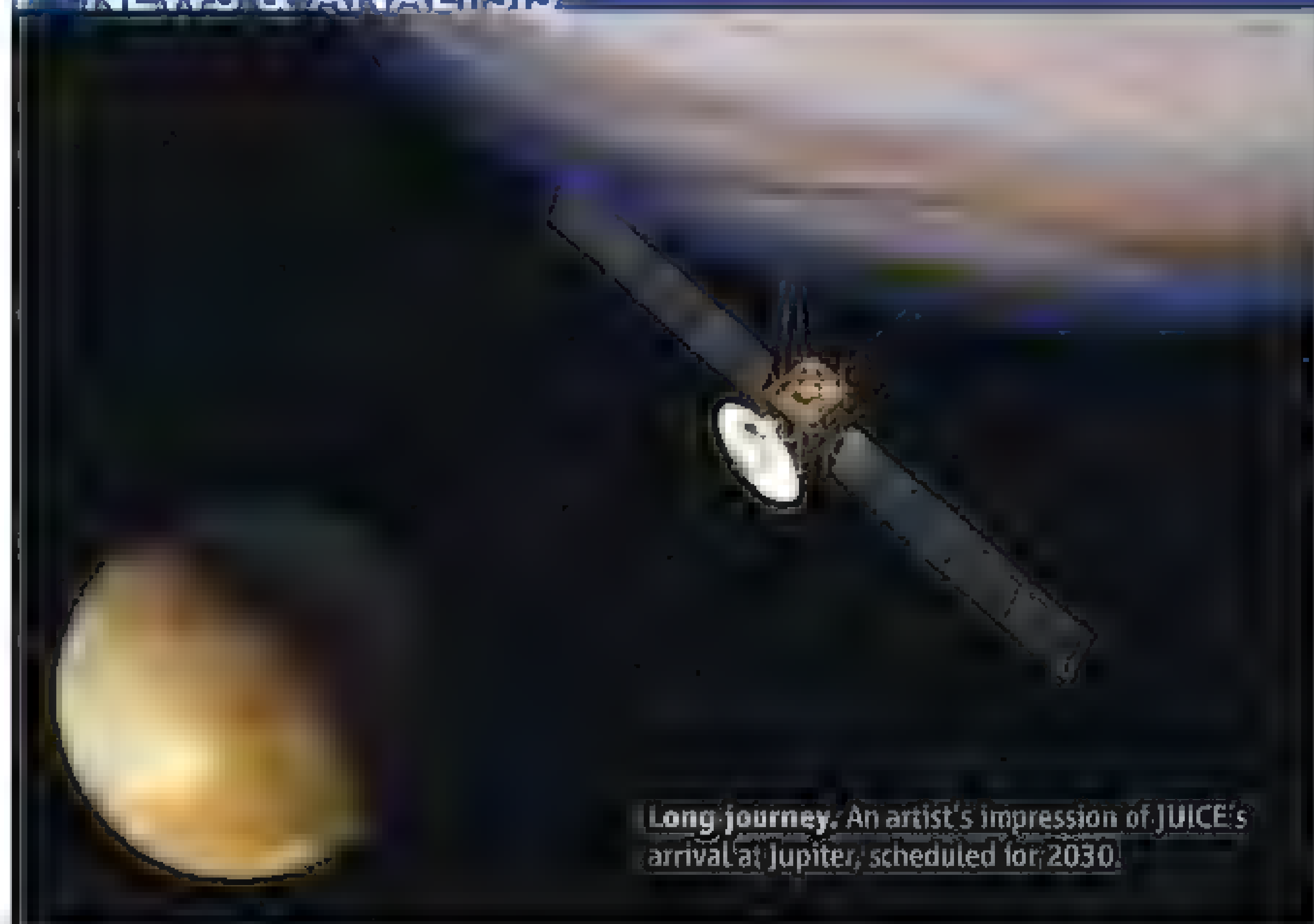
the mechanics of walking as well as liquid sloshing, an interplay of accelerations, torques, and forces. They asked a person, filled mug in hand, to walk at different speeds, either focusing on the mug or looking straight ahead. A camera recorded the person's motion and the mug's trajectory while a tiny sensor on the mug recorded the instant of spillage.

In their paper published last month in *Physical Review E*, Krechetnikov and Mayer show that everyday mug sizes produce natural frequencies that happen to match those of a person's leg movements during walking. So walking alone is tuned to drive coffee to oscillate in a mug. But small irregularities in walking can amplify oscillations, or sloshing.

So how to avoid a spill? Walk more slowly, the researchers say, and leave a gap between the top of the coffee and the mug's rim. And watch what you're doing—so long as your mug isn't filled too high, a watched mug almost guarantees a clean run. <http://scim.ag/spilledcoffee>

Science LIVE

Join us on Thursday, 17 May, at 3 p.m. EDT for a live chat on the roots of war and conflict among humans <http://scim.ag/science-live>



SPACE SCIENCE

Europe Picks Jupiter Probe; Runners-Up Vow to Press On

While American space scientists gaze on with envy, Europe is setting its sights on a solo run to Jupiter. Last week, the European Space Agency (ESA) announced that it had chosen a €1 billion satellite to study three icy moons of Jupiter as its next major science mission, scheduled to be launched in 2022. Scientists believe the moons orbiting Jupiter are potentially homes of primitive life and could be models for life on planets and moons beyond our solar system.

The news caused elation among the leaders of the Jupiter Icy Moon Explorer (JUICE), but came as a blow to two rival missions that had also hoped to secure ESA's funding: the New Gravitational Wave Observatory (NGO) and the Advanced Telescope for High-Energy Astrophysics (ATHENA), an x-ray observatory. Some scientists working on those missions complained that ESA hasn't properly explained its choice—but they hope to be chosen for the agency's next available launch, currently planned for 2028.

The winning mission will be the first L-class (large) mission—meaning it needs the heavy Ariane-5 rocket for launch—in ESA's Cosmic Vision 2015–2025 program. It will study the interaction between Jupiter and its moons to better understand how the Jovian system formed and, by extension, how the solar system as a whole came into being.

The mission will also investigate whether

the moons have the conditions needed to sustain life. Oceans of liquid water are believed to exist on Europa, Callisto, and Ganymede, the latter is particularly tantalizing because its structure, thought to involve a metallic core, a silicate mantle, and liquid water trapped between layers of ice, is believed to be common in extrasolar planetary systems, says Michele Dougherty of Imperial College in London, JUICE's lead scientist. "If Ganymede turns out to have the right conditions, it could be the most common potential habitat for life in the universe," Dougherty says.

JUICE received the unanimous backing of ESA's member states in a vote held in Paris on 2 May, following endorsements by the agency's directors and its Space Science Advisory Committee (SSAC). That panel has

not explained publicly why it favored JUICE, but an ESA document says that the committee "came to a consensus" after extensive discussion. In an e-mail to *Science*, SSAC Chair Willy Benz of the University of Bern in Switzerland said that all three proposals "were of very high caliber and worthy of being flown." JUICE, however, will improve our understanding of the solar system and exoplanets, possibly change our thinking about where conditions suitable for life might be found, and "demonstrate the ability of Europe to explore the outer planets of the solar system on its own," he added.

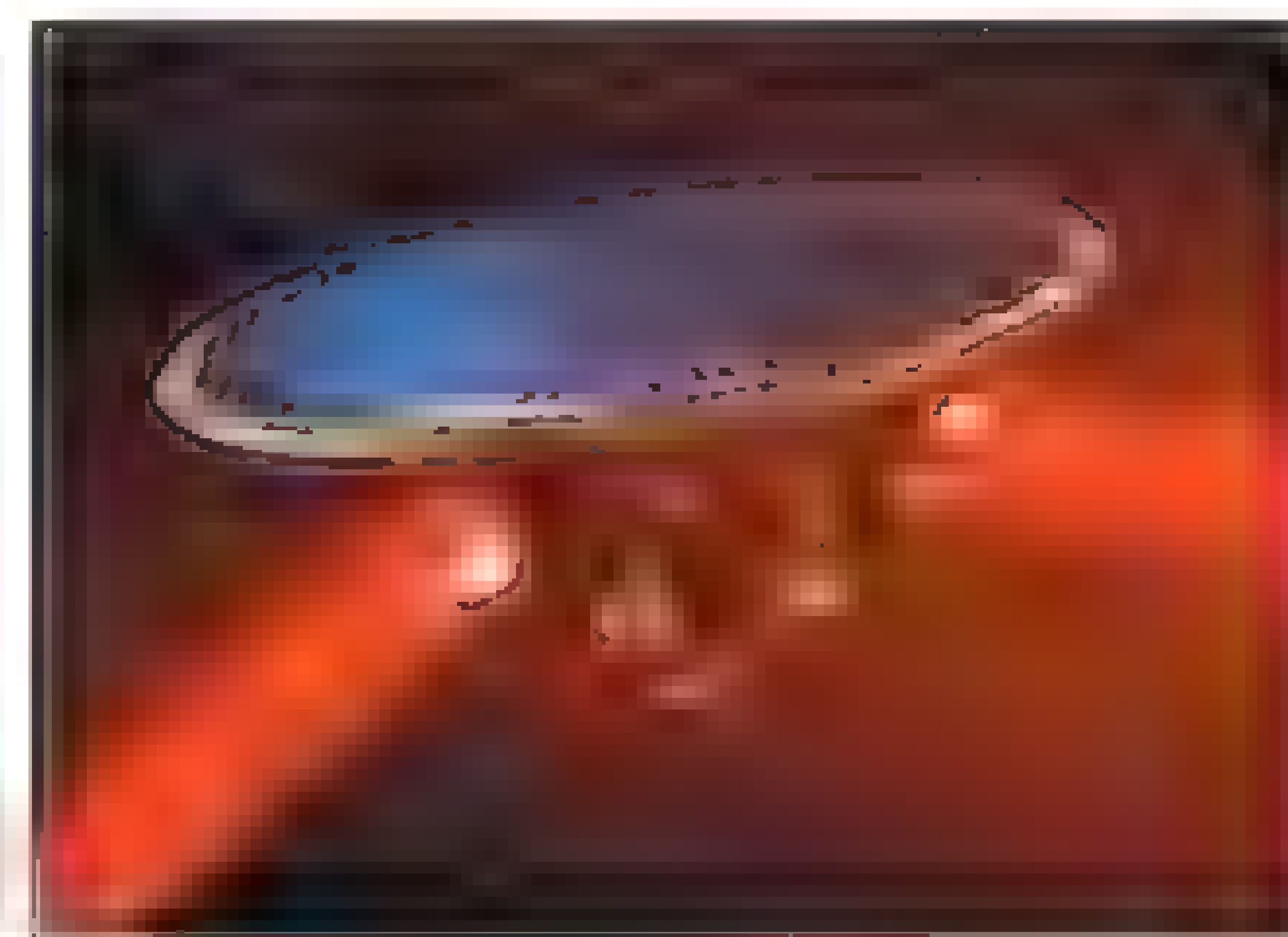
All three mission proposals were scaled-down versions of larger projects that ESA was to have carried out jointly with its U.S. counterpart, NASA, which pulled out last year because of funding problems. The Jupiter mission envisaged a European spacecraft orbiting the jovian moon Ganymede while a U.S. orbiter would have encircled Europa. JUICE will now take on some of the work of the latter, arriving at Jupiter in 2030, performing fly-bys of Europa and extensive studies of Callisto before finally settling into an orbit around Ganymede in 2032, where it is due to remain for about 9 months.

Robert Pappalardo of NASA's Jet Propulsion Laboratory in Pasadena, California, who led U.S. science efforts to develop a Europa orbiter, says that JUICE will "provide for superb science" but believes a dedicated Europa mission is still needed to pin down the moon's potential for hosting life. He and a team of scientists and engineers have given NASA chiefs a range of options for an independent mission that would cost about \$2 billion, less than half the price of the earlier plans. Pappalardo says Congress has requested to see the new plans, and he's hopeful that work on the new mission might start "in the next year or two."

Leaders of the two losing proposals insist that their missions, too, should eventually be



Not giving up. Scientists involved in the proposed missions ATHENA (left) and NGO (right) hope to secure a launch spot in 2028.



funded. "Obviously not being selected has a bitter taste, but I think the development of NGO is a must," says Stefano Vitale of the University of Trento in Italy, the principal investigator for LISA Pathfinder, a mission slated for launch in 2014 that will test some of the technology needed for NGO.

Xavier Barcons of the Physics Institute of Cantabria in Spain, who chairs ATHENA's science working group, says he is "very disappointed." With NASA's Chandra observatory and ESA's XMM-Newton satellite probably retiring around the end of the decade, x-ray astronomers may be without a space telescope soon, he points out. The lack of an explanation for the decision is "particularly frustrating," adds Barcons, who would like to know "if the advisers to ESA think it is more exciting to go to Jupiter's moons than to study black holes," one of ATHENA's targets. "We don't know, so we can't even disagree with them," he says.

Vitale says that NGO failed to get the backing of SSAC "for programmatic reasons." NGO would take longer to launch than JUICE, he points out, and ESA has estimated that the extremely complex project would cost some €200 million more. NGO would involve firing laser beams off free-falling test masses inside three spacecraft spaced a million kilometers apart in order to measure distance changes of just a few trillionths of a meter brought about by a passing gravitational wave. Testing the free-falling test masses on Earth is impossible, which is why LISA Pathfinder is needed. Because that mission won't take place until 2014, NGO probably won't launch before 2025, ESA says.

ESA is planning to issue a new call for large missions next year. Vitale says it is important that the winner is picked only after LISA Pathfinder has flown. If the test craft "has problems, then NGO is not a runner anymore, but if it flies well it will be hard not to choose NGO," he says.

Barcons says the ATHENA team will soon start discussions with ESA leaders about the mission's future. But he believes the agency has to return to its practice of approving large missions up to 2 decades in advance. "Going by elimination, as we have done this time, I think makes very little sense," he says, because of the wasted effort for those missions not chosen. In the past, Barcons says, "everyone knew which missions were going to be launched, and so everyone worked towards the same goal."

—EDWIN CARTLIDGE

Edwin Cartledge is a science writer in Rome.

LAB EXPOSURE

Death of California Researcher Spurs Investigation

Local and federal health agencies are investigating the death of Richard Din, a 25-year-old research associate at the Veterans Affairs (VA) Medical Center in San Francisco, California. Din died on 28 April of meningococcal disease, which authorities believe he contracted from exposure to bacteria in the lab where he worked.

Din began complaining of headache and nausea the previous evening, says Harry Lampiris, chief of infectious diseases at the San Francisco VA and the person authorized to speak about the incident. (Din worked in a lab run by Gary Jarvis, an infectious disease researcher.) By the next morning, Din's symptoms had worsened, and friends took him to the hospital. His condition deteriorated quickly, and he died 17 hours after his symptoms first appeared.

Din had worked in a lab that studies *Neisseria meningitidis*, a bacterium that causes roughly 1000 cases of meningococcal disease and 75 fatalities in the United States each year. A 2005 paper in the *Journal of Clinical Microbiology* identified 19 cases worldwide of lab workers infected with *N. meningitidis* between 1985 and 2002; eight of those were fatal. Vaccines have been available since the 1960s for several strains of *N. meningitidis*, but not against so-called serotype B strains, which Din was working with the week before his death. Developing a vaccine against these strains is a goal of the lab where Din worked, Lampiris says.

Tests confirmed the presence of serotype B *N. meningitidis* in Din's blood, Lampiris says. The VA has sent additional samples to the Centers for Disease Control and Prevention (CDC) in Atlanta for genetic tests to determine whether the specific strains Din handled in the lab match those in his blood.

What went wrong is not yet clear. "An internal group investigated the lab and found no evidence of spills, or malfunctions, or problems with the biosafety hood," Lampiris says. "People in the lab felt that [Din] was a hard-working and fastidious person and was following the appropriate precautions."

N. meningitidis spreads by inhalation and is classified as a biosafety level 2 (BSL-2) pathogen. That means any lab procedures with viable organisms should be done under

a hood fitted with air filters, and researchers should wear a face shield or mask and goggles during procedures that could release the bacteria into the air, says Leonard Mayer, chief of the CDC's meningitis lab. "People that work in the lab normally are vaccinated, although with serotype B that doesn't provide any protection," Mayer says. He adds that there's been discussion

in the research community about elevating serotype B to BSL-3, but he doubts any one incident will have much impact on that decision. Din's death should, however, cause other researchers who work with these pathogens to redouble their safety efforts, Mayer says. "We will definitely be discussing this at our weekly lab meeting and reminding people that this is a life-threatening disease."

Lampiris says the lab will remain closed pending investigations by the VA, the San Francisco and California public health departments, and the federal and state Occupational Safety and Health Administration, which could take up to 6 months. Lab members, as well as Din's personal contacts and health workers who were exposed to him, have been treated prophylactically with antibiotics. "Obviously our whole institution is devastated," Lampiris says.

—GREG MILLER



Primary suspect. Exposure to *Neisseria meningitidis* bacteria in a San Francisco laboratory may have killed a 25-year-old researcher.

ASTRONOMY

Venus's Rare Sun Crossing May Aid Search for Exoplanets

It's the last call. Early next month, skywatchers will get their second—and final—chance this century to observe a rare mini-eclipse in which Venus crosses in front of the sun. As seen from Earth on 5–6 June, the silhouette of Venus, as big as a large sunspot, will adorn the sun's orange disk with a fleeting beauty mark. Venus's passages, or transits, occur in pairs spaced 8 years apart every 105 or 122 years. The next transit isn't until 2117.

In past centuries, astronomers and explorers including Captain James Cook observed transits to measure the scale of the solar system. Next month, several scientists plan to study the phenomenon as a benchmark to refine models of exoplanets that pass in front of suns light-years beyond our own.

At the time of Venus's last passage, in 2004, astronomers had detected the transits of only two exoplanets, both the size of Jupiter, by measuring the tiny drop in starlight as the giant orbs crossed in front of their parent stars. Now, thanks largely to NASA's dedicated Kepler spacecraft, they have spotted more than 1000 transiting exoplanets. Kepler researchers say they are on the verge of finding exoplanets the size of Earth or Venus orbiting their stars at comparable distances.

But how can astronomers tell a potentially habitable, water-rich exo-Earth from a hazy and hot exo-Venus? Haze may itself provide a way to distinguish the two types of planets, and clues may come from studying the Venus transit at several different wavelengths, or colors, says Thomas Widemann of the Observatory of Paris in Meudon, France. In 2004, scientists observed the transit in white light, he says. This time, Widemann and colleagues will have nine portable 10-centimeter telescopes at sites including Japan, China, Australia, and Hawaii—some of the best places to view the entire transit (<http://venustex.oca.eu>). Each telescope will observe the transit through a variety of color filters.

The team will focus on the aureole, a thin arc or halo of light that surrounds the black disk of Venus for about 25 minutes just before and again after the planet crosses the face of the sun, a trip that takes about 6.5 hours. The ring is caused by sunlight refracted through the planet's dense upper atmosphere, and the intensity of the ring depends on the den-

sity and composition of Venus's atmosphere, including the presence of a haze layer. "Being able to detect the signature of a haze layer like the one on Venus would tell a lot" about the atmosphere of an exoplanet and shed light on whether the orb has the right stuff for life, Widemann says. Because light absorption by clouds or hazes can hide the presence of biomarkers such as ozone and water vapor, it's critical to know whether an exoplanet has a significant haze layer, he adds.

"We consider that 2004 was essentially a

reflected off Earth's moon. Because different components of Venus's atmosphere absorb different amounts of light at particular wavelengths, the slight drop in sunlight as Venus travels across the solar disk should vary across the spectrum, says Jean-Michel Désert of the Harvard-Smithsonian Center for Astrophysics in Cambridge, Massachusetts, a member of the Hubble project. If it works, the technique—called transmission spectroscopy—could help future missions identify the atmospheric constituents of transiting exoplanets.

"Because we know the atmosphere of Venus, we know what we will have to find with our technique," Désert says. "If our technique fails to retrieve the atmospheric composition of Venus, then we will have to reconsider the [validity of the] method."

Other scientists will use the transit to explore an enduring puzzle about Venus's atmosphere: its superfast rotation. The upper atmosphere rotates around the planet in just 4 days, compared to the 243 days it takes for the planet to spin on its axis.

During the transit, ground-based telescopes trained on the aureole will team up with the European Space Agency's Venus Express spacecraft, launched a year after the 2004 transit, to determine whether temperature fluctuations in the atmosphere vary with time or latitude. That information may offer clues about how solar heating and some kind of atmospheric instability may drive the fast rotation, Widemann says. Another recently launched craft, NASA's Solar Dynamics Observatory, will record the sharpest images of the transit to measure the sun's diameter to unprecedented accuracy.

Even after Venus makes its final passage across the sun this century as observed from Earth, astronomer Glenn Schneider of the University of Arizona, Tucson, hopes to take more data. As seen from Jupiter, Venus will pass in front of the sun on 20 September. Schneider has requested that Hubble attempt to observe that transit by recording the reflected sunlight from the giant planet. Schneider won't know until 15 June if his proposal will get the green light.

—RON COWEN

Ron Cowen is based in Silver Spring, Maryland, and writes about physics, astronomy, and the history of technology.



On the brink. In images of the 2004 transit recorded by a ground-based telescope in South Africa, Venus crawls toward the edge of the solar disk—the most fruitful place for scientific observations.

test, as nobody alive had seen a Venus transit before," says Paolo Tanga of the Lagrange Laboratory of the Observatory of the Côte d'Azur in Nice, France. "In 2012, we are ready for a more detailed characterization, thanks to better models and to the observations previously done in 2004."

One newcomer to transit studies, the Hubble Space Telescope, will attempt to emulate what the Venus transit would look like if it were taking place in a distant solar system. Hubble's optics are too sensitive to stare directly at the sun; instead, it will observe how the transit appears in sunlight

CONDENSED-MATTER PHYSICS

Reprise of First Experiment Casts Doubt on Supersolid Helium

Nine years ago, two physicists reported that ultracold solid helium appeared to flow like the thinnest possible liquid, a bizarre phenomenon akin to rock salt slipping through a sieve. Since then, physicists have debated whether such “supersolidity” exists, with evidence piling up on both sides of the argument. Now, another duo has found further evidence that solid helium doesn’t flow—ironically, by tweaking the experiment that started the controversy in the first place.

“It certainly takes away one of the consistency arguments” for supersolidity, says John Beamish of the University of Alberta in Edmonton, Canada, who studies solid helium but was not involved in the new work.

Supersolidity would be an even weirder version of a bizarre phenomenon in ultracold liquid helium called superfluidity. When chilled below 4 K, helium liquefies; below 2.17 K, the liquid of the isotope helium-4 loses all viscosity and flows without resistance. That flow arises as atoms crowd into a single macroscopic quantum wave. In the 1960s, theorists predicted that solid helium-4, which forms when liquid helium is squeezed to more than 25 times atmospheric pressure, might flow in the same way even though the atoms in it are more or less locked in place. In January 2004, Moses Chan of Pennsylvania State University, University Park, and Eunseong Kim, now at the Korea Institute for Advanced Science and Technology (KAIST) in Daejeon, South Korea, reported signs of such flow (*Science*, 1 July 2005, p. 38).

The two placed a cylinder of a sponge-like, porous glass called Vycor in a can atop a thin shaft. They packed the glass’s nanometer-sized pores with solid helium and set the can twisting on the shaft. When Kim and Chan cooled their “torsional oscillator” below 175 millikelvin, the frequency of twisting shot up. That signal suggested that some helium atoms had let go of their neighbors and were standing still, making the can effectively lighter. To do that, they had to slip through the rest of the helium without drag. Kim and Chan soon spotted the effect in solid helium alone.

Supersolidity has proved controversial, however. In March 2006, John Reppy of Cornell University showed that he could make the signal in an oscillator disappear if he briefly warmed the solid helium to remove defects in its crystal structure—evidence that a per-

fect crystal doesn’t flow (*Science*, 24 March 2006, p. 1693). In December 2007, Beamish used a different technique to show that solid helium becomes stiffer at the same temperature at which flow appears to commence. In a torsional oscillator, such stiffening could mimic flow, although modeling suggests that it can’t fully account for the measured signals. Beamish says a picture has emerged in which solid helium stiffens at low temperatures as threadlike defects in it freeze into place. Atoms might flow along the defects—or not.

Now, Reppy has put a twist on the first Kim and Chan experiment that undermines the case for flow. He and undergraduate student Xiao Mi also used a cell filled with Vycor. But they put it on a more complex oscillator that gyrates at two frequencies instead of one. The “double oscillator” has a weight halfway down its shaft and can twist in two patterns or “modes”: a low-frequency one in which the can and the weight twist in the same direction, and a high-frequency one in which they twist in opposite directions.

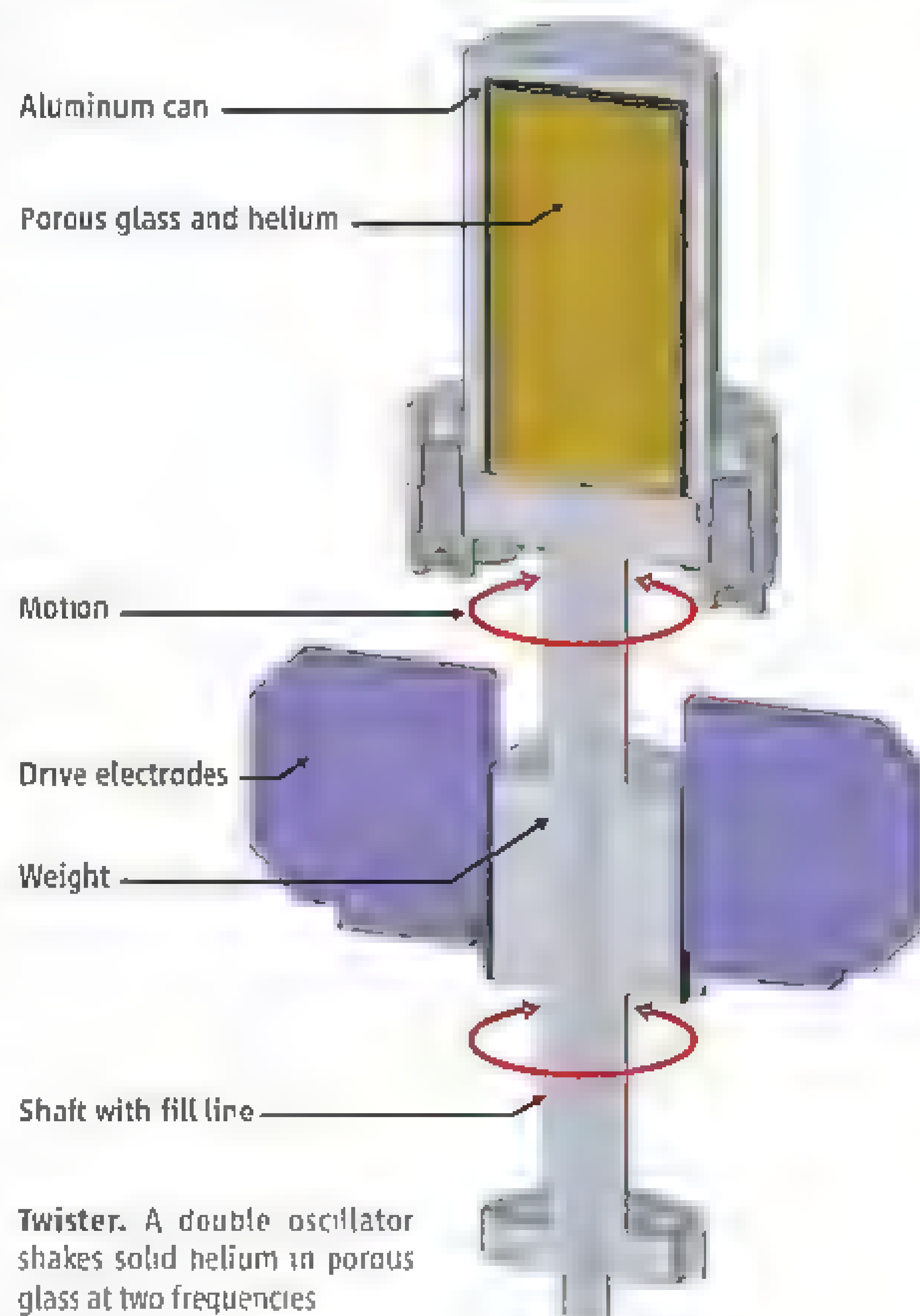
The new experiment, described in a paper in press in *Physical Review Letters*, lets Reppy and Mi compare signals at two frequencies to check for consistency. They can also compare a supersolid signal to a superfluid signal because the Vycor’s pores can also be coated with a film of liquid helium.

For liquid films, Reppy and Mi see self-consistent signals of superfluidity: At a given temperature, the sizes of frequency shifts for the two modes show that the same fraction of atoms has let go. That is exactly what should happen in a superfluid scenario, in which the fraction of the helium that’s become superfluid depends on only the temperature. In contrast, for solid helium at a given temperature, the two frequency shifts suggest that different amounts of helium have let go. That observation clashes with the supersolidity scenario, in which the fraction of the helium that flows should also depend on only the temperature.

Instead, the way the signals vary with frequency suggests they originate in some “dynamical effect” such as stiffening, which can depend on frequency, Reppy says. “At least with Vycor, it doesn’t look good” for supersolidity, he says. Beamish agrees that the simplest explanation is that nothing flows in the solid, although he adds that Reppy hasn’t proved there is no flow.

But Reppy’s experiment has its own consistency issue. The glass is far stiffer than the helium in it, so it’s hard to see how a change in the helium could affect the overall stiffness of the sample cell. “Where does this dynamical effect come from?” Chan says. “That’s what’s puzzling all of us.”

As for the case for supersolidity, some evidence is hard to dismiss, Beamish says. In particular, in November 2010, KAIST’s Kim and colleagues showed that if they put



a twisting oscillator on a rotating platform, the supersolid signal goes down (*Science*, 19 November 2010, p. 1033). That’s what should happen if there is quantum-mechanical flow, as rotation squelches such flow. Chan says he’s “hesitant to say, ‘No, there’s definitely no supersolidity.’” Still, the new data take a chunk out of a cornerstone of the field.

—ADRIAN CHO

Primeval Land Rises From the Ashes

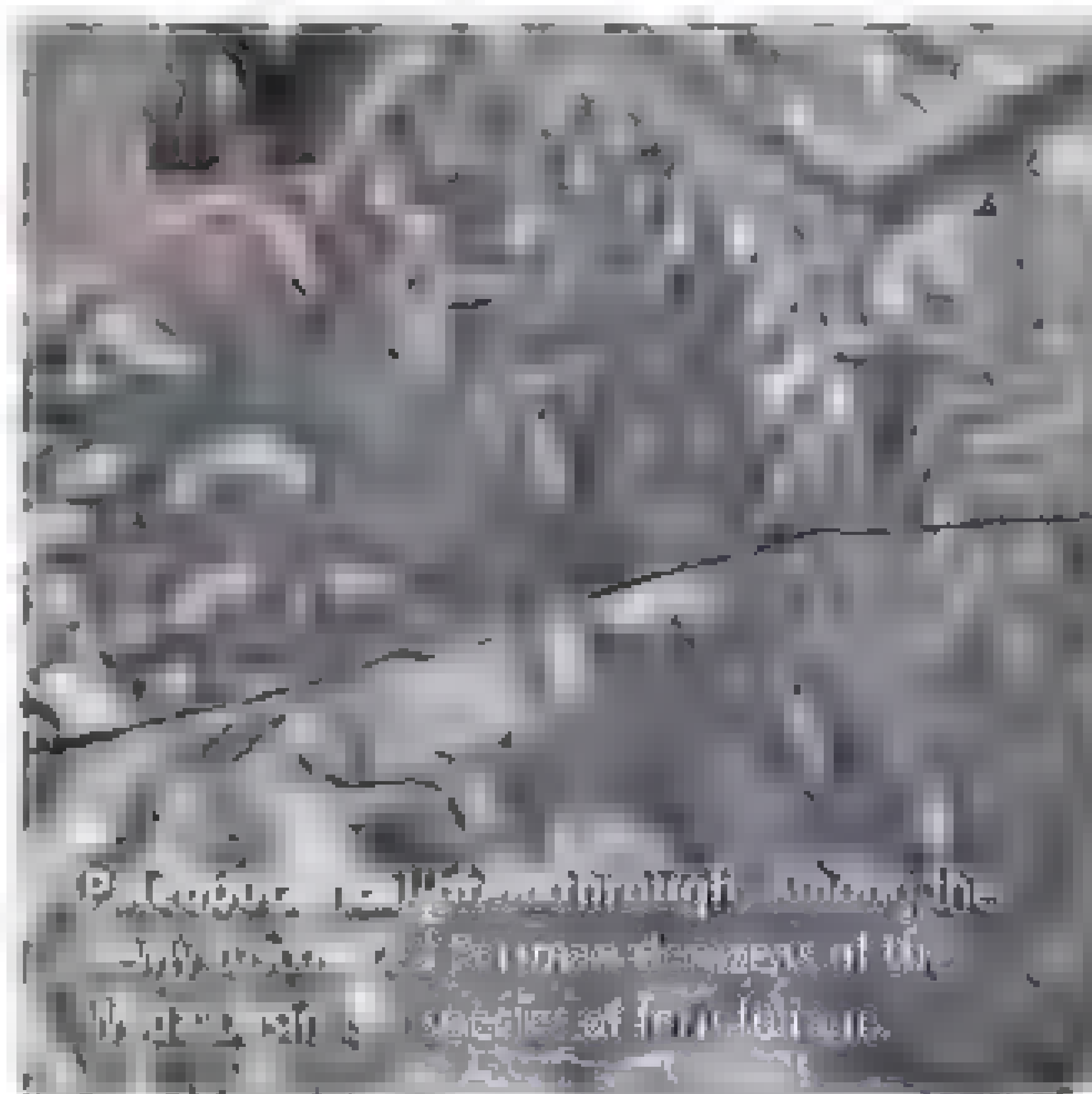
A vegetational Pompeii on peat and coal deposits is shedding light on ecosystem structure and climate during the Permian period

WUDA, CHINA—Black dust swirls across a gutted, wind-whipped land. Here at an open-pit coal mine in Inner Mongolia, sooty dogs skulking nearby cringe at the blasts as coal seams are opened up for extraction. Few landscapes are as bleak as this one, but to Wang Jun, these desolate pits in the Wuda basin are a lost paradise: Sandwiched between the coal layers is the imprint of a lush forest from the Early Permian period. Prowling the mine with a pickax, Wang, a paleobotanist at the Chinese Academy of Sciences' Nanjing Institute of Geology and Palaeontology, is enchanted. "I call this a 'vegetational Pompeii,'" he says.

The forest, whose imprint spans an estimated 20 square kilometers, was preserved when a volcano erupted roughly 298 million years ago. Ash hardened into a 66-centimeter-thick band of chalklike tuff that entombed trunks, branches, and even whole trees. Wang chips away at tuff exposed by mining. In minutes, he and a graduate student have amassed about a dozen fossils—most of which they dismiss as too small and toss aside.

Such selectivity is a luxury, says Wang, who holds that the preservation of Wuda's fossils is nonpareil. Around the world, just a few ancient forests are known to have been preserved under ash. The Wuda tuff flora—the first discovered in Asia—is remarkably

accessible and thick, says Stanislav Opluštil, a geologist with the Institute of Geology and Palaeontology in Prague. Analyzing three patches of forest that together measure 1000 square meters, Wang, University of Pennsylvania geologist Hermann Pfefferkorn, and two colleagues pieced together the forest's rough makeup last February in an article published in the *Proceedings of the National Academy of Sciences (PNAS)*. Their findings illuminate a puzzling group of extinct fern-like plants. Wuda's exquisite preservation enabled the team to "look at the ancient landscape in essentially the same way an ecologist



◀ **Tuff luck.** Wang Jun scored a treasure trove of plant fossils in western China entombed by a volcanic eruption 298 million years ago

examines a modern landscape," says William DiMichele, curator of fossil plants at the Smithsonian Institution in Washington, D.C., who has studied a fossilized forest from the Carboniferous period in an Illinois coal basin.

Wang and colleagues hope to refine their reconstruction of this Permian ecosystem through further field studies. But protecting the remaining tuff bed long enough to study it will be no small feat. This hardscrabble region's economy depends on coal. Mining has already claimed parts of the fossilized forest, while excavations to extinguish coal-seam fires have destroyed other swaths. Wang estimates that only about 10% of the original tuff bed is left. Unless he can convince local officials of the importance of the paleobotanical treasures beneath their feet, the last sliver of Wuda's primeval forest will soon be lost.

Paradise lost and found

In the Early Permian period, the land that is now the Wuda basin lay in the continent of North China, which was separated from South China and other continents by the Paleo-Tethys Ocean. The steamy Late Carboniferous period had just ended, and the supercontinent Euramerica, which encompassed modern-day North America and Europe, had become drier. But a warm, wet climate persisted in North China, and peat accumulated in its sandy soil. In the early Wuda forest, ferns dominated the lower canopy, while exotic, cattail-like *Sigillaria* trees stretched to a height of more than 20 meters.

Life in the forest came to an abrupt end after a distant volcano blanketed the Wuda basin in ash. Reconstructing ancient ecosystems based on plant fossils in most locations has been devilishly complex. Plant materials can travel hundreds of meters by wind or water before lodging in sediment, confounding scientists with a jumble of puzzle pieces. But at Wuda, fossilization occurred in one fell stroke, capturing a snapshot of an ancient era much in the way the eruption of Mount Vesuvius in 79 C.E. froze the Roman city of Pompeii in time.

Wang got his first glimpse of the hidden world of Wuda in 1999 as a postdoctoral researcher. An adviser had passed along a 2-centimeter-long fragment of a cone belonging to the poorly understood plant group Noeggerathiales, an order of small, spore-bearing trees related to ferns. The adviser had found the fossil at Wuda, and Wang visited the site hoping to find a complete cone

CREDITS (TOP TO BOTTOM): MADA HUSTENDAH; NANJING INSTITUTE OF GEOLOGY AND PALAEONTOLOGY

Instead, he came back with abundant fossils of Noeggerathiales leaves and branches.

The next year, at the International Organization of Paleobotany's quadrennial meeting, Wang corralled Pfefferkorn, who had recently published a study on the mysterious plant group. Noeggerathiales plants had been identified in scattered sites in North America, but they remained so poorly understood that some textbooks omitted them altogether. Wuda offered a sudden wealth of material. In 2003, Pfefferkorn and Wang visited Wuda and unearthed fossilized trunks—the first indication that an entire forest lay buried under ash.

The paleobotanists set out to unravel the forest's ecology. Their work became urgent in 2006, when a government coal-fire-extinguishing initiative got under way. Intensive strip mining at Wuda had revealed the layer of tuff for geologists but also exposed coal seams to oxygen, leading to spontaneous combustion. Instead of injecting coolants to extinguish the flames, as is done elsewhere, project directors brought in hundreds of machines to rapidly excavate the remaining coal—and the tuff along with it. Wang and Pfefferkorn collected specimens as fast as they could, but the Permian forest was disappearing before their eyes.

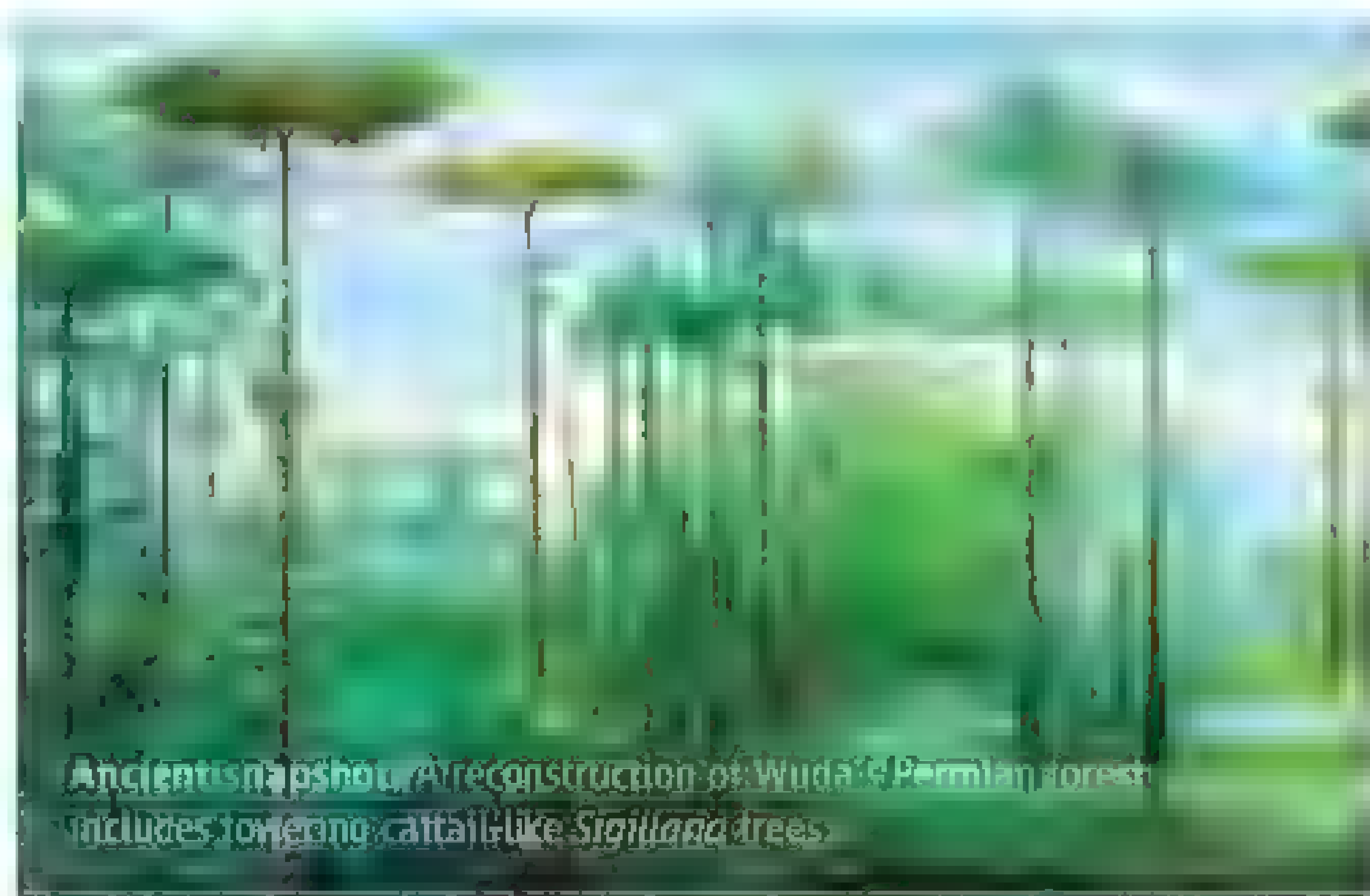
For any hope of protecting Wuda, Wang realized, he would have to make friends in the local government and mining company. In 2007, he had a stroke of luck when Zhang Haiwang, a coal official in the county governing Wuda, got word of the research. That year, Zhang, an ethnic Mongolian who has a passion for fossils, managed to delay the coal-fire project by 2 weeks, giving Wang and Pfefferkorn just enough time to sketch out the forest's basic structure.

To guide their reconstruction, they turned to research on a tuff flora outcrop in the Radnice coal basin in the Czech Republic. The Czech forest is older by some 16 million years and shows little overlap with Wuda at the species level, but a similar diversity of plants colonized both forests. Of more practical use was a mapping method Opluštil pioneered at Radnice in 2002. Borrowing a technique from archaeology, Opluštil had divided the site with a grid that allowed him to catalog fossils precise locations.

Over 8 years of fieldwork, Wang and Pfefferkorn uncovered nearly complete Noeggerathiales specimens. Geologists working in the Illinois coal basin and other sites had hypothesized that it was an upland

plant that grew in isolated patches. In contrast, at Wuda, Noeggerathiales was a dominant wetland tree that covered more than 60% of the forest. “The Wuda material is nothing short of spectacular,” DiMichele says. The discovery of whole Noeggerathiales specimens “solves all sorts of riddles.”

The Wuda fossils will also help researchers reconstruct North China's climate in the Permian period. The fossils show that wet-



Ancient snapshot: A reconstruction of Wuda's Permian forest includes towering, cattail-like *Sigillaria* trees.

lands vegetation had evolved relatively little since the late Carboniferous period—and that some of the plants that occupied Euramerica in that earlier period continued to thrive in North China.

With excavators bearing down on them, Wang and Pfefferkorn worked quickly. As a result, in the *PNAS* paper, they could only paint the lost forest in broad strokes. Last September, they returned to Wuda with Opluštil and other colleagues to scrutinize a small area in more detail. This time they cordoned off an 18-square-meter area of tuff to catalog species and probe aspects of forest ecology missed in the earlier study. Merging the fine-grained and wide-angle views will give a more complete picture, revealing the composition of plants as well as their positions in the forest, Opluštil says.

It didn't take long for that tiny site to be ravaged. Returning to the Wuda basin in March, Wang finds only a broken piece of cord used to stake out the grid. The hills are strewn with garbage. He shakes his head at the pace of mining. “It's faster than I expected,” he says. “If we don't stop it soon, everything will be like this.”

Running out of time

Over a feast in a Mongolian yurt featuring a roasted lamb and vats of steaming milk tea, Wang appeals to local officials to protect the

Wuda outcrop. Zhang, who helped secure research rights in 2007, chimes in. “It won't affect the GDP,” he assures the other officials, who nod. “Eventually there won't be any coal to mine,” one points out. “We have to think about what comes next.”

Wang's proposal is modest. He wants the county government to give geologists a few weeks to work with the remaining tuff flora before gutting it, and to indefinitely protect a patch—roughly 1 square kilometer—for research. The Czech Republic and Germany have protected tuff flora for science. Wang has also urged the government to set up a museum showcasing the fossilized forest. The first specimens, he says, could be an impressive array of Permian trunks compressed in a band of tuff overlooking a power plant.

If local officials consent to another round of research, Wuda may yield more secrets. Wang hopes to find a fossilized cycad plant hidden in the tuff; he has already found the seeds. The site may ultimately divulge which ferns and seed plants covered the forest floor in Permian North China. “There are a lot of questions about what groundcover looked like before grasses had evolved,” DiMichele says. Wuda's flora predates grasses by millions of years. And since North China in the Early Permian had a similar climate and character to Euramerica during the Carboniferous, the Wuda fossils may also shed light on the supercontinent's ecology in an earlier era.

More broadly, Wuda may have implications for our understanding of climate change today. “The relationships between plants and distances between trees can tell us a lot about the climatic changes of the past,” Opluštil says. As Wang notes, “This is also a period when the Earth was changing from an icehouse to a greenhouse.”

The veteran paleobotanist leads a team to a corner of the basin untouched by scientific hands. He stops near the entrance to an abandoned mining tunnel and chips away at tuff. Wang tosses aside a few disappointing fossil fragments—and then stumbles on a specimen that makes him giggle. “Ah!” he cries. He connects two pieces to show a jagged, dark shape, joking that it is the imprint of a head of Chinese cabbage. “This is a new species,” he says.

An explosion booms from just over the next hill.

—MARA HVISTENDAHL

Online

sciencemag.org

Podcast interview with author Mara Hvistendahl (http://scim.ag/pod_6082)



Barge ahead: A new research barge will screen ballast water for invaders.

INVASIVE SPECIES

Researchers Set Course To Blockade Ballast Invaders

As U.S. regulations loom, scientists are working to test new devices that can remove potentially invasive organisms from ships' ballast water

BALTIMORE, MARYLAND—Standing aboard one of the newest research vessels in the United States, Mario Tamburri looks more like a plumber than a marine ecologist. Blame it on the pipes: Bright red, blue, and green tubes twist and turn across the deck of the repurposed barge, Tamburri, who is based in Solomons and directs the Maritime Environmental Resource Center (MERC), part of the University of Maryland Center for Environmental Science, points to a narrow outlet. It's here, he says, that researchers can tap into the barge's precious scientific cargo: its ballast water and the organisms that live in it.

Ballast is crucial to balancing the weight of giant cargo ships as they ply the world's oceans. But as these ships pump millions of liters of ballast in and out of their hulls, they also help spread sometimes microscopic stowaways, including invasive shellfish and algae that have damaged marine ecosystems and local economies worldwide. Blocking these invasions is the goal of Tamburri's science barge, officially christened the *Mobile Ballast Water Treatment Test Platform*. Recently, he and his colleagues began using it to test ship-based technologies—including mechanical filters and chemical weapons—capable of removing most organisms from ballast water. The experiments are part of a larger international effort to prevent ship-

borne invasions. Earlier this year, for example, the United States adopted new rules that limit how many ballast organisms commercial ships can release into coastal waters and require ship owners to install proven water-treatment systems. It's not clear, however, which technologies will meet the new standards—or how researchers can validate the effectiveness of various devices. That's where MERC's barge, and several other floating laboratories like it, come in: "We're here to provide unbiased, independent data to regulators [and] shipbuilders," Tamburri says.

The stakes are high for ecosystems and shippers. Big cargo ships dock in U.S. waters an estimated 90,000 times each year and unload nearly 200 million tons of ballast. Even relatively isolated ports, such as those in the Great Lakes, "are connected to almost every other port on the planet through four or five ship voyages," says David Lodge, an ecologist at the University of Notre Dame in South Bend, Indiana. Those linkages have enabled some organisms to travel far from home. Roughly one-half of the 59 invasive species known to have colonized the Great Lakes since the late 1950s, for instance, likely arrived in ballast tanks, according to a 2007 report to the U.S. National Academy of Sciences's Transportation Research Board. Those invaders include the now-pervasive

zebra mussel (*Dreissena polymorpha*), which has clogged industrial pipes and displaced native animals. Overall, such invasions cost about \$130 million annually in the Great Lakes alone, Lodge and colleagues estimated in a February 2011 study in the journal *Ecosystems*. And saltwater habitats haven't fared much better. Researchers suspect that ballast tanks carried troublesome Asian shore crabs (*Hemigrapsus sanguineus*) to the Northeast coast of the United States, and Asian clams (*Potamocorbula amurensis*) to San Francisco Bay—although it's possible that some invaders simply hitched a ride on the outer hulls of ships (see sidebar, p. 665).

For the past decade, U.S. regulations required most ships entering U.S. waters to flush and refill ballast tanks far offshore, where waters are less likely to harbor organisms that might take hold in coastal seas. But many environmental groups are pressing the government to set tighter standards. In 2011, the U.S. National Research Council asked scientists to examine just how tight such standards would need to be. In other words, how many ballast organisms does it take to start an invasion? The answer, says panelist Gregory Ruiz, a zoologist at the Smithsonian Environmental Research Center (SERC) in Edgewater, Maryland, depends on a number of factors, from the saltiness of the water to the presence of predators. But one thing is certain: "The lower you go, the lower the risk."

That's the thinking behind new U.S. Coast Guard regulations published on 23 March. The rules—which echo standards proposed or adopted by the United Nations' International Maritime Organization and the U.S. Environmental Protection Agency (EPA)—require most ships built after December 2013 and planning to enter U.S. waters to install

CREDIT: MARITIME ENVIRONMENTAL RESOURCE CENTER

an approved, onboard ballast-treatment system. The aim is to thin, but not necessarily eliminate, the aquatic herds living in ballast water. The rules require culling the biggest hitchhikers—such as most mussel larvae and crustaceans—down to nine living individuals or fewer per cubic meter of water.

The rules don't specify which treatment systems ship owners must use. But the best candidates rely on a combination of approaches, according to a 2011 EPA report. Many start with brute force, using mesh screens to filter out bigger organisms or even spinning the water to flush them out. Then the systems typically go for the kill, using a toxic chemical such as chlorine to poison survivors. Other systems bombard organisms with damaging ultraviolet rays (UV) or suffocate them by removing oxygen. Whatever the approach, ballast-cleaning equipment is expected to be expensive, costing from \$1 million to \$3 million per ship. As a result, shippers and regulators want to find out which technologies really work—a task that has fallen to scientists such as Tamburri. "There's going to be a real push" for rigorous testing, he says.

The MERC team, for instance, plans to use funding from private and public sources to screen about three privately developed treatment systems per year aboard their barge. Last month, the researchers installed their first prototype, a system that pairs filtration with UV rays. Over the next month, the researchers will see how it cleans nearly 300 metric tons of ballast water that the barge can store in one of its dual deck tanks. The results may determine whether the equipment receives the Coast Guard's approval for wider use. And later this year, a tugboat is scheduled to push the barge around the Chesapeake Bay, where the scientists will test how the equipment treats water with a range of salinities, including brackish and fresh water. "The more sources you can pull water from, the more confident you are that water from around the world can be treated successfully," says Nick Welschmeyer, who studies plankton at Moss Landing Marine Laboratories in California. He also serves as chief scientist of the Golden Bear Facility, a similar testing platform based in San Francisco Bay. A third U.S. effort, called the Great Ships Initiative, operates in the Great Lakes.

All three U.S. facilities and their European counterparts, however, face sizable technical obstacles. One of the most fundamental is that larvae and algae aren't easy to count. To get a sample representative of an entire ballast tank, for instance, technicians need to tally tiny organisms living in as much as 7 cubic meters of water (about the volume of seven

A Foul Problem

Not all potential invaders lurk inside cargo ships. Many live in plain sight, clinging to vessels' outer hulls. From mussels to barnacles to algae, studies suggest that such "hull-fouling" organisms could pose an invasion threat that is "equally strong if not stronger" than that from ballast creatures, says zoologist Gregory Ruiz of the Smithsonian Environmental Research Center in Edgewater, Maryland.

So far, however, regulators haven't addressed the hull-fouling issue, in part because it's not clear how boats can effectively get rid of their clinging hitchhikers. Researchers are also still trying to understand which hull organisms can withstand long sea journeys that are fraught with extreme swings in temperatures and salinities.

To replicate such stresses, Louise McKenzie, a postdoctoral researcher in Ruiz's laboratory, has been subjecting small clutches of hull-fouling animals, including blue mussels (*Mytilus edulis*) and tunicates called sea grapes (*Molgula manhattensis*), to simulated voyages.

First, she places the organisms in rows of tanks. Then over hours or days, she changes the temperature and salinity of the water, replicating the fluctuating conditions at sea. She recently took her passengers on a faux voyage from New York to Melbourne, Australia; to simulate passing through the Panama Canal, McKenzie plunged the animals into fresh water, then back again into a salty solution. Sometimes, McKenzie says, the toll of such shifts is obvious just by sniffing the air in her laboratory: "It can be a bit smelly if a few things have died."

Researchers hope that McKenzie's study and others like it will help them identify shipping routes with a high risk of carrying organisms overseas. Others, meanwhile, are developing new tools to keep creatures off hulls, such as nonstick surfaces and improved cleaning methods. But one thing is clear, says Mario Tamburri, director of the University of Maryland's Maritime Environmental Resource Center in Solomons: "We're only solving half of the problem with ballast-water treatment." —D.S.

average-sized hot tubs), Tamburri and colleagues reported in 2011 in *Environmental Science & Technology*. Welschmeyer says the process can be "so cumbersome it hurts."

That pain was on display recently aboard the MERC barge. Darrick Sparks, a member of the SERC team, sat in a cramped trailer peering at dozens of small animals called rotifers through a microscope. To determine if the creatures were alive or dead, he used an ice pick–like instrument to poke idle rotifers to see whether they moved.

Scientists like Welschmeyer and Tamburri are working on tricks to make the process easier. For instance, measuring how much chlorophyll, a pigment common in many photosynthesizing organisms, is in a water sample can give officials a reasonable guess of the abundance of algae. It's the "whoa, that is way too green" to meet regulations approach, Tamburri says.

Such techniques may be critical if the U.S. government follows some states in further tightening ballast standards. California, for example, has adopted tougher rules that are slated to enter into full force in 2020, and environmentalists want the U.S. and other nations to follow suit.

But many in the shipping industry are pushing back, citing a 2011 EPA report that concluded that no current ship-based technology can meet California's tighter standards. The struggle highlights the need to think ahead, says Thom Cmar, an attorney with the Natural Resources Defense Council in Chicago, which is pushing for tighter limits. The technologies shipbuilders choose could stay on vessels for decades, he notes, so "the time is really now, before the vessels have started installing those systems, to get it right."

—DANIEL STRAIN

Daniel Strain is a journalist in Washington, D.C.



Cling-ons. Divers survey marine organisms (inset) clinging to a vessel's hull.



Specimens. Mateo with a display of *Triatoma infestans*, the bug that carries the Chagas parasite

CHAGAS DISEASE

With Novel Paint, Chemist Aims To Vanquish the *Vinchuca*

Spanish chemist Pilar Mateo invented a clever way to package insect-control agents in paint; after a decade of trying, she's persuaded Bolivia to give it a test

URUNDAYTI, BOLIVIA—The old woman walks slowly toward the car with a toothless smile. “*Doctorita*,” she says. Pilar Mateo jumps from the SUV, launching a hug so tight the frail elder looks like she might break in two. As they walk back toward the cluster of faded colorful mud homes, a crowd emerges to greet *la Doctorita*, a Spanish chemist who invented a remarkable insecticidal paint that covers the village’s buildings. Mateo is one step away from sainthood for this region’s indigenous Guarani people. “She made the bugs disappear,” the old woman whispers in my ear.

Urundayti lies in the heart of the Gran Chaco—a vast dry forest region in Bolivia, Argentina, and Paraguay that’s ground zero for Chagas disease, endemic in the Americas. Infection often begins with a bite from a large beak-nosed bug known as the *vinchuca* (*Triatoma infestans*) that emerges at night to feed. Through its feces, it transmits the *Trypanosoma cruzi* parasite that causes Chagas, a slow-developing illness that can lead to extreme lethargy and even organ failure.

Thirty years ago, the *vinchuca* infestation covered 628 million hectares of South America. A continent-wide effort of massive and repetitive insecticide application has whittled that zone down to 12% of the initial area. (Worldwide, the disease affects more than

8 million people.) Bolivia has the globe’s highest Chagas infection rates, and the Bolivian Chaco remains the epicenter of transmission, with more than 80% of homes still infested in many villages. Ranging between 150 and 300 meters above sea level, the Chaco is prime *vinchuca* terrain because of its warm, dry climate. Entrenched poverty is partly complicit. The vector makes its home in the walls of mud or adobe huts and feeds on farm animals like the ubiquitous goats and chickens.

Research shows that shoddy and sporadic fumigation has resulted in a pesticide-tolerant bug population. “This region presents such deep challenges that traditional pesticide application methods don’t seem capable of overcoming them,” says David Gorla, director

of the Regional Center for Scientific Investigation and Technological Transfers of Anillaco, La Rioja (CRILAR) in Argentina and one of the continent’s primary *T. infestans* experts.

Mateo believes that her patented paint Inesfly 5A IGR, sold through her company, Inesba in Valencia, Spain—is the solution. Studies published in 2008 and 2009 show it is effective for four to 20 times longer than traditional pesticide applications, and its microcapsule packaging of active agents reduces environmental and toxic risks.

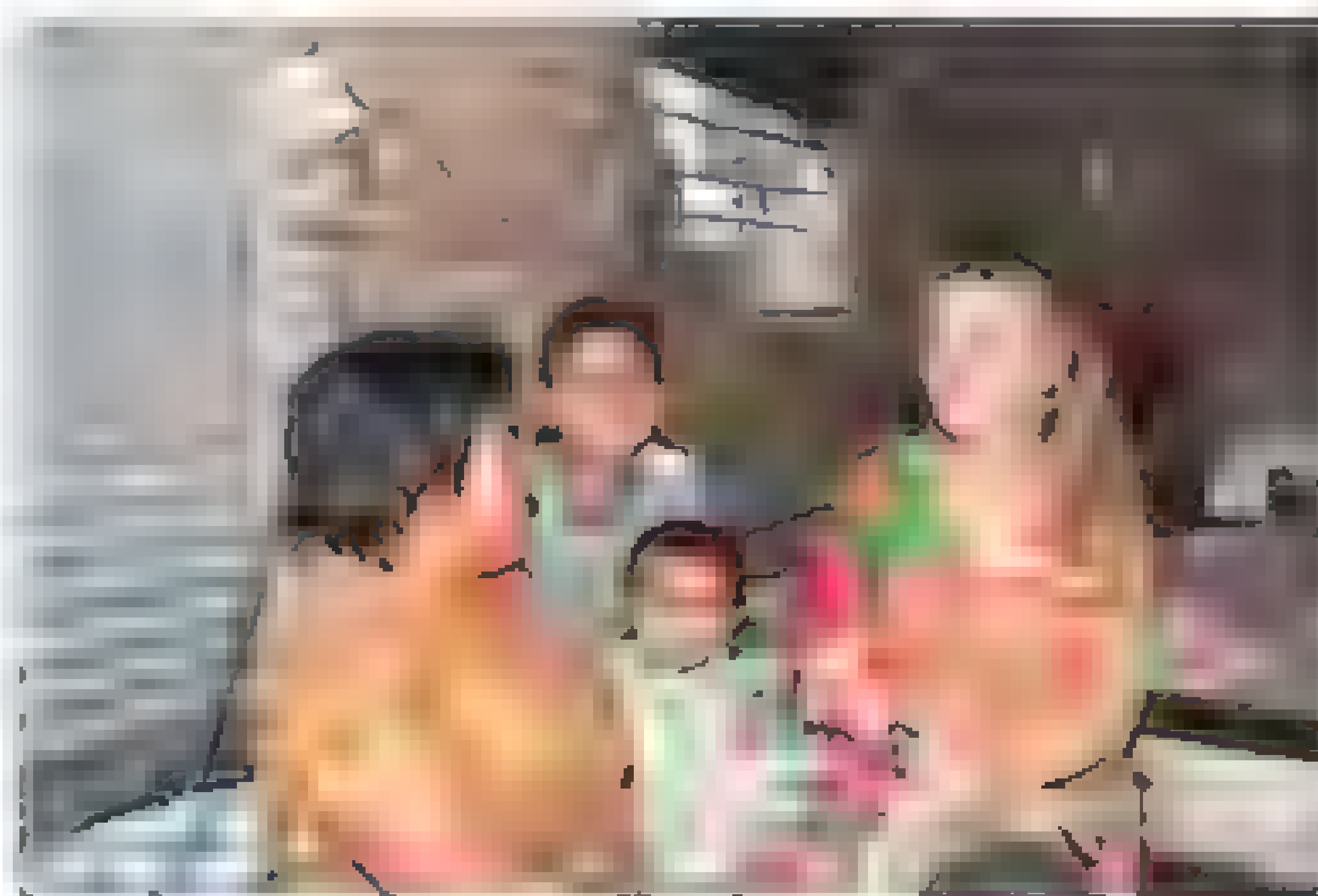
For the past decade, she’s been trying to paint her way across the Gran Chaco region. But adoption of Inesfly has been slow, partly because it lacks the approval of the World Health Organization’s Pesticide Evaluation Scheme (WHOPES), the gateway to biocide use in the developing world. Mateo’s go-it-alone approach, some say, has been a factor, too. No large pharma company is helping escort Inesba through its trials; Mateo has ruled out such partnerships.

But Inesfly now seems poised for a debut. A version that targets the malaria-carrying *Anopheles gambiae* mosquito has cleared two of the four WHOPES stages in Africa, where it will soon undergo a test of its ability to reduce malaria infections. And after a decade of obstacles, WHOPES evaluations of the anti-Chagas formula may begin here in Bolivia within the year.

The invention

Mateo’s odyssey began in Spain 2 decades ago when she read about a local hospital being closed because of a bug infestation. The young Ph.D. in chemical engineering and daughter of a paint factory owner had a thought: If walls are homes for many common pests, then walls could also be a first line of defense. Her initial attempts at mixing pesticides and water-based paint were disastrous. Residual activity was null, and toxic chemicals leached. Mateo wondered whether coating the active ingredients in a nanocapsule would enable slow release and minimize health risks. In 1995, she patented the “microcapsule” packaging, and Inesfly was born. “I thought I’d make a fortune ridding wealthy people’s homes of cockroaches and flies,” Mateo says.

But that changed when, in 1998, a Bolivian doctor named Cleto Caceres showed up on her doorstep in Spain. “My entire village is dying of a disease called Chagas. Can you



Hot zone. With a family in Bolivia’s Chaco region.

CREDITS: SILVINA DEL ISOLA

help?" Mateo recalls him saying. She hesitated. "I didn't make the paint to save lives." But Cáceres proved convincing. A year later, Mateo traveled to his Chaco homeland and was stunned to see that the Guaraní were so tormented by the *vinchuca* in their homes that they slept outside to escape the nightly feeding frenzies. Mateo, now 53, remembers thinking, "My life has changed forever."

When Mateo arrived in Urundayti in 2006, she recalls, "the WHO had said it would be impossible to eliminate the *vinchuca* here." The village had been fumigated for several years, but the *vinchuca* kept returning. Mateo and residents painted home walls, fences, and community buildings later that year. The bugs left, and Urundayti is still *vinchuca*-free. Since 1998, approximately 7000 houses in the region have been painted with Inesfly. According to evaluations by SEDES Santa Cruz, the local office of Bolivia's health ministry, areas formerly registering 90% infestation levels have gone to zero vector presence, often with one paint application. No painted communities have suffered reinfestation, the reports say.

No side effects or environmental complications have been reported, says Abraham Gemio, a scientist who joined Mateo's company in 2006 and now manages its new paint projects and postpaint evaluations. "We can make history here in the Chaco," says Gemio, arguably Bolivia's most knowledgeable *T. infestans* scientist, who helped established Bolivia's national Chagas program in 1980 and led it for 25 years before joining Mateo's firm.

"The great advantage of this paint is that it solves the most important shortcomings in vector-control programs such as short residual activity," says CRILAR's Gorla, who has published papers on the paint in *Parasites & Vectors* and in the journal of the Oswaldo Cruz Institute in Rio de Janeiro. In natural conditions, Inesfly has a kill rate of 100% for at least 6 months and 22% for 34 months after application, according to his research.

A key to the paint's effectiveness, researchers say, is the microcapsules' inclusion of insect growth regulator (IGR) compounds such as pyriproxyfen and diflubenzuron, which prevent the insects from developing fully. These have no effect on humans but attack insects' young and eggs, which insecticides rarely reach. As a long-term agent, IGR is better than pesticides alone, because it does not select resistant organisms for survival, says Jorge Méndez Galván, former director of vector-transmitted diseases for the Mexican government. João Carlos Pinto Dias, a renowned Chagas researcher at the Oswaldo

Cruz Institute with half a century of experience, adds that painted homes lead to "greater self-esteem among the poor and improved [living] conditions."

Into the labyrinth

With so many fans, why is Inesfly still relatively unknown? "In international meetings of Chagas experts, there's a general feeling of skepticism," says one expert who requested anonymity. "Everyone asks: If it works so well, then why hasn't she gotten [WHOPES] approval?"

"The lack of approval is a commercial problem," says Javier Lucientes Curd of the University of Zaragoza in Spain, who's been studying Inesfly's potential for containment of insect-borne animal diseases for years.

According to Mateo, the reasons are numerous. First, WHOPES is a complex labyrinth that requires rigorous testing of each formulation at specified centers. Without a host country's support—which Mateo lacked until recently—it is hard to launch a WHOPES review. And each evaluation can cost millions—a reach for Mateo's 12-person company, which operates with \$1 million annually.

Inesba rarely charges more than cost of production for the paint (\$100 covers a standard Chaco house). The company earns most of its income from other products such as Inesba's joint venture with Dow Chemicals Spain to microencapsulate agricultural pesticides, and a lice shampoo.

Revenues underwrite Inesfly, S.L. in Spain, an independent company that researches new uses for microcapsules. Inesba also supports Mateo's foundation, Science and Knowledge in Action, which funds women's empowerment and community-development projects worldwide. Though Mateo says she was apolitical earlier in life, she's now a born-again revolutionary. She readily lambastes what she calls the elite, profit-driven pharmaceutical world and says that "the real solution" for eradicating diseases of poverty such as Chagas is to end global inequality—not distribute paint.

Chris Schofield, coordinator for the European Community Latin America Network for Research on the Biology and Control of Triatominae (ECLAT) and honorary senior lecturer at the London School of Hygiene and Tropical Medicine, praises Mateo as "an excellent formulation chemist who has developed a splendid technology." Yet he sees a risk

in her anticorporate stance: "It's like if you develop a new medicine that you know works. Unless you partner with a large company with the resources to make it available throughout the world, it's going to stay unknown."

Mateo has focused on proving the paint's safety, obtaining relatively benign toxicity ratings from laboratories in Latin American and Europe. But she says that for more than a decade, the Bolivian health ministry refused to expand the Inesfly painting test area. "We can't go skirting international guidelines just because the paint seems like a good idea," says Max Enriquez, director of Bolivia's Chagas program, who says only WHOPES approval will lift his doubts.

Mateo was incensed. Frustrated by what



Mixing it up. Mateo and colleagues Franz Espejo (left) and Johny Bauda prepare paint for use against *vinchuca* (below).

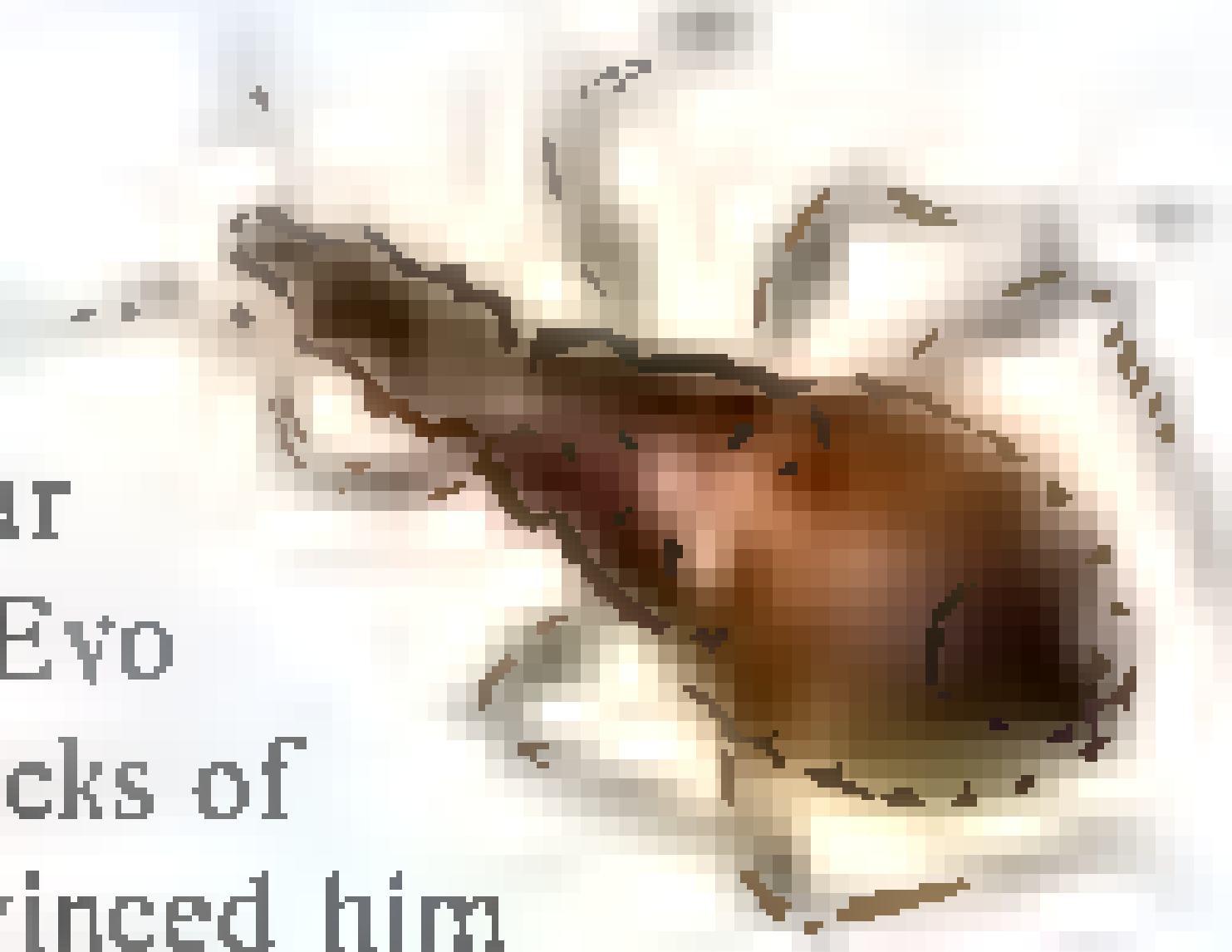
she calls "two-legged pests," she took her case last year directly to President Evo Morales. Armed with stacks of scientific data, she convinced him within an hour of the paint's worth. He has now authorized every indigenous Guaraní home in the Chaco to be painted—and has demanded that the health ministry facilitate the initiation of WHOPES trials.

With this decision, the last piece of the WHOPES puzzle—a national sponsor for *vinchuca* control—has fallen into place. World Chagas experts and financial backing have been waiting in the wings: The trials, set to begin this year, will be led by Pedro Albajar Viñas, coordinator of the Chagas program of WHO's neglected tropical diseases unit, in collaboration with ECLAT, Barcelona's Hospital Vall d'Hebron, and Spain's development agency, AECID, Mateo says.

Pinto Dias is deeply pleased: "I hope with all my heart that this product soon becomes available. ... As a witness to its effectiveness, I truly wish that others have a chance to use this important tool."

—JEAN FRIEDMAN-RUDOVSKY

Jean Friedman-Rudovsky is a journalist in La Paz, Bolivia.



LETTERS

edited by Jennifer Sills

Conservation Concerns in the Deep

IN THEIR PERSPECTIVE “A DIVE TO CHALLENGER DEEP” (20 APRIL, P. 301), R. A. Lutz and P. G. Falkowski highlight the exciting advancements in engineering that allowed director James Cameron to dive to Challenger Deep, the deepest point on Earth. As Lutz and Falkowski point out, ever-improving submarine technologies are broadening scientific research capabilities in the planet’s largest and least-explored ecosystem—the deep sea. Cameron’s historic dive, and the international attention it garnered, has reinvigorated humanity’s fascination with this otherworldly ecosystem. Missing from most reports, however, is that although reaching the deepest points on Earth requires great feats of engineering, the deep sea is not beyond the touch of human activities.

At depths close to that of Challenger Deep, bovine DNA was found in the guts of scavenging amphipods, presumably from ship galley dis-

cards (1). Moreover, large-scale disposal of refuse and extraction of resources such as fishes, hydrocarbons, and soon minerals currently threaten this ecosystem, and changes in ocean temperature, oxygen availability, and pH

are expected to have increasing impacts in coming decades (2). Thus, when considering future research objectives, it is important to consider not only the scientific and natural history gains to be made, but also the conservation concerns that are both notable and accelerating



Hironella gigas. Collected in the Challenger Deep.

NextGenVOICES

Experiences That Changed Us:
Last Call

Did a particular person, conversation, reading, or event inspire you to pursue science or change your course of study?

Submit your story to NextGen VOICES by 18 May!
Go to <http://scim.ag/NextGen3> and answer this question:

Describe a specific experience and how it changed your science, training, or career goals.

Members of the *Science* editorial team share their memorable moments:

Career-wise, my “Eureka!” moment didn’t arrive until the job posting for my current position, Associate Editor at *Science*, arrived in my inbox one morning. I had never been fascinated by my research project and I often found myself in seminars or journal clubs thinking about how much more interesting that particular line of research seemed. I also was tiring of the hours spent in front of the flow cytometer, the waiting for various crosses of mice to bear the right genotypes, the experiments that didn’t work due to technical problems—all the mundane day-to-day activities of research science. And so at that moment I decided: Not only am I qualified to be an editor, but it would be the perfect way to stay immersed in research science while not doing any benchwork myself. If not now, when? And so I dropped everything and talked to anyone who knew anyone who was an

editor. I prepared my application and then practiced for my interview. The rest is history. But the lesson learned was that sometimes you just need to take that leap.

Kristen L. Mueller

During my junior year, I was fortunate enough to be chosen by Jim Ammerman to work in his laboratory as part of Texas A&M University’s Research Experience for Undergraduates summer program. Being an undergraduate in a research lab mostly means grunt work. I washed a lot of glassware. I made many, many liters of growth media to fill many, many petri dishes. But midway through the program came an opportunity to collect seawater from Galveston Bay. Jim suggested that I bring back a liter of water and learn how to do bacteria cell counts from an environmental sample.

The water was gray and had an odd smell. After applying a fluorescent dye that bound to DNA to the filter, I poured the water through to a low the filter to catch the bacteria. Then I put the filter on a microscope slide and had a look. What I saw through the microscope were hundreds of pin points, shining like stars in a night sky. I almost couldn’t believe that the muddy, gray water contained so many living organisms. And we know probably fewer than 1% of all bacteria species, so almost every one of those pin points was a mystery to science. That was my “aha!” moment, when I was sure that I wanted graduate school and that I wanted to study bacteria. The scope of discovery was enormous if only people were willing to take a second look at the almost-impossibly small. Trista Wagoner

Deadline for submissions is 18 May. A selection of the best responses will be published in the 6 July issue of *Science*. Submissions should be 250 words or less. Anonymous submissions will not be considered.

in the farthest reaches of our planet. Further exploration of the type championed by James Cameron will lead to greater understanding of species interactions and geochemical cycling in the deep sea. With this ever-growing knowledge, we must protect and manage deep-sea resources in a sustainable manner, and in doing so avoid destruction borne from ignorance like that on the imaginary planet Pandora in Cameron's other recent success—the film *Avatar*.

AARON C. HARTMANN* AND LISA A. LEVIN

Center for Marine Biodiversity and Conservation, Scripps Institution of Oceanography, La Jolla, CA 92043, USA

References

1. L. E. Blankenship, L. A. Levin, *Limnol. Oceanogr.* **52**, 1685 (2007)
2. E. Ramirez-Llodra *et al.*, *PLoS One* **6**, e22588 (2011)

Presumed Guilt in the Anthrax Case

IN REVIEWING MY BOOK *AMERICAN ANTHRAX*, (“Have we ‘met the enemy?’,” 3 February, p. 540), D. A. Relman referred to a “number of positive samples from a clandestine effort

to assess a possible overseas source of the spores” used in the 2001 anthrax letter attacks. In samples taken in 2004 from the overseas site, understood to be in Kandahar, DNA tests on three samples gave mixed results, and none yielded viable *Bacillus anthracis* [supplemental documents for (1)]. Subsequently, 1254 more samples were collected from the same site. None yielded viable *Bacillus anthracis*, and all DNA tests were negative. The committee judged “these data to be inconclusive” [(1), p. 67]. In my book, I gave a balanced account of the facts and agreed with the committee's conclusion.

JEANNE GUILLEMIN

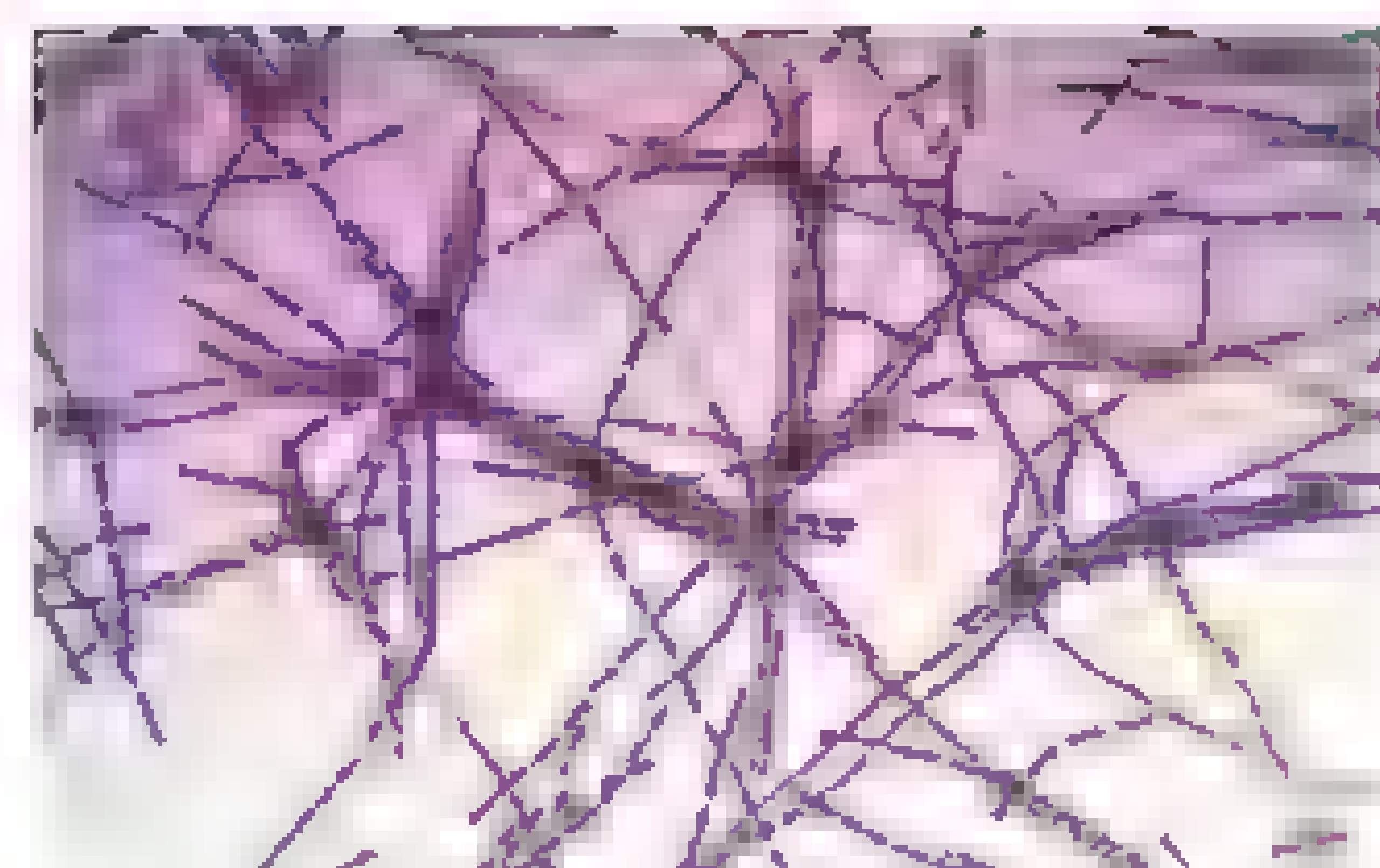
Security Studies Program, Massachusetts Institute of Technology, Cambridge, MA 02139, USA. E-mail: jeg@mit.edu

Reference

1. National Research Council. “Review of the scientific approaches used during the FBI's investigation of the 2001 anthrax letters” (National Academies Press, Washington, DC, 2011). www.nap.edu/catalog.php?record_id=13098

Response

IN MY REVIEW OF *AMERICAN ANTHRAX*, I sought to highlight the valuable contributions of this book to the public understanding of this complex and controversial case,



Bacillus anthracis

as well as the book's shortcomings. It is true that Guillemin makes no explicit statement about her position regarding the guilt or innocence of Ivins. However, statements such as, “the FBI had solid scientific proof that the spores in the anthrax letters matched those in a flask, labeled RMR (Reference Material Receipt)-1029, that was in Ivins' keeping at the Army's medical institute at Detrick” (p. xxii), and “a criminal—either Ivins or someone else—had used the institute's Ames anthrax spores to commit murder” (p. 251), misrepresent the strength of the scientific evidence that points to this flask as the source of the spores in the letters (and by infer-



Learn how current events are impacting your work.

ScienceInsider, the new policy blog from the journal *Science*, is your source for breaking news and instant analysis from the nexus of politics and science.

Produced by an international team of science journalists, *ScienceInsider* offers hard-hitting coverage on a range of issues including climate change, bioterrorism, research funding, and more.

Before research happens at the bench, science policy is formulated in the halls of government. Make sure you understand how current events are impacting your work. Read *ScienceInsider* today.

www.ScienceInsider.org

ScienceInsider

Breaking news and analysis from the world of science policy



THE SCIENCE TECHNOLOGIES

Proteomics

Spot-on Protein Microarrays

An Old Proteomics Tool Learns New Tricks

In This Issue

When it comes to 'omics-inspired bioscience tools, next-gen DNA sequencing is the undisputed king. The previous champ was the DNA microarray, with the protein array its logical successor. Yet while DNA arrays achieved their potential, protein arrays never really took off, owing largely to the fact that, while every DNA oligo behaves more or less identically, the same cannot be said of proteins. They're also harder to synthesize, purify, and stabilize. Still, to paraphrase Mark Twain, the rumor of protein array's death has been greatly exaggerated. Today, new array formats and strategies have made the protein microarray a viable and growing tool for biomarker discovery, interactome research, functional genomics, and more.

See full story on page 748.

Upcoming Features

Digital imaging June 8

Nanotechnology July 6

Proteomics, Clinical Diagnostics August 31

ence, Ivins and/or the Army's institute at Fort Detrick, Maryland). A variety of weaknesses in the FBI's scientific investigation are discussed in detail in the NRC Report (1) (issued by a committee on which I served as vice chair), but unfortunately, these weaknesses are not given much coverage in her book.

DAVID A. RELMAN

VA Palo Alto Health Care System, Stanford University, Palo Alto, CA 94304, USA. E-mail: relman@stanford.edu

Reference

1. National Research Council., "Review of the scientific approaches used during the FBI's investigation of the 2001 anthrax letters" (National Academies Press, Washington, DC, 2011); www.nap.edu/catalog.php?recordid=11098

Letters to the Editor

Letters (~300 words) discuss material published in *Science* in the past 3 months or matters of general interest. Letters are not acknowledged upon receipt. Whether published or not, all letters are subject to editing for clarity and style. Letters submitted, published, or posted elsewhere in print or online will be disqualified. To submit a letter, go to www.submit2science.org.

CORRECTIONS AND CLARIFICATIONS

Editors' Choice: "Bacteria hedge their bets" and "No fix for broken ends" (6 April, p. 13). The image that accompanies "Bacteria hedge their bets" should have instead accompanied "No fix for broken ends."

Science Prize for Inquiry-Based Instruction: "Adapting to osmotic stress and the process of science" by B. J. Gasper *et al.* (30 March, p. 1590). The first (CCU/TUES) NSF grant number was incorrect; it is 0941921. The number has been corrected in the HTML and PDF versions online.

Reports: "The geometric structure of the brain fiber pathways" by V. J. Wedeen *et al.* (30 March, p. 1628). In (26), the book title should be *Three Dimensional Geometry and Topology*. In (27), the first two authors should be spelled "C. W. Misner, K. S. Thorne."

Review: "The control of the metabolic switch in cancers by oncogenes and tumor suppressor genes" by A. J. Levine and A. M. Puzio-Kuter (3 December 2010, p. 1340). In the third column on page 1342, the phrase "which lowers the intracellular concentrations of fructose 2,6 biphosphatase (FBPase)" was incorrect. It should be "which lowers the intracellular concentrations of fructose 2,6 biphosphate." The TIGAR protein decreases the levels of the metabolite, not the enzyme.

Reports: "Relating introspective accuracy to individual differences in brain structure" by S. M. Fleming *et al.* (17 September 2010, p. 1541). The authors have detected a minor programming error in their original analysis of brain structure. Thus spatial coordinates for a subset of results should be corrected by ± 2 mm (see the table below for the correct coordinates). No other aspects of their results or interpretations are affected.

Contrast	Region	Peak voxel reported in paper (MNI)	Corrected peak voxel (MNI)
GM positive A_{acc}	Right BA10	24, 65, 18	26, 66, 16
GM-positive A_{acc}	Precuneus	6, -57, 18	8, -57, 19
WM-positive A_{acc}	Anterior corpus callosum	2, 26, -2	2, 27, -2

MNI, Montreal Neurological Institute; GM, grey matter volume; WM, white matter (fractional anisotropy); A_{acc} , a quantitative measure of metacognitive accuracy.

A new way to look at science

The new *Science* Reader App for iPad® from AAAS puts *Science* in your hands, wherever you go. Read abstracts, career advice, and highlights from our newest journals, *Science Signaling* and *Science Translational Medicine*. Plus, AAAS members can access full text articles from *Science*.

Visit iTunes App StoreSM or content.aaas.org/ipad for details.



NEUROSCIENCE

Recalling Space and Time

Laura Lee Colgin

Vincent van Gogh's *Memory of the Garden at Etten* vibrantly depicts a recollection from his boyhood of his mother and sister walking through a garden. This painting of a past experience remembered is as vivid as any of his paintings of his perceptions of the world in front of him. Certainly a large part of the richness of human existence comes from memories. But how do we record and relive our experiences in such vivid detail? This question is at the center of Michael E. Hasselmo's *How We Remember: Brain Mechanisms of Episodic Memory*.

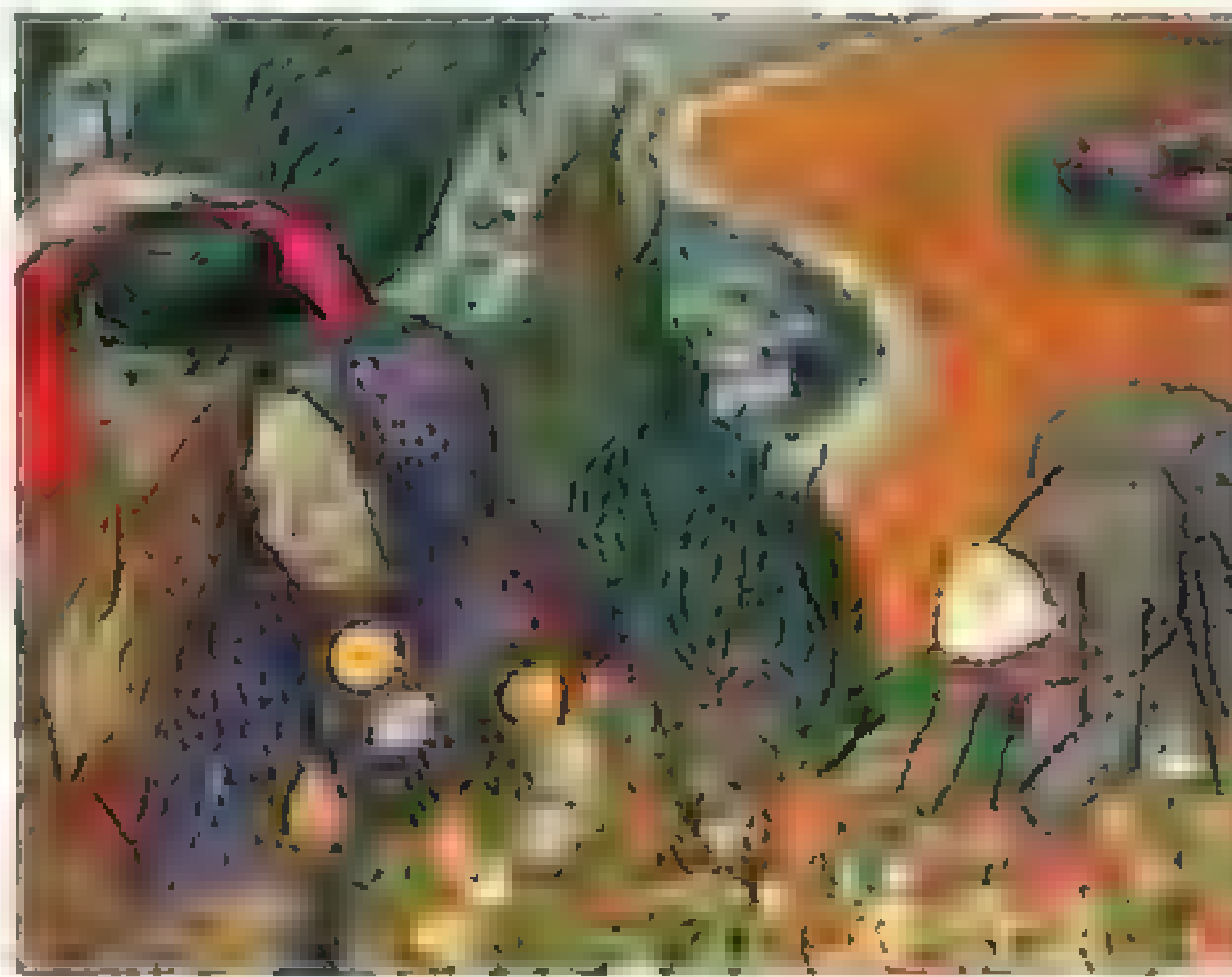
"Episodic memory" refers to "the memory of specific events occurring at a specific place and time." Hasselmo (a neuroscientist at Boston University) describes his own episodic memory of meeting Henry Molaison (HM), a patient whose hippocampus and entorhinal cortex had been surgically removed years earlier in a last-ditch attempt to treat his epilepsy. After his surgery, HM was unable to form new memories of ongoing events. Hasselmo describes how testing HM and other patients led to the discovery that the hippocampus and entorhinal cortex are essential for the formation of episodic memories and how this has since been corroborated by many other studies in humans.

Although human studies have revealed the anatomical structures involved in episodic memory, they have provided much less information about how memories emerge from individual brain cells (neurons). It is not possible to observe the activity of individual neurons in healthy humans, so much of what we know about how neurons code memories comes from recording their activity in the hippocampus and entorhinal cortex of rats. However, many researchers believe that episodic memory is a capacity unique to humans, raising the question of whether rat studies are relevant.

Hasselmo views episodic memory not as a unique feature of human existence but instead more generally as "a detailed repre-

sentation of a complex spatiotemporal trajectory on which a range of detailed items and events can be fastened." He describes how his typical daily experiences can be viewed this way, as a journey through various locations, encountering different people and objects along the way. In a standard experiment, a rat also visits various places where different items, such as food rewards, are encountered. Hasselmo uses this parallel between human and rat experiences to provide the framework for his theory of episodic memory.

Defining episodic memory "as occurring at a specific place," Hasselmo finds that "the



Vincent van Gogh's *Memory of the Garden at Etten* (1888).

sentation of location is essential to episodic memory." He takes location to be represented by neurons that are selectively activated in particular regions of space, neurons that are known to exist in rodents ("place cells" in the hippocampus and "grid cells" in the entorhinal cortex). Many aspects of Hasselmo's theory arise from insights gained by studying these neurons.

Theta oscillations in the hippocampus and entorhinal cortex reflect periodically synchronized activity of place cells and grid cells. Hasselmo advocates the view that theta oscillations provide a phase code, whereby spatial location is represented by the phase of theta at the time that a cell fires. He also

proposes that functionally distinct phases of theta set up appropriate conditions for either memory retrieval or memory encoding. This separation prevents memory interference effects in his model.

Hasselmo has an exceptionally diverse neuroscience background. He has firsthand experience with neuronal recording in active rats and monkeys, intracellular recording in

extracted brain tissue, mathematical modeling, and psychological testing and brain imaging in humans. This almost certainly underlies his seamless switching throughout the book from one discipline to another in order to best explain his theory. The chapter describing drug effects on memory

is a good example. Hasselmo explains how a drug that blocks the brain chemical acetylcholine impairs human subjects' ability to learn word pairs. The impairment worsens when words to be learned overlap with

words that were learned previously. This effect demonstrates "proactive memory interference," which occurs when new information is not remembered due to interference from older memories. Hasselmo describes analogous findings in rats and monkeys and explains how proactive interference creates serious problems for computational models of memory. Hasselmo then discusses how acetylcholine's effects on neuronal activity, revealed through studies of extracted brain tissue, could explain how the brain avoids proactive interference. During memory encoding, high acetylcholine levels suppress retrieval of old memories by selectively reducing neurotrans-

mitter release in the circuits mediating memory retrieval. This suppression of the retrieval machinery allows encoding of new information to occur without interference caused by retrieval of similar memories.

How We Remember reviews a broad range of seminal episodic memory studies while also introducing new ways of thinking about the topic. Readers with a general interest in memory will learn a lot from reading this thoughtful book. Hasselmo suggests many novel hypotheses concerning the mechanisms of episodic memory, so memory researchers who read this book will almost certainly get ideas for new experiments. I definitely did.

10.1126/science.1220742



ENERGY

The Wind at Our Backs

Dan Reicher

Philip Warburg's *Harvest the Wind* chronicles the dramatic growth—and current challenges—of the modern wind industry, with a focus on the United States. I read the book while traveling in China. I also brought along a dog-eared copy of Palmer Putnam's 1948 *Power from the Wind (I)*. I enjoyed an ideal setting, and two fine books, to help take stock of where the wind industry came from and where it is headed.

In 1941, Putnam, a geologist turned energy innovator, switched on the world's first large electricity-generating wind turbine on Grandpa's Knob in Vermont. At 1.25 megawatts (MW), similar in size to today's turbines, his machine was a major breakthrough

wind began to gain support as power needs surged. A substantial Chinese industry eventually developed; currently four of the top ten turbine manufacturers are Chinese companies, with Sinovel second only to Vestas in worldwide production.

Warburg, an environmental lawyer and writer, makes it clear that with this kind of growth the issue with wind power is no longer whether: wind is fast becoming a mainstream part of the global energy system. Nor is it how: key challenges to the broad-scale deployment of wind are being solved. Instead, the unsettled question is who will be the leaders in the research, manufacturing, financing, and deployment of wind on a massive scale? More specifically, will the United States have a prominent role or be a bit player to China, the European Union, India, and others?

On the technical front, Warburg nicely addresses several thorny issues: For turbine noise and impacts on birds and bats, the effects are real, but we're getting better at managing them. On the challenge of integrating intermittent wind-generated electricity into the electric grid, the options are growing and now include innovative "smart grid" technologies and storage opportunities such as plug-in cars. Warburg also emphasizes the critical need for more transmission capacity to tap U.S. wind resources, and he examines how to pay for it.

On the policy front, Warburg describes how uncertain policy support is harming the wind industry in the United States. He highlights the wind production tax credit that over the past two decades has expired several times—and, unless renewed by Congress, will do so again at the end of 2012—resulting in uncertainty that chills U.S. wind farm development. He also decries the imbalance between unreliable federal renewables policy and the comparatively consistent policy support enjoyed by traditional energy sources.

In addition, the author addresses the serious challenge of siting wind turbines in the United States. He tells the story of the large Meridian Way project in Kansas, where local residents enjoy a substantially expanded tax base, a community college wind train-

ing program, and well-paying jobs. In contrast, Warburg describes how a project near Grandpa's Knob in Vermont and the nation's first offshore wind project near Nantucket have stalled because of local opposition.

Turning to China, Warburg notes that whereas only 100 MW were installed in 2003, by 2010 that figure had grown to 18,900 MW (about half the global new capacity that year).

He describes a meeting with a top Chinese energy planner whose goal is to put 150,000 MW of wind on-line by 2020, roughly three times the capacity installed in the United States by the end of 2011. Warburg describes how this massive market—the additional capacity will cost over \$150 billion

may develop, including the challenges foreign companies face in getting a meaningful share of this very large pie.

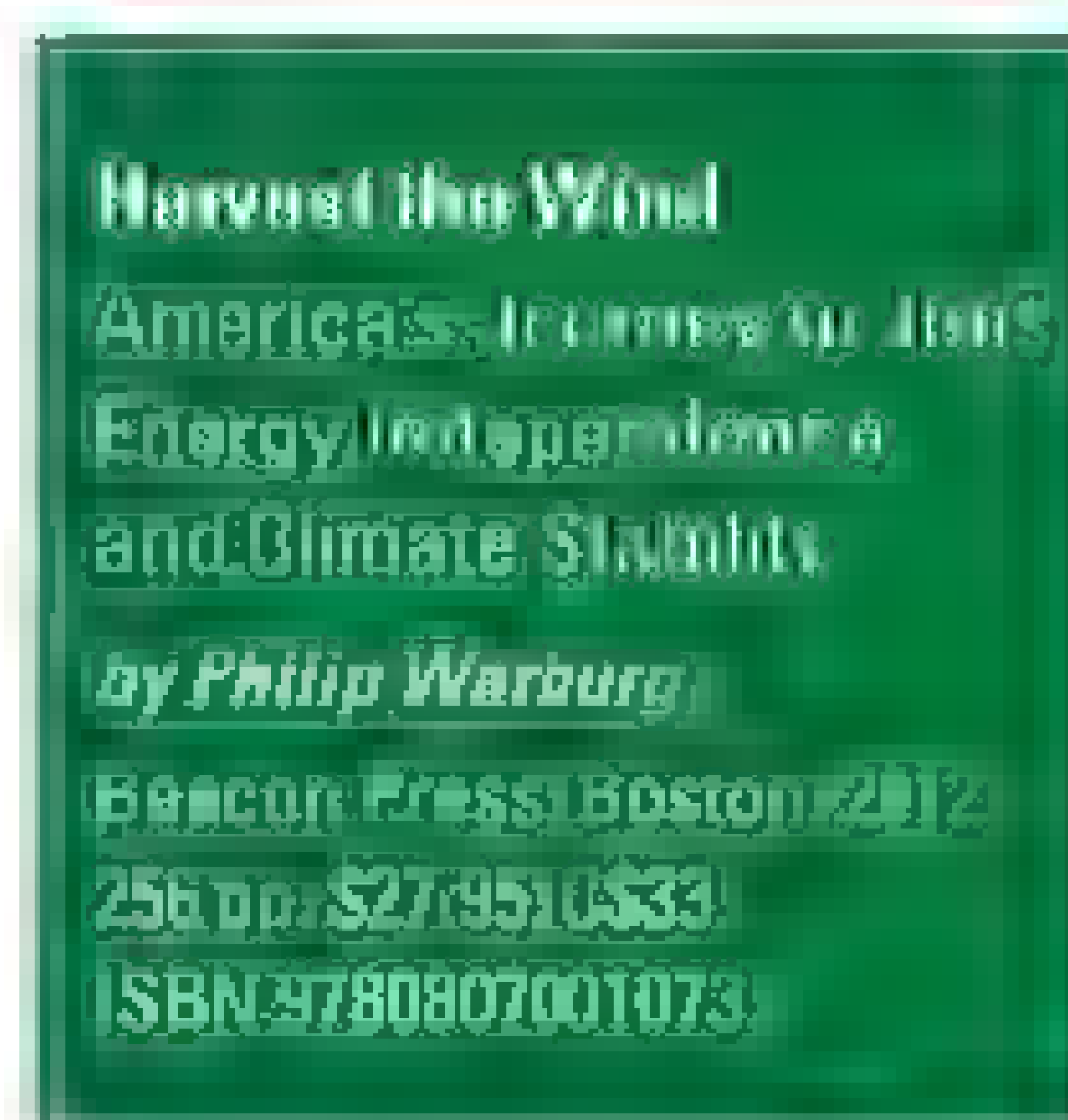
Warburg also raises concerns about China's fast-paced march to wind, noting that "[p]rivate property rights scarcely exist" and "[g]overnment policies and plans are announced, not debated." But with fast-rising electricity demand, serious air pollution problems, and keen interest in leading the global wind industry, China is making an extraordinary push. It should therefore not be surprising that Vestas recently opened the largest turbine factory in the world—in China, not Denmark.

Meanwhile, U.S. companies are increasingly considering the same path. Ohio-based Timken, the world's leading manufacturer of precision bearings, sees wind energy as its most promising new market. Although much of Timken's current wind-related work is in the United States, Warburg reports that company executives will not hesitate to move it to China if the market, and associated support, develops there rather than at home.

Despite this serious global competition, Warburg ends *Harvest the Wind* with a modestly hopeful tone about wind energy in the United States. He comments that continued progress will clearly require innovation but also sound investment and careful planning. Warburg concludes, "With strong collaboration between government and the private sector, wind can truly become the heartland's new harvest."

References

1. P. C. Putnam, *Power from the Wind* (Van Nostrand, New York, 1948).



Wind farm, Smoky Hills, Kansas.

and decades ahead of its time. Fast forward to the 1980s, when a wind rush hit California, with developers installing thousands of turbines from more than a dozen manufacturers. But, because of inadequate testing and standards, many of these machines failed almost as fast as they were erected.

Enter Denmark, where Vestas and two other long-standing companies designed, tested, and built standardized wind turbines. By 1987, Danish turbines had captured 90% of the California market. However, U.S. support for wind energy waxed and waned over the following years. Vestas and other manufacturers turned much of their attention to other countries, including China, where

The reviewer is at the Steyer-Taylor Center for Energy Policy and Finance, Stanford University, Stanford, CA 94305, USA. E-mail: dreicher@stanford.edu

RESEARCH PRIORITIES

ELSI 2.0 for Genomics and Society

Jane Kaye,^{1*} Eric M. Meslin,² Bartha M. Knoppers,³ Eric T. Juengst,⁴ Mylène Deschênes,⁵ Anne Cambon-Thomsen,⁶ Donald Chalmers,⁷ Jantina De Vries,⁸ Kelly Edwards,⁹ Nils Hoppe,¹⁰ Alastair Kent,¹¹ Clement Adebamowo,¹² Patricia Marshall,¹³ Kazuto Kato¹⁴

Anticipating and addressing the ethical, legal, and social implications (ELSI) of scientific developments has been a key feature of the genomic research agenda (1–4). Research in genomics is advancing by developing common infrastructures and research platforms, open-access and sharing policies, and new forms of international collaborations (5–12). In this paper, we outline a proposal to establish a “collaboratory” (13) for ELSI research to enable it to become more coordinated, responsive to societal needs, and better able to apply the research knowledge it generates at the global level. Current ELSI research is generally nationally focused, with investigator-initiated approaches that are not always aligned with the developments in international genomics research. This makes it difficult to efficiently leverage findings that impact global practice and policy. Moreover, as translational genomic research design challenges become more pressing (14), ELSI research will need to develop greater capacity to respond rapidly to new developments. The ELSI 2.0 Initiative is designed to catalyze international collaboration in ELSI genomics and to enable those in the field to better assess the impact and dynamics of global genome research.

Vision

The aim of ELSI 2.0 is to accelerate the translation of ELSI research findings into practice and policy. To do this, we will build on successful examples of international ELSI research. To succeed, ELSI 2.0 must be grounded in a commitment to the shared values of mutual respect, trust, and active collaboration. It will require the development of new methods and frameworks for the strategic targeting of

research to overcome current barriers to international, interdisciplinary research. Through ELSI 2.0, ELSI researchers can be globally connected while still carrying out locally sensitive research. By enabling large-scale global collaborations among a range of stakeholders, ELSI research will become more effective, efficient, and economical—leading to development of better local, regional, and international practice and policy.

Design and Methods: The Collaboratory

The collaborative Web-based infrastructure (see the figure) will be open to all ELSI researchers, national and international agencies, and other research “consumers,” including the general public and advocacy groups. It will provide ways for ELSI research to make an impact on policy and practice. It will be an active, generative space, distinct from discussion boards or networks. The Collaboratory will provide information on research resources, prospective projects, and workspaces for online collaboration, as well as educational webinars and workshops. ELSI 2.0 will facilitate a variety of activities—including networking, rapid response, “crowd-sourcing,” modeling, forecasting, and the development of proactive strategies to coordinate and enable international ELSI research.

It will give a sense of the terrain of the international ELSI landscape, which will be used to identify overlaps and similarities that exist in different localities despite there being different national cultures, legal systems, and policy regimes in play. Identifying and appreciating regional differences can strengthen our understanding of the complexity of bioethics issues and provides a basis for shared learning. For example, the works of Phelan *et al.* (15) and Sankar *et al.*

We need an international infrastructure for the ethical, legal, and social implications of genomic research.

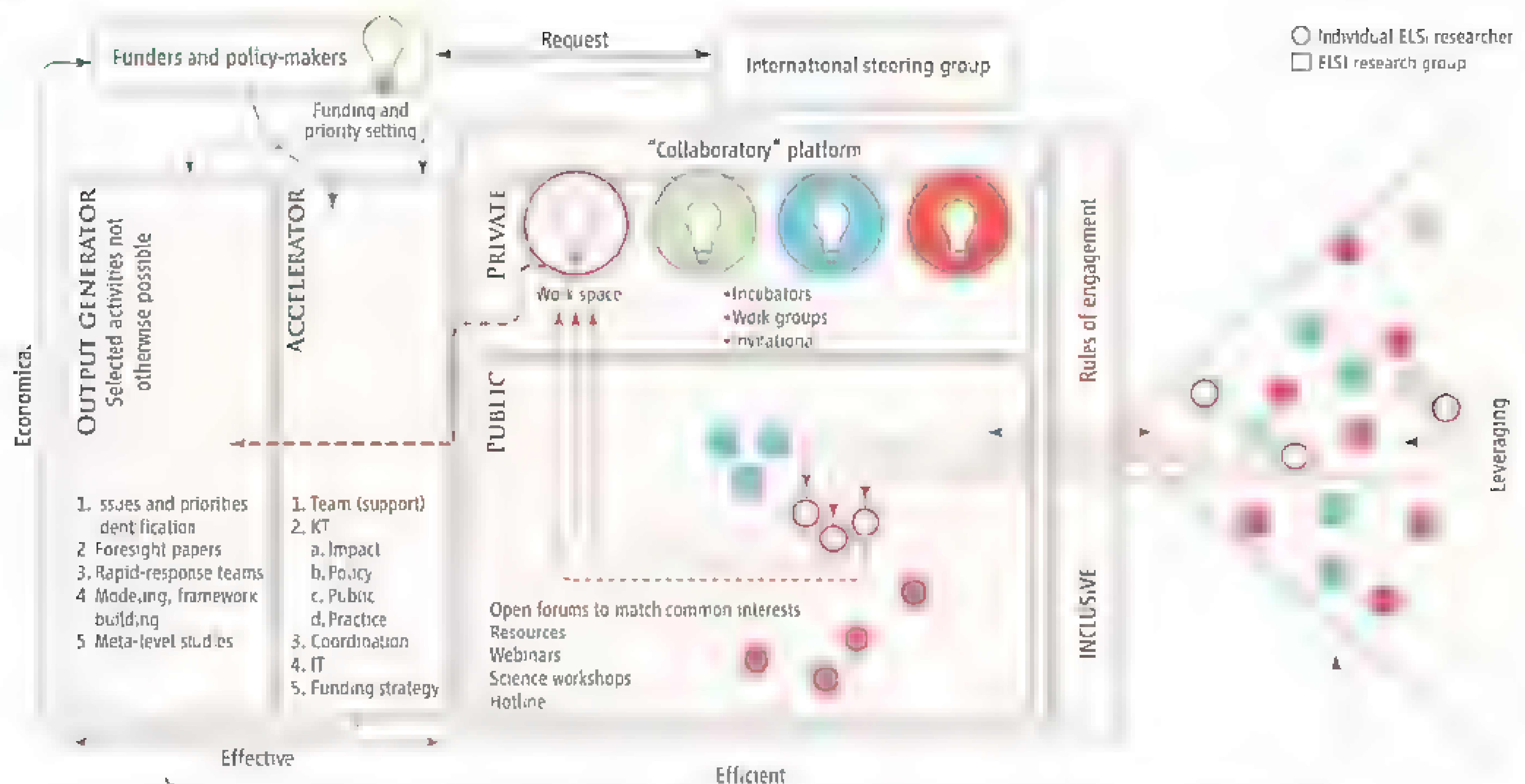
(16) on genetic discrimination are proving to be extremely informative in designing a project on stigma in genomics in Africa. By using ELSI 2.0, tracking and coordinating ELSI research will also be possible at a global level and will accelerate the impact of research on policy.

For an ELSI scholar in Africa, ELSI 2.0 could be a place to connect with other scholars or to tap into resources not otherwise readily available. For a U.S.-based advocacy organization, the Collaboratory will provide essential services to extend the reach of work otherwise locked up in the academic literature. A funder in the European Union could request a rapid response team to respond to ad hoc, short-notice requests related to emerging issues or to forecast important policy directions. A patient could become an active participant in ELSI research or find literature and experts on subjects such as direct-to-consumer testing. For a scholar in Asia looking to fund a multicountry effort, the Collaboratory could help identify funding sources, collaborators, and workshops for the idea. Scholars could choose to be observers or builders and creators (posing projects for a workspace or a crowd-sourced effort) or to motivate collaborators who would not otherwise be accessible (clinicians, patients, policy-makers). In this way, ELSI 2.0 will continually build and support global ELSI research and policy-making capacity.

The Collaboratory will stimulate creativity and communication between researchers, diverse publics, funders, and policy-makers in a variety of ways. It will provide a Web-based infrastructure with the same capabilities as the collective platforms used in large-scale, international genomics science and elsewhere and will draw on a variety of approaches to maximize interactions, including networking, rapid response, crowd-sourcing, modeling, forecasting, and the development of proactive strategies and comparative methodologies to enable international ELSI research in genomics. This will include modeling exercises for the construction of international frameworks and approaches to issues. These provisions will promote efficient use of research and resources, avoiding redundancy and duplication of effort. A clearer under-

¹HeLEX, Department of Public Health, University of Oxford OX3 7LF, Oxford, UK. ²Center for Bioethics, Indiana University, Bloomington, IN 46202, USA. ³Centre for Genomics and Policy, McGill University, Montreal H3A 1A4, Canada. ⁴UNC Center for Bioethics, University of North Carolina, Chapel Hill, NC 27599, USA. ⁵P3G, Montreal H3V 1A2, Canada. ⁶UMR 1027, INSERM, Epidemiology and analyses in public health, 31000 Toulouse, France. ⁷JMR 1027, Faculté de médecine Purpan, Université Paul Sabatier Toulouse, 31000 Toulouse, France. ⁸Faculty of Law, University of Tasmania, Hobart, Tasmania 7000, Australia. ⁹Faculty of Health Sciences, University of Cape Town, South Africa. ¹⁰Department of Bioethics and Humanities, University of Washington, Seattle, WA 98195, USA. ¹¹CELLS, Leibniz Universität, 30167 Hannover, Germany. ¹²Genetic Alliance UK, London N1 3QP, UK. ¹³Institute of Human Virology, Garki, Abuja, Nigeria. ¹⁴University of Maryland School of Medicine, Baltimore, MD 21201, USA. ¹⁵Department of Bioethics, Case Western Reserve University, Cleveland, OH 44106, USA. ¹⁶Osaka University, Suita 565-0871, Japan.

*Author for correspondence. E-mail: jane.kaye@law.ox.ac.uk



Collaboratory scheme. Relations among the parts of the proposed Collaboratory are shown. KT, knowledge transfer; IT, information technology.

standing of the international ELSI landscape will be invaluable in informing and coordinating future research, tracking the impact of research on policy, and continually building ELSI research and policy-making capacity.

To be fully responsive to emerging issues, the Collaboratory will establish an "Accelerator Team" with experience and skills in the translation and delivery of ELSI research to different publics, patient groups, the media, and policy-makers. It is envisaged that ELSI 2.0 could provide funding organizations with access to reliable assessments of research priorities to assist with the planning of research agendas and strategy.

Together, the users of the Collaboratory infrastructure will develop a governance approach consistent with the vision and values of ELSI 2.0. An international steering group will guide and support the operation and development of the overall initiative. A regular evaluation process with measurable goals and targets will be used to ensure the effectiveness and efficiency of the initiative. ELSI 2.0 will be hosted through the P3G Consortium, which has parallel aims and established policies (17).

Conclusion

The success of ELSI 2.0 will be realized by the energy, enthusiasm, and diversity of those who join and participate. We invite all those interested in ethical, legal, and social issues in genomics to become involved as active

contributors. Initial pilot efforts using current open-source tools will test proof of concept to gauge further support and participation. Our next step will be to have a series of meetings to publicize and gather support for the initiative and details of these meetings, which can be found on the P3G Web site. The first meeting will be held on 26 June 2012 as a satellite workshop of the International Association of Bioethics meeting in Rotterdam (18). We shall pursue an international coordinated funding strategy, as has been achieved for large-scale genome science collaborations like the International Cancer Genome Project (7). Our initial estimates are that establishment costs will be in the region of U.S.\$2 million per year for 2 to 3 years. We believe that ELSI 2.0 has the potential to radically transform and enhance the international genomics and society research agenda. In doing so, it will be possible to better anticipate and address the challenges raised by the globalization of genomic research.

References and Notes

1. F. S. Collins, *N. Engl. J. Med.* **341**, 28 (1999).
2. E. M. Meslin, E. J. Thomson, J. T. Boyer, *Kennedy Inst. Ethics J.* **7**, 291 (1997).
3. E. T. Juengst, *Soc. Philos. Policy* **13**, 63 (1996).
4. A. Wolfe, in *Encyclopedia of Ethical, Legal and Policy Issues in Biotechnology* (Wiley, New York, 2003); 10.1002/0471250597.mlr045.10.1002/0471250597.mlr045.
5. E. Birney et al., *Nature* **461**, 168 (2009).
6. See also CCC as a model for international collaboration.
7. T. J. Hudson et al., *Nature* **464**, 993 (2010).
8. W. Burke, M. J. Khoury, A. Stewart, R. L. Zimmerman, *Genet. Med.* **8**, 451 (2006).

9. E. A. Achidi et al., *Nature* **456**, 732 (2008).
10. P. A. Singer, A. S. Daar, *Science* **294**, 87 (2001).
11. E. Calva, M. J. Cardoso, J. V. Gavilondo, *Trends Biotechnol.* **20**, 368 (2002).
12. T. O. Ogundiran, *Soc. Policy* **1**, 66 (2005).
13. W. A. Wu, *Science* **261**, 854 (1993).
14. E. D. Green et al., *Nature* **470**, 204 (2011).
15. J. C. Phelan, R. Cruz-Rojas, M. Redf., *Am. J. Psychiatr. Rehabil.* **6**, 159 (2002).
16. P. Sankar, M. K. Cho, P. R. Wolpe, C. Scharrer, *Genet. Med.* **8**, 33 (2006).
17. The P3G Consortium is located at McGill University, Montreal, Canada; www.p3g.org/.
18. Online registration is now open at <http://elsirotterdam.eventbrite.com/>.

Acknowledgments: We thank the Brocher Foundation and the Wellcome Trust (097671/2/11/2) for their generous support for a meeting held at the Brocher Foundation 16 to 19 November 2011. In addition, the authors are supported under the following grants: J.K., Wellcome Trust (096599/2/11/2) and BioSHaRE-EU (261433); E.M.M., Richard M. Fairbanks Foundation and National Center for Research Resources, NIH (JL1RR025761-01); B.M.K., Canada Research Chair in Law and Medicine; Genome Canada/Quebec and BioSHaRE-EU (261433); A.C.T., CAGEKD (a collaboration on kidney cancer genomics) (241669), BioSHaRE-EU (261433), Genetic European Variation in Disease (GEUVADIS) (261123), and Genotype to Phenotype Databases: A Holistic Approach (GEN2PHEN) (200754); D.C., National Health and Medical Research Council, Australia (490037); J.D.V., Postdoctoral Fellowship from the University of Cape Town, K.E., Center for Genomics and Healthcare Equality, National Human Genome Research Institute (NHGRI), NIH (P50-HG3374), C.A., West African Bioethics Training Program Fogarty International Center (FIC), NIH (R25TW007091); P.M., The Center for Genetic Research Ethics and Law (CGREAL), a Center for Excellence in ELSI Research, NHGRI, NIH (P50-HG-03390-07); K.K., Ministry of Education, Culture, Sports, Science and Technology (MEXT) (22150002), Japan.

10.1126/science.1218015

CELL BIOLOGY

FGF21 Takes a Fat Bite

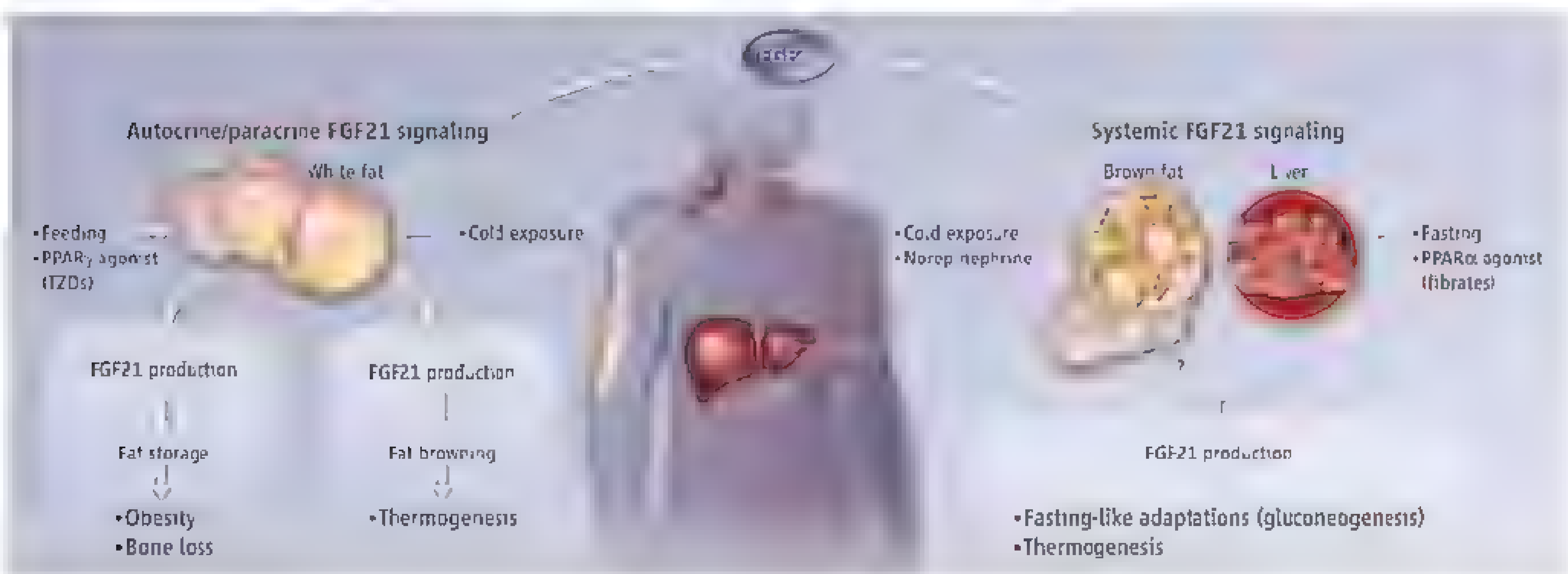
Carlos Cantó¹ and Johan Auwerx²

The quest for secreted peptides with metabolic actions has identified several autocrine, paracrine, and exocrine growth factors—including neuregulins, platelet-derived growth factor, and members of the fibroblast growth factor (FGF) family—that stimulate glucose uptake and regulate mitochondrial function in key metabolic tissues. Among them, FGF21 has become particularly interesting because its endocrine actions endow it with potential therapeutic uses.

FGF21 has less than 35% homology to other family members and, unlike most

sue (5, 6). Most likely, the activation of the transcription factor peroxisome proliferator-activated receptor- γ (PPAR γ) accounts for this up-regulation, as PPAR γ agonists [thiazolidinediones (TZDs)] induce FGF21 expression in white fat (1, 5, 7). Intriguingly, FGF21 controls the sumoylation of PPAR γ , thereby preventing its inhibition; as a consequence, FGF21-null mice have less adipose tissue. TZDs also failed to increase adiposity and insulin sensitivity in these mice (5). That FGF21 might favor adiposity is striking, as exogenous administration of FGF21

A growth factor's varied effects on adipose tissue and thermogenesis may be attributable to its local and systemic actions.



other FGFs, it diffuses upon secretion and functions as a hormone (1). FGF21 is expressed predominantly in white adipose tissue, liver, and pancreas (1), with most circulating FGF21 originating from the liver. Because its production is induced in murine livers by starvation (2, 3), and because many of its actions—induction of gluconeogenesis, fat oxidation, and ketogenesis, coupled to a state of torpor (2–4)—mimic the effects of fasting, FGF21 has been considered a possible starvation signal. This may reflect only one aspect of FGF21 biology because recent studies show that feeding can promote FGF21 synthesis in white adipose tis-

to animal models of diabetes and obesity is generally associated with weight loss (1, 8). However, the mechanistic link between FGF21 and PPAR γ sumoylation requires further study, as does the physiological relevance of PPAR γ sumoylation. In this context, the apparent physiological discrepancies between localized and systemic FGF21 increases might be resolved through analysis of how local FGF21 production affects energy balance, lipolysis, and adipocyte differentiation. The generation of adipose tissue-specific FGF21-deficient mouse models, as well as mice genetically engineered to express constitutively sumoylated or desumoylated PPAR γ , should help to clarify the tissue-specific effects of FGF21.

Because PPAR γ activation inhibits bone formation (9), bone fractures are one of the major comorbidities observed in patients treated with TZDs. Given the link between PPAR γ and FGF21, it is not surprising that

FGF21 actions. FGF21 can act both locally and systemically to affect metabolism

(11, 12). Further understanding of these facets of FGF21 biology is hence imperative if these side effects of TZDs are to be reduced.

Another twist in the unfolding roles of FGF21 is in the browning of white fat in response to cold or adrenergic stimulation (13). FGF21 is linked with increased thermogenic activity (14). However, although FGF21 actions on mouse neonatal brown fat function result from the regulation of systemic FGF21 concentrations (14), this does not seem to be the case for the browning of white fat, as the amount of circulating FGF21 did not change upon cold exposure, which suggests autocrine-paracrine signaling. To promote the browning of white fat, FGF21 enhances PPAR γ coactivator 1 α (PGC-1 α) activity, potentially through inducing its post-

¹Nestlé Institute of Health Sciences, Ecole Polytechnique Fédérale de Lausanne (EPFL) Campus, Quartier de l'Innovation, Bâtiment G, CH-1015 Lausanne, Switzerland
²Laboratory of Integrative and Systems Physiology, EPFL, SV-B, Building AI, Station 15, CH-1015 Lausanne, Switzerland
 E-mail: carlos.cantoalvarez@rd.nestle.com, admin.auwerx@epfl.ch

translational modifications (13). The pathway through which FGF21 activates PGC-1 α and browning is not yet established, but the signaling pathway involving the enzymes AMP-activated protein kinase (AMPK) and sirtuin 1 (SIRT1) warrants scrutiny. Activation of AMPK and the deacetylation of PGC-1 α by SIRT1 are essential for FGF21 to trigger PGC-1 α activity and enhance mitochondrial function (15). Moreover, pharmacological activation of AMPK enhances the browning of epididymal white adipose tissue, although it is not clear whether this derives from a direct effect of AMPK in white adipocytes (16). The actions of FGF21 on hepatic lipid metabolism also require PGC-1 α (4), further suggesting that activation of the AMPK-SIRT1 signaling axis may be a general downstream feature linking FGF21 and PGC-1 α activity.

Human data have established FGF21 as a starvation hormone; the amount of circulating FGF21 displays no apparent circadian variation or a feeding-fasting cycle, and prolonged fasting (7 days) increases plasma

FGF21 concentration (17). But circulating FGF21 concentration also increases in overweight patients with various features of the metabolic syndrome (18), potentially hinting at the existence of an obesity-induced FGF21-resistant state (19), although this is debated (20). Future work will have to establish whether local changes in adipose tissue FGF21 production contribute to the increase in circulating FGF21 concentration observed in metabolic disease. Furthermore, the molecular and physiological pathways that endow FGF21 with the capacity to promote both white and brown fat tissue deserve further attention. It also will be important to evaluate the extent to which FGF21's thermogenic effects and PPAR γ -activating effects contribute to its beneficial effects on weight and glycemic control, and how such improvements can be achieved in the clinic while bypassing potential side effects such as bone loss. These fascinating enigmas testify to our still-evolving understanding of FGF21 biology.

References

1. E. S. Muijs et al., *Mol. Pharmacol.* **74**, 403 (2008).
2. M. K. Badman et al., *Cell Metab.* **5**, 426 (2007).
3. T. Inagaki et al., *Cell Metab.* **5**, 415 (2007).
4. M. J. Potthoff et al., *Proc. Natl. Acad. Sci. U.S.A.* **106**, 10853 (2009).
5. P. A. Dutchak et al., *Cell* **148**, 556 (2012).
6. K. Oishi, M. Konishi, Y. Murata, N. Itoh, *Biochem. Biophys. Res. Commun.* **412**, 396 (2011).
7. H. Wang, L. Qiang, S. R. Farmer, *Mol. Cell Biol.* **28**, 188 (2008).
8. A. Kharitonov et al., *Endocrinology* **148**, 774 (2007).
9. T. A. Cock et al., *EMBO Rep.* **5**, 1007 (2004).
10. W. Wei et al., *Proc. Natl. Acad. Sci. U.S.A.* **109**, 3143 (2012).
11. S. E. Nissen, K. Wolski, *N. Engl. J. Med.* **356**, 2457 (2007).
12. A. M. Lefebvre et al., *Nat. Med.* **4**, 1053 (1998).
13. F. M. Fisher et al., *Genes Dev.* **26**, 271 (2012).
14. E. Hondares et al., *Cell Metab.* **11**, 206 (2010).
15. M. D. Chau, J. Gao, Q. Yang, Z. Wu, J. Gromada, *Proc. Natl. Acad. Sci. U.S.A.* **107**, 12553 (2010).
16. R. Vila-Bedmar, M. Lorenzo, S. Fernández-Vetado, *Endocrinology* **151**, 980 (2010).
17. C. Gálman et al., *Cell Metab.* **8**, 169 (2008).
18. W. W. Chen et al., *Exp. Clin. Endocrinol. Diabetes* **116**, 65 (2008).
19. F. M. Fisher et al., *Diabetes* **59**, 2781 (2010).
20. C. Hale et al., *Endocrinology* **153**, 69 (2012).

10.1126/science.1222646

GEOPHYSICS

Understanding Earthquakes

Paul Segall

Progress in understanding the mechanics of earthquakes has come from improvements in data collection, laboratory experiments, and theory, allowing numerical simulations that are ever more “Earthlike” in character (1). On page 707 of this issue, Barbot *et al.* (2) compare sophisticated dynamical simulations to a sequence of well-recorded moment magnitude (M_w) 6.0 earthquakes along the Parkfield segment of the San Andreas Fault. Parkfield was the site of the only official earthquake forecast in the United States, with an intensive effort undertaken to obtain high-resolution data near a moderate-sized shock (3). Although the earthquake failed to occur within the expected time window, it did provide a wealth of data that can be compared to the predictions of dynamical models (4).

Despite the basic physics of earthquakes having been known for roughly a century (5, 6), it remains challenging to construct dynamical models of earthquakes. In the case of a plate-bounding fault, such as the San Andreas, the relative motion of the

Pacific and North American plates leads to a gradually increasing shear stress on the locked section of the fault (the upper 10 to 15 km). At some point in space and time, the shear stress overcomes the frictional resistance and slip initiates. As the fault slides, the frictional resistance decreases and slip accelerates, leading to an expanding inertially limited rupture that radiates seismic waves as it propagates.

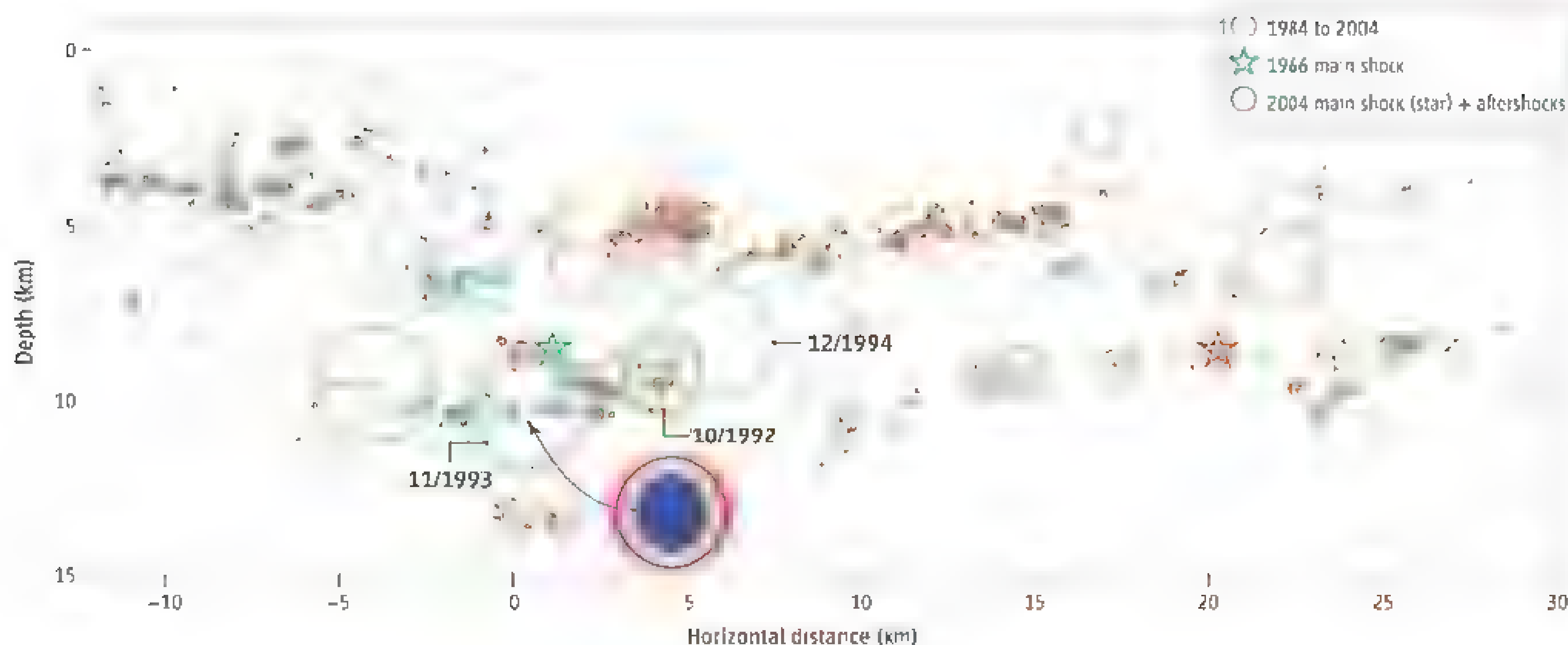
Modeling earthquakes is computationally demanding, with details of the propagating rupture requiring fine spatial and temporal discretization. At the same time, the interval between earthquakes can be decades to centuries, and ruptures may reach hundreds of kilometers. Also, observations of processes operating many kilometers deep are limited by sensors that are restricted to (or near) Earth's surface. Limitations in knowledge include the details of how friction weakens, particularly at seismic slip speeds; the detailed geometry of faults; the pressure of pore fluids within fault zones and how they respond to slip; and the nature of fault zones below the seismically active crust, where earthquakes do not image fault structure.

Sophisticated numerical models can reproduce a wide range of seismic activity at the Parkfield segment of the San Andreas Fault.

There have been important advances in our understanding of friction, in numerical methods for dynamical earthquake simulation, and in data collection in the near field of large earthquakes. Laboratory experiments have shown that friction depends on instantaneous slip speed (rate) as well as past slip history (7). Steady-state frictional resistance can either be an increasing (strengthening) or decreasing (weakening) function of slip rate, depending on rock type and temperature. Stability analyses using these friction laws have given rise to what could be considered the standard model for earthquakes—that earthquakes can only nucleate in regions that are steady-state velocity weakening over a sufficiently large fault patch. In contrast, areas that are steady-state velocity strengthening tend to exhibit stable creep.

Barbot *et al.*'s model incorporates slow interseismic stressing and dynamic rupture propagation, and compares to both seismic and geodetic observations. The locations of small earthquakes are used to infer spatial transitions in frictional properties, outlining a velocity-weakening region that hosts M_w 6.0 earthquakes from velocity-strengthening surroundings. They also use the aver-

Department of Geophysics, Stanford University, Stanford, CA 94305-2215, USA. E-mail: segall@stanford.edu.



Movers and shakers. Cross section along the San Andreas Fault at Parkfield; earthquake locations (13) shown as circles (radius scaled with magnitude). 1966 and 2004 M_w 6.0 nucleation points shown as stars. Earthquakes repeat in the same streaks, both before and after the 2004 mainshock. The Parkfield prediction (3) anticipated a M_w 6.0 to nucleate near the 1966 focus (blue star). Even though strain had built up by early 1990's (11), earthquakes in 1992 ($M_w \sim 4.4$), 1993 ($M_w \sim 4.7$), and 1994 ($M_w \sim 4.9$) failed to trigger the expected event. The inset shows how the static stress decreases (blue) inside the earthquake slip region, but increases at its periphery (red). The numerical models of Barbot *et al.*, may help to explain why the stress increase, as well as the dynamic stressing which would have been even larger, did not trigger a M_w 6.0 at the expected site (blue star). Data from (13).

age repeat time of Parkfield earthquakes and geodetic observations to constrain physical properties of the fault. Their modeled results bear many similarities to observed Parkfield earthquake sequences, including magnitude and average repeat times.

M_w 6.0 earthquakes in 1922, 1934, and 1966 all nucleated at the northwest end of the Parkfield segment (8) and ruptured to the southeast. It thus came as a surprise when the 2004 Parkfield shock started at the southeastern end and ruptured to the northwest. The simulations of Barbot *et al.* reproduce this directivity switching, but only by including a locked-to-creeping transition at the southeastern end of the segment. The lateral transitions in frictional behavior at the ends of the model segment serve both to stop dynamic ruptures and to stress the velocity-weakening patch causing model earthquakes to preferentially nucleate at the ends. A limitation of the model is that the southeastern locked-to-creeping transition is not detected by geodetic or creepmeter data (4). Further work is needed to establish whether the model transition could be a proxy for a more subtle stress concentration at depth.

The numerical earthquake sequences are more periodic than the observed sequence of seven Parkfield earthquakes, which have interevent times as short as 12 years and

as long as 38 years. Current models do not capture the full range of physical processes, including interaction with neighboring faults (9), irregular fault geometry (10), and important frictional weakening processes at high slip speeds (1). Computational limitations also prevent current models from including sufficiently small spatial scales to simulate the full size range of small earthquakes observed. The Barbot *et al.* simulations include only a few M_w 2.5 to 4.0 earthquakes.

For the 38-year interval between the two most recent Parkfield earthquakes (1966 to 2004), geodetic data suggested that sufficient strain had accumulated to power a repeat of the 1966 quake by the early 1990s (11). At that time, a sequence of three M_w 4.4 to 4.9 quakes struck very close to the expected Parkfield hypocenter (12), yet none of them expanded into a M_w 6.0 (see the figure). Intriguingly, the Barbot *et al.* simulations occasionally exhibit M_w 2.0 to 4.0 events near the segment ends, interpreted as failed nucleation of M_w 6.0 events, that are associated with directivity switching and the longest interevent times.

The 2011 M_w 9.0 Tohoku-Oki earthquake in Japan raises important questions about the standard model and the ability of current dynamical models to have predictive power. Before 2011, northeastern

Japan experienced earthquakes up to M_w 8.0, many of which seemed to repeat in the same locations, dubbed seismic asperities. These were assumed to represent velocity-weakening fault segments. Global Positioning System measurements after these earthquakes exhibited large post-earthquake transients, assumed to represent slip in velocity-strengthening regions surrounding the asperities. Some models suggested that the largest quakes in that region would be at most M_w 8.5, yet the 2011 event apparently ruptured asperity and nonasperity regions with equal facility.

Although we still have much to learn from detailed observations of earthquakes and careful comparisons to the predictions of numerical models, the work of Barbot *et al.* presents an appreciable step forward in this process.

References

1. H. Noda, E. M. Dunham, J. R. Rice, *J. Geophys. Res.* **114**, B07302 (2009).
2. S. Barbot, N. Lapusta, J.-P. Avouac, *Science* **336**, 707 (2012).
3. W. H. Bakun, A. G. Lindh, *Science* **229**, 619 (1985).
4. W. H. Bakun *et al.*, *Nature* **437**, 969 (2005).
5. G. K. Gilbert, *Am. J. Sci.* **27**, 49 (1884).
6. H. F. Reid, in *The California Earthquake of April 18, 1906, Report of the State Earthquake Investigation Commission* A. C. Lawson, Ed. (Carnegie Institute of Washington, Washington, DC, 1910), vol. II, pp. 3–55.
7. C. Marone, *Annu. Rev. Earth Planet. Sci.* **26**, 643 (1998).
8. W. H. Bakun, T. V. McEvilly, *J. Geophys. Res.* **89**, (B5), 3051 (1984).
9. S. Toda, R. S. Stein, *J. Geophys. Res.* **107**, 2126 (2002).
10. E. M. Dunham, D. Belanger, L. Cong, J. Kozdon, *Bull. Seismol. Soc. Am.* **101**, 2308 (2011).
11. J. Murray, P. Segall, *Nature* **419**, 287 (2002).
12. J. B. Fletcher, P. Spudis, *J. Geophys. Res.* **103**, 835 (1998).
13. C. Thurber, *Bull. Seismol. Soc. Am.* **96**, 538 (2006).

10.1126/science.1220946

STRUCTURAL BIOLOGY

PARP-1 Activation—Bringing the Pieces Together

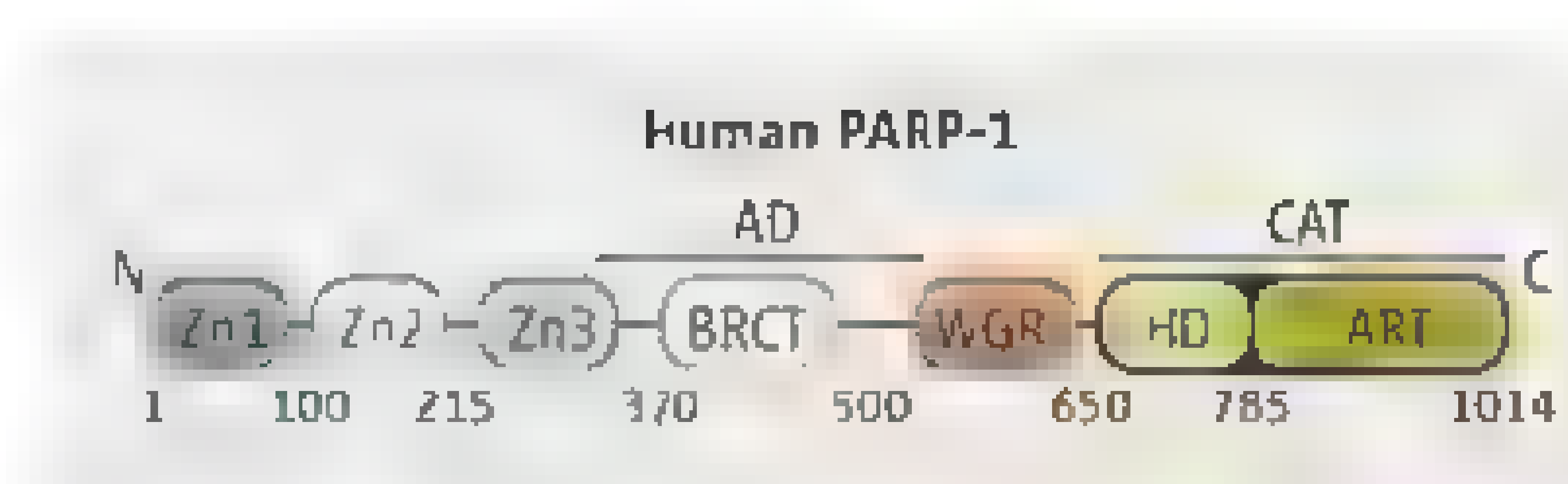
Jean-Philippe Gagné, Michèle Rouleau, Guy G. Poirier

The repair of DNA strand breaks is crucial for cell survival. In higher eukaryotes, cellular responses to DNA strand breaks are coordinated by a process called poly(ADP-ribosylation) (where ADP is adenosine diphosphate). This highly dynamic process begins with the hydrolysis of NAD (nicotinamide adenine dinucleotide) by poly(ADP-ribose) polymerases (PARPs), resulting in the polymerization of ADP-ribose moieties onto a substrate protein. The most active PARP in DNA damage recognition, PARP-1, is highly stimulated by single- and double-strand breaks (1). Because it is a clinically important molecular target in the treatment of several cancers, including breast and ovarian cancers (2), understanding how PARP-1 is activated after binding DNA strand breaks is an ongoing challenge. On page 728 of this issue, Langeher *et al.* (3) report key structural information about PARP-1 domain organization around a DNA double-strand break (DSB) that explains this activation.

DNA-dependent PARP activation has been characterized extensively at the biochemical level. The identification of zinc-finger (Zn) structures in the amino-terminal region of PARP-1 as DNA-binding modules helped to elucidate the molecular mechanisms underlying DNA-dependent PARP-1 activation (4). However, PARP-1 is a large multidomain protein, in which the amino-terminal DNA-binding domain is separated from the carboxyl-terminal catalytic domain (CAT) by several regions, including a central automodification domain (AD) and a WGR domain [defined by the conserved residues tryptophan (W), glycine (G), and arginine (R)] of unknown function (see the first figure). It has been unclear how signals from the DNA-interacting regions are relayed to the catalytic domain. Crystallographic studies have elucidated individual PARP-1 domains and molecular interactions with DNA or inhibitors, but a global mechanistic understanding of the domain rearrangements that underlie PARP-1 activation has been elusive.

CHUQ Research Center—CHUL, Cancer Research Unit, Laval University, Quebec, Canada. E-mail: guy.poirier@crchu.ulaval.ca

A model structure sheds light on how the PARP-1 protein is activated in DNA repair.



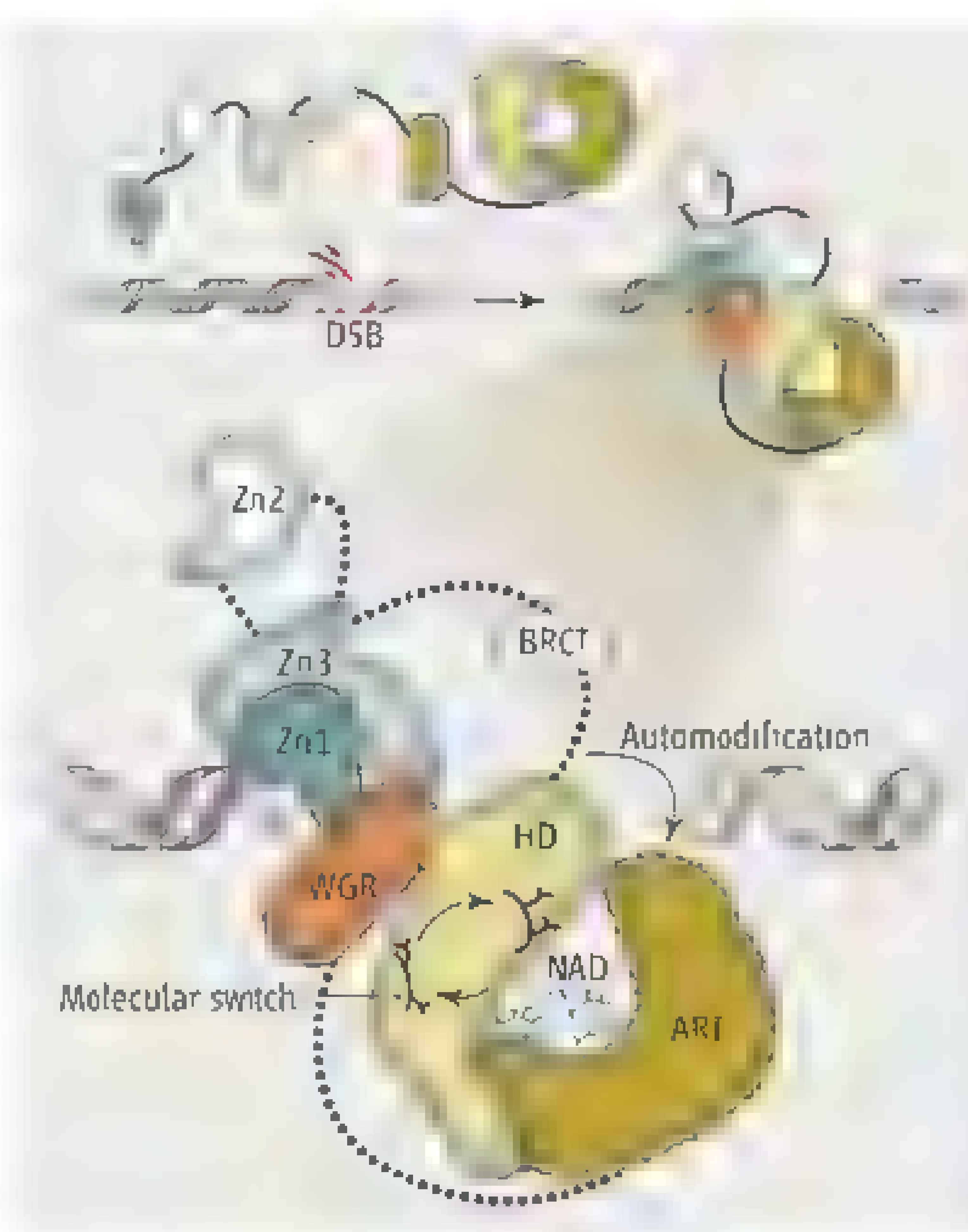
Modular domain architecture of human PARP-1. Approximate domain boundaries are indicated by residue numbers. ART, ADP-ribosyl transferase domain.

To address these issues, Langeher *et al.* constructed the minimal assembly of domains that supports DNA DSB-dependent PARP-1 activation, consisting of the first and third zinc fingers coupled to the WGR and catalytic domains (Zn1, Zn3, WGR-CAT), and used it as a basis for their structure-function

tion study. Although lacking Zn2 and the protein interaction module BRCT [Breast cancer type 1 susceptibility protein (BRCA1) C-terminal region], this truncated but active PARP-1 structure is the nearest to the full-length protein crystallized to date.

On the basis of their structural and functional data, Langeher *et al.* propose a PARP-1 activation model that involves the formation of a compact PARP-1 DNA complex, in which the DSB-interacting zinc fingers and the CAT domain lie on opposite faces of the WGR (see the second figure). This conformation distorts the helical subdomain (HD) within the CAT, thereby inducing a change in conformational flexibility of the CAT and repositioning the AD near the active site. This rearrangement explains the propensity of PARP-1 for poly(ADP-ribosylating itself rather than target protein substrates, but raises the question of how PARP-1 accommodates the broad range of its known protein substrates.

The tertiary model (see the second figure) also indicates that PARP-1 does not form a dimer at the DSB, consistent with a previous structural study in which PARP-1 interacted with damaged DNA as a monomer (5). Yet, PARP-1 dimerization has been a recurrent theme in the literature, and many have reported PARP-1 as a catalytic dimer (6–8). Self-association behavior of PARP-1 through BRCT domains has also been reported (9), but a more recent characterization of the solution structure of PARP-1 BRCT domain indicated that this domain does not engage in dimer formation (10). Although Langeher *et al.* show that PARP-1 can be fully automodified as a monomer, it may also function as a dimer in certain contexts; for example, inactive mutants can complement each other (11).



Model for DNA double-strand break-dependent activation of PARP-1. Langeher *et al.* show that upon DSB generation, PARP-1 engages DNA as a monomer and adopts a compact conformation centered on the WGR domain. In this conformation (inset, magnified view), the WGR domain makes interdomain contacts with Zn1 and Zn3 and contributes to the formation of the DNA-binding interface. This rearrangement triggers a molecular switch in the HD region of the CAT domain, alters the flexibility and dynamics of the ART domain, and thereby activates PARP-1. It also places the BRCT/AD close to the CAT, making it available for intramolecular modification.

Although the poorly characterized WGR domain is necessary for PARP-1 activation (11), the crucial contribution of this domain to the formation of a DNA damage recognition interface along with Zn1 and Zn3, as shown by Langelier *et al.*, is unexpected. This central role of the WGR domain in PARP-1 activation may explain the observation that PARP-1 automodification is mainly restricted to a small region of the AD (11). In the model proposed by Langelier *et al.*, the PARP-1 DNA structure has limited flexibility, and the small region of the AD prone to poly(ADP-ribosylation) is found near the catalytic pocket (12). Thus, Langelier *et al.*'s results could lead to a redefinition of what is currently considered the AD of PARP-1.

Furthermore, one could hypothesize from the model of Langelier *et al.* that the WGR could mediate PARP activation through DNA-independent signals. It is of considerable interest to determine whether atypical substrates will only trigger subtle distortions to the compact structure model or induce larger domain rearrangements. The WGR domain deserves further characterization as a substrate-recognition module. A WGR-

centered activation mechanism would provide a strong rationale for developing small-molecule inhibitors specific to PARP-1.

Langelier *et al.*'s study is an impressive advance in our understanding of PARP-1 activation by DSBs. It provides the basis for unraveling the mechanism of PARP-1 activation in the context of a full-length protein. Examining essential domains for the binding of single-strand breaks will be highly informative, especially as regards Zn2, which appears to be critical for the interaction of PARP-1 with single-strand breaks (13). Furthermore, the study paves the way for designing a new generation of PARP-1 specific inhibitors that could disrupt the domain-domain interactions required for forming an active PARP-1 conformation.

Although PARP-1 displays robust DSB-binding activity (14), its identification as an integral component in either of the two main DSB repair pathways, homologous recombination and nonhomologous end joining (NHEJ), has not been rigorously demonstrated. However, recent studies strongly support interplay between DNA protein kinase (DNA PK) and PARP-1 in the DNA dam-

age response through the NHEJ pathway (15, 16). The mechanism by which PARP-1 and DNA PK bind to DNA DSBs must be elucidated before the precise role of these proteins in DNA repair can be understood.

References

1. M. El Jareb, S. Teolia, R. S. Lamb, *BMC Evol. Biol.* **10**, 308 (2010).
2. M. Rouleau, A. Pate, M. J. Hendze, S. H. Kaufmann, G. G. Poirier, *Nat. Rev. Cancer* **10**, 293 (2010).
3. M.-F. Langelier *et al.*, *Science* **336**, 728 (2012).
4. S. Petrucco, R. Percudani, *FEBS J.* **275**, 883 (2008).
5. W. Luyestrom, M. J. van der Woerd, N. Clark, K. Luger, *J. Mol. Biol.* **395**, 983 (2010).
6. H. Mendoza-Alvarez, R. Alvarez-Gonzalez, *J. Biol. Chem.* **268**, 22575 (1993).
7. E. Pion *et al.*, *Biochem.* **44**, 14670 (2005).
8. M. F. Langelier, K. M. Servent, E. E. Rogers, J. M. Pascal, *J. Biol. Chem.* **283**, 4105 (2008).
9. P. T. Boonink *et al.*, *J. Biol. Chem.* **280**, 30206 (2005).
10. P. A. Loeffler *et al.*, *BMC Struct. Biol.* **11**, 37 (2011).
11. M. Altmeyer, S. Messner, P. O. Hassa, M. Fey, M. O. Hothiger, *Nucleic Acids Res.* **37**, 3723 (2009).
12. E. Pic, J. P. Gagné, G. G. Poirier, *Expert Rev. Proteomics* **8**, 759 (2011).
13. S. Eustermann *et al.*, *J. Mol. Biol.* **407**, 149 (2011).
14. T. J. Jorgensen *et al.*, *J. Mol. Recognit.* **22**, 446 (2009).
15. L. Spagnolo, J. Barbeaud, N. J. Curtin, E. P. Morris, L. H. Pearl, *Nucleic Acids Res.* **40**, 1093/naa/gkr1231 (2012).
16. A. G. Piel, J. N. Sarkaria, S. H. Kaufmann, *Proc. Natl. Acad. Sci. U.S.A.* **108**, 3406 (2011).

10.1126/science.1221870

PHYSICS

Intertwining Electron Tunneling with Light

Marzena H. Szymańska

If we try to lob a ball over a building but throw it too slowly, it bounces off. But a quantum-mechanical “ball” (e.g., an electron) also has a wave nature, and thus has a finite chance of tunneling through the barrier (as if our classical ball disappeared into the building and came out the other side). Quantum tunneling underlies natural processes such as radioactive decay and is harnessed in the operation of many devices, such as tunnel junctions and scanning tunneling microscopes. In these applications, tunneling rates are controlled by changing the barrier height or width, either by altering the design (e.g., changing the thickness of an insulating layer) or by applying an external electric field. In a study reported on page 704 of this issue, Cristofolini *et al.* (1) controlled electron tunneling optically by entangling the electron into a complex quasipar-

ticle—which they call a “dipolariton”—partially made of light. This result opens up a wide range of optoelectronic applications based on coherent transfer between a photon state and an electron tunneling state.

This new quasiparticle is unusual in that it has an extremely small mass and a large static electric dipole moment. The small mass allows the room-temperature formation of a Bose-Einstein condensate (BEC), in which the quantum phase of these bosonic particles synchronizes and creates a single macroscopic quantum object. The large dipole moment leads to strong long-range or anisotropic dipolar interactions, which are known to cause exotic physical phenomena (2): novel anisotropic superfluids, supersolids, and topological phases that are currently being sought in ultracold vapors of dipolar atomic gases. It also allows for easy electrical trapping and manipulation.

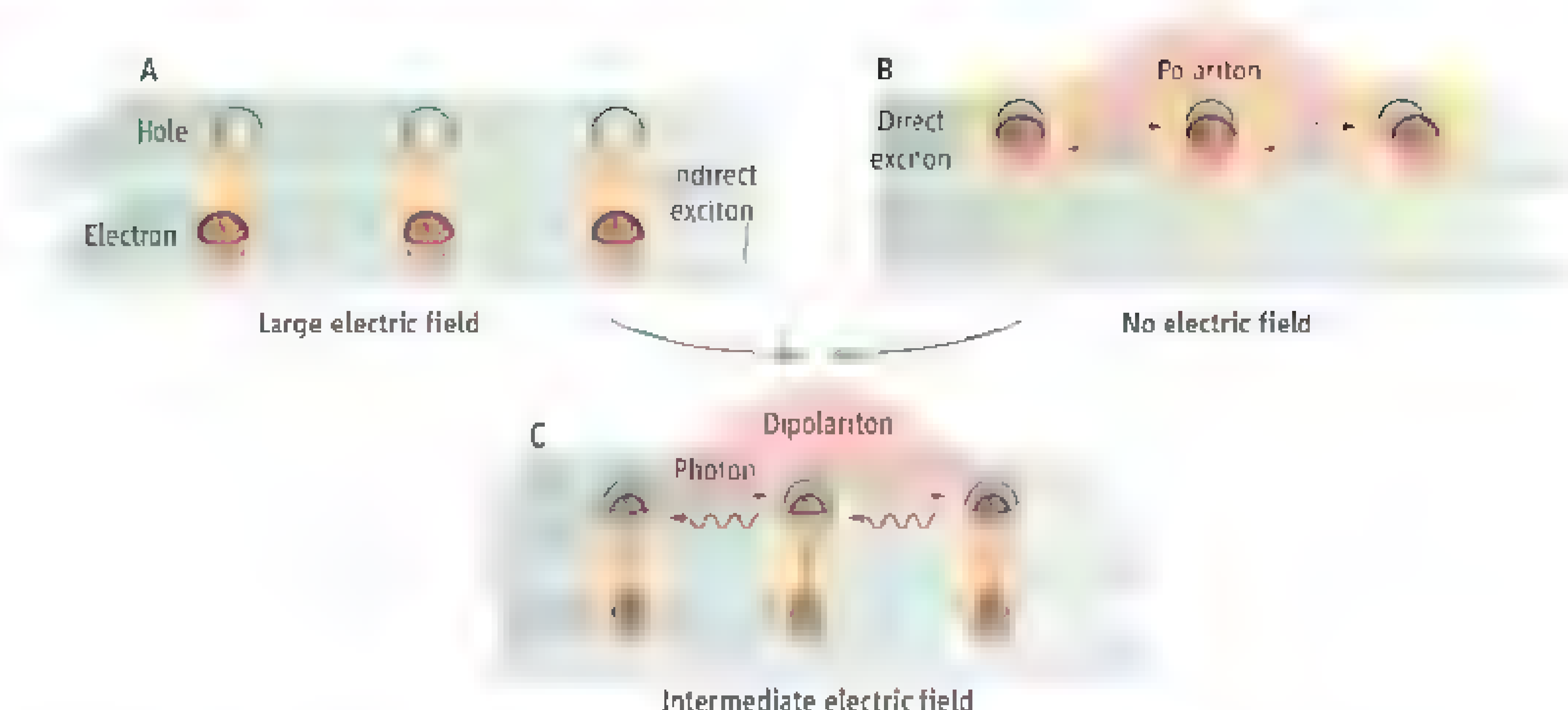
The road to forming BECs from excitons has been a long one. Excitons form

The tunneling of electrons through barriers can be controlled when photons are coupled to excited states of electrons trapped in quantum wells.

when an electron in one energy band of a semiconductor is attracted by a positively charged empty electronic level (a “hole”) in another band. The mass of this bound exciton state is less than that of a typical atom by six orders of magnitude, but the exciton is short-lived—it collapses within a nanosecond, emitting light in the process. Longer exciton lifetimes can be achieved by creating indirect excitons, in which the electron and hole are separated into two neighboring semiconductor layers, called coupled quantum wells, divided by a thin potential barrier by applying an electric field. This barrier is thin enough so that the electron and hole have sufficient Coulomb attraction to form an excitonic bound state, but is still able to hinder electron-hole overlap that leads to their annihilation.

Indirect excitons have lifetimes that are tens of thousands of times those of direct excitons (where the electron and hole are in the same layer) and have been successfully

Department of Physics, University of Warwick, Coventry CV4 7AL, UK. E-mail: m.h.szymanska@warwick.ac.uk



Recipe for photon control of tunneling. Cristofolini *et al.* fabricated two layers of semiconductor separated by a thin barrier of coupled quantum wells that trap negative and positive current carriers (electrons and holes). Mirrors create an optical cavity for photons similar to that used in a laser. Depending on the applied electric (E) field, different type of quasiparticles can form in which the electrons and holes form “atoms” called excitons. (A) At high E fields, “indirect” excitons form in which the electrons and holes occupy different layers and are separated by a barrier, but do not interact with photons. (B) With no E field, direct excitons form in the same layer. When they decay and emit light, the trapped light can reexcite more excitons and form a polariton. However, no electric field control is possible. (C) At intermediate E fields, the indirect excitons can interact with light and form dipolaritons. Light can be introduced into the cavity and can control the rate at which electrons tunnel through the barrier between the layers.

trapped and thermalized (3–5). However, half a century after the theoretical proposals (6), experimental evidence for excitonic BECs remains elusive (7). One reason is that the methods that can be used to create BECs from alkali gases—laser and evaporative cooling to temperatures near absolute zero (8)—do not work for charge carriers in semiconductors. Exciton condensation in semiconductors must rely on increasing their density, which favors outcomes other than condensation, such as annihilation.

Adding photons to the system leads to a solution. The radiated photon from exciton annihilation can be sent back into the semiconductor with mirrors; the photon reexcites an identical bound electron-hole pair. The coherent mixture of exciton and photon forms a new quasiparticle called a polariton. The photon component causes polaritons to have extremely low mass (less than that of excitons by more than three orders of magnitude; less than that of typical atoms by more than nine orders of magnitude), and this low mass makes achievable densities sufficient for the formation of polariton BECs. The realization of a polariton condensate in 2006 (9) was followed by a blossoming of experimental activity (10), with quantum effects even reaching room temperatures (11).

Nonetheless, polaritons do have their limitations. They are neutral particles with tiny dipole moments and so they do not respond

well to external fields, making polaritons difficult to trap and transport. An obvious solution would be to create polaritons out of indirect dipolar excitons, but indirect excitons were originally designed not to interact with light, and so do not form polaritons.

Cristofolini *et al.* managed to overcome this limitation by exploiting quantum tunneling. Their sample consists of asymmetric coupled quantum wells grown inside an optical cavity (see the figure). In the absence of an applied electric field, electrons naturally opt to pair with holes in the same layer and form polaritons. At high applied fields, the indirect excitons are energetically more favorable. Between these two limits, the electron energy levels in both layers can be tuned to a resonance that allows an electron to tunnel across the barrier and delocalize into both quantum wells. The quantum mixing of the two types of excitons, along with a photon, leads to a three-state dipolariton system (lower, middle, and upper). The middle dipolariton is especially useful for condensate formation. It can consist of just the indirect exciton and photon that maximizes the electric dipole strength and still has a strong photonic component, despite the complete absence of any direct interactions between the exciton and the photon.

The work of Cristofolini *et al.* on creating and characterizing dipolaritons can lead to control over fascinating optical phenomena in their collective behavior. A state similar to

a dipolariton, called a dark polariton, seen in atomic systems lies at the heart of electromagnetically induced transparency and slow light (12). These three-state systems give rise to media with amazing optical properties because direct optical transitions between one pair of states are “forbidden,” resulting in so-called lambda schemes. Normally, materials with large refractive indices that slow down light propagation come at the price of increased absorption, but the lambda scheme produces perfectly transparent media in which light can be slowed down or even halted and stored.

Thus quantum interference effect can be switched on for one light beam by the presence of another. However, if one of the optical

transitions is replaced in the lambda scheme by an electron tunneling transition, as in Cristofolini *et al.*’s system, it might be possible for the transparency and slowing of light to be controlled by an electric field rather than by another laser beam—an electrically induced transparency. A photon beam tuned to the desired polariton frequency and momentum could influence the electron tunneling process and then lead to an enhanced or suppressed tunneling rate fully controlled by photons. For now, let the race begin to condense dipolaritons into exotic superfluids or to use them to halt light via electric fields.

References

1. P. Cristofolini *et al.*, *Science* **336**, 704, 10.1126/science.1219010 (2012).
2. M. A. Baranov, *Phys. Rep.* **464**, 71 (2008).
3. L. V. Butov, C. W. Lai, A. L. Ivanov, A. C. Gossard, D. S. Chemla, *Nature* **417**, 47 (2002).
4. A. T. Hammack *et al.*, *Phys. Rev. Lett.* **96**, 227402 (2006).
5. Z. Vörös, D. W. Snoke, L. Pfeiffer, K. West, *Phys. Rev. Lett.* **97**, 016803 (2006).
6. L. V. Keldysh, Y. V. Kopaev, *Fiz. Tverd. Tela* **6**, 2791 (1964) [*Sov. Phys.* **6**, 2219 (1965)].
7. D. W. Snoke, *Adv. Condens. Matter Phys.* **2011**, 938609 (2011).
8. W. D. Phillips, *Rev. Mod. Phys.* **70**, 721 (1998).
9. J. Kasprzak *et al.*, *Nature* **443**, 409 (2006).
10. H. Deng, H. Haug, Y. Yamamoto, *Rev. Mod. Phys.* **82**, 1489 (2010).
11. S. Christopoulos *et al.*, *Phys. Rev. Lett.* **98**, 126405 (2007).
12. M. Fleischhauer, A. Imamoglu, J. P. Marangos, *Rev. Mod. Phys.* **77**, 633 (2005).

10.1126/science.1221416

MOLECULAR BIOLOGY

RNA Plays Meiotic Matchmaker

Abby F. Dernburg^{1,2,3,4}

Most eukaryotic cells contain two homologous sets of chromosomes, one inherited from each parent. Meiosis, the cell division process required for sexual reproduction, involves a single round of DNA replication and two successive rounds of cell division. A hallmark of meiosis is the pairing of homologous chromosomes, which enables them to recombine and then separate from each other. Despite recent progress in understanding the forces that promote chromosome interactions, the molecular basis for homologous chromosome recognition—even the temporal and spatial scales on which it acts—are still mysterious. On page 732 in this issue, Ding *et al.* (1) describe a pairing mechanism in which RNA mediates homologous chromosome association during meiosis in the fission yeast *Schizosaccharomyces pombe*.

In mammals, plants, and fungi, robust association of homologous chromosomes requires the initiation of recombination through the formation of DNA double-strand breaks and the activity of DNA repair enzymes (homologs of the bacterial RecA proteins). However, homolog pairing in some metazoans proceeds in the absence of DNA breaks, implying the existence of other homology-detecting mechanisms. It is likely that other processes, including the attachment of telomeres (the ends of chromosomes) to the nuclear envelope and motor-driven chromosome motion, contribute to preliminary alignment, which can then be reinforced or rejected during recombination. But it is unclear whether initial recognition is mediated through protein-protein interactions, DNA base-pairing, or other chromosomal features.

In vivo imaging of chromosome dynamics in *S. pombe* shows that during meiotic prophase, all telomeres associate with the nuclear envelope and form a tight cluster associated with the spindle pole body (2, 3). The spindle pole body organizes an array of cytoplasmic microtubules and drags the

nucleus back and forth through the cytoplasm. During this telomere-led “horse-tail” stage, loci along the chromosome arms undergo dynamic pairing and unpairing, but as recombination events gradually reinforce homologous interactions, pairing becomes more and more prevalent (4).

Ding *et al.* observed that the *sme2* locus pairs earlier and more robustly than other loci at similar distances from telomeres, even in the absence of meiotic recombination. This locus encodes a noncoding RNA called meiotic RNA (meiRNA), which enables cells to switch from mitosis to meiosis by binding two proteins, Mei2 and Mmi1. These proteins are positive and negative regulators, respectively, of meiotic entry. Mmi1 binds to more than 100 meiRNAs that contain a hexanucleotide motif and destabilizes them to prevent precocious meiosis (5–8); meiRNA acts as a “decoy” to sequester the activity of Mmi1 and allow for expression of meiotic genes. Mei2 inactivates Mmi1 during meiosis.

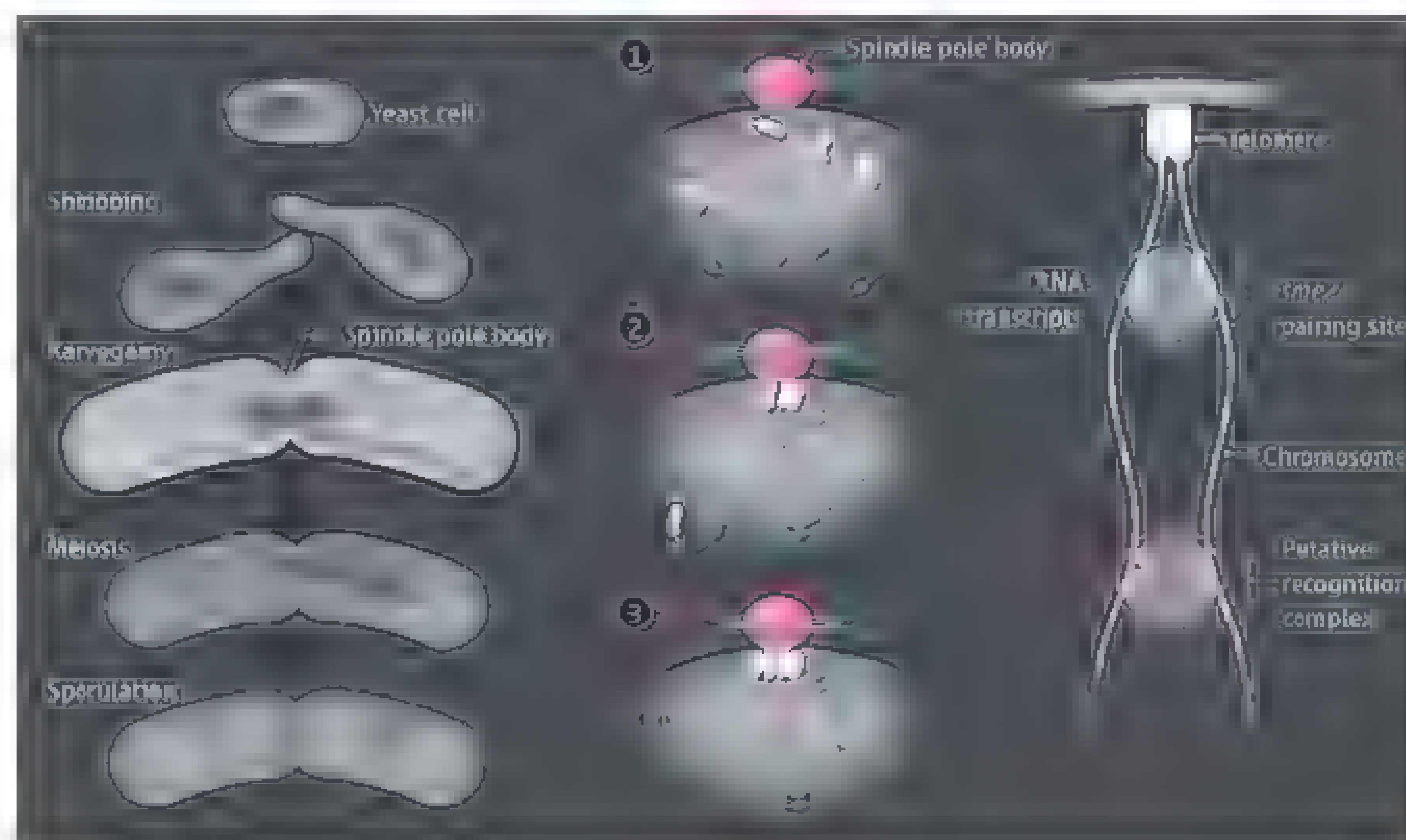
Ding *et al.* found that a longer noncoding RNA, meiRNA-L, is transcribed from this site and is responsible for the recombination-independent pairing of homologous loci. The authors mapped the pairing activity to the 3′ end of meiRNA-L and showed that transcripts must originate from both

RNA plays a role in homologous chromosome pairing during meiosis

homologs to promote pairing. By tagging meiRNA-L with a protein-binding aptamer, they observed that the nascent RNAs converge to form a single dot in the nucleus even when two dots are still detected for the chromosomal loci, indicating that RNA pairing precedes chromosome pairing. This activity is independent of the RNA interference machinery, can be uncoupled from Mei2 binding, and occurs even more robustly in the presence of a mutant allele of Mmi1 with reduced regulatory function.

There had been little experimental evidence to support the notion that RNAs might play a role in meiotic chromosome pairing. In hilly and mouse meiocytes, a subset of the genome is transcribed during early meiotic prophase, concomitant with homolog pairing, but a causal link was never demonstrated (9). In dipteran insects, homologous chromosomes are paired even in somatic cells (10, 11). In *Drosophila melanogaster* embryos, this pairing is established at roughly the same time that zygotic transcription becomes highly active (12), and initiates at multiple points along each chromosome (13). However, there is no evidence that somatic pairing is mediated by or requires transcription.

Stronger evidence for RNA-mediated homologous pairing comes from studies of X-chromosome inactivation in mamma-



Homolog recognition. In *S. pombe*, telomeres tether chromosomes to the nuclear envelope and associate with the spindle pole body. In the model of Ding *et al.*, complexes containing RNA transcripts emanating from loci along the chromosome act as recognition sites to align homologs.

¹Howard Hughes Medical Institute, Chevy Chase, MD 20815, USA. ²Department of Molecular and Cell Biology, University of California, Berkeley, CA 94720, USA. ³Life Sciences Division, Lawrence Berkeley National Laboratory, Berkeley, CA 94720, USA. ⁴California Institute for Quantitative Biosciences, Berkeley, CA 94720, USA. E-mail: afdernburg@bl.gov

lian cells. This process, which equalizes the expression of genes on the X chromosome in males and females, depends on the X-inactivation center (Xic) locus. This large (~500 kb), complex region templates the transcription of numerous noncoding RNAs that specify which X chromosome will remain active. All other X chromosomes in the cell are silenced through epigenetic modification. Selection of the active X involves transient association between Xic loci on different X chromosomes (14), and this homologous pairing requires transcription of at least two noncoding RNAs from the Xic locus, Tsix and Xite. However, it is unclear whether noncoding RNAs or simply the act of transcription is important for pairing (15).

Several features of RNA make it a good candidate for mediating homologous pairing. A nascent transcript anchored to a chromosome could emanate from the site of its transcription, providing a “feeler” to search for a homologous sequence. Some RNAs, such as ribosomal RNAs, are localized to

discrete nuclear bodies, and recruitment of nascent transcripts could promote colocalization of the homologous loci. Although RNA-mediated pairing may not occur at all loci, a limited number of sites along a chromosome could serve as landmarks to establish a coarse alignment between homologs, which might subsequently be reinforced (or rejected) through recombination-based homology search or other processes. The mechanisms used by many eukaryotes to suppress the transcription of transposons and other high-copy DNA elements in germ cells could also serve to exclude these sequences from RNA-based homology search mechanisms.

Although it remains unclear how extensive a role is played by RNA in matching up homologous chromosomes during meiosis, even in *S. pombe*, the work by Ding *et al.* will motivate experiments in other model organisms. Identifying other components important for pairing at the *sme2* locus, such as protein factors that keep the nascent meiRNAs

tethered in cis to their sites of transcription, and/or other loci that also pair robustly in the absence of recombination, will help to clarify the role of RNA in homologous recognition.

References

1. D.-Q. Ding *et al.*, *Science* **336**, 732 (2012).
2. Y. Chikashige *et al.*, *Science* **264**, 270 (1994).
3. Y. Chikashige *et al.*, *Cell* **125**, 59 (2006).
4. D. Q. Ding, A. Yamamoto, T. Haraguchi, Y. Hiraoka, *Dev Cell* **6**, 329 (2004).
5. H. M. Chen, B. Fitcher, J. Leatherwood, *PLoS ONE* **6**, e26804 (2011).
6. M. Yamamoto, *Proc. Jpn. Acad., Ser. B, Phys. Biol. Sci.* **86**, 788 (2010).
7. Y. Hiraoka *et al.*, *Nature* **442**, 45 (2006).
8. A. Yamashita *et al.*, *Open Biol.* **2**, 120014 (2012).
9. Y. Hotta, S. Tabata, L. Stubbs, H. Stern, *Cell* **40**, 785 (1985).
10. N. M. Stevens, *J. Exp. Zool.* **5**, 359 (1908).
11. C. W. Metz, *J. Exp. Zool.* **21**, 213 (1916).
12. Y. Hiraoka *et al.*, *J. Cell Biol.* **120**, 591 (1993).
13. J. C. Fang, W. F. Marshall, A. Demburg, D. A. Agard, J. W. Sedat, *J. Cell Biol.* **141**, 5 (1998).
14. N. Xu, C.-L. Tsai, J. T. Lee, *Science* **311**, 1149 (2006).
15. N. Xu, M. E. Donohoe, S. S. Silva, J. T. Lee, *Nat. Genet.* **39**, 1390 (2007).

10.1126/science.1222647

CLIMATE CHANGE

The Ice Age Carbon Puzzle

Edward Brook

Between about 24,000 years ago and today, the large ice sheets covering most of Canada and parts of Europe and Asia melted away, sea level rose by 120 m, Earth warmed by about 5°C, and rainfall and vegetation patterns shifted, sometimes abruptly. This dramatic natural climate experiment was set in motion by cyclic variations in the geometry of Earth's orbit, but a complex system of feedbacks governed the transition from a glacial to an interglacial state. One of the most important of these feedbacks was a well-documented change in the atmospheric greenhouse gas carbon dioxide (CO₂) (1). On page 711 of this issue, Schmitt *et al.* (2) provide important new carbon isotopic data that help to explain these changes.

Multiple studies of air trapped in polar ice have shown that ~17,500 years ago CO₂ levels started to rise from ice age levels of about 180 parts per million (ppm), reaching about 265 ppm 10,000 years ago (see the figure). Over the next 10,000 years, CO₂ slowly rose by another 20 ppm, until the rapid increase

that started in the industrial age took over. Looking farther back in time, CO₂ variations appear to be a fundamental characteristic of ice age cycles (3).

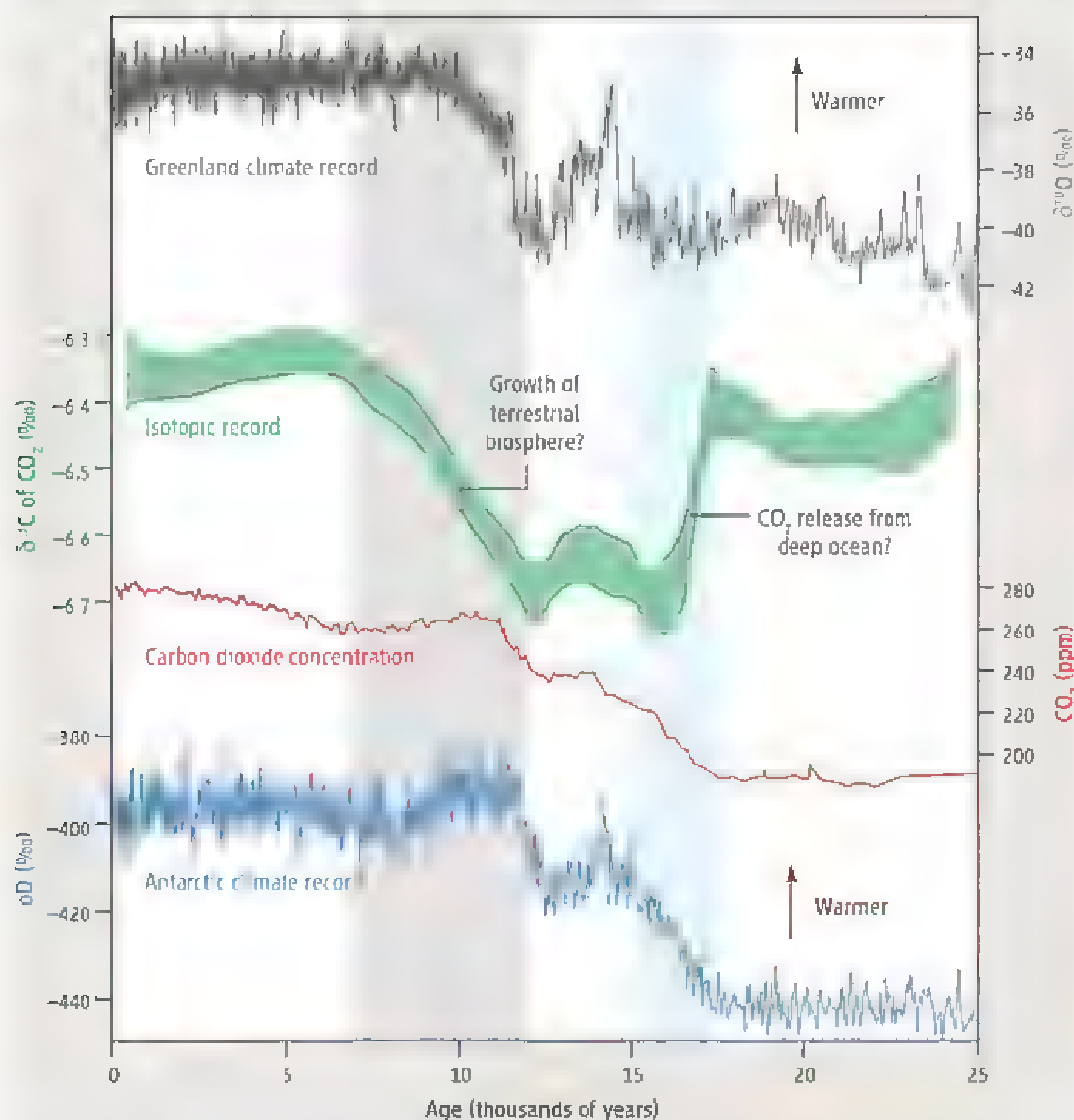
Exactly why CO₂ changed like this has been vexing geochemists for decades. The carbon cycle involves uptake and release of CO₂ from both land and oceanic reservoirs, and these processes operate on many time scales. No one unified theory fits all available evidence, nor is the available evidence sufficient to test all hypotheses. The stable carbon isotopic composition of CO₂ could help to resolve these issues. This is because various carbon cycle processes fractionate the heavy isotope ¹³C from the lighter ¹²C. Photosynthesis, for example, preferentially removes ¹²C from the atmosphere, and isotope fractionation during inorganic partitioning of CO₂ between the atmosphere and ocean is also important. However, apart from the clear isotopic signature of fossil fuel CO₂ input since the industrial revolution (4) and some hints from pioneering work (5, 6), ice core isotopic measurements have not been detailed or precise enough to yield consistent patterns. Schmitt *et al.* now move the isotopic story forward with an important data set.

A carbon isotope record helps to explain why carbon dioxide concentrations change during ice age cycles.

The primary problems to overcome have been technical. Available ice samples tend to be small, and the isotopic variations are also relatively small, making it both difficult and necessary to make precise measurements. Extracting air for CO₂ measurements requires either mechanical disaggregation or sublimation under vacuum, plus purification of CO₂, all of which can introduce artifacts. Furthermore, at deeper depths in the great ice sheets, air slowly changes from being occluded in bubbles to a solid hydrate form. Releasing air from hydrates by mechanical means is inefficient, and fractionation between bubbles and hydrates can cause further problems.

Schmitt *et al.* have overcome some of these challenges to produce the best record to date of the glacial to interglacial variations in stable carbon isotopes of CO₂. They adapted and painstakingly refined a traditionally cumbersome technique of sublimating ice and coupled it with a sensitive mass spectrometric technique to measure isotope ratios (7). Schmitt *et al.* augmented their latest sublimation data set with several others, although the results are primarily drawn from one Antarctic ice core. To create a unified picture of isotopic variations for the past 24,000 years,

College of Earth, Ocean, and Atmospheric Sciences, Oregon State University, Corvallis, OR 97331, USA. E-mail: brooke@oregonstate.edu.



they smoothed the combined record using a method that incorporates analytical uncertainty. The resulting curve provides a good picture of isotopic variations on thousand-year time scales, at the expense of losing resolution of more detailed variations.

The data provide much food for thought. Going forward in time from 24,000 years ago, the isotopic pattern resembles a somewhat distorted letter W. The first event is a rapid 0.3 per mil depletion in ^{13}C between about 17,500 and 14,000 years, a time when the CO_2 concentration rose by about 60 ppm. Schmitt *et al.* suggest that this is consistent with release of CO_2 from a previously isolated deep-ocean reservoir that accumulated carbon as a result of oxidation of organic detritus sinking from the surface ocean. Variants of this hypothesis have been presented recently (8, 9), and the idea gains support from the fact that the amount of radioactive ^{14}C in the atmosphere dropped drastically at about the same time as the carbon isotope ratio decreased (10). Studies of ^{14}C in fossil organisms found in deep sea sediments,

which can provide estimates of the age of ancient deep ocean water, both support (11, 12) and call into question (13) the existence and ventilation of the isolated reservoir.

The middle section of the W, between about 14,000 and 12,000 years ago, is subdued (see the figure). There are hints of variations that may be related to abrupt climate change seen in ice cores and other records, but they are too small to be interpreted clearly. This interval contains most of the remaining glacial-interglacial change in CO_2 , and the lack of major isotopic change may indicate a different mechanism for this change than for the previous increase.

The other end of the W-shaped pattern is a slow rise in the isotope ratio between about 12,000 and 7000 years ago. Schmitt *et al.* suggest that this increase may reflect growth of the terrestrial biosphere, which preferentially removes ^{12}C from the atmosphere.

Schmitt *et al.* provide plausible interpretations of their results, but the role of other processes—including the input of magmatic CO_2 and the release of carbon from the terres-

Glacial-interglacial change. Over the course of the past 24,000 years, CO_2 concentrations have risen (red curve) (1) as Earth emerged from glaciation, as shown by climate records from Greenland and Antarctica (gray and blue curves, respectively) (14, 15). Schmitt *et al.* (2) report a record of the change in the $^{13}\text{C}/^{12}\text{C}$ ratio of CO_2 during this time (green curve). The isotopic ratio is expressed in delta notation, where $\delta^{13}\text{C}$ is the deviation of a sample ratio from that of an internationally expected standard, expressed in parts per thousand. Comparison of the CO_2 record with the isotopic record provides insights into the mechanisms behind the CO_2 rise. D, deuterium.

trial biosphere, among others, remains to be fully evaluated. Large-scale carbon cycle models will be needed to explore the full significance of these long-awaited data.

One limitation of the results is that the smoothed record does not allow us to see more rapid changes in the isotopic ratio of CO_2 . Such changes are possible and could provide important clues to why so many of the inflection points during the glacial-interglacial CO_2 rise seem to correspond to abrupt shifts in climate seen in ice cores in Greenland and Antarctica (see the figure).

Schmitt *et al.* have paved the way for more laborious lab work that may further unwrap these and other mysteries, and may ultimately lead to a more complete understanding of carbon cycle feedbacks. Such feedbacks will operate during the current human experiment with the climate system, and therefore are important to understand.

References

1. E. Monnin *et al.*, *Science* **291**, 112 (2001).
2. J. Schmitt *et al.*, *Science* **336**, 711 (2012); 10.1126/science.1217161.
3. D. Lüthi *et al.*, *Nature* **453**, 379 (2008).
4. R. J. Francey *et al.*, *Tellus B*, **51**, 170 (1999).
5. A. Lourantou *et al.*, *Global Biogeochem. Cycles* **24**, GB2015 (2010).
6. H. J. Smith, H. Fischer, M. Wahlen, D. Mastrosianni, B. Deck, *Nature* **400**, 248 (1999).
7. J. Schmitt, R. Schneider, H. Fischer, *Atmos. Meas. Tech.* **4**, 1445 (2011).
8. R. F. Anderson *et al.*, *Science* **323**, 1443 (2009).
9. D. M. Sigman, M. P. Rayn, G. H. Haug, *Nature* **466**, 47 (2010).
10. W. Broecker, S. Barker, *Earth Planet. Sci. Lett.* **256**, 90 (2007).
11. D. C. Lund, A. C. Mix, J. Southon, *Not. Geosci.* **4**, 771 (2011).
12. A. Burke, L. F. Robinson, *Science* **335**, 557 (2012).
13. L. C. Skinner, S. Fallon, C. Waelbroeck, E. Michel, S. Barker, *Science* **328**, 1147 (2010).
14. P. M. Grootes, M. Stahler, *J. Geophys. Res.* **102**, 26455 (1997).
15. J. Jouzel *et al.*, *Science* **317**, 793 (2007).

Published online 29 March 2012;
10.1126/science.1219710

Dawn at Vesta: Testing the Protoplanetary Paradigm

C. T. Russell,^{1*} C. A. Raymond,² A. Coradini,³ H. Y. McSween,⁴ M. T. Zuber,⁵ A. Nathues,⁶ M. C. De Sanctis,³ R. Jaumann,⁷ A. S. Konopliv,² F. Preusker,⁷ S. W. Asmar,² R. S. Park,² R. Gaskell,⁹ H. U. Keller,⁶ S. Mottola,⁷ T. Roatsch,⁷ J. E. C. Scully,⁸ D. E. Smith,⁵ P. Tricarico,⁹ M. J. Toplis,¹⁰ U. R. Christensen,⁶ W. C. Feldman,⁹ D. J. Lawrence,¹¹ T. J. McCoy,¹² T. H. Prettyman,⁹ R. C. Reedy,⁹ M. E. Sykes,⁹ T. N. Titus¹³

The Dawn spacecraft targeted 4 Vesta, believed to be a remnant intact protoplanet from the earliest epoch of solar system formation, based on analyses of howardite-eucrite-diogenite (HED) meteorites that indicate a differentiated parent body. Dawn observations reveal a giant basin at Vesta's south pole, whose excavation was sufficient to produce Vesta-family asteroids (Vestoids) and HED meteorites. The spatially resolved mineralogy of the surface reflects the composition of the HED meteorites, confirming the formation of Vesta's crust by melting of a chondritic parent body. Vesta's mass, volume, and gravitational field are consistent with a core having an average radius of 107 to 113 kilometers, indicating sufficient internal melting to segregate iron. Dawn's results confirm predictions that Vesta differentiated and support its identification as the parent body of the HEDs

Meteoritic evidence indicates that Vesta probably formed within 2 million years of the first condensation of solids within the nebula of gas and dust that became our solar system (1). Short-lived radioactive nuclides, ²⁶Al and ⁶⁰Fe, were present in these first few million years (2), trapping heat inside objects accreting at that time. Bodies that formed very early and incorporated the live radioactive material should have melted and differentiated (3), whereas bodies of a slightly younger age may not have. These early-forming objects, both differentiated and undifferentiated, are considered to be protoplanets and constitute the material that coalesced to form the terrestrial planets. Determining whether Vesta was a surviving protoplanet became the objective of Dawn, NASA's ninth Discovery mission, designed to orbit successively the two most massive survivors from the earliest days of the solar system, 4 Vesta

and 1 Ceres. On 27 September 2007, Dawn began its 4-year trip to Vesta. After a Mars gravity assist in February 2009, Dawn reached Vesta on 16 July 2011 and slipped into orbit with no critical injection burn

Vesta is substantially larger than anybody encountered by previous reconnaissance missions within the main asteroid belt (Fig. 1),

dwarfed only by its sibling Ceres. It appears to be an intact original protoplanet that has survived the collisional environment of the asteroid belt since its formation over 4.56 billion years ago. Vesta has been identified as the source of a very common class of meteorites, the howardite-eucrite-diogenites (5), which make up ~6% of the meteorites seen to fall on Earth. These meteorites appear to have been liberated from the crust and possibly the mantle of a small differentiated body. Unlike the explorations of the Moon, Mercury, Mars, and Venus, which were undertaken initially without prior knowledge of the target's composition, our exploration of Vesta begins with a rich petrologic and geochemical understanding. Dawn will be providing the geological context for this insight

Dawn arrived in vestan southern summer, allowing a complete survey of the south polar region. Rheasilvia, a giant impact basin (6), dominates this region. Its large central peak is higher than Mauna Kea on Hawaii (with respect to the underlying ocean floor) and rivals the height of Olympus Mons on Mars (Fig. 2). This impact alone could have liberated most of the material that composes the Vestoids, which display orbits and reflectance spectra similar to those of Vesta (7, 8), possibly as recently as 1 billion years ago (9). The giant Rheasilvia impact has resulted in a strong dichotomy between the northern and southern hemispheres, reflected in surface albedo and crater densities, but did not erase evidence of an older, underlying large impact basin, possibly providing an earlier additional source of HEDs.

¹Institute of Geophysics and Planetary Physics, University of California, Los Angeles, CA 90095-1567, USA. ²Jet Propulsion Laboratory, California Institute of Technology, Pasadena, CA 91109, USA. ³Istituto di Astrofisica e Planetologia Spaziali, Istituto Nazionale di Astrofisica, Rome, Italy. ⁴Department of Earth and Planetary Sciences, University of Tennessee, Knoxville, TN 37996-1410, USA. ⁵Massachusetts Institute of Technology, Cambridge, MA 02139-4307, USA. ⁶Max-Planck-Institut für Sonnensystemforschung, Katlenburg-Lindau, Germany. ⁷Institute of Planetary Research, DLR, Berlin, Germany. ⁸Department of Earth and Space Sciences, University of California, Los Angeles, CA 90095-1567, USA. ⁹Planetary Science Institute, Tucson, AZ 85719, USA. ¹⁰Institut de Recherche en Astrophysique et Planétologie, Université de Toulouse, France. ¹¹Johns Hopkins University Applied Physics Laboratory, Laurel, MD 20723, USA. ¹²Smithsonian Institution, Washington, DC 20560, USA. ¹³U.S. Geological Survey, Flagstaff, AZ 86001, USA

*To whom correspondence should be addressed. E-mail: crussel@igpp.ucla.edu



Fig. 1. Collage of Vesta in comparison with other asteroids visited to date for which good images exist. This south polar view of Vesta shows the south pole mountain and the Rheasilvia impact basin surrounding this central peak.

Dawn's orbital mission provides the surface coverage, observation time, and spatial resolution necessary to comprehensively characterize Vesta's complex structure and composition. Spectral mapping reveals a diverse surface consistent with the mineralogy of the HED meteorites (10). Tracking and imaging allowed improvements in geophysical parameters relevant to understanding Vesta's internal structure and dynamics (Table 1). The average density, a key parameter in deducing its interior structure, is determined from the volume of our image-derived shape model (11);

and the mass is determined by means of radiometric tracking (12). Before Dawn's arrival, the best estimates of Vesta's mass depended on the asteroid's perturbation of Mars, whose position can be determined to within about 5 m from landers and orbiters. The perturbation of the Dawn spacecraft by Vesta's gravitational field (12) yields a mass within the bounds of error of estimates from the Mars data (13) but with a significantly reduced uncertainty (Table 1).

Extensive imagery and tracking data from orbit enable the development of a high-accuracy

control point network to determine the spin axis orientation (14), significantly different than that derived from Hubble Space Telescope (HST) observations (Table 1). The spin period has also been refined. The north pole was dark upon Dawn's arrival and will remain so until about 20 August 2012; the unmeasured shape of the northern polar region results in a small uncertainty in the current volume estimate. The shape model was also used to calculate a best-fit ellipsoid (Table 1). The new volume estimate, using the previous HST shape model (15) to fill in the unmapped northern polar region, is $74,970 \times 10^6 \text{ km}^3$, yielding an average density of 3456 kg m^{-3} . This value is at the lower end of bulk densities previously derived, which ranged from 3500 to 3900 kg m^{-3} and were uncertain within a range of 3100 to 4700 kg m^{-3} (15). It is comparable to bulk silicate compositions having densities of 3320 to 3630 kg m^{-3} predicted by HED analyses (16) that assume negligible porosity. Although bulk density is formally accurate to better than 1 part in 10^3 , a conservative estimate of uncertainty is $\pm 1\%$ (17), the final answer depends on the shape determined after the complete surface has been mapped.

This density estimate is combined with Dawn's measurement of 0.03178 for the gravitational moment J_2 (18) derived from radiometric tracking to explore the range of models of Vesta's interior consistent with the geophysical and geochemical constraints. The J_2 predicted from Vesta's shape for a homogeneous density is 0.0350. Thus, the measured J_2 confirms the presence of a central mass concentration. The size of J_2 , resulting from this central mass concentration depends on its density and shape. Ignoring non-hydrostatic contributions (19), a mass-balance approach was used to investigate Vesta's internal structure to obtain constraints on the size of the core, as a function of its shape, from a sphere to an oblate spheroid with flattening $(a-c)/a$ of 0.15, where a and c are the major and minor axes, respectively, of the elliptical cross section. A flattening of a factor of 0.14 is predicted if Vesta's shape of mean radius 263 km has reached hydrostatic equilibrium, whereas the flattening of the core is expected to be smaller. The measured flattening of Vesta is ~ 0.21 . The difference between the predicted and measured values could be the result of the massive excavation of the south polar basin due to giant impacts

For assumed core densities of 7100 and 7800 kg m^{-3} , consistent with densities of iron meteorites (1, 20), the core size and bulk silicate density were derived using a two-layer mass-balance model that can reproduce J_2 (Fig. 3). The assumption of an iron-nickel core is supported by the observed siderophile element depletion seen in HEDs (21). It is difficult to estimate the sulfur content of the cores of differentiated bodies, but studies of iron meteorites suggest small sulfur abundances at the weight % level (22), so we have not made density corrections for sulfur. For

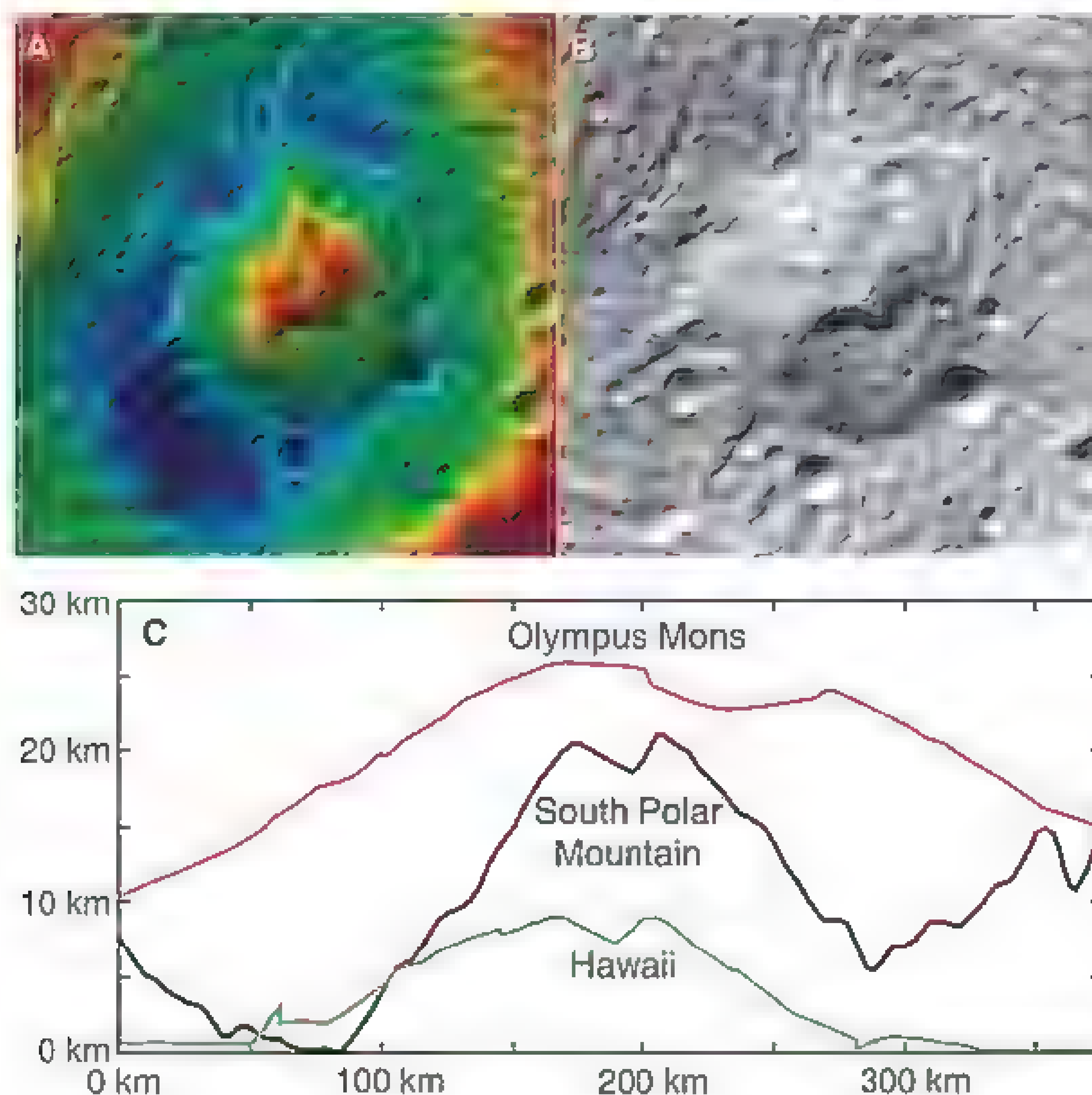


Fig. 2. Cross sections of the central peak of the Rheasilvia impact basin, shown in color-contoured topography (A) and as an orthorectified image mosaic (B) compared with the cross section of Olympus Mons on Mars and Hawaii on Earth (C). The topography of the Rheasilvia basin is relative to a reference ellipsoid of $285 \times 285 \times 229 \text{ km}$.

Table 1. Vesta physical parameters from Dawn compared to the previous HST values.

Parameter	Dawn	Previous knowledge
Major axes (km)	$(286.3/278.6/223.2) \pm 0.1$	$(280 \times 289 \times 229) \pm 5$ (15)
Mean radius (km)	262.7 ± 0.1	264.6 ± 5 (15)
Volume (km^3)	$74,970 \times 10^6$	$77.60 \pm 8.7 \times 10^6$ (15)
Mass (kg)	$2.59076 \pm 0.00001 \times 10^{20}$	$2.6 \pm 0.3 \times 10^{20}$ (13)
Bulk density (kg m^{-3})	$3456 \pm 1\%$	$3800 \pm 15.8\%$ (15)
Gravitational flattening (J_2)	$0.0317799 \pm 0.0005\%$	—
Spin pole right ascension (deg)	309.03 ± 0.01	$301^\circ \pm 5^\circ$ (15)
Spin pole declination (deg)	42.23 ± 0.01	$41^\circ \pm 5^\circ$ (15)
Rotation rate (deg/day)	1617.333119 ± 0.000003	1617.332776 (15)

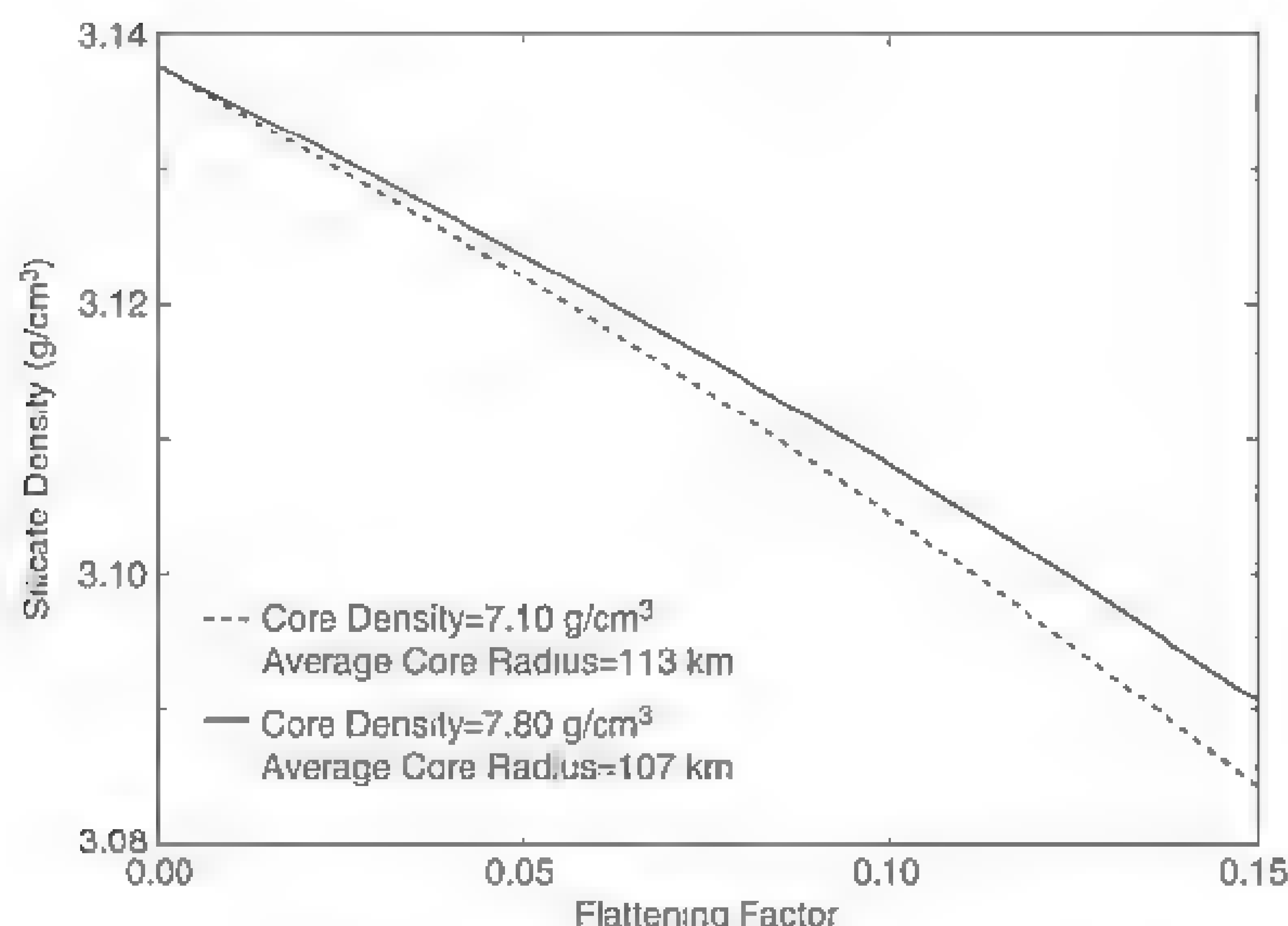


Fig. 3. Forward calculations of the bulk silicate densities and core-flattening factors that match the observed J_2 of Vesta for two values of core density and their derived average equivalent spherical core sizes.

flattening greater than zero and less than 0.15, the range of values of core size and silicate density that fits J_2 is constrained narrowly, indicating that the unknown shape of the core does not lead to a significant error in the size estimate. The resulting average core size (equivalent spherical core size) has a radius of 107 to 113 km, resulting in a core mass fraction (~18%) similar to that deduced from analysis of the HEDs (16, 21). The core size and shape that fit J_2 are only weakly dependent on the core density, rather, the density of the silicate fraction controls the fit for a given flattening.

The derived core size, constrained by the densities of iron meteorites, the chemistry of the HEDs, and petrogenic models of Vesta's interior evolution (16, 23, 24), is consistent with a magma ocean scenario (16). A vestan mantle of olivine plus orthopyroxene having diogenite compositions (25) will have a bulk silicate density of 3400 to 3500 kg m⁻³, assuming zero porosity. The bulk silicate density for this range of iron core density, size, and shape, however, is 3085 to 3138 kg m⁻³, which is lower than previous estimates that neglect porosity (16, 26, 27). When the less dense crustal layer is taken into account, the mantle density will be higher (~3200 kg m⁻³). Although it is clear that neglecting nonhydrostatic contributions to J_2 results in an error in the derived bulk silicate density (19), it is nevertheless low compared to nonporous HED densities (16), and it does agree with recent HED bulk densities that include porosity, which cluster between 2800 and 3200 kg m⁻³ (27). The lower bulk density estimate derived from Dawn data suggests 5 to 6% porosity in the mantle and crust, which is consistent with Vesta's intense bombardment history as revealed by Dawn.

As detailed here and in accompanying papers, Dawn's exploration has confirmed that Vesta is a surviving protoplanet whose properties are as inferred from HED meteorites. Vesta appears to have accreted early and differentiated, forming an iron core that may have sustained a magnetic dynamo (28). The surface of Vesta records its collisional evolution over its 4.5-billion-year history (8, 29). The Rheasilvia impact basin is consistent with the production of the HEDs and the Vestoids (6). Vesta's thick regolith has the mineralogy expected for HED meteorites (10). Still, it preserves the record of its early magmatic processing, reflected in distinct surface regions with more color variation than other asteroids (30). Dawn has also provided geologic enigmas: the circumplanetary troughs (29), patches of bright and dark material (10, 29, 30), and significant mass wasting (29), all revealing a complex petrologic, geochemical, and tectonic history. Vesta's rapid growth, large size, and massive iron core may help explain how this protoplanet was able to withstand the intense pummeling to which it obviously has been subjected.

References and Notes

1. H. Y. McSween, G. R. Huss, *Cosmochemistry* (Cambridge Univ. Press, Cambridge, 2010).
2. H. C. Urey, *Proc. Natl. Acad. Sci. U.S.A.* **41**, 127 (1955).
3. A. Coradini et al., *Space Sci. Rev.* **164**, 25 (2011).
4. C. T. Russell, C. A. Raymond, *Space Sci. Rev.* **163**, 1 (2011).
5. I. B. McCord, J. B. Adams, T. V. Johnson, *Science* **168**, 1445 (1970).
6. P. Schenk et al., *Science* **336**, 694 (2012).
7. R. P. Binzel, S. Xu, *Science* **260**, 186 (1993).
8. F. Marzari et al., *Astron. Astrophys.* **316**, 248 (1996).
9. S. Marchi et al., *Science* **336**, 690 (2012).
10. M. C. De Sanctis et al., *Science* **336**, 697 (2012).
11. Vesta's volume was estimated using three methods. (1) a stereophotoclinometrically derived (SPC) shape model

that filled in the unmeasured northern latitudes with spherical harmonics fit to the measured region; (2) the SPC shape model that used the Thomas shape model (21) to fill in the northern cap; and (3) the stereophotogrammetrically derived shape model filled in the north with the SPC harmonics. The differences were 0.28% between models 1 and 2 and 0.059% between 1 and 3, indicating that the unmeasured northern cap is unlikely to cause a large uncertainty in the volume estimate. Model 2 is used throughout this report.

12. A. Konopliv et al., *Space Sci. Rev.* **163**, 461 (2011).
13. A. Konopliv et al., *Icarus* **211**, 401 (2011).
14. See supplementary materials on Science Online.
15. P. Thomas et al., *Icarus* **128**, 88 (1997).
16. A. Ruzicka, G. A. Snyder, L. A. Taylor, *Meteorit. Planet. Sci.* **32**, 825 (1997).
17. The error in bulk density was estimated by assuming uncertainties in the axial dimensions of a best fit ellipsoid of 100 m equatorial and 500 m polar, and forward-calculating the density variation. The quoted value is three times that estimate.
18. J_2 is the gravitational moment associated with the normalized spherical harmonic coefficient of the Legendre polynomial $P_2 - C_{20}$ and is related to the gravitational flattening (31).
19. Vesta's shape and the values of J_2 , C_{22} , and S_{22} (C_{22} , 0.0043590 ± 0.0000003, S_{22} , 0.000254 ± 0.000005) indicate that Vesta is not currently in hydrostatic equilibrium, but its rotation dominates the second harmonic of its gravity field. Vesta may have been closer to hydrostatic equilibrium at the time of core formation, in which case its core may have frozen in an oblate shape. The dependence of the derived bulk silicate density on the core's shape demonstrates that its influence is weak.
20. V. F. Buchwald, *Handbook of Iron Meteorites* (Univ. of California Press, Berkeley, CA, 1975).
21. K. Righter, M. J. Drake, *Meteorit. Planet. Sci.* **32**, 929 (1997).
22. N. L. Chabot, B. Haack, in *Meteorites and the Early Solar System*, D. S. Lauretta, H. Y. McSween, Eds. (Univ. of Arizona Press, Tucson, AZ, 2006), pp. 747–771.
23. H. Y. McSween et al., *Space Sci. Rev.* **163**, 141 (2010) and references therein.
24. M. T. Zuber et al., *Space Sci. Rev.* **163**, 77 (2011) and references therein.
25. A. W. Beck, H. Y. McSween Jr., *Meteorit. Planet. Sci.* **45**, 850 (2010).
26. G. Dreibus, H. Wanka, *Z. Naturforsch. C* **35a**, 204 (1980).
27. D. Britt et al., *Lunar Planet. Sci. Conf.* **41**, 1869 (2010).
28. B. P. Weiss et al., *Science* **322**, 713 (2008).
29. R. Jaumann et al., *Science* **336**, 687 (2012).
30. V. Reddy et al., *Science* **336**, 700 (2012).
31. W. Kaada, *Theory of Satellite Geodesy: Applications of Satellites to Geodesy* (Dover, Mineola, NY, 2000).
32. R. Greeley, G. Batson, *Planetary Mapping* (Cambridge Univ. Press, Cambridge, 1990).

Acknowledgments. We thank the Dawn team for the development, cruise, orbital insertion, and operations of the Dawn spacecraft at Vesta. C.T.R. is supported by the Discovery Program through contract NNM05AA86C to the University of California, Los Angeles. A portion of this work was performed at the Jet Propulsion Laboratory, California Institute of Technology, under contract with NASA. Dawn data are archived with the NASA Planetary Data System.

Supplementary Materials

www.sciencemag.org/cgi/content/full/336/6082/684/DC1
Supplementary Text
Figs. S1 and S2

19 January 2012, accepted 22 March 2012
10.1126/science.1219381

Vesta's Shape and Morphology

R. Jaumann,^{1,2*} D. A. Williams,³ D. L. Buczowski,⁴ R. A. Yingst,⁵ F. Preusker,¹ H. Hiesinger,⁶ N. Schmedemann,² T. Kneissl,² J. B. Vincent,⁷ D. T. Blewett,⁴ B. J. Buratti,⁸ U. Carsenty,¹ M. W. Denevi,⁴ M. C. De Sanctis,⁹ W. B. Garry,⁵ H. U. Keller,¹⁰ E. Kerster,¹ K. Krohn,¹ J.-Y. Li,¹¹ S. Marchi,¹² K. D. Matz,¹ T. B. McCord,¹³ H. Y. McSween,¹⁴ S. C. Mest,⁵ D. W. Mittlefehldt,¹⁵ S. Mottola,¹ A. Nathues,⁷ G. Neukum,² D. P. O'Brien,⁵ C. M. Pieters,¹⁶ T. H. Prettyman,⁵ C. A. Raymond,⁸ T. Roatsch,¹ C. T. Russell,¹⁷ P. Schenk,¹⁸ B. E. Schmidt,¹⁹ F. Scholten,¹ K. Stephan,¹ M. V. Sykes,⁵ P. Tricarico,⁵ R. Wagner,² M. T. Zuber,²⁰ H. Sierks⁷

Vesta's surface is characterized by abundant impact craters, some with preserved ejecta blankets, large troughs extending around the equatorial region, enigmatic dark material, and widespread mass wasting, but as yet an absence of volcanic features. Abundant steep slopes indicate that impact-generated surface regolith is underlain by bedrock. Dawn observations confirm the large impact basin (Rheasilvia) at Vesta's south pole and reveal evidence for an earlier, underlying large basin (Veneneia). Vesta's geology displays morphological features characteristic of the Moon and terrestrial planets as well as those of other asteroids, underscoring Vesta's unique role as a transitional solar system body.

The Dawn spacecraft (1) arrived at Vesta on 17 July 2011 and began science operations at the highest of three orbital altitudes. During the first orbital period of 22 days (which define the survey phase), starting on 6 August 2011, the Dawn Framing Camera (FC) (2) and the Visible and Infrared Spectrometer (VIR) (3) mapped the surface from an altitude of ~2700 km with image scales of ~260 m/pixel (FC) and ~700 m/pixel (VIR), respectively. The survey mapping campaign was designed to obtain at least three different viewing geometries of Vesta, under similar illumination conditions, in order to construct a model of surface topography and to generate a base map by using stereophotogrammetric analyses. Because of Vesta's oblique axis, the north-polar region above 50°N remains dark until late August of 2012, when the spacecraft departs Vesta (4). In total, the Dawn FC acquired 1179 stereoscopic images during the survey orbit covering ~80% of Vesta's surface. The presence of an igneous crust on Vesta

raises the prospect of surface morphology consistent with differentiated terrestrial planets (5). Stereophotogrammetric analysis (6) of Vesta yields an overall relief from -22.3 to 19.1 km (with respect to a biaxial reference ellipsoid of 285 km by 229 km), which slightly exceeds previous estimates of relief based on Hubble Space Telescope (HST) data [-25.4 to +13.7 km with respect to the same ellipsoid (7)] by about 8%. The observed relief to size ratio of 15% is consistent with previous discussions and predictions [e.g., (7, 8)] on the dynamic range of topography of solar system bodies.

Vesta's surface exhibits complex topography at all spatial scales imaged so far (Fig. 1). Previous HST data revealed a large south polar basin with a central mound (9). This feature has been named Rheasilvia and is centered at about 301°E and 75°S (4) (Figs. 1 and 2). Stereo data reveal an approximately circular impact basin with a diameter of 500 ± 20 km (the mound is ~180 km in diameter) displaying apparent lower crater density (10) and smoother texture distinctive from the surrounding terrain. A steep scarp defines part of the outer perimeter of the

basin. Besides the south polar region, other large depressions can also be identified and may be remnants of large impact basins (Fig. 1) (10). A region with elevated topography, on average 20 km higher than its surrounding, occurs between ~25°N to 35°S and ~200°E to 300°E and is called Vestalia Terra. The southernmost part of this region merges into the rim area of the Rheasilvia basin. Such irregularly high plateaus like Vestalia Terra form parts of the Rheasilvia basin rim and are comparable to large arcuate ridges of asymmetric ejecta blankets as predicted by impact models of rapidly rotating bodies (11). However, their overall appearance does not completely fit the model assumptions such as the impact direction. The western margin (at about 210°E) of Vestalia Terra, with an elevation change of ~2000 m, separates it from the young crater Marcia and adjacent craters to the north (Fig. 1). A scarp almost completely surrounds Vestalia Terra. Its northern edge is curvilinear, with a shape suggestive of an impact basin margin at about 225°E to 270°E and 15°N. Additional elevated topography, on average ~15 km higher than the surroundings, extends between 10°S to 55°S and 310°E to 110°E longitude with its southern boundary again marked by the Rheasilvia basin rim. A second large and older basin 400 ± 20 km wide, named Veneneia and centered at 170°E and 52°S, is partly overlapped by the Rheasilvia structure.

Large-scale structural features occur in the equatorial and northern regions of Vesta (Fig. 2), including sets of equatorial and northern troughs. By mapping the troughs directly onto the Vesta shape model, they can be modeled as planes that cut through the asteroid. A cluster of pole directions represents similarly oriented planes (Fig. 2) and implies a common formation mechanism of corresponding structures. The primary set of Vesta structures approximately encircle the asteroid, roughly oriented along the equator. In total, 86 linear structures with this orientation were mapped at an image scale of about 260 m/pixel. The equatorial troughs are wide, flat-floored, and

¹German Aerospace Center (DLR), Institute of Planetary Research, Berlin, Germany. ²Freie Universität Berlin, Planetary Sciences, Germany. ³Arizona State University, Tempe, AZ 85287, USA. ⁴Johns Hopkins University Applied Physics Laboratory, Laurel, MD 20723, USA. ⁵Planetary Science Institute, Tucson, AZ 85719, USA. ⁶Westfälische Wilhelms-Universität Münster, Germany. ⁷Max Planck Institute for Solar System Research (MPS), Katlenburg-Lindau, Germany. ⁸Jet Propulsion Laboratory, California Institute of Technology, Pasadena, CA 91109, USA. ⁹Istituto di Astrofisica e Planetologia Spaziale, Istituto Nazionale di Astrofisica (INAF), Roma, Italy. ¹⁰Universität Braunschweig, Germany. ¹¹University of Maryland, College Park, MD 20742, USA. ¹²National Aeronautics and Space Administration (NASA) Lunar Science Institute, Boulder, CO 80309, USA. ¹³Bear Fight Institute, Winthrop, WA 98862, USA. ¹⁴Department of Earth and Planetary Sciences, University of Tennessee, Knoxville, TN 37996, USA. ¹⁵Astromaterials Research Office, NASA Johnson Space Center, Houston, TX 77058, USA. ¹⁶Brown University, Planetary Geosciences Department, Providence, RI 02912, USA. ¹⁷Institute of Geophysics and Planetary Physics, University of California Los Angeles (UCLA), Los Angeles, CA 90095, USA. ¹⁸Lunar and Planetary Institute, Houston, TX 77058, USA. ¹⁹Institute for Geophysics, University of Texas, Austin, TX 78712, USA. ²⁰Massachusetts Institute of Technology, Cambridge, MA 02139, USA.

*To whom correspondence should be addressed. E-mail: ralf.jaumann@dlr.de

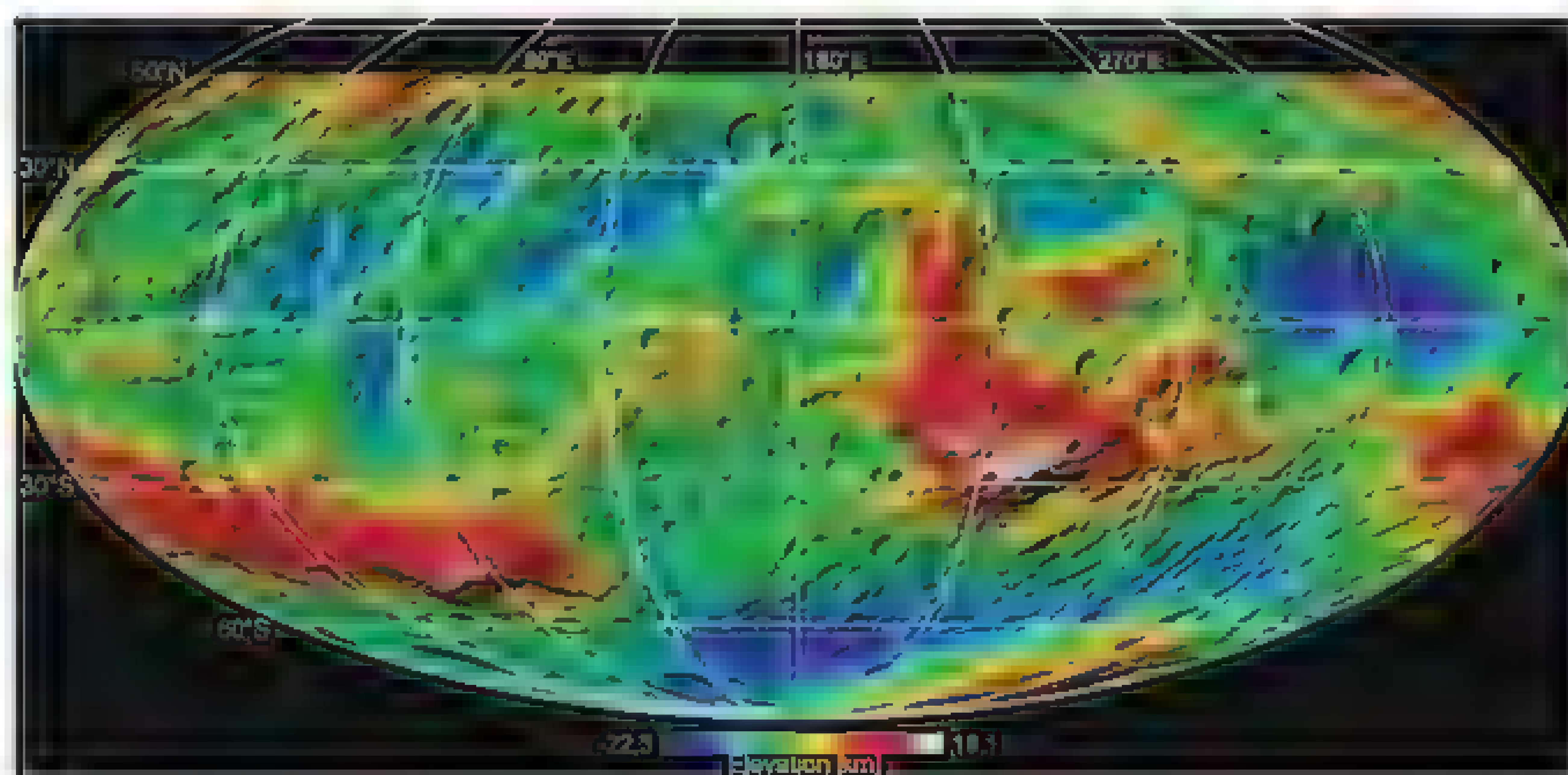


Fig. 1. Global, colored, hill-shaded digital terrain model in Mollweide projection (equal area).

bounded by steep scarps along $\sim 240^\circ$ of longitude, circling about two-thirds of the asteroid. Troughs are mostly co-planar, have lengths that vary from 19 to 380 km, and can be as wide as 15 km. Muted troughs, grooves, and pit crater

chains are evident in the remaining longitude range of the asteroid, from $\sim 150^\circ\text{E}$ to $\sim 270^\circ\text{E}$. The poles of the equatorial troughs cluster at about 120°E to 240°E and $78^\circ (\pm 10^\circ)\text{S}$. The other set of large-scale linear structures extends to

the northwest oriented $\sim 30^\circ$ from the equatorial troughs, starting at $\sim 300^\circ\text{E}$ longitude (Fig. 2). The most prominent structure in this group is 390 km long and 38 km wide. Although larger than the equatorial troughs, the walls of the north-

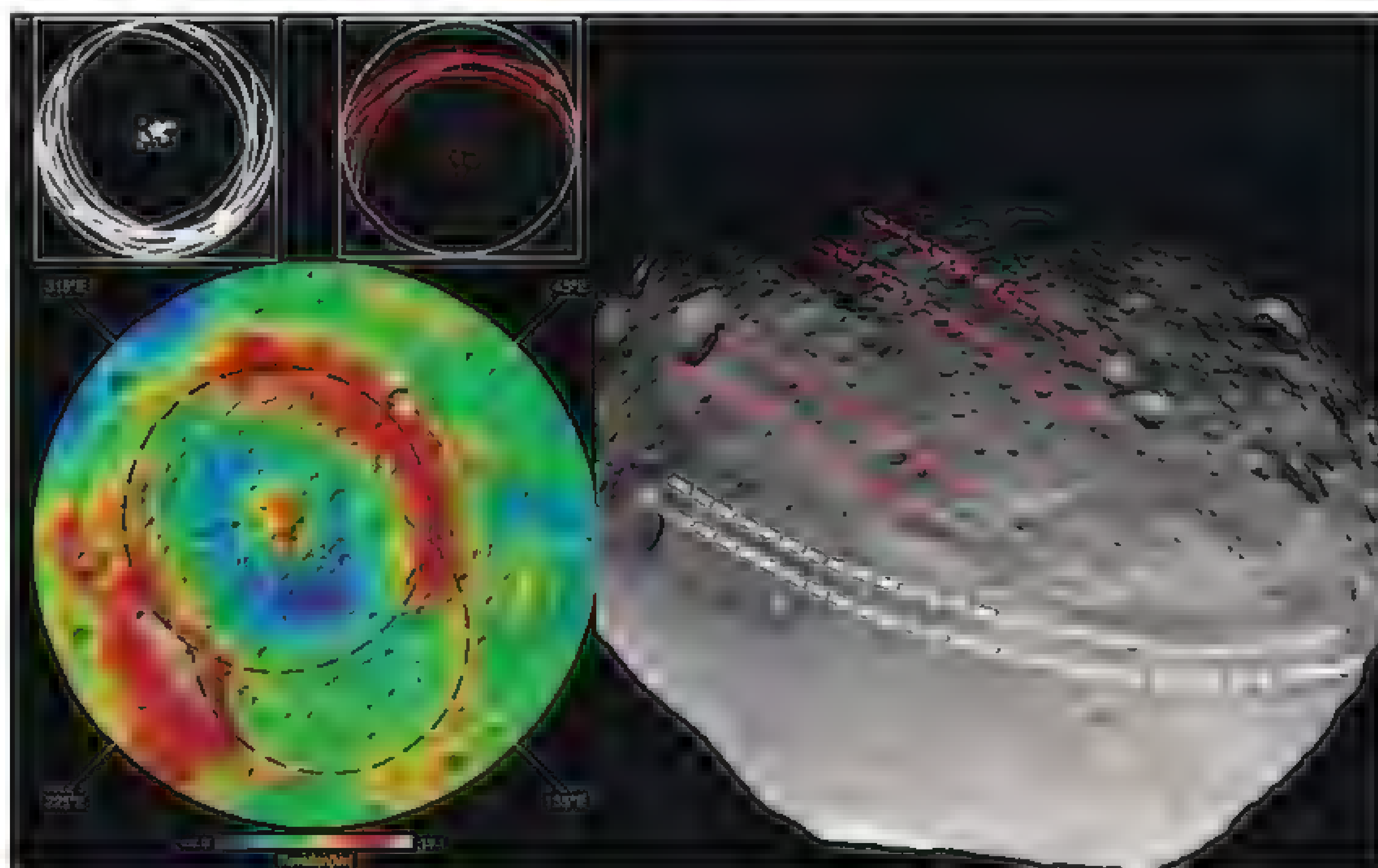


Fig. 2. Large-scale troughs are oriented along Vesta's equator (white dashed lines) and also form the equator to the north (red dashed lines). The center positions of these circular troughs relative to the equatorial plane of Vesta (top left) correspond to the center of the two southern basins (red and white \times bottom left).

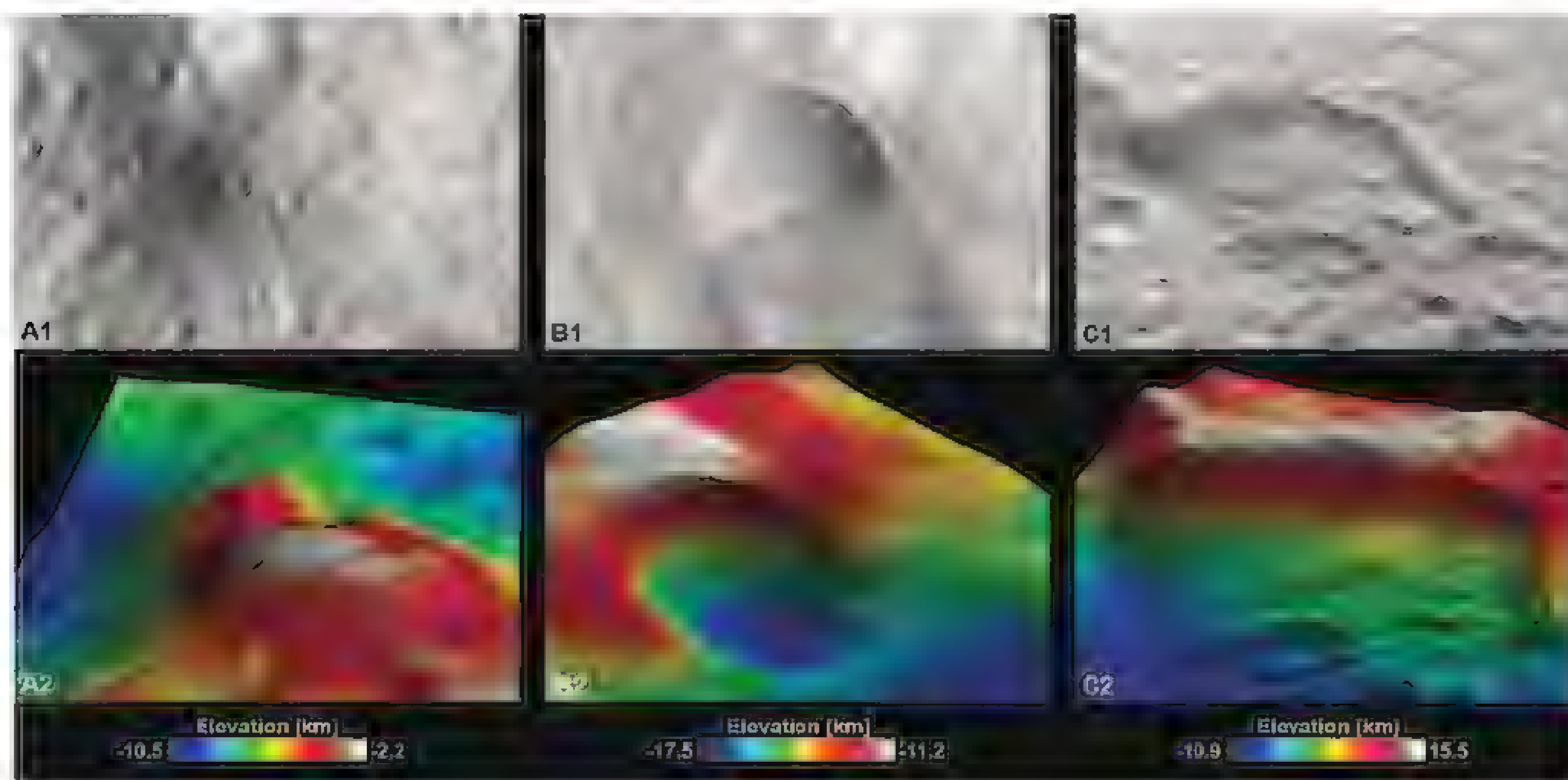


Fig. 3. Detailed views of Vesta's surface. (A1) Mountain with dark material exposed (image width = 48 km, 61°E , 10°N); (B1) crater on a slope with a sharp crest uphill and slumping material covering the lower rim (image width = 44 km, 201°E , 58°S); (C1) scarp with mass wasting features (image width = 180 km, 92°E , 55°S); (A2, B2, and C2) color-coded image-textured three-dimensional perspective views corresponding to the terrains in (A1), (B1), and (C1), respectively.

ern troughs display gentler slopes and rounded edges. They show considerable infilling and heavy cratering, suggesting an older age. Analyses indicate that seven smaller troughs (31 to 212 km long) define planes that are parallel to the plane described by this large-scale structure, also indicating that they all share a common formation mechanism. Their pole directions cluster at about 190°E and 60° ($\pm 10^\circ$)S. The poles of the global troughs agree within error bounds with the basin center of Rheasilvia at 310°E , 75°S and Veneneia at 170°E , 52°S (Fig. 2). This strongly suggests that the formation of the troughs is related to the formation of the basins. The orientations of both sets of large-scale structures are consistent with models of large impacts into an asteroid that predict fracturing concentric to the point of impact (12, 13). In addition, the older set of troughs is exposed only on the northern hemisphere, which

may be due to obliteration of their southern extension by the Rheasilvia impact. This is consistent with the younger age of Rheasilvia and also indicates that all structures down to the equator were destroyed or at least affected by the Rheasilvia impact.

Impact-related processes have played a dominating role in (re-)shaping Vesta's surface (Fig. 3). Impact craters on Vesta can be divided into four different degradation states: fresh craters, showing sharp, unmodified rims and ejecta deposits; craters with degraded, softened rims; craters with heavily degraded rims; and impact crater ruins showing almost no visible rims (fig. S1). These different crater degradation states can be identified in a sample area covered by the ejecta of a nearby 45-km-diameter crater at 307°E and 16°N named Lepida (fig. S1). The largest craters that are completely filled and covered in this area

have diameters of about 4 km. The crater depth to diameter ratio for simple craters (6) implies a thickness of ejecta (regolith) in this area of about 0.8 ± 0.1 km (14).

Topography plays an important role in crater formation and modification processes on Vesta. There are numerous cases of craters formed on slopes, where pronounced collapse, slumping, and ejecta deposition occurred on the upslope side as well as the downslope side of the craters. This results in a strongly asymmetric morphology with a wider upslope crater wall topped by a sharp crest and a narrower downslope wall with a smoothed crater rim (Fig. 3). Impact on steep slopes also causes asymmetric ejecta deposition with the downslope ejecta covering and smoothing the corresponding crater rim. Compared with its radius, Vesta has significant relief, resulting in relatively steep slopes, locally

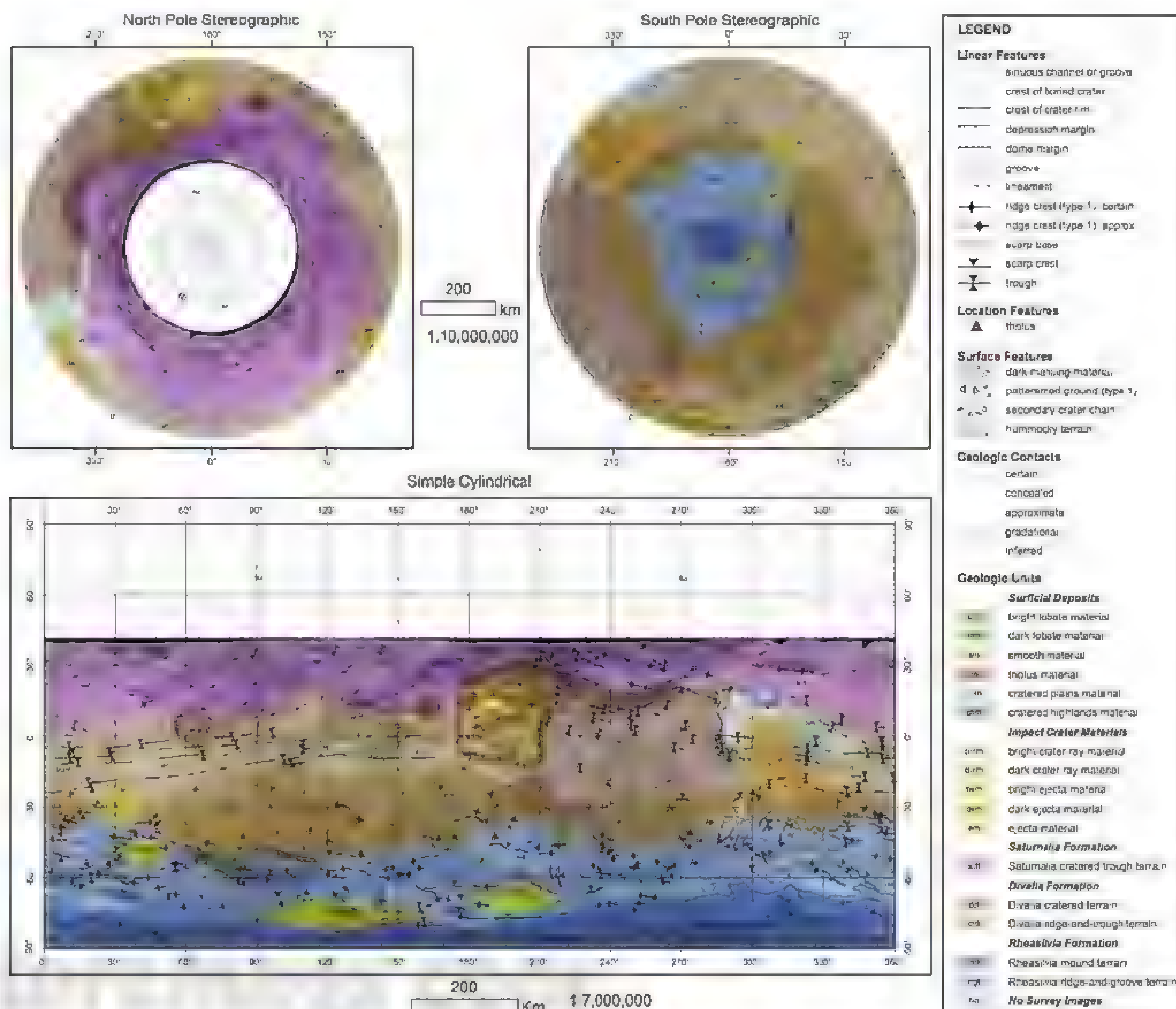


Fig. 4. Geologic maps of Vesta based on survey orbit data.

exceeding 40° when referred to the ellipsoid. Gravitational slopes are slightly less steep but also reach up to ~40° on a lower-resolution shape model (~700 m). A considerable number of slopes on Vesta are most probably above the angle of repose and indicative of intact bedrock beneath (15). This is also consistent with the appearance of large boulders in some parts of the ejecta. Impacts onto such steep surfaces, followed by slope failure, make resurfacing because of impacts, subsequent gravitational modifications, and seismic activity important geologic processes on Vesta that substantially alter the morphology of geologic features and add to the complexity of Vesta's surface evolution.

Smooth, flat regions occur in the interiors of some craters and in small depressions as pondlike accumulations (16) with well-defined geological contacts, indicating that they are younger than their surroundings (Fig. 3). These ponds are not randomly distributed across the surface but preferentially occur in a band between 10°S and 30°N with fewer ponds north of ~30° and even fewer ponds in the Rheasilvia region. However, poor lighting conditions in the northern hemisphere may bias this observation. Similar, but smaller (<230 m diameter) smooth ponds were also reported from the surface of asteroid Eros (17). Ponds on Vesta and Eros show several similarities, including preferred occurrence in equatorial regions, downslope asymmetry within craters on slopes, stratigraphic relationships with adjacent terrain, and formation within craters and depressions without evidence for material flowing into these craters and depressions. On the basis of current observations, several scenarios for the origin of these deposits seem plausible, including volcanism, impact sedimentation, impact melt, dust levitation and transport, seismic shaking, or slumping of fine material.

Dark material is common on Vesta; it is locally concentrated and mostly associated with impacts (fig. S2). Dark material is either exogenic in origin because of carbon-rich material from low-velocity impactors (18) (i.e., from the impact of a carbonaceous chondrites) or endogenic because of freshly exposed mafic material or impact melt locally mixed into the subsurface and excavated by later impacts. Dark material on Vesta can be divided into four major geomorphologic classes (6): material emanating from the rims or walls of impact craters or running downslope in fans into the crater and on the crater floor because of mass wasting processes; dark material associated with crater ejecta patches or continuous ejecta blankets; material associated with hill flanks and related to impacts on hills; and clusters of dark spots and extended linear dark features. Dark material exposed by impact excavation often shows line structures indicating a spotty admixture within the regolith. Deposits of dark material are unevenly distributed across Vesta's surface. The major regions with dark material are at about 110°E to 160°E and 10°S to 10°N, 170°E to 225°E and 10°S to

20°N, and 290°E to 330°E and 0° to 20°S (fig. S2 and Fig. 4).

No unambiguous volcanic deposits have been identified, although they might be expected given evidence from howardite-eucrite-diogenite meteorites (19). All features with lobate, lava flow-like morphologies occur in close proximity to impact craters or topographic heights and are best interpreted as gravity-driven mass flow deposits, impact ejecta deposits, or impact melt deposits, although the amount of impact melt is expected to be small (20). One feature, morphology similar to a terrestrial basaltic spatter vent feeding a dark flow-like deposit, occurs in the dark ejecta field of an impact crater. This feature could also be interpreted as impact ejecta or melt deposits; thus, positive identification remains ambiguous at image scales of 70 m/pixel. Two positive relief features containing dark materials appear to be impact-sculpted hills (Fig. 3). The materials associated with these dark or dark-rayed impact craters suggest either an exogenic origin of the dark material or excavation and exposure of subsurface volcanic dikes by the impacts (6). The present lack of volcanic relicts detected on Vesta suggests that such features were only produced during the short period of rapid cooling of Vesta's interior within the first 100 million years after formation and have been eroded and gardened by impacts, in part evidenced by the dark materials seen in the walls of many impact craters. Volcanic materials should be deeply buried by impact ejecta from the Rheasilvia and other large basins whose ejecta must cover the surface.

References and Notes

1. C. T. Russell, C. A. Raymond, *Space Sci. Rev.* **163**, 3 (2011).
2. H. Sierks et al., *Space Sci. Rev.* **163**, 263 (2011).

3. C. M. De Sanctis et al., *Space Sci. Rev.* **163**, 329 (2011).
4. C. T. Russell et al., *Science* **336**, 684 (2012).
5. M. T. Zuber et al., *Space Sci. Rev.* **163**, 77 (2011).
6. Methods and additional materials are available as supplementary materials on Science Online.
7. P. C. Thomas et al., *Icarus* **128**, 88 (1997).
8. T. V. Johnson, T. R. McGetchin, *Icarus* **18**, 612 (1973).
9. P. C. Thomas et al., *Science* **277**, 1492 (1997).
10. S. Marchi et al., *Science* **336**, 690 (2012).
11. M. Jutz, E. Asphaug, *Geophys. Res. Lett.* **38**, L01102 (2011).
12. E. Asphaug et al., *Icarus* **120**, 158 (1996).
13. B. E. Schmidt, thesis, UCLA, Los Angeles, CA (2011).
14. The error on ejecta thickness is estimated by multiplying the crater depth-to-diameter ratio with the bin width (500 m) of the crater sizes at which the slope of the crater frequency distribution curve is changing because of resurfacing (fig. S1).
15. A. F. Cheng et al., *Icarus* **155**, 51 (2002).
16. A. F. Cheng, N. Zernberg, C. R. Chapman, M. T. Zuber, *Meteorit. Planet. Sci.* **37**, 1095 (2002).
17. M. S. Robinson, P. C. Thomas, J. Veverka, S. Murchie, B. Carcich, *Nature* **413**, 396 (2001).
18. D. P. O'Brien, M. Sykes, *Space Sci. Rev.* **163**, 41 (2011).
19. H. Y. McSween, D. W. Mittlefehldt, A. W. Beck, R. G. Mayne, T. J. McCoy, *Space Sci. Rev.* **163**, 141 (2011).
20. L. Wilson, K. Kei, *Meteorit. Planet. Sci.* **32**, 813 (1997).

Acknowledgments: We thank the Dawn team for the development, cruise, orbital insertion, and operations of the Dawn spacecraft at Vesta. Portions of this work were performed at the DLR Institute of Planetary Research and at the Jet Propulsion Laboratory under contract with NASA and were supported by the NASA Dawn participating scientist program and the DLR Dawn data are archived with the NASA Planetary Data System.

Supplementary Materials

www.sciencemag.org/cgi/content/full/336/6082/687/DC1

Supplementary Text

Figs. S1 and S2

References (21–32)

13 January 2012; accepted 18 April 2012

10.1126/science.1219122

The Violent Collisional History of Asteroid 4 Vesta

S. Marchi,^{1*} H. Y. McSween,² D. P. O'Brien,³ P. Schenk,⁴ M. C. De Sanctis,⁵ R. Gaskell,³ R. Jaumann,⁶ S. Mottola,⁶ F. Preusker,⁶ C. A. Raymond,⁷ T. Roatsch,⁶ C. T. Russell⁸

Vesta is a large differentiated rocky body in the main asteroid belt that accreted within the first few million years after the formation of the earliest solar system solids. The Dawn spacecraft extensively imaged Vesta's surface, revealing a collision-dominated history. Results show that Vesta's cratering record has a strong north-south dichotomy. Vesta's northern heavily cratered terrains retain much of their earliest history. The southern hemisphere was reset, however, by two major collisions in more recent times. We estimate that the youngest of these impact structures, about 500 kilometers across, formed about 1 billion years ago, in agreement with estimates of Vesta asteroid family age based on dynamical and collisional constraints, supporting the notion that the Vesta asteroid family was formed during this event.

Asteroid 4 Vesta is the second most massive body in the main asteroid belt and, according to models (1–5), its early evolution occurred in an environment where collisions with other asteroids were much more frequent than they are today. One notable fea-

ture emerging from early observations of the Dawn mission (6) is that the surface of Vesta is dominated at all scales by impact craters. Dawn's framing camera extensively imaged Vesta during its survey phase, at an altitude of ~2700 km. These data have been used to build a global

visual image mosaic with a resolution of 260 meters per pixel, covering $\sim 80\%$ of Vesta's surface and leaving only a portion of the northern hemisphere unseen. We used the global mosaic and digital terrain models (DTMs) (7) to map craters larger than 4 km in diameter (Fig. 1). Numerous large, shallow topographic depressions are inferred to be degraded impact structures (Fig. 1B)

The shape of Vesta has been noticeably modified by a $\sim 500 \pm 25$ -km-diameter impact structure, named Rheasilvia, located near the south pole (8, 9). The formation of this structure obliterated the older cratering record of Vesta's southern hemisphere, including nearly half of a ~ 400 -km-diameter basin, named Veneneia, whose rim remnants are visible in the DTMs (Fig. 1B) (9). The volume of material excavated by the impact that formed Rheasilvia (9) is an order of magnitude larger than the estimated volume of asteroidal members of Vesta's dynamical family (10), the so-called Vestoids. Vestoids are thought to be the immediate parent bodies of howardite, eucrite, and diogenite (HED) meteorites (11–15).

The cratering record shows that the northern hemisphere escaped such violent resetting, with the density of craters increasing from the Rheasilvia rim to northern latitudes. The crater density has a distinctive pattern, reaching maximum values in two heavily cratered terrains (HCTs) centered at about 348°E , 17°N and 110°E , 17°N (Fig. 2). The overall crater density in the northern hemisphere and the extent of the HCTs appear to have been shaped by the formation of large craters that obliterated preexisting craters. The best examples are two craters with diameters of ~ 50 and 60 km and located at 195°E , 10°N in the Marcia quadrangle (6). These craters produced ejecta blankets that, along with impact-induced seismic shaking, apparently obliterated the previous cratering record up to a distance of about one crater radius from their rims (16). The northward extension of the HCTs is presently unmapped, so it is possible that the highest crater density has yet to be detected.

Interestingly, some local topography seems to be correlated with crater areal density. The highest-relief terrains (HRTs) of Vesta correspond to the high-standing flanks immediately proximal to the rim of Rheasilvia and extend in northward direction (outlined in Fig. 2) (7, 9). These areas generally have crater densities intermediate between HCTs and the low crater density seen on Rheasilvia's floor (Fig. 2).

The cumulative crater size-frequency distributions of Rheasilvia's floor, HRTs, and HCTs are

shown in Fig. 3A. The clear separation in terms of crater density indicates that HCTs are much older than Rheasilvia. Although the crater retention age of Rheasilvia may not necessarily correspond to its formation age, it is concluded that most mass-wasting on Rheasilvia's floor occurred shortly after its formation as a consequence of complex crater-floor collapse (9). The plot also shows the curve corresponding to the 10% level of the geometric crater saturation curve (17, 18). Although the empirical lunar saturation may well not apply to Vesta, given the different impactor populations and crater sizes investigated, the fact that lunar terrains saturate at the 3 to 5% level of geometric saturation (17) suggests that the heavily cratered terrains on Vesta may be close to saturation. Note that the HCT's size-frequency distributions are characterized by a slope transition (19) at about crater size $D = 10$ km. Craters

in the 4- to 10-km size range have a cumulative slope of -1.9 ± 0.1 , which is close to the geometric saturation slope -2 , whereas the cumulative slope is -2.9 ± 0.2 for craters in the 10- to 20-km size range. These observations are consistent with the overall behavior of saturated terrains (17), in which the shallower branch of the distribution is controlled by saturation, and the steeper branch would represent the crater production curve (16). Even if the crater distribution on the HCTs has not reached a fully saturated state, the overall crater density is high enough that crater obliteration by repeated impacts may have still played an important role. These observations, along with large uncertainties in the impactor flux over time, make the process of cratering age determination for HCTs uncertain.

The HRT crater size-frequency distribution shows a slightly higher crater density (by a factor

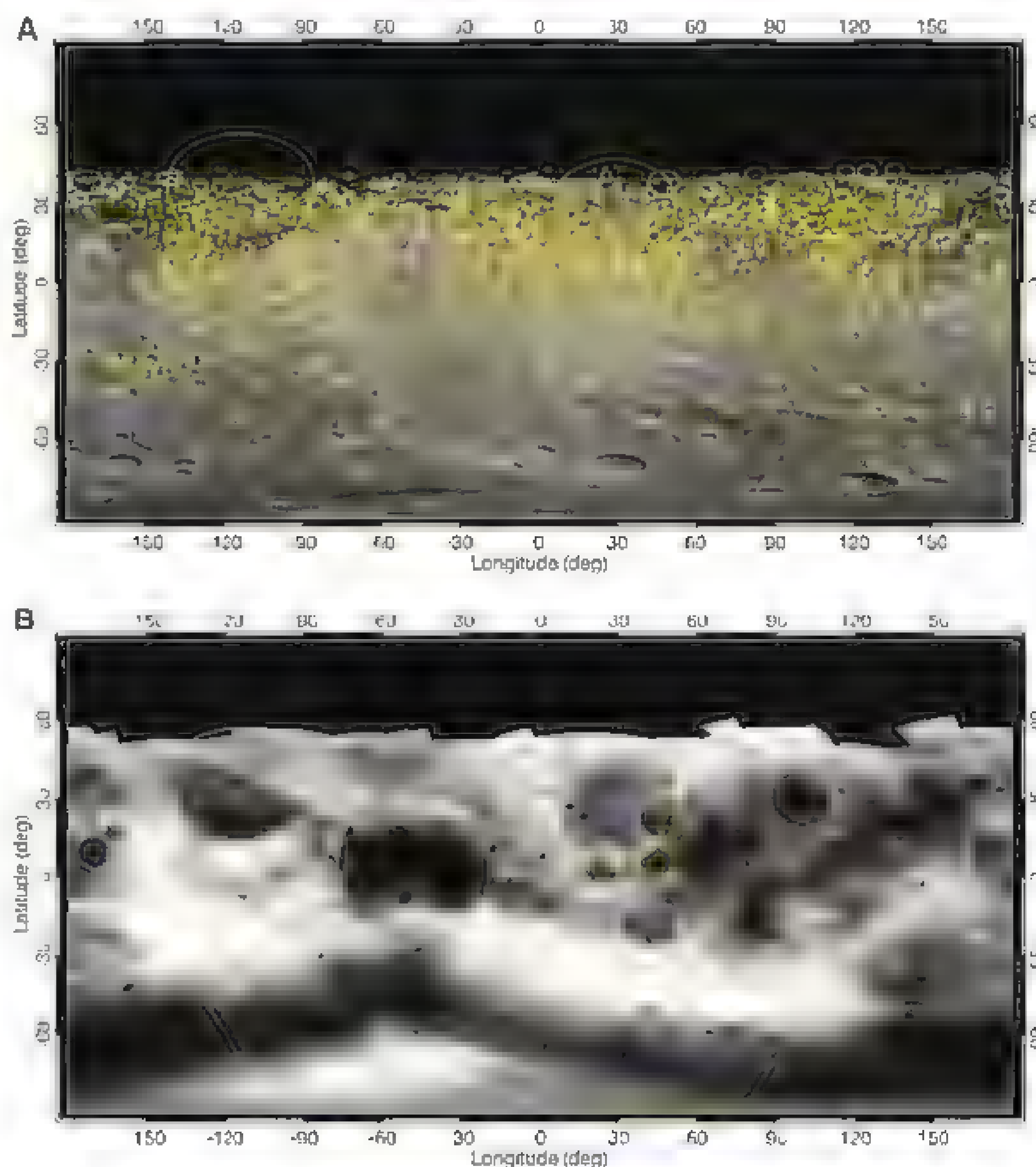


Fig. 1. Vesta's global crater distribution. (A) Location of the 1872 identified craters ≥ 4 km superposed on the survey phase global mosaic (260 meters per pixel). Illumination conditions are not uniform over the mosaic: On average, the northern quadrants have low incidence angles, whereas equatorial quadrants have high incidence angles. Consequently, the detectability of craters is not uniform across the surface. Despite these limitations, the quality of the mosaic allows a uniform detection limit for craters ≥ 4 km. (B) Recognized craters ≥ 50 km (yellow solid lines) superposed on DTM topography referred to the reference 285-by-285-by-229-km ellipsoid. Minimum and maximum elevations are about -22 km and 19 km, respectively. The large crater Rheasilvia appears to be the youngest structure among the largest craters (except for the two 50- to 60-km craters in Marcia quadrangle visible at the left-hand side of the map). The number of observed large craters is probably a lower limit. It is possible that other large irregular depressions in the northern hemisphere are impact features (red dashed lines), although their identification is presently unclear.

¹NASA Lunar Science Institute, Boulder, CO, USA. ²University of Tennessee, Knoxville, TN, USA. ³Planetary Science Institute, Tucson, AZ, USA. ⁴Lunar and Planetary Institute, Houston, TX, USA. ⁵Istituto di Astrofisica e Planetologia Spaziali, Istituto Nazionale di Astrofisica, Rome, Italy. ⁶German Aerospace Center (DLR), Institute of Planetary Research, Berlin, Germany. ⁷Jet Propulsion Laboratory, California Institute of Technology, Pasadena, CA, USA. ⁸University of California, Los Angeles, CA, USA.

*To whom correspondence should be addressed. E-mail: marchi@boulder.swri.edu.

of ~ 1.6 at $D = 4$ km) than that of Rheasilvia. The reduced crater densities associated with the HRTs proximal to the Rheasilvia rim are most simply explained by coverage with a thick ejecta blanket from Rheasilvia, in rough agreement with recent modeling (20), whereas Rheasilvia secondaries may be responsible for the slightly higher crater density. Similar conclusions also apply to the subequatorial region (21) between 0° and 100° E longitude close to a sharp segment of Rheasilvia's rim, named Matronalia Rupes (Fig. 2). Although Vesta's capability of forming secondary craters requires detailed analysis, a recent model (22) shows that secondary craters can be important on small saturnian satellites whose gravity is comparable with Vesta's (0.22 m/s^2).

The crater size-frequency distribution of large degraded craters (LDCs) is reported in Fig. 3B. Its overall cumulative slope (-0.8 ± 0.2) is considerably shallower than that of HCTs, although, for craters larger than 100 km, its slope is close to that estimated using the model main-belt population (2) and the Pi-group crater scaling law (23). On the other hand, the crater size-frequency distribution of the younger Rheasilvia floor matches the model main-belt crater production function quite well (Fig. 3B) (16). Although preliminary, these results show that the current main-belt crater production does not bridge the overall crater distribution from small craters on HCTs to large degraded craters, the latter being in excess by a factor of ~ 4 with respect to small craters, according to the present main belt (Fig. 3B). This result suggests either that the overall HCT-LDC distribution is saturated or that HCTs have been reset by a recent event, whereas the LDCs record an older population. The latter hypothesis is not supported by the distribution of recognized large craters (Fig. 1B). The first scenario, however, is at odds with the observation that the HCT crater size-frequency distribution for craters in the size range 10 to 20 km is steeper than the main-belt crater production function (Fig. 3B). This result supports the idea that the steep slope may be due to secondary craters from Rheasilvia or other LDCs, arguing against the saturation of the overall HCT-LDC distribution. Thus, it appears that the overall HCT-LDC cumulative slope may indicate a much shallower main-belt size-frequency distribution in early solar system history.

The Rheasilvia model best fit presented in Fig. 3B can also be used to derive a crater retention age (24, 25). The present intrinsic collisional probability of other main-belt asteroids with Vesta is $\sim 2.8 \times 10^{-18} \text{ km}^{-2} \text{ year}^{-1}$ (26, 27), which yields a very young crater retention age of $\sim 1.0 \pm 0.2$ billion years (Gy), assuming a constant impact rate over that time span, consistent with the results of geological mapping and independent crater counting (9). The estimated probability for such an impact to occur over the past 1 Gy is $\sim 25\%$ (28). Rheasilvia's young cratering age agrees with its undegraded morphology (9) and with the steep Vestoid size-frequency distribution (10, 16, 29). According to collisional

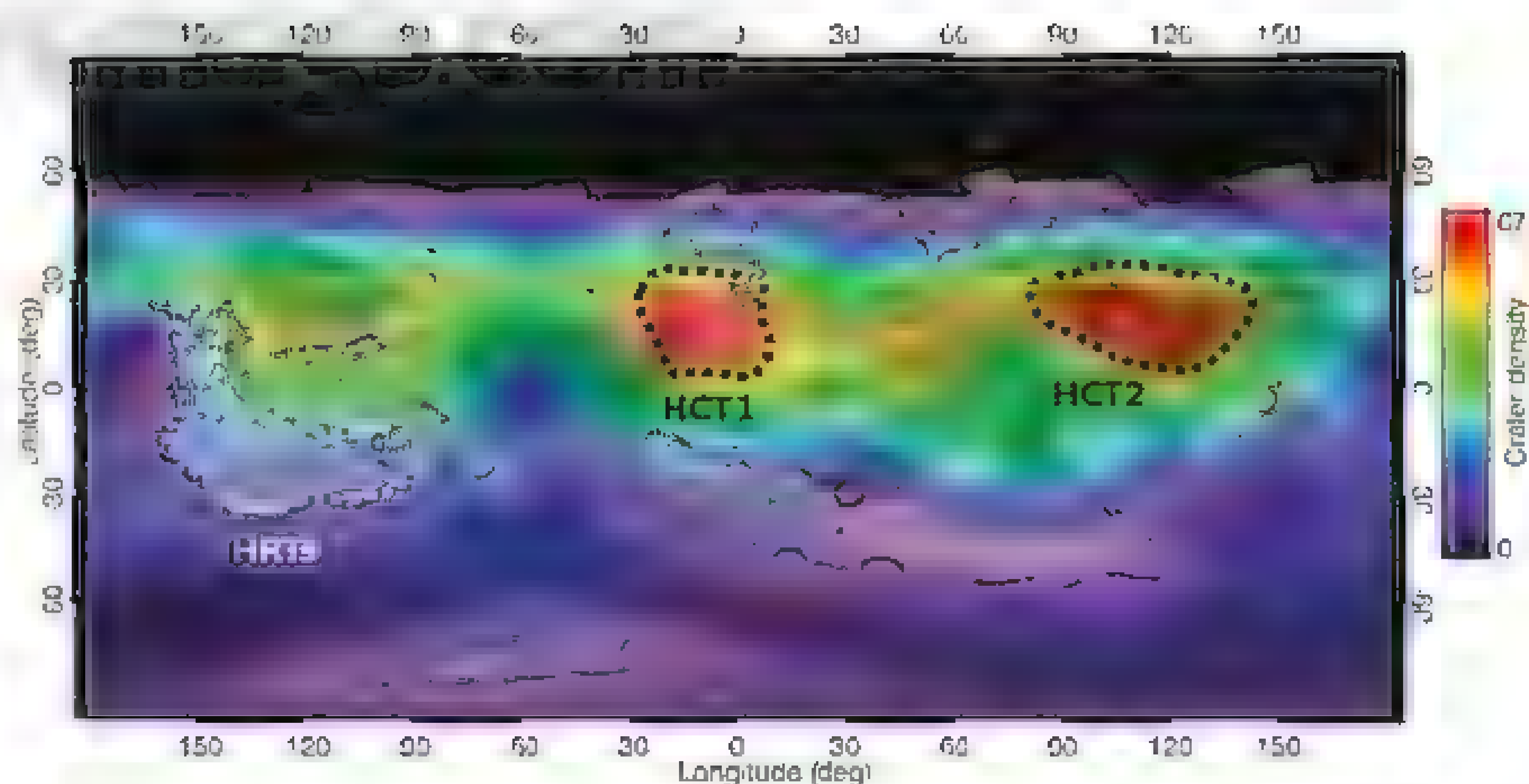


Fig. 2. Global crater areal density ($D \geq 4$ km). Crater density (in number of craters per 10^4 km^2) was derived by averaging over a radius of 80 km. Black solid lines indicate the contour level for the HRTs, as derived by DTM topography, and correspond to elevations of 12, 13.5, 15, and 16.5 km (referred to the reference ellipsoid). This region corresponds to the southern part of the larger high-elevation terrains, named Vestalia Terra. The same contour levels also define Rheasilvia's central mound (300°E , 70°S). The vertical gradient in the crater density for latitudes $\geq 30^\circ\text{N}$ (yellow dotted line) is an artifact due to the lack of data at high latitudes.

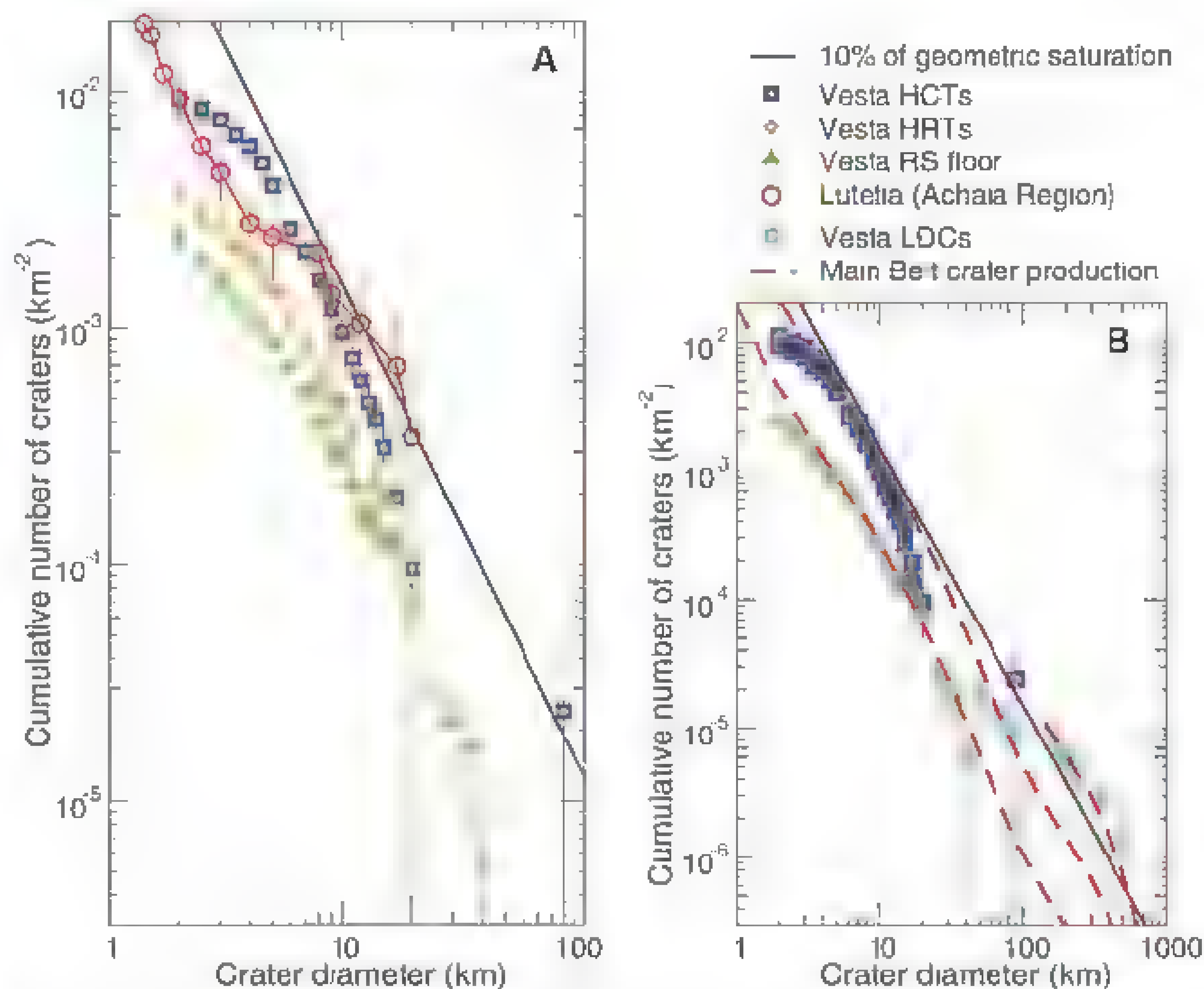
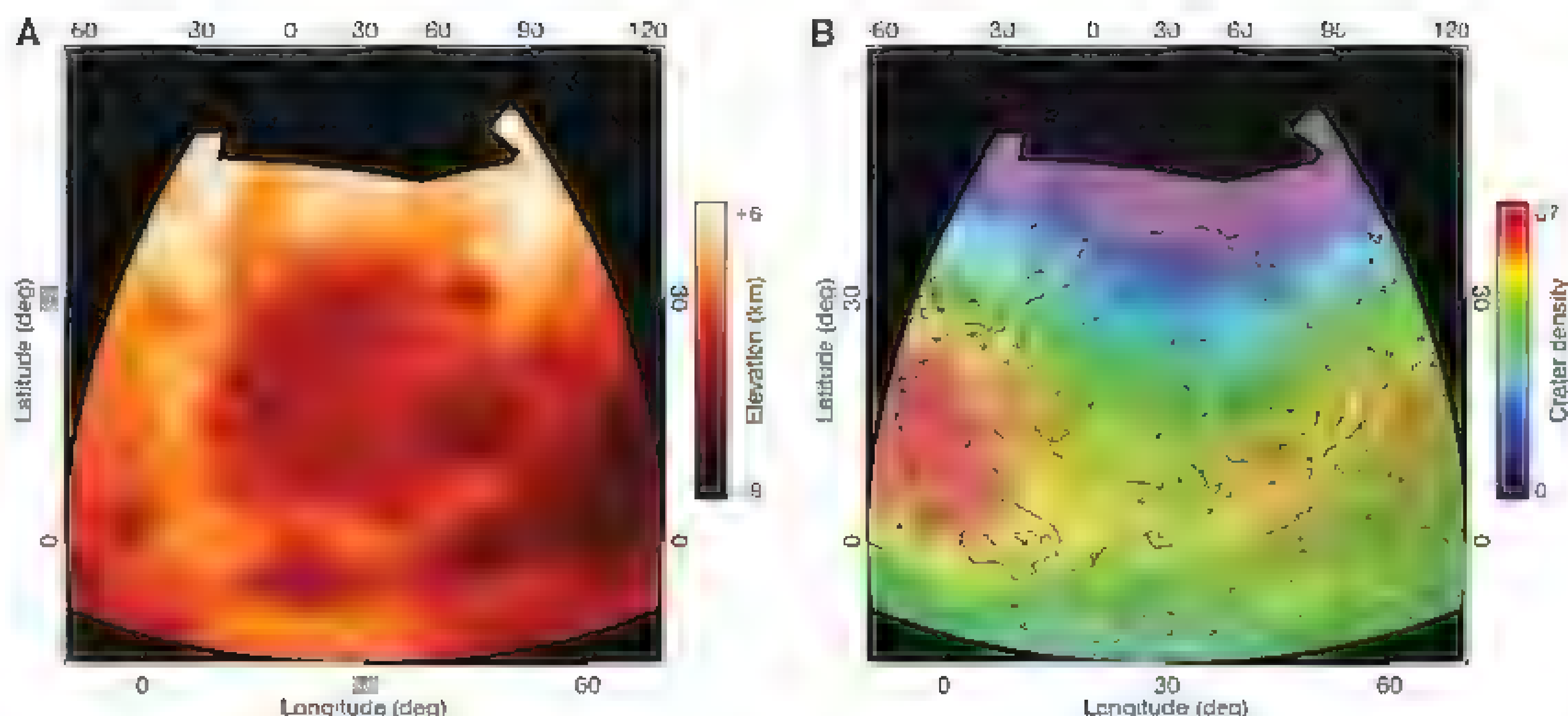


Fig. 3. Crater size-frequency distributions of key units on Vesta. (A) Cumulative crater size-frequency distributions of Rheasilvia's (RS) floor, HCTs (composite of HCTs 1 and 2) (Fig. 2), and HRTs. The 10% level of geometric crater saturation (17, 18) is reported, as well as the crater size-frequency distribution of the oldest unit observed on 21 Lutetia (Achaia region), the second-largest asteroid imaged by a spacecraft (25). Vesta's HCT crater size-frequency distributions appear steeper than Lutetia's, although the overall crater densities are rather similar. Moreover, none of Vesta's crater size-frequency distributions exhibit the characteristic kink shown by Lutetia crater size-frequency distribution at $D = 5$ to 8 km, which is interpreted to result from inhomogeneous properties (25). (B) Vesta's HCT crater size-frequency distribution compared with that of large craters observed on the imaged surface. The main-belt crater production functions for three different levels of crater density are given for comparison (red dashed curves).

Fig. 4. Close-up view of one of the largest impact structures detected in the northern hemisphere. This structure is ~180 km across and located at the border of the Bellicia and Gegania quadrangles (Fig. 1B). (A) Color-coded topography. (B) Color-coded crater areal density (number of craters per 10^4 km²) superposed on topographic contour levels for elevations of -13, -9, -6, -1, and 0.5 km with respect to the reference ellipsoid. The formation of these large craters locally reset the previous crater record and is responsible for the observed pattern in the overall crater density. These large impact structures have shallow concavities due to erosion by numerous superposed impact craters, reaching maximum



relative depths with respect to surrounding terrains of ~10 to 15 km. A similar conclusion also applies to other large degraded craters in the northern hemisphere.

evolution models (29), if the Vesta family were older than ~1 Gy, its size-frequency distribution would have evolved by collisional grinding to match the background population of main-belt asteroids. This is also the minimum time scale required for “fugitive” V-type asteroids (spectrally related but dynamically distinct from the Vesta family) to migrate away from the family under the action of secular perturbations (16). The fact that our Rheasilvia crater retention age is in agreement with the time scales for age and evolution of the Vesta family provides strong support for the Rheasilvia event being the primary source of the Vesta family, although a minor contribution from older family-populating impact events cannot be ruled out.

Unraveling the convoluted collisional evolution of Vesta is required for a global understanding of Dawn data and for interpreting HED meteorites. In this respect, the north-south cratering dichotomy is responsible for much of the compositional diversity across Vesta’s imaged surface. The occurrence of superposed craters having very different sizes in the northern hemisphere (Fig. 1) indicates that they excavated through different depths of Vesta’s crust and produced extensive local mixing, as inferred from HED meteorites. Similar processes likely occurred in the southern hemisphere before the terrains were excavated by the formation of the south pole basins, whose ejected material may be sampled by HED meteorites. The Visible and Infrared Spectrometer data indicate that most of Vesta’s surface resembles howardites (30), composed of admixed eucrite and diogenite components, confirming the mixing inferred from crater imagery. Moreover, the observation that the overall composition of the equator and low-latitude northern hemisphere is compatible with eucrite-enriched howardites (30) may suggest that the large impact structures in the northern

hemisphere did not expose substantial portions of the diogenitic crust, unlike the Rheasilvia basin, which contains diogenite-enriched howardite. The DTM-based depths of the largest craters in the northern hemisphere (Fig. 4) are <15 km, which is less than the average estimated crustal depth of ~20 km, assuming that Vesta’s bulk composition is chondritic (13). A few small regions with less eucritic-enriched howardite composition have been identified beyond the floor of Rheasilvia. One is found on Rheasilvia’s smooth ejecta units (9), possibly indicating diogenite-enriched ejecta.

The early Dawn observations of Vesta’s surface reveal a collision-dominated world. From very large basins to HCTs, most of Vesta’s surface properties have been affected by impacts. These observations suggest that the HCTs may have reached an equilibrium level for craters with sizes ranging from 4 to 10 km. In addition, the slope of the overall size-frequency distribution from ~4-km craters to craters hundreds of kilometers in size is considerably shallower than predicted by the present main-belt population, possibly revealing that the primordial main belt had a greater proportion of large asteroids, as envisaged by recent dynamical models (31). One of the most intriguing results from our work is the young crater retention age of the Rheasilvia basin, estimated to have formed ~1 Gy ago. This major impact event dramatically altered the inner main belt by producing the massive Vesta asteroid family and may have generated a cascade of events that we are just beginning to fully understand.

References and Notes

1. G. W. Wetherill, *Icarus* **100**, 307 (1992).
2. W. F. Bottke Jr. et al., *Icarus* **179**, 63 (2005).
3. D. P. O’Brien, A. Morbidelli, W. F. Bottke, *Icarus* **191**, 434 (2007).

4. A. Morbidelli, R. Brasser, R. Gomes, H. F. Levison, K. Tsiganis, *Astron. J.* **140**, 1391 (2010).
5. D. Turner, G. Magni, A. Coradini, *Mon. Not. R. Astron. Soc.* **413**, 2439 (2011).
6. C. T. Russell et al., *Science* **336**, 684 (2012).
7. R. Jaumann et al., *Science* **336**, 687 (2012).
8. P. C. Thomas et al., *Science* **277**, 1492 (1997).
9. P. Schenk et al., *Science* **336**, 694 (2012).
10. D. Nesvorný et al., *Icarus* **193**, 85 (2008).
11. T. B. McCord, J. B. Adams, T. V. Johnson, *Science* **168**, 1445 (1970).
12. T. H. Burbine et al., *Meteorit. Planet. Sci.* **36**, 761 (2001).
13. H. Y. McSween, D. W. Mittlefehdt, A. W. Beck, R. G. Mayne, T. J. McCoy, *Space Sci. Rev.* **163**, 141 (2011).
14. M. C. De Sanctis et al., *Astron. Astrophys.* **533**, A77 (2011).
15. It is also possible that a part of the Vestoids and HED meteorites have been originated by the older 400-km basin underneath Rheasilvia.
16. Methods and additional data are available as supplementary materials on Science Online.
17. D. E. Gault, *Radio Sci.* **5**, 273 (1970).
18. H. J. Melosh, *Oxford Monographs on Geology and Geophysics*, no. 11 (Clarendon Press, Oxford, 1989).
19. The slope of a cumulative crater size-frequency distribution is defined by $\Delta \log(N)/\Delta \log(D)$, where N is the cumulative number of craters and D is the crater size.
20. M. Jutzi, E. Asphaug, *J. Geophys. Res.* **38**, 101102 (2011).
21. Note that this region excludes the floor of the large basin underneath Rheasilvia, and it extends for about 10° to 15° degrees northward starting from Rheasilvia’s rim.
22. E. B. Berghaus, L. Dones, J. L. Avaris, K. Zahnle, *Icarus* **218**, 602 (2012).
23. K. A. Holsapple, K. R. Housen, *Icarus* **187**, 345 (2007).
24. S. Marchi et al., *Planet. Space Sci.* **58**, 1116 (2010).
25. S. Marchi et al., <http://arxiv.org/abs/1111.3628> (2011).
26. P. Farnella, D. R. Davis, *Icarus* **97**, 111 (1992).
27. Intrinsic collisional probabilities among asteroids are computed by analytical means using the orbital distribution of asteroids >10 km (25). The main source of uncertainty in the age-estimation process, which is considered in the final error estimate, is due to the lack of detailed knowledge of the impactor size-frequency distribution.
28. The estimated size of the impactor that produced Rheasilvia is ~50 km or larger (e.g., (20)), resulting in an impact every ~16 Gy, according to the present

main-belt impact rate. The knowledge that the event did happen in 4.5 Gy implies a 25% probability of occurrence in the past 1 Gy

29. F. Marzari *et al.*, *Astron. Astrophys.* **316**, 248 (1996)

30. M. C. De Sanctis *et al.*, *Science* **336**, 697 (2012)

31. A. Morbidelli, W. F. Bottke, D. Nesvorný, H. F. Levison, *Icarus* **204**, 558 (2009)

Acknowledgments: We thank the Dawn Science, Instrument, and Operations Teams for support. This work was supported by the Italian Space Agency and NASA's Dawn at Vesta Participating Scientists Program. A portion of this work was performed at the Jet Propulsion Laboratory, California Institute of Technology, under contract with NASA. S. Marchi thanks Istituto Nazionale d'Astrofisica for the support in carrying on this work

Supplementary Materials

www.sciencemag.org/content/full/336/6082/690/DC1

Materials and Methods

Figs. S1 to S3

References (32–43)

5 January 2012, accepted 16 April 2012

10.1126/science.1218757

The Geologically Recent Giant Impact Basins at Vesta's South Pole

Paul Schenk,^{1*} David P. O'Brien,² Simone Marchi,³ Robert Gaskell,² Frank Preusker,⁴ Thomas Roatsch,⁴ Ralf Jaumann,⁴ Debra Buczkowski,⁵ Thomas McCord,⁶ Harry Y. McSween,⁷ David Williams,⁸ Aileen Yingst,² Carol Raymond,⁹ Chris Russell¹⁰

Dawn's global mapping of Vesta reveals that its observed south polar depression is composed of two overlapping giant impact features. These large basins provide exceptional windows into impact processes at planetary scales. The youngest, Rheasilvia, is 500 kilometers wide and 19 kilometers deep and finds its nearest morphologic analog among large basins on low-gravity icy satellites. Extensive ejecta deposits occur, but impact melt volume is low, exposing an unusual spiral fracture pattern that is likely related to faulting during uplift and convergence of the basin floor. Rheasilvia obliterated half of another 400-kilometer-wide impact basin, Veneneia. Both basins are unexpectedly young, roughly 1 to 2 billion years, and their formation substantially reset Vestan geology and excavated sufficient volumes of older compositionally heterogeneous crustal material to have created the Vestoids and howardite-eucrite-diogenite meteorites.

Hubble Space Telescope (HST) imaging of asteroid Vesta revealed a major depression at the south pole that is inferred to be a giant impact basin (*1*) nearly as large as Vesta itself. A large basin fit well with the paradigm of Vesta as the parent body of the HED (howardite-eucrite-diogenite) meteorites, on the basis of spectroscopic and petrologic evidence (*2, 3*), proximity to asteroid resonances that can deliver material to near-Earth space (*4*), and the dynamically related family of "Vestoids" (*5*), with the basin as the likely source of these bodies. Determination of the structure, shape, and age of this feature—all of which provide critical parameters for modeling the formation of Vestoids and HEDs—are key Dawn objectives (*6*).

Dawn has resolved Vesta's south polar feature into two large distinct overlapping impact basins. The largest and youngest of these, Rheasilvia (Fig. 1 and fig. S1), is centered at 301° W, 75° S, ~15° from the south pole and, at 500 ± 25 km (or ~114° of arc) in diameter and 19 ± 6 km deep (*7*), is both deeper and larger than estimated from HST (*1*). The multiple concentric terraces and ring scarps—broad flat-lying melt sheets

and central depressions associated with large multiring basins on the Moon or Mercury (*8*)—are absent at Rheasilvia. Dawn instead observed three main structural components (Fig. 1 and fig. S1): a large central massif, a broad sloping basin floor, and an outer margin. The central massif is a 180-km-wide, 20-to-25-km-high conical dome (Fig. 1), with a "craggy" surface of small irregular rounded knobs and patches of relatively smooth material on steep slopes. The knobs may represent exposures of uplifted fractured or disrupted bedrock material, and the smoother material may be unconsolidated debris, impact melt drained down slope, or both. Two arcuate scarps ~5 to 7 km high near the crest of the central massif suggest partial failure of the central massif. The rugged surface morphology is consistent with uplift of highly disrupted material during impact, as observed in large complex craters on other bodies (*8*).

The bowl-shaped floor of Rheasilvia is a broad annular unit characterized by rolling plains. The floor is pervasively deformed by linear and curvilinear ridge and inward-facing scarps 1 to 5 km high (Fig. 2) forming well-organized radial and (clockwise) spiral patterns extending from within the central massif out to the basin margins. Flat-lying deposits indicative of deep ponded impact melt and debris are absent within Rheasilvia (Fig. 1). This is consistent with the low apparent unconsolidated debris, impact melt drained down slope, or both. Two arcuate scarps ~5 to 7 km high near the crest of the central massif suggest partial failure of the central massif. The rugged surface morphology is consistent with uplift of highly disrupted material during impact, as observed in large complex craters on other bodies (*8*).

The bowl-shaped floor of Rheasilvia is a broad annular unit characterized by rolling plains. The floor is pervasively deformed by linear and curvilinear ridge and inward-facing scarps 1 to 5 km high (Fig. 2) forming well-organized radial and (clockwise) spiral patterns extending from within the central massif out to the basin margins. Flat-lying deposits indicative of deep ponded impact melt and debris are absent within Rheasilvia (Fig. 1). This is consistent with the low apparent unconsolidated debris, impact melt drained down slope, or both. Two arcuate scarps ~5 to 7 km high near the crest of the central massif suggest partial failure of the central massif. The rugged surface morphology is consistent with uplift of highly disrupted material during impact, as observed in large complex craters on other bodies (*8*).

posite sides of the basin. Fractured slump blocks are observed at the base of these rim scarps [figure 3 in (*10*)]. The ridged slump material on the rim has a more coherent structure than that of the rugged slump material on the flank of the central massif. This may reflect a difference in rock properties, with the rim flank being less fragmented than the central massif.

All terrains within ~100 km of Rheasilvia's rim (and further in some areas) show evidence of extensive mantling by debris (Fig. 3), which is consistent with ejecta deposition. Smooth and striated surfaces are common, and nearly complete erasure of craters within 50 km or so of the rim (Fig. 1) gives way to the north to decreasing degrees of partial burial of craters (Fig. 3), which is consistent with the observed increase in crater densities away from the Rheasilvia rim (*11*) and the thinning of ejecta. Differences in crater density provide indirect evidence for nonuniform ejecta deposition, but no direct evidence for the extreme predicted asymmetric ejecta deposition due to rotation (*12*) has as yet been found. The multispectral color signature most consistent with diogenite (*13, 14*) is offset from the basin center toward 45°E longitude (fig. S1) (*15*) and suggests either oblique impact and enhanced ejecta deposition in one direction or that the impact occurred in a compositionally heterogeneous region, possibly because of the formation of older basins such as Veneneia.

The basic structure at Rheasilvia is surprisingly similar to that observed in very large craters on low-gravity worlds elsewhere in the solar system (Fig. 1) (*15*). Large impact craters on the midsize icy satellites Hyperion, Rhea, and Iapetus are also characterized by deep steep-sided depressions and broad domical central peaks that account for 0.35 to 0.5 of the crater diameter (*D*) (compared with 0.36 for Rheasilvia). These basins also have $D_{\text{crater}}/D_{\text{target}}$ ratios of 0.4 to 0.9 compared with 0.95 for Rheasilvia. This basic morphology, in which large central uplift (Fig. 1 and fig. S2) dominates over rim failure, may be characteristic of large complex crater formation on smaller planetary bodies or on bodies where melt production is low, regardless of composition (*15*), although planetary curvature may also play a role.

The basic structure at Rheasilvia is surprisingly similar to that observed in very large craters on low-gravity worlds elsewhere in the solar system (Fig. 1) (*15*). Large impact craters on the midsize icy satellites Hyperion, Rhea, and Iapetus are also characterized by deep steep-sided depressions and broad domical central peaks that account for 0.35 to 0.5 of the crater diameter (*D*) (compared with 0.36 for Rheasilvia). These basins also have $D_{\text{crater}}/D_{\text{target}}$ ratios of 0.4 to 0.9 compared with 0.95 for Rheasilvia. This basic morphology, in which large central uplift (Fig. 1 and fig. S2) dominates over rim failure, may be characteristic of large complex crater formation on smaller planetary bodies or on bodies where melt production is low, regardless of composition (*15*), although planetary curvature may also play a role.

¹Lunar and Planetary Institute, Houston, TX 77058, USA. ²Planetary Science Institute, Tucson, AZ 85719, USA. ³NASA Lunar Science Institute, Boulder, CO 12489, USA. ⁴Institute of Plan-

Determination of the structure, shape, and age of this feature—all of which provide critical parameters for modeling the formation of Vestoids and HEDs—are key Dawn objectives (*6*).

Dawn has resolved Vesta's south polar feature into two large distinct overlapping impact basins. The largest and youngest of these, Rheasilvia (Fig. 1 and fig. S1), is centered at 301° W, 75° S, ~15° from the south pole and, at 500 ± 25 km (or ~114° of arc) in diameter and 19 ± 6 km deep (*7*), is both deeper and larger than estimated from HST (*1*). The multiple concentric terraces and ring scarps—broad flat-lying melt sheets

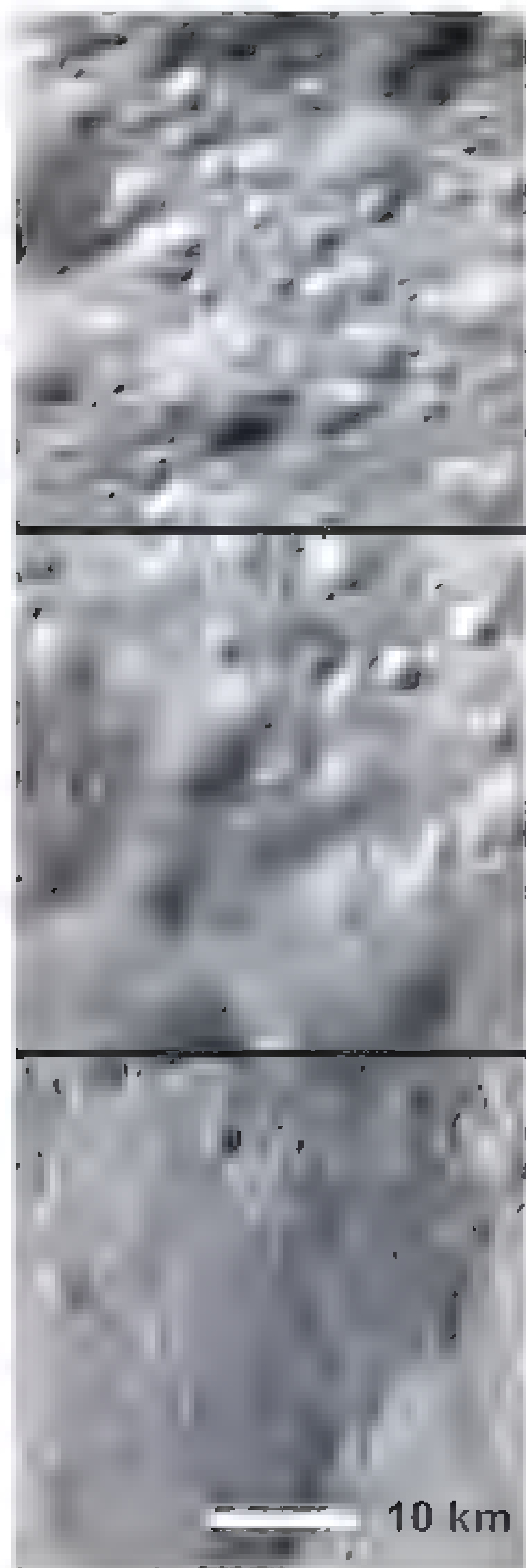


Fig. 3. Dawn image mosaics showing ejecta of Rheasilvia basin. Each image was acquired at 62 m resolution and show areas 35 km across. From top to bottom, they show terrains with increasing degree of mantling by ejecta in regions ~125 km, 75 km, and 50 km from the rim of Rheasilvia.

cratered, or obscured by Rheasilvia. A third older basin ~250 km wide (5°N, 315°E) is also cross-cut and heavily mantled by Rheasilvia (fig. S4) (11).

Independent crater counts of Rheasilvia floor, central massif, and proximal ejecta by three different workers all converge on a relatively young crater retention and formation age for Rheasilvia on the order of 1.0 ± 0.2 billion years (Fig. 4) (11). Crater counts also suggest a crater retention age for Veneneia of 2.1 ± 0.2 billion years (Fig. 4), predating Rheasilvia. Mantling of Veneneia by Rheasilvia ejecta may allow for an older age, but the relatively intact rim topography of Veneneia suggests that it is not ancient.

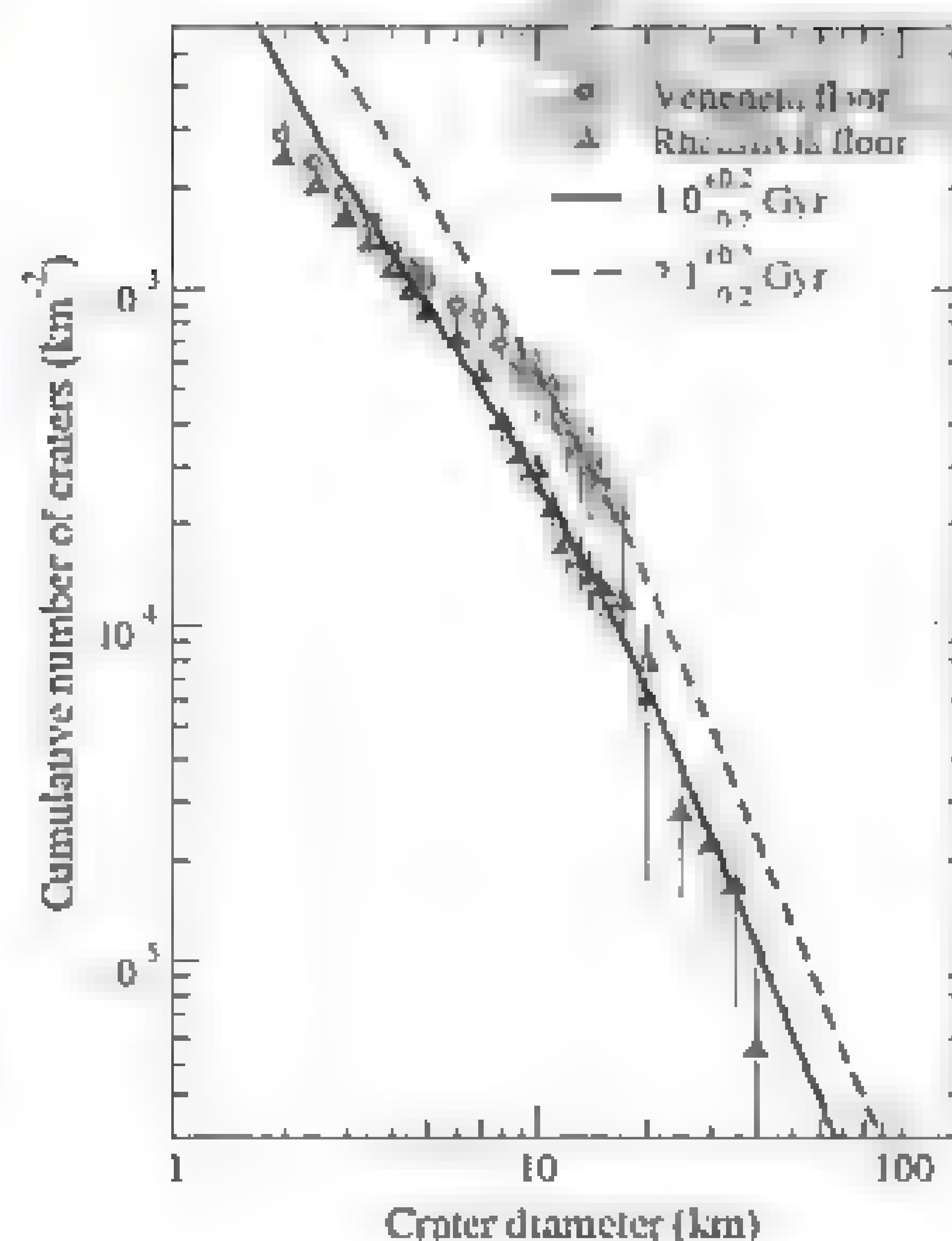


Fig. 4. Crater counts and ages for Rheasilvia (solid triangles) and Veneneia (gray circles) basins. Estimated ages (12) are 1.0 ± 0.2 (Rheasilvia) and 2.1 ± 0.2 billion years (Veneneia).

The proximity of the two large basins of similar age near the south pole suggests the possibility of a binary asteroid impact. However, the arcuate rim of Rheasilvia clearly truncates Veneneia, and there is no indication that the expanding ejecta or basin of Veneneia interfered with the development or shape of Rheasilvia, as would have been expected during an impact of binary objects (19). This indicates a minimum formation interval of at least several hours, during which the putative second object would likely have missed Vesta (20). Thus, while Rheasilvia and Veneneia are both relatively young impact features, they likely formed at different times.

The two large impact events at the south pole also excavated large amounts of rock that may have been the source of Vestoids and HEDs (1). A provisional estimated minimum volume of excavated material at Rheasilvia based on the observed concavity and the nominal volume of the modeled transient excavation crater (15) is $\sim 1 \times 10^6$ to 3×10^6 km³, or ~2 to 4% of the total volume of Vesta. Some Rheasilvia ejecta were retained on the surface (Fig. 3), however. Obliteration of preexisting craters <20 km wide out to ~50 km from the rim implies ejecta thicknesses of order 4 to 5 km at this range, increasing to the rim and decreasing outward to negligible thickness north beyond a range of about 100 km. Modeling of impact ejecta on Vesta (12) also predicts average thicknesses on this order.

Assuming an average ejecta thickness of 5 km over a range of 100 km, we obtain a provisional volume of ejecta on the surface Vesta of roughly 5×10^5 km³ (15), suggesting that more than half of Rheasilvia's ejecta was lost to space, which is a relatively high fraction. The fraction lost to space is significantly more than the estimated $<1 \times 10^5$ km³ volume of the Vesta family (21), which is consistent with the ejection into space of Rheasilvia ejecta to form the Vestoids. The suggestion of a smaller second dynamical family

of Vestoids (21) could potentially be explained by ejecta from the somewhat older giant Veneneia basin (Fig. 1), which has a nominal excavation volume ~65% that of Rheasilvia and likely excavated an additional several 10^5 km³ to space.

As discussed in (11), the young ages we find for these basins are consistent with the preservation of the Vesta family's steep size distribution (22, 23). Fugitive V-type asteroids take ~1 billion years or more to migrate away from the family (21), so many could have originated from Rheasilvia, or from an older large family populating impact event such as Veneneia.

At least seven basins larger than 150 km have been identified on Vesta, including Rheasilvia and Veneneia (fig. S4) (11). Most of the thermal alteration recorded in the argon-argon (Ar-Ar) ages of HED meteorites (24–26) may have occurred in thick slow-cooling units such as ejecta or basin floor deposits rather than directly during the impact events themselves (27), and Vesta's surface may be a patchwork of basin-formed units of distinct ages (11). The geologically recent formation of Rheasilvia into at least two preexisting large basins and their associated floor and ejecta deposits could have easily provided a ready source of large volumes of thermally altered rocks with different resetting ages that could be launched to form the Vestoids and the HED meteorite suite.

References and Notes

1. P. C. Thomas *et al.*, *Science* **277**, 1492 (1997).
2. L. B. McCord, J. B. Adams, T. V. Johnson, *Science* **168**, 1445 (1970).
3. G. J. Consolmagno, M. J. Drake, *Geochim. Cosmochim. Acta* **41**, 1271 (1977).
4. J. Wisdom, *Nature* **315**, 731 (1985).
5. R. P. Binzel, S. Xu, *Science* **260**, 186 (1993).
6. C. T. Russell *et al.*, *Science* **336**, 684 (2012).
7. The estimated depths for the basins are reported with respect to the current reference ellipsoid shape of Vesta: 285 by 229 km (6, 10). Otherwise, heights are reported with respect to local minimum and maximum elevations. The basin rim is defined here topographically and

- structurally by the inward facing scarp, arcuate ridge, or break in slope.
8. H. J. Melosh, *Impact Cratering* (Oxford Univ. Press, Oxford, 1989).
 9. K. Keil, D. Stollner, S. Love, E. Scott, *Meteorit. Planet. Sci.* **32**, 349 (1997).
 10. R. Jaumann *et al.*, *Science* **336**, 687 (2012).
 11. S. Marchi *et al.*, *Science* **336**, 690 (2012).
 12. M. Jutzi, E. Asphaug, *Geophys. Res. Lett.* **38**, L01102 (2011).
 13. M. C. De Sanctis *et al.*, *Science* **336**, 697 (2012).
 14. V. Reddy *et al.*, *Science* **336**, 700 (2012).
 15. Materials and methods are available as supplementary materials on Science Online.
 16. B. Knies, E. Shoemaker, K. Herkenhoff, *J. Geophys. Res.* **104**, 18867 (1999).
 17. T. Kenkmann, *Geology* **30**, 231 (2002).
 18. P. Allemand, P. Thomas, *J. Geophys. Res.* **104**, 16501 (1999).
 19. W. Bottke, H. J. Melosh, *Icarus* **124**, 72 (1996).
 20. If the formation time scale of Veneneia is a few hours, then to avoid interference with Rheasilvia a binary impactor would need a separation of at least $\sim 3600 \text{ s} \times 5 \text{ km/s} \sim 18,000 \text{ km}$ or ~ 70 Vesta radii. The probability of both binary bodies hit Vesta would then be very small.
 21. D. Nesvorný *et al.*, *Icarus* **193**, 85 (2008).
 22. F. Marzari, P. Farnetani, D. R. Davis, *Icarus* **142**, 63 (1999).
 23. F. Marzari *et al.*, *Astron. Astrophys.* **316**, 248 (1996).
 24. D. Bogard, *Meteoritics* **30**, 244 (1995).
 25. D. Bogard, D. Garrison, *Meteorit. Planet. Sci.* **38**, 669 (2003).
 26. D. Bogard, *Chem. Erde Geochem.* **71**, 207 (2011).
 27. Ar-Ar age resetting requires an extended time to diffuse Ar from the rocks; there is insufficient time to accomplish this in just the initial shock.

Acknowledgments: The authors thank D. Bogard, E. Asphaug, and H. J. Melosh for helpful discussions and comments.

and the NASA Dawn at Vesta Participating Scientist program for support. We thank the Dawn team for the development, cruise, orbital insertion, and operations of the Dawn spacecraft at Vesta. A portion of this work was performed at the Jet Propulsion Laboratory, California Institute of Technology, under contract with NASA. Dawn data are archived with the NASA Planetary Data System.

Supplementary Materials

www.sciencemag.org/cgi/content/full/336/6082/694/DC1

Materials and Methods

Supplementary Text

References (28, 29)

12 April 2012; accepted 20 April 2012

10.1126/science.1223272

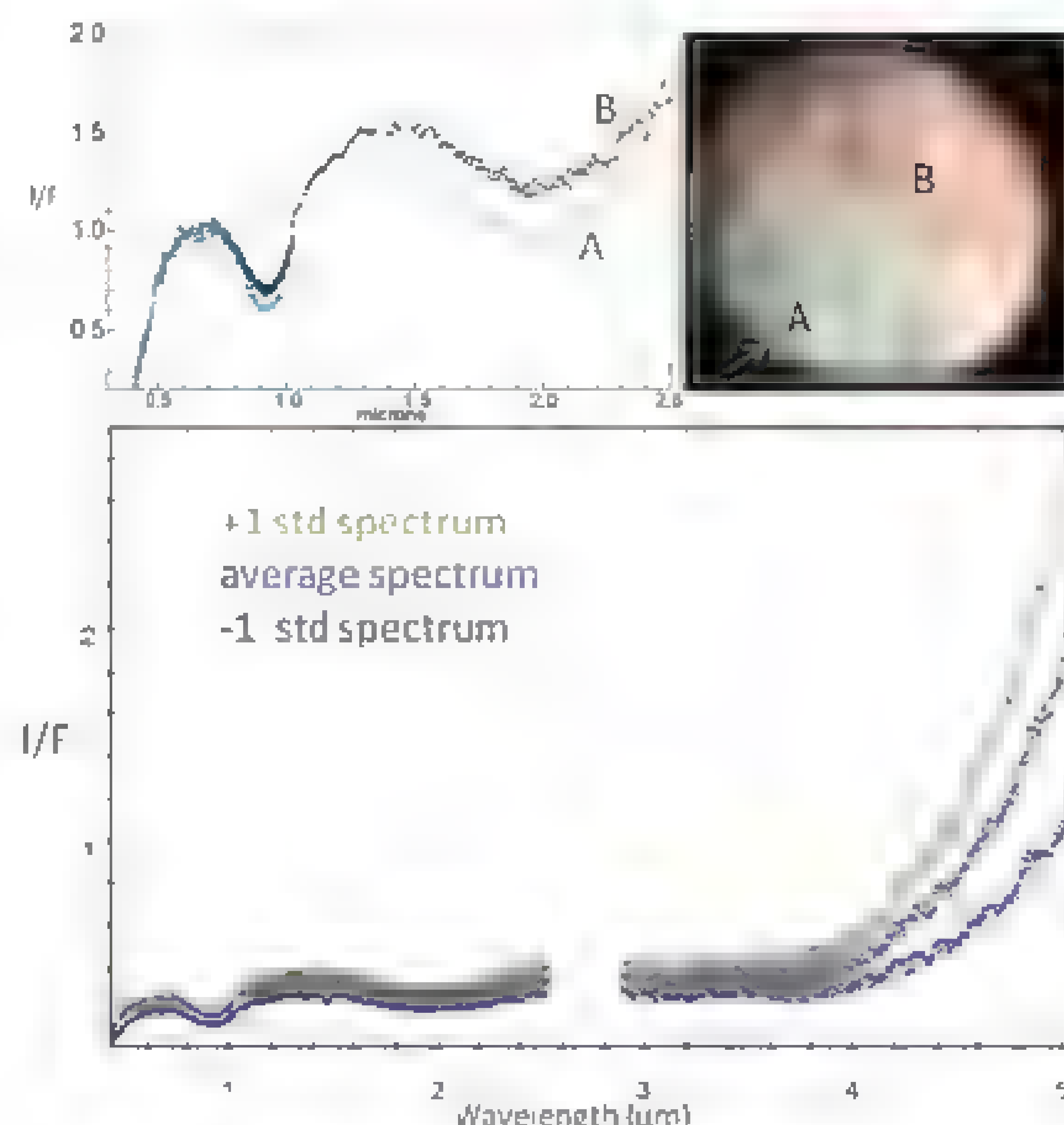
Spectroscopic Characterization of Mineralogy and Its Diversity Across Vesta

M. C. De Sanctis,^{1*} E. Ammannito,¹ M. T. Capria,¹ F. Tosi,¹ F. Capaccioni,¹ F. Zambon,¹ F. Carraro,² S. Fonte,¹ A. Frigeri,¹ R. Jaumann,² G. Magni,¹ S. Marchi,³ T. B. McCord,⁴ L. A. McFadden,⁵ H. Y. McSween,⁶ D. W. Mittlefehldt,⁷ A. Nathues,⁸ E. Palomba,¹ C. M. Pieters,⁹ C. A. Raymond,¹⁰ C. T. Russell,¹¹ M. J. Toplis,¹² D. Turrini¹

The mineralogy of Vesta, based on data obtained by the Dawn spacecraft's visible and infrared spectrometer, is consistent with howardite-eucrite-diogenite meteorites. There are considerable regional and local variations across the asteroid: Spectrally distinct regions include the south-polar Rheasilvia basin, which displays a higher diogenitic component, and equatorial regions, which show a higher eucritic component. The lithologic distribution indicates a deeper diogenitic crust, exposed after excavation by the impact that formed Rheasilvia, and an upper eucritic crust. Evidence for mineralogical stratigraphic layering is observed on crater walls and in ejecta. This is broadly consistent with magma-ocean models, but spectral variability highlights local variations, which suggests that the crust can be a complex assemblage of eucritic basalts and pyroxene cumulates. Overall, Vesta mineralogy indicates a complex magmatic evolution that led to a differentiated crust and mantle.

Telescopio visible and near-infrared spectroscopy shows that the asteroid Vesta has a basaltic surface dominated by the spectral signature of pyroxene. Vesta spectra show many similarities to those of howardite-eucrite-diogenite (HED) meteorites (1), leading to the consensus that Vesta is differentiated and is the parent body of the HED achondrites (2–4). Nu-

Fig. 1. (Top left) Spectra (normalized at 0.7 μm) of regions A and B indicated in the VIR image. (Top right) VIR color composite (red = 0.92 μm , green = 0.62 μm , blue = 0.44 μm). Spatial resolution is ~ 25 km. Arrow indicates the south pole. (Bottom) Average Vesta spectrum with ± 1 SD of the average. The data between 2.5 and 2.8 μm have been removed because they are not yet fully calibrated in this region.



¹Istituto di Astrofisica e Planetologia Spaziali, Istituto Nazionale di Astrofisica, Rome, Italy. ²Institute of Planetary Research, German Aerospace Center (DLR), Berlin, Germany. ³NASA Lunar Science Institute, Boulder, CO, USA. ⁴Bear Fight Institute, Winthrop, WA, USA. ⁵NASA, Goddard Space Flight Center, Greenbelt, MD, USA. ⁶Department of Earth and Planetary Sciences, University of Tennessee, Knoxville, TN, USA. ⁷NASA Johnson Space Center, Houston, TX 77058, USA. ⁸Max-Planck-Institut für Sonnensystemforschung, Katlenburg-Lindau, Germany. ⁹Brown University, Providence, RI, USA. ¹⁰Jet Propulsion Laboratory, California Institute of Technology, Pasadena, CA, USA. ¹¹Institute of Geophysics and Planetary Physics, University of California, Los Angeles, CA, USA. ¹²Observatoire Midi-Pyrénées, Toulouse, France.

*To whom correspondence should be addressed. E-mail: manacrisbna.desanctis@iaps.inaf.it

geological context relevant to the question of its formation history

The visible and infrared spectrometer (VIR) on Dawn is a high-resolution imaging spectrometer with a spectral range of 0.25 to 5.01 μm and a spatial sampling of 250 μrad (15). It combines two data channels in one compact instrument: the visible-infrared (0.25 to 1.07 μm) and the infrared (0.95 to 5.1 μm) channels, with a spectral sampling of $\Delta\lambda_{\text{VIS}} = 1.8$ nm per band and $\Delta\lambda_{\text{IR}} = 9.8$ nm per band, respectively.

VIR obtained spatially resolved hyperspectral images of Vesta (fig. S1) with a nominal spatial sampling up to ~ 0.7 km. The orientation of Vesta's spin axis and Dawn's orbital characteristics (16)

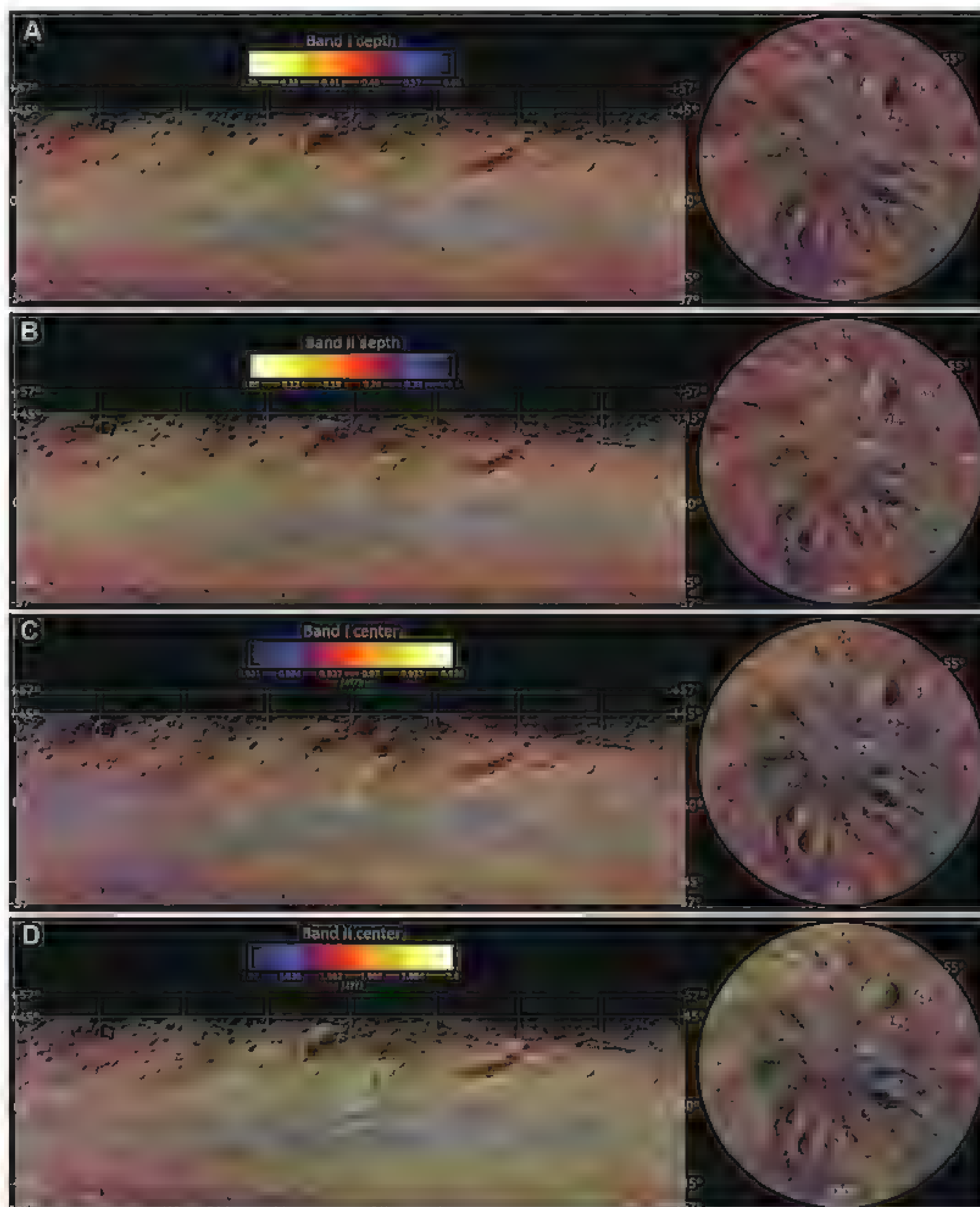
have allowed $>65\%$ of the surface to be imaged, ranging from the south pole up to about 45°N (the northern polar region was in shadow). VIR has acquired about four million spectra of Vesta's surface under different illumination conditions, with phase angles from 67.8° to 7.9° .

The first data, at a resolution twice that of the Hubble Space Telescope, were obtained from a distance of $\sim 99,200$ km (Fig. 1). The spectra show clear evidence of pyroxene absorption bands at 0.9 and 1.9 μm (hereafter B1 and B2). Different regions of Vesta are characterized by distinctly different band depths, widths, shapes, and centers. Beyond ~ 3.5 μm , thermal emission of the surface becomes increasingly important, and the spec-

tral variations also reflect diurnal changes with the corresponding surface temperature changes (Fig. 1).

The color composite image of Vesta (Fig. 1) demonstrates that there are large-scale variations in the spectral properties of the surface material and that these variations are greater in magnitude than those described on other asteroids (17, 18). In this image, the reddish color of the northern hemisphere indicates greater reflectivity at 0.92 μm , and hence shallower pyroxene bands compared with the southern hemisphere. The representative spectrum from region A shows stronger absorption at 0.92 μm relative to the continuum at 0.7 μm than does region B.

Fig. 2. Cylindrical and stereographic projections of spectral parameters obtained by VIR. (A) B1 depths. (B) B2 depths. (C) B1 centers. (D) B2 centers. Band depths and centers were computed after continuum removal (fig. S2).



Although the surface of Vesta exhibits spectral variations at both large and small scales, the materials on the surface are always dominated by rocks formed by mafic magmatism, as indicated by the ubiquitous BI and BII pyroxene signatures.

These bands are caused by absorption of photons, primarily by Fe^{2+} , and their exact position and shape are driven by the relative proportion of Fe to Mg in the M1 and M2 sites of pyroxene crystal structures (19, 20)

VIR spatial resolution allows for the definition of localized mineralogical units. The results indicate a complex geological and collisional history (21–23) and reveal a crust that was differentiated before impact bombardment. The spectral variations indicate that Vesta's crust is compositionally variable at vertical scales from a few hundred meters to 20 km, the depth of excavation of the southern impact basins (16)

A global-scale spectral difference is observed between the equatorial and southern Rheasilvia regions, as shown on maps of BI and BII depths and centers (Fig. 2). In the south pole region, pyroxene bands are, on average, deeper and wider than in the equatorial region (fig. S3). In general, BI depths in the equatorial region are ~ 0.35 to 0.4 , whereas those in the Rheasilvia basin are commonly 0.45 to 0.55 . Similarly, BII depths in the equatorial region are typically ~ 0.15 to 0.2 ,

whereas in the southern region they are ~ 0.25 to 0.3 . The depth of an absorption band is mainly determined by the abundance of the absorbing minerals, the grain size distribution, and the abundance of opaque phases. The process known as space weathering also modifies reflectance spectra and can make lithological interpretation difficult. Regolithic howardites show some characteristics of exposure to the space environment, such as high noble gas and siderophile element contents, and impact-produced glass, but these characteristics are not as well developed as in mature lunar regolith breccias (24, 25). Vesta retains a reflectance spectrum dominated by pyroxene absorption bands (fig. S5), indicating that the effects of space weathering are much less pronounced on Vesta compared with the Moon or Mercury.

Thus, the VIR data suggest that the region of the Rheasilvia basin is richer in pyroxene than the equatorial regions or that the regolith in this region has a larger average grain size distribution and/or contains fewer opaque minerals. A larger grain size would be consistent with less impact comminution in the southern region because of the younger age of the Rheasilvia basin (23). The lower crust is also expected to have had a coarser initial grain size because pyroxene grain sizes vary from diogenites, which are much larger than cumulate eucrites, which are larger than basaltic eucrites (12)

Fig. 3. BI center versus BII center. Green, yellow, and violet ovals are the distribution of howardites, eucrites, and diogenites, respectively. The scatter plot represents the distribution of the VIR BI and BII centers acquired during the Survey phase.

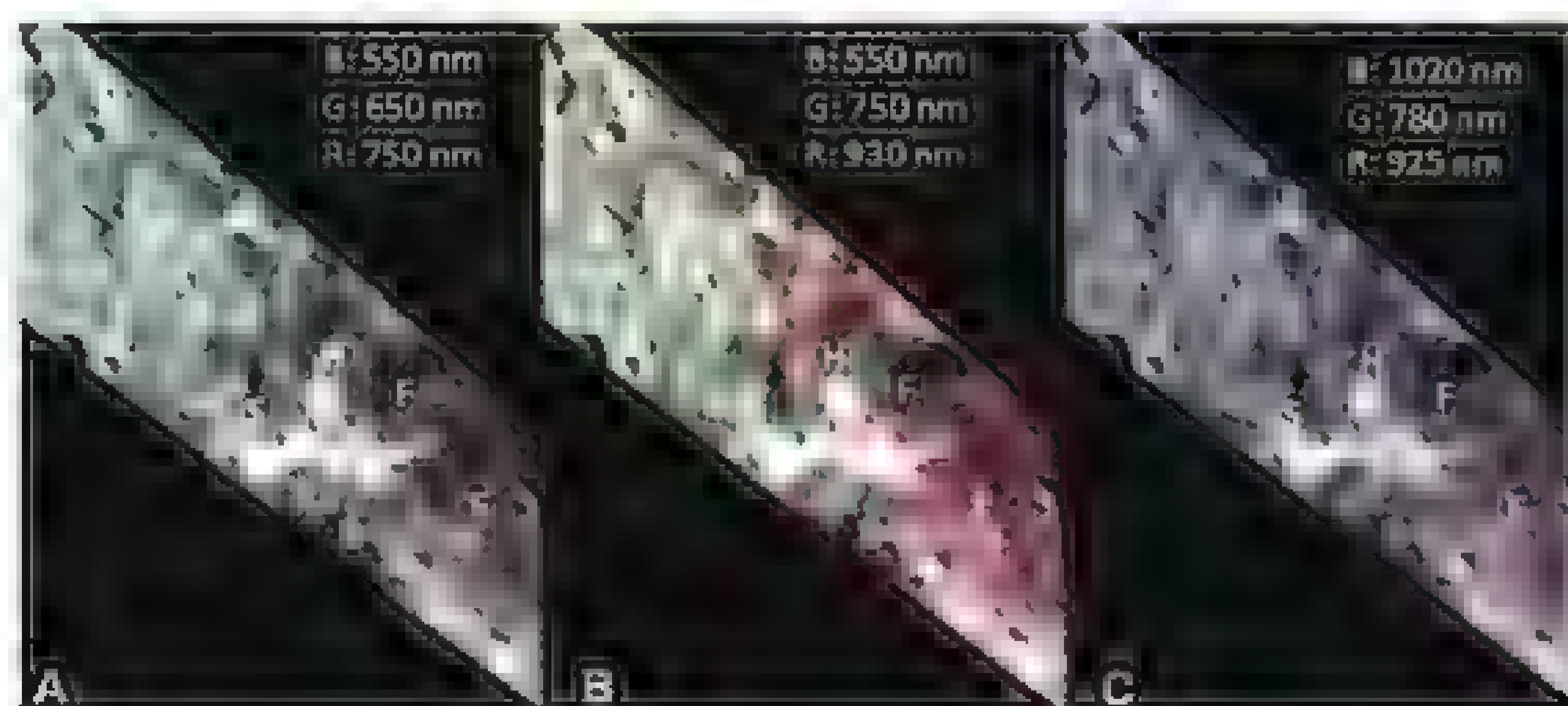
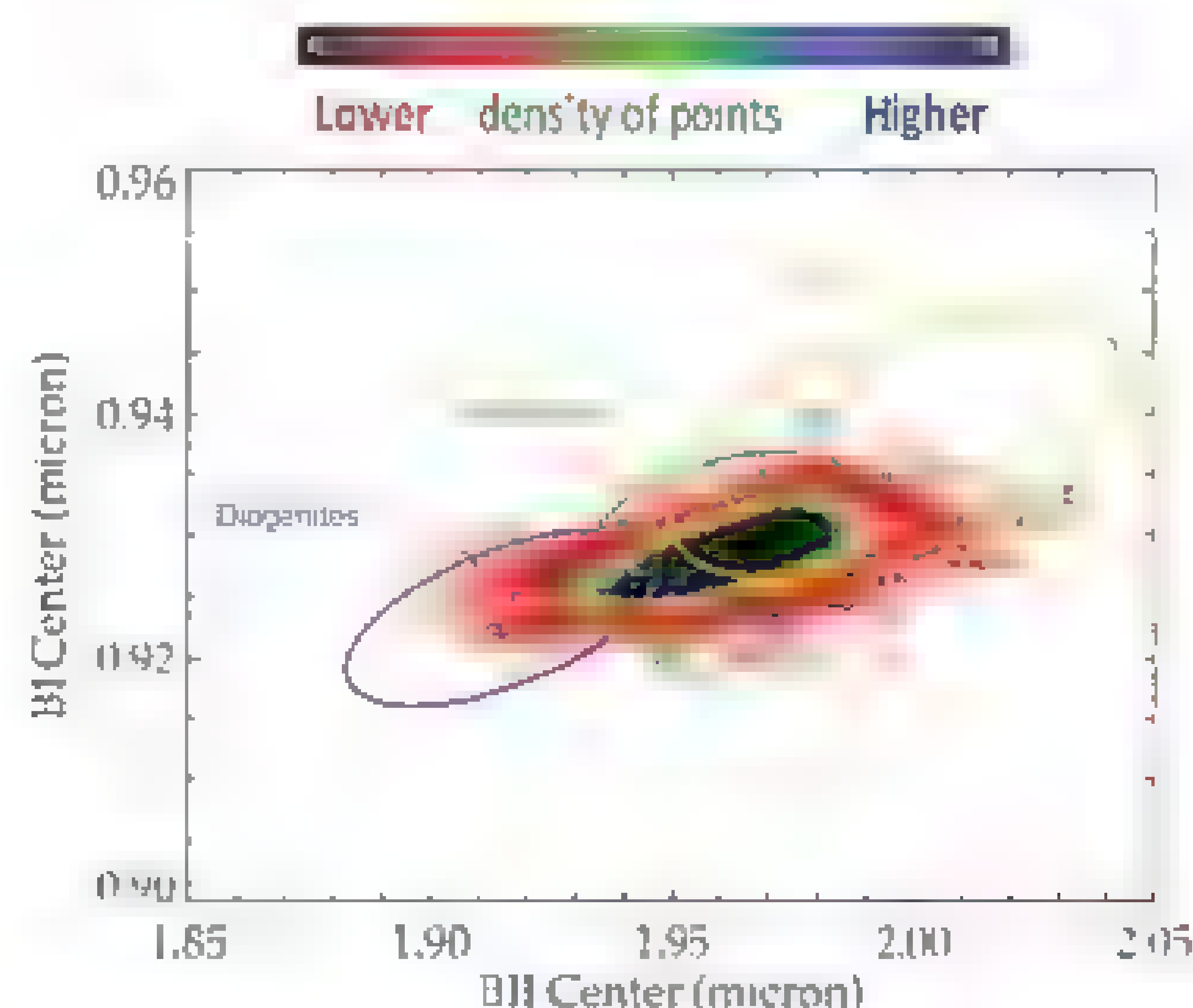


Fig. 4. The vestan surface near Oppia crater. E, Oppia ejecta; F, Oppia crater floor; H, Oppia crater walls; S, small crater near Oppia. (A) False-color image in the visible continuum. (B) Lithologic diversity around the central crater with copious "red" ejecta (shallower absorption bands) and deeper pyroxene bands on the crater walls. (C) Image made by combining colors defining the 930-nm band depth, where the small crater near the Oppia rim (S) is clearly seen.

The global asymmetry evident in the distributions of pyroxene band depths is also demonstrated by variations in band center wavelengths (Fig. 2, C and D). Laboratory studies indicate that band centers for BI and BII pyroxene absorptions are systematically different for diogenites and eucrites (26). To directly compare Vesta band centers with HEDs, we computed the band centers of HEDs by applying the same method to both data sets (Fig. 3). BI and BII centers are at slightly shorter wavelengths for diogenites than for eucrites (Fig. 3), a consequence of more Mg-rich pyroxenes with lower Ca concentrations in the former (26). Howardites, because of their intermediate nature, lie between, but partially overlap the fields of diogenites and eucrites.

The BI and BII centers in the VIR spectra form a trend from diogenites to eucrites, and most plot in the howardites region. Band center values are not uniformly distributed on Vesta, but they differ systematically between the equatorial and southern regions, and band center values often correlate inversely with band depths (Fig. 2). Equatorial regions are prevalently characterized by band centers at longer wavelengths (average BI = $0.930 \mu\text{m}$ and BII = $1.96 \mu\text{m}$) and typically have intermediate to shallow band depths. In contrast, band centers in the Rheasilvia basin are at shorter wavelengths (average BI = $0.926 \mu\text{m}$ and BII = $1.94 \mu\text{m}$), and these often correspond to the deepest pyroxene absorption bands (Fig. 2)

Overall, the correlations between band depths and band centers can be interpreted in terms of diogenite/eucrite content of the different terrains. Diogenites contain ~ 90 to 95 volume % (vol %) pyroxene (27), whereas basaltic eucrites contain ~ 50 vol % pyroxene (28), implying that, for a given grain size, the diogenites spectra have stronger bands with respect to eucrites, as confirmed by HED spectra (table S1). The correspondence of stronger pyroxene absorptions with shorter BI and BII centers in the Rheasilvia basin is consistent with a greater proportion of diogenite on the surface in this deeply excavated region.

Spectra from the equatorial regions have band centers shifted to longer wavelengths, indicating more Fe-rich pyroxenes, and intermediate or shallow band depths, indicating lower pyroxene abundance, both consistent with a greater eucrite component. However, the equatorial region is not spectrally uniform. An extensive area at about 40°E has measurably deeper absorption bands and shorter wavelengths, suggesting a lower proportion of eucritic material in this region, possibly related to the influence of Rheasilvia ejecta (23–25). Overall, the mineralogical north-south diversity indicates that the lower crust exposed in Rheasilvia is dominated by pyroxene-rich, diogenitic material.

Although the difference between the south polar and equatorial regions is the dominant first-order feature (Fig. 2), VIR data also demonstrate that Vesta's surface and subsurface show variations at local scales, that is, bright and dark localized areas (fig. S4). Study of geological structures at scales of tens of kilometers, in particular impact craters with copious ejecta and

mass movements often show associated spectral differences. For example, the Oppia region's surface exhibits variations in albedo and spectral slope that indicate differences in surface materials (Fig. 4A). Moreover, the area around the (Fig. 3) fresh Oppia crater (E) and the crater floor (F) have shallower BI depths (Fig. 4B), revealing material poorer in pyroxene. The cratering process here results in inverted stratigraphy of roughly the upper third of the target lithology in the ejecta blanket nearest the rim [e.g., (29)]. The crater floor and material part-way up the walls have a reddish hue similar to the ejecta just outside the rim, consistent with the lower layers in this crater being composed of rock poorer in pyroxene. The cyan color indicates that the soils just below the rim (H) have stronger BI absorption and thus have higher pyroxene content or different grain size (Fig. 4C). The small crater (S) is surrounded by a halo of bright and green materials, similar to the layer exposed in Oppia (H), suggesting a similar composition. VIR thus reveals that the Oppia impact exposed different kinds of materials, suggesting complex, small-scale crustal stratigraphy on Vesta.

At all scales, pyroxene absorptions are the most prominent spectral features on Vesta and, on average, the spectral parameters of Vesta resemble those of howardites (fig. S5). The VIR spectra are thus consistent with a surface covered by a howardite-like regolith containing varying proportions of eucrite and diogenite at different locations. This firmly supports the link between Vesta and the HEDs, providing geologic context for these samples, which furthers our understanding of the formation and evolution of Vesta.

Furthermore, Vesta exhibits large color and spectral variations that often reflect geological structures, indicating a complex geological and

evolutionary history, more similar to that of the terrestrial planets than to other asteroids visited by spacecraft (17, 18). The occurrence of a greater proportion of diogenite at depth is a critical finding, not demonstrated by data from the Hubble Space Telescope or telescopic observations (30, 31), and broadly consistent with magma ocean models for Vesta's differentiation. On the other hand, the fact that mixtures of diogenite and eucrite appear ubiquitous in all regions, coupled with the occurrence of smaller-scale variations in mineralogy, make it premature to distinguish between a simple layered crust of eucrite and underlying diogenite (32) or a complex eucrite crust with intruded diogenitic plutons (14). The Dawn mission provides the first spatially detailed view of the distribution of the rock types, allowing insight into the magmatic processes that formed the solar system's "smallest planet."

References and Notes

1. T. B. McCord, J. B. Adams, T. V. Johnson, *Science* **168**, 1445 (1970).
2. M. A. Feinberg, M. J. Drake, *Science* **209**, 805 (1980).
3. G. J. Consolmagno, M. J. Drake, *Geochim. Cosmochim. Acta* **41**, 1271 (1977).
4. M. J. Drake, in *Asteroids*, T. Gehrels, Ed. (Univ. Arizona Press, Tucson, AZ, 1979), pp. 765–782.
5. R. P. Binzel et al., *Icarus* **128**, 95 (1997).
6. M. C. De Sanctis et al., *Astron. Astrophys.* **533**, A77 (2011).
7. A. Moscovitz et al., *Icarus* **208**, 773 (2010).
8. M. C. De Sanctis et al., *Mon. Not. R. Astron. Soc.* **412**, 2318 (2011).
9. K. Righter, M. J. Drake, *Meteorit. Planet. Sci.* **32**, 929 (1997).
10. P. H. Warren, *Meteorit. Planet. Sci.* **32**, 945 (1997).
11. R. C. Greenwood, A. Franchi, A. Jambon, P. C. Buchanan, *Nature* **435**, 916 (2005).
12. D. W. Mittlefehldt et al., in *Planetary Materials. Reviews in Mineralogy* **36**, J. J. Papike, Ed. (Mineralogical Society of America, Chantilly, VA, 1998), pp. 4–14–195.
13. A. Beck, H. Y. McSween Jr., *Meteorit. Planet. Sci.* **45**, 850 (2010).
14. J.-A. Barrat, A. Yamaguchi, B. Zanda, C. Bolinger, M. Bohn, *Geochim. Cosmochim. Acta* **74**, 6218 (2010).

15. M. C. De Sanctis et al., *Space Sci. Rev.* (2010).
16. C. T. Russell et al., *Science* **336**, 684 (2012).
17. A. Coradini et al., *Science* **334**, 492 (2011).
18. J. Veveřka et al., *Science* **289**, 2088 (2000).
19. R. G. Burns, *Mineralogical Applications of Crystal Field Theory* (Cambridge Univ. Press, Cambridge, 1993).
20. L. A. McFadden, T. B. McCord, C. Pieters, *Icarus* **31**, 439 (1977).
21. P. Schenk et al., *Science* **336**, 694 (2012).
22. R. Jaumann et al., *Science* **336**, 687 (2012).
23. S. Marchi et al., *Science* **336**, 690 (2012).
24. P. H. Warren, G. W. Kammerdorn, H. Huber, F. Uff-Möller, W. Choe, *Geochim. Cosmochim. Acta* **73**, 5918 (2009).
25. L. Wilkening, D. Lal, A. M. Reid, *Earth Planet. Sci. Lett.* **10**, 334 (1971).
26. M. J. Gaffey, *J. Geophys. Res.* **81**, 905 (1976).
27. L. E. Bowman, M. N. Sprade, J. J. Papike, *Meteorit. Planet. Sci.* **32**, 869 (1997).
28. J. S. Deane, M. Prinz, H. Takeda, *J. Geophys. Res.* **89**, (suppl.), C251 (1984).
29. H. J. Melosh, *Impact Cratering: A Geologic Process* (Oxford Univ. Press, Oxford, 1989).
30. Telescopic data suggested a prominent diogenite region. In the adopted coordinate system, this diogenite spot was moved to the northern hemisphere, where VIR does not find this evidence.
31. J. Y. Li et al., *Icarus* **208**, 238 (2010).
32. H. Takeda, *Icarus* **40**, 455 (1979).

Acknowledgments: VIR is funded by the Italian Space Agency and was developed under the leadership of NAF-Istituto di Astrofisica e Planetologia Spaziali, Rome, Italy. The instrument was built by Selex-Galileo, Florence, Italy. The authors acknowledge the support of the Dawn Science, Instrument, and Operations Teams. This work was supported by the Italian Space Agency, and NASA's Dawn at Vesta Participating Scientists Program. A portion of this work was performed at the Jet Propulsion Laboratory under contract with NASA.

Supplementary Materials

www.sciencemag.org/cgi/content/full/336/6082/697/DC1

Supplementary Text

Figs. S1 to S5

Table S1

17 January 2012, accepted 16 April 2012

10.1126/science.1219270

Color and Albedo Heterogeneity of Vesta from Dawn

Vishnu Reddy,^{1,2*} Andreas Nathues,¹ Lucille Le Corre,¹ Holger Sierks,¹ Jian-Yang Li,³ Robert Gaskell,⁴ Timothy McCoy,⁵ Andrew W. Beck,⁵ Stefan E. Schröder,¹ Carle M. Pieters,⁶ Kris J. Becker,⁷ Bonnie J. Buratti,⁸ Brett Denevi,⁹ David T. Blewett,⁹ Ulrich Christensen,¹ Michael J. Gaffey,² Pablo Gutierrez-Marques,¹ Michael Hicks,⁸ Horst Uwe Keller,¹⁰ Thorsten Maue,¹ Stefano Mottola,¹¹ Lucy A. McFadden,¹² Harry Y. McSween,¹³ David Mittlefehldt,¹⁴ David P. O'Brien,⁴ Carol Raymond,⁸ Christopher Russell¹⁵

Multispectral images (0.44 to 0.98 μm) of asteroid (4) Vesta obtained by the Dawn Framing Cameras reveal global color variations that uncover and help understand the north-south hemispherical dichotomy. The signature of deep lithologies excavated during the formation of the Rheasilvia basin on the south pole has been preserved on the surface. Color variations (band depth, spectral slope, and eucrite-diogenite abundance) clearly correlate with distinct compositional units. Vesta displays the greatest variation of geometric albedo (0.10 to 0.67) of any asteroid yet observed. Four distinct color units are recognized that chronicle processes—including impact excavation, mass wasting, and space weathering—that shaped the asteroid's surface. Vesta's color and photometric diversity are indicative of its status as a preserved, differentiated protoplanet.

The Dawn spacecraft rendezvoused with the asteroid Vesta on 16 July 2011, and the Framing Cameras (FCs) (1) acquired images

in seven colors (0.44 to 0.98 μm) and one broadband clear filter, mapping the entire sun-lit surface at a detail of ~ 9 to ~ 0.016 km/pixel. We used

¹Max Planck Institute for Solar System Research, Max-Planck-Strasse 2, 37191 Katlenburg-Lindau, Germany. ²Department of Space Studies, University of North Dakota, Grand Forks, ND 58202, USA. ³Department of Astronomy, University of Maryland, College Park, MD 20742, USA. ⁴Planetary Science Institute, 1700 East Fort Lowell, Suite 106, Tucson, AZ 85719, USA. ⁵Department of Mineral Sciences, Smithsonian National Museum of Natural History, 10th and Constitution NW, Washington, DC 20560-0119, USA. ⁶Department of Geological Sciences, Brown University, Providence, RI 02912, USA. ⁷Astrogeology Science Center, U.S. Geological Survey, Flagstaff, AZ 86001, USA. ⁸Jet Propulsion Laboratory, California Institute of Technology, 4800 Oak Grove Drive, Pasadena, CA 91109, USA. ⁹Johns Hopkins University Applied Physics Laboratory, Laurel, MD 20723, USA. ¹⁰Institut für Geophysik und extraterrestrische Physik, TU Braunschweig Mendelssohnstrasse 3, DE 38106 Braunschweig, Germany. ¹¹Deutsches Zentrum für Luft und Raumfahrt (DLR)—German Aerospace Center, Institute of Planetary Research, Rutherfordstrasse 2, D-12489 Berlin, Germany. ¹²NASA/Goddard Space Flight Center, Mail Code 160, Greenbelt, MD 20771, USA. ¹³Department of Earth and Planetary Sciences, University of Tennessee, 1412 Circle Drive, Knoxville, TN 37996-1410, USA. ¹⁴Asteromaterials Research Office, NASA Johnson Space Center, Mail Code KR, Houston, TX 77058, USA. ¹⁵Institute of Geophysics and Planetary Physics, University of California Los Angeles, Los Angeles, CA 90024-1567, USA.

*To whom correspondence should be sent. E-mail: redy@mps.mpg.de

these images to determine the global color characteristics and compositional heterogeneity of the asteroid's surface. The diversity of collected meteorites indicates that in the early solar system, the main asteroid belt held more than 100 large asteroids that were partially or totally melted but subsequently destroyed by collisions (2). Today, Vesta is the only surviving silicate-rich differentiated object (3). Two major goals of the Dawn mission are to help answer why Vesta is the only remaining member of this class and to use its history to understand terrestrial planet formation.

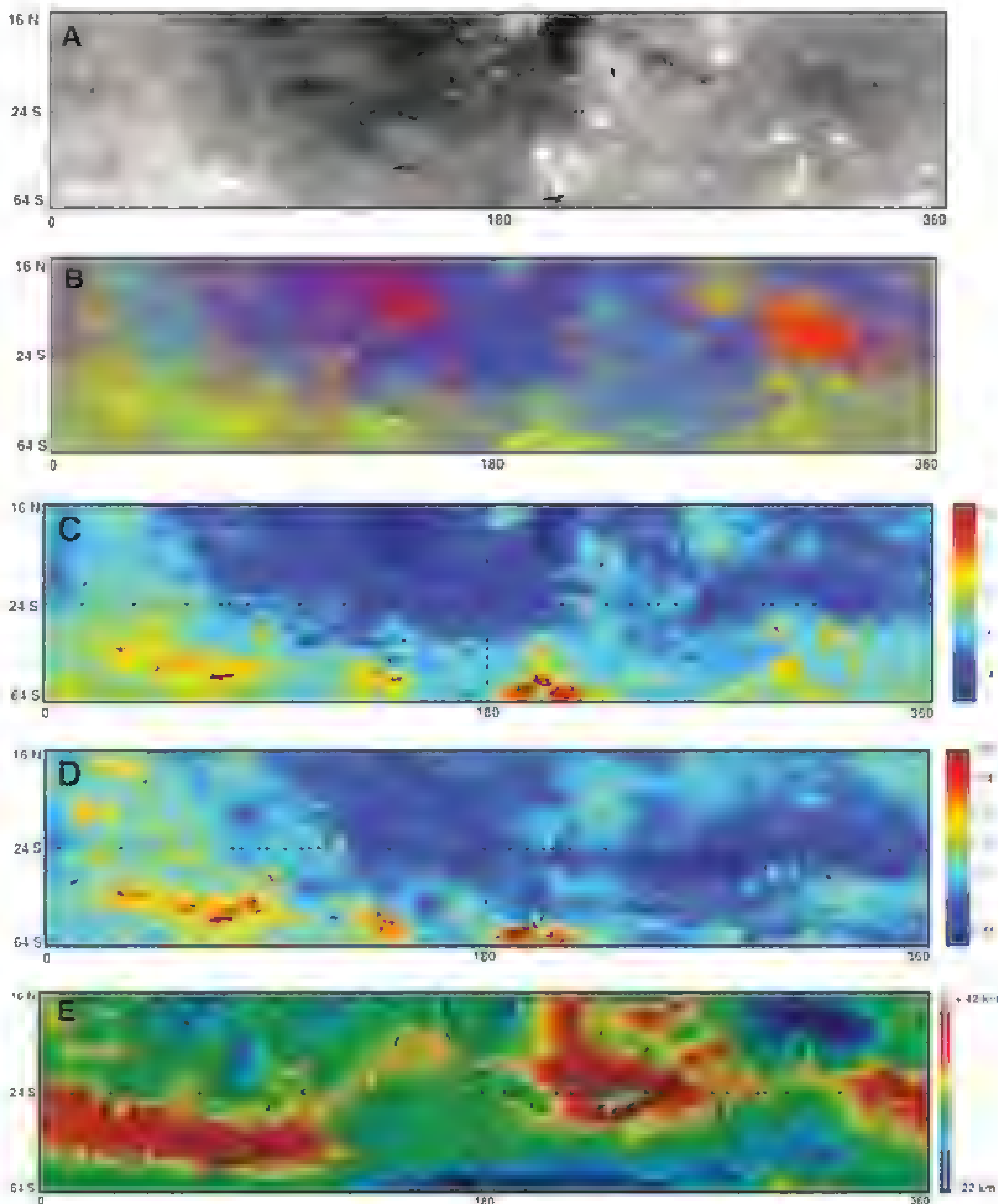
Vesta is the likely parent body of the howardite-eucrite-diogenite (HED) meteorites. Eucrites are crustal basalts, petrologically similar to terrestrial basalts; diogenites are ultramafic cumulates,

likely formed in the lower crust of the asteroid; and howardites are physical mixtures (regolith) of eucrites and diogenites formed by impact processes. Spectroscopic (4) and petrologic evidence (5) originally suggested a HED-Vesta link, and the 3:1 mean-motion resonance with Jupiter at 2.5 AU could provide a pathway for pieces ejected from Vesta to near-Earth space (6). This connection was further solidified by the detection of the "Vestoids," a group of smaller (<10 km) asteroids that are spectrally similar to Vesta and span the orbital region between Vesta and the 3:1 resonance (7).

We converted the FC images to reflectance (I/F) by dividing the observed radiance by the solar irradiance from a normally solar-illuminated

Lambertian disk, photometrically corrected to standard viewing geometry (30° incidence and 0° emergence and 30° phase angles). This was accomplished by using Hapke functions derived from disk-integrated ground-based telescopic observations of Vesta and Vestoids, as well as resolved data from the approach phase of the mission (8). A fit of the Dawn survey data in the wideband clear filter to Hapke's model yields fits to the Hapke parameters of 0.52 for the single scattering albedo (SSA), -0.29 for the backscattering parameter (confirming that Vesta's surface is backscattering as other asteroids are), and 20° for the mean slope angle defining macroscopic roughness. For each color acquisition, subpixel coregistration was accomplished to

Fig. 1. Color mosaics of Vesta obtained during the approach phase (~480 m/pixel) in simple cylindrical projection. (A) Photometrically corrected 0.75- μ m filter global mosaic showing east-west and north-south dichotomies in reflectance. (B) Clementine color ratios mosaic using $C_R = R(0.75)/R(0.45)$, $C_G = R(0.75)/R(0.92)$, and $C_B = R(0.45)/R(0.75)$, where $R(\lambda)$ is the reflectance in a filter centered at λ (micrometer) and C_R , C_G , C_B are the colors red, green, and blue, respectively. Greener areas have deeper bands, and redder areas have steeper visible slopes relative to bluer areas. (C) Rainbow-color coded map of $R(0.75)/R(0.92)$ ratio (proxy for 0.90- μ m pyroxene band depth) showing areas with deeper bands as red. (D) Rainbow-color coded map of $R(0.98)/R(0.92)$ ratio (Eucrite-Diogenite) showing diogenite-rich regions as red and eucrite-rich regions as blue (8). (E) Color-shaded topographic map of Vesta with white corresponding to the highest elevation and blue the lowest. Minimum and maximum elevations are computed relative to a 285- \times -229-km reference ellipsoid. All maps are based on the new Claudia coordinate system, which is different from the older Olbers system used with the Hubble Space Telescope data. Olbers reference longitude is located approximately at 210°E in the Claudia system.



align the seven color frames in order to create color cubes before analysis

Global maps show variations in 0.75- μm albedo (Fig. 1A) and the 0.90- μm pyroxene absorption depth $R(0.75)/R(0.92)$ (Fig. 1C). The ratio $R(0.98)/R(0.92)$ qualitatively identifies eucrite- and diogenite-rich terrains (Fig. 1D). All of these features show a weak relation to topography (Fig. 1E). A false color composite quantifies band depth and visible slope (Fig. 1B). Because eucrites have more ferroan pyroxene than diogenites (fig. S1), their 0.90- μm pyroxene band is shifted toward longer wavelengths (fig. S2) (8, 9), causing the $R(0.98)/R(0.92)$ to be closer to 1 for eucrites but higher for diogenites (Fig.

1D). We further confirmed the compositional identification of specific color units with laboratory spectra of HED meteorites using several spectral criteria (10)

The maps (Fig. 1, A to E) reveal a hemispherical scale dichotomy on Vesta. The brightest point (in clear filter) is on a crater wall near the south pole that has a SSA of ~ 0.82 and a geometric albedo of ~ 0.67 ; the darkest area has a SSA of ~ 0.15 and a geometric albedo of only ~ 0.10 . This range is much higher than is seen in other asteroids (8). The global albedo map also exhibits an overall lower reflectance in the eastern hemisphere as compared with the western (3, 11). The area located between 30°S and the

Rheasilvia Formation at the south pole also has higher albedo as compared with that of the northern hemisphere (Fig. 2, A and B). In addition, two distinct lower albedo units are associated with the ejecta of the Marcia (10°N, 190°) and Oppia (8°S, 309°) impact craters

This dichotomy reflects both Vesta's composition and regolith processes. Abundance of mafic minerals (iron abundance), space weathering, grain size, and presence of opaque minerals are known to affect the $R(0.75)/R(0.92)$ ratio (8). Laboratory study of HED meteorites suggests that grain size is a major cause for band depth dichotomy (8). Unlike the Moon, where the highland units have higher albedo as compared with those of lower and darker mare, Vesta does not seem to have distinct global correlation between topography and albedo or color

Along with global color dichotomy, we have identified various terrains on Vesta that are further evidence for surface heterogeneity. We have classified these areas as bright, dark, gray, and orange terrains (Fig. 3, A to H). Fresh impact craters have higher reflectance (30 to 40% in the 0.75- μm filter) than that of background surface and are associated with bright terrains (such as the Canuleia crater) (Fig. 3, A and B). They also have deeper 0.90- μm pyroxene absorption band. In the south, several fresh craters appear redder in the eucrite/diogenite (ED) ratio maps, suggesting that diogenite-rich material was excavated within Rheasilvia. By comparing the color spectra of bright material with global average, we find that the $R(0.75)/R(0.92)$ ratio is 16% deeper, and the visible spectral slope (0.45 to 0.55 μm) is also steeper (Fig. 4, A and B).

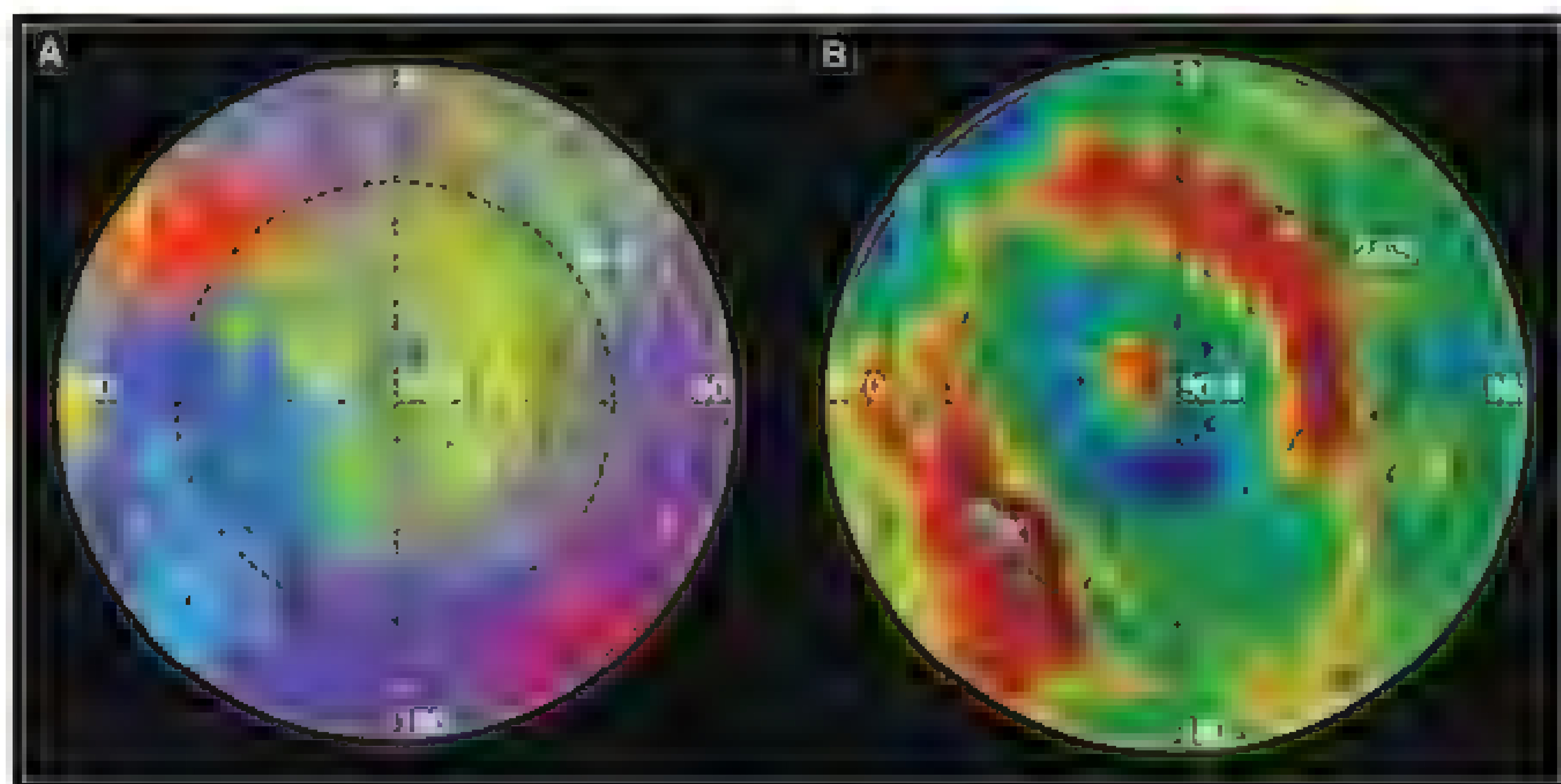


Fig. 2. Stereographic projection centered on the south pole of (A) the color mosaic in Clementine color ratios overlaid on a shaded-relief map and of (B) the color-shaded topographic map.

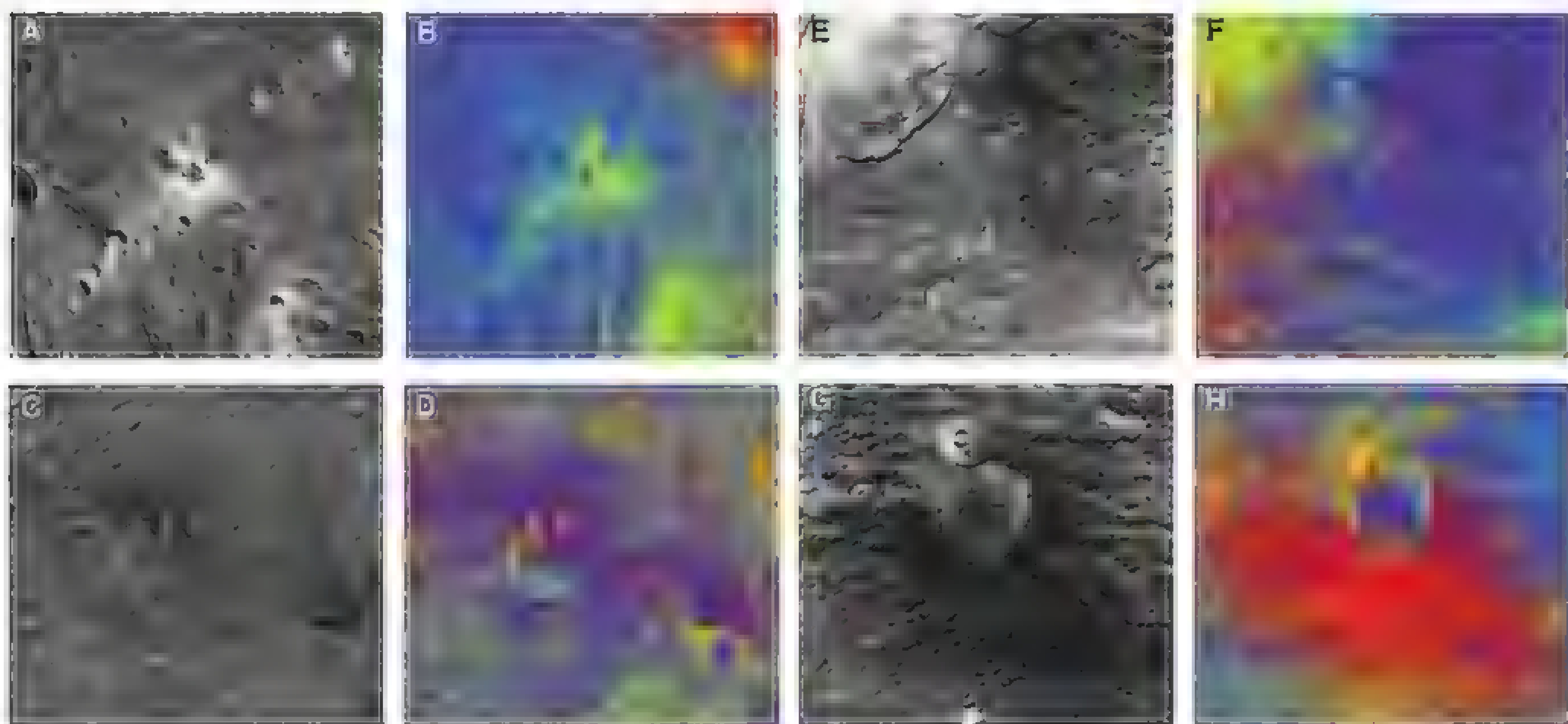


Fig. 3. Examples of diverse color terrains on Vesta in 0.75- μm filter (left) and Clementine ratio (right). (A and B) Bright ejecta around the 11.2-km diameter fresh impact crater Canuleia located at 33.7°S, 294.5°E. (C and D) Dark material on the crater wall and in the surroundings of the 30-km diameter

Numisia crater located at 7°S, 247°E. (E and F) Gray ejecta blanket of the 58-km diameter Marcia crater (top left) located at 10°N, 190°E. (G and H) The 34-km diameter impact crater Oppia located at 8°S, 309°E, with orange ejecta blanket.

Dark material is commonly associated with impact craters (such as the Nanus crater (Fig. 3, C and D), but dark deposits are also seen elsewhere in >25 locations. In some cases—Lucaria Tholus—dark material is associated with a topographic high. In addition, several fresh impact craters exhibit excavation of bright and dark material within the crater walls and ejecta blankets (Fig. 3, C and D). They have lower reflectance (8 to 13% at 0.75 μm), weaker band depth (Fig. 4, A and B) and have a redder visible spectral slope. Either the excavation of a darker subsurface layer or the incorporation of dark material by an impactor could explain the observed morphology of these units. The dark material on Vesta may indicate the presence of impact melts and exogenous carbonaceous material (8), both of which are seen in the HED meteorites.

Most of the surface of Vesta is covered with gray material (0.75- μm reflectance, ~15 to 30%). This material has a moderate $R(0.75)/R(0.92)$ ratio (Fig. 4, A and B). In craters, downslope movements have unveiled underlying bright material. Hence, gray material could correspond to a mixture of bright and dark material or space-weathered bright material. Space weathering affects optical properties of the regolith of planetary bodies without an atmosphere. A second type of gray material is associated with ejecta blankets around large impact craters such as the Marcia crater (Fig. 3, E and F) and is possibly impact melt. This gray material has a 0.75- μm reflectance of ~15%, a shallow visible slope, and the second weakest $R(0.75)/R(0.92)$ ratio (Fig. 4, A and B).

The Oppia crater displays asymmetric orange ejecta in the Clementine ratio map (Fig. 3, G and H) that is spread toward the southeast. The morphology of Oppia could be explained by an oblique impact or an impact on a slope. This particular unit has a steep visible spectral

slope (redder in Clementine ratios) and a weak $R(0.75)/R(0.92)$ ratio; thus, it has a shallower 0.90- μm pyroxene band as compared with the global mean spectrum (Fig. 4, A and B). Several lighter “orange patches” are also observed to the west and north around Oppia (Fig. 3, G and H).

Band depth and ED maps (Fig. 1, C and D) show that areas with deeper $R(0.75)/R(0.92)$ ratios also tend to have higher $R(0.98)/R(0.92)$ ratios (8). This correlation suggests that diogenite-rich material has a deeper $R(0.75)/R(0.92)$ ratio as compared with that of eucrite-rich material. Terrains with higher ratios surround Rheasilvia basin in the south, whereas Vesta has lower ratios in the north (Fig. 1, C and D). The observed variance is consistent with diogenite-rich terrains (red) in the south and more eucritic terrains (blue) in the north, which is in agreement with Visible and Infrared Imaging Spectrometer observations (12). This north-south dichotomy is disrupted by a swath (~0 to 90°E) of relatively higher $R(0.75)/R(0.92)$ and $R(0.98)/R(0.92)$ ratio material that protrudes to the northern extent of Dawn's observations (Fig. 1, C and D). This swath is probably impact ejecta from the Rheasilvia forming event because it is topographically higher than adjacent terrains (Fig. 1E) and has similar $R(0.75)/R(0.92)$ and $R(0.98)/R(0.92)$ ratios to Rheasilvia material (Fig. 1, C and D). Also, meteoritical evidence suggests that diogenitic material probably formed deep beneath the surface of Vesta (13). The central peak of the Rheasilvia basin has a strong $R(0.75)/R(0.92)$ ratio (Fig. 2A), implying that it is dominated by material with a strong 0.90- μm pyroxene band (diogenite-rich).

The high rim of Rheasilvia (Figs. 1, C and D, and 2, A and B) is dominated by high $R(0.75)/R(0.92)$ and $R(0.98)/R(0.92)$ ratio material, which is consistent with diogenite-rich rocks that have been excavated from depth and deposited as ejecta. However, the abundance of deeper-band material is not homogeneous along the entire Rheasilvia

rim. The eastern portion, between ~0 and 130°E, has higher concentrations of high-band-ratio material than the western portion (210 to 300°E), which is consistent with the western portion containing relatively more eucritic material. The origin of this variation is not immediately clear. Given that the western portion of the rim is topographically higher (Figs. 1E and 2B), we would expect it to contain higher concentrations of diogenite material (ejecta), which it does not. This may be an indication that the western portion of the Rheasilvia ejecta rim sampled previously reworked lithologies, which may be linked to the large pre-Rheasilvia basin impact (14).

Two localized concentrations of the highest $R(0.75)/R(0.92)$ and $R(0.98)/R(0.92)$ ratio material occur in areas associated with Rheasilvia (Figs. 1, C to E, and 2, A and B). The first (43 to 55°S, 51 to 87°E) coincides with a large scarp face, possibly indicating diogenite-rich material exposed along the rim and wall of the basin, and deposited nearby in the ejecta material. The second location (53 to 64°S, 180 to 230°E) is at a topographical low in the Rheasilvia basin floor and corresponds to the Antonia crater and its associated ejecta. Given the likely depth of excavation and the high-band-ratio signature, this material may be an *in situ* diogenitic lithology that has been exposed by the Rheasilvia impact event.

In a magma ocean model, a single, deep-seated layer of diogenitic material is expected (15), and if this region in the Rheasilvia basin is the only region with *in situ* diogenitic material identified on Vesta, a magma ocean model may be favored. Our analyses show that Vesta was large enough to accrete material and differentiate during the first few million years of Solar System formation. Although battered by multiple impacts, Vesta remains intact today probably because of its differentiated internal structure. These catastrophic events have not only excavated deeper

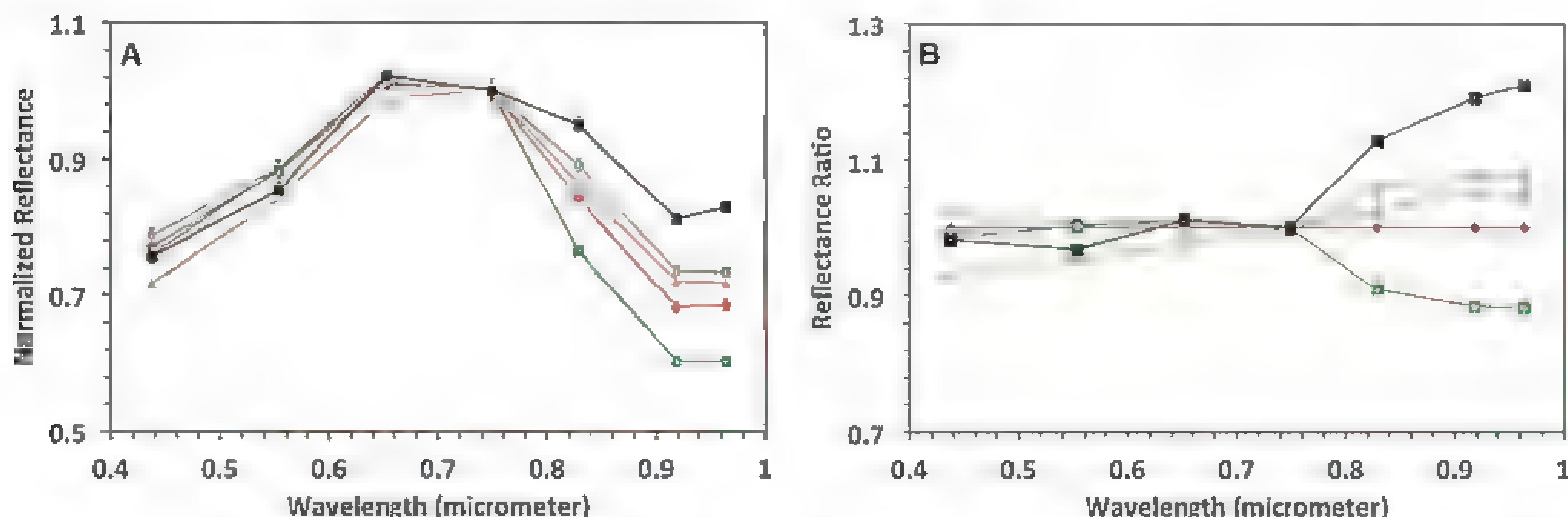


Fig. 4. (A) Color spectra of bright (green), dark (black), gray (gray) and orange terrains (orange) on Vesta. The red spectrum corresponds to the global average spectrum of Vesta. Errors shown are 1σ . (B) Ratios of the same color spectra divided by the global average spectrum (red). Dark,

gray, and orange terrains have weaker $R(0.75)/R(0.92)$ ratios, whereas bright material has deeper ratio as compared with the global average. The orange ejecta exhibits the steepest visible slope with respect to global average.

compositional units but also delivered exogenous carbon-rich material to Vesta, a key ingredient for the formation and evolution of life on Earth.

References and Notes

1. H. Sierks *et al.*, *Space Sci. Rev.* **163**, 263 (2011).
2. K. Keil, in *Asteroid III*, William F. Bottke, Alberto Cellino, Paolo Paolicchi, Richard P. Binzel, Eds. (Univ. of Arizona Press, Tucson, 2002), pp. 573–584.
3. P. C. Thomas *et al.*, *Icarus* **128**, 88 (1997).
4. T. B. McCord, J. B. Adams, T. V. Johnson, *Science* **168**, 1445 (1970).
5. G. J. Consolmagno, M. J. Drake, *Geochim. Cosmochim. Acta* **41**, 1271 (1977).
6. J. Wisdom, *Nature* **315**, 731 (1985).

7. R. P. Binzel, S. Xu, *Science* **260**, 186 (1993).
8. Materials and methods are available as supplementary materials on Science Online.
9. M. J. Gaffey, *J. Geophys. Res.* **81**, 905 (1976).
10. L. Le Corre, V. Reddy, A. Nathues, E. A. Cloutis, *Icarus* **216**, 376 (2011).
11. J.-Y. Li *et al.*, *Icarus* **208**, 238 (2010).
12. M. C. De Sanctis *et al.*, *Science* **336**, 697 (2012).
13. D. W. Mittlefehdt *et al.*, *Planet. Mot.* **36**, 4–1 (1998).
14. P. Schenk *et al.*, *Science* **336**, 694 (2012).
15. A. Ruzicka, G. A. Snyder, *Meteor. Planet. Sci.* **32**, 825 (1997).

Acknowledgments: We thank the Dawn team for the development, cruise, orbital insertion, and operations of the Dawn spacecraft at Vesta. The Framing Camera project is

financially supported by the Max Planck Society and the German Space Agency, DLR. We also thank the Dawn at Vesta Participating Scientist Program for funding the research. A portion of this work was performed at the Jet Propulsion Laboratory, California Institute of Technology, under contract with NASA. Dawn data are archived with the NASA Planetary Data System.

Supplementary Materials

www.sciencemag.org/cgi/content/full/336/6082/700/DC1
Materials and Methods

Figs. S1 and S2

References (16–31)

13 January 2012, accepted 13 April 2012

10.1126/science.1219088

Coupling Quantum Tunneling with Cavity Photons

Peter Cristofolini,¹ Gabriel Christmann,¹ Simeon I. Tsintzos,^{1,2} George Deligeorgis,^{2*} George Konstantinidis,² Zacharias Hatzopoulos,² Pavlos G. Savvidis,^{2,3} Jeremy J. Baumberg^{2,†}

Tunneling of electrons through a potential barrier is fundamental to chemical reactions, electronic transport in semiconductors and superconductors, magnetism, and devices such as terahertz oscillators. Whereas tunneling is typically controlled by electric fields, a completely different approach is to bind electrons into bosonic quasiparticles with a photonic component. Quasiparticles made of such light-matter microcavity polaritons have recently been demonstrated to Bose-condense into superfluids, whereas spatially separated Coulomb-bound electrons and holes possess strong dipole interactions. We use tunneling polaritons to connect these two realms, producing bosonic quasiparticles with static dipole moments. Our resulting three-state system yields dark polaritons analogous to those in atomic systems or optical waveguides, thereby offering new possibilities for electromagnetically induced transparency, room-temperature condensation, and adiabatic photon-to-electron transfer.

Strong coupling of photons to the interband exciton transition in a semiconductor microcavity leads to the formation of polaritons, bosonic quasiparticles whose properties are governed by their mixed light-matter composition. Owing to their quantum indistinguishability and the interplay of their Coulomb interactions, microcavity polaritons show unusually strong light-matter interactions and many-body quantum effects. In particular, their small effective mass allows observation of quantum degeneracy effects at temperatures from 10 to 300 K, such as Bose condensation (1–4) and superfluidity flow dynamics (5), and their tunable interactions make them ideal candidates for future quantum optoelectronic devices (6) working at room temperature (7). By contrast, spatially separating the electrons and holes in coupled double quantum wells yields indirect excitons with sufficiently long lifetimes for thermalization and a large static dipole moment (8). These properties enable ef-

ficient in-plane electrostatic traps (9, 10) and the coherent control of electron spins (11). By embedding double quantum wells inside a conventional microcavity in the strong coupling regime, we unite the concepts of indirect excitons and microcavity polaritons to produce optically active quasiparticles with transport properties, named dipolaritons. These offer the advantages of both systems: electrical trapping and tuning of excitons, strong optical coupling to low-mass quasiparticles with large de Broglie wavelength, and excellent control over the dipole properties and interactions (12, 13).

Microcavities are formed from p-i-n semiconductor multilayers surrounded by doped multilayer mirrors (7) (Fig. 1A; details in the supporting online material) and pumped with a non-resonant laser. Quantum wells (QWs) of InGaAs inside the cavity are arranged in asymmetric pairs separated by a thin barrier (of width L_B) that allows electrons to tunnel between the two wells (Fig. 1A). Because of the large effective hole mass and the wide energy separation of hole levels in neighboring QWs, hole tunneling is negligible, and only the low-energy left QW (LQW) hole state is considered. Without tunneling, there are two types of exciton in this system. The direct exciton (DX) has both electron and hole in the left QW (Fig. 1B, top) and therefore strongly couples to the cavity mode, with its induced di-

pole moment oriented randomly in the QW plane. The indirect exciton (IX) has the hole in the left QW and the electron in the right QW thus possessing an additional static dipole moment aligned perpendicularly to the plane—and has a very small overlap of electron and hole wave functions, hence low oscillator strength. When a bias voltage is applied to bring the electron levels into resonance, the electron states in the two QWs mix to give symmetric and antisymmetric electron wave functions (red in Fig. 1A), which, together with the low-energy hole states (blue) in the left QW, produce the exciton modes $(1/\sqrt{2})\{|IX\rangle \pm |DX\rangle\}$, split by the tunneling energy $\hbar J$ (where \hbar is Planck's constant divided by 2π). These modes combine the large oscillator strength of the DX with the large static dipole moment of the IX (Fig. 1B, bottom).

Embedding DX and IX excitons in the microcavity with cavity mode C now forms a three-state system similar to the atomic Λ -scheme (14, 15), which is coupled optically by the vacuum Rabi frequency Ω and electronically by the electron tunneling rate J (Fig. 1C). Although J and Ω are intrinsic to the microcavity design, full control of the dipolariton modes is possible through bias voltage control of tunneling and angle tuning of the cavity mode. In the strong coupling regime, when J is larger than the carrier escape rate from the coupled QWs and Ω is faster than the photon decay rate, the system displays three distinct eigenmodes: the lower (LP), middle (MP), and upper (UP) dipolaritons. Thus, a conventional microcavity polariton (Fig. 1D, black) can be simply bias-tuned to yield the dipolariton spectrum (red) in the strong tunneling regime.

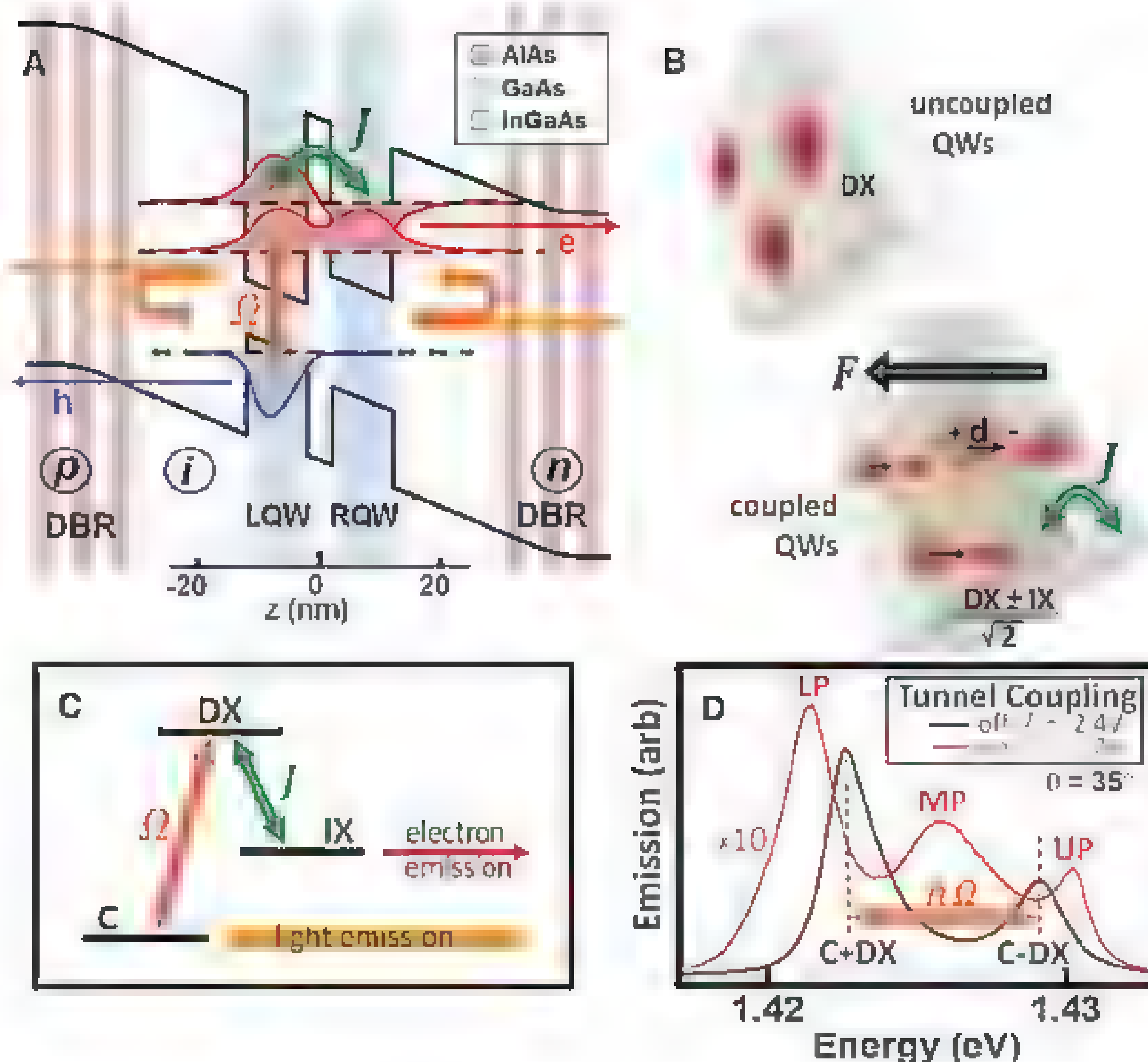
The bias dependence of the photoluminescence (PL) of a mesa with barrier width $L_B = 4$ nm (Fig. 2) clearly reveals these three dipolariton modes. Because in-plane wave vectors k are conserved, photons emitted at an angle θ directly measure dipolaritons at k . At normal incidence (Fig. 2, A and C) the narrow cavity mode is detuned below the excitons, whereas at 35° (Fig. 2, B and D) the uncoupled modes are all degenerate. For higher electric fields, the PL emission weakens because electrons escape the coupled QW system before they can recombine radiatively with a left QW hole, and eventually two of the modes vanish, leaving only the most cavity-

¹NanoPhotonics Centre, Cavendish Laboratory, University of Cambridge, Cambridge CB3 0HE, UK. ²FORTH-IESL, Post Office Box 1527, 71110 Heraklion, Crete, Greece. ³Department of Materials Science and Technology, University of Crete, Post Office Box 2208, 71003 Heraklion, Greece.

*Present address: CNRS, LAAS, 7 avenue de Colonel Roche, F-31077 Toulouse Cedex 4, France.

†To whom correspondence should be addressed. E-mail: jjb12@cam.ac.uk

Fig. 1. (A) Schematic band structure of coupled quantum wells in a microcavity at tunneling resonance. As a result of tunneling coupling J , electrons (red wave functions) extend over both wells while holes (blue) are confined in the LQW. Strong optical coupling to cavity photons Ω gives rise to dipolaritons. DBR, distributed Bragg reflector. (B) Conventional in-plane excitons (top) acquire a static out-of-plane dipole moment at resonance (bottom). (C) Three-level Λ -scheme coupling cavity C and direct (DX) and indirect (IX) exciton modes by classical intense laser pump Ω and quantum tunneling J . (D) Spectra of standard polaritons (black) and dipolaritons (red) tuned with bias.



like dipolariton. A simple harmonic oscillator model coupling the modes $\{|IX\rangle, |DX\rangle, |C\rangle\}$ gives a deeper understanding of these dipolaritons. The Hamiltonian H is

$$H = \hbar \begin{pmatrix} \omega_{IX} & J/2 & 0 \\ J/2 & \omega_{DX} & \Omega/2 \\ 0 & \Omega/2 & \omega_C \end{pmatrix} \quad (1)$$

where $|DX\rangle$ couples to both $|IX\rangle$ and $|C\rangle$, whereas there is no direct interaction between $|IX\rangle$ and $|C\rangle$ (Fig. 1C) (16). Independent control over all parameters in this model is practical: Angle tuning shifts the cavity frequency, bias voltage tunes both the IX level (directly) and the DX level (as a result of the quantum confined Stark effect), the barrier width sets the intrinsic tunneling rate J , and Ω is set by the microcavity design and geometry. Diagonalization of H yields the three dipolariton modes $|LP\rangle$, $|MP\rangle$, and $|UP\rangle$, which provide an excellent account of the PL (Fig. 2, A and B, and Fig. 3A, solid lines, with uncoupled modes dashed)

At normal incidence (Fig. 2, A and C), the cavity mode is detuned 10 meV below the excitons and hence is effectively decoupled from the excitons. The weak exciton PL nonetheless directly resolves their tunnel splitting $\hbar J$ at the anticrossing bias $U = 3.2$ V (Fig. 3D, black curve). This situation changes at high angle (Fig. 2, B and D), where the cavity mode is resonant with both the direct and indirect exciton transition. For low bias voltage, IX is far detuned and

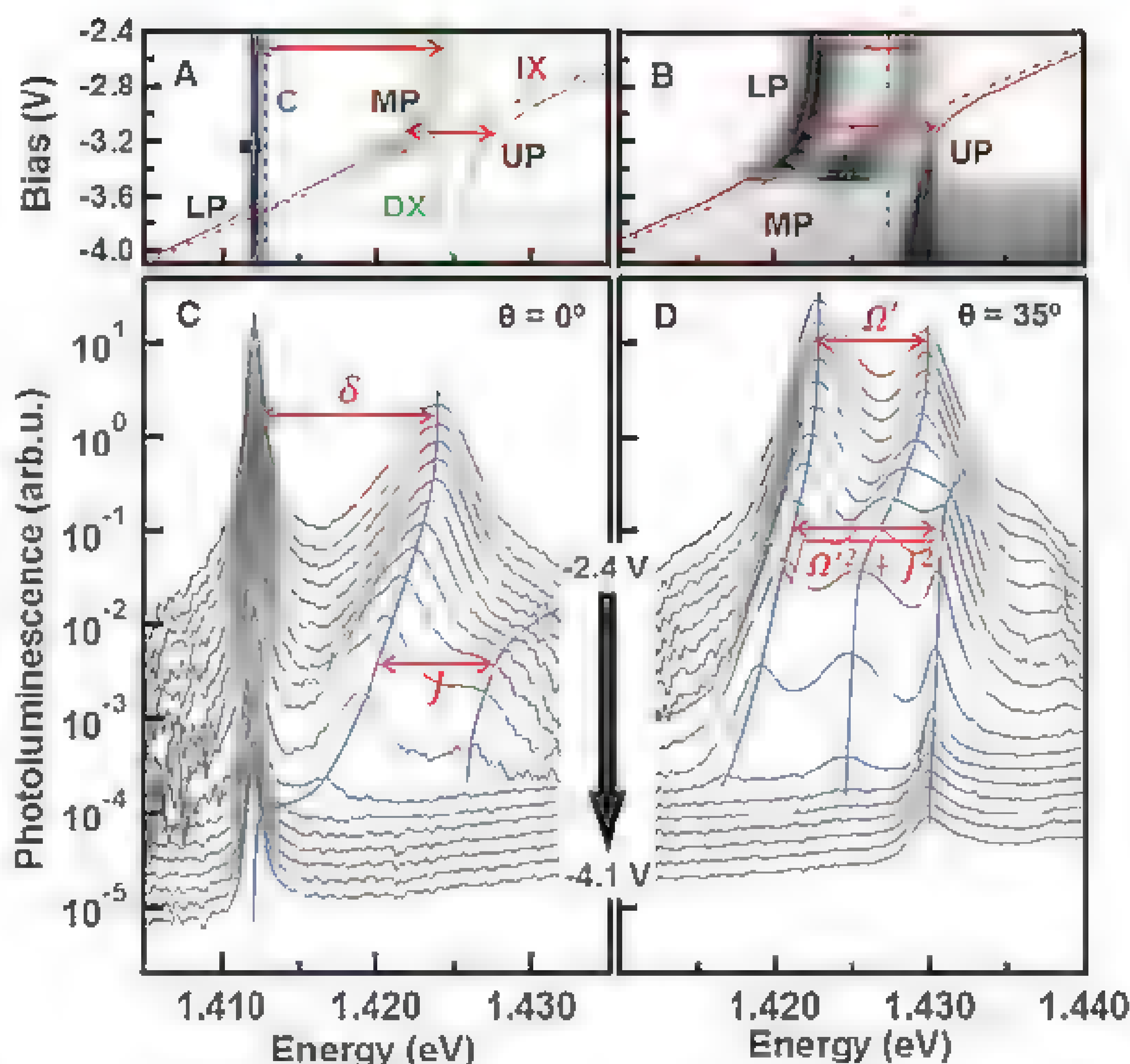


Fig. 2. (A to D) Normalized PL spectra with bias voltage for the off-resonant cavity [(A) and (C)] and close to resonance [(B) and (D)] for a mesa with $L_B = 4$ nm. Polaron lines LP, MP and UP in (A) and (B) are fits to the coupled oscillator model of Eq. 1; dashed lines show the uncoupled modes: cavity (C, blue), direct (DX, green), and indirect (IX, red) excitons. In (C) and (D) the spectra are shifted for clarity; blue lines are guides to the eye.

the system behaves as a single-QW microcavity with direct excitons only, producing detuned Rabi splitting $\Omega' = \sqrt{\Omega^2 + \delta^2}$, where $\delta(U, \theta)$ is the detuning of DX below C at each bias and angle. Simultaneous resonance of DX, IX, and the cavity mode is reached again at $U = -3.2$ V and appears as three clearly distinct dipolariton branches spanned by an anticrossing of width $S = \sqrt{\Omega'^2 + J^2}$. The eigenvectors at resonance (when $\omega_C = \omega_{IX} = \omega_{DX} + \delta$) are

$$|MP\rangle = \alpha\{|C\rangle + |IX\rangle - J|DX\rangle\} \quad (2)$$

$$\begin{pmatrix} |UP\rangle \\ |LP\rangle \end{pmatrix} = \beta\{J|IX\rangle + \Omega|C\rangle - (\delta + S)|DX\rangle\} \quad (3)$$

Remarkably, although the central MP has no DX admixture at resonance (independent of the detuning δ), it is clearly visible in emission through the tunneling interaction with the cavity photon (and is almost as strong as the other dipolaritons). The absence of DX in the MP arises from the destructive interference of transition amplitudes, as seen in Fig. 3B, which shows the composition of each of the dipolariton modes versus bias, extracted from the coupled oscillator model of Fig. 3A. With increasing field, the MP turns from an ordinary DX polariton to a pure dipolariton at resonance (black arrow), consisting only of $|IX\rangle$ and $|C\rangle$ (Eq. 2), with the electron and hole located in different QWs and possessing a static dipole moment oriented perpendicularly to the QW plane (Fig. 1B).

In atomic physics, this state is known as a dark polariton (14, 15) and is used for electromagnetically induced transparency (EIT) (17) in atomic media or waveguides (18), for drastic slowing of light propagation (19), and for light storage (20, 21). The MP dipolariton differs from atomic dark polaritons in that the role of the second probe laser in the Λ -scheme is now taken by the bias-controlled electron tunneling transition. Applying EIT to a condensed dipolariton population could thus map photonic states onto electron tunneling states that can be read out in charge transport. This suggests new strategies for quantum readout and optical interconnects—for example, as a variable pulse delay element in dipolariton signal processing. Furthermore, interactions between dipolaritons with vertically aligned dipole moments are much stronger (by a factor of 100) than for typical dipole-dipole scattering between in-plane excitons (22) and resemble an ensemble of Rydberg atoms in an electric field (23). The stronger repulsion of dipolaritons over conventional polaritons leads to increased stimulated scattering rates, and hence lower condensation thresholds (22). We suggest that this is a fruitful approach to accessing room-temperature polariton condensates.

The bare tunneling rate J controls the coupling between the two exciton modes and is set by the width and height of the barrier between the QWs. To test the tunnel control of dipolaritons, we fabricated devices with barrier widths of 4 nm, 7 nm, and 20 nm. Emission PL

measurements (Fig. 3A and fig. S2) confirm the dependence of strong coupling dipolariton modes on this tunneling rate. Extracting the polariton Rabi splittings from each sample gives $\hbar\Omega = 6.0$ meV, whereas the tunnel splitting varies from $\hbar J = 0$ to 6 meV (Fig. 3A, inset), which proves that small tunneling barriers L_B are required to see dipolaritons. The tunnel splitting J exactly matches (Fig. 3A, line in inset) that from parameter-free solutions of the Schrödinger equation for this asymmetric double QW with electric field (13), showing the expected exponential decrease in splitting with increased barrier width. The excellent fits confirm the simple explanatory power of this model for the observed modes.

Resonant dipolariton systems offer new ways to control tunneling. When Rabi flopping is faster than tunneling ($J < \Omega$), the dipolariton spends half of the time rapidly oscillating between a cavity photon and a DX (Fig. 3C). Because the excitation is not available for tunneling when it is a cavity photon, this results in a reduced effective tunneling rate $J_{\text{eff}} = J/\sqrt{2}$. On the other hand, in the fast tunneling limit $J > \Omega$, the electron is only in the left QW for half the time, which reduces the coupling to the cavity photon and hence

reduces the effective Rabi splitting. Thus, modifying the admixture of C and DX in the MP allows optical control of the tunneling process: Optical and electrical detunings determine the amount of time the electron spends shuttling between the left and right QWs or Rabi flopping on the DX transition. The anticrossings in the energy dispersion of LP-MP and MP-UP (figs. S4 and S5) quantify this effective tunneling rate J_{eff} , depending on J , Ω , and detunings between the modes.

Such polariton mesas can be sensitively switched (fig. S3), toggling between the regimes of conventional polaritons and of strongly tunnel-coupled dipolaritons with a small change in bias voltage U (Fig. 1D) or in cavity angle θ (Fig. 3D). Furthermore, electrical manipulation of the coupling of the dipolariton static dipole moment to light is possible (fig. S4D).

The observation and control of dipolaritons in these electrical devices opens up interesting regimes for quantum optoelectronics, combining quantum tunneling with light-matter coupling. The full control of the modes in this system (with bias voltage tuning and angle tuning), together with the enhancement of dipolariton repulsion relative to conventional microcavity polaritons,

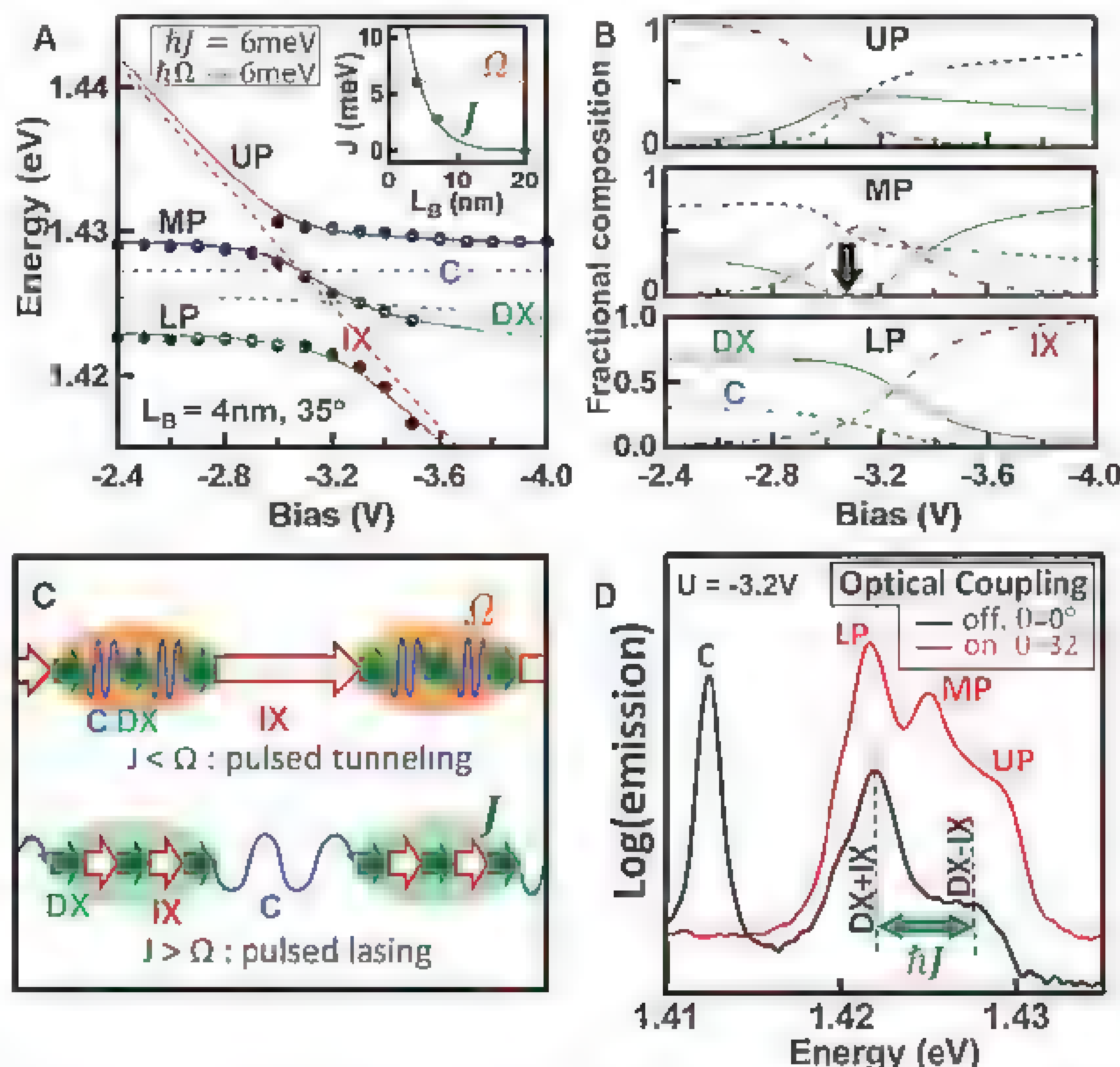


Fig. 3. (A) Bias-dependent polariton modes observed in photoluminescence for $L_B = 4$ nm with fits to the coupled oscillator model of Eq. 1. Inset: Extracted intrinsic tunneling rate J as a function of the barrier width (points) together with theory (line). (B) Bias dependence of the polariton composition; black arrow for MP marks position of the pure dipolariton of Eq. 2. (C) For $J < \Omega$, tunneling is suppressed; for $J > \Omega$, the Rabi frequency is reduced. (D) Optical control of the dipolariton regime by changing from red-detuned cavity (black) to resonance (red) through angle tuning

implies that they are strong candidates for high-temperature condensates with tunable interactions. The pure dipolariton EIT state, consisting only of cavity and indirect exciton components, offers a transition scheme amenable to building coherence between light and matter states, and thereby directly applicable to novel adiabatic photon-to-electron transfer.

References and Notes

1. J. Kasprzak *et al.*, *Nature* **443**, 409 (2006).
2. S. Christopoulos *et al.*, *Phys. Rev. Lett.* **98**, 126405 (2007).
3. R. Balili, V. Hartwell, D. Snoke, L. Pfeiffer, K. West, *Science* **316**, 1007 (2007).
4. K. G. Lagoudakis, B. Pietka, M. Wouters, R. André, B. Deveaud-Fledran, *Phys. Rev. Lett.* **105**, 120403 (2010).
5. A. Amo *et al.*, *Nature* **457**, 291 (2009).
6. F. Capasso, *Science* **235**, 172 (1987).
7. S. I. Tsintzos, N. T. Pelekanos, G. Konstantinidis, Z. Hazopoulos, P. G. Savvidis, *Nature* **453**, 372 (2008).
8. Z. Voros, D. W. Snoke, L. Pfeiffer, K. West, *Phys. Rev. Lett.* **103**, 016403 (2009).
9. A. A. High, E. E. Novitskaya, L. V. Butov, M. Hanson, A. C. Gossard, *Science* **321**, 229 (2008).
10. G. Schinner *et al.*, *Phys. Rev. B* **83**, 165308 (2011).
11. M. Poggio *et al.*, *Phys. Rev. B* **70**, 121305 (2004).
12. G. Christmann *et al.*, *Phys. Rev. B* **82**, 113308 (2010).
13. G. Christmann *et al.*, *Appl. Phys. Lett.* **98**, 081111 (2011).
14. M. Fleischhauer, M. D. Lukin, *Phys. Rev. Lett.* **84**, 5094 (2000).
15. M. D. Lukin, S. F. Yelin, M. Fleischhauer, *Phys. Rev. Lett.* **84**, 4232 (2000).
16. The minimal splitting between LP and MP in Fig. 2A illustrates the absence of direct coupling between IX and C, justifying $H_{13} = H_{31} = 0$ in Eq. 1.
17. M. Mücke *et al.*, *Nature* **465**, 755 (2010).
18. M. F. Yanik, W. Suh, Z. Wang, S. Fan, *Phys. Rev. Lett.* **93**, 233903 (2004).
19. M. D. Lukin, A. Imamoglu, *Nature* **413**, 273 (2001).
20. D. F. Phillips, A. Fleischhauer, A. Mair, R. L. Walsworth, M. D. Lukin, *Phys. Rev. Lett.* **86**, 783 (2001).
21. C. Liu, Z. Dutton, C. H. Behroozi, L. V. Hau, *Nature* **409**, 490 (2001).
22. A. Filinov, N. V. Prokof'ev, M. Bonitz, *Phys. Rev. Lett.* **105**, 070401 (2010).
23. D. Møller, L. B. Madsen, K. Mølmer, *Phys. Rev. Lett.* **100**, 170504 (2008).

Acknowledgments: Supported by UK Engineering and Physical Sciences Research Council grants EP/G060649/1 and EP/F011393, European Union grants CLERMONT4 PITNGA-2009-235114 and NDEX FP7 2011-289968, and the POLATOM European Science Foundation Research Network Programme

Supporting Online Material

www.sciencemag.org/cgi/content/full/1219010/DC1
Materials and Methods
Figs. S1 to S5
Reference (24)

11 January 2012, accepted 20 March 2012

Published online 5 April 2012

10.1126/science.1219010

Under the Hood of the Earthquake Machine: Toward Predictive Modeling of the Seismic Cycle

Sylvain Barbot,^{1*} Nadia Lapusta,^{1,2} Jean-Philippe Avouac¹

Advances in observational, laboratory, and modeling techniques open the way to the development of physical models of the seismic cycle with potentially predictive power. To explore that possibility, we developed an integrative and fully dynamic model of the Parkfield segment of the San Andreas Fault. The model succeeds in reproducing a realistic earthquake sequence of irregular moment magnitude (M_w) 6.0 main shocks—including events similar to the ones in 1966 and 2004—and provides an excellent match for the detailed interseismic, coseismic, and postseismic observations collected along this fault during the most recent earthquake cycle. Such calibrated physical models provide new ways to assess seismic hazards and forecast seismicity response to perturbations of natural or anthropogenic origins.

Seismic and geodetic observations provide an increasingly detailed insight into fault motion over a wide range of temporal and spatial scales, from rapid seismic rupture to slower postseismic slip and complex interseismic behavior, including slow episodes of accelerating slip and tremor (1–5). Laboratory experiments and theoretical developments (6–13) provide an increasingly detailed physical basis for understanding the entire earthquake cycle. Yet, models capable of capturing a wide range of observations are still in their infancy. Existing models are either restricted to specific aspects of fault behavior (e.g., progression of a single dynamic rupture or evolution of postseismic slip) or simplify some stages of the fault deformation (14–20). Recently developed numerical methods (21–23) allow us to resolve, in one physical model, slow tectonic loading, earthquake nucleation, and

rupture propagation—including the radiation of seismic waves—and the afterslip transient that follows main shocks, but so far these methods have been applied to qualitative studies of conceptual fault scenarios (24).

We have developed a fully dynamic model of the earthquake cycle capable of quantitatively reproducing a wide range of observations for the Parkfield segment of the San Andreas Fault (SAF) (Fig. 1). The Parkfield sequence of moment magnitude (M_w) 6.0 events, their inferred similarities, and their short recurrence times inspired one of the most famous prediction experiments and prompted the installation of modern seismic and geodetic networks (25, 26). The latest rupture of 2004 defied the expectations by taking place a decade later than anticipated and initiating on the opposite end of the segment compared with previous events (27). Interestingly, a series of smaller earthquakes occurred in 1993 around the location where the 1966 event had nucleated (Fig. 1), but they failed to generate the M_w 6.0 event that was expected at the time (1). Due to the dense instrumentation networks and other observational facilities, such as the San Andreas Fault Observatory at Depth

(13), installed to monitor the Parkfield segment, the pattern of strain buildup, microseismic activity in the interseismic period, as well as co- and postseismic deformation related to the 2004 earthquake cycle, have been relatively well constrained (27–31).

Our dynamic model of the earthquake cycles at Parkfield is constrained by multiple sets of observations and previous theoretical findings. We use the spatial pattern of microseismicity, the time series of Global Positioning System (GPS) displacements in the 1999 to 2010 period, the interferometric synthetic aperture radar (InSAR) data, and the GPS offsets of the 2004 earthquake (2, 4, 19, 29, 32). We also consider the slip distribution of the 1966 event and the historical catalog of recurrence times and hypocenter locations of M_w 6.0 events (25). As an integration device for all observations, we adopt a strike-slip fault segment embedded into an elastic medium, loaded by a deep-seated slip at the long-term slip rate, and governed by rate- and state friction, a well-established empirical constitutive law for fault strength (6–8, 10). The area with rate-weakening friction, where seismic slip can nucleate, is bounded to the north and south by rate-strengthening patches. The northern rate-strengthening patch accounts for the creeping segment of the SAF. The southern one is more speculative; it serves as a possible proxy for the kind of barrier effect needed to account for the repetition of similar events arresting in that area and for an as-yet-unknown source of localized stressing (33).

The model results in a rich history of fault slip with spontaneous nucleation and ruptures of earthquakes of magnitudes ranging from M_w 2.0 to 6.0 (Fig. 2 and movie S1). The simulated M_w 6.0 earthquake cycles reproduce co-, post-, and interseismic behavior of the Parkfield segment, with most coseismic slip occurring in the area circumscribed by microseismicity. The simulated sequence of earthquakes includes the nucleation of a rupture near the hypocenter of the

¹Division of Geological and Planetary Sciences, California Institute of Technology, 1200 East California Boulevard, Pasadena, CA 91125, USA. ²Division of Engineering and Applied Sciences, California Institute of Technology, 1200 East California Boulevard, Pasadena, CA 91125, USA.

*To whom correspondence should be addressed. E-mail: sbarbot@caltech.edu

Fig. 1. (A) Tectonic setting and seismic cycle at Parkfield. The SAF accommodates most of the relative motion between the Pacific (PAC) and North-American (N-AM) plates in central California and produces localized microseismicity (black dots). Deformation during the co-, post-, and interseismic periods is monitored by various arrays of instruments, including GPS (black triangles and pre-2004 velocity vectors) and broad-band seismometers (gray squares). (B) Spatial distribution of fault slip and microseismicity on the SAF during the earthquake cycle. Aseismic creep occurs above and below the SZ. The area between the microseismic streaks is coupled. The coseismic slip distribution of the 2004 main shock (20-cm red contours) may be concentrated in the domain circumscribed by background seismicity. (C) Paleoseismic cycle of the largest earthquakes since 1881 (with interevent times between 12 and 38 years). Smaller events occurred in 1992 to 1994, culminating with the November 1993 M_w 4.6 and the December 1994 M_w 4.7 earthquakes.

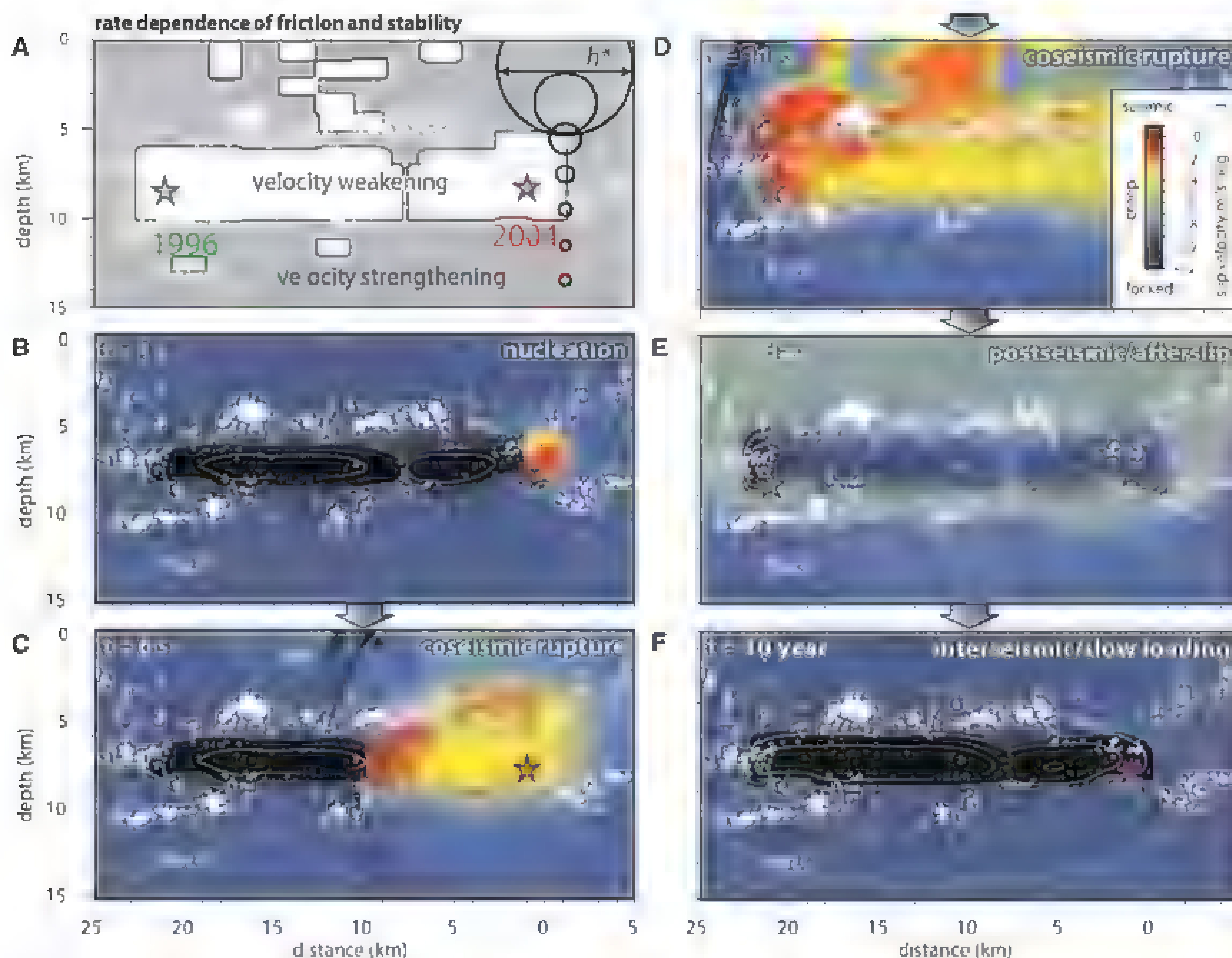
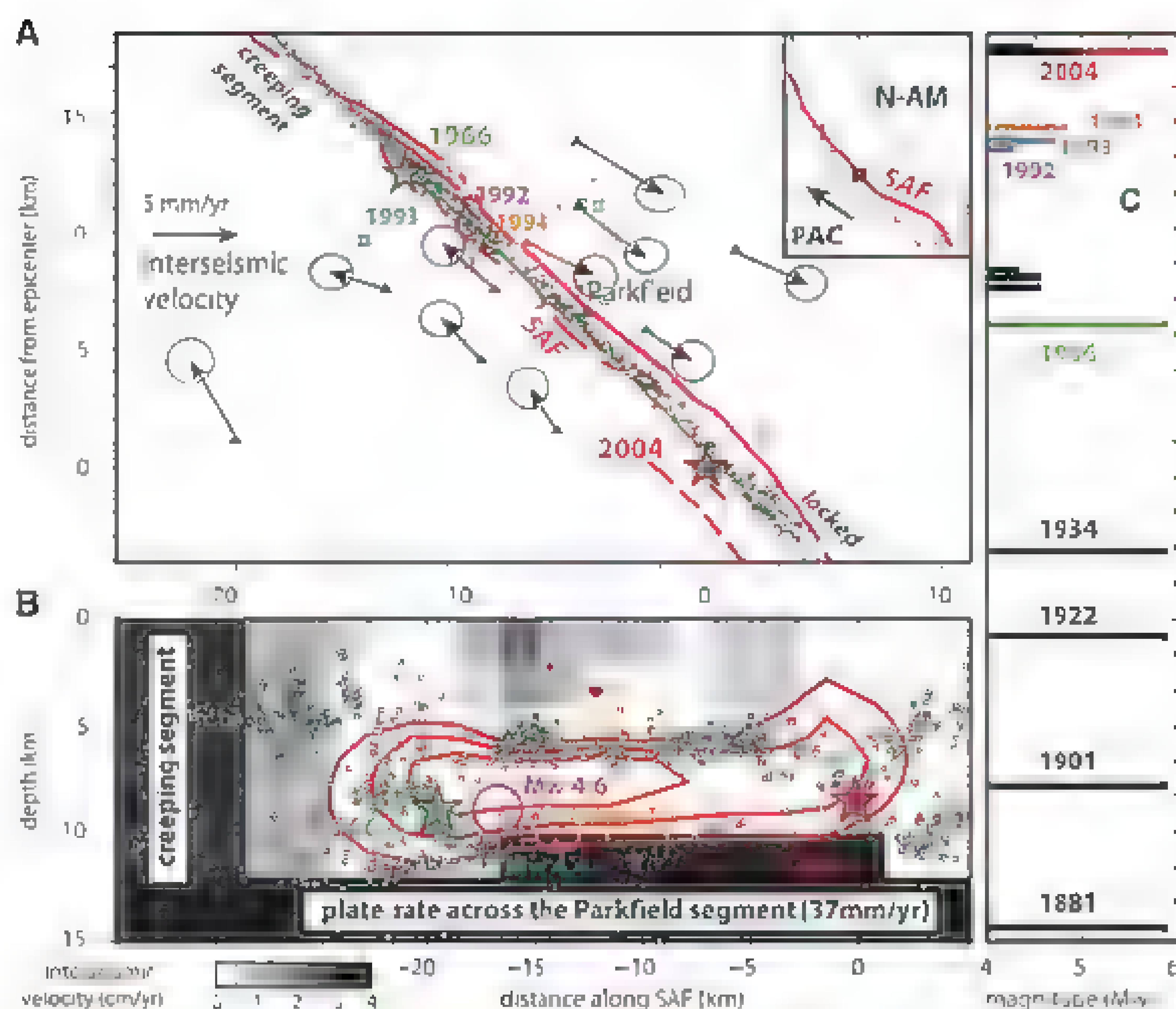


Fig. 2. Model that reproduces the entire seismic cycle at Parkfield. (A) Spatial distribution of rate-weakening (white) and rate-strengthening (gray) friction properties ($a - b$), with rate-weakening values in the SZ delineated by the background seismicity, a few shallow patches required to explain near-field GPS data, and two deeper patches included for illustration purposes. The critical size h^* for unstable slip is shown in black circles (see supplementary text). (B to F) Snapshots of a M_w 6.0 seismic

cycle with rupture nucleating spontaneously to the south near the Parkfield 2004 earthquake hypocenter (B), propagating to the north and rupturing the entire SZ [(C) and (D)], and followed by a slow postseismic transient (E), with interseismic loading of the partially locked SZ (F). Another M_w 6.0 event nucleates 20 years later. Zero time is chosen for plotting convenience. The solid gray profiles indicate the contours of the cumulative slip at 0.1-m intervals.

2004 M_w 6.0 event (Fig. 2B). The rupture propagates northward, slows down in the vicinity of the velocity-strengthening obstacle (Fig. 2C), and proceeds to rupture the entire seismogenic zone (SZ), arresting at the creeping segment (Fig. 2D), similarly to what occurred during the 2004 event. The resulting seismic moment corresponds to a M_w 6.0 earthquake. During the rupture, the shallow asperities slip with aseismic sliding velocity below 0.1 m/s. After the coseismic rupture, the SZ becomes locked, and afterslip expands around it (Fig. 2E). The after-

slip slows down with time, eventually leading to the pattern of the locked SZ surrounded by interseismic creep (Fig. 2F). During the interseismic period, creep penetrates into the SZ, building conditions for earthquake nucleation. Eventually, the cycle repeats, with a mean recurrence time of ~ 20 years.

Our model explains the longer-term behavior of the earthquake cycle at Parkfield. Some of the events produced offer an excellent fit to the coseismic and the postseismic displacements measured at the GPS stations, indicating an adequate

representation of faulting over a range of time scales (Fig. 3 and fig. S3). It also qualitatively reproduces the switch in the hypocenter location from earthquakes nucleating at the northern end to earthquakes nucleating at the southern end, as occurred in 2004 at Parkfield (Fig. 4). The southern and northern corners of the SZ are favorable nucleation sites because of their location near local stress concentrations due to both horizontal and vertical boundaries between domains of stable and unstable sliding. The domain with stable sliding at the northern end of the SZ is clearly seen in geodetic inversions; no equivalent domain is observed to the south (Fig. 1B). It is possible that there is a local zone of creep not resolvable with the data used in these inversions but sufficient to induce a local reloading, at least in the early postseismic period. In our model, the transition between the two nucleation sites occurs after a few smaller earthquakes (M_w 2.0 to 4.0) that can be interpreted as tailed nucleation attempts of the main event. The transition in nucleation location is coincidental with the longest simulated recurrence time ($T_r^{\max} = 23.1$ years, compared with the smallest, $T_r^{\min} = 15$ years) of the sequence (Fig. 4 and movie S2).

In view of these results, the delay of the latest M_w 6.0 2004 event at Parkfield and its unexpected change of hypocenter may have been at least partially caused by the smaller earthquakes in 1992 to 1994, a series of arrested M_w 6.0 nucleations. On 20 October 1992, close to the expected time of a M_w 6.0 earthquake, a M_w 4.6 event occurred near the 1966 hypocenter (33) as a part of an accelerated slip episode between 1992 and 1994 (1). The M_w 4.6 event failed to grow to a M_w 6.0 event, indicating that the surrounding area was not yet ready to sustain rupture propagation due to cycle-to-cycle variations inherent in such a nonlinear system, outside perturbations, or finer-scale heterogeneity. The stress drop associated with the M_w 4.6 event may have prevented nucleation of the next M_w 6.0 event in that area.

Our results indicate that the Parkfield anomalies in the earthquake cycle can at least partially result from a spontaneous behavior of rate-and-state faults after a complex sequence of smaller interseismic events. The model succeeds in producing returning M_w 6.0 events irregularly spaced in time, which we attribute to stress redistributions induced by smaller events. However, the distribution of the recurrence time in our simulation, between 15 and 25 years, is not as wide as the observed variability at Parkfield (fig. S4). Reproducing the full spread of recurrence times since 1881 may require taking into account additional aspects of fault dynamics, including stress transfers from remote earthquakes and their postseismic transient, the effect of deeper crustal processes (5, 34), or more sophisticated friction laws (11, 12). Representing coseismic fault behavior by the standard rate-and-state formulation with rate weakening is an effective but simplified approach, akin to the typical practice

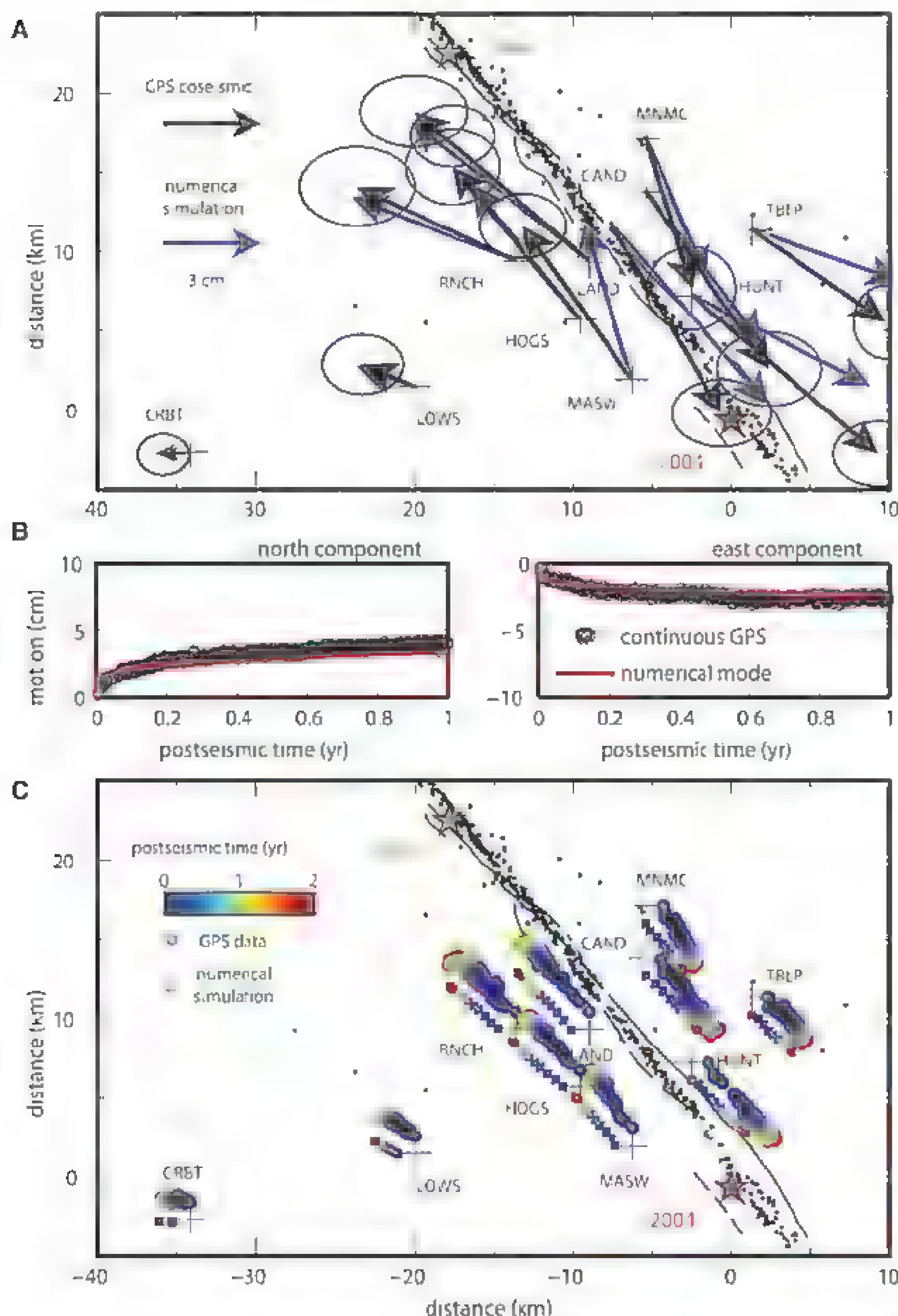


Fig. 3. (A) Comparison between the observed surface displacements of the 2004 M_w 6.0 Parkfield earthquake and those predicted by our numerical simulation. (B) Sample time series of postseismic displacements during a 1-year period after the earthquake: GPS time series at station MASW (black dots) and numerical simulations (red solid line). (C) Map view of postseismic transients in a 2-year period at the Southern California Integrated GPS Network stations: GPS data (circles) and model (squares).

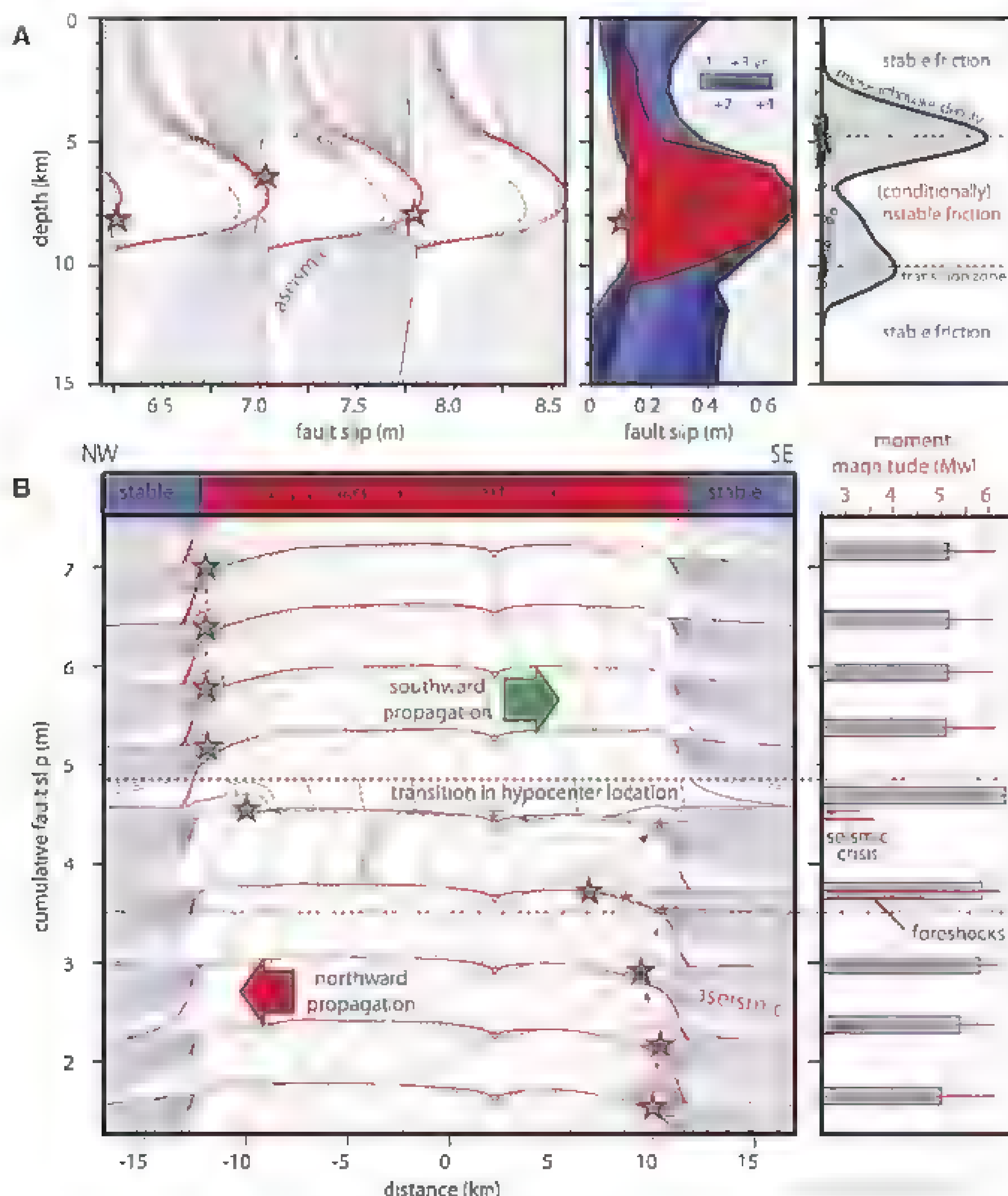


Fig. 4. Comparison between modeled and inferred slip history at Parkfield. **(A)** Depth profiles in the middle of the SZ comparing the modeled history of fault slip for three events to the one inferred from our inversion of InSAR and GPS data in the period 1999 to 2010. The red stars indicate the location of hypocenters. The seismicity concentrates around the area of maximum coseismic slip. **(B)** Horizontal profiles in the middle of SZ, at 7.5-km depth, showing a series of 11 simulated ruptures. The series captures a complex transition of hypocenter location from one side of the SZ to another, punctuated by foreshocks and a seismic crisis consisting of M_w 2.0 to 4.0 earthquakes and giving rise to the longest recurrence time of a M_w 6.0 quake. The red dashed profiles represent cumulative coseismic slip at 1-s intervals; the blue solid profiles are cumulative aseismic slip at 1-year intervals taking place during the post- and interseismic periods.

of using linear slip weakening laws to simulate dynamic rupture (15, 17).

The presented study demonstrates the possibility of creating comprehensive physical models of fault zones that integrate geodetic and seismological observations for all stages of the earthquake cycle. As computational resources and methods improve, more realistic fully dynamic simulations will be able to incorporate near-fault damage, local fault nonplanarity, and additional coseismic weakening mechanisms. Such simulations could in principle be used to assess the full range of earthquake patterns that a particular fault system might produce or to

assimilate observation about past earthquakes and interseismic loading to assess future seismicity (20). The resulting region-specific models may then reveal how the entire earthquake cycle is affected by various additional factors, such as static and/or dynamic triggering and human intervention in the form of geothermal energy harvesting and CO_2 sequestration.

References and Notes

1. R. M. Nadeau, T. V. McEvilly, *Science* **285**, 718 (1999).
2. F. Waldhauser, W. L. Ellsworth, D. P. Schaff, A. Cole, *Geophys. Res. Lett.* **31**, L18608 (2004).
3. A. O. Konca *et al.*, *Nature* **456**, 631 (2008).
4. Z. Peng, P. Zhao, *Nature Geosci.* **2**, 877 (2009).

5. D. R. Shelly, *Nature* **463**, 648 (2010).
6. T. H. Dettner, *J. Geophys. Res.* **84**, 2161 (1979).
7. A. Ruina, *J. Geophys. Res.* **88**, 10359 (1983).
8. T. E. Tullis, *Proc. Natl. Acad. Sci. U.S.A.* **93**, 5803 (1996).
9. N. M. Beeler, T. E. Tullis, M. L. Blanpied, J. D. Weeks, *J. Geophys. Res.* **101**, 8697 (1996).
10. C. J. Marone, *Annu. Rev. Earth Planet. Sci.* **26**, 643 (1998).
11. J. R. Rice, *J. Geophys. Res.* **111**, B05311 (2006).
12. F. Ferri, G. D. Toro, T. Hirose, T. Shimamoto, *Terra Nova* **22**, 347 (2010).
13. D. A. Lockner, C. Morrow, D. Moore, S. Hickman, *Nature* **472**, 82 (2011).
14. Y. Ben-Zion, J. R. Rice, R. Dmowska, *J. Geophys. Res.* **98**, 2135 (1993).
15. K. B. Olsen, R. Madanaga, R. J. Archuleta, *Science* **278**, 834 (1997).
16. F. Yamashita, E. Fukuyama, K. Omura, *Science* **306**, 261 (2004).
17. S. Ma, S. Castrodio, R. J. Archuleta, P. Liu, *J. Geophys. Res.* **113**, B02301 (2008).
18. T. Hori, N. Kato, K. Hirahara, T. Baba, Y. Kaneda, *Earth Planet. Sci. Lett.* **228**, 215 (2004).
19. S. Barbot, Y. Fialko, Y. Bock, *J. Geophys. Res.* **114**, B07405 (2009).
20. J. H. Dettner, K. B. Richards-Dinger, *Pure Appl. Geophys.* **167**, 1087 (2010).
21. N. Lapusta, J. R. Rice, Y. Ben-Zion, G. Zheng, *J. Geophys. Res.* **105**, 23765 (2000).
22. N. Lapusta, Y. Liu, *J. Geophys. Res.* **114**, B09303 (2009).
23. H. Noda, N. Lapusta, *J. Geophys. Res.* **115**, B12314 (2010).
24. Y. Kaneko, J.-P. Avouac, N. Lapusta, *Nat. Geosci.* **3**, 363 (2010).
25. W. H. Bakun, A. G. Lindh, *Science* **229**, 619 (1985).
26. M. Wyss, P. Bodin, R. E. Habermann, *Nature* **345**, 426 (1990).
27. W. H. Bakun *et al.*, *Nature* **437**, 969 (2005).
28. P. Segall, Y. Du, *J. Geophys. Res.* **98**, 4527 (1993).
29. C. Thurber *et al.*, *Bull. Seismol. Soc. Am.* **96**, 538 (2006).
30. F. Brengner *et al.*, *Science* **321**, 1478 (2008).
31. T. Uchide, S. Ide, G. C. Beroza, *Geophys. Res. Lett.* **36**, L04307 (2009).
32. I. A. Johanson, E. J. Fielding, F. Rolandone, R. Bürgmann, *Bull. Seismol. Soc. Am.* **96** (4B), S269 (2006).
33. J. B. Fletcher, P. Spudich, *J. Geophys. Res.* **103**, 835 (1998).
34. L. Bruhat, S. Barbot, J. P. Avouac, *J. Geophys. Res.* **116**, B08401 (2011).
35. D. H. Oppenheimer, W. H. Bakun, A. G. Lindh, *J. Geophys. Res.* **95**, 8483 (1990).

Acknowledgments: This study was supported partly by the National Science Foundation (grant EAR 0548277 to N.L.), the Gordon and Betty Moore Foundation, and the Southern California Earthquake Center (SCEC). This is Tectonics Observatory contribution #194 and SCEC #1600. Numerical simulations for this study were carried out on the CITerra Dell cluster at the Division of Geological and Planetary Sciences of the California Institute of Technology. J.P.A. worked on this study while on sabbatical at GFZ (German Research Centre for Geosciences) Potsdam, Germany) with support from the Humboldt Foundation. GPS data used in this study are available from the Scripps Orbit and Permanent Array Center. Numerical data are available upon request to the authors.

Supplementary Materials

www.sciencemag.org/cgi/content/full/336/6082/707/DC1
Materials and Methods
Supplementary Text
Figs. S1 to S4
References (36–74)
Movies S1 and S2
Data File S1

6 January 2012, accepted 30 March 2012
10.1126/science.1218796

Carbon Isotope Constraints on the Deglacial CO₂ Rise from Ice Cores

Jochen Schmitt,^{1,2*} Robert Schneider,¹ Joachim Elsig,¹ Daiana Leuenberger,¹ Anna Lourantou,^{3†} Jérôme Chappellaz,³ Peter Köhler,² Fortunat Joos,¹ Thomas F. Stocker,¹ Markus Leuenberger,¹ Hubertus Fischer^{1,2}

The stable carbon isotope ratio of atmospheric CO₂ ($\delta^{13}\text{C}_{\text{atm}}$) is a key parameter in deciphering past carbon cycle changes. Here we present $\delta^{13}\text{C}_{\text{atm}}$ data for the past 24,000 years derived from three independent records from two Antarctic ice cores. We conclude that a pronounced 0.3 per mil decrease in $\delta^{13}\text{C}_{\text{atm}}$ during the early deglaciation can be best explained by upwelling of old, carbon-enriched waters in the Southern Ocean. Later in the deglaciation, regrowth of the terrestrial biosphere, changes in sea surface temperature, and ocean circulation governed the $\delta^{13}\text{C}_{\text{atm}}$ evolution. During the Last Glacial Maximum, $\delta^{13}\text{C}_{\text{atm}}$ and atmospheric CO₂ concentration were essentially constant, which suggests that the carbon cycle was in dynamic equilibrium and that the net transfer of carbon to the deep ocean had occurred before then.

During the past 800,000 years, atmospheric CO₂ concentrations have varied in close relation to Antarctic temperatures (1, 2) and the general waxing and waning of continental ice sheets. In particular, CO₂ rose from a stable level of 190 parts per million by volume (ppmv) during the Last Glacial Maximum to about 280 ppmv in preindustrial times, showing pronounced differences in atmospheric CO₂ rates of change in the course of the last glacial-interglacial transition (3). Many processes have been invoked in attempts to explain these CO₂ variations, but it has become evident that none of these mechanisms alone can account for the 90-ppmv increase in atmospheric CO₂. A combination of processes must have been operating (4, 5), with the sequence of events, their durations, and their amplitudes being crucial. However, a unique solution to the deglacial carbon cycle changes has not yet been found.

In this respect, high-resolution and precise $\delta^{13}\text{C}_{\text{atm}}$ records from Antarctic ice cores are needed to better constrain the evolution of carbon cycle changes during the last deglaciation. On millennial time scales, $\delta^{13}\text{C}_{\text{atm}}$ is primarily influenced by the $\delta^{13}\text{C}$ of dissolved inorganic carbon (DIC) ($\delta^{13}\text{C}_{\text{DIC}}$) and by sea surface temperature (SST), which controls the isotopic fractionation during air/sea gas exchange. The continuous rain of isotopically light organic material to the interior of the ocean draws carbon down from the surface layer to intermediate and deep waters, where the organic carbon is remineralized. Consequently, a vertical $\delta^{13}\text{C}_{\text{DIC}}$ gradient is established, controlled by the inter-

play of the ocean circulation with this so-called “biological pump.” The more intense the circulation, the smaller the gradients are for $\delta^{13}\text{C}_{\text{DIC}}$, DIC, oxygen, and nutrients. Superimposed on these marine carbon cycle processes are climate-induced changes in terrestrial biosphere carbon storage, which result in a net change in the carbon isotopic composition of the ocean-atmosphere system. On orbital time scales, weathering and sedimentation of CaCO₃ affect $\delta^{13}\text{C}_{\text{DIC}}$, $\delta^{13}\text{C}_{\text{atm}}$, and the atmospheric CO₂ concentration as well.

Until recently (6), analytical constraints represented a fundamental limitation on the utility of $\delta^{13}\text{C}_{\text{atm}}$ ice core records (7, 8). Here, we provide evidence (Fig. 1) about possible causes of carbon cycle changes with measurements of $\delta^{13}\text{C}_{\text{atm}}$ from two Antarctic ice cores—EPICA (European Project for Ice Coring in Antarctica) Dome C and Talos Dome—performed with three independent methods in two different labs (referred to as Bern sublimation, Bern cracker, and Grenoble mill data) (6, 9). One of our records is based on a novel sublimation method (10) that avoids the effects associated with incomplete gas extraction and thus yields more precise results (see supplementary materials). A stringent residual analysis of the three data sets shows virtually no offset between the two Bern data sets and only a small, systematic offset between the Bern and Grenoble data of 0.16 per mil (‰), which can be explained by a method-dependent systematic fractionation. After correction of this offset, we used an error-weighted Monte Carlo bootstrap approach to combine the three $\delta^{13}\text{C}_{\text{atm}}$ records over the past 24,000 years. This method showed that all three data sets are essentially compatible within their analytical uncertainties. Although all our conclusions are supported by the individual records, we combined all three data sets to make full use of the resolution and precision of the data. The final data set consists of 201 individual measurements, each reflecting typically two to four replicates and with an analytical 1 σ error between 0.04 and 0.12‰. Because the resulting Monte Carlo average (MCA) removes most of the analytical uncertainties, it contains less high-frequency

variability relative to the raw data. This is in line with the centennial-scale low-pass filtering inherent in the firm densification process, which gradually encloses air bubbles, finally leading to the atmospheric archive. Accordingly, the retained variability can be regarded as the signal most representative of millennial $\delta^{13}\text{C}_{\text{atm}}$ changes (see supplementary materials for details regarding the MCA and its uncertainty).

Our $\delta^{13}\text{C}_{\text{atm}}$ data are in good agreement with previously published lower-resolution records (6, 9). Our record shows a very stable level between 24,000 and ~19,000 years before present (B.P., where present is defined as 1950), with an average $\delta^{13}\text{C}_{\text{atm}}$ of -6.45‰ (tables S1 and S2), similar to the -6.35‰ of the Late Holocene (Fig. 2B). Given the fact that a large set of environmental parameters such as atmospheric CO₂, global SST, terrestrial carbon storage, and ocean circulation have varied between the LGM and the Late Holocene, almost identical $\delta^{13}\text{C}_{\text{atm}}$ values indicate that opposing effects must have offset each other (11). This becomes clear if we look at three first-order effects on $\delta^{13}\text{C}_{\text{atm}}$: A SST rise of 1 K translates into a 0.1‰ increase in $\delta^{13}\text{C}_{\text{atm}}$, due to temperature-dependent fractionation between atmospheric CO₂ and marine DIC species (12). The assumption of a global LGM-to-Holocene SST rise of 3 K would result in about 0.3‰ higher $\delta^{13}\text{C}_{\text{atm}}$ for the Holocene, provided that SST distribution and CO₂ gross flux exchange patterns remained constant. This effect is further augmented by the uptake of isotopically light carbon by the land biosphere and is counterbalanced by the smaller vertical gradient in $\delta^{13}\text{C}_{\text{DIC}}$ in the Holocene ocean, supported by marine data (13). The fact that both $\delta^{13}\text{C}_{\text{atm}}$ and CO₂ show little variation from 24,000 to 19,000 years B.P. points to the carbon cycle being essentially in dynamic equilibrium at that time. As can also be seen in Fig. 2, the climate variations related to Heinrich stadial 2 (HS2) and Dansgaard-Oeschger event 2 (DO2) had little effect on the global carbon cycle during this time interval. However, given the opposing trends for reconstructed atmospheric $\Delta^{14}\text{C}$ ($\Delta^{14}\text{C}_{\text{atm}}$) (14, 15) and the expected $\Delta^{14}\text{C}_{\text{atm}}$ evolution (16) based on variations in ¹⁴C production rate (17, 18), the global ¹⁴C budget was not balanced (Fig. 2A).

After a very small increase in $\delta^{13}\text{C}_{\text{atm}}$ at the very end of the glacial, a sharp drop in $\delta^{13}\text{C}_{\text{atm}}$ starting at 17,500 years B.P. parallels the onset of increasing atmospheric CO₂. Taken at face value, the small local maximum would point to an early SST rise that preceded the onset of the CO₂ increase. When we apply a crude SST correction to our $\delta^{13}\text{C}_{\text{atm}}$ data, on the basis of a global estimate of SST temperature changes during the transition (see supplementary materials), this $\delta^{13}\text{C}_{\text{atm}}$ increase vanishes (Fig. 2B). Note, however, that this 0.06‰ excursion is within the uncertainties of our data and that other effects could also lead to this small enrichment in $\delta^{13}\text{C}_{\text{atm}}$. The 0.3‰ drop in $\delta^{13}\text{C}_{\text{atm}}$ after the onset of the transition at 17,500 years B.P. is accompanied by

¹Climate and Environmental Physics, Physics Institute, and Oeschger Centre for Climate Change Research, University of Bern, CH-3012 Bern, Switzerland. ²Alfred Wegener Institute for Polar and Marine Research, 27570 Bremerhaven, Germany. ³UIF-Grenoble 1/CNRS, Laboratoire de Glaciologie et Géophysique de l'Environnement (LGGE) UMR 5183, 38041 Grenoble, France.

*To whom correspondence should be addressed. E-mail: schmitt@climate.unibe.ch

†Present address: Laboratoire d'Océanographie et du Climat (LOCEAN), Institut Pierre Simon Laplace, Université P. et M. Curie, 75005 Paris, France

a CO_2 increase of about 35 ppmv and a 19‰ drop in $\Delta^{14}\text{C}_{\text{atm}}$ (19), which has been attributed to a release of old carbon from the deep ocean. This coeval drop in $\delta^{13}\text{C}_{\text{atm}}$ and $\Delta^{14}\text{C}_{\text{atm}}$ during the so-called “mystery interval,” 17,500 to 14,000 years B.P. (19), is arguably the most enigmatic carbon cycle change in the course of the transition (see below).

After the broad $\delta^{13}\text{C}_{\text{atm}}$ minimum is reached at about 16,000 years B.P., $\delta^{13}\text{C}_{\text{atm}}$ increases slightly by 0.1‰ during the pronounced Bolling-Allerod warming. Other than circulation changes in the Southern Ocean (20), the regrowth of the terrestrial biosphere in the northern hemisphere could contribute to this increase in $\delta^{13}\text{C}_{\text{atm}}$ (4). However, because the SST-corrected $\delta^{13}\text{C}$ evolution (Fig. 2B) does not show any increase, a robust process attribution requires precisely dated SST reconstructions and transient carbon cycle modeling.

An almost linear rise by 0.06‰ per 1000 years follows the second $\delta^{13}\text{C}_{\text{atm}}$ minimum at 12,200 years B.P., leading to maximum values of -6.33‰ at around 6000 years B.P. This rise might be largely explained by the continuing regrowth of the terrestrial biosphere (21), in concert with smaller contributions from SST warming and changes in circulation and export production (9, 22). From this mid-Holocene maximum, $\delta^{13}\text{C}_{\text{atm}}$ values decline slightly to

reach values of -6.35‰ at 500 years B.P., as previously reported (6).

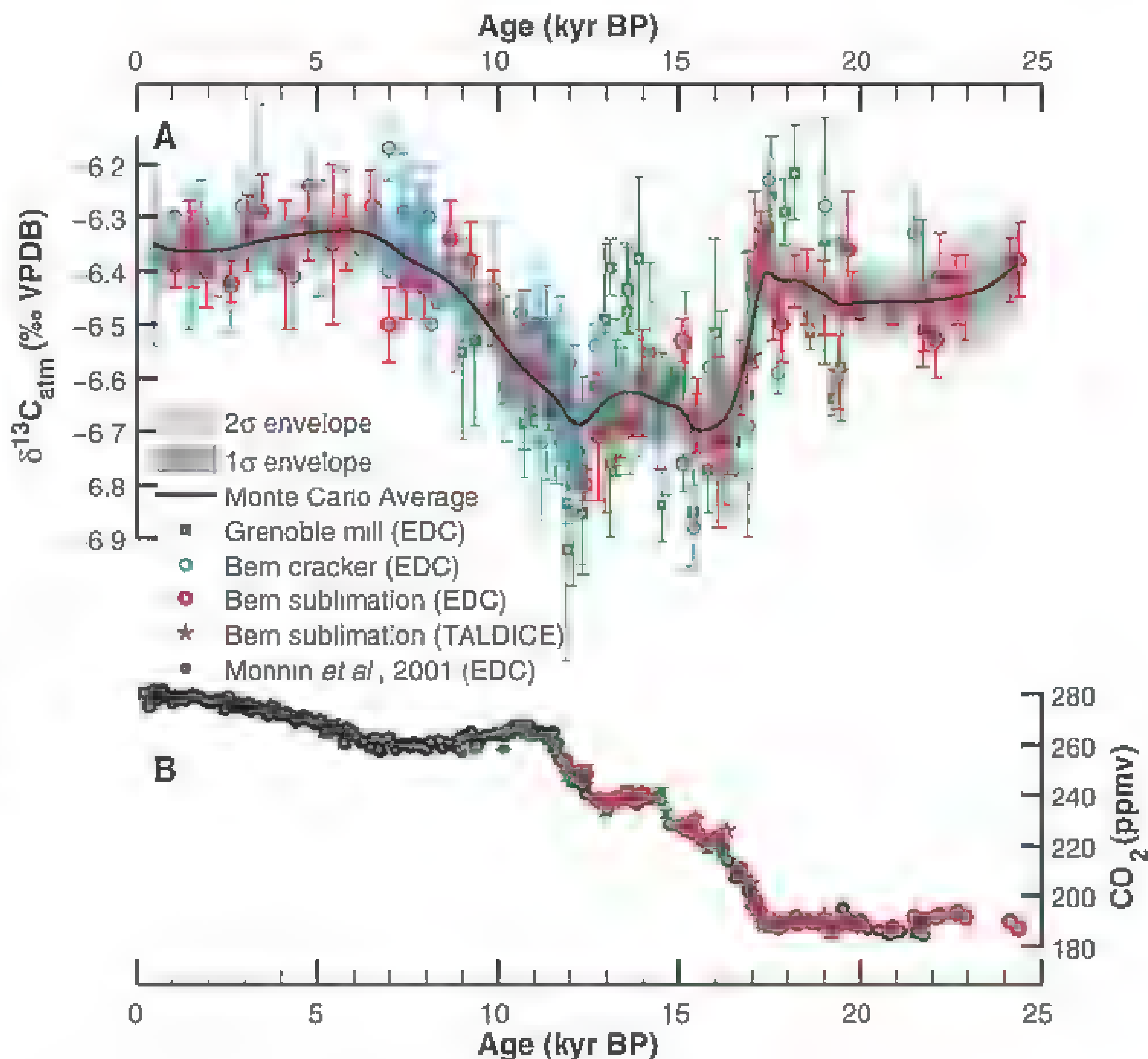
As mentioned above, the carbon cycle changes during the mystery interval have been a matter of intense debate (19, 20, 23). Our high-resolution $\delta^{13}\text{C}_{\text{atm}}$ record, together with other records of carbon cycle changes and insights from models, may help to constrain hypotheses put forward to explain the mystery interval. The rise in CO_2 and the decline in $\delta^{13}\text{C}_{\text{atm}}$ and $\Delta^{14}\text{C}_{\text{atm}}$ between 17,000 and 15,000 years B.P. fit the concept of bringing DIC-rich waters with old carbon into exchange with the atmosphere. Indicative ^{14}C signals of upwelling of old, CO_2 -enriched deep water were found in Pacific intermediate waters (24), but other studies (23) ruled out such old water in the northeast Pacific, and evidence for a ^{14}C -depleted glacial deep ocean remains elusive (19, 23, 25). These $\Delta^{14}\text{C}$ studies were usually confronted with variable reservoir age between benthic and planktonic foraminifera. A study using deep sea corals now circumvents this problem by applying absolute U-Th dating and shows that the deep glacial Southern Ocean indeed ventilated its ^{14}C -depleted reservoir during the mystery interval (26).

The constant $\delta^{13}\text{C}_{\text{atm}}$ values during the late glacial indicate that the buildup of such an old, DIC-rich reservoir must have occurred before 24,000 years B.P. A large number of records

mark the start of the deglaciation around 17,000 years B.P. (Fig. 2). Within the uncertainty in marine and ice core age scales, the CO_2 increase, the pronounced $\Delta^{14}\text{C}_{\text{atm}}$ drop (15), the resumption of vigorous Southern Ocean upwelling as recorded in intense deposition of biogenic opal (20), and the launch of ice-rafted debris layers at the beginning of the Heinrich 1 stadial (27) all occurred simultaneously.

Our $\delta^{13}\text{C}_{\text{atm}}$ record shows its largest deviation of 0.3‰—that is, the entire $\delta^{13}\text{C}_{\text{atm}}$ decrease from the LGM to the Preboreal—within the first 2000 years after the start of the deglaciation. Within the same 2000-year interval, CO_2 rose from 190 ppmv to 220 ppmv (i.e., only 35% of the LGM-Preboreal rise). Together with the trend reversal in $\delta^{13}\text{C}_{\text{atm}}$ toward the end of the mystery interval, this indicates that only a fraction of the glacial/interglacial CO_2 increase can be explained by an intensification of deep ocean ventilation bringing isotopically depleted and carbon-rich water to the surface of the Southern Ocean. Our new, high-resolution $\delta^{13}\text{C}_{\text{atm}}$ data constrain this release of isotopically depleted carbon from the deep ocean to the atmosphere to the period 17,400 to 15,000 years B.P. This interpretation of the proxy records is quantitatively in line with dynamical ocean model results that link deep ocean ventilation, atmospheric CO_2 , $\delta^{13}\text{C}_{\text{atm}}$, $\delta^{13}\text{C}_{\text{DIC}}$, opal burial, and radiocarbon (28).

Fig. 1. Ice core reconstructions of atmospheric $\delta^{13}\text{C}$ and CO_2 concentration covering the past 24,000 years (24 kyr). (A) $\delta^{13}\text{C}_{\text{atm}}$ of atmospheric CO_2 measured with three different methods on two different ice core drill sites. Blue circles, Bern cracker data, green squares, Grenoble mill data (9) after offset correction, red circles, Bern sublimation data. Red stars indicate values from the sublimation method but measured on Talos Dome Ice Core (TALDICE). Error bars represent SD of replicate measurements where available and the mean SD for single measurements. The black line is the result of 4000 Monte Carlo simulations representing an error-weighted average of the different $\delta^{13}\text{C}_{\text{atm}}$ data sets. The light and dark shaded areas represent the 2 σ and 1 σ error envelope around the Monte Carlo average (MCA). (B) CO_2 concentration. Black circles represent earlier measurements on EPICA Dome C (EDC) (3); other symbols are the same as in (A). All ice core records are plotted on a synchronized age scale (32).



Alternative hypotheses (29, 30) invoking the release of old carbon from permafrost or carbon locked under continental ice sheets are unlikely to explain the carbon cycle changes in the mystery interval, because the amount of terrestrial carbon needed to account for the ^{14}C drop is very large [about 5000 Gt (25)] and would conflict

with the moderate 30-ppmv rise in atmospheric CO_2 . Moreover, it would lead to an overall decline in $\delta^{13}\text{C}_{\text{DIC}}$, which is not observed in benthic foraminifera in the deep ocean (13, 22). Also, a carbonate dissolution event at the sea floor that would have to accompany such a large terrestrial carbon release into the atmosphere-ocean system

is not imprinted in the deglacial marine CaCO_3 record (31).

Consequently, even though the search for an extremely ^{14}C -depleted deep water mass in marine records has so far not been successful (23) and might not even be essential to explain the $\Delta^{14}\text{C}_{\text{atm}}$ anomaly (26), the release of carbon from the deep ocean remains the most plausible scenario to explain the early deglacial drop in our new $\delta^{13}\text{C}_{\text{atm}}$ record. Furthermore, model results suggest that a $\delta^{13}\text{C}_{\text{atm}}$ decrease of 0.3‰ and a CO_2 increase of about 30 ppmv can be accommodated by relatively small (about 20‰) and spatially complex changes in deep ocean $\Delta^{14}\text{C}$ (28). These changes may remain undetected in attempts to use benthic foraminifera as clues to the location of old abyssal water (19, 25). However, such changes are also too small to explain the reconstructed $\Delta^{14}\text{C}_{\text{atm}}$ decline during the mystery interval. Because of these considerations, the currently available marine and ice core information cannot be reconciled with the atmospheric radiocarbon record in a straightforward manner. One possible way to resolve this issue is to consider the possibility of a larger change in ^{14}C production between the Holocene and the glacial, and to work toward independent verification of the $\Delta^{14}\text{C}_{\text{atm}}$ history.

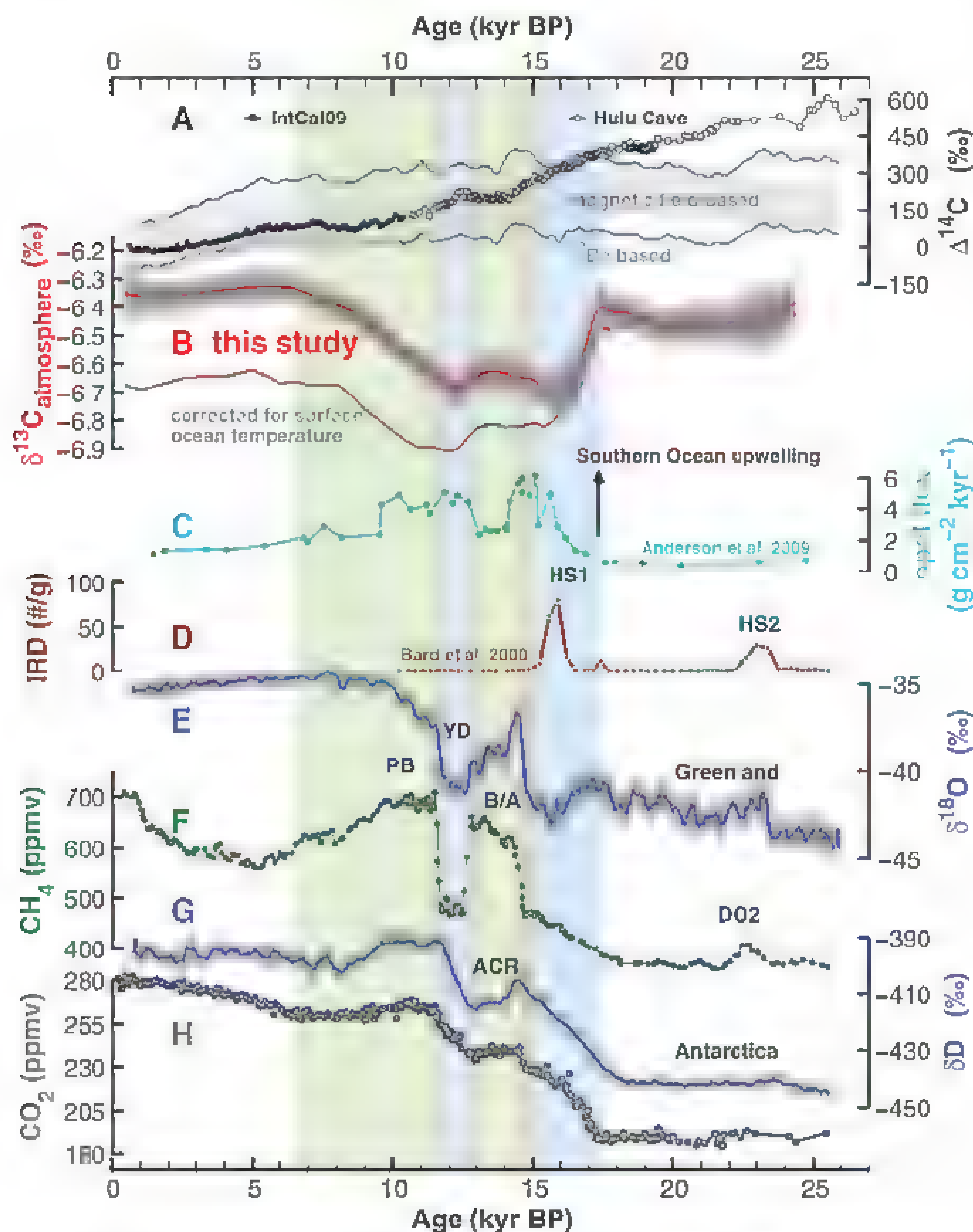


Fig. 2. Ice core reconstructions and marine records illustrating the evolution of major components of the Earth climate system over the past 24,000 years. (A) Reconstructed $\Delta^{14}\text{C}_{\text{atm}}$ from IntCal09 (14) and the ^{230}Th -dated Hulu Cave $\Delta^{14}\text{C}_{\text{atm}}$ record (15) compared with modeled (16) $\Delta^{14}\text{C}_{\text{atm}}$ assuming a constant carbon cycle under preindustrial conditions but considering temporal changes in ^{14}C production [based on ^{10}Be (18), upper and lower estimates (gray lines), or based on paleomagnetic field intensity (17), hatched area]. (B) Monte Carlo average (this study) of the evolution of $\delta^{13}\text{C}_{\text{atm}}$ before SST correction (red line represents the MCA; 2σ and 1σ envelopes are in gray) and after SST correction (gray line). (C) Opal flux in the Southern Ocean as a proxy for local upwelling (20). (D) Record of ice-rafted debris (IRD) in the North Atlantic associated with Heinrich stadials HS1 and HS2 (27). (E) Greenland temperature proxy $\delta^{18}\text{O}$ (33). (F) Reconstructed atmospheric CH_4 concentration (34). (G) Antarctic temperature proxy δD from the EDC ice core (35). (H) Compilation of reconstructed CO_2 shown in Fig. 1B. Green bars indicate intervals with a strong net terrestrial carbon buildup; blue bars indicate intervals where sequestered deep ocean CO_2 was released back to the atmosphere. Note that ice core records are plotted on a synchronized age scale (32), whereas other records are plotted on their individual age scales. PB, Preboreal; YD, Younger Dryas; B/A, Bolling-Allerød warming; DO2, Dansgaard-Oeschger event 2; ACR, Antarctic Cold Reversal.

References and Notes

1. D. Lüthi et al., *Nature* **453**, 379 (2008).
2. H. Fischer et al., *Quat. Sci. Rev.* **29**, 193 (2010).
3. E. Monnin et al., *Science* **291**, 112 (2001).
4. P. Kohler, H. Fischer, G. Munhoven, R. E. Zeebe, *Global Biogeochem. Cycles* **19**, GB4020 (2005).
5. D. M. Sigman, M. P. Hain, G. H. Haug, *Nature* **466**, 47 (2010).
6. J. Etsig et al., *Nature* **461**, 507 (2009).
7. H. J. Smith, H. Fischer, M. Wahlen, D. Mastroianni, B. Deck, *Nature* **400**, 248 (1999).
8. M. Leuenberger, U. Siegenthaler, C. C. Langway, *Nature* **357**, 488 (1992).
9. A. Lourantou et al., *Global Biogeochem. Cycles* **24**, GB2015 (2010).
10. J. Schmitt, R. Schneider, H. Fischer, *Atmos. Meas. Tech.* **4**, 1445 (2011).
11. P. Köhler, H. Fischer, J. Schmitt, *Paleoceanography* **25**, PA1213 (2010).
12. J. Zhang, P. D. Quay, D. O. Wilbur, *Geochim. Cosmochim. Acta* **59**, 107 (1995).
13. K. C. Oliver et al., *Clim. Past* **6**, 645 (2010).
14. P. J. Reimer et al., *Radiocarbon* **51**, 1111 (2009).
15. J. Southon, A. L. Noronha, H. Cheng, R. L. Edwards, Y. Wang, *Quat. Sci. Rev.* **33**, 32 (2012).
16. P. Köhler, R. Muscheler, H. Fischer, *Geochim. Geophys. Geosyst.* **7**, Q11N06 (2006).
17. C. Laj, C. Kissel, J. Beer, in *Timescales of the Paleomagnetic Field*, J. E. T. Channell, D. V. Kent, W. Lowrie, J. G. Meert, Eds. (American Geophysical Union, Washington, DC, 2004), pp. 255–265.
18. R. Muscheler, R. Beer, P. W. Kubik, H. A. Synal, *Quat. Sci. Rev.* **24**, 1849 (2005).
19. W. Broecker, S. Barker, *Earth Planet. Sci. Lett.* **256**, 90 (2007).
20. R. F. Anderson et al., *Science* **323**, 1443 (2009).
21. P. Carr et al., *Nat. Geosci.* **5**, 74 (2012).
22. M. Yu et al., *Science* **330**, 1084 (2010).
23. D. C. Lund, A. C. Mix, J. Southon, *Nat. Geosci.* **4**, 771 (2011).
24. I. Stott, J. Southon, A. Timmermann, A. Koutavas, *Paleoceanography* **24**, PA2223 (2009).
25. W. Broecker, E. Clark, *Geophys. Res. Lett.* **37**, L13606 (2010).
26. A. Burke, L. F. Rodionov, *Science* **335**, 557 (2012).

27. E. Bard, F. Rostek, J. L. Taron, S. Gendreau, *Science* **289**, 1321 (2000)
28. T. Tschumi, F. Joos, M. Gehlen, C. Heinze, *Clim. Past* **7**, 171 (2011)
29. R. Zech, Y. Huang, M. Zech, R. Tarozo, W. Zech, *Clim. Past* **7**, 501 (2011)
30. N. Zeng, *Clim. Past* **3**, 135 (2007)
31. D. A. Hodell, C. D. Charles, F. J. Sierra, *Earth Planet. Sci. Lett.* **192**, 109 (2001)
32. B. Lemieux-Dudon *et al.*, *Quat. Sci. Rev.* **29**, 8 (2010)
33. North Greenland Ice Core Project members, *Nature* **431**, 147 (2004)
34. EPICA Community Members, *Nature* **444**, 195 (2006)
35. B. Stenni *et al.*, *Science* **293**, 2074 (2001)

Acknowledgments: We thank two anonymous reviewers for carefully reviewing the manuscript. Supported in part by Deutsche Forschungsgemeinschaft, Heimholtz Gemeinschaft and Schweizerischer Nationalfonds. This work is a contribution to EPICA, a joint European Science Foundation/European Commission (EC) scientific program, funded by the EC under the Environment and Climate Program and by national contributions from Belgium, Denmark, France, Germany, Italy, the Netherlands, Norway, Sweden, Switzerland, and the UK. The main logistic support at Dome C was provided by the Institut Polaire Français–Paul Emile Victor (IPEV) and PNRA. Ice core material was also used from TALDICE, a joint European program led by Italy and funded by national contributions from Italy, France, Germany, Switzerland, and the UK. The main logistical support at

Talos Dome was provided by PNRA. This is EPICA publication 284. The data are accessible online at <http://doi.pangaea.de/10.1594/PANGAEA.772713>.

Supplementary Materials

www.sciencemag.org/cgi/content/full/science.1217161/DC1
Materials and Methods

Figs. S1 to S7

Tables S1 to S3

References (36–49)

28 November 2011; accepted 19 March 2012

Published online 29 March 2012,

10.1126/science.1217161

Ancient Maya Astronomical Tables from Xultun, Guatemala

William A. Saturno,^{1*} David Stuart,² Anthony F. Aveni,³ Franco Rossi⁴

Maya astronomical tables are recognized in bark-paper books from the Late Postclassic period (1300 to 1521 C.E.), but Classic period (200 to 900 C.E.) precursors have not been found. In 2011, a small painted room was excavated at the extensive ancient Maya ruins of Xultun, Guatemala, dating to the early 9th century C.E. The walls and ceiling of the room are painted with several human figures. Two walls also display a large number of delicate black, red, and incised hieroglyphs. Many of these hieroglyphs are calendrical in nature and relate astronomical computations, including at least two tables concerning the movement of the Moon, and perhaps Mars and Venus. These apparently represent early astronomical tables and may shed light on the later books.

The Maya have long been noted for their astronomical proficiency, believed by many to be on par with that of the cultures of the ancient Middle East. Most of what we know about Maya astronomical methodology, and the precision of their understanding of the movement of the Sun, Moon, and planets, comes from studies of the codices, painted bark paper documents dated to a century or two before Spanish contact. Here we report on a source several centuries earlier, a wall painting accompanied by a numerical table and a series of long numbers that appear to have functioned like those found in astronomical tables in the codices.

Though systematic archaeological investigations began only in 2008 (1), the Maya ruins of Xultun, Guatemala, were first reported in 1915 (2). Despite formal scientific expeditions to map and record the site's monuments in the 1920s (2) and again in the 1970s (3, 4), illicit excavations have left the largest mark on the site. In March 2010, Maxwell Chamberlain identified the presence of a heavily eroded mural painting on the west wall of a small masonry-vaulted structure exposed by looting (5). The structure (Fig. 1), designated 10K-2, is located within a residential compound and was modified by the Maya over

several construction phases. The most recent of these phases saw the room filled with rubble and earth, and the final phase built over it, effectively preserving its interior paintings. The looters' excavation broke through this final-phase veneer and exposed the southernmost portion of the room's

west wall. They later abandoned their excavation, and the exposed painting began to weather.

We continued excavating this structure in 2010 and 2011, revealing that three of the structure's interior walls (west, north, and east), as well as its vaulted ceiling, were once covered by mural paintings. The fourth (south) wall consisted mainly of a doorway, with the remainder destroyed by the looters. The state of preservation of the murals varies considerably, owing to the damaging effects of water, roots, and insects. The east wall, located closest to the exterior surface of the covering mound, has eroded the most.

The paintings on the east wall include a large number of small, delicately painted hieroglyphs, rendered in a variety of sizes and in black or red line near the two (possibly three) seated figures that once dominated the imagery. Thin coats of plaster were reapplied over existing texts to provide a clean slate for others. Still other texts are incised into the plaster surface. Given their arrangement around and on the figural painting and

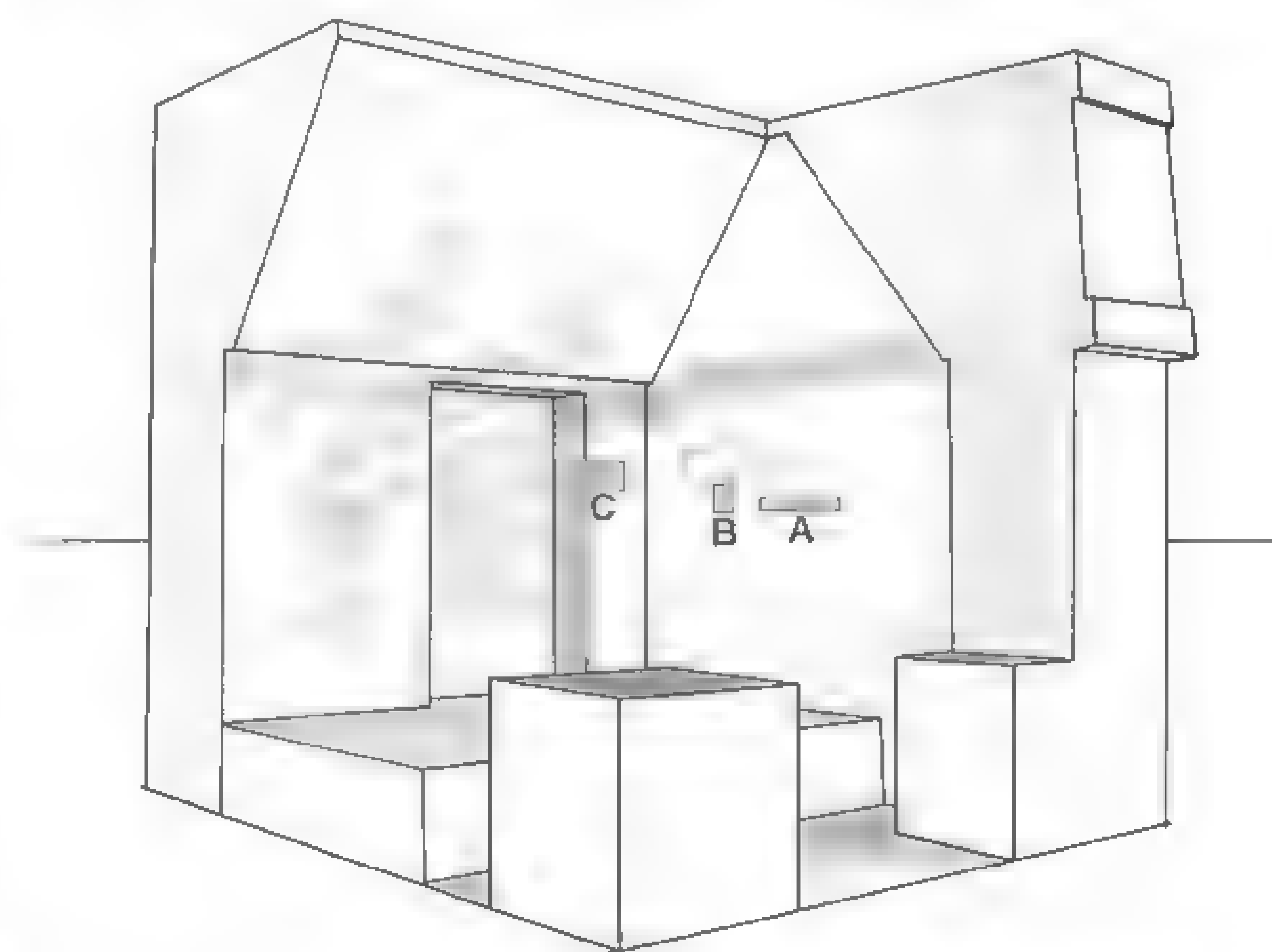


Fig. 1. Artist's reconstruction of Structure 10K-2, Xultun, Guatemala, showing painted figures from the north and east walls, as well as the locations of numerical arrays discussed in the text. (A) Lunar table. (B) "Ring Number." (C) Intervals. [Drawing by H. Hurst]

¹Archaeology Department, Boston University, Boston, MA 02215, USA. ²Department of Art and Art History, University of Texas at Austin, Austin, TX 78712, USA. ³Department of Physics and Astronomy, Department of Sociology and Anthropology, Cengage University, Hamilton, NY 13346, USA. ⁴Archaeology Department, Boston University, Boston, MA 02215, USA.

*To whom correspondence should be addressed. E-mail: saturno@bu.edu

earlier texts, as well as the variety of sizes and method of execution of the preserved glyphs, there is little doubt that texts were not integral to the original design of the chamber's mural decoration, but were created during the room's continual use.

The remains of many bar-and-dot numbers arranged in vertical columns can be seen along the southern portion of the east wall. Only a handful of legible columns are left (Fig. 2 and fig. S2), but faint remains of other bar-and-dot numbers can be seen, suggesting a lengthy array of columns spanning some 48 cm (fig. S3). The columns contain no more than three numerals, and they resemble calendrical and astronomical tables in the *Dresden Codex*, an ancient Maya hieroglyphic manuscript composed centuries later (6, 7).

Visible atop at least five of the columns are individual "Moon" glyphs combined with facial profiles. Enough detail is visible on two of these glyphs to see that they are deities. Elsewhere, similar hieroglyphs are used to record Moon ages in Maya date records—as part of the so-called Lunar Series identified by Teeple (8). Lunar months, as Teeple showed, are grouped into sets of six, forming the 177- or 178-day Maya lunar "semester" (~ 29.5 days $\times 6$) (8–10). The presence of these lunar deity heads suggests that the number columns also have a lunar meaning.

The final three number columns are:

12	12	13
5	14	5
?	6	4

Given their similarity to numerical records in the *Dresden Codex* and other hieroglyphic manuscripts, we take these numbers to represent records of elapsed days using periods of the Long Count calendar. The upper number would therefore rep-

resent multiples of the 360-day "tun" unit, the middle number multiples of 20-day units known as the "winal," and the final number would represent units of single days, known as "k'in." These three columns thus represent a progression of ever-increasing quantities of days with the last two columns equal to 4606 (12.14.6) and 4784 (13.5.4) days, respectively. The bottommost number of the previous column is eroded, but enough remains to indicate that it must be a number between 7 and 9 (12.5.?), implying that the column's quantity is between 4427 and 4429.

The span between the final two columns is a lunar "semester" of 178 days. Subtracting either 177 or 178 from the penultimate number (4606), we arrive at 4429 (12.5.9) or 4428 (12.5.8) days, both of which fit with what remains of the third-from-last column. In this light, it is reasonable to suggest that the Xultun number array represents a running sequence of consecutive multiples of 177 or 178 with only the last three totals well preserved. The numbers 177 and 178 are important in ancient Maya astronomy. The eclipse tables on pages 51 to 58 of the *Dresden Codex* are based on these same intervals. The *Dresden* tables use this basic unit, along with an interspersed correction span of 148 days, or five lunations, to represent patterns in both lunar and solar eclipses (8, 11). The 4784-day Xultun array represents 162 cumulative 6-month lunations ($162 \times 29.530589 = 4783.9554$), or twice that of the Palenque lunar reckoning system (8). Moreover, the layout of the Xultun table closely resembles the successive columns of cumulative totals in the *Dresden Eclipse Table*. However, unlike the *Dresden* tables, the Xultun array does not seem corrected to correlate with precise eclipse phenomena. It would seem rather to be a simpler tally spanning a period

of roughly 13 years. This end point is suggestive, because years and other time periods grouped in thirteens were of deep cosmological significance to the ancient Maya, forming the foundation of their "Grand Long Count" calendar (12).

Additional similarity between the Xultun paintings and codical tables emerges in the form of an incised "Ring Number" on the east wall (fig. S5). Ring Numbers typically serve to establish the temporal starting points for various tabulations and almanacs, including astronomical tables. The relationship between this Ring Number and the other Xultun texts is at present unclear.

A second array consisting of four columns painted in red is found on the eastern portion of the north wall (Fig. 3 and fig. S4). Each column begins with a tzolk'in day station in the uppermost hieroglyph, followed in a vertical line by a series of five numbers, as follows.

A	B	C	D
1 Kawak (Kaban?)	9 K'an	13 Chikchan	? Manik'
8	2	17	12
6	7	0	5
1	9	1	3
9	0	3	3
0	0	0	0

Unfortunately, the tzolk'in stations are not all legible. The middle two are fairly clear as 9 K'an and 13 Chikchan, respectively. The day record atop the first column bears the coefficient 1 with what looks to be Kawak or Kaban, and the final column shows a clear Manik' day sign without a legible coefficient.

The columns of five numbers appear at first glance to be Long Count dates, yet they are not—at least not in the conventional sense. By their nature, standard Long Count dates reckon elapsed

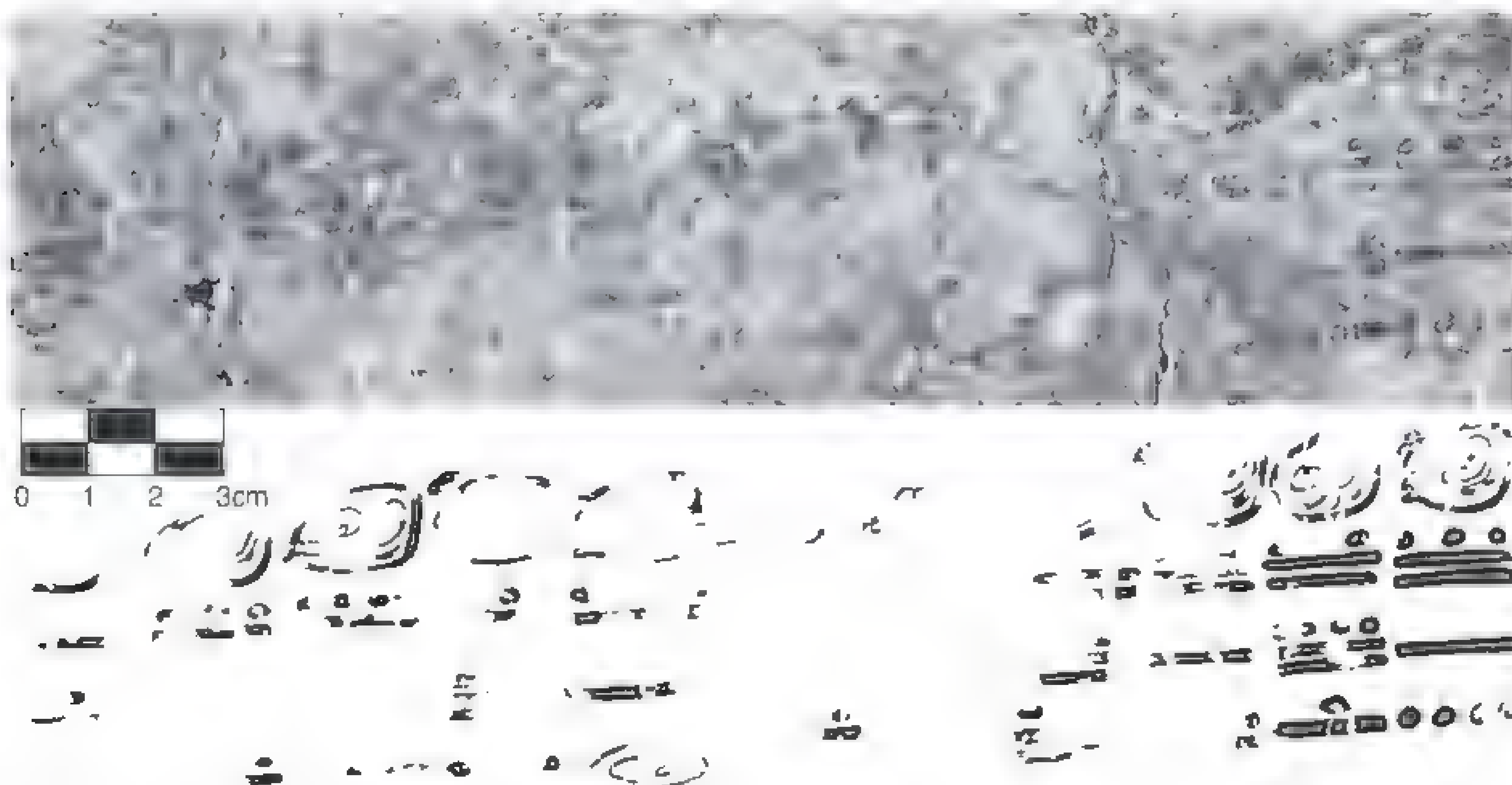


Fig. 2. Portion of lunar table, Structure 10X-2, Xultun, Guatemala. [Image by W. Saturno, drawing by D. Stuart]

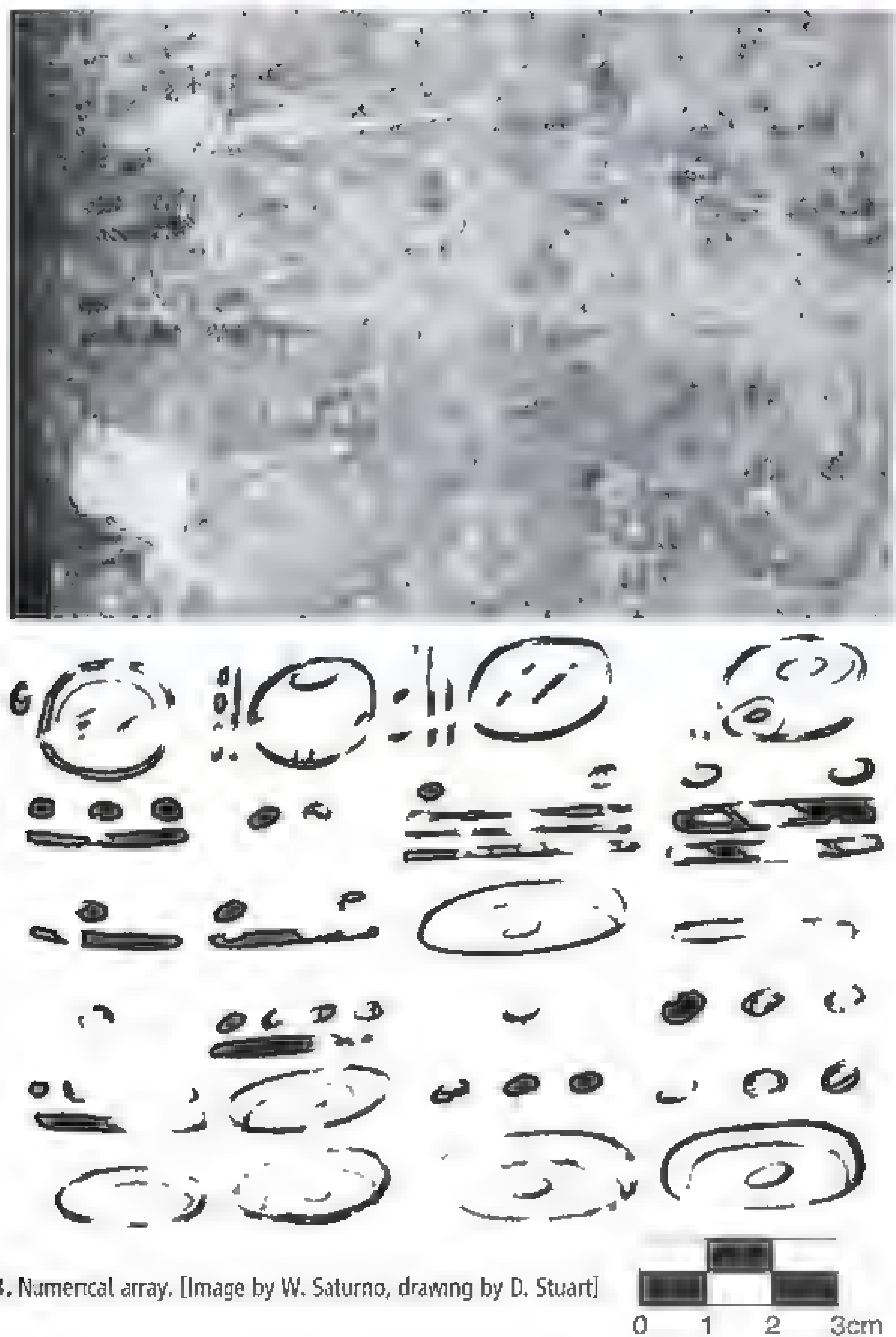


Fig. 3. Numerical array. [Image by W. Saturno, drawing by D. Stuart]

Table 1. Maya calendrical and astronomical commensurabilities with the Xultun intervals. Explanation of entries: 1, Xultun intervals (base 20); 2, base-10 equivalent; 3, tzolk'in or 260-day round of 13×20 days; 4, haab or 365-day year (the Maya did not use leap years); 5, Calendar Round (CR), 18,980 days, which commensurates tzolk'in and haab: $52 \times 365 = 73 \times 260$ days; 6, computing year, or 364 days, a conveniently factorable approximation to the 365-day year used to facilitate calculations; 7, canonic Venus period (VP), 584 days (actual 583.92 days); 8, five canonic VP, or 2920 days, the length of one pass of five stations through the

No.	(1) Interval	(2) Decimal equivalent	(3) Tzolk'in	(4) Haab	(5) CR	(6) Computing year	(7) (VP) Canonic Venus period	(8) 5VP	(9) 2340-day cycle	(10) Length of Venus Table	(11) (MP) Canonic Mars period	(12) 56,940- day cycle	(13) Length of Eclipse Table
A	8.6.1.9.0	1,195,740	4599	3276	63	3285	$2047+0.5VP$	409.5	511	$31+1CR$	1533	21	$100-260^d$
B	2.7.9.0.0	341,640	1314	936	18	$938+4 \times 52^d$	585	117	146	9	438	6	$28.5+780$
C	17.0.1.3.0	2,448,420	9417	6708	129	$6726+3 \times 52^d$	$4192+0.5VP$	838.5	$1046+780^d$	$64+1CR$	3139	43	$204.5+10 \times 260$
D	12.5.3.3.0	1,765,140	6789	4836	93	$4849+2 \times 52^d$	$3022+0.5VP$	604.5	$754+780^d$	$46+1CR$	2263	31	$147.5+4 \times 260$

Venus table, which commensurates VP and haab: $5 \times 584 = 8 \times 365$; 9, 2340 days, a cycle commensurating the cycle of the nine lords of the night, the 13-day numbers, the VP, and possibly the period of Mercury (actual 115.9 days): $9 \times 13 = 117$ days; $20 \times 117 = 2340 = 4VP + 4$ days; 10, length of the Venus table = $37960 = 65 \times 584 = 2CR$; 11, canonic Mars period (MP) = 780 days (actual 779.9 = $2 \times 260 - 0.1$ days); 12, $56,940 =$ largest common divisor of CR and MP = $3 \times 18,980 = 73 \times 780$; 13, length of the Eclipse Table in the Dresden Codex = $11960 = 46 \times 260 = 405$ lunar synodic months. d, days.

time from the base of 13.0.0.0.4 Ahaw 8 Kumk'u. These spans are usually between 3000 and 4000 years. The Xultun columns, by contrast, appear different, expressing a wide range of accumulated time, some smaller and others considerably larger. Similar lengthy tallies of days appear as so-called Distance Numbers in both the monumental inscriptions and in the *Dresden Codex*, often involving periods above the Bak'tun (13-15). In addition, the Xultun intervals do not link the different tzolk'in day stations noted at the top of each column, suggesting that each column is self-contained, expressing accumulations of days wedded, for reasons still undetermined, to the individual tzolk'in days recorded at the top.

The intervals might be commensurate with other canonic astronomical periods and significant computational numbers found in the much later codices, where they were contrived to perform long-term corrections to astronomical tables and to provide schemes for ordering tabulated base dates. One of the likenesses to the Xultun numbers is on page 24 of the Venus Table in the *Dresden Codex*. The so-called Long Round (LR) number (16), 9.9.16.0.0—which may be added to a date prior to the era beginning 13.0.0.0.0 to reach a date in the historical era—is a whole multiple not only of the 260-day tzolk'in, the 365-day haab, and the 584-day Venus canonic synodic cycle, but also of the 18,980-day Calendar Round, the length of the Venus Table (37,960 days; also a double Calendar Round), and the 2340-day cycle, which commensurates the table with the $9 \times 13 = 117$ -day cycle associated with the nine Lords of the Night (17). The number 117 is also an approximation to the synodic period of Mercury (115.9 days), for which there is some documented reference in codical texts (18). The largest common divisor of each of the four Xultun intervals, 56,940, is a whole multiple of both the Calendar Round ($3 \times 18,980$) and the canonic Mars period (73×780).

Although the Xultun intervals and the aforementioned submultiples can be generated solely

as a consequence of their relationship to the Calendar Round, it is also possible that these long numbers were designed at least in part to serve astronomical ends (Table 1). That the Xultun numbers are divisible by integral and half-integral multiples (give or take additive or subtractive small multiples of 52 and 260) is reminiscent of the character of numbers one finds in the upper portions of multiplication tables that accompany astronomical reckonings in the codices. The latter were developed to place canonic events in closer proximity to the occurrence of actual sky phenomena, e.g., an eclipse, the start of a retrograde loop of Mars, or a heliacal rise of Venus.

Though the *Dresden Codex* dates to ca. the 15th century, there are Long Count entry dates to the Eclipse table on the same page as the multiplication table dated to 755 C.E. (19), which corresponds well with the 800 C.E. date for Xultun 10K-2. Codical tables were likely copied and re-copied over many generations, with updates, based on observational data, incorporated periodically. Thus, the known Postclassic written documents derived from others of classical origin.

One goal of the Maya calendar keepers, gleaned from studies of the codices, was to seek harmony between sky events and sacred rituals. The Xultun paintings may represent an expression of the same ambition several centuries earlier. Although the higher multiples in the multiplication table attached to the *Dresden Codex* Venus Table consist of near whole multiples of important Venus numbers, and the Mars and Eclipse tables exhibit similar properties with respect to Mars and Eclipse periods, respectively, the four (undoubtedly carefully contrived) Xultun numbers may have been devised to create schemes for synchronizing predictable events connected with the movement of Mars, Venus, the Moon, and possibly Mercury. Why these four particular numbers were used, which range in duration from 935 to 6703 years, is uncertain.

Though human portraits adorn most of the interior space, painted when the room was built and decorated in the early 9th century C.E. (texts associated with the main figures of the mural and their actions seem to cluster around 814 C.E.), the smaller, more ephemeral texts represent the continued use and modification of the room up until the time it was intentionally buried. To date, 12 painted or incised texts (not including the presented tables), ranging in length from 5 to 30 glyphs, have been identified. This continued astronomical and calendrical writing is confined to the area along the sunlit portions of east and north walls. These repeatedly replastered sections may have been used as a kind of reference for the preparation of other more permanent or public monuments. The tidy hand-writing on the wall might even have been copied from Classic period screenfold books, the plastered and replastered surfaces reflecting a perpetual negotiation and elaboration in Maya reckonings of time, astronomical cycles, and the written words that conveyed them.

References and Notes

1. W. Saturno, M. Urquiza, *Proyecto Arqueológico Reg. San Bartolo, Informe No. 7* (Instituto de Antropología e Historia, Guatemala, 2008).
2. S. Morley, in *The Inscriptions of Peten* (Carnegie Institution of Washington, Washington, DC, 1938), vols. 1–4, pp. 383–385.
3. E. Von Ew, *Corpus of Maya Hieroglyphic Inscriptions*, vol. 5, no. 1: *Xultun* (Peabody Museum of Archaeology and Ethnology, Cambridge, MA, 1978).
4. E. Von Ew, J. Graham, *Corpus of Maya Hieroglyphic Inscriptions*, vol. 5, no. 2: *Xultun, La Honradéz, Uaxactun* (Peabody Museum of Archaeology and Ethnology, Cambridge, MA, 1984).
5. W. Saturno, D. Del Cid, F. Rossi, *Nuevos Descubrimientos en el Sitio Arqueológico Xultun, in Informe Preliminar, No. 9, Novena Temporada 2010* (Instituto de Antropología e Historia, Guatemala, 2010), pp. 106–108.
6. E. Forstemann, *Commentary on the Maya Manuscript in the Royal Public Library of Dresden* (Papers of the Peabody Museum of American Archaeology and Ethnology, Harvard Univ., vol. 4, no. 2 (Salem Press, Cambridge, MA, 1906)).
7. E. Thompson, *Maya History and Religion* (Univ. of Oklahoma Press, Norman, 1970).
8. J. Teeple, *Maya Astronomy*, in *Contributions to American Archaeology*, 1/2 (Carnegie Institution of Washington, Washington, DC, 1930).
9. L. Schele, N. Grube, F. Falsen, *Texas Notes on Pre-Columbian Art, Writing and Culture*, No. 29 (Univ. of Texas, Austin, 1992).
10. J. Linden, *The Dotted Head Variants of Glyph C*, in *Eighth Palenque Round Table* (Pre-Columbian Art Research Institute, San Francisco, 1996), pp. 343–356.
11. H. Bricker, V. Bricker, *Curr. Anthropol.* **24**, 1 (1983).
12. D. Stuart, *The Order of Days* (Harmony, New York, 2011).
13. J. E. S. Thompson, *Maya Hieroglyphic Writing: An Introduction* (Carnegie Institution of Washington Publication 589 (Univ. of Oklahoma Press, Norman, 1950)).

14. J. E. S. Thompson, in *A Commentary of the Dresden Codex, A Maya Hieroglyphic Book*, APS Memoir 93 (American Philosophical Society, Philadelphia, 1972), pp. 20–22.
15. L. Satterthwaite, *Concepts and Structures of Maya Calendrical Arithmetics* (Joint Publication no. 3 of the Univ. of Pennsylvania Museum and the Philadelphia Anthropological Society, 1947).
16. H. Bricker, V. Bricker, in *Astronomy in the Maya Codices* (American Philosophical Society, Philadelphia, 2011), p. 76.
17. F. Lounsbury, in *Dictionary of Scientific Biography*, vol. 15, (Scribners, New York, 1978), suppl. 1, p. 787.
18. H. Bricker, V. Bricker, *Astronomy in the Maya Codices* (American Philosophical Society, Philadelphia, 2011), pp. 235ff, 330–331.
19. H. Bricker, V. Bricker, *Astronomy in the Maya Codices* (American Philosophical Society, Philadelphia, 2011), pp. 275f.

Acknowledgments: The data reported in this paper are available in the supplementary materials. Excavations by the Proyecto Regional San Bartolo–Xultun between 2008 and 2012 were supported by Boston University as well as through grants from the National Geographic Society, Committee for Research and Exploration (grants 8782-10, 8991-11, 9091-12), and the National Geographic Society, Expeditions Council (EC0497-11). We also thank the Guatemalan Ministerio de Cultura, Instituto de Antropología e Historia, and the Departamento de Monumentos Prehistóricos for their support.

Supplementary Materials

www.sciencemag.org/cgi/content/full/336/6082/714/DC1

Materials and Methods

Supplementary Text

Figs. S1 to S5

5 March 2012, accepted 5 April 2012

10.1126/science.1221444

A Stem Cell–Based Approach to Cartilage Repair

Kristen Johnson,^{1,†} Shoutian Zhu,^{2,†} Matthew S. Tremblay,^{1,2} Joshua N. Payette,² Jianing Wang,² Laure C. Bouchez,² Shelly Meeusen,¹ Alana Althage,¹ Charles Y. Cho,¹ Xu Wu,³ Peter G. Schultz^{2*}

Osteoarthritis (OA) is a degenerative joint disease that involves the destruction of articular cartilage and eventually leads to disability. Molecules that promote the selective differentiation of multipotent mesenchymal stem cells (MSCs) into chondrocytes may stimulate the repair of damaged cartilage. Using an image-based high-throughput screen, we identified the small molecule kartogenin, which promotes chondrocyte differentiation (median effective concentration = 100 nM), shows chondroprotective effects in vitro, and is efficacious in two OA animal models. Kartogenin binds filamin A, disrupts its interaction with the transcription factor core-binding factor β subunit (CBF β), and induces chondrogenesis by regulating the CBF β -RUNX1 transcriptional program. This work provides new insights into the control of chondrogenesis that may ultimately lead to a stem cell–based therapy for osteoarthritis.

Over 70% of Americans between the ages of 55 and 70 are affected by osteoarthritis (OA), which is characterized by the progressive breakdown of articular cartilage (1) and ultimately leads to the functional failure of synovial joints. OA is mediated by several pathogenic mechanisms, including enzymatic degradation of extracellular matrix, deficient new matrix formation, cell death, and abnormal activation and hypertrophic differentiation of cartilage cells

(2). The only current therapeutic options for OA are pain management and surgical intervention (3). Mesenchymal stem cells (MSCs), which reside in bone marrow and many adult tissues, are capable of self-renewal and differentiation into a variety of cell lineages, including chondrocytes, osteoblasts, and adipocytes (4, 5). MSCs have been identified in healthy and diseased cartilage and appear to retain at least some potential to regenerate cartilage in vivo (6, 7). Here we

describe the identification and characterization of a small molecule that selectively directs MSC differentiation into chondrocytes for cartilage regeneration.

An image-based high-throughput screen was established with primary human bone marrow MSCs [CD29⁺ CD44⁺ CD166⁺ CD105⁺ CD45⁻, termed hMSCs (5)] in a 384-well format. Chondrogenic nodules containing cartilage-specific matrix components (proteoglycans and type II collagen) were positively stained by rhodamine B to identify the early cell condensation phenotype associated with the induction of chondrogenesis (Fig. 1B). Of 22,000 structurally diverse, heterocyclic, druglike molecules screened, one compound, kartogenin (KGN) (Fig. 1A), promoted chondrocyte differentiation from hMSCs in a dose-dependent manner [median effective concentration (EC₅₀) = 100 nM, fig. S1]. Lineage-specific differentiation in the presence of KGN was further confirmed by fluorescent immunostaining of chondrocyte-specific proteins, including type II collagen, SOX9, and aggrecan under both monolayer and high-density conditions (fig. S2). Reverse transcriptase polymerase chain reaction (RT-PCR) with mRNA isolated

from differentiated cells confirmed the expression of gene products associated with chondrocytes, including lubricin (superficial zone protein), aggrecan, and type II collagen (2). There were only slight changes in the expression of gene products associated with chondrocyte hypertrophy and calcification, such as osteocalcin, alkaline phosphatase, discoidin domain receptor, Indian hedgehog (IHH), and type X collagen, in either hMSCs or chondrocytes (Fig. 1C and figs. S2 to S4). In a three-dimensional 21-day hMSC pellet culture, up-regulation of tissue inhibitor of metalloproteinase 1, type II collagen, and aggrecan was observed upon KGN treatment (Fig. 1D), indicating retention of the cartilage phenotype and inhibition of further matrix breakdown by matrix metalloproteinases (MMPs). Increased production of collagen is often associated with an increase in MMP activity in osteoarthritic cartilage (8). However, KGN did not alter either MMP-3, MMP-13, or aggrecanase expression in primary chondrocytes and MSCs (figs. S3 to S5), nor did it show any inhibition of aggrecanase or MMP13 *in vitro* (fig. S6). In addition, no toxicity was observed with KGN at 100 μM in hMSCs, chondrocytes, osteoblasts, and synoviocytes (fig. S7).

We next evaluated the effects of KGN on articular chondrocytes under pathophysiological conditions. Primary bovine articular chondrocytes and cartilage explants were grown in the presence of tumor necrosis factor α (TNF-α) and oncostatin M to mimic cytokine-induced damage during OA pathogenesis (9). When treated with this cytokine cocktail, cultured primary chondrocytes released four to five times (50 μM) more nitric oxide (NO) than did un-

treated chondrocytes, as measured by the Griess reaction. Upon treatment with 1 to 5 μM KGN, NO release was significantly inhibited (up to 70%). In cartilage explant organ cultures treated with 5 μM KGN, the cytokine-induced release of glycosaminoglycans (GAGs) was also reduced by up to 60% (Fig. 1E). These data suggest that KGN also protects existing chondrocytes under the pathological conditions of OA.

OA is considered to be the consequence of a variety of etiologic factors, including abnormal biomechanical stress, genetics, and abnormalities of the articular cartilage or bone (10). To evaluate the efficacy of KGN *in vivo*, we took advantage of two widely used rodent models: the collagenase VII-induced chronic joint injury model (11) and the acute surgical model, involving transection of three of the major ligaments in the joint (12). In the collagenase VII-induced model, a 3-day period of mild inflammation is followed by collagenase-induced destabilization of the joint, resulting in mild to moderate cartilage destruction based on pathological alteration of joint morphology (Fig. 2, A and C). Intra-articular (IA) administration of KGN (10 μM in 4 μl of saline on days 7 and 21) and subsequent histological analysis and grading of the medial tibial plateau [based upon the Osteoarthritis Research Society International scoring system (13)] revealed regeneration in the cartilage matrix as indicated by a decrease in the fibrillations in the superficial and midzone of the articular cartilage (Fig. 2, C and D). Peripheral blood was collected during the 8-week period to measure the serum level of cartilage oligomeric matrix protein (COMP), which is elevated in the plasma of patients with OA and correlates with

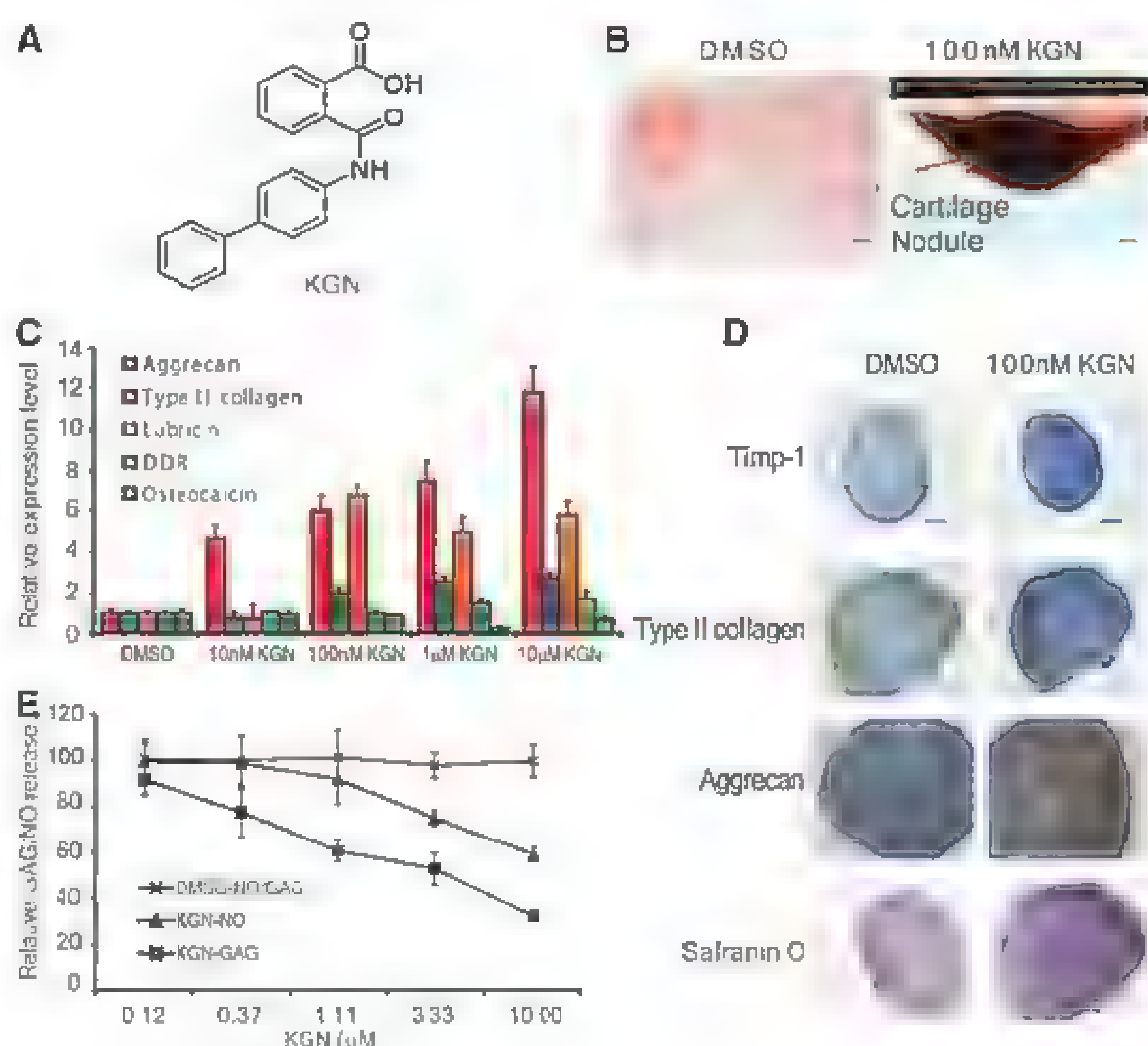
¹Genomics Institute of the Novartis Research Foundation, 10675 John Jay Hopkins Drive, San Diego, CA 92121, USA.

²The Scripps Research Institute, 10550 North Torrey Pines Road, La Jolla, CA 92037, USA. ³Massachusetts General Hospital, Cutaneous Biology Research Center, Harvard Medical School, Building 149, 13th Street, Room 3219 Charlestown, MA 02129 USA.

*To whom correspondence should be addressed. E-mail: schultz@scripps.edu (P.G.S.), kjohnson@gnf.org (K.J.)

†These authors contributed equally to this work.

Fig. 1. KGN induces chondrocyte differentiation from hMSCs and protects articular chondrocytes *in vitro*. (A) Structure of KGN. (B) KGN induces chondrocyte nodule formation in primary hMSCs. Cells were grown in serum-free DMEM under high-density conditions for 3 days and stained with rhodamine B (1 μg per milliliter of phosphate-buffered saline). Scale bars, 100 μm. (C) KGN increases chondrocyte-specific gene expression in hMSCs. Cells were treated with KGN as indicated for 72 hours. Relative mRNA levels were determined with Taqman gene-specific assays (*n* = 3). Fold change relative to a dimethyl sulfoxide (DMSO) control is shown. DDR, discoidin domain receptor. (D) Long-term hMSC pellet cultures treated with KGN exhibit cartilage properties. Cells were treated with compound for days 1 to 3 of the 21-day differentiation period, fixed, and stained to assess chondrocyte differentiation. Scale bars, 400 μm. (E) KGN inhibits NO and GAG release induced by cytokines. Primary bovine articular chondrocytes were induced to release NO by stimulation with 20 ng/ml TNF-α and 10 ng/ml oncostatin M (OSM) with and without KGN. After 48 hours, NO released into the media was determined by the Griess reaction (*n* = 12 experiments). Bovine cartilage (femoral groove only) explants were treated as above for 72 hours. GAG content was determined by the dimethylene blue reaction (*n* = 6 experiments). Relative levels of NO and GAG, normalized to that of DMSO-treated controls, are shown.



the severity of disease (14). At both days 13 and 56, there were significantly lower levels of COMP in the mice treated with KGN (Fig. 2E).

In the acute surgical model, the majority of the lesions were located on the lateral tibial plateau (Fig. 2, B and F). After KGN treatment, there was a 50% reduction in the joint score (Fig. 2G) as compared to that with vehicle treatment alone. Furthermore, there was a 1.8-fold reduction in the levels of circulating type II collagen fragments [a peptide that is released during

cartilage damage (15)] (Fig. 2H). Next, alleviation of OA-induced pain was assessed by incapacitation measurements on the basis of weight distribution between the surgically treated and untreated legs. Forty-two days after surgical induction of joint damage and four weekly drug treatments (days 7, 21, 28, and 35), treatment with as little as 1 μ M KGN produced significant improvement as compared to the vehicle-treated injured knees (Fig. 2I). Although we do not know the IA exposure of KGN, systemic exposure

of KGN is minimal after IA injection (half-life 2 hours, maximum concentration 0.1% of IA dose). This result suggests that KGN acts at the diseased joint, and systemic exposure is minimal. Consistent with this result, no obvious adverse effects (weight loss, significant swelling, or signs of pain or distress) were observed in either animal model. Collectively, the *in vitro* and *in vivo* data strongly support the notion that directed differentiation of cartilage resident MSCs leads to improvements in the damaged joints when given at early stages of the disease. The overall *in vivo* efficacy of KGN may be attributable to a combination of both a regenerative/repair effect and a protective effect; further *in vivo* studies will be required to analyze the relative contribution of each.

To elucidate the biological mechanism of KGN, we performed a focused structure-activity-relationship study. Among a group of derivatives of KGN, we found that cyano-KGN (KGN-CN, fig. S1) has very similar chondrocyte differentiation activity ($EC_{50} = 137$ nM) to that of the parent molecule. We therefore synthesized a close structural analog of KGN-CN as an affinity probe that contains a biotin moiety and a phenyl azide photo-cross-linker [biotin-kartogenin-azide (BKA), fig. S1]. We incubated the probe with hMSCs and cross-linked it to cellular targets by ultraviolet irradiation. Western blotting with antibodies to biotin identified 90- and 280-kD bands in an SDS-polyacrylamide gel electrophoresis gel of ammonium sulfate-precipitated fractions of the cell lysates (fig. S8). The intensity of both bands decreased in the presence of 100 μ M free KGN (50 times in excess of BKA). The two bands were identified as filamin A (FLNA) by mass spectrometry. FLNA, a member of the filamin family of proteins, is a 280-kD protein that can be cleaved in certain cells to afford a 90-kD C-terminal fragment (16). Knockdown of FLNA in hMSCs using lentiviral particles expressing short hairpin RNAs (shRNAs) targeting FLNA (>70% knockdown, fig. S9) resulted in up to a fivefold increase in chondrocyte formation as compared to the control virus (expressing nontargeting shRNA)-infected cells (Fig. 3A), suggesting that KGN induces MSC differentiation through its association with FLNA.

FLNA is an actin-binding protein that cross-links actin filaments, thereby regulating cytoskeletal network organization and dynamics (17). Previously, cytoskeleton rearrangement has been shown to induce chondrocyte differentiation (18). However, treatment of hMSCs with KGN revealed no significant effects on either the G-actin (monomeric) or F-actin (filamentous) fractions, nor altered distribution of FLNA in the two fractions (fig. S10), which is consistent with binding of KGN distal to the actin-binding domain at the N terminus of the protein. Three C-terminal fragments of FLNA (Fig. 3B) were then cloned and incubated with BKA and photo-cross-linked. Only FC-1 was labeled (Fig. 3C). Among the known binding partners of the FC-1 fragment of

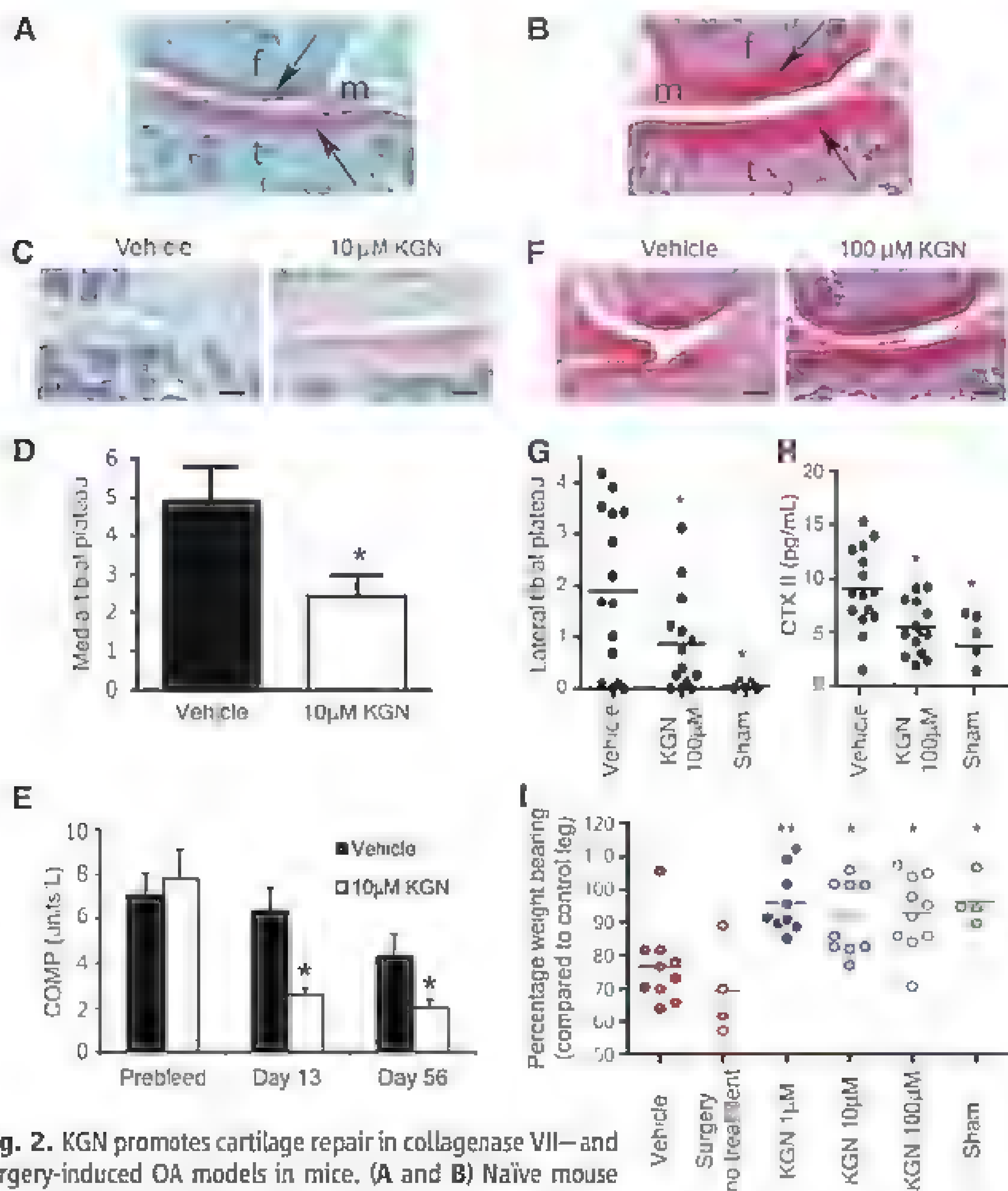


Fig. 2. KGN promotes cartilage repair in collagenase VII- and surgery-induced OA models in mice. (A and B) Naïve mouse knee joints were stained with safranin O/methyl green (A) and safranin O (B). Note the thickness and the smooth surfaces of the intact cartilage. Arrows indicate the stained cartilage. f, femur; t, tibia; m, meniscus. (C) Representative images of the medial tibial plateau stained with safranin O/methyl green to evaluate the pathological changes 8 weeks after IA injection of collagenase VII on day 1, and IA injections of vehicle or 10 μ M KGN on days 7 and 21. Scale bars, 100 μ m. (D) The medial tibial plateau joint score in the collagenase model, based on the OARSI (Osteoarthritis Research Society International) scoring system. (E) The circulating COMP levels in peripheral blood were determined on days 13 and 56 after collagenase VII treatment ($n = 15$ mice). (F) Representative images of the lateral tibial plateau stained with safranin O to evaluate the pathological changes 4 weeks after surgical transection of the anterior cruciate ligament, medial collateral ligament, and medial meniscotibial ligament. Vehicle and 100 μ M KGN IA treatment were given on days 7, 14, and 21 after surgery. Scale bars, 100 μ m. (G) The lateral tibial plateau joint score in the surgical model, based on the OARSI scoring system. (H) Cleaved collagen type II fragment levels in plasma on day 28 after surgery ($n = 15$ mice). (I) OA-induced joint pain was alleviated in KGN-treated animals as compared to vehicle-treated ones as monitored by incapacitation measurements on day 42 after surgery of the percentage of weight the mice distributed to each hind leg ($n = 10$ mice). In (G) to (I), asterisks indicate statistically significant differences between compound and vehicle treatments, * $P < 0.05$, ** $P < 0.01$, t test.

FLNA is core-binding factor β subunit (CBF β), which has recently been shown to bind to the hinge 2 and immunoglobulin-like repeat 24 region of FC-1 (19). We confirmed the association between CBF β and FC-1 (but not FC-2 or FC-3) in an *in vitro* pull-down experiment and observed that KGN blocks this interaction at its active concentrations (Fig. 3, D and E). The specific interaction between FLNA and CBF β was further confirmed in hMSC cell lysates by a coimmunoprecipitation assay (Fig. 3F) and could again be disrupted by KGN.

CBF β is the regulatory subunit of the heterodimeric core-binding factor transcription complex; the other subunit is one of the runt-related transcription factor (RUNX) family members, which include RUNX1, RUNX2, and RUNX3 (20). In the resting state, CBF β is sequestered in the cytoplasm by binding to its cytoplasmic partner, FLNA; upon activation, it dissociates from FLNA and translocates into the nucleus, where it binds the RUNX factors and regulates transcription (19). When hMSCs were treated

with 5 μ M KGN, CBF β nuclear localization was significantly increased (Fig. 4, A and B). We next overexpressed CBF β in hMSCs and saw that cells overexpressing CBF β showed increased chondrocyte differentiation as compared to empty vector-transfected cells (Fig. 4C and fig. S11). Moreover, knockdown of CBF β expression by shRNAs blocked KGN's effect on chondrocyte differentiation in hMSCs (Fig. 4D and fig. S11). Thus, KGN appears to induce chondrogenesis by regulating the nuclear localization of CBF β .

The RUNX proteins are highly regulated by complex signaling networks [IHH, fibroblast growth factor (FGF), WNT (21), and RUNX themselves (22)] in a context-dependent manner that correlates with their distinct roles in musculoskeletal development and maintenance. RUNX1 has been shown to play a critical role in chondrogenesis, chondrocyte proliferation, and survival (23, 24). RUNX2 is a key factor in osteogenesis (25–27) and also plays a pivotal role in chondrocyte hypertrophy (the terminal differentiation of chondrocytes often associated with OA). Knock-

down of RUNX2 diminishes bone formation and blocks chondrocyte hypertrophy, cartilage calcification, and the development of OA (28). Recently, evidence has also suggested a possible role for RUNX3 in chondrocyte differentiation (29). Microarray gene expression analysis revealed that 5 of the 39 genes affected by KGN (>1.5 fold at 6 or 24 hours) are associated with the RUNX1 network, including *DOX5*, *SPN*, and *THRAP3* (fig. S12) (30). In addition, *ANKRD1*, a downstream target gene of RUNX2, was down-regulated upon KGN treatment in hMSCs; and altered transcription of shared downstream target genes of RUNX1 and RUNX2 [e.g., *anaphase-promoting complex subunit 10* (*ANAPC10*)] was also observed. Quantitative RT-PCR analysis showed an interesting pattern of expression for RUNX family members and CBF β in hMSCs, chondrocytes, and osteoblasts: RUNX1 is highly expressed in all cell types, with slight up-regulation in chondrocytes; RUNX2 and RUNX3 are expressed at low levels in hMSCs, significantly up-regulated in osteoblasts, and almost

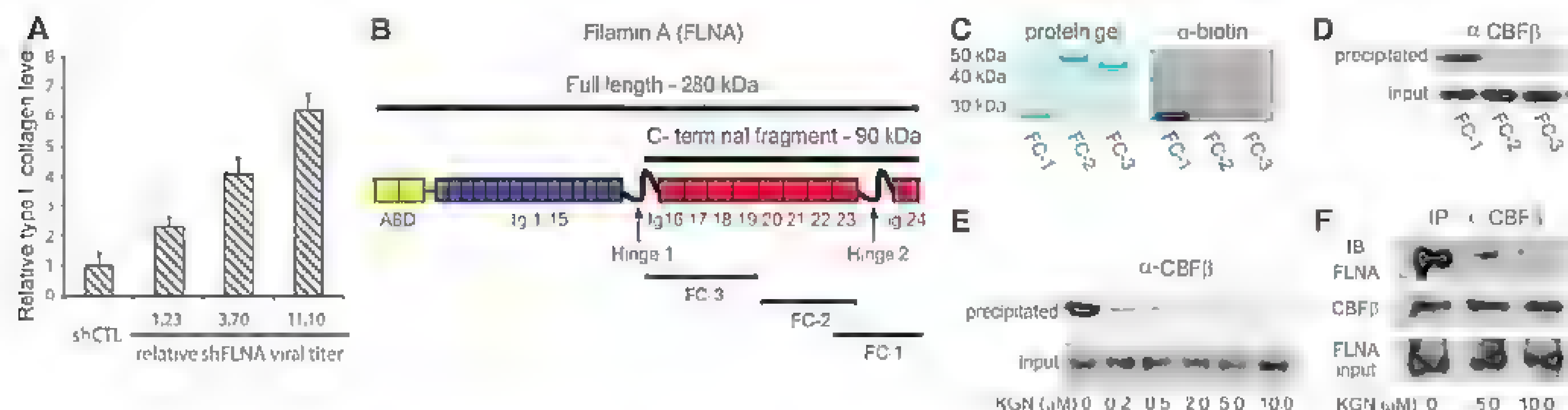


Fig. 3. KGN binds to the FC-1 fragment of FLNA and regulates its interaction with CBF β . (A) Knockdown of FLNA with shRNA-expressing lentiviral particles increased chondrocyte differentiation from hMSCs. Type II collagen expression levels were normalized to nontargeting shRNA control virus-infected cells ($n = 6$ experiments). (B) Human FLNA structure and fragment cloning. Fragments: FC-1, nucleotides 7264 to 7941 (relative to ATG start codon), contains immunoglobulin-like (Ig) repeat 23, hinge 2, and Ig repeat 24; FC-2, nucleotides 6391 to 7566, contains Ig repeats 20 to 23; FC-3, nucleotides 5275 to 6390, contains partial hinge 1 and Ig repeats 16 to 19.

ABD, actin-binding domain. (C) Western blotting shows the specific labeling of the FC-1 fragment but not the other two FLNA fragments by BKA (anti-biotin). (D) The specific interaction between the FC-1 fragment and CBF β was demonstrated by pull-down of purified recombinant CBF β (400 ng) using FLNA fragments fused to glutathione *S*-transferase. (E) KGN treatment disrupts the interaction between FC-1 and CBF β . (F) KGN disrupts the interaction between FLNA and CBF β in hMSC cell lysates. The FLNA-CBF β complex was immunoprecipitated with antibody to CBF β and probed with antibodies to FLNA and CBF β .

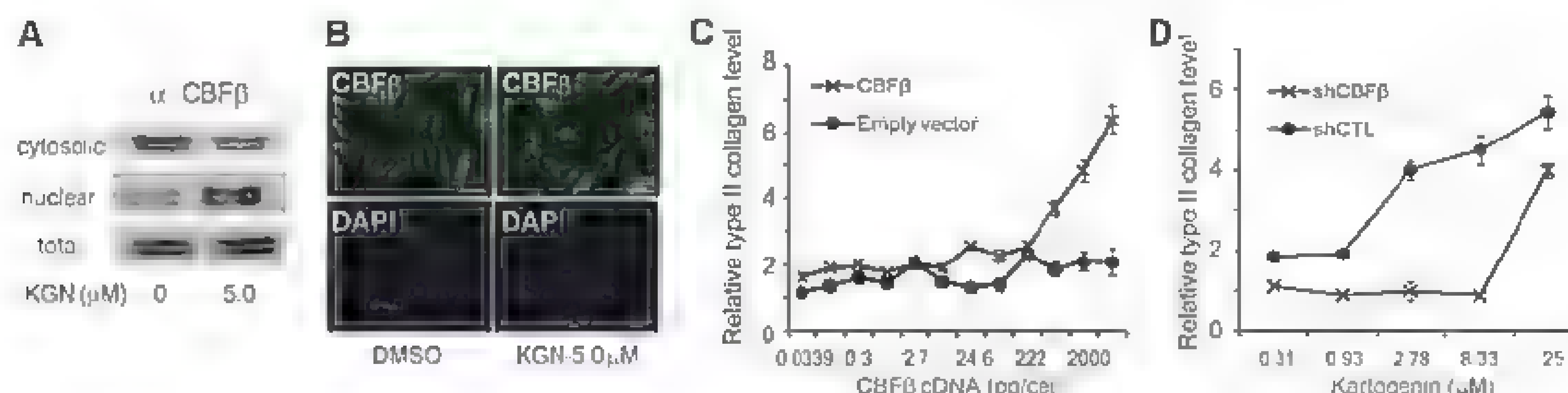


Fig. 4. KGN enhances the nuclear localization of CBF β and induces hMSC chondrocyte differentiation. (A and B) KGN treatment induces CBF β nuclear localization in hMSCs, as demonstrated by (A) nuclear fractionation followed by Western blotting and (B) fluorescent immunostaining. Scale

bars, 20 μ m. (C) CBF β overexpression mimics the effect of KGN in hMSCs ($n = 6$ experiments). (D) CBF β knockdown in hMSCs blocks chondrocyte differentiation induced by KGN with shRNA-expressing lentiviral particles ($n = 6$ experiments).

undetectable in chondrocytes; CBF β is expressed in all cell types at comparable levels (figs. S13 and S14). Fluorescent immunostaining of mouse joint tissue sections also showed coexpression of CBF β and RUNX1 in cartilage cells (fig. S15). These results are consistent with previous findings about the roles of the genes in chondrogenesis and osteogenesis, and lead us to speculate that RUNX1, rather than RUNX2 or RUNX3, is probably the downstream effector of KGN. When we knocked down RUNX1 expression in hMSCs with shRNAs, KGN-induced chondrocyte differentiation was blocked (fig. S16). Furthermore, *RUNX2* transcription has been shown to be suppressed by RUNX2 through an autoregulation mechanism in different types of cells (31). Given the fact that all RUNX family members recognize the same DNA sequence, it is plausible that the RUNX1-CBF β complex also suppresses *RUNX2* transcription, thus keeping RUNX2 at a relatively low level, which inhibits osteoblast and terminal chondrocyte differentiation.

The development of disease-modifying osteoarthritis drugs has to date focused on (i) slowing the erosion of cartilage by inhibiting matrix-degrading enzymes; (ii) protecting chondrocytes from catabolic activity with antagonists of interleukin-1 β and TNF- α or inhibitors of p38, MEK, and caspases; and (iii) the development of anabolic agents, such as FGF18, which promote chondrocyte and chondrocyte progenitor cell proliferation (3, 32, 33). This work is based on small-molecule effectors of endogenous stem cell populations and may prove synergistic with other

efforts currently in development. KGN functions by binding FLNA and disrupting its interaction with CBF β , which in turn modulates the RUNX family of transcription factors. Recently, two other examples have been reported (34, 35) in which small druglike molecules selectively regulate transcription factor subcellular localization and downstream transcriptional activities. Thus, small molecules appear to be useful tools for selectively modulating gene transcription in cells and whole organisms, and in this case have provided new insights into chondrocyte biology that may lead to novel therapies for the treatment of this degenerative disease.

References and Notes

1. J. Y. Reginster, N. G. Khaltayev, *Rheumatology (Oxford)* **41** (suppl. 1), 1 (2002).
2. M. B. Goldring, S. R. Goldring, *Ann. N.Y. Acad. Sci.* **1192**, 230 (2010).
3. D. J. Hunter, *Nat. Rev. Rheumatol.* **7**, 13 (2011).
4. P. Charbord, *Hum. Gene Ther.* **21**, 1045 (2010).
5. M. F. Pittenger et al., *Science* **284**, 143 (1999).
6. S. P. Grogan, S. Miyaki, H. Asahara, D. D. O. Lima, M. K. Lotz, *Arthritis Res. Ther.* **11**, R85 (2009).
7. S. Koelling et al., *Cell Stem Cell* **4**, 324 (2009).
8. G. N. Smith Jr., *Front. Biosci.* **11**, 3081 (2006).
9. M. Rutgers, D. B. Saris, W. J. Dhert, L. B. Creemers, *Arthritis Res. Ther.* **12**, R114 (2010).
10. S. J. Read, A. Dray, *Expert Opin. Investig. Drugs* **17**, 619 (2008).
11. P. M. van der Kraan, E. L. Vitters, L. B. van de Putte, W. B. van den Berg, *Am. J. Pathol.* **135**, 1001 (1989).
12. S. S. Glasson, T. J. Blanchet, E. A. Morris, *Osteoarthritis Cartilage* **15**, 1061 (2007).
13. K. P. Pritzker et al., *Osteoarthritis Cartilage* **14**, 13 (2006).
14. L. S. Lohmander, T. Sakne, D. K. Heidegård, *Ann. Rheum. Dis.* **53**, 8 (1994).
15. M. Rejman et al., *Arthritis Rheum.* **50**, 2471 (2004).

16. Y. Wang et al., *Oncogene* **26**, 6061 (2007).
17. J. B. Gorlin et al., *J. Cell Biol.* **111**, 1089 (1990).
18. J. T. Connelly, A. J. Garcia, M. E. Levenston, *J. Cell. Physiol.* **217**, 145 (2008).
19. N. Yoshida et al., *Mol. Cell. Biol.* **25**, 1003 (2005).
20. N. Adya, L. H. Castilla, P. P. Liu, *Semin. Cell Dev. Biol.* **11**, 361 (2000).
21. T. Komori, *J. Cell. Biochem.* **112**, 750 (2011).
22. D. Levanon, Y. Groner, *Oncogene* **23**, 4211 (2004).
23. Y. Wang et al., *J. Bone Miner. Res.* **20**, 1624 (2005).
24. S. Wotton et al., *Oncogene* **27**, 5856 (2008).
25. G. S. Stein et al., *Oncogene* **23**, 4315 (2004).
26. T. Komori et al., *Cell* **89**, 755 (1997).
27. F. Otto et al., *Cell* **89**, 765 (1997).
28. S. Kamekura et al., *Arthritis Rheum.* **54**, 2462 (2006).
29. O. Y. Soung et al., *J. Bone Miner. Res.* **22**, 1260 (2007).
30. P. M. van der Kraan, E. N. Baney Davidson, W. B. van den Berg, *Arthritis Res. Ther.* **12**, 201 (2010).
31. H. Drissi et al., *J. Cell. Biochem.* **86**, 403 (2002).
32. M. K. Lotz, V. B. Kraus, *Arthritis Res. Ther.* **12**, 211 (2010).
33. J. Clouet et al., *Drug Discov. Today* **14**, 913 (2009).
34. S. Zhu et al., *Cell Stem Cell* **4**, 416 (2009).
35. H. Wardak et al., *Proc. Natl. Acad. Sci. U.S.A.* **107**, 16542 (2010).

Acknowledgments: This work was funded by grants from the California Institute for Regenerative Medicine (R2-01829 to P.G.S.). We are grateful to J. Walker for help in gene expression analysis. Microarray data have been deposited in the National Center for Biotechnology Information's Gene Expression Omnibus with accession number GSE35546. A patent application has been submitted by the authors on the use of kartogenin for chondrogenesis.

Supplementary Materials

www.sciencemag.org/content/full/science.1215157/DC1
Materials and Methods
Figs. S1 to S16

11 October 2011; accepted 3 March 2012
Published online 5 April 2012;
10.1126/science.1215157

Differential Diffusivity of Nodal and Lefty Underlies a Reaction-Diffusion Patterning System

Patrick Müller,^{1*} Katherine W. Rogers,¹ Ben M. Jordan,^{2†} Joon S. Lee,^{1†} Drew Robson,¹ Sharad Ramanathan,^{1,3} Alexander F. Schier^{1,3*}

Biological systems involving short-range activators and long-range inhibitors can generate complex patterns. Reaction-diffusion models postulate that differences in signaling range are caused by differential diffusivity of inhibitor and activator. Other models suggest that differential clearance underlies different signaling ranges. To test these models, we measured the biophysical properties of the Nodal/Lefty activator/inhibitor system during zebrafish embryogenesis. Analysis of Nodal and Lefty gradients revealed that Nodals have a shorter range than Lefty proteins. Pulse-labeling analysis indicated that Nodals and Leftys have similar clearance kinetics, whereas fluorescence recovery assays revealed that Leftys have a higher effective diffusion coefficient than Nodals. These results indicate that differential diffusivity is the major determinant of the differences in Nodal/Lefty range and provide biophysical support for reaction-diffusion models of activator/inhibitor-mediated patterning.

In 1952, Alan Turing put forward the reaction-diffusion model, in which two interacting and diffusing species of molecules can generate complex patterns (1). Gierer and Meinhardt postulated that pattern formation in reaction-diffusion

models requires a short-range activator that enhances both its own production and that of a long-range inhibitor (2) (Fig. 1A). Despite the prominence of reaction-diffusion models and the widespread occurrence of short-range acti-

vators and long-range inhibitors in development (3–10), it is unclear how differences in activator and inhibitor ranges arise in vivo. The classic reaction-diffusion models postulate that the inhibitor is more diffusive than the activator (text S1), but more recent studies suggest that differential signal clearance might be a major determinant of differences in signaling range (11–18) (Fig. 1B). This question has not been resolved because the biophysical properties of diffusion and clearance have not been measured for any activator/inhibitor pair.

The transforming growth factor- β superfamily signals Nodal and Lefty constitute an activator/inhibitor-based system in animals as different as sea urchin and mouse (3–5, 16, 18–22) (text S2). Nodals activate signaling during mesendoderm induction and left-right patterning,

¹Department of Molecular and Cellular Biology, Harvard University, Cambridge, MA 02138, USA. ²Department of Organismic and Evolutionary Biology, Harvard University, Cambridge, MA 02138, USA. ³FAS Center for Systems Biology and Harvard Stem Cell Institute, Harvard University, Cambridge, MA 02138, USA.

*To whom correspondence should be addressed. E-mail: pmueller@fas.harvard.edu (P.M.); schier@fas.harvard.edu (A.F.S.)

†These authors contributed equally to this work.

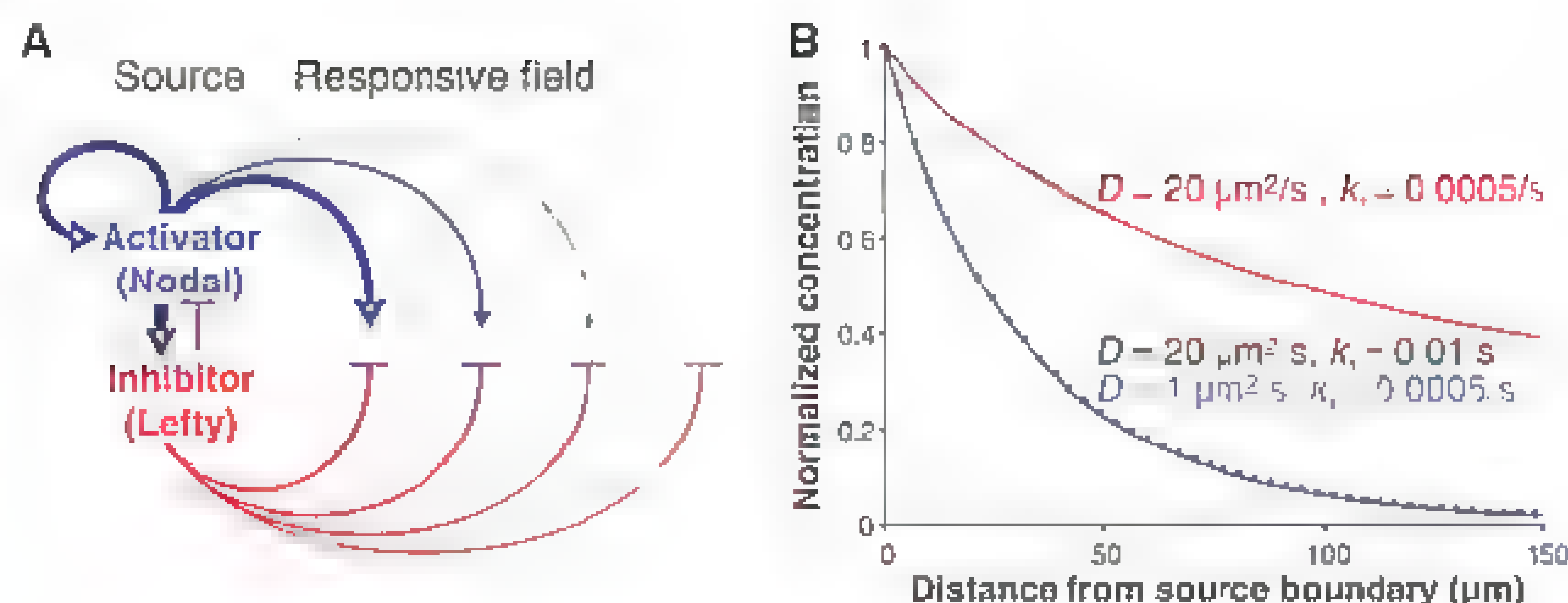
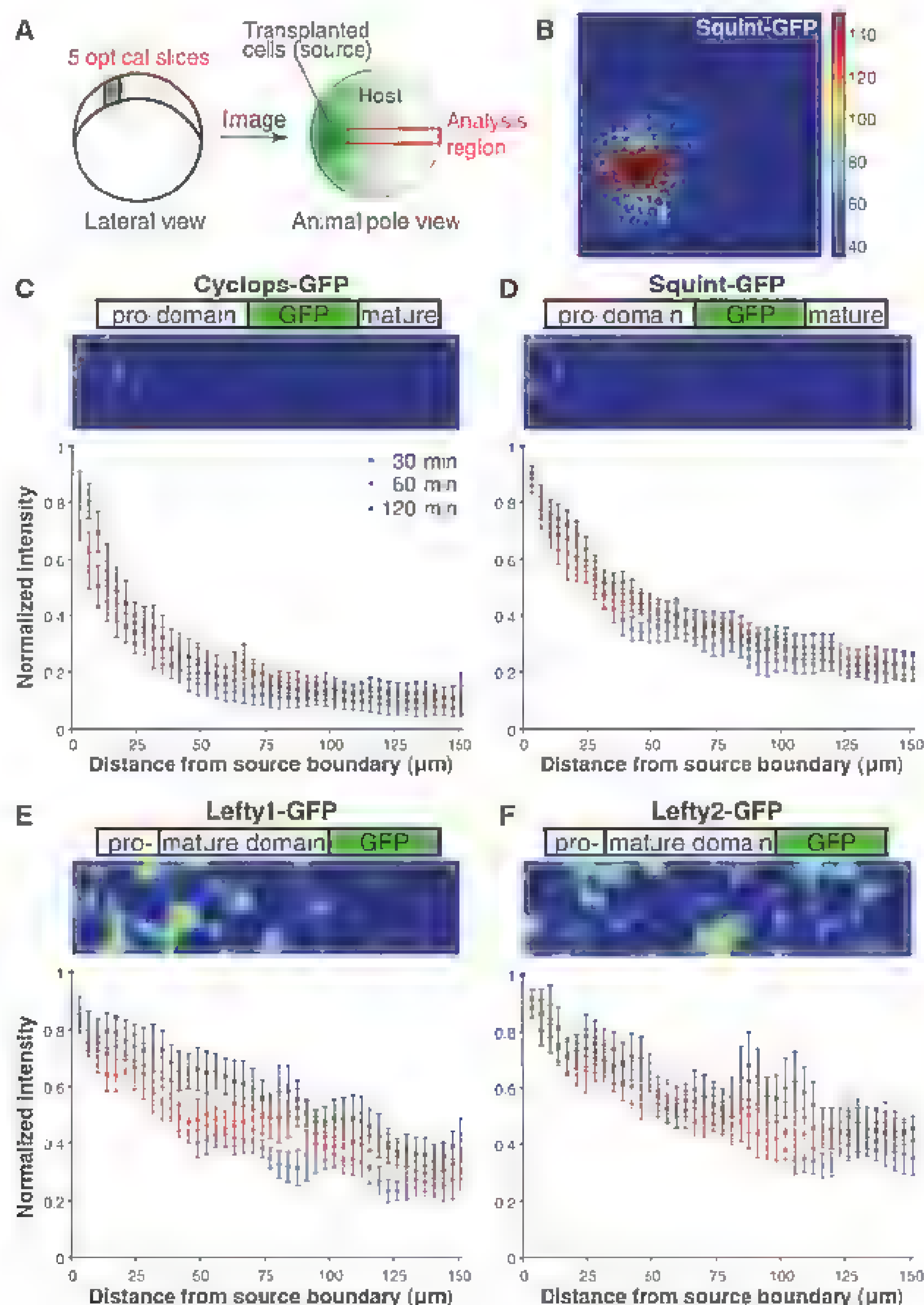


Fig. 1. Model of the Nodal/Lefty activator/inhibitor reaction-diffusion system and regulation of range. (A) In the source, Nodal signals (blue) activate their own expression as well as the expression of Lefty (red), which inhibits Nodal production. Nodal signaling in the responsive field is inhibited by the long-range inhibitor Lefty. (B) Distribution is controlled by both diffusivity, D , and clearance, k_1 . Highly mobile molecules that are rapidly cleared from the extracellular space (black circles) can form gradients similar to those formed by poorly diffusive molecules that are slowly cleared (blue). Decreasing the clearance of the more diffusive species results in a long-range gradient (red). Simulations were performed as described in text S7.

Fig. 2. Measurement of Nodal-GFP and Lefty-GFP distributions. (A) At late blastula stages, about 40 cells secreting Nodal-GFP or Lefty-GFP proteins were transplanted from donor embryos into wild-type hosts (text S4). The gradient profile was determined using a maximum-intensity projection of five confocal slices encompassing a depth of 20 μm (about one cell). (B) A representative projection is shown for Squint-GFP. (C to F) Construct schematic, representative maximum-intensity projection, and distribution profiles 30, 60, and 120 min after transplantation for Cyclops-GFP (C), Squint-GFP (D), Lefty1-GFP (E), and Lefty2-GFP (F). Embryos that did not undergo transplantation were used for background subtraction, and all intensities were normalized to the value most proximal to the source. Error bars indicate SE. Numbers of embryos analyzed at 30, 60, and 120 min after transplantation, respectively: for Cyclops-GFP, $n_{30} = 7$, $n_{60} = 7$, $n_{120} = 7$; for Squint-GFP, $n_{30} = 12$, $n_{60} = 17$, $n_{120} = 20$; for Lefty1-GFP, $n_{30} = 8$, $n_{60} = 8$, $n_{120} = 13$; for Lefty2-GFP, $n_{30} = 12$, $n_{60} = 10$, $n_{120} = 12$.



whereas Leftys block pathway activation. The Nodal/Lefty system fulfills two of the tenets of activator/inhibitor reaction-diffusion models: (i) Nodals are short- to mid-range activators that enhance their own expression, and (ii) Leftys are long-range inhibitors that are activated by Nodals (3, 5, 19, 22). Genetic and embryological studies in zebrafish have shown that during mesendoderm induction, the two Nodal signals Cyclops and Squint and the two Nodal signaling inhibitors Lefty1 and Lefty2 have different activity ranges: Cyclops is a short-range activator of mesendodermal gene expression, Squint acts at a medium range, and Lefty1 and Lefty2 are long-range inhibitors (6, 23). Moreover, these Nodal signals induce their own expression as well as the expression of Leftys (5, 19, 22) (Fig. 1A). However, the biophysical properties that control the different activity ranges of Nodals and Leftys are unknown. It therefore remains unclear whether

one of the central tenets of reaction-diffusion models—differential diffusivity of activator and inhibitor—is fulfilled in vivo (4–6, 15, 16, 19, 22, 24). To address this question, we performed measure-

ments of Nodal and Lefty distribution, clearance, and diffusivity during zebrafish embryogenesis.

To visualize Nodal and Lefty proteins in vivo, we generated active fusions of green fluorescent

protein (GFP) with Cyclops, Squint, Lefty1, and Lefty2 (see figs. S2 to S11 and texts S3 and S4 for analyses of fusion protein activity, processing, localization, and distribution). When expressed from a localized source in blastula embryos, the fusion proteins had activity ranges similar to those of their untagged counterparts (figs. S5 and S10). In vivo imaging revealed that the distribution profiles of the fusion proteins reflected their activity ranges: The gradient formed by Cyclops-GFP exhibited a punctate distribution and dropped steeply as the distance from the source increased, whereas the gradient formed by Squint-GFP was more diffuse and reached farther (Fig. 2, C and 2D). The distributions of Lefty1-GFP and Lefty2-GFP were more shallow and were long-range and super-long-range, respectively (Fig. 2, E and F).

To determine whether differential clearance underlies the different ranges of Nodal and Lefty signals, we developed a pulse-labeling assay to measure extracellular clearance rate constants. We fused the monomeric green-to-red photoconvertible protein Dendra2 (25) to Nodals and Leftys and uniformly expressed these active fusions in blastula embryos (figs. S2 to S10 and text S3). We then switched the fluorescent state of Dendra2 from green to red throughout the embryo and monitored the decrease in intensity of the extracellular red signal for 300 min (Fig. 3 and movie S1). By fitting the data with an exponential decay model, we obtained clearance rate constants (k_1) and calculated the inversely related extracellular half-lives, $\tau = \ln(2)/k_1$ (see figs. S12 to S16 and text S5 for control experiments and detailed measurements). We found half-lives of 95 to 218 min with clearance rate constants of $1.22 (\pm 0.13) \times 10^{-4}/s$ for Cyclops-Dendra2, $1.00 (\pm 0.06) \times 10^{-4}/s$ for Squint-Dendra2, $0.53 (\pm 0.05) \times 10^{-4}/s$ for Lefty1-Dendra2, and $0.69 (\pm 0.07) \times 10^{-4}/s$ for Lefty2-Dendra2 (Fig. 3B and fig. S12). Thus, protein half-lives increased only slightly as ranges increased, which suggests that differential clearance is only a minor contributor to the differences in Nodal and Lefty range.

To determine whether differential diffusivity underlies the different ranges of Nodals and Leftys, we measured their effective diffusion coefficients using fluorescence recovery after photobleaching (FRAP) (12, 13, 18, 26). FRAP assays can measure diffusivity over developmentally relevant length and time scales by observing the diffusion-dependent reappearance of fluorescence after photobleaching (text S6). To perform FRAP assays, we ubiquitously expressed Nodal-GFP and Lefty-GFP fusion proteins in blastula embryos and photobleached a cuboidal volume containing several hundred cells. We then monitored the recovery of fluorescence in the bleached region over a period of 50 min (3000 s) (Fig. 4A and figs. S18 to S23). Photobleaching was nearly uniform (fig. S22) and had no apparent toxic effects on the embryo, and fluorescence recovery occurred from regions adjacent to the bleached window (fig. S23). We determined the effective

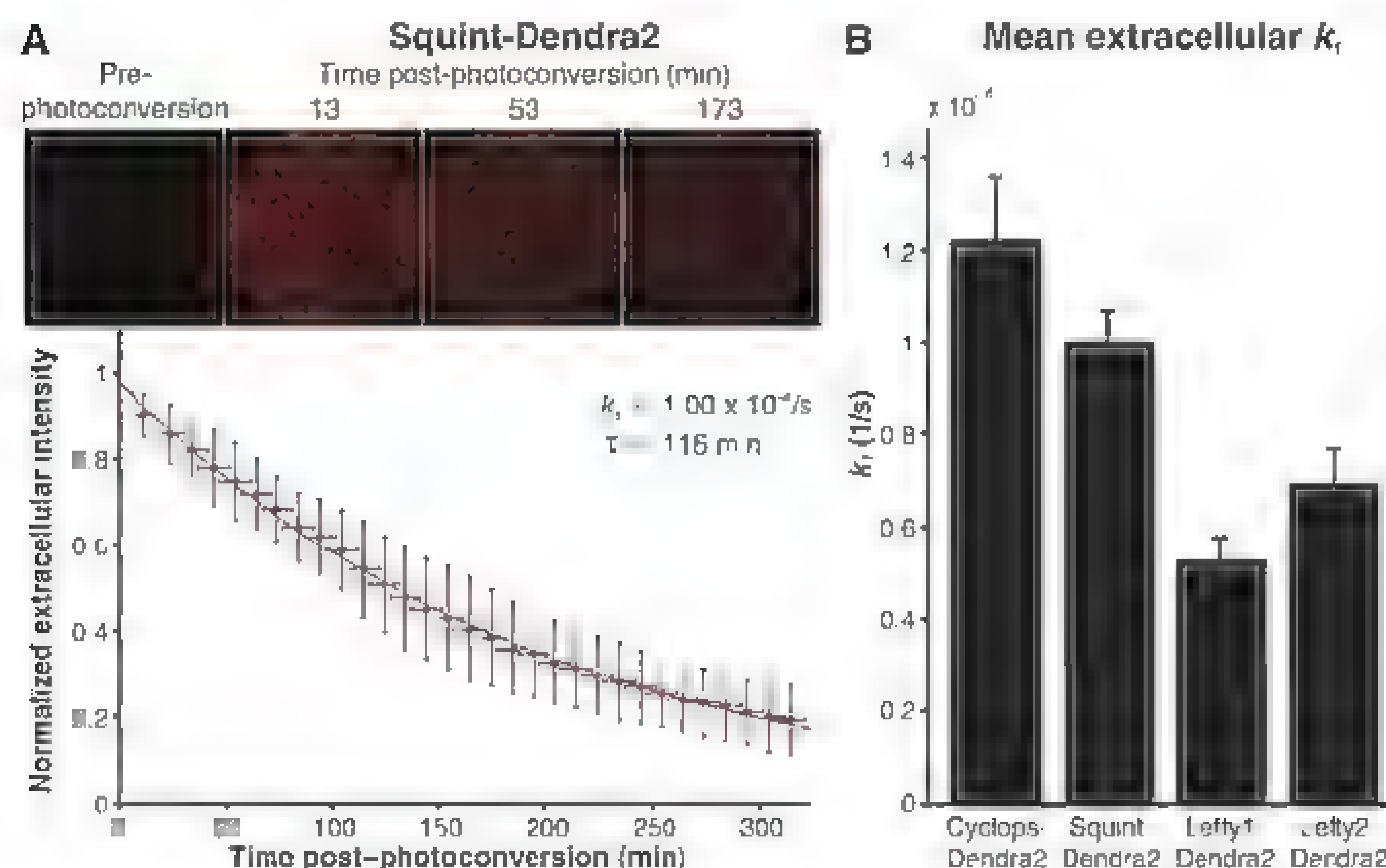


Fig. 3. Measurement of extracellular clearance rate constants. (A) Uniformly expressed Nodal-Dendra2 or Lefty-Dendra2 fusion proteins were photoconverted using an ultraviolet pulse. The average extracellular photoconverted Dendra2 intensity was monitored over time and used to determine the clearance rate constants (k_1) and half-lives ($\tau = \ln(2)/k_1$) by fitting exponential functions to data from individual embryos (text S5). The normalized average intensity from Squint-Dendra2 experiments at 10-min intervals (black, $n = 11$) is shown fitted with an exponential function (red). Error bars indicate SD. See fig. S12 for Cyclops-Dendra2, Lefty1-Dendra2, and Lefty2-Dendra2 results. (B) Summary of mean extracellular k_1 values. Error bars indicate SE.

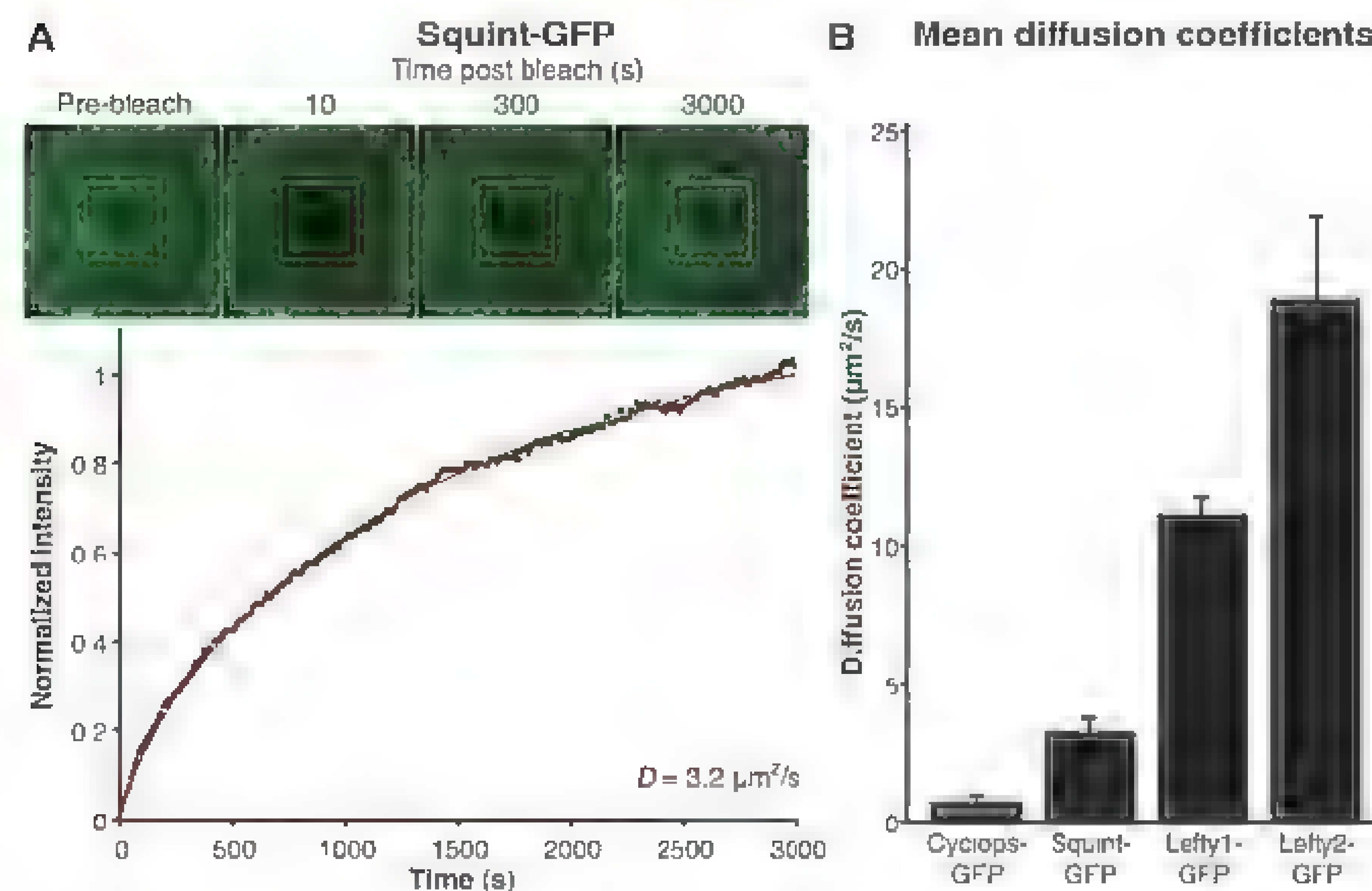


Fig. 4. Measurement of effective diffusion coefficients. (A) Uniformly expressed Nodal-GFP or Lefty-GFP fusion proteins were locally photobleached (yellow boxes) at blastula stages. Fluorescence recovery was monitored over time, and the effective diffusion coefficient D was determined by fitting the resulting recovery profile (black) with simulated recovery curves (red) that were numerically generated using a model that includes diffusion, production, and clearance in a three-dimensional embryo-like geometry (text S6). Results for an individual Squint-GFP embryo are shown. See fig. S18 for Cyclops-GFP, Lefty1-GFP, and Lefty2-GFP results. (B) Summary of mean diffusion coefficients. Error bars indicate SE.

diffusion coefficients of the fusion proteins by fitting a three-dimensional diffusion model to recovery profiles (text S6 and figs. S19 to S21). We obtained effective diffusion coefficients of $0.7 \pm 0.2 \mu\text{m}^2/\text{s}$ for Cyclops-GFP, $3.2 \pm 0.5 \mu\text{m}^2/\text{s}$ for Squint-GFP, $11.1 \pm 0.6 \mu\text{m}^2/\text{s}$ for Lefty1-GFP, and $18.9 \pm 3.0 \mu\text{m}^2/\text{s}$ for Lefty2-GFP (Fig. 4B, figs. S18 to S23, and text S6). Thus, increased protein diffusivities reflect increased ranges, indicating that differential diffusivity is a major contributor to the differences in Nodal and Lefty range.

To test whether the experimentally determined values for diffusivity and clearance accurately predict the measured distribution profiles, we numerically simulated signal secretion from a localized source, diffusion, and clearance (12, 14, 26) in a three-dimensional geometry appropriate for blastula embryos (text S7). Using the measured values for diffusivity and clearance, these simulations yielded distribution profiles similar to the experimentally determined protein distributions (fig. S26) and thus provided independent support for the validity of the experimental approaches.

Our results have two major implications. First, differential diffusivity underlies differences in activator/inhibitor range. The differences in range (Cyclops < Squint < Lefty1 < Lefty2) are reflected in the differences in effective diffusion coefficients (Cyclops < Squint < Lefty1 < Lefty2). There is a similar trend in half-lives, but the differences in diffusivity are much more pronounced than the differences in clearance. During embryogenesis, the sources of Nodal and Lefty overlap, but Nodal signaling is active near the source and is inhibited by Lefty farther away. Our results suggest that the lower mobility of Nodal allows its accumulation close to the site of secretion, whereas the high mobility of Lefty leads to rapid long-range dispersal and prevents accumulation near the source. Thus, the differential diffusivity of Nodal and Lefty signals serves as the biophysical basis for the spatially restricted induction of cell fates during embryogenesis.

Second, the previously described network topology of the Nodal/Lefty system and the biophysical properties of Nodals and Leftys measured here support the activator/inhibitor reaction-diffusion model of morphogenesis: A less diffusive activator (Nodal) induces both its own production and that of a more diffusive inhibitor (Lefty) (3, 4). The Nodal/Lefty reaction-diffusion system is further constrained by pre-patterns and rapid cell fate specification; thus, the system results in graded pathway activation during mesendoderm induction and exclusive pathway activation on the left during left-right specification (see text S2 for detailed discussion). Mathematical models have postulated that the inhibitor in reaction-diffusion systems must have a higher diffusion coefficient than the activator. Several models suggest that clearance-normalized inhibitor and activator diffusion coefficients differ by a factor of at least 6, that is, $\mathcal{R} = (D/k_1)_{\text{inhibitor}}/(D/k_1)_{\text{activator}} > 6$ (8, 16, 27–29).

The average ratio of the normalized diffusivities of Leftys and Nodals measured here is $\mathcal{R} \approx 14$, providing biophysical support for these modeling studies (see text S8 for comparison of reaction-diffusion systems). The different diffusivities in the Nodal/Lefty biological system have counterparts in chemical reaction-diffusion systems. For example, patterns can be generated in a starch-loaded gel by combining an activator (iodide) with an inhibitor (chlorite) in the presence of malonic acid (30). In this *in vitro* system, diffusion of the activator is hindered by binding to the starch matrix and is thought to result in a higher (factor of ~ 15) diffusivity of the inhibitor. These models and our measurements raise the possibility that differential binding interactions and a ratio of at least a factor of 5 to 15 of inhibitor and activator diffusivities might be a general feature of reaction-diffusion-based patterning.

References and Notes

1. A. M. Turing, *Philos. Trans. R. Soc. London Ser. B* **237**, 37 (1952).
2. A. Gierer, H. Meinhardt, *Kybernetik* **12**, 30 (1972).
3. S. Kondo, T. Miura, *Science* **329**, 1616 (2010).
4. H. Meinhardt, *Cold Spring Harb. Perspect. Biol.* **1**, a001362 (2009).
5. H. Shiratori, H. Hamada, *Development* **133**, 2095 (2006).
6. Y. Chen, A. F. Schier, *Curr. Biol.* **12**, 7124 (2002).
7. D. E. Klein, V. M. Nappi, G. T. Reeves, S. Y. Shvartsman, M. A. Lemmon, *Nature* **430**, 1040 (2004).
8. S. Sick, S. Reinker, J. Timmer, T. Schlake, *Science* **314**, 1447 (2006).
9. D. Ben-Zvi, B. Z. Shilo, A. Fainsod, N. Barkai, *Nature* **453**, 1205 (2008).
10. A. D. Economou et al., *Nat. Genet.* **44**, 348 (2012).
11. P. Müller, A. F. Schier, *Dev. Cell* **21**, 145 (2011).
12. A. Kicheva et al., *Science* **315**, 521 (2007).
13. O. Wartlick et al., *Science* **331**, 1154 (2011).
14. S. R. Yu et al., *Nature* **461**, 533 (2009).

15. J. A. Le Good et al., *Curr. Biol.* **15**, 31 (2005).
16. T. Nakamura et al., *Dev. Cell* **11**, 495 (2006).
17. S. Zhou et al., *Curr. Biol.* **10.1016/j.cub.2012.02.065** (2012).
18. K. W. Rogers, A. F. Schier, *Annu. Rev. Cell Dev. Biol.* **27**, 377 (2011).
19. A. F. Schier, *Cold Spring Harb. Perspect. Biol.* **1**, a003459 (2009).
20. V. Duboc, F. Lapraz, L. Besnardeau, T. Lepage, *Dev. Biol.* **320**, 49 (2008).
21. C. Grande, N. H. Paley, *Nature* **457**, 1007 (2009).
22. M. M. Shen, *Development* **134**, 1023 (2007).
23. Y. Chen, A. F. Schier, *Nature* **411**, 607 (2001).
24. L. Marjoram, C. Wright, *Development* **138**, 475 (2011).
25. L. Zhang et al., *Bioelectrochem.* **42**, 446, 443, 450 (2007).
26. T. Gregor, E. F. Wieschaus, A. P. McGregor, W. Bialek, D. W. Tank, *Cell* **130**, 141 (2007).
27. M. I. Granero, A. Porat, D. Zanacca, *J. Math. Biol.* **4**, 21 (1977).
28. S. Kondo, R. Asai, *Nature* **376**, 765 (1995).
29. M. Yamauchi, E. Yoshimoto, S. Kondo, *Proc. Natl. Acad. Sci. U.S.A.* **104**, 4790 (2007).
30. I. Lengyel, I. R. Epstein, *Science* **251**, 650 (1991).

Acknowledgments: We thank X. Zhang for help with the cloning of Cyclops constructs, H. Othmer and A. Lander for helpful discussions, J. Dubrèlle for discussions and primers for quantitative reverse transcript on polymerase chain reaction, and S. Mango for comments on the manuscript. Supported by European Molecular Biology Organization and Human Frontier Science Program (HFSP) Long-Term Fellowships (P.M.), the NSF Graduate Research Fellowship Program (K.W.R.), N.H. grant 5R01GM56211, and HFSP grant RGP0066/2004-C.

Supplementary Materials

www.sciencemag.org/cgi/content/full/science.1221920/DC1

Texts S1 to S8

Tables S1 to S8

Figs. S1 to S26

Movie S1

References (31–109)

14 March 2012; accepted 5 April 2012

Published online 12 April 2012.

10.1126/science.1221920

Mechanical Control of Morphogenesis by Fat/Dachsous/Four-Jointed Planar Cell Polarity Pathway

Floris Bosveld,^{1*} Isabelle Bonnet,^{1*} Boris Guirao,^{1*} Sham Tlili,^{1†} Zhimin Wang,¹ Ambre Petitalot,¹ Raphaël Marchand,¹ Pierre-Luc Bardet,¹ Philippe Marcq,² François Graner,¹ Yohanns Bellaïche^{1‡}

During animal development, several planar cell polarity (PCP) pathways control tissue shape by coordinating collective cell behavior. Here, we characterize by means of multiscale imaging epithelium morphogenesis in the *Drosophila* dorsal thorax and show how the Fat/Dachsous/Four-jointed PCP pathway controls morphogenesis. We found that the proto-cadherin Dachsous is polarized within a domain of its tissue-wide expression gradient. Furthermore, Dachsous polarizes the myosin Dachs, which in turn promotes anisotropy of junction tension. By combining physical modeling with quantitative image analyses, we determined that this tension anisotropy defines the pattern of local tissue contraction that contributes to shaping the epithelium mainly via oriented cell rearrangements. Our results establish how tissue planar polarization coordinates the local changes of cell mechanical properties to control tissue morphogenesis.

Tissue morphogenesis requires the coordination of cell behaviors during development. Planar cell polarity (PCP) pathways, which coordinate the polarization of cells in the

tissue plane, have been shown to play a fundamental role in morphogenesis of vertebrates and invertebrates (1). It remains largely unknown how PCP pathways control local cell mechan-

ical properties to drive global tissue deformation. The Fat/Dachsous(Ds)/Four-jointed(Fj) PCP pathway plays fundamental roles in the regulation of tissue growth, the orientation of cell polarity across the tissue, and the regulation of morphogenesis (1, 2). *fat* and *ds* encode proto-cadherins, whereas *fj* encodes a Golgi kinase modulating Fat/Ds binding (3–8). In many *Drosophila* tissues, *ds* and *fj* are expressed in tissue-wide opposing gradients (4, 5, 9, 10). Fat and Ds are reported to be homogeneous at the cell membrane (10, 11). Yet, the heterophilic binding of Fat and Ds between adjacent cells is proposed to generate

a tissue-wide polarity (7, 8, 10, 12–15). Through a poorly understood mechanism involving Fat signaling and the DHHC palmitoyltransferase Approximated (16), this polarity promotes the asymmetric distribution of the myosin Dachs, which controls division orientation and apical cell size (12, 16–19). The role of the Fat/Ds/Fj pathway in tissue morphogenesis has been studied by using indirect measurements such as the shape of clones and division orientation (19, 20), conversely, measurements of tissue dynamics have so far characterized its role in tissue rotation (21). Here, we assessed whether, where, and how the Fat/Ds/Fj pathway affects local cell mechanical properties to drive tissue deformations.

We implemented a multiscale imaging method to record morphogenesis of the *Drosophila* dorsal thorax during metamorphosis (22). This monolayered epithelium is composed of a posterior region, the scutellum, and of a large anterior region, the scutum (Fig. 1A and fig. S1, A and B). Cells were labeled with E-Cadherin: green fluorescent protein (GFP), and the tissue was imaged from 11 hours after pupa formation

(hAPF) to 36 hAPF by acquiring high-resolution three-dimensional stacks tiling the thorax at each time-point (Fig. 1A and movie S1). This multi-scale imaging enabled us to follow $\sim 10^4$ cells over several cell cycles with unprecedented dynamics: 5 min resolution over 26 hours of development and $0.32 \mu\text{m}$ resolution over the $\sim 750 \times 700 \mu\text{m}^2$ of the tissue. At the cell-scale, the spatial and temporal resolutions facilitated the determination and the tracking of cell apex areas, cell shapes, divisions, cell rearrangements, and apoptoses (Fig. 1, B to D, fig. S1, C and D; and movie S2). At the tissue scale, we measured local tissue flow over the whole tissue by means of image correlation, using a length scale of 10 to 20 cells and a time scale of 2 hours. This revealed the different periods of development (fig. S2 and movie S3). In particular, between 17:20 and 21:20 hAPF the velocity map showed morphogenetic movements both in the scutum and the scutellum (Fig. 1E, shaded regions). This tissue flow promoted tissue contraction and elongation in the lateral scutum and the medial scutellum, resulting in their anterior-posterior and medial-

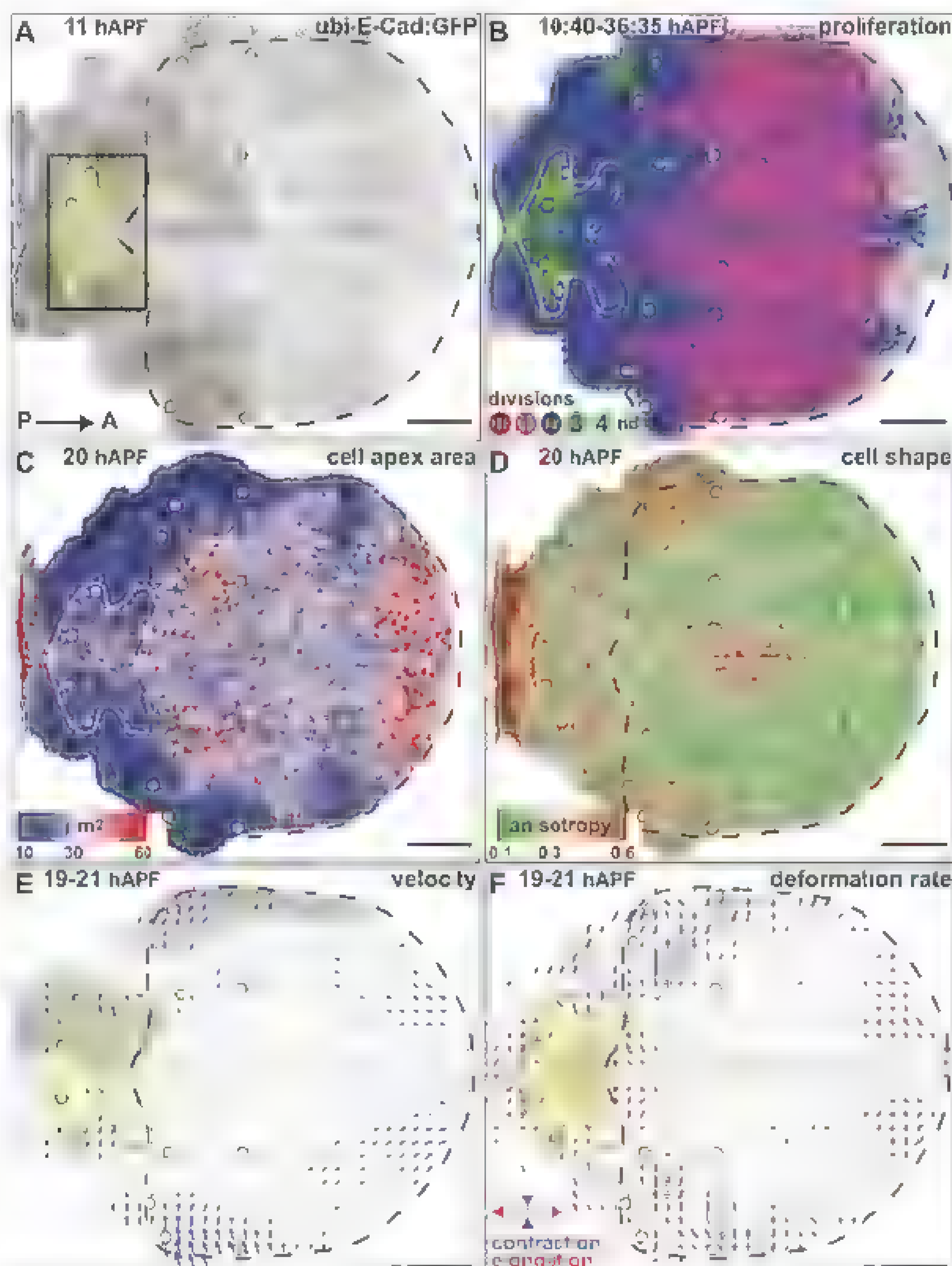
¹Polarity, Division and Morphogenesis Team, Institut Curie, CNRS UMR 3215, INSERM U934, 26 Rue d'Ulm, 75248 Paris Cedex 05, France. ²Laboratoire Physico-Chimie Curie, Institut Curie, CNRS UMR 168, Université Pierre et Marie Curie, 26 Rue d'Ulm, 75248 Paris Cedex 05, France.

*These authors contributed equally to this work.

†Present address: Matière et Systèmes Complexes, Université Paris Diderot, CNRS UMR 7057, 10 Rue Alice Domon et Léonie Duquet, 75205 Paris Cedex 13, France.

‡To whom correspondence should be addressed. E-mail: yohannis.bellard@cne.fr

Fig. 1. The *Drosophila* dorsal thorax as a system for morphogenesis. In all figures, yellow circles, macrochaetae; cyan dashed line, midline. (A) Dorsal thorax tissue labeled with E-Cad:GFP. Yellow region, scutellum; dashed black line, scutum. The black box cut by the midline defines the two “hemiscutella”. (B to D) Maps of proliferation (B), apex area (C), and anisotropy (D), defined as 1 minus the ratio of minor and major axes of the fitting ellipse. White cells are sensory organ precursor cells. (E) Velocity field averaged between 19 and 21 hAPF, represented as arrows. Gray regions are scutum and scutellum flows. (F) Deformation rates averaged between 19 and 21 hAPF, represented as ellipses. Red, elongation; Blue, contraction. Anterior (A). Posterior (P). Scale bars, $100 \mu\text{m}$, $9 \times 10^{-2} \mu\text{m}/\text{min}$ [(E), blue arrow], $2.4 \times 10^{-3} \text{min}^{-1}$ [(F), blue bar].



lateral elongations, respectively (Fig. 1F, scutellum in yellow). Collectively, our multiscale imaging and measurements provide a resource to investigate how signaling pathways control tissue morphogenesis.

Looking for regulators of these morphogenetic movements, we observed that *ds* and *fj* were both expressed in the scutellum (fig. S3), their opposing gradients forming an inverted V-shaped domain pointing toward the midline (thereafter referred to as A shape) in each hemi-scutellum (Fig. 2A and fig. S3). To understand the role of Fat/Ds/Fj signaling in tissue morphogenesis, we thus focused on the contraction and elongation taking place in the scutellum. The average tissue deformation rate map between 17:20 and 21:20 hAPF revealed that tissue deformation was not homogenous along the *ds* and *fj* gradients (Fig. 2B and fig. S4). This suggests that Fat/Ds/Fj activation might vary along the *ds* and *fj* gradients and emphasizes the need to define where the Fat/Ds/Fj pathway is active to investigate its role in morphogenesis. Given the evidence indicating that the subcellular localization of the myosin Dachs is controlled by Fat activity (17, 18, 23), we generated a Dachs:GFP (D:GFP) rescue construct and imaged it in the scutellum (movie S4). This revealed that (i) D:GFP was polarized in the A-shaped domain, where the opposing expression gradients of *ds* and *fj* meet (Fig. 2C); and (ii) within the regions of D:GFP planar polarization, cell boundaries enriched in D:GFP were aligned with each other, leading to D:GFP planar polarity lines (Fig. 2C, arrowheads).

Loss of *ds* or *fat* function as well as overexpression of *fj* disrupted D:GFP polarization (fig. S5, A to D). In agreement with the fact that D:GFP was mostly polarized in the region where the *ds* and *fj* gradients were opposed, clonal overexpression of either *ds* or *fj* induced repolarization of D:GFP only in regions where *fj* or *ds* were expressed, respectively (fig. S5, E and F). We then analyzed the subcellular localization of Fat, Ds, and Fj in relation with the Dachs polarization domain (fig. S6, A to C'') and established that Ds was polarized in regions where D:GFP was polarized (Fig. 2D and fig. S6, A to A''). Ds polarization required the *fj* gradient and Fat activity but was independent of Dachs activity (fig. S6, D to G'). Both Ds and D:GFP polarized toward high levels of *fj* expression and colocalized at the junctions (Fig. 3, A to C''). Furthermore, D:GFP can pull down the Flag:Ds intracellular domain (Fig. 3D). Altogether, our results revealed that Ds is planar polarized in the region where the opposing gradients of *ds* and *fj* meet. In turn, the interaction between Ds and Dachs promotes the polarization of Dachs (fig. S7, model).

The ectopic accumulation of Dachs reduces cell apex area, suggesting its possible implication in mechanical apex constriction (19). To directly assess whether the Fat/Ds/Fj pathway modulates cell mechanical properties via Dachs polarization, we performed laser ablation of junc-

tions and observed that the tension of junctions enriched in D:GFP was on average twofold higher as compared with junctions devoid of D:GFP (Fig. 3E, fig. S8, and movie S5). To confirm that Dachs polarization leads to anisotropic junction tension, we generated *fat* clones that induced an increased polarization and an accumulation of Dachs in mutant junctions facing the wild-type ones (fig. S9, A and C). Such junctions displayed an increased tension that depends on Dachs activity (fig. S9B). Last, MyosinII was not polarized at the *fat* clone boundaries and did not exhibit a stronger anisotropy than the one due to cell shape itself, along the Dachs polarity lines (fig. S9, D to H). This shows that Dachs polarity regulates the anisotropy of junction tension and suggests that the opposing *ds* and *fj* gradients generate a tension anisotropy along Ds and Dachs polarity lines.

Fig. 2. Ds and Fj expression gradients locally polarize Dachs and Ds. Panels show right side hemi-scutellum. (A) Quantification of the average gradients of Ds and *fj-lacZ* ($n = 7$ hemi-scutella). (B) Mean deformation rates ($n = 5$ hemi-scutella) between 17:20 and 21:20 hAPF. Deformation rates represented as ellipses. Red, elongation; Blue, contraction. (C and D) Dachs:GFP (D:GFP) and Ds localization. Arrowheads: D:GFP (C) and Ds (D) polarity lines. Yellow ellipses indicate average macrochaete positions \pm 5D. Scale bars, 10 μ m, 10^{-3} min $^{-1}$ [(B), blue bar].

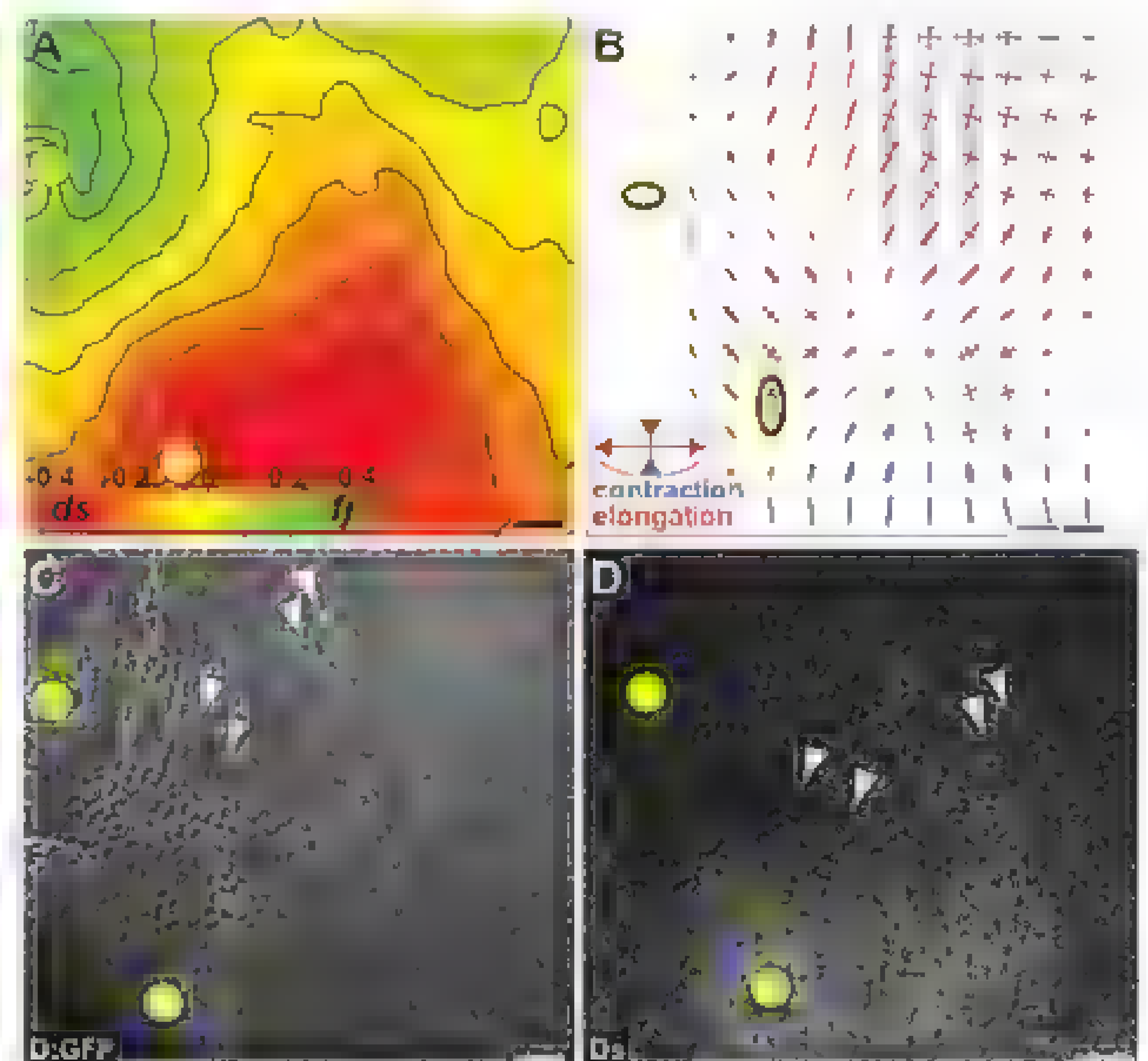
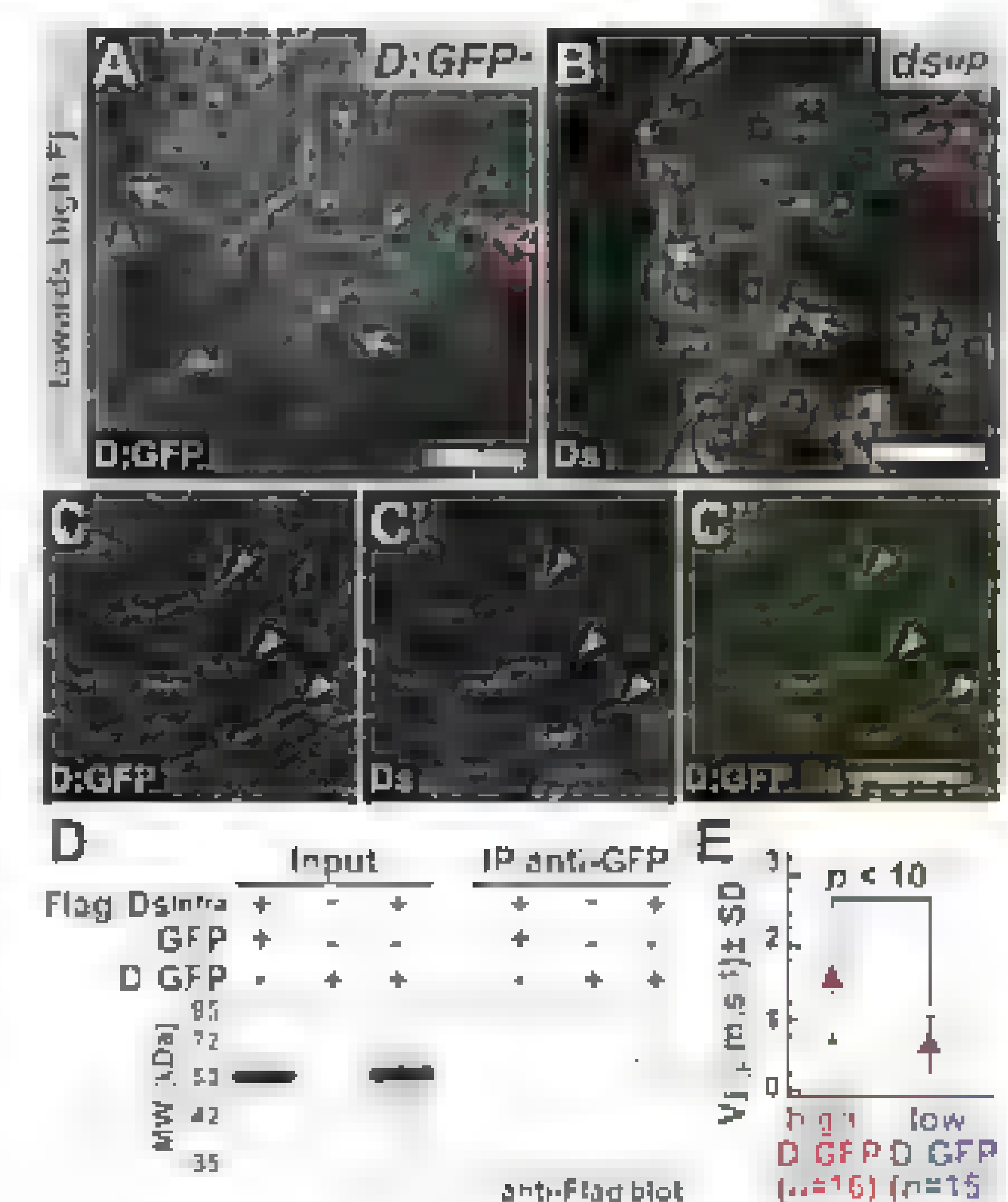


Fig. 3. Ds and Dachs colocalize and Dachs polarization is associated with tension anisotropy. (A and B) Cells located in a region of the Fj gradient expressing D:GFP and lacking D:GFP (D:GFP $^{-}$) (A), or overexpressing *ds* (*ds^{UP}* cells marked by mRFP, not shown) (B) accumulate D:GFP and Ds at junctions facing the higher Fj concentration (green arrowheads), whereas they are absent at junctions facing the lower Fj concentration (red arrowheads). Yellow arrows: direction of polarization. Yellow dots: *dsUP* cells abutting the wild-type (WT) cells (B). (C to C'') D:GFP [(C) and (C'')] and Ds [(C') and (C'')] colocalize (arrowheads). (D) Anti-Flag blot of GFP-immunoprecipitates from cells expressing Flag Ds intra and GFP; Flag:Ds intra ; Flag:Ds intra and D:GFP; Molecular weight (MW) markers in kilodaltons. Although a nonspecific GFP binding was observed, a larger amount of Flag:Ds intra was reproducibly coprecipitated with D:GFP. (E) Plot of the mean speed of vertex relaxation after ablation of junctions with high or low D:GFP. Scale bars: 10 μ m.

To investigate whether the tension anisotropy along the Dachs polarity lines control tissue morphogenesis, we developed a physical model that provides a general method to analyze the morphogenetic contribution of a specific signaling pathway within elaborate morphogenetic movements. In our case, it predicted that Dachs tension anisotropy is sufficient to modulate the local contraction rate (supplementary text). It provided a quantitative test to determine whether Dachs contributes to morphogenesis: Upon subtraction of the contraction rate of any mutant condition abrogating Dachs function or polarization from the contraction rate of the wild-type condition, the resulting difference in contraction rate is expected to be aligned with the Dachs polarity pattern.

To analyze the role of Dachs polarization, we first quantified the Dachs polarity pattern



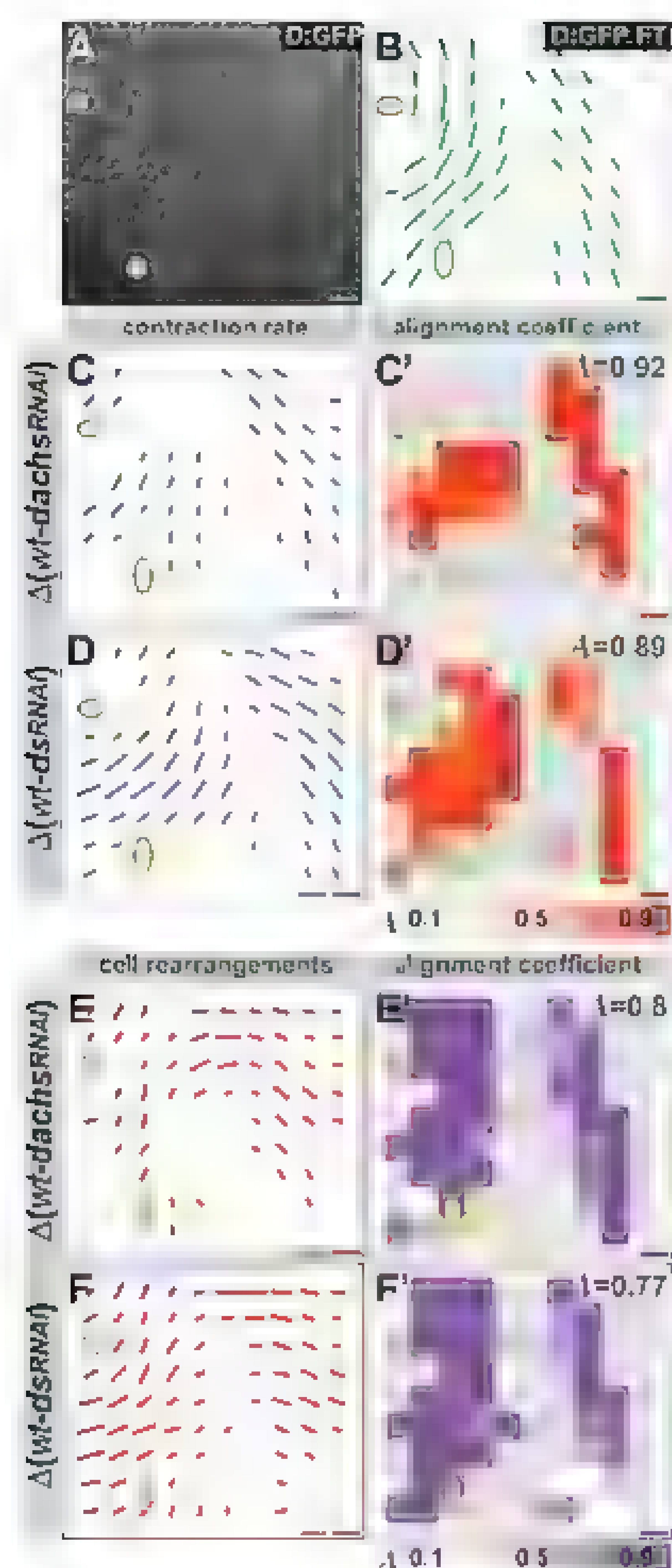


Fig. 4. Dachs polarity lines promote local contractions mainly via cell rearrangements. Averaged maps between 17:20 and 21:20 hAPF. (A and B) Localization of D:GFP (A) and map of D:GFP magnitude and anisotropy (B) quantified by Fourier Transform (FT, $n = 3$ hemi-scutella) (C to F) Maps of subtractions of *dachs*^{RNAi} ($n = 5$ hemi-scutella) from WT ($n = 11$ hemi-scutella) and of *ds*^{RNAi} ($n = 5$ hemi-scutella) from WT ($n = 11$ hemi-scutella) for contraction rates [(C) and (D)] and for cell rearrangements [(E) and (F)]. Bars indicate amplitudes and orientations of the differences of contraction rates or cell rearrangements. Maps of the alignment coefficients between the D:GFP FT pattern and the differences in contraction rates [(C') and (D')] or between the differences in contraction rates and cell rearrangements within the D:GFP FT pattern [(E') and (F')] for WT and *dachs*^{RNAi} [(C') and (E')] and for WT and *ds*^{RNAi} [(D') and (F')]. Local alignment scores [(C') and (D'), orange; (E') and (F'), purple] go from 0 (fully anticorrelated), to 1 (fully correlated), through 0.5 (noncorrelated). Significant data are green (B), blue [(C) and (D)], and red [(E) and (F)] bars; other are gray bars [(B) to (F)]. The average score A is calculated over nongray regions. Scale bars, 10 μm , $5.5 \times 10^{-4} \text{ min}^{-1}$ [(C) and (D), blue bars], $1 \mu\text{m}^2 \text{ min}^{-1}$ [(E) and (F), red bars].

(Fig. 4, A and B, green bars, and fig. S10). We then knocked down Dachs or Ds function by expressing *dachs* (*dachs*^{RNAi}) or *ds* (*ds*^{RNAi}) hairpins during pupal development and averaged between 17:20 and 21:20 hAPF the map of differences of the local contraction rates between wild-type and *dachs*^{RNAi} or between wild-type and *ds*^{RNAi} pupae. We observed significant differences in the local contraction rates between wild-type and *dachs*^{RNAi} tissues or between wild-type and *ds*^{RNAi} within the A-shaped domain of D:GFP polarization (Fig. 4, C and D, blue bars, and fig. S11, A to C). The orientations of the significant differences were aligned with the local orientations of the D:GFP anisotropy distribution (Fig. 4, C' and D'). These results demonstrate that Dachs polarization regulates tissue morphogenesis by increasing the rate of contraction along its polarity lines.

We then studied how Dachs polarization controls the cell dynamics that makes up the local tissue contractions. Our analyses of cell division rate and orientation argue against a major contribution of division orientation (fig. S12). We therefore quantified the respective contributions of cell rearrangements and cell shape changes to tissue contraction rates (fig. S13). In the wild-type tissue, Dachs polarization correlates with the cell rearrangement pattern both in magnitude and orientation (fig. S14, A to C', red bars), whereas it poorly correlates with cell shape changes (fig. S14, D and D', cyan bars). Accordingly, both the differences in tissue contraction rates between wild-type and *dachs*^{RNAi} and between wild-type and *ds*^{RNAi} were mainly associated with a decrease in the contribution of cell rearrangements to tissue contractions in the regions of Dachs polarization and, to a lesser extent, to cell shape changes ($P < 10^{-12}$) (Fig. 4, E to F', and figs. S11, A' to C', and fig. S15). Similar results for tissue contraction rate and cell dynamics were obtained in *fat*^{RNAi} and *fj*^{LP} mutant conditions (fig. S16). Accordingly, *ds*^{RNAi}, *fj*^{LP}, *fat*^{RNAi}, and *dachs*^{RNAi} pupae manifest similar defects in the adult scutellum shape (fig. S17).

Altogether, we found that Ds polarization promotes Dachs polarization within a domain of the opposing tissue-wide *ds* and *fj* gradients. Their local polarization produces an anisotropic distribution of junction tensions, which increases the contraction rates along the lines of Ds and Dachs planar polarization to shape the epithelial tissue mainly through oriented cell rearrangements (fig. S18). The Dachs myosin has the necessary domains to be an actin-binding motor (fig. S9) and, in complex with Dachsous, may directly contribute to junction contractility, favoring cell rearrangements (24). future work should dissect the respective roles of Dachs and MyosinII in these processes. Morphogenesis is accomplished by the concerted activity of multiple signaling pathways. Our subtractive method of tissue deformation rates is general enough to isolate the contribution of a

given pathway to morphogenesis without making assumptions on its magnitude and its spatial dependence. Last, given the multitude of cell shapes, cell sizes, and division patterns occurring in the thorax epithelium, future work on this tissue should reveal how multiple signaling pathways are integrated to regulate proliferation, planar polarization, and morphogenesis.

References and Notes

1. L. V. Goodrich, D. Strutt, *Development* **138**, 1877 (2011).
2. F. A. Grusche, H. E. Richardson, K. F. Harvey, *Curr. Biol.* **20**, R574 (2010).
3. P. A. Mahoney *et al.*, *Cell* **67**, 853 (1991).
4. H. F. Clark *et al.*, *Genes Dev.* **9**, 1530 (1995).
5. M. H. B. Odsky, H. Steller, *Dev. Biol.* **173**, 428 (1996).
6. H. O. Ishikawa, H. Takeuchi, R. S. Halbwanger, K. D. Irvine, *Science* **321**, 401 (2008).
7. M. A. Simon, A. Xu, H. O. Ishikawa, K. D. Irvine, *Curr. Biol.* **20**, 811 (2010).
8. A. L. Brittle, A. Repiso, J. Casal, P. A. Lawrence, D. Strutt, *Curr. Biol.* **20**, 803 (2010).
9. C. H. Yang, J. D. Axelrod, M. A. Simon, *Cell* **108**, 675 (2002).
10. D. Ma, C. H. Yang, H. McNeill, M. A. Simon, J. D. Axelrod, *Nature* **421**, 543 (2003).
11. H. Strutt, D. Strutt, *Dev. Cell* **3**, 851 (2002).
12. E. Cho, K. D. Irvine, *Development* **131**, 4489 (2004).
13. H. Matakatsu, S. S. Blair, *Development* **131**, 3785 (2004).
14. J. Casal, P. A. Lawrence, G. Struhl, *Development* **133**, 4561 (2006).
15. H. Matakatsu, S. S. Blair, *Development* **133**, 2315 (2006).
16. H. Matakatsu, S. S. Blair, *Curr. Biol.* **18**, 1390 (2008).
17. Y. Mao *et al.*, *Development* **133**, 2539 (2006).
18. D. Rogujs, C. Rauskolb, K. D. Irvine, *Dev. Cell* **15**, 309 (2008).
19. Y. Mao *et al.*, *Genes Dev.* **25**, 131 (2011).
20. L. A. Baena-López, A. Baonza, A. García-Beil, *Curr. Biol.* **15**, 1640 (2005).
21. B. Argouy *et al.*, *Cell* **142**, 773 (2010).
22. Materials and methods are available as supplementary materials on Science Online.
23. G. Schwank *et al.*, *Dev. Cell* **20**, 123 (2011).
24. T. Lecuit, P. F. Lenne, E. Munro, *Annu. Rev. Cell Dev. Biol.* **27**, 157 (2010).

Acknowledgments: We thank J. Axelrod, S. Blair, Y. Hong, K. Irvine, E. Martin-Bianco, M. Simon, D. Strutt, S. Tsukita, the Bloorington Drosophila Stock Center, Transgenic RNAi Project, and Vienna Drosophila RNAi Center for reagents; M. Coppey, A. Houdusse, F. Mouno, S. Ritzenthaler, F. Serman, J. Shi, and the PICT-BISA@BDD for help; V. Hakim, E. Heard, J. Lopez-Gay, M. Labouesse, and A.-M. Lennon for comments. This work was supported by ARC 4830, L'Agence Nationale de la Recherche-MorphoDro, and European Research Council-CePoDro grants, a Fondation pour la Recherche Médicale grant to I.B.; and a Nederlandse Organisatie voor Wetenschappelijk Onderzoek-Rubicon grant to F.B.

Supplementary Materials

www.sciencemag.org/content/336/6186/1221071/DC1
Materials and Methods

Supplementary Text

Figs. S1 to S20

References

Movies S1 to S5

27 February 2012; accepted 30 March 2012

Published online 12 April 2012.

10.1126/science.1221071

Structural Basis for DNA Damage–Dependent Poly(ADP-ribosylation) by Human PARP-1

Marie-France Langelier, Jamie L. Planck, Swati Roy, John M. Pascal*

Poly(ADP-ribose) polymerase-1 (PARP-1) (ADP, adenosine diphosphate) has a modular domain architecture that couples DNA damage detection to poly(ADP-ribosylation) activity through a poorly understood mechanism. Here, we report the crystal structure of a DNA double-strand break in complex with human PARP-1 domains essential for activation (Zn1, Zn3, WGR-CAT). PARP-1 engages DNA as a monomer, and the interaction with DNA damage organizes PARP-1 domains into a collapsed conformation that can explain the strong preference for automodification. The Zn1, Zn3, and WGR domains collectively bind to DNA, forming a network of interdomain contacts that links the DNA damage interface to the catalytic domain (CAT). The DNA damage–induced conformation of PARP-1 results in structural distortions that destabilize the CAT. Our results suggest that an increase in CAT protein dynamics underlies the DNA-dependent activation mechanism of PARP-1.

Poly(ADP-ribose) polymerase-1 (PARP-1) (ADP, adenosine diphosphate) creates poly(ADP-ribose) (PAR) covalently attached onto target proteins that mediate gene transcription, DNA damage repair, and cell-death signaling (1, 2), and it has emerged as a promising drug target for the treatment of cancer due to its role in maintaining genome stability (3, 4). The primary target for PARP-1 mediated poly(ADP-ribosylation) is PARP-1 itself (1). PARP-1 binding to DNA strand breaks dramatically elevates PAR synthesis activity over a low basal level (1). The modular architecture of PARP-1 contains six domains (Fig. 1A). Two zinc-binding domains, Zn1 and Zn2, enable PARP-1 to recognize particular DNA structures (5–9), and a third zinc-binding domain, Zn3, has a distinct structure and function from that of Zn1 and Zn2 (10, 11). The automodification domain (AD) bears the major sites of automodification and contains a BRCT (BRCA1 C terminus) fold (1). The WGR is an essential domain of unknown function (12). The catalytic domain (CAT) is composed of two subdomains, the helical subdomain (HD) and the ART subdomain, which is conserved in other ADP-ribosyl transferases (ARTs), and includes the amino acids involved in catalysis and binding of nicotinamide adenine dinucleotide (NAD⁺) (13, 14).

We determined the x-ray crystal structure of human PARP-1 domains Zn1, Zn3, and WGR-CAT bound to a DNA double-strand break (DSB) (15). These domains are essential for PARP-1 activity in the presence of DNA DSBs (5, 10–12) and represent the minimal assembly of domains that supports DNA-dependent PARP-1 activity.

The Zn1 and Zn3 domains stimulate PAR synthesis of the WGR-CAT fragment in the presence of DNA (Fig. 1B). The Zn2 and BRCT domains are dispensable for PARP-1 activity in the presence of DNA DSBs (fig. S1) (5, 12, 16). Crystals of the PARP-1/DNA complex diffract anisotropically to 3.25 Å; we determined the structure by molecular replacement (fig. S2 and table S1).

The PARP-1/DNA structure reveals the assembly of PARP-1 domains on DNA damage. The WGR domain is a central component of the complex, interacting with Zn1, Zn3, CAT, and the DNA (Fig. 1, C and D). Zn1 and Zn3 rest next to each other on the DNA, both domains interacting with one face of WGR. The opposite face of WGR contacts the HD of the CAT. PARP-1 contacts with the DNA break are transmitted to the CAT through a network of interdomain communication that acts on the HD. In contrast, the ART subdomain is not involved in direct contacts with DNA or PARP-1 regulatory domains.

We constructed a model of full length PARP-1 (including Zn2 and BRCT) based on the relative locations of the N and C termini of domains present in the structure (Fig. 1E) (see supplementary text). In the model, the AD is anchored between Zn3 and WGR in close proximity to the CAT and is available for *in cis* modification, explaining the strong preference of PARP-1 to perform automodification over heteromodification of target proteins (17). The PARP-1/DNA complex contains a single copy of each domain, and the model for full-length PARP-1 indicates that a monomeric PARP-1 polypeptide can assume the active conformation. A monomeric mode of DNA binding has been reported recently for PARP-1 (5, 6, 18, 19); however, an earlier study reported that the Zn1-Zn2 fragment binds to DNA as a dimer under certain conditions (supplementary text) (8). Our sedimentation analysis

indicates that full-length PARP-1 exists as a highly extended monomer in solution in the absence of DNA and that PARP-1 domains compact upon binding to DNA as a monomer with a 1:1 stoichiometry (fig. S3), consistent with the PARP-1/DNA structure.

The PARP-1/DNA structure and biochemical experiments demonstrate that the Zn1, Zn3, and WGR domains collaboratively bind to DNA damage (Fig. 2, fig. S4, and table S2). PARP-1 domains primarily contact the ribose-phosphate backbone of the DNA and, therefore, mediate sequence-independent interactions. PARP-1 engages the break in the DNA through hydrophobic contacts with exposed nucleotide bases (Fig. 2, A and B), a common feature of damaged DNA structures (fig. S5). Zn1 binds to DNA using two conserved regions termed the backbone grip and the base-stacking loop (Fig. 2, A and B), as observed previously (5). Zn3 binds to DNA adjacent to Zn1 using its N-terminal α -helical region to span the minor groove (Fig. 2A). WGR binds to the 5'-terminus of one DNA strand, holding the DNA backbone between the central β sheet and the α helix of WGR (Fig. 2A). WGR residue Trp⁵⁸⁹ stacks against the ribose sugars of nucleotides located at the end of the 5'-terminated DNA strand (Fig. 2, A and B).

The PARP-1/DNA structure reveals a network of interdomain contacts formed upon DNA binding (Fig. 3). The Zn1 base-stacking loop and the Zn3 extended loop provide a two-point contact surface with the appropriate orientation and spacing for engaging WGR (Fig. 3, A and B). A key Zn1-WGR contact is a salt bridge formed between Asp⁴⁵ of Zn1 and Arg⁵⁹¹ of WGR (Fig. 3C). Arg⁵⁹¹ also interacts with HD, thus, WGR provides a bridge between the Zn1 DNA damage interface and the CAT. Zn3 contacts WGR and HD using the extended loop of its zinc ribbon fold, with residue Trp³¹⁸ occupying a central location at this interface (Fig. 3D). Zn3 forms a second interface in the PARP-1/DNA complex, using its N-terminal helical region to interact with Zn1, near their points of contact with the DNA duplex (Fig. 3E). Mutation of full-length PARP-1 at residues located at domain interfaces resulted in severe to moderate defects in DNA-dependent activity relative to wild-type (WT) PARP-1 (Fig. 3F) (5, 20, 21). These biochemical results confirm that the interdomain contacts observed in the PARP-1/DNA structure are critical for DNA-dependent activation of full-length PARP-1.

The PARP-1/DNA structure reveals that the HD is distorted when compared with structures of isolated CAT domains (Fig. 4, A and B, and fig. S6). The HD region surrounding α C is remodeled and moved away from α F and α B and toward the WGR interface, displacing conserved residues Leu⁶⁰⁸ and Leu⁷⁰¹ from the HD hydrophobic core (Fig. 4B). In contrast, the ART is similar to isolated CAT domain structures (Fig. 4A and fig. S6). Thus, the DNA-dependent regulatory domains of PARP-1 act to distort the HD

Department of Biochemistry and Molecular Biology, The Kimmel Cancer Center, Thomas Jefferson University, Philadelphia, PA 19107, USA.

*To whom correspondence should be addressed. E-mail: john.pascal@kimmelcancercenter.org

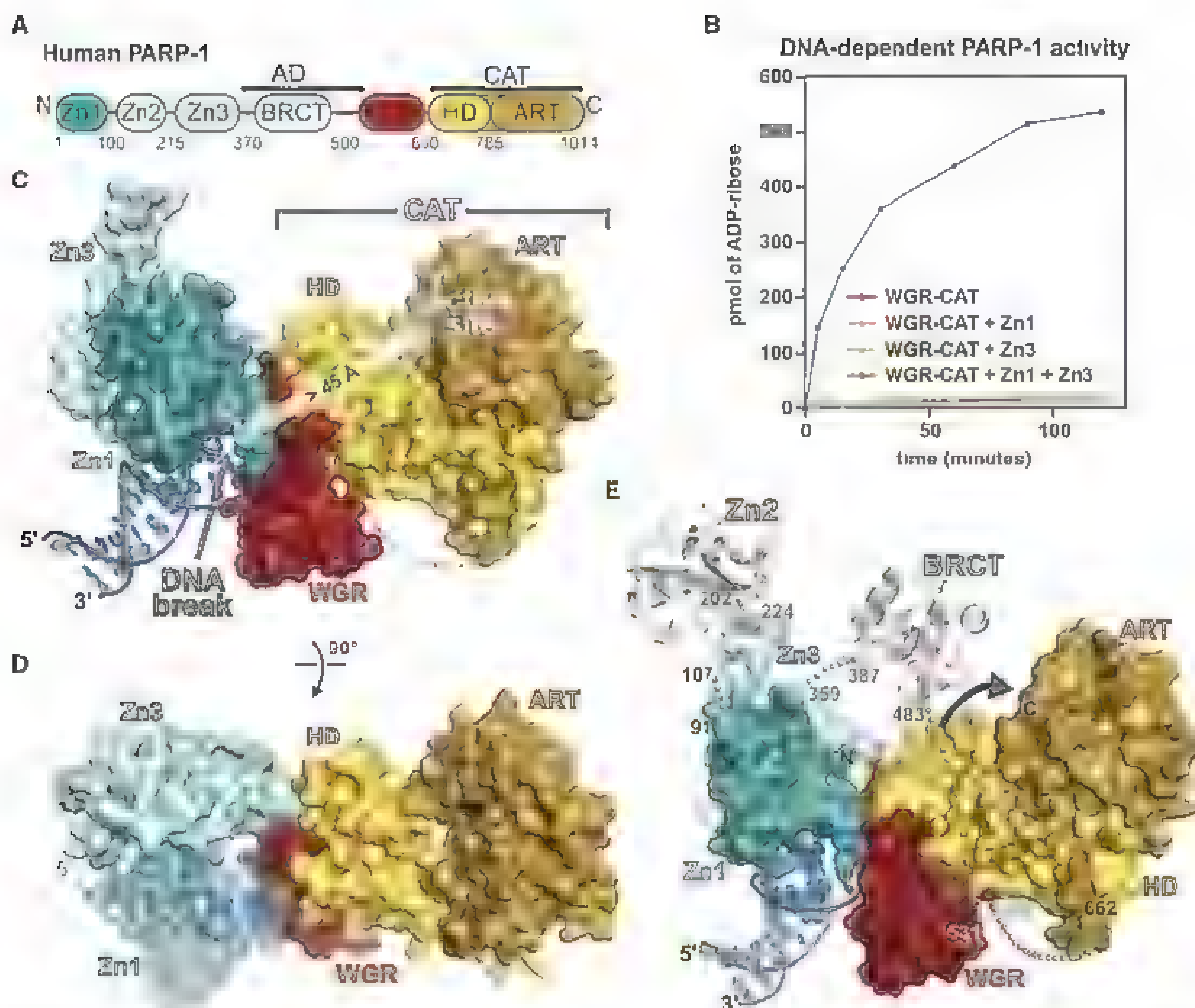


Fig. 1. Overview of the PARP-1/DNA crystal structure. (A) Modular domain architecture of human PARP-1. (B) Colorimetric assay of PARP-1 DNA-dependent automodification using the indicated domain combinations (see also fig. S1, A and B). (C) Surface representation of the PARP-1/DNA structure. (D) A 90°

rotation was applied to the view in (C). (E) The Zn2 and BRCT domains (light gray) were manually positioned on the PARP-1/DNA structure using the structures of Zn2 and BRCT (PDB codes 3ODC and 2COK, respectively). The arrow accents the close proximity of AD and CAT.

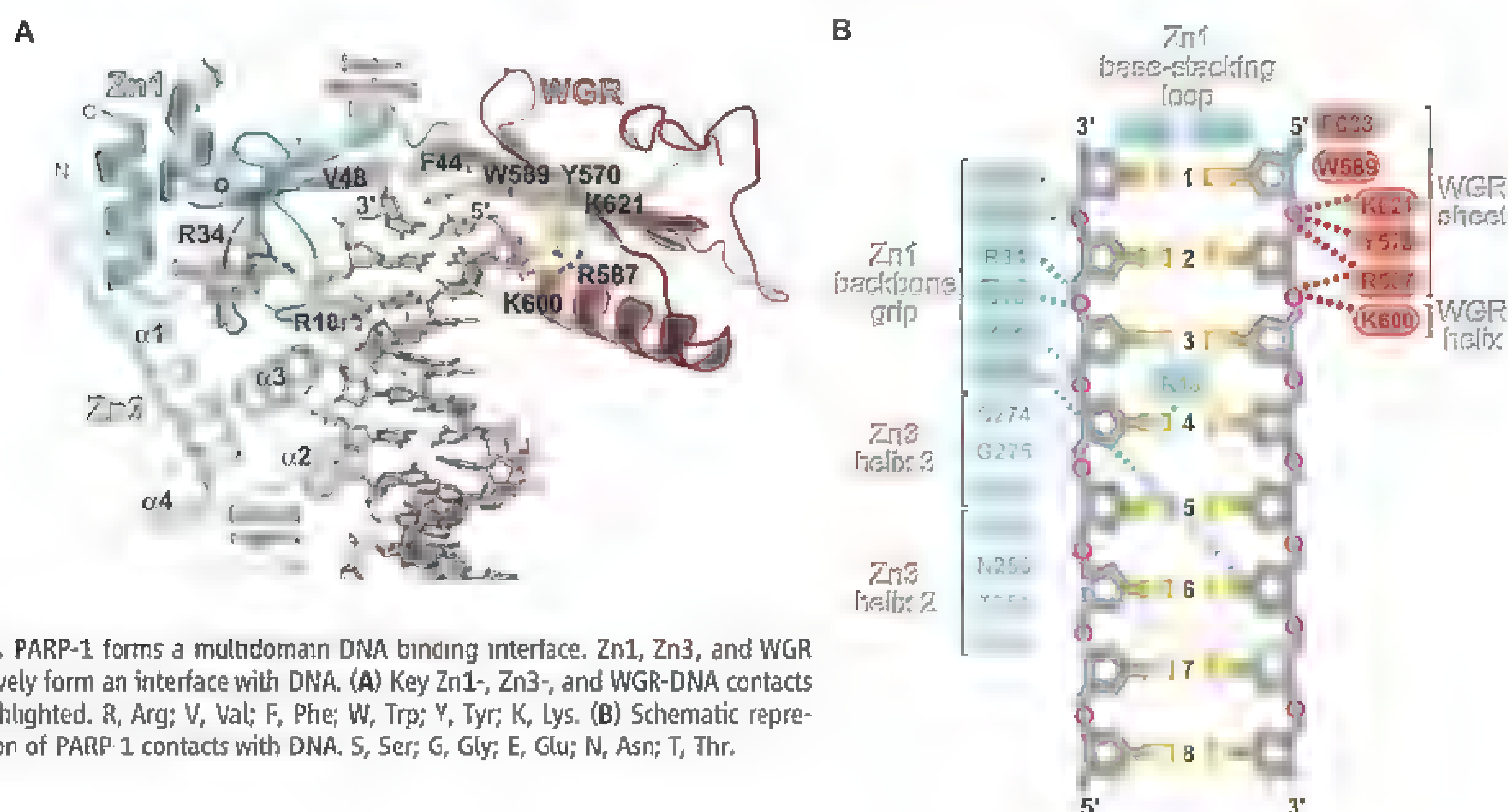


Fig. 2. PARP-1 forms a multidomain DNA binding interface. Zn1, Zn3, and WGR collectively form an interface with DNA. (A) Key Zn1-, Zn3-, and WGR-DNA contacts are highlighted. R, Arg; V, Val; F, Phe; W, Trp; Y, Tyr; K, Lys. (B) Schematic representation of PARP-1 contacts with DNA. S, Ser; G, Gly; E, Glu; N, Asn; T, Thr.

hydrophobic core, suggesting that HD distortion underlies DNA-dependent activation. We tested whether mutagenesis of the HD could simulate the observed HD distortions and thereby mimic the effect of PARP-1 interaction with DNA. We observed an increase in DNA-independent PARP-1 activity for mutations that targeted the

HD hydrophobic core (Fig. 4, C to E, and fig. S7). In contrast, mutation of HD residues facing away from the hydrophobic interior had no effect on DNA-independent activity (Fig. 4, C to E, and fig. S7). Random mutagenesis previously identified a hydrophobic core mutant Leu⁷¹³→Phe⁷¹³ (L713F) that activates PARP-1 in the absence of

DNA (22), consistent with our biochemical analysis. HD hydrophobic core mutants mimic the effect of DNA damage-induced HD distortions, increasing PARP-1 DNA-independent activity up to ~20-fold and elevating the catalytic efficiency of poly(ADP-ribosyl)ation while not affecting affinity for NAD⁺ (figs. S8 and S9)

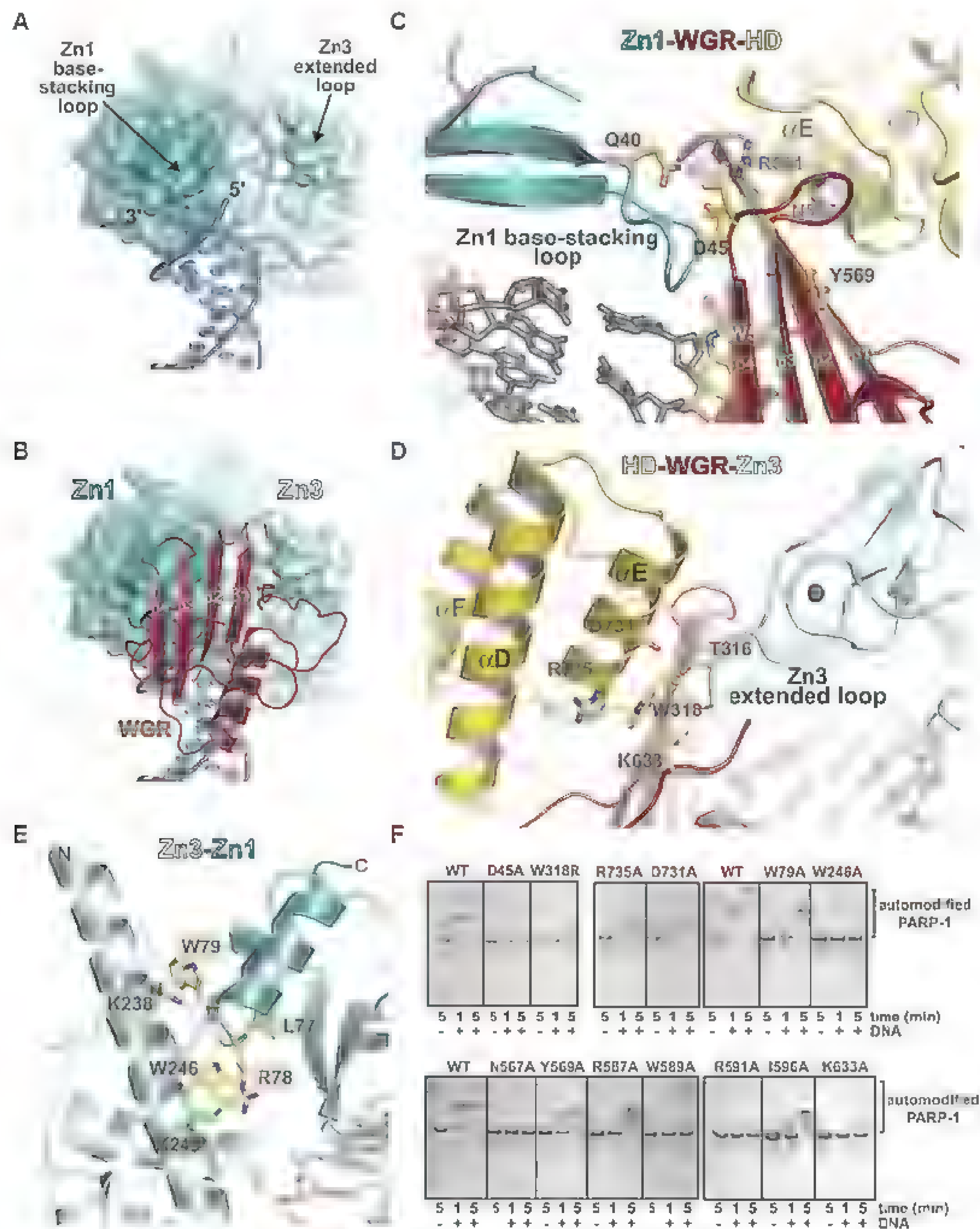


Fig. 3. DNA-induced interdomain contacts are critical for DNA-dependent PARP-1 activation. (A) Surface representation of Zn1 and Zn3 bound to DNA. WGR and CAT have been omitted for clarity. (B) The Zn1 base-stacking loop, the Zn3 extended loop, and the 5'-terminated DNA strand form a binding site for WGR. (C) The Zn1-WGR-HD interface. Q, Gln; I, Ile; D, Asp. (D) The HD-WGR-Zn3 interface. (E) The Zn3-Zn1 interface. Resi-

dues targeted for mutagenesis are labeled in yellow; residues identified in a random screen for inactive mutants (22) are shown in green. L, Leu. (F) SDS-polyacrylamide gel electrophoresis assay of DNA-dependent PARP-1 automodification activity. The wild type and the indicated mutants were monitored for a shift in migration due to the covalent addition of PAR. A, Ala

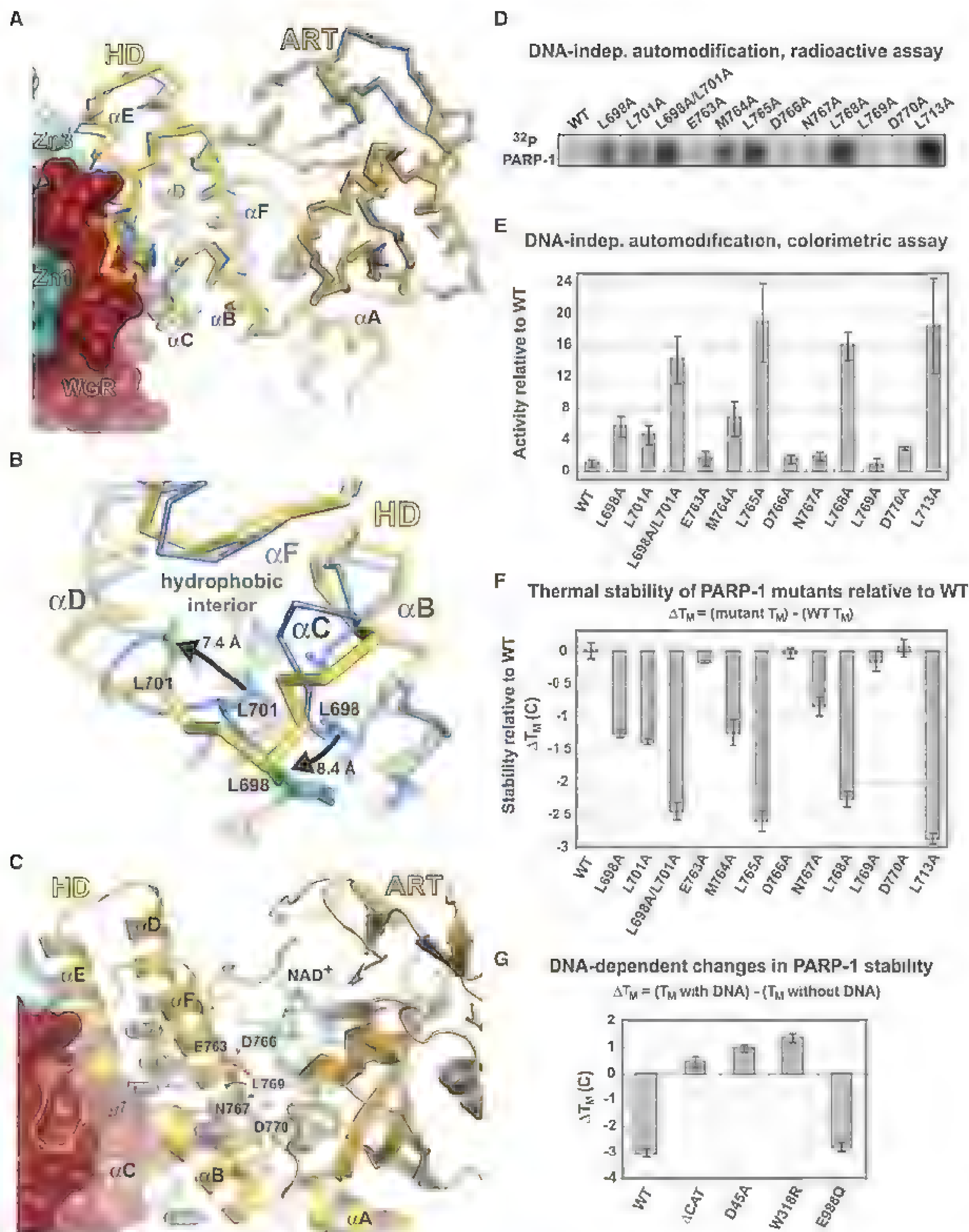


Fig. 4. Distortion of the HD structure modulates PARP-1 catalytic activity. **(A)** Co trace of CAT structure in the absence of DNA and regulatory domains (PDB code 1A26; blue) and CAT in the PARP-1/DNA structure (yellow/brown). **(B)** Detailed view of Leu⁶⁹⁸ and Leu⁷⁰¹ contributions to the HD hydrophobic interior of the isolated CAT (blue) and their repositioning in the PARP-1/DNA structure (yellow with green side chains). **(C)** Ribbon representation of CAT in the PARP-1/DNA complex. Residues mutated are drawn in pink and labeled in white (HD interior hydrophobic core) and black (HD exterior). The position of NAD⁺ was modeled for

reference. M, Met. **(D)** Radioactive assay of DNA-independent PARP-1 automodification using ³²P-NAD⁺. **(E)** Colorimetric assay of DNA-independent PARP-1 automodification. Values represent quantification of the 90-min time point of a time-course experiment (fig. S7) and are an average of three independent experiments with associated SDs (error bars). **(F)** Relative thermal stability of PARP-1 mutants obtained by differential scanning fluorimetry. Changes in thermal stability (ΔT_M) were calculated as shown. **(G)** Relative change in thermal stability upon DNA binding. ΔT_M were calculated as shown.

A strong anticorrelation exists between catalytic activity and relative thermal stability of HD mutants. HD hydrophobic core mutants exhibit increased DNA-independent activity and decreased thermal stability relative to WT PARP-1, whereas mutants that face the exterior of the HD hydrophobic core have the same activity and stability as the wild type (Fig. 4, E and F). The HD mutations that elevate DNA-independent activity act solely through alterations to CAT and do not depend on the regulatory domains. Indeed, the isolated CAT bearing HD hydrophobic core mutation L713F exhibited elevated DNA-independent activity and decreased thermal stability relative to WT CAT (fig. S10). Consistent with the mutational analysis, full-length PARP-1 in the presence of DNA exhibited a decrease in thermal stability that depended on the presence of the CAT domain and residues mediating interdomain contacts in the PARP-1/DNA structure (Fig. 4G). As a control, the catalytic ART mutant Glu⁹⁸⁸→Gln⁹⁸⁸ (E988Q) (23, 24), expected to form all interdomain contacts observed in the PARP-1/DNA structure, showed the same decrease in thermal stability as the wild type (Fig. 4G). Collectively, our results demonstrate that the stability of the CAT decreases upon PARP-1 binding to DNA damage, and the change in stability depends on the interdomain contacts that mediate HD distortion in the PARP-1/DNA structure.

PARP-1 binding to DNA damage organizes the Zn1, Zn3, and WGR domains into a conformation that distorts the hydrophobic core of the HD and thereby decreases the thermal stability of CAT (fig. S11). The observed HD distortions are unlikely to have a substantial influence on active site access to the NAD⁺ substrate or target protein substrate (supplementary text). Rather, we propose that distortions to the structure and stability of HD are linked to the stability of ART and that changes in the stability and conformational dynamics of ART underlie the DNA-dependent activation mechanism of PARP-1 (fig. S11). The positioning of the AD in close proximity to the CAT could also contribute to PARP-1 DNA-dependent activity by increasing CAT domain exposure to protein substrate. Our study illustrates a DNA damage-dependent intramolecular mechanism for rapidly elevating the low basal level of PARP-1 activity and suggests the structural basis for PARP-1 preference for auto-modification. The critical requirement of domain interfaces for PARP-1 DNA-dependent activity suggests that these domain interfaces represent targets for the design of novel PARP-1 inhibitors.

References and Notes

- O. D'Amours, S. Desnoyers, I. D'Silva, G. C. Poirier, *Biochem. J.* **342**, 249 (1999).
- R. Krishnakumar, W. L. Kraus, *Mol. Cell* **39**, 8 (2010).
- P. C. Fong et al., *N. Engl. J. Med.* **361**, 123 (2009).
- M. Rouleau, A. Patel, M. J. Hendzel, S. H. Kaartmann, G. G. Poirier, *Nat. Rev. Cancer* **10**, 293 (2010).
- M. F. Langeier, J. L. Planck, S. Roy, J. M. Pascal, *J. Biol. Chem.* **286**, 10690 (2011).
- S. Eastermann et al., *J. Mol. Biol.* **407**, 149 (2011).
- I. Lonskaya et al., *J. Biol. Chem.* **280**, 17076 (2005).
- E. Pion et al., *Biochemistry* **42**, 12409 (2003).
- I. D'Silva et al., *Biochim. Biophys. Acta* **1430**, 119 (1999).
- M. F. Langeier, K. M. Servent, E. E. Rogers, J. M. Pascal, *J. Biol. Chem.* **283**, 4105 (2008).
- Z. Tao, P. Gao, D. W. Holtman, H. W. Liu, *Biochemistry* **47**, 5804 (2008).
- M. Altmeyer, S. Messner, P. O. Hassa, M. Fey, M. O. Hottiger, *Nucleic Acids Res.* **37**, 3723 (2009).
- A. Ruf, G. de Murcia, G. E. Schultz, *Biochemistry* **37**, 3893 (1998).
- A. Ruf, J. Menissier de Murcia, G. de Murcia, G. E. Schultz, *Proc. Natl. Acad. Sci. U.S.A.* **93**, 7481 (1996).
- Materials and methods are available as supplementary materials on Science Online.
- D. A. Wacker et al., *Mol. Cell. Biol.* **27**, 7475 (2007).
- N. Ogata, K. Ueda, M. Kawauchi, O. Hayaishi, *J. Biol. Chem.* **256**, 4135 (1981).
- W. Liljestrom, M. J. van der Woerd, N. Clark, K. Lager, *J. Mol. Biol.* **395**, 983 (2010).
- L. Spagnolo, J. Barbeau, N. J. Curtin, E. P. Morns, L. H. Pearl, *Nucleic Acids Res.* **10**, 1093/nar/gkr1231 (2012).
- M. F. Langeier, D. D. Ruhl, J. L. Planck, W. L. Kraus, J. M. Pascal, *J. Biol. Chem.* **285**, 18877 (2010).
- C. Trucco, E. Flatter, S. Enbourg, G. de Murcia, J. Menissier-de Murcia, *FEBS Lett.* **399**, 313 (1996).
- E. A. Miranda, F. Dantzer, M. O'Farrell, G. de Murcia, J. M. de Murcia, *Biochem. Biophys. Res. Commun.* **212**, 317 (1995).
- G. T. Marsischky, B. A. Wilson, R. J. Collier, *J. Biol. Chem.* **270**, 3247 (1995).
- A. Ruf, V. Rouil, G. de Murcia, G. E. Schultz, *J. Mol. Biol.* **278**, 57 (1998).

Acknowledgments: This work was supported by funds from the N.H. (R01087282), the American Cancer Society (RSG0918301), and the Kimmel Cancer Center X-ray Crystallography and Molecular Characterization Facility at Thomas Jefferson University (P30CA56036). We thank the National Synchrotron Light Source staff for access and assistance with data collection (beamlines X6A and X29A Brookhaven National Laboratory); G. Cingolani, Y. M. Hou, and J. D. Steffen for helpful discussions; and S. Carney for cloning the Zn1/Zn3 interface mutants. The structure of the complex has been deposited under accession number 4DQY in the Protein Data Bank (PDB).

Supplementary Materials

www.sciencemag.org/cgi/content/full/336/6082/728/DC1

Materials and Methods

Supplementary Text

Figs. S1 to S11

Tables S1 and S2

References (25–48)

8 November 2011; accepted 19 March 2012

10.1126/science.1216338

Meiosis-Specific Noncoding RNA Mediates Robust Pairing of Homologous Chromosomes in Meiosis

Da-Qiao Ding,¹ Kasumi Okamasa,¹ Miho Yamane,¹ Chihiro Tsutsumi,¹ Tokuko Haraguchi,^{1,2} Masayuki Yamamoto,³ Yasushi Hiraoka^{1,2*}

Pairing and recombination of homologous chromosomes are essential for ensuring reductional segregation in meiosis. However, the mechanisms by which chromosomes recognize their homologous partners are poorly understood. Here, we report that the *sme2* gene encodes a meiosis-specific noncoding RNA that mediates homologous recognition in the fission yeast *Schizosaccharomyces pombe*. The *sme2* locus shows robust pairing from early in meiotic prophase. The *sme2* RNA transcripts accumulate at their respective gene loci and greatly enhance pairing of homologous loci. Deletion of the *sme2* sequence eliminates this robust pairing, whereas transposition to other chromosomal sites confers robust pairing at those ectopic sites. Thus, we propose that RNA transcripts retained on the chromosome play an active role in recognition of homologous chromosomes for pairing.

Meiosis, essential for sexually reproducing eukaryotes, involves reductional segregation of homologous chromosomes in meiosis I. Pairing and recombination of homologous chromosomes are crucial for this process. Clustering of telomeres in meiotic prophase spatially aligns homologous chromosomes

to promote their pairing (1–6). In some organisms, pairing requires double strand-break (DSB) formation, whereas in other organisms it occurs independently of DSB formation (6–11). It remains unknown how chromosomes recognize their homologous partners in order to pair with each other.

We have examined the process of homologous chromosome pairing in meiosis by monitoring fluorescently tagged chromosome loci in live cells of *Schizosaccharomyces pombe* (2). In this organism, initiation of meiosis is regulated by Mei2, an RNA-binding protein essential for entry into meiosis (12, 13). Mei2 forms a distinct nuclear dot at the *sme2* locus on chromosome II in

¹Advanced ICT Research Institute Kobe, National Institute of Information and Communications Technology, Kobe 651-2492, Japan. ²Graduate School of Frontier Biosciences, Osaka University, Suita 565-0871, Japan. ³Department of Biophysics and Biochemistry, Graduate School of Science, The University of Tokyo, Tokyo 113-0033, Japan.

*To whom correspondence should be addressed. E-mail: hiraoka@bs.osaka-u.ac.jp

the meiotic prophase “horsetail” nucleus (13, 14). The *sme2* gene encodes noncoding polyadenylated RNAs, *meiRNA-S* and *meiRNA-L* (Fig. 1A), that

are required for Mei2 dot formation (12, 15, 16). Another major *sme2* RNA binding protein, Mmi1, which selectively eliminates meiotically essen-

tial mRNAs in mitotic cells, is sequestered to the Mei2 dot in meiotic prophase to allow the progression of meiosis (16, 17). Because the

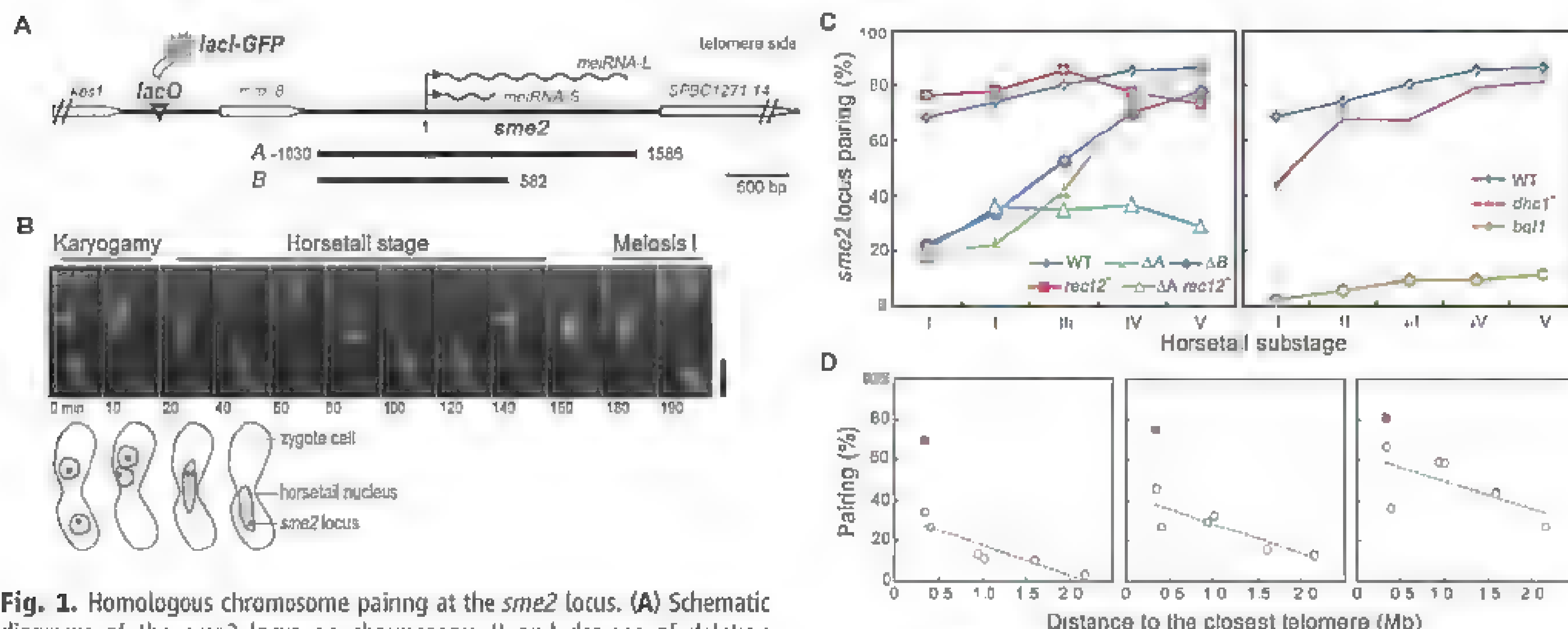


Fig. 1. Homologous chromosome pairing at the *sme2* locus. (A) Schematic diagrams of the *sme2* locus on chromosome II and designs of deletion mutants: 0.5-kb noncoding RNA *meiRNA-S* (12) and 1.5-kb *meiRNA-L* (16). Black triangle indicates the position of the *lacO*-repeat array. DNA fragments A and B were replaced with the marker gene in deletion experiments. Numbers indicate nucleotide residues with 1 corresponding to the first residue of the annotated *sme2* transcript (12). (B) Projection of three-dimensional (3D) image stacks of selected frames from time-lapse observations of the *sme2* locus (*lacO*–*lacI*-GFP) in a living cell. Scale bar, 5 μ m. Illustrations of the first four time points are shown under the image. (C) Pairing frequencies

of the *sme2* locus in WT and various mutant backgrounds (strain list, table S1). Statistical analyses are summarized in fig. S5. (D) Pairing frequencies of multiple loci on chromosome II plotted as a function of the distance to the telomere for the first three horsetail substages: *sme2* locus, filled red square. Six other chromosome loci examined previously (2), open blue circles (from left to right): 0.3, 0.4, 0.94, 1.0, 1.6, and 2.2 Mb from the telomere. Blue dashed line, linear regression of the pairing frequencies at those loci

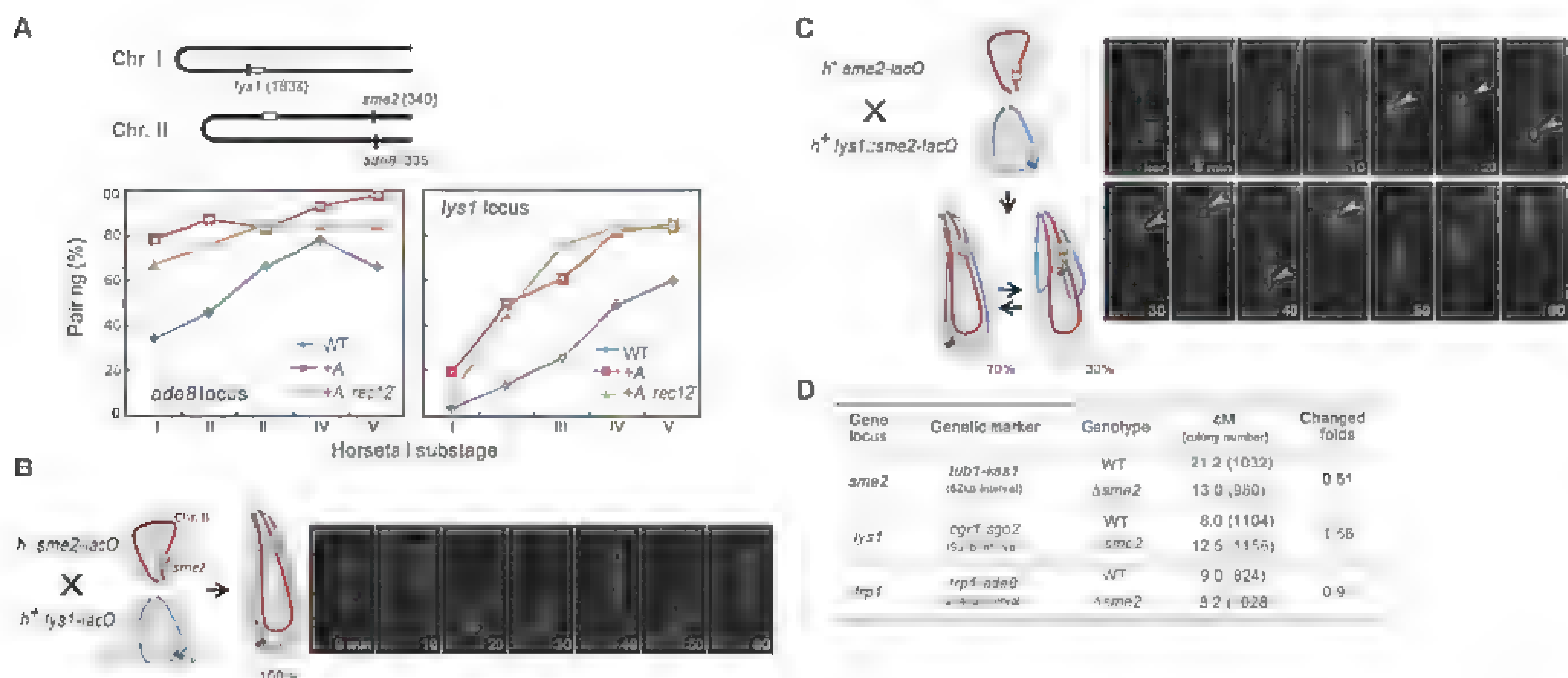


Fig. 2. Transposition of the *sme2* sequence confers robust pairing. (A) (Top) Schematic diagrams of chromosome I and II showing the positions of *lys1*, *sme2*, and *ade8*. Numbers in parentheses indicate the distance (kb) from their proximal telomeres. The open squares indicate the position of the centromeres. (Bottom) The pairing frequencies of *ade8* and *lys1* loci with (+A) or without (WT) the ectopic *sme2* insertion in a WT or *rec12* background are shown. Statistical analyses in fig. S5. (B and C) Diagrams (left): Chromosomal locations of the *sme2* (shaded square), *lys1* (black bar), and *lacO* array (green circle) in a haploid

and a horsetail nucleus. Time-lapse observations (right): (B) *h⁺ sme2-lacO* crossed with *h⁺ lys1-lacO*. (C) *h⁺ sme2-lacO* crossed with *h⁺ lys1::sme2-lacO*. Images are projections of 3D image stacks. Close localizations of the two GFP signals are indicated by arrowheads. Scale bar, 5 μ m. (D) Intergenic recombination frequency. Genetic distance (cM) was calculated from recombination frequency with Haldane’s formula, $cM = -50 \ln(1 - 2R)$, where *R* is fraction of recombinant spores among total spores (23). Cumulative number of spore colonies from three independent crosses in parentheses.

Mei2 dot is formed at the *sme2* locus on each haploid chromosome, two Mei2 dots are expected in a diploid zygotic cell. However, in most

cases only one dot of Mei2-GFP was observed. In live-cell observations of Mei2-GFP, a Mei2 dot formed in each of the haploid cells before

nuclear fusion, they quickly joined each other after nuclear fusion and remained as one dot for most of the horsetail stage (fig. S1, A and B).

Fig. 3. The *sme2* transcript is essential for pairing. (A) Schematic diagrams of the *sme2* locus. Fragments C to F were replaced with a selective marker gene in deletion experiments. (B) Pairing frequencies of the *sme2* locus in ΔC , ΔD , and *sme2-m* backgrounds. The *sme2-m* is a TATA-box mutant (14). (C) Pairing frequencies of the *sme2* locus in heterozygous crosses: A WT cell was crossed with a ΔC or *sme2-m* cell. (D) Pairing frequencies of the *sme2* locus in ΔE and ΔF backgrounds. Statistical analyses in fig. S5. (E) Northern blotting analysis of *sme2* expression in various *h⁹⁰* mutant cells induced to enter meiosis: nucleotides 618 to 1057 of the *sme2* gene as the detection probe, meiosis-specific *bqt2* probe (18) as the internal control to monitor the induction of meiosis, and 28S ribosomal RNA as the loading control. JZ464 is an insertion-disrupting mutant in which a portion of the *sme2* gene was replaced by a *ura4⁺* gene (12). The arrow indicates the 1.5-kb *sme2* transcript.

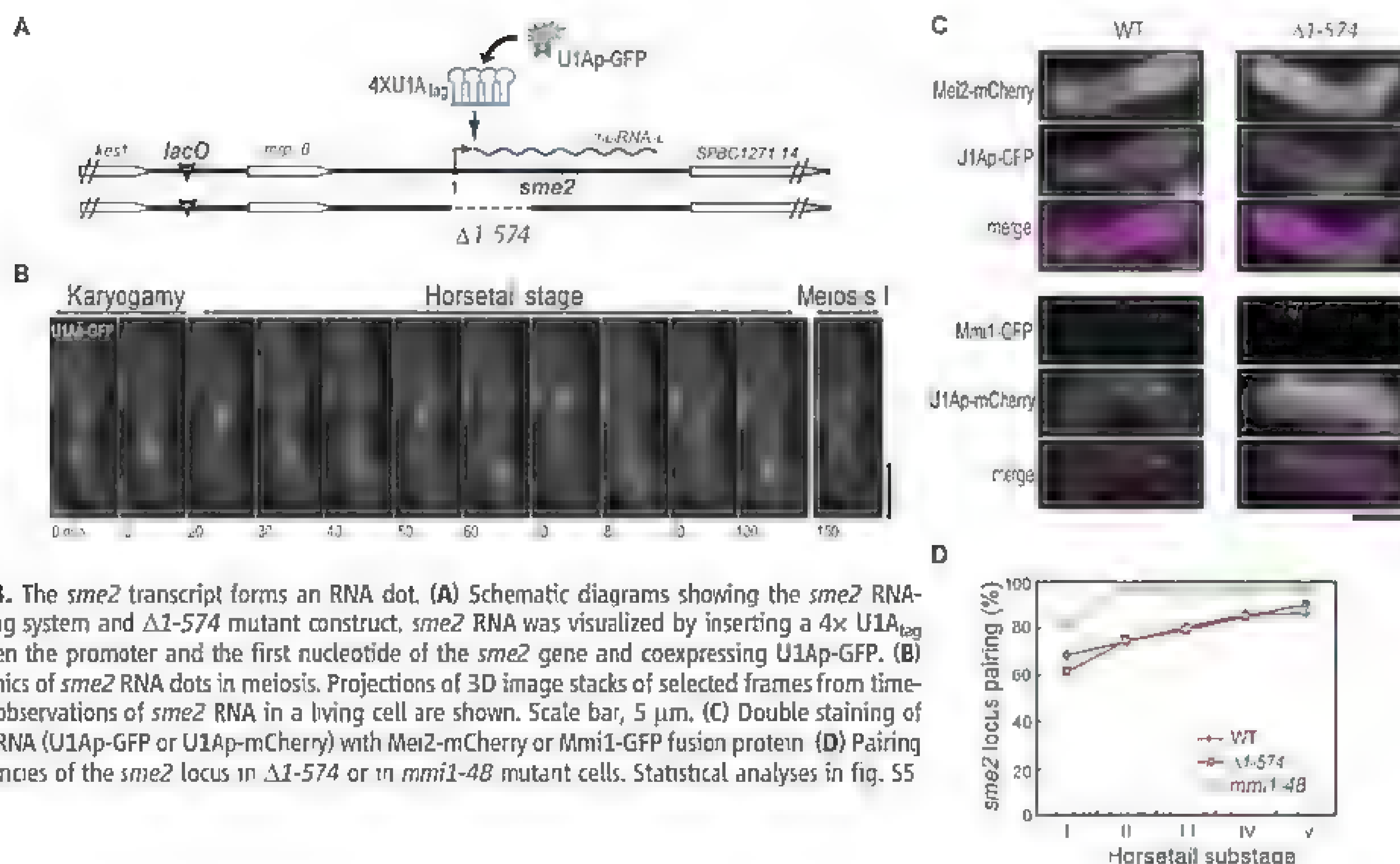
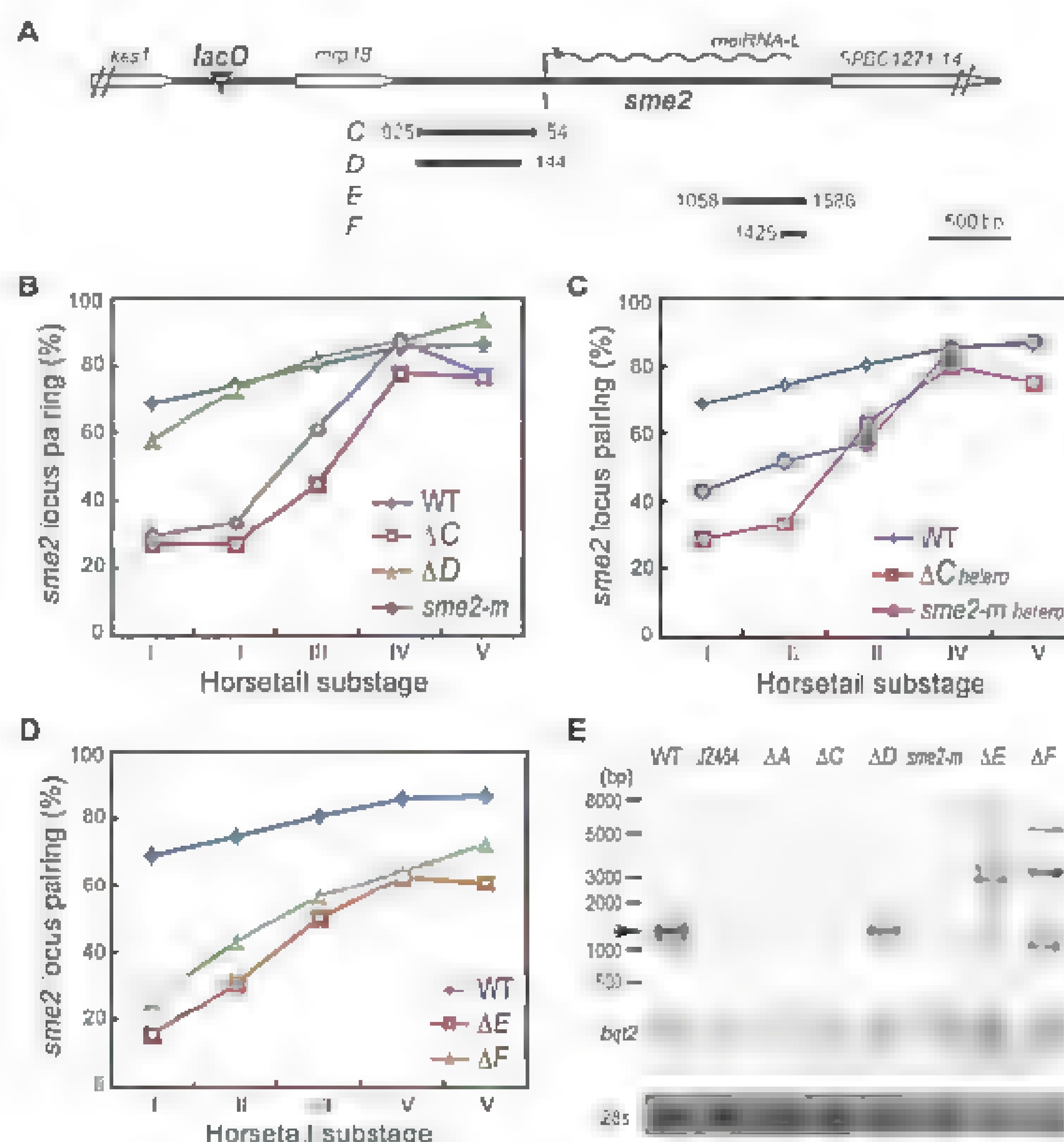


Fig. 4. The *sme2* transcript forms an RNA dot. (A) Schematic diagrams showing the *sme2* RNA-labeling system and $\Delta 1-574$ mutant construct, *sme2* RNA was visualized by inserting a 4x U1A_{tag} between the promoter and the first nucleotide of the *sme2* gene and coexpressing U1Ap-GFP. (B) Dynamics of *sme2* RNA dots in meiosis. Projections of 3D image stacks of selected frames from time-lapse observations of *sme2* RNA in a living cell are shown. Scale bar, 5 μ m. (C) Double staining of *sme2* RNA (U1Ap-GFP or U1Ap-mCherry) with Mei2-mCherry or Mmi1-GFP fusion protein. (D) Pairing frequencies of the *sme2* locus in $\Delta 1-574$ or in *mmi1-48* mutant cells. Statistical analyses in fig. S5.

Then, we followed homologous pairing of the *sme2* loci directly by chromosomally inserting *lacO* arrays visualized with lacI fused with green fluorescent protein (lacI-GFP) (Fig. 1A) (14). The *sme2* loci also displayed robust pairing as early as the onset of the horsetail stage [Fig. 1B, wild type (WT) in Fig. 1C], after the pairing of Mei2 dots (fig. S1C). Telomere clustering and horsetail movement spatially align homologous chromosomes to promote their contact, as a consequence, pairing frequency, in general, depends on the distance from the telomere (2). However, the pairing frequency of the *sme2* loci was significantly higher than for any other chromosomal loci examined, especially during the earlier horsetail substages (Fig. 1, C and D). This robust pairing was impaired in *bqt1* and *dhl1* mutants (Fig. 1C, right), which are defective in telomere clustering and horsetail movement, respectively (18, 19). The robust pairing at the *sme2* locus was, however, independent of recombination. In *rec12* mutant cells lacking Rec12 (Spo11 homolog) as required for DSB formation, the frequency of pairing of the *sme2* loci was comparable with that in WT cells (*rec12* in Fig. 1C, left). These results suggest that the *sme2* loci display robust pairing, independent of recombination.

To confirm that the *sme2* locus is required for the robust pairing observed at this region, we deleted the DNA sequence spanning the *sme2* locus (fragments A or B indicated in Fig. 1A). In these deletion experiments, we inserted fragment A into the *lys1* locus to rescue the *sme2* gene function for meiosis. Deletion of fragment A or B resulted in the loss of robust pairing at this locus (ΔA and ΔB in Fig. 1C, left). Pairing increases gradually in a recombination-dependent manner as in an ordinary arm region (compare ΔA and ΔA *rec12* in Fig. 1C, left).

Next, to test if the *sme2* locus is sufficient to induce robust pairing, we translocated the DNA sequence containing the *sme2* locus (fragment A indicated in Fig. 1A) to the *ade8* locus and the *lys1* locus (Fig. 2A). Pairing of homologous chromosomes at these loci was highly elevated (+A in Fig. 2A), and again, these increases were independent of recombination (+A *rec12* in Fig. 2A). These data suggest that the observed recombination-independent robust pairing is due to the presence of the *sme2* locus. Note that *sme2*-mediated pairing at the *lys1* locus is delayed compared with that at the *ade8* locus, which reflects the distance from the telomere.

When two copies of the *sme2* gene are present on nonhomologous chromosomes, these loci associated transiently during the horsetail stage. We generated a zygote nucleus containing one copy of the *lacO* array at the *sme2* locus and the other copy at the *lys1* locus. These arrays never associated with each other (Fig. 2B). However, when an additional copy of *sme2* was inserted at the *lys1* locus (Fig. 2C), transient ectopic pairing was observed in 30% of the horsetail nuclei ($n = 131$); this transient ectopic association

persisted from 5 to 30 min and then was resolved during the horsetail stage. Clearly, the *sme2* loci are capable of recognizing each other even when located on nonhomologous chromosomes, but their pairing is dominated by telomere-mediated alignment of homologous chromosomes.

The effect of *sme2* on robust pairing remained significant 100 kb from the *sme2* locus, but almost disappeared at 200 kb (fig. S2A). As a consequence of enhanced pairing, the chromosome region containing the *sme2* locus has a high recombination frequency (Fig. 2D). Deletion of the *sme2* sequence decreased recombination frequency at the *sme2* locus (*tub1* to *kes1* interval), and insertion of the *sme2* sequence next to the *lys1* locus increased recombination frequency at this locus (*cgr1* to *sgo2* interval). As a control, an unrelated locus (*trp1* to *ade8* interval) showed no changes in recombination frequency.

We demonstrate that the *sme2* transcripts (*meiRNA*) are necessary for robust pairing. First, we deleted the putative *sme2* promoter region (fragments C and D indicated in Fig. 3A). In the ΔC strain, transcription of *sme2* decreased to a level similar to that of the ΔA strain in which the entire *sme2* sequence was deleted (Fig. 3E), and pairing decreased to a level similar to that in the ΔA mutant (compare Fig. 3B with Fig. 1C). In contrast, robust pairing was observed in the mutant with the shorter deletion (ΔD in Fig. 3B). In the *sme2-m* cells bearing mutations in the TATA box sequence (14), transcription was significantly reduced (Fig. 3E), and the pairing decreased to a level similar to that of the promoter-deleted ΔC mutant (Fig. 3B). Furthermore, when a WT cell was crossed with a ΔC or *sme2-m* cell, the robust pairing was lost or severely impaired in the resulting heterozygous zygotes (Fig. 3C), which suggests that transcripts from both homologous chromosomes are required for robust pairing. In addition, deletion of the 3' regions of *sme2* also impaired robust pairing (ΔE and ΔF in Fig. 3D). In the ΔE and ΔF mutants, which lack a polyadenylation site (16), longer read-through transcripts were expressed (Fig. 3E). From these results, we concluded that the 1.5-kb *meiRNA-L* was required for robust pairing. The robust pairing was observed in mutants defective in *dicer* (*dcl1*) or argonaute (*ago1*) (fig. S2B), major components of RNA interference machinery (20, 21).

Using a *U1A₃₃₃-sme2* gene and a U1Ap-GFP fusion construct to visualize the localization of RNA transcripts in living cells (Fig. 4, A and B) (22), we found that the *sme2* RNA transcripts accumulated in the Mei2 dot (Fig. 4C). Deletion of a 5' region of the *sme2* gene (ΔI 574), on the other hand, resulted in loss of the Mei2 dot, but the ΔI 574 *meiRNA-L* still accumulated on the chromosome (Fig. 4C, top right). Furthermore, the Mmi1 protein was also colocalized with ΔI -574 *meiRNA-L* on the chromosome (Fig. 4C, bottom right). Pairing frequencies of the *sme2* locus in ΔI -574 mutant cells were as robust as in WT cells (Fig. 4D). Thus, the 3'

region of the *meiRNA-L* is sufficient for robust pairing at the *sme2* locus, and the 5' region of the *meiRNA-L* is necessary for recruiting Mei2 protein to the locus, but Mei2 recruitment is not necessary for robust pairing at the *sme2* locus. In the termination-defective ΔE and ΔF mutants, *sme2* transcripts did not accumulate at the *sme2* locus (fig. S3, A and B), and Mei2 and Mmi1 were also dispersed. In those cells, the homologous pairing was reduced (Fig. 3D). In an *mmi1-48* mutant (17), robust pairing was enhanced compared with that of WT cells (Fig. 4D). The *meiRNA-L* level is up-regulated in *mmi1* mutants because *meiRNA-L* is a target of Mmi1-mediated degradation by the exosome (16, 17). Taken together, these results support the idea that *meiRNA-L* mediates robust pairing of the *sme2* loci.

In *S. pombe*, chromosomes are first aligned by telomere clustering and horsetail nuclear movement (2). However, telomere clustering itself cannot provide chromosome specificity. Our results demonstrate that accumulation of *meiRNA-L* transcript at the *sme2* locus acts as a cis-acting pairing factor. On the other hand, even though local pairing and recombination was greatly reduced when the *sme2* locus was removed from chromosome II, no obvious defects in chromosome segregation or spore formation were detected in such strains. These observations raise the possibility that other, as yet undiscovered, pairing sites may also exist on chromosome II. Thus, we propose a model in which RNA-containing complexes along each chromosome act as chromosome-specific identifiers (fig. S4).

References and Notes

1. Y. Chikashige et al., *Science* **264**, 270 (1994).
2. D. Q. Ding, A. Yamamoto, T. Haraguchi, Y. Hiraoka, *Dev. Cell* **6**, 329 (2004).
3. Y. Chikashige, T. Haraguchi, Y. Hiraoka, *Chromosoma* **116**, 497 (2007).
4. Y. Hiraoka, A. F. Dernburg, *Dev. Cell* **17**, 598 (2009).
5. R. Koszul, N. Kieckhefer, *Trends Cell Biol.* **19**, 716 (2009).
6. D. Q. Ding, T. Haraguchi, Y. Hiraoka, *FEBS J.* **277**, 565 (2010).
7. B. D. McKee, *Biochim. Biophys. Acta* **1677**, 165 (2004).
8. K. S. McKim, *Cell* **123**, 989 (2005).
9. J. L. Gerton, R. S. Hawley, *Nat. Rev. Genet.* **6**, 477 (2005).
10. U. Zickler, *Chromosoma* **115**, 158 (2006).
11. A. Barzel, M. Kupiec, *Nat. Rev. Genet.* **9**, 27 (2008).
12. Y. Watanabe, M. Yamamoto, *Cell* **78**, 487 (1994).
13. Y. Watanabe, S. Shirozaki-Yabana, Y. Chikashige, Y. Hiraoka, M. Yamamoto, *Nature* **386**, 187 (1997).
14. T. Shimada, A. Yamashita, M. Yamamoto, *Mol. Biol. Cell* **14**, 2461 (2003).
15. A. Yamashita, Y. Watanabe, N. Nukina, M. Yamamoto, *Cell* **95**, 115 (1998).
16. A. Yamashita et al., *Open Biol.* **2**, 120014 (2012).
17. Y. Harigaya et al., *Nature* **442**, 45 (2006).
18. Y. Chikashige et al., *Cell* **125**, 59 (2006).
19. A. Yamamoto, R. R. West, J. R. McIntosh, Y. Hiraoka, *J. Cell Biol.* **145**, 1233 (1999).
20. P. Provost et al., *Proc. Natl. Acad. Sci. U.S.A.* **99**, 16648 (2002).
21. T. Volpe et al., *Chromosome Res.* **11**, 137 (2003).
22. T. Andoh, Y. Oshiro, S. Hayashi, H. Takeo, T. Tam, *Biochem. Biophys. Res. Commun.* **351**, 999 (2006).

23 C. Elmerter, G. R. Smith, *Proc. Natl. Acad. Sci. U.S.A.* **102**, 10952 (2005)

Acknowledgments: We thank T. Andoh and T. Tani for providing the RNA visualizing system, J. Nakayama for *S. pombe* strains, A. Yamashita for discussions, C. Mori and N. Sakurai for technical support. This work was supported

by KAKENHI grants from MEXT of Japan to D.-Q.D., T.H., M. Yamamoto, and Y.H.

Supplementary Materials

www.sciencemag.org/content/tbl/336/6082/732/DC1
Materials and Methods

Figs. S1 to S5

Table S1

References (24–26)

23 January 2012, accepted 19 March 2012
10.1126/science.1219518

Epigenomic Enhancer Profiling Defines a Signature of Colon Cancer

Batool Akhtar-Zaidi,^{1,2} Richard Cowper-Sal-lari,³ Olivia Corradin,¹ Alina Saiakhova,¹ Cynthia F. Bartels,¹ Dheepa Balasubramanian,¹ Lois Myeroff,⁴ James Lutterbaugh,⁴ Awad Jarrar,⁵ Matthew F. Kalady,^{4,5,6} Joseph Willis,^{4,7} Jason H. Moore,³ Paul J. Tesar,^{1,4} Thomas Laframboise,^{1,4} Sanford Markowitz,^{1,4,8} Mathieu Lupien,^{3,9} Peter C. Scacheri^{1,2,4,*}

Cancer is characterized by gene expression aberrations. Studies have largely focused on coding sequences and promoters, even though distal regulatory elements play a central role in controlling transcription patterns. We used the histone mark H3K4me1 to analyze gain and loss of enhancer activity genome-wide in primary colon cancer lines relative to normal colon crypts. We identified thousands of variant enhancer loci (VELs) that comprise a signature that is robustly predictive of the *in vivo* colon cancer transcriptome. Furthermore, VELs are enriched in haplotype blocks containing colon cancer genetic risk variants, implicating these genomic regions in colon cancer pathogenesis. We propose that reproducible changes in the epigenome at enhancer elements drive a specific transcriptional program to promote colon carcinogenesis.

Although noncoding functional elements play a central role in establishing gene expression patterns that drive normal development, cell-type identity, and evolutionary processes, their potential involvement in the context of common cancers remains unknown. The mono- and dimethylated forms of histone 3 lysine 4 (H3K4me1/2) broadly mark multiple classes of gene enhancer elements (1–3). Here, we present an epigenomic comparison of H3K4me1-marked gene enhancer elements in a cohort of colorectal cancer (CRC) cell lines and normal colon epithelial crypt cells, from which colon cancer is derived.

We performed H3K4me1 chromatin immunoprecipitation sequencing (ChIP-seq) analysis on

three preparations of normal epithelial crypts as well as primary CRC cell lines derived from two early-stage tumors (V432 and V703), two late-stage tumors (V8 and V9P), and five liver metastases (V400, V457, V481, V503, V9M). On average, we detected ~71,000 peaks significantly enriched for H3K4me1 at a false discovery rate of less than 5% (table S1). The distribution of H3K4me1 relative to annotated genes is similar between colon cancer samples and crypt controls, with most H3K4me1 sites mapping to intergenic and intronic regions located distal to transcription start sites (fig. S1). We compared H3K4me1 patterns between all 12 colon samples and 9 unrelated human cell types (4). H3K4me1 patterns in tumors are more similar to those of colon crypt than of noncolon cells, consistent with the notion that colon tumors are derived from colon crypts (fig. S2). Moreover, there is less variation between the colon samples than between unrelated cell types.

We identified thousands of H3K4me1 sites, or variant enhancer loci (VELs), that are differentially enriched (lost or gained) in each of the CRC samples compared to normal colon crypts (Fig. 1A). On average, less than 0.05% of VELs map to regions altered in DNA copy number, and thus, the vast majority of VELs are unlikely to be the result of copy-number variations related to malignant transformation. VELs comprise 28 to 61% of all putative enhancers present in a given CRC sample (Fig. 1B). ChIP-seq analysis of H3K27ac, an epigenetic mark of active enhancer elements, revealed that ~40% of gained VELs acquire H3K27ac in CRC. Of lost VELs, 70% are

enriched for H3K27ac in normal crypts and show virtually no detectable levels of H3K27ac in CRC (fig. S3). We also performed global mapping of deoxyribonuclease I (DNase I)-hypersensitive sites in two CRC lines using DNase-seq (5). Consistent with acquisition and loss of enhancer marks, virtually all gained VELs map to open chromatin sensitive to DNase I digestion, and lost VELs map to DNase I-insensitive regions (fig. S3, D and E). Collectively, the data indicate that multiple changes in chromatin state and function accompany the changes in H3K4me1 at VELs. Lastly, we verified that H3K4me1 sites are functionally active using luciferase reporter assays (fig. S4).

A higher number of VELs than expected by random chance are common to multiple CRC samples. Specifically, we detected 2604 gained VELs common to five or more lines, and 2047 lost VELs common to six or more CRC lines ($P < 0.001$). Both unique and common VELs are distributed relatively evenly among the CRC samples (Fig. 1D); 197 VELs are shared between all 9 CRC samples. The universally common VELs are dispersed throughout the genome on multiple chromosomes and do not appear to cluster in any meaningful way (fig. S5).

We ranked VELs by their level of specificity in crypts and nine unrelated cell types. Compared to a control set of H3K4me1 sites invariant between CRC samples and crypts, lost VELs are highly crypt specific, whereas gained VELs are relatively noncrypt specific (fig. S6A). These relationships also held true for common VELs (fig. S6B). We also determined that 67 to 92% of gained VELs map to H3K4me1-marked loci in any one of the nine noncolon cell types, compared to 9 to 11% for lost VELs and 24 to 31% for control enhancers (Fig. 1E). Collectively, these data indicate that in colon cancer, the chromatin configuration is altered by acquisition of putative enhancer marks that are normally found in noncolon cell types, and by loss of putative enhancer marks that typify normal crypt differentiation status; the net effect leading to a less colon-specific phenotype.

Multiple approaches were used to assess the relationship between VELs and gene expression. Compared to control genes not linked to gained VELs, genes linked to gained VELs are generally more highly expressed in CRC samples than in crypts, and genes linked to lost VELs are expressed at a lower level in CRC samples than in crypts (Fig. 2A and fig. S7). For all CRC samples, the effect of lost VELs on gene repression is more pronounced than the effect of gained VELs on gene overexpression, indicating that lost VELs are more likely than gained VELs to

¹Department of Genetics and Genome Sciences, Case Western Reserve University, Cleveland, OH 44106, USA. ²Department of Molecular Medicine of the Cleveland Clinic Lerner College of Medicine, Case Western Reserve University, Cleveland, OH 44106, USA. ³Norms Cotton Cancer Center, Institute for Quantitative Biomedical Sciences, Department of Genetics, Dartmouth Medical School, Lebanon, NH 03756, USA. ⁴Case Comprehensive Cancer Center, Case Western Reserve University, Cleveland, OH 44106, USA. ⁵Department of Colorectal Surgery, Cleveland Clinic Foundation, Cleveland, OH 44195, USA. ⁶Cancer Biology Department, Lerner Research Institute, Cleveland Clinic Foundation, Cleveland, OH 44195, USA. ⁷Department of Pathology, Case Western Reserve University, Cleveland, OH 44106, USA. ⁸Department of Medicine, Case Western Reserve University, Cleveland, OH 44106, USA. ⁹Ontario Cancer Institute, University Health Network and Department of Medical Biophysics, University of Toronto, Toronto, Ontario, M5G 1L7, USA.

*To whom correspondence should be addressed at Department of Genetics, Case Western Reserve University, School of Medicine, 10900 Euclid Avenue, BRB 627, Cleveland, OH 44106, USA. E-mail: psc183@case.edu.

confer a functional effect. Overexpressed genes are 1.6 to 6.2 times more likely than randomly selected control genes to have gained VELs (Fig. 2B). Repressed genes are 2.8 to 8.7 times more likely than controls to have lost VELs (Fig. 2C). One VEL is generally sufficient to confer an effect on gene expression, and additional VELs confer more marked changes in a relatively quantitative fashion (Fig. 2, D and E, and fig. S8). Genes associated with gained VELs are generally expressed at high levels in crypt controls, and their expression is further elevated in CRC (Fig. 2F and fig. S9). Genes associated with lost VELs are expressed at mid to high levels in crypt controls and generally become either attenuated or

silenced in CRC (Fig. 2F and fig. S9). These results are consistent with the above findings indicating that the majority of lost VELs lose the active H3K27ac enhancer mark, whereas the minority of gained VELs acquire H3K27ac. We also found that correlations of global gene expression between CRC samples and crypts improved when VEL genes were not considered (fig. S10A). Common VELs are also enriched for genes frequently dysregulated in the CRC cell lines (fig. S10B). Collectively, the data indicate that gained and lost VELs are highly predictive of local cancer-specific overexpressed and repressed genes, respectively. Consistent with these positive correlations, lost VEL gene promoters often show decreases in

H3K4me3 and/or H3K27ac in CRC relative to crypts, and gained VEL gene promoters show increases in H3K4me3 and/or H3K27ac in CRC relative to crypts (fig. S11). However, there is also a class of VEL genes that do not show measurable differences in promoter-associated H3K4me3/H3K27ac between normal crypts and CRC, but clearly show expression changes (fig. S11, B and C).

If VELs are indeed cancer-related events, then aberrantly expressed genes associated with common VELs ought to validate as aberrantly expressed in primary tumors. We determined that overexpressed genes associated with gained VELs common to five to nine lines, and repressed genes associated with lost VELs common to six to eight lines, validated as aberrantly expressed in primary tumors at a rate two to eight times higher than that determined when the VEL was not considered (Fig. 3, A and B). These results suggest that VELs are a signature predictive of the *in vivo* colon cancer transcriptome more robustly than the aberrant gene expression patterns associated with the colon cancer cell lines from which the VELs themselves were identified. 15-Hydroxyprostaglandin dehydrogenase (PDGH), a colon tumor suppressor gene associated with the VEL signature and repressed in CRC, is shown in Fig. 3C (6).

Twenty single-nucleotide polymorphisms (SNPs) have been identified through genome-wide association studies to confer risk to CRC (7–18). We used variant set enrichment analyses (VSEs) to test whether enhancers and VELs were significantly enriched among the 20 CRC-risk SNPs [or variants in linkage disequilibrium (LD) with the CRC risk SNPs (clusters), designated as the annotated variant set (AVS)]. Among the 20 clusters of SNPs comprising the AVS, 16 (80%) overlapped at least one H3K4me1 site in colon crypt (Fig. 4A). Similar analyses in nine other cell types indicated that the CRC AVS association was specific to H3K4me1 enhancers in colon crypt and HepG2 cells (Fig. 4B). Furthermore, significant associations were detected between the AVS and low-frequency lost VELs (L1 and L2, Fig. 4B), and not common gained or lost VELs. An example is shown in Fig. 4C. Of the eight SNPs associated with unique lost VELs, five (rs719725, rs6983267, rs10505477, rs7014346, and rs3802842) were associated with enhancers in crypt and HepG2 cells, and not in any other cell types, indicating that SNP/enhancer associations exclusive to the disease-relevant tissue are particularly important. Although VSE tests for enrichment of enhancers in linkage disequilibrium with the CRC AVS as a whole, we did detect multiple instances in which individual risk SNPs (or variants in strong LD with the risk SNP) overlapped VELs, despite the lack of significance with the entire AVS. For example, rs4444235 was significantly associated with gains common to seven CRC lines ($P = 0.004$). Rs4444235 maps to the enhancer of BMP4 and increases its expression (19). Accordingly, gained VELs at this locus

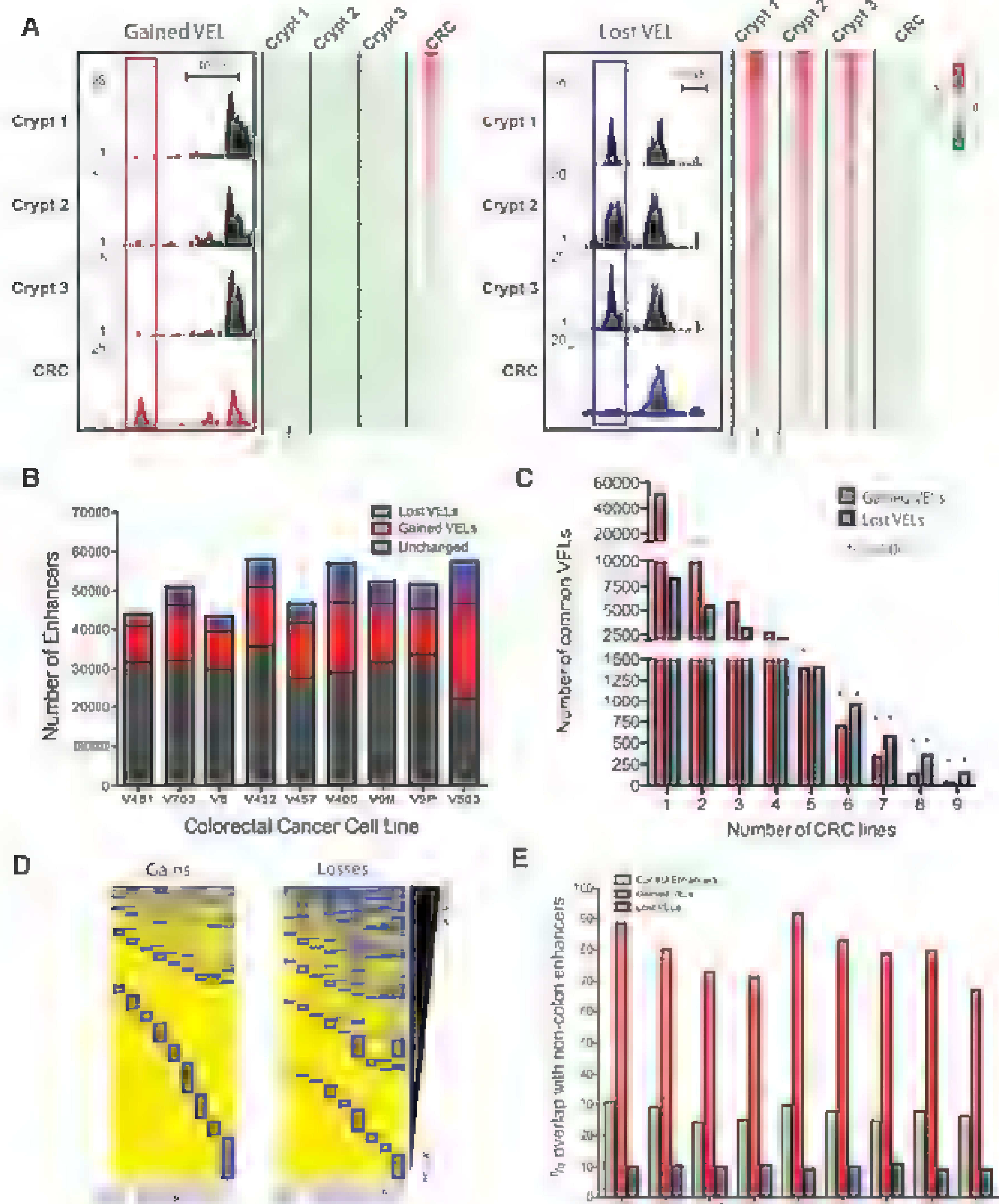


Fig. 1. H3K4me1 ChIP-seq identifies variant enhancer loci (VELs). (A) UCSC browser views of H3K4me1 profiles from three normal crypts and a CRC cell line (V400), illustrating an example of a gained (left) and a lost (right) VEL. Heatmaps show the corresponding H3K4me1 ChIP-seq signals ± 5 kb of VEL midpoints. (B) Number of VELs and unchanged H3K4me1 sites in CRC samples relative to normal controls. (C) Number of unique and common VELs. (D) Distribution of VELs among CRC lines. VELs are shown in blue. (E) Percentage of control enhancers and VELs that overlap with H3K4me1 sites in any of nine noncolon cell types. All comparisons are significant by χ^2 test ($P < 10e-10$).

correlate with increased BMP4 expression in CRC cell lines. Furthermore, lost VELs associated with risk SNPs rs719725 and rs9929218 were associated with reduced expression of potential target genes, JMJD2C and TMED6, in CRC samples containing the lost VELs. Collectively, these findings provide further evidence that enhancers and VELs are relevant to CRC pathogenesis.

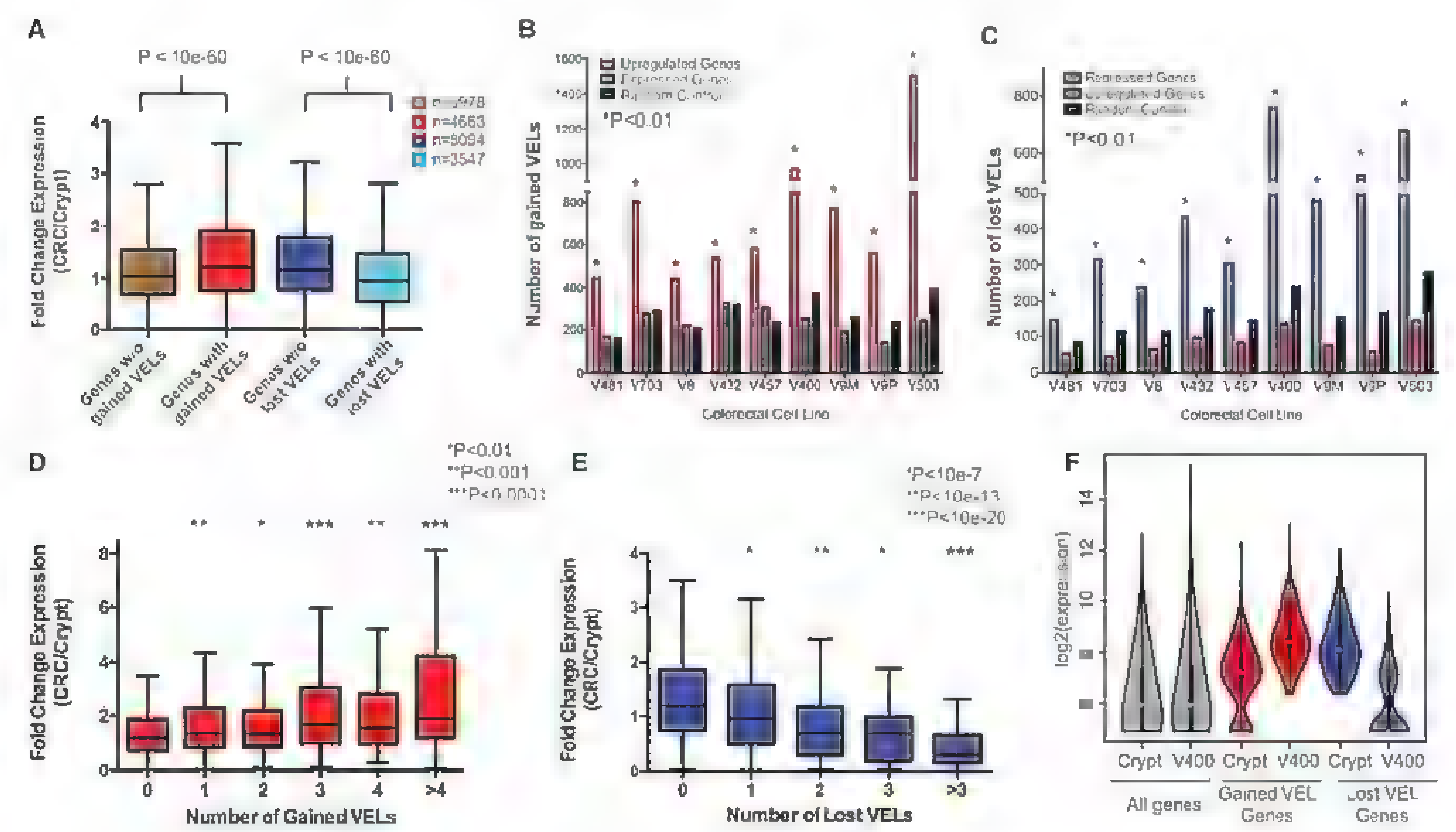
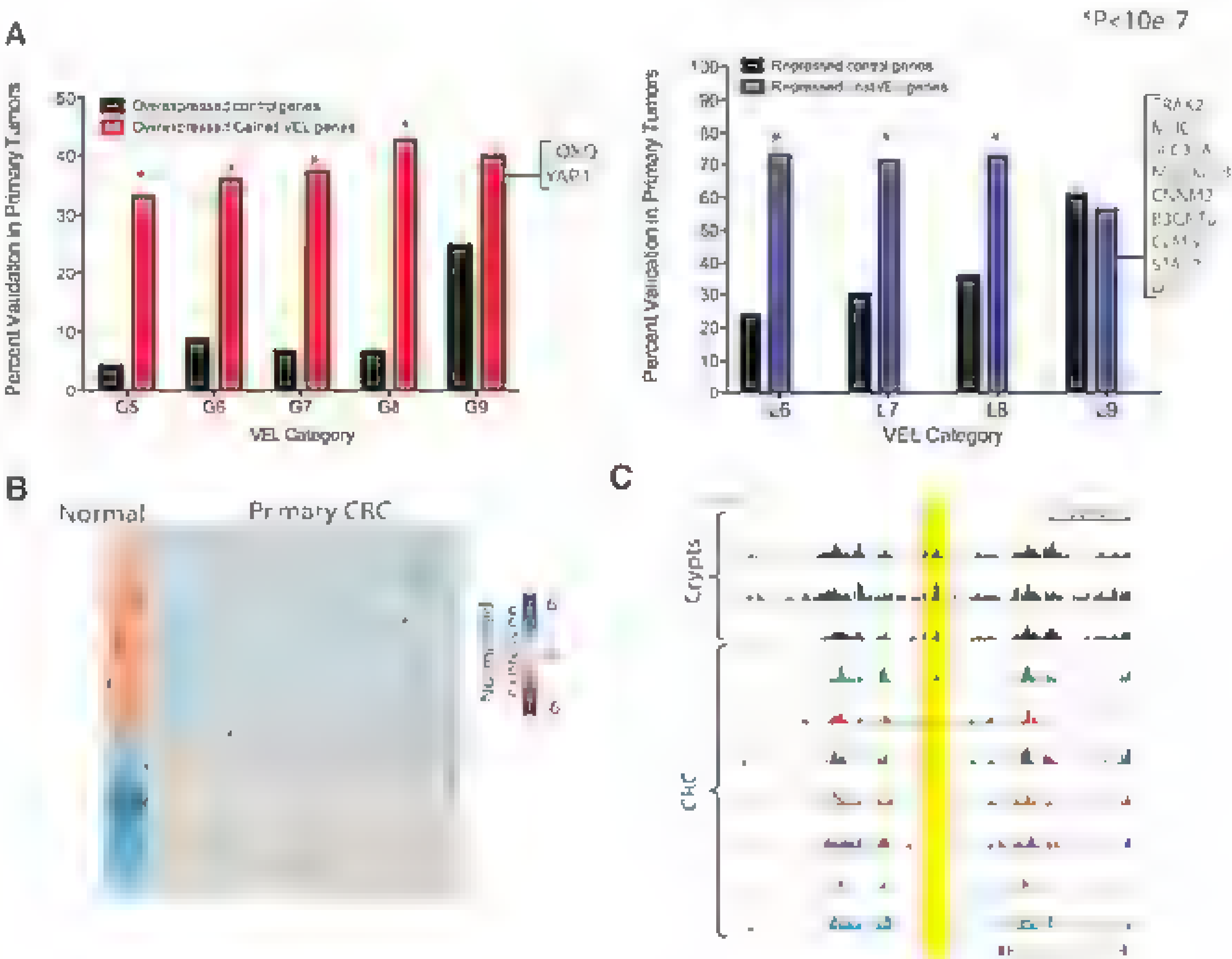


Fig. 2. VELs correlate with aberrant gene expression. (A) Fold change in expression of VEL and control genes for a representative CRC line (V400). Number of (B) gained and (C) lost VELs associated with overexpressed and repressed genes, respectively. Fold change in expression of genes associated with variable numbers of (D) gained VELs and (E) lost VELs in CRC sample V400. (F) Levels of all genes (gray) and aberrantly expressed genes (>1.5-fold relative to crypts) associated with VELs in CRC sample V400.

Fig. 3. Common VELs predict aberrant gene expression in primary tumors. (A) (Left) Red bars represent the percentage of overexpressed genes associated with gained VELs common to five or more lines (G5 to G9) that validate as overexpressed in primary tumors. Black bars represent the baseline predictive power when the VEL is not considered, i.e., the percentage of overexpressed genes in five or more cell lines that validate as overexpressed in primary tumors. G9 genes that validated as overexpressed in primary tumors are listed in brackets. (Right) Same as left, but for lost VELs common to six or more lines (L6 to L9). (B) Heatmap of expression of VEL associated genes in (A) (red and blue bars) in normal colon tissue ($n = 16$) and primary CRC tumors ($n = 120$). (C) UCSC Browser view of H4K4me1 ChIP-seq signals across the PDGF locus, associated with a lost VEL common to six CRC samples (highlighted in yellow).



Our epigenomic comparison of H3K4me1-marked gene enhancer elements in colon cancer cells suggest that central changes at enhancers drive a specific transcriptional program to promote colon carcinogenesis. Lost VELs appear to contribute to this signature more than gained VELs, as lost VELs confer a greater functional effect on expression than gained VELs, are better predictors of gene expression in primary tumors than gained VELs, typify colon crypt identity, are far more concordant across tumors than gained VELs, and are more robustly as-

sociated with CRC-risk SNPs than gained VELs. Most, but not all, VELs are linked to changes in promoter-associated H3K4me3 and H3K27ac. Thus, VELs capture novel and global information about the chromatin state that is related to gene expression. Moreover, these findings suggest that some of the VEL genes identified in this study would likely remain undiscovered through analysis of these promoter marks alone. Lastly, most VELs are common to at least two of nine (>20%) CRC samples. The commonality of the epigenetic colon cancer signature captured

by VELs contrasts with the marked heterogeneity in mutations in colon cancer candidate driver genes revealed by genome sequencing and suggests either that VELs capture pathway outputs that are downstream of sets of gene mutations or that they capture epigenetic alterations that are independent of and more common than gene mutations (20–22). Clearly, the number of enhancers consistently altered across multiple CRC tumors is likely far greater than genes commonly mutated in colon cancer. These findings, even when adjusted for the notion that enhancers are two to five times more prevalent than genes, suggest that the epigenetic terrain at gene enhancer elements in colon cancer is less heterogeneous than the genetic landscape of protein-coding genes.

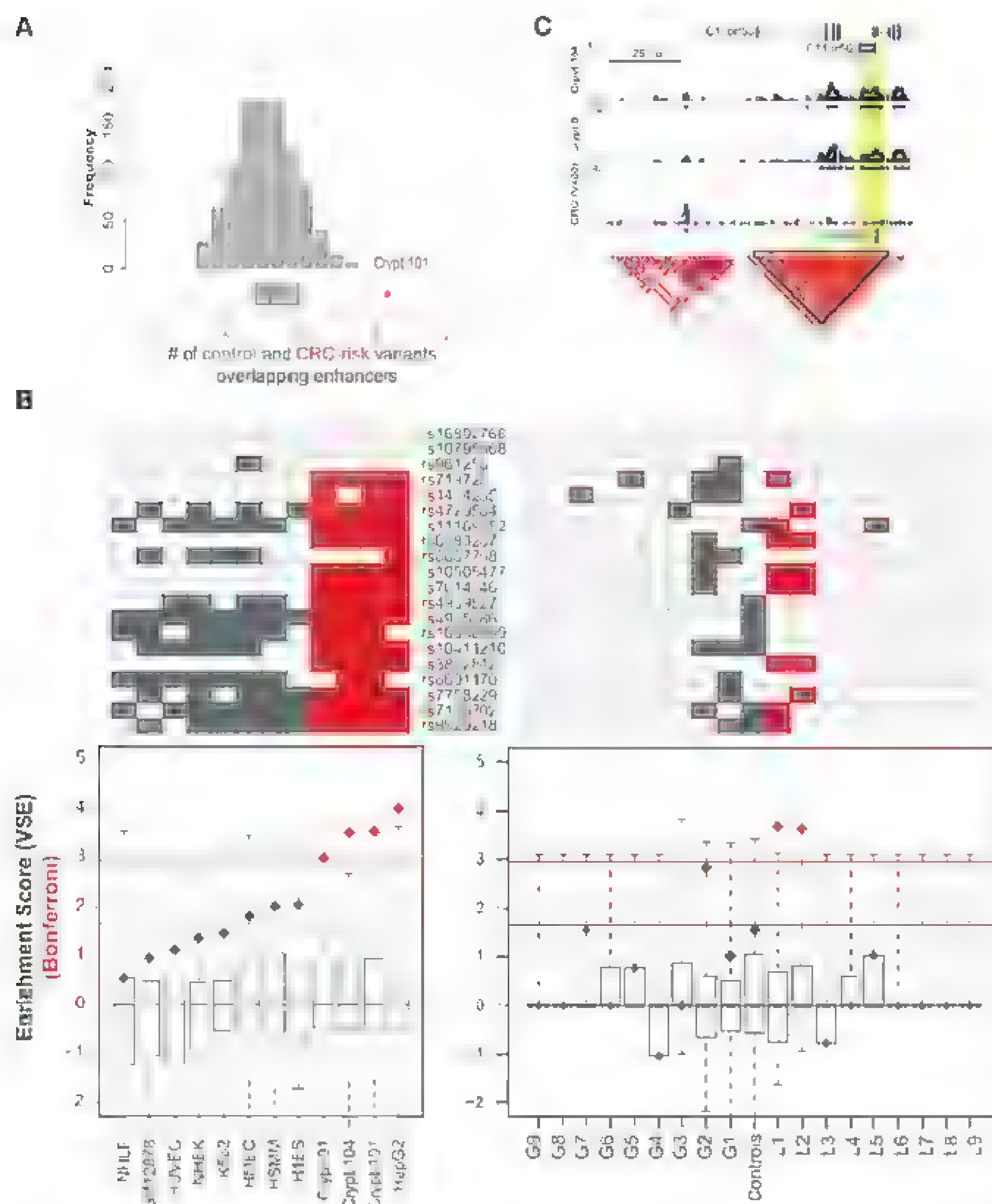


Fig. 4. Colon enhancers and VELs are associated with genetic risk variants for CRC. (A) Results of VSE analysis showing that 16 of 20 CRC-risk SNP clusters map to H3K4me1-marked enhancers in a colon crypt sample (C101, red diamond), compared to a null distribution (gray). (B) (Left) The results of VSE analyses testing the association between CRC-risk SNPs and H3K4me1 sites in 10 cell types. The red line represents the significance threshold. The lower horizontal line represents the unadjusted significance threshold. The individual CRC SNPs found to be associated with H3K4me1 enhancers in each cell type are indicated in boxes, above each boxplot. (Right) VSE analysis of the CRC-risk SNPs and VELs. Control enhancers are H3K4me1 sites that are unchanged between CRC samples and crypts. L1 corresponds to unique lost VELs; L2 to L9 correspond to losses common to two to nine lines. G1 corresponds to unique gained VELs; G2 to G9 correspond to gains shared between two and nine lines. (C) Example of a lost VEL directly overlapping a CRC risk SNP shown within the relevant haplotype block structure (red).

References and Notes

1. N. D. Heintzman *et al.*, *Nature* **459**, 108 (2009).
2. A. Rada-Iglesias *et al.*, *Nature* **470**, 279 (2011).
3. G. E. Zentgraf, P. J. Tesar, P. C. Schachner, *Genome Res.* **21**, 1273 (2011).
4. J. Ernst *et al.*, *Nature* **473**, 43 (2011).
5. A. P. Boyle *et al.*, *Cell* **132**, 311 (2008).
6. S. J. Myung *et al.*, *Proc. Natl. Acad. Sci. U.S.A.* **103**, 12098 (2006).
7. U. Peters *et al.*, *Hum. Genet.* **131**, 217 (2012).
8. J. C. Figueiredo *et al.*, *Cancer Epidemiol. Biomarkers Prev.* **20**, 758 (2011).
9. R. Cui *et al.*, *Gut* **60**, 799 (2011).
10. R. S. Houlston *et al.*, *Nat. Genet.* **42**, 973 (2010).
11. R. S. Houlston *et al.*, *Nat. Genet.* **40**, 1426 (2008).
12. I. P. Tomlinson *et al.*, *Nat. Genet.* **40**, 623 (2008).
13. A. Tenesa *et al.*, *Nat. Genet.* **40**, 631 (2008).
14. P. Brodenck *et al.*, *Nat. Genet.* **39**, 1315 (2007).
15. J. Lascorz *et al.*, *Carcinogenesis* **31**, 1612 (2010).
16. B. W. Zanke *et al.*, *Nat. Genet.* **39**, 989 (2007).
17. J. N. Poynter *et al.*, *Cancer Res.* **67**, 11128 (2007).
18. L. A. Hindorf *et al.*, www.genome.gov/qwastudies (2012).
19. S. J. Lubbe *et al.*, *Oncogene* **30**, 1038/anc.2011.564 (2011).
20. A. J. Bass *et al.*, *Nat. Genet.* **43**, 964 (2011).
21. T. Sjöblom *et al.*, *Science* **314**, 268 (2006).
22. L. D. Wood *et al.*, *Science* **318**, 1108 (2007).

Acknowledgments: We thank A. Ting and K. Guda for helpful comments and discussion, Z. Zhang for providing Perl scripts for data analysis; P. Manerikov for assistance with data visualization; and S. Edelfelt, N. Beckloff, and N. Molyneux from the Case Western Reserve University Genomics Core for sequencing and informatics assistance. This work was supported in part by N.H. grants R01HD056369 and R01CA160356 (to P.C.S.), R01CA1555004 (to M.L.), R01LM009012 and R01LM010098 (to J.H.M. and R.C.S.), 1P50CA150964 and N.H. U01CA152756 (to S.M.), and 5T32GM008056-29 (to D.C.). B.A.-Z. is a predoctoral student in the Molecular Medicine Ph.D. Program of Cleveland Clinic and Case Western Reserve University, funded in part by the Med into Grad initiative of the Howard Hughes Medical Institute. All data are available in Gene Expression Omnibus through the accession numbers GSE36401, GSE36204, and GSE36400.

Supplementary Materials

www.sciencemag.org/cgi/content/full/336/6127/DC1

Materials and Methods

Figs. S1 to S14

Table S1

References

30 November 2011; accepted 22 March 2012

Published online 12 April 2012,

10.1126/science.1217277

Recent Explosive Human Population Growth Has Resulted in an Excess of Rare Genetic Variants

Alon Keinan^{1*} and Andrew G. Clark^{1,2}

Human populations have experienced recent explosive growth, expanding by at least three orders of magnitude over the past 400 generations. This departure from equilibrium skews patterns of genetic variation and distorts basic principles of population genetics. We characterized the empirical signatures of explosive growth on the site frequency spectrum and found that the discrepancy in rare variant abundance across demographic modeling studies is mostly due to differences in sample size. Rapid recent growth increases the load of rare variants and is likely to play a role in the individual genetic burden of complex disease risk. Hence, the extreme recent human population growth needs to be taken into consideration in studying the genetics of complex diseases and traits.

The human global population has recently grown (1) from a few million people roughly 10,000 years ago to an estimated 7 billion today (2, 3). The extent of this growth—more than three orders of magnitude within fewer than 400 generations—can be divided into one epoch of moderate exponential growth followed by accelerated explosive growth starting fewer than 100 generations ago (Fig. 1). This situation implies massive departures from population genetic equilibrium. In particular, rapid recent growth generates a load of rare variation, due to recent mutations, which may play a role in complex disease risk.

Studies modeling the demographic history of human populations from genetic data have considered a recent epoch of exponential growth of effective population size [effective population size, which is typically smaller than the real population size, determines the genetic properties of a population (4)]. Earlier studies used small amounts of data or had ascertainment biases toward an excess of common variants—which tend to be due to less recent mutations—and did not observe population growth. Recent studies (5, 6) observed an excess of rare variants in resequencing data and modeled past population growth by comparing the prediction of a model with the observed site frequency spectrum (SFS). For European history, these studies estimated as much as 0.5% growth in effective population size per generation since the split of the ancestors of Europeans and East Asians ~1000 generations ago, resulting in an effective population size of a few tens of thousands today (Table 1). However, these studies did not

capture the full scope of human expansion, which may be due to the models not allowing for a recent acceleration in growth rate (5). We hypothesize, however, that the limited sample size of these studies (at most 60 individuals), which only allowed capturing variants of frequency as low as ~1% in the sample, has provided a limited view of rare variants in the population. Rare variation adds information

on mutations that have occurred during recent epochs of accelerated explosive growth and that may be identified from sequencing larger sample sizes (7–10). Several ongoing projects are sequencing ever-larger numbers of individuals genome-wide (11, 12).

Learning from the frequencies of genetic variants about the demographic history during the past 10,000 years requires capturing variants that entered the population in that time span. Many such variants are likely to be rare in the population as a whole (i.e., frequency <0.1%, see below), requiring sequencing of a larger sample of individuals than previously considered in demographic studies. Although it is now economically feasible to sequence a sufficiently large number of individuals, such an effort introduces a new scale to the problem of false positives among newly identified variants such as single-nucleotide polymorphisms (SNPs). Specifically, the ability to easily distinguish SNPs present only once in the sample (singletons) from sequencing errors decreases as the sample size increases.

Despite an improvement in the accuracy of sequencing technologies, some errors remain unavoidable. For example, with a sequencing error rate of 1 in 10,000 bases, in a sample of 10,000 individuals, each base pair will exhibit two errors on average across the sample and the majority of monomorphic sites will appear poly-

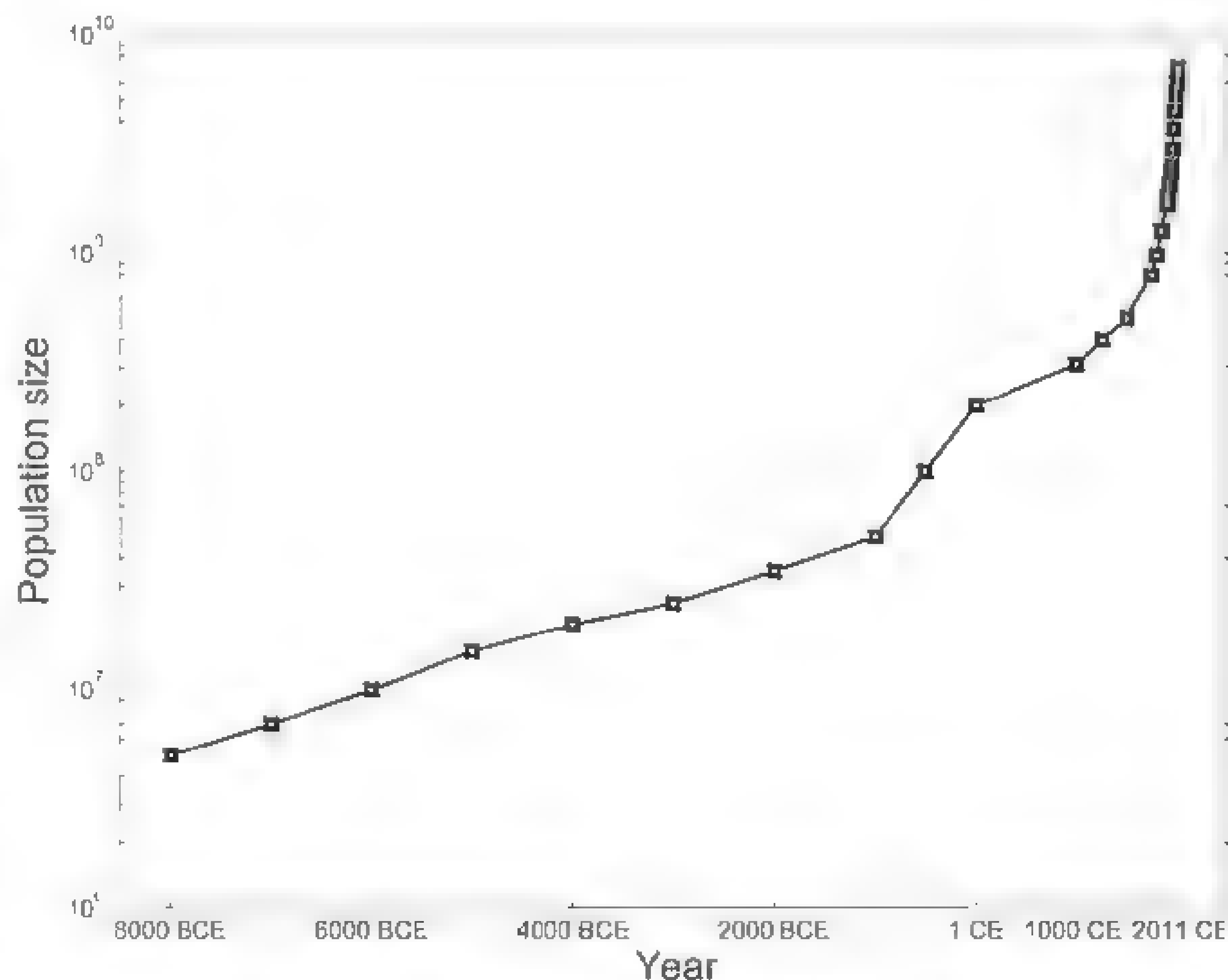


Fig. 1. Census (rather than effective) population size is presented on a logarithm scale over the past 10,000 years, from about 5 million at 8000 BCE to about 7 billion today from data in (1, 3, 30, 31). The depicted linear increase (on the log scale) through most of the presented epoch denotes exponential growth of relatively constant percentage increase in population size per year. An acceleration of that increase starting in the Common Era is evident.

¹Department of Biological Statistics and Computational Biology, Cornell University, Ithaca, NY 14853, USA. ²Department of Molecular Biology and Genetics, Cornell University, Ithaca, NY 14853, USA.

*To whom correspondence should be addressed. E-mail: ak735@cornell.edu

morphic (most often as a singleton or a doubleton; i.e., with the rare allele present in one or two copies in the sample). On the other hand, strict filtering of the data will lead to missing many rare variants because they are not observed as reliably. Hence, any analysis of large sample sizes must account for the uncertainty inherent in sequencing by considering the variant calls probabilistically, and secondary validation of rare variants by an alternate sequencing procedure is essential.

For accurate analysis of human genetic data, it is also necessary to address how assumptions underlying most population genetic analysis tools are violated with samples of thousands or more individuals (13). This may require generalizations of population genetics theory to cases in which the sample size is not necessarily smaller than the historical effective population size (13–17).

A recent study (18) analyzed a large sample size through Sanger resequencing data for two genes (*KCNJ11* and *HHEX*) in 10,422 European Americans from the Atherosclerosis Risk in Communities (ARIC) study (19). They estimated the fraction of variants that are validated by Roche/454 sequencing, which in turn recalibrated the probabilities of genotype calls and accuracy of calling rare variants. The entire SFS was considered probabilistically, with a total expected number of 262 and 317 SNPs in the two genes, respectively (18). Considering a sample of 10,000 individuals, the number of singletons estimated was at least 5 times that predicted by the standard Wright-Fisher model (18). Similarly, the expected number of doubletons was at least 3 times the prediction. Subsamples of the data show that the number of singletons increases almost linearly with sample size. As a result, in the collection of all SNPs in this sample, more than 50% are singletons. Qualitatively similar results have been reported

from sequencing of 202 genes in 15,000 individuals from different populations (20) and whole exomes of 2440 individuals of European and African ancestry (12).

By focusing on “neutral” sites—defined in (18) as synonymous SNPs and sites at least 30 base pairs from a coding region—the authors estimated a model of European demographic history from comparison of the model-predicted SFS with the probabilistically observed SFS (18) while allowing for the sample size to exceed the effective population size (13). The model estimates pointed to a recent extreme growth of 9.4% per generation [95% Bayesian credible interval (CI), 4.5 to 14.5%], starting 1400 years ago (95% CI, 900 to 2800 years ago) (Table 1). [The current global human population growth rate is estimated at 1.1% per year, equivalent to about 30% per generation (3).] The present effective population size of Europeans as estimated by the model is 1.1 million (95% CI, 0.3 to 1.9 million) (18), compared to the present effective population size of only a few tens of thousands estimated by previous models that incorporated recent exponential growth (5, 6) (Table 1).

There are several differences between the models of population history assumed by the different studies that considered recent population growth—as well as between the inference methods used—that can potentially explain the differences in results (Table 1). However, we hypothesize that the very different results are mostly due to differences in sample size. A larger sample size allows identification of rarer polymorphisms that are, on average, due to more recent mutations. Singletons in studies of 20 to 60 individuals have a frequency on the order of 1% and are due to much older mutations than the singletons of 0.005% frequency in a sample of 10,000. In the latter sample, 80% of the variants were observed in fewer than 10 copies

(<0.05%), with the vast majority of these being due to mutations that arose in the past 2500 years, according to the estimated model (18). In contrast, the majority of common SNPs with frequency greater than 5% have been segregating for several tens of thousands of years. For neutral SNPs of 5% frequency, fewer than one is expected to have arisen across the entire genome during the past 2500 years, and only ~8% during the past 10,000 years (18). Thus, the larger the sample size, the more recent the epoch it probes.

The excess of rare variants found with a large sample size predicts a growth of 5 to 14% per generation over the past 900 to 2800 years, compared to models of smaller sample size that predicted growth of between 0.2 and 0.7% over a longer period of 20,000 to 30,000 years (5, 6). A demographic history consistent with the archaeological and historical records of Europe (Fig. 1) emerges by bringing together the different models: The human population has been expanding for at least hundreds of generations, and the excess of very rare variation indicates that the rate of expansion has accelerated substantially over at least the last several dozen generations (18) (Table 1). Additional data and future modeling with additional parameters are required to estimate more accurately these different phases of population growth.

We contrasted three simplified models of population history to exemplify the general effects of recent explosive growth and sample size on the SFS: (i) a population of constant size throughout history, (ii) a model of European history with two population bottlenecks (21), and (iii) a variant of the second model that adds recent exponential growth, as supported by previously estimated parameters (Table 1) and the archaeological record (Fig. 1). The expected SFS under the three models (Fig. 2) points to considerable inflation in the fraction of variants that are singletons when recent growth is introduced in model 3: For a sample of 500 individuals, where a singleton corresponds to a frequency of 0.1%, model 1 predicts 13% of variants to be singletons, whereas the addition of the population bottlenecks in model 2 inflates this percentage to 18%. The addition of recent exponential growth in model 3 results in an increase to 64% (Fig. 2). The effect of recent explosive growth, as captured in model 3, seems restricted to an inflation of singletons (Fig. 2). However, the observed deflation of other rare frequency categories is due to the inflation in the proportion of singletons and the SFS capturing relative proportions from all variants. Indeed, after removal of singletons and renormalization of other frequency categories (accounting for the possibility of filtering singletons from data because of rare variants having not been validated), the SFS exhibits inflation in doubletons and other rare variants (fig. S1).

The simulated SFS supports the conclusion that differences between previously estimated

Table 1. Genetic estimates of recent exponential growth in Europe.

Study	Sample size (n)*	Time growth started (years ago)†	Initial N_e ‡	Growth per generation (%)
Gravel <i>et al.</i> (5)	60	23,000§ (21,000–27,000)	1032 (677–1290)	0.48 (0.30–0.75)
Gutenkunst <i>et al.</i> (6) (including New World modeling)	22	26,400§ (21,700–30,700)	1500 (900–2200)	0.23 (0.16–0.34)
Gutenkunst <i>et al.</i> (6) (excluding New World modeling)	22	21,200§ (17,600–23,900)	1000 (500–1500)	0.4 (0.26–0.57)
Schaffner <i>et al.</i> (29)	62	8750	7700	0.73
Coventry <i>et al.</i> (18)	10,422	1400 (900–2800)	7700#	9.4 (4.5–14.5)

*Number of individuals of European ancestry used for inference.

†Number of years ago, on the basis of 25 years per generation. All studies assumed growth to continue into the present.

‡Effective population size (N_e) before the start of the exponential growth phase.

§Time of growth was assumed in these studies to coincide with the split of the ancestors of Europeans and East Asians, hence the split and growth were estimated as a single parameter.

| Fixed parameters that were not estimated from the data, and which are hence not considered in the discussion in the main text. (Growth is instantaneous to a fixed value of $N_e = 100,000$, which is approximately equivalent to exponential growth of 0.73% per generation.)

#A fixed parameter, following (29).

models of population expansion (Table 1) can be explained by differences in sample size. The inflation in singletons in model 3 relative to model 2 ranges from only 8% (which can easily be missed in model fitting) for a very small sample size to almost 500% for a large sample (Fig. 2). This relative increase is compounded by the fact that the proportion of singletons decreases as sample size increases (in the absence of explosive growth) and that the proportion of singletons for model 3 is actually increasing as a function of sample size, from 33% to 74%, because in a larger sample singletons represent rarer variants due to more recent mutations (Fig. 2). As a result, a standard sample size of 50 to 100 only provides a glimpse into

the inflation in singletons. In our models, a sample size of 50 individuals identifies a quarter of the inflation relative to a sample size two orders of magnitude larger (Fig. 2). This effect of sample size is even more pronounced for rare variants that are not singletons (fig. S1).

The inflation in the number of rare variants due to explosive growth implies that, even in large samples, many variants will be restricted to a single individual. We thus examined the individual burden of mutations, defined here as the proportion of heterozygote variants in each newly sequenced individual that are novel (i.e., completely absent from a previously sequenced large sample from the same population). We estimated the expectation of this quantity in the

three idealized demographic models described above and measured this quantity in populations of European and East Asian ancestry on the basis of ENCODE regions from HapMap 3 (22). Model 2 predicts that 1.3% of heterozygous positions in a new individual are otherwise completely monomorphic in a population sample of 90 individuals (Fig. 3). This percentage underpredicts the empirically observed 2.9% in a sample of European ancestry (Fig. 3), and its prediction is almost as poor as that of a model of constant population size (1.1%). Adding recent explosive growth changes the prediction to 3.3% of heterozygous positions and provides a much better fit to the observed data in European and East Asian populations (Fig. 3).

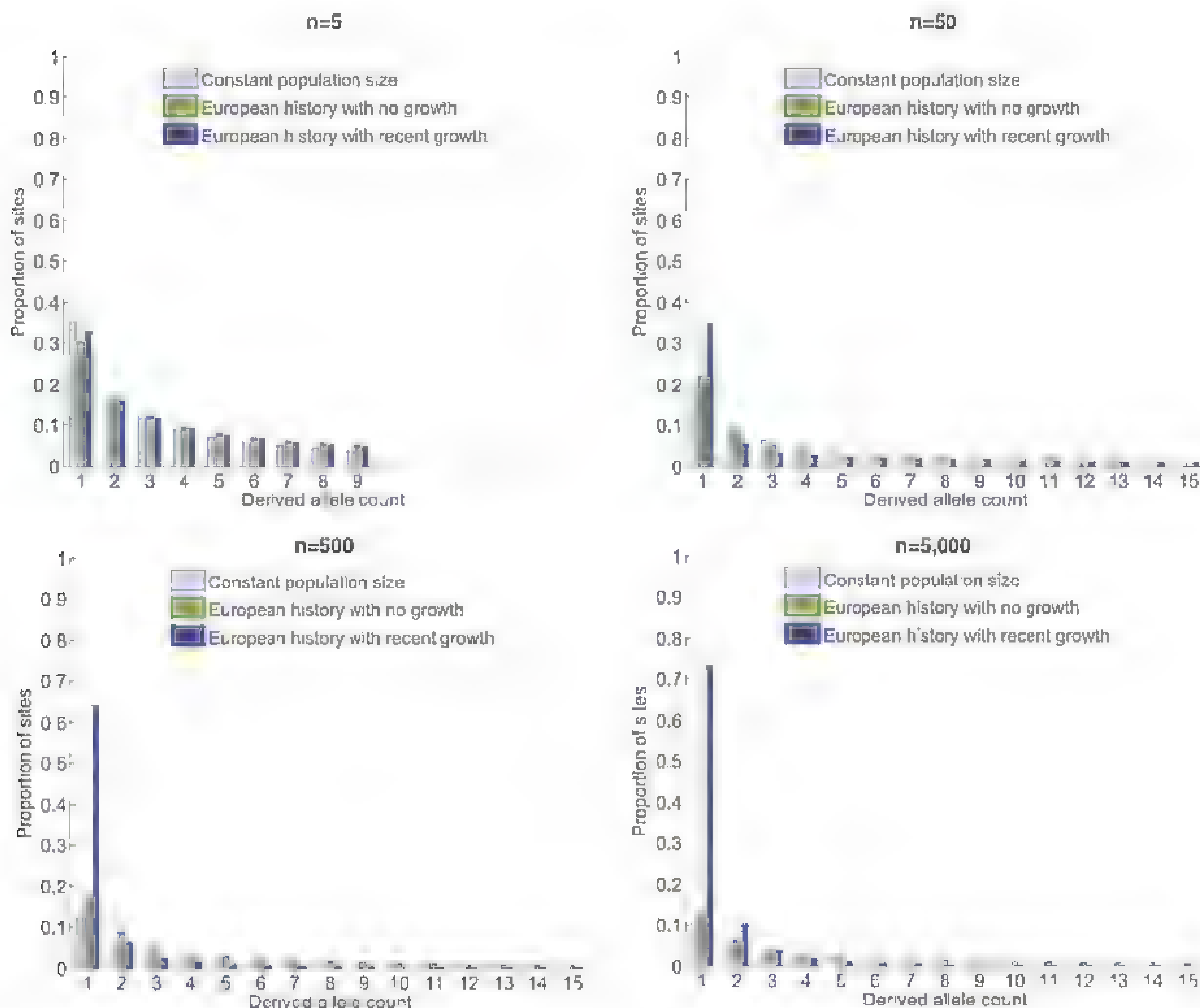


Fig. 2. The expected site frequency spectrum (SFS) of the derived allele (the new mutation arisen in the population) for three different demographic models: (i) a population that has been of constant size throughout history; (ii) a model previously fit to the derived allele frequency spectrum of Europeans, which includes an out-of-Africa population bottleneck and a second, more recent, population bottleneck (22); and (iii) the same two-bottleneck model of European history with the addition of recent exponential growth from a population size of 10,000 at the advent of agriculture to an extant

effective population size of 10,000,000, which amounts to 1.7% growth per generation during the last 400 generations. The results presented are based on sequences of 5, 50, 500, and 5000 diploid individuals. Figures are from 10 million coalescent simulations (32); the expectation of models 1 and 2 were also validated analytically (21). In all panels, the proportions of all possible derived allele counts, ranging from 1 to $2n - 1$, sum up to 1, although only those for 1 through 15 are presented. See fig. S1 for a version of this figure in which singletons are excluded and the SFS renormalized.

The fraction of novel variants discovered in each sequenced genome decreases in all models as more individuals are sequenced (Fig. 3), because increasing sample size results in a greater likelihood that a variant has already been ascertained. Interestingly, though, the discrepancy between the prediction of models with and without population growth increases as more individuals are sequenced: Whereas explosive growth predicts a 150% increase in the proportion of unique mutations for 90 previously sequenced genomes (3.3% versus 1.3%), in the case of 1000 previously sequenced genomes it predicts a 1200% increase (Fig. 3). The model predicts that even in the 1001st genome sequenced, about 1.9% of the variants (which number about 57,000) would be novel. These models are limited to neutral mutations, and deleterious mutations would likely exhibit an even larger percentage of novel rare variants (23).

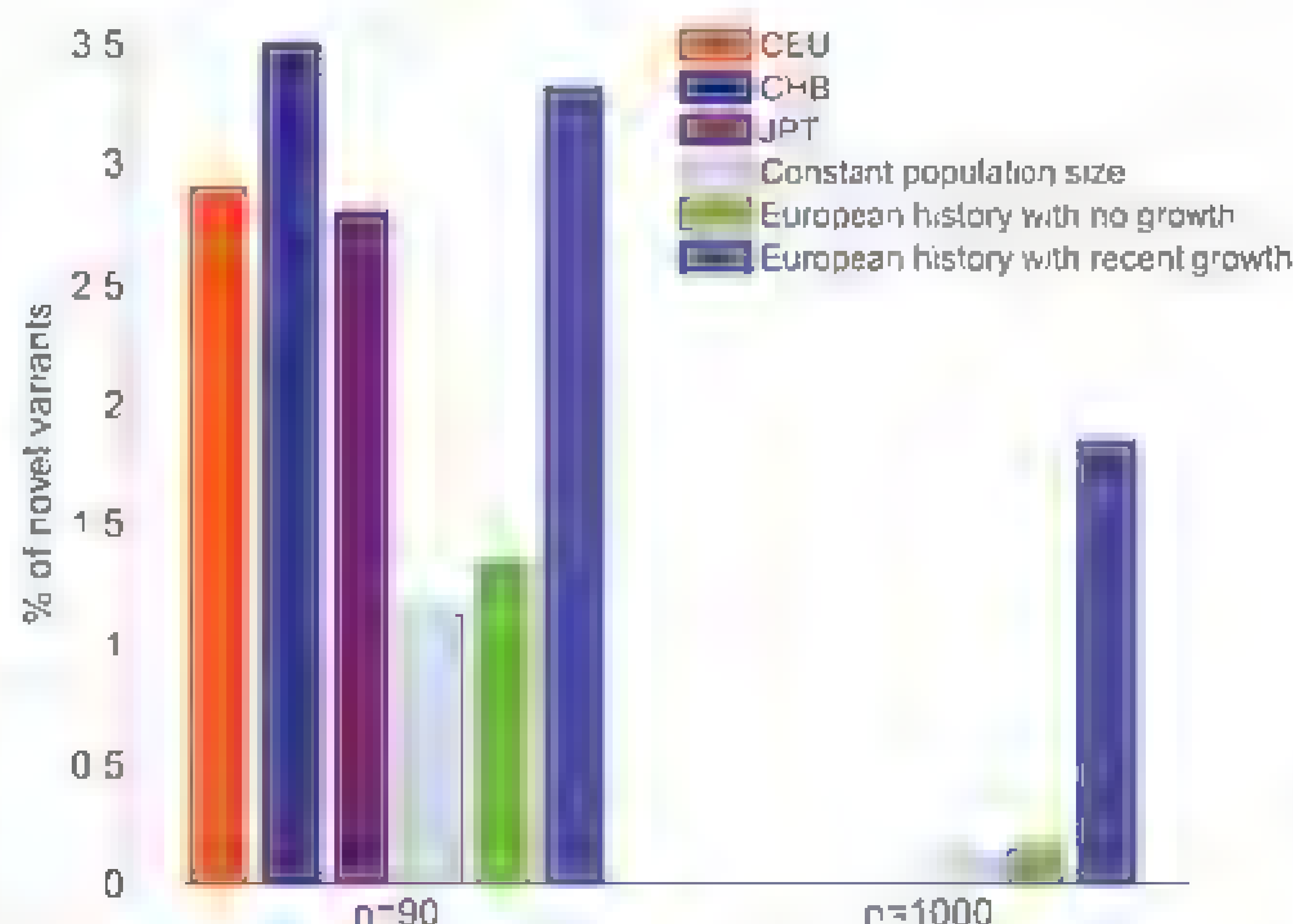
With disease-gene association studies moving in the direction of exome and whole-genome sequencing, models of the genetics of complex traits need to accommodate recent, rapid human population growth. The medical implications of an excess of rare genetic variation and increased individual mutational load are of particular interest in light of the limited success of genome-wide association studies at explaining the genetic basis of complex human diseases (24–27). Some degree of genetic risk for complex disease may be due to this recent rapid expansion of rare variants in the human population. A better understanding of the population genetic consequences of such recent, explosive growth for how genetic variation will be structured in populations is needed for optimal sampling designs that most efficiently identify disease risk variants. The extraordinary growth implies

a massive departure from equilibrium, such that populations will continue to accumulate genetic variability until a new equilibrium is reached. Our models showed a skewed SFS, with nearly normal counts of SNPs in all frequency classes other than the very rarest classes, which are highly inflated. These rare variants are so recent that they appear as novel mutations, with relatively little time for natural selection to operate.

Explosive growth also results in a haplotype structure that deviates from the prediction of standard population genetics because recombination will not have broken down linkage disequilibrium between rare mutations and neighboring common variants. This results in a deviation in the distribution of haplotypes that contain both common variants with deep evolutionary history and recent mutations. However, it presents an opportunity for mapping methods that are based on the structure of haplotypes or that aggregate signals from multiple variants according to their inferred biological impact (so-called burden tests). Furthermore, the skewed genealogical structure when the sample size exceeds the historical effective population size can result in excess sharing of identical-by-descent blocks among affected individuals, which can be used for associating rare variants (13). Optimization of association-testing methods will clearly benefit from expanding our understanding of the population genomic variation in rapidly expanding populations.

To shed further light on recent epochs in the history of modern humans, large-scale sequencing of many thousands of individuals is needed (28), together with more elaborate demographic modeling. The sequenced population should exhibit as little substructure as possible because sequencing several closely related populations—

Fig. 3. Percentage of novel variants in a sequenced individual. Bars denote the fraction, out of all sites for which a given individual is heterozygous, that are also monomorphic in a separate sample of 90 (left) or 1000 (right) individuals from the same population. Expected fraction is presented for the same three demographic models as in Fig. 2. For $n = 90$ —a value chosen on the basis of availability of empirical data—the observed fraction for three populations of European (CEU), Chinese (CHB), and Japanese (JPT) ancestry is also provided, from resequencing data of ENCODE regions from the HapMap 3 Project (22). We averaged over all possible choices of an individual out of each sample in these data. The empirical results are inconsistent with the two models excluding growth, and they match a simplistic model that includes recent exponential expansion. We note that the empirical estimates are likely slight underestimates due to stringent quality control filters (22). No empirical data are available for a sample of size 1000.



while optimizing other criteria of variant discovery (11)—does not accurately capture the frequency of rare variants due to mutations that postdate population split. It is also imperative to understand the impact of natural selection during the phase of explosive growth, an aspect that our models did not attempt to capture.

References and Notes

1. J. E. Cohen, *How Many People Can the Earth Support?* (Norton, New York, ed. 1, 1995).
2. L. Roberts, *Science* **333**, 540 (2011).
3. United Nations Department of Economic and Social Affairs Population Division, 2011.
4. D. Hartl, A. Clark, *Principles of Population Genetics* (Sinauer, Sunderland, MA, 2007).
5. S. Gravel et al., 1000 Genomes Project, *Proc. Natl. Acad. Sci. U.S.A.* **108**, 11983 (2011).
6. R. N. Gutenkunst, R. D. Hernandez, S. H. Williamson, C. D. Bustamante, *PLoS Genet.* **5**, e1000695 (2009).
7. J. C. Cohen, E. Boenink, T. H. Mosley Jr., H. H. Hobbs, *N. Engl. J. Med.* **354**, 1264 (2006).
8. K. A. Fawcett et al., *Diabetes* **59**, 741 (2010).
9. C. E. Glatz et al., *Nat. Genet.* **27**, 435 (2001).
10. C. T. Johansen et al., *Nat. Genet.* **42**, 684 (2010).
11. R. M. Durbin et al., *Nature* **467**, 1061 (2010).
12. J. Akey, *Genome Biol.* **12** (suppl. 1), 1 (2011).
13. See supplementary materials on Science Online.
14. J. Wakeley, T. Takahashi, *Mol. Biol. Evol.* **20**, 208 (2003).
15. J. Pitman, *Ann. Probab.* **27**, 1870 (1999).
16. S. Sagitov, *J. Appl. Probab.* **36**, 1116 (1999).
17. J. Schweinsberg, *Electron. J. Probab.* **5**, 1 (2000).
18. A. Coventry et al., *Nat. Commun.* **1**, 131 (2010).
19. The ARIC Investigators, *Am. J. Epidemiol.* **129**, 687 (1989).
20. J. Novembre et al., abstr. 6, presented at the 12th International Congress of Human Genetics, 12 October 2011, Montreal.
21. A. Keinan, J. C. Munkin, N. Patterson, D. Reich, *Nat. Genet.* **39**, 1251 (2007).
22. D. M. Altshuler et al.; International HapMap 3 Consortium, *Nature* **467**, 52 (2010).
23. M. Lynch, *Proc. Natl. Acad. Sci. U.S.A.* **107**, 961 (2010).
24. T. A. Manolio et al., *Nature* **461**, 747 (2009).
25. K. A. Frazer, S. S. Murray, N. J. Schork, E. J. Topol, *Nat. Rev. Genet.* **10**, 241 (2009).
26. B. Maher, *Nature* **456**, 10 (2008).
27. E. E. Eichler et al., *Nat. Rev. Genet.* **11**, 446 (2010).
28. J. A. Tennessen, T. D. O'Connor, M. J. Bamshad, J. M. Akey, *Genome Biol.* **12**, 127 (2011).
29. S. F. Schaffner et al., *Genome Res.* **15**, 1576 (2005).
30. C. Haub, *Popul. Today* **23**, 4 (1995).
31. M. Kremer, *Q. J. Econ.* **108**, 681 (1993).
32. R. R. Hudson, *Bioinformatics* **18**, 337 (2002).

Acknowledgments. We thank R. Bexhman, E. Boeswinkle, C. D. Bustamante, A. Coventry, E. Gazave, S. Gravel, H. Hunter-Zinck, J. M. Kidd, L. Ma, C. F. Sing, and the 1000 Genomes Project for discussion and ongoing collaborations that substantively advanced this project. Supported by NIH grants U01-HG005715, GM065509, and HL102419, and by an Alfred P. Sloan Research Fellowship (A.K.).

Supplementary Materials

www.sciencemag.org/cgi/content/full/336/6082/740/DC1
Supplementary Text

Fig. S1

References (33–40)

30 November 2011, accepted 15 March 2012
10.1126/science.1217283

Transcription-Independent Function of Polycomb Group Protein PSC in Cell Cycle Control

Adone Mohd-Sarip,¹ Anna Lagarou,^{1*†} Cecile M. Doyen,^{1†} Jan A. van der Knaap,^{1†} Ülkü Aslan,¹ Karel Bezstarosti,² Yasmin Yassin,³ Hugh W. Brock,³ Jeroen A. A. Demmers,² C. Peter Verrijzer^{1†}

Polycomb group (PcG) proteins control development and cell proliferation through chromatin-mediated transcriptional repression. We describe a transcription-independent function for PcG protein Posterior sex combs (PSC) in regulating the destruction of cyclin B (CYC-B). A substantial portion of PSC was found outside canonical PcG complexes, instead associated with CYC-B and the anaphase-promoting complex (APC). Cell-based experiments and reconstituted reactions established that PSC and Lemming (LMG, also called APC11) associate and ubiquitylate CYC-B cooperatively, marking it for proteosomal degradation. Thus, PSC appears to mediate both developmental gene silencing and posttranslational control of mitosis. Direct regulation of cell cycle progression might be a crucial part of the PcG system's function in development and cancer.

Polycomb group (PcG) proteins are transcriptional repressors that maintain cell fate decisions and control cell proliferation (1–5). They function as part of distinct multiprotein complexes that modulate chromatin structure. The RING domain protein Posterior sex combs (PSC) is a subunit of Polycomb repressive complex 1 (PRC1) and dRING-associated factors (dRAF), which mediate monoubiquitylation

of histone H2A (2–6). A substantial portion of PSC is part of neither PRC1 nor dRAF (6), suggesting that PSC might have additional functions. We compared the effect of depleting either Polycomb (PC), Polyhomeotic (PH), PSC, or dRING by treating S2 cells with the appropriate double-stranded RNAs (dsRNAs) (see supplementary materials and methods section and fig. S1). PC, PH, PSC, and dRING form the

core of PRC1, whereas dRING, PSC, and dKDM2 are the central subunits of dRAF (2–6). Knock-down (KD) of PH or PSC decreased cell accumulation, whereas depletion of PC or dRING had no appreciable effects (Fig. 1A). Fluorescence-activated cell sorter (FACS) analysis indicated that cells lacking PSC primarily accumulated at the G₂-M phase of the cell cycle (Fig. 1B). Loss of other PcG proteins did not give a clear cell cycle arrest. Therefore, PSC might function in cell cycle regulation, independent of PRC1 or dRAF.

Consistent with the G₂-M arrest caused by loss of PSC, maternal effect mutations of *Psc* cause mitotic segregation defects in early *Drosophila* embryos (7). This is illustrated by the mitotic chromosome bridges, frequently detected in the progeny of *Psc*^{h27} maternal mothers (Fig. 1C). Because early embryos have nonconventional checkpoint mechanisms, problems at either S phase or mitosis can lead to segregation defects

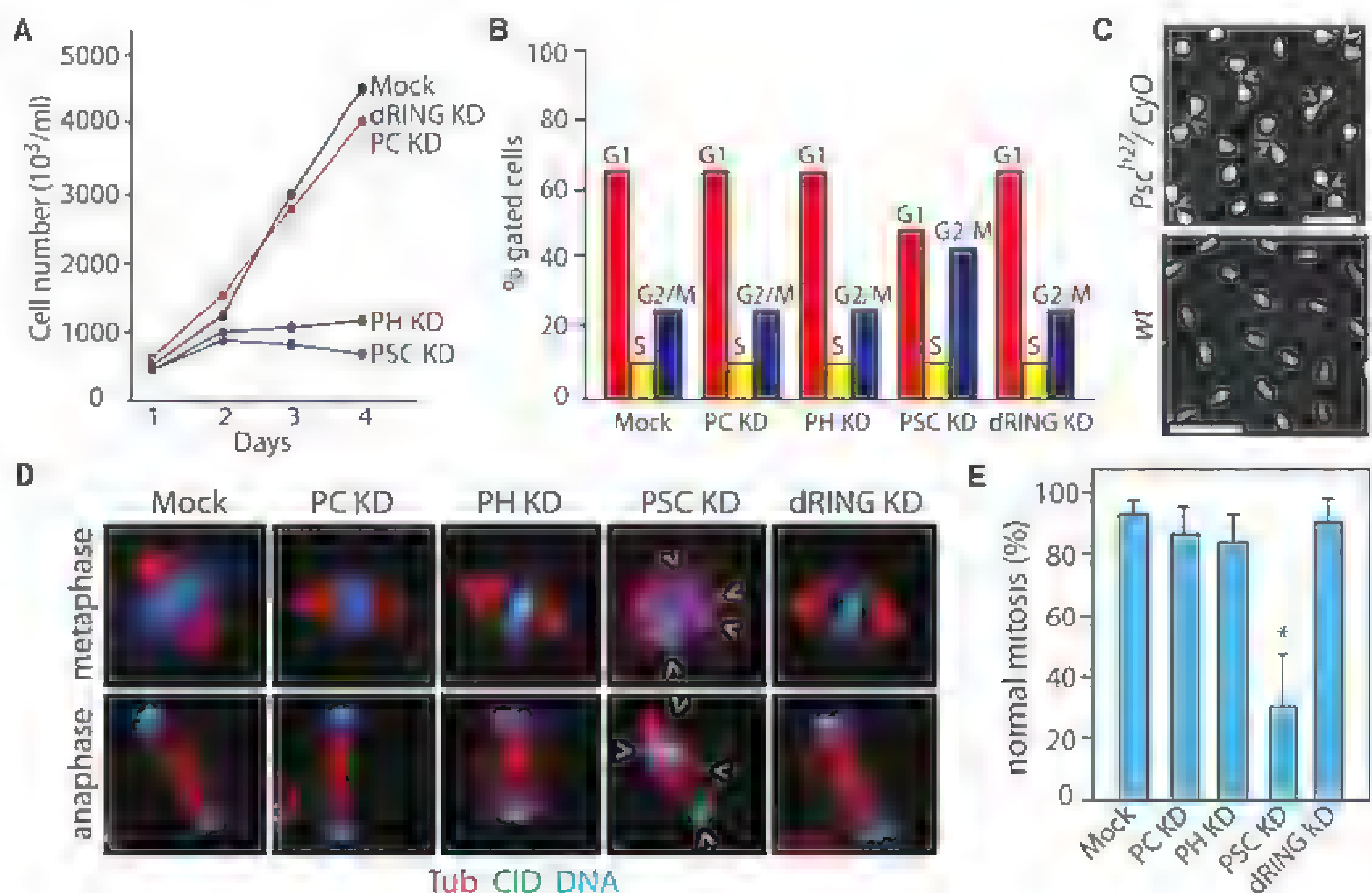
¹Department of Biochemistry and Centre for Biomedical Genetics, Erasmus University Medical Centre, Post Office Box 1738, 3000 DR, Rotterdam, Netherlands. ²Proteomics Centre, Erasmus University Medical Centre, Post Office Box 1738, 3000 DR, Rotterdam, Netherlands. ³Department of Zoology, University of British Columbia, Vancouver, BC, Canada

*Present address: Biomedical Sciences Research Center Alexander Fleming, 16672 Vari, Greece

†These authors contributed equally to this work.

‡To whom correspondence should be addressed. E-mail: c.verrijzer@erasmusmc.nl

Fig. 1. PSC function in mitosis. (A) S2 cell accumulation after RNAi-mediated KD of PC, PH, PSC, or dRING. (B) Cell cycle distribution of S2 cells after KD of the indicated proteins, determined by FACS. (C) Micrograph of cell cycle 11 embryos from a cross of *Psc*^{h27}/CyO females mated to wild-type (wt) fathers displaying chromatin bridges (yellow arrowheads). A comparable wt embryo is shown for comparison. Scale bars, 10 μ m. (D) Indirect immunofluorescence of mitotic S2 cells after KD of PC, PH, PSC, or dRING. Cells were stained with antibodies against α -tubulin (red) and centromere identifier (CID) (green); DNA was visualized by 4',6-diamidino-2-phenylindole (blue). Arrowheads indicate misalignment and missegregation. (E) Number of cells with normal mitosis was plotted as a percentage of the total number of mitotic cells. 95% confidence intervals are indicated (error bars). The asterisk marks the significant difference between mock- and PSC KD cells ($P < 0.0001$), as determined by a χ^2 test. See also table S1.



(7, 8). In S2 cells, which have a conventional cell cycle, depletion of PSC caused severe mitotic defects (Fig. 1D). After depletion of PSC, ~68% of mitotic cells displayed an abnormal phenotype, whereas loss of the other PcG proteins did not affect mitosis. (Fig. 1E and table S1). The PcG system has been implicated in the regulation of cell cycle genes (9–12). Yet, because the integrity of PcG complexes is required for silencing (1–5), we suspected that PSC's role in mitosis extends beyond transcription repression. Indeed, a portion of cellular PSC does not appear to be part of PRC1 nor dRAF (6).

To identify interaction partners, we used three distinct, affinity-purified antibodies to isolate PSC from whole-cell extracts of 0- to 12-hour-old *Drosophila* embryos. Mass spectrometric analysis revealed that, in addition to PRC1 and dRAF subunits, cyclin B (CYC-B), cell division cycle 2 (CDC2, also called cyclin-dependent protein kinase 1), and key subunits of the anaphase-promoting complex (APC) associated with PSC (Fig. 2A and table S2). Although PSC was present in PC, dRING, and PH purifications, CYC-B and the APC were absent. The APC is a multisubunit E3 ubiquitin ligase that is pivotal to cell cycle regulation (13–23). CYC-B ubiquitylation by the APC, marking it for destruction by the proteasome, is required for completion of ana-

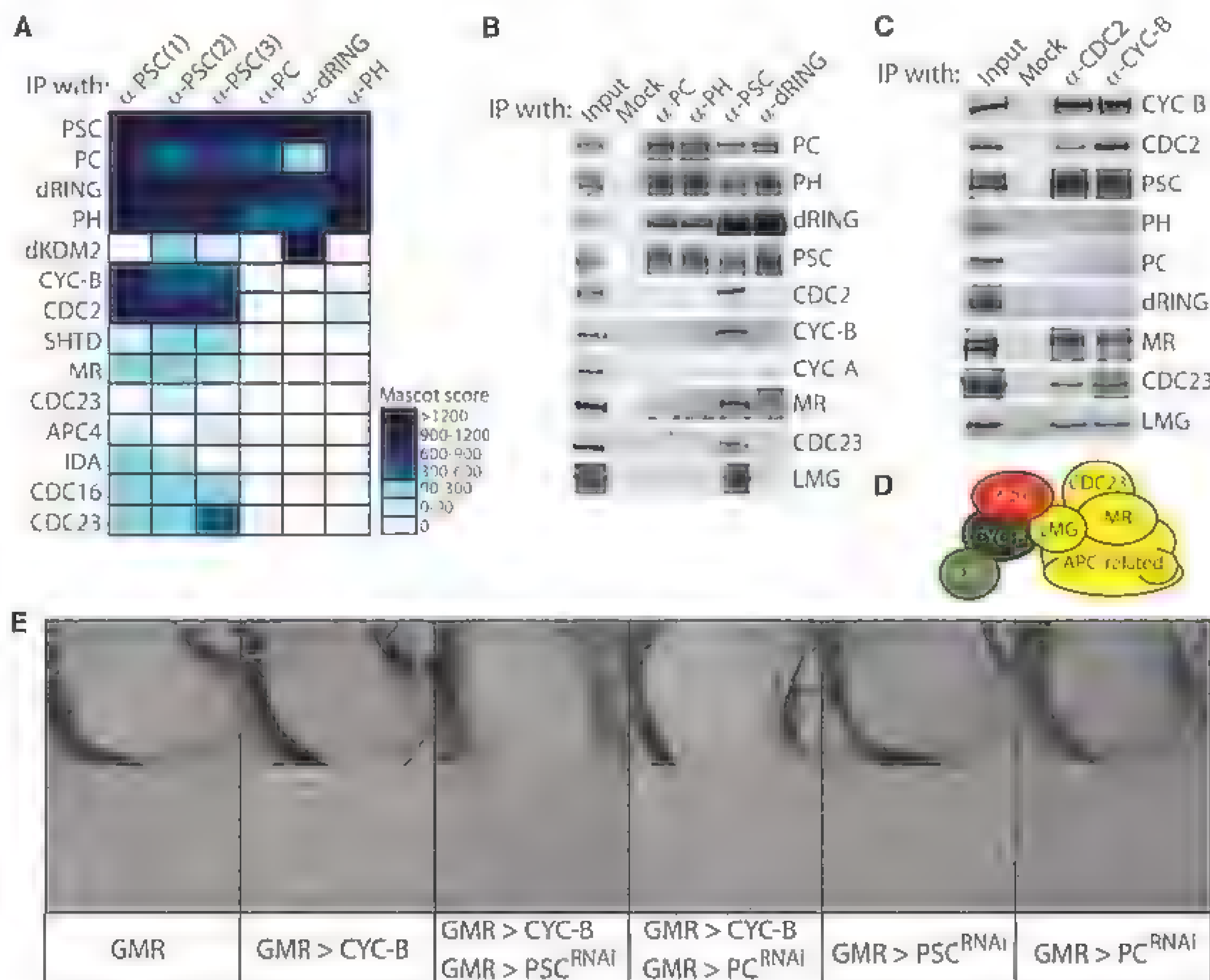
phase and cytokinesis (16–23). We confirmed the selective association of PSC with CYC-B and APC by a series of immunoprecipitations (IPs) combined with protein immunoblotting. IPs of PcG proteins (Fig. 2B) showed that only PSC associated with CYC-B; CDC2; and the APC subunits MORULA (MR, also called APC2), CDC23 (APC8), and LEMMING (LMG, also called APC11). Reverse IPs further established the unique association of PSC with CYC-B (Fig. 2C) and the APC (fig. S2). LMG is a small 85-amino acid protein, comprising mainly a RING domain, that is essential for the ubiquitin ligase activity of the APC (20–23). Many RING domain proteins are E3 ubiquitin ligases and frequently function as homo- or heterodimers (20). For example, PSC and its mammalian homolog BMI1 bind dRING or RING1B, respectively, and stimulate histone H2A ubiquitylation (2, 6, 24–26). We found that the RING domain of PSC was necessary and sufficient to bind LMG, whereas its C-terminal region bound CYC-B (fig. S3). Thus, PSC appears to associate with LMG and CYC-B directly (Fig. 2D).

To complement these biochemical experiments with a genetic-interaction assay, we employed the GAL4-UAS system in *Drosophila* (27). We used the *glass multimer reporter* (GMR) to drive ectopic CYC-B expression (GMR>CYC-

B) in the developing eye (Fig. 2E). Ectopic CYC-B caused a mild rough-eye phenotype, characterized by disorganized ommatidia and loss of bristles. Concomitant expression of dsRNA directed against *Psc* mRNA [GMR>CYC-B; GMR>PSC^{RNAi} (RNAi, RNA interference)] enhanced the GMR>CYC-B phenotype, consistent with the notion that PSC is a negative regulator of CYC-B. In contrast, expression of dsRNA directed against *Pc* had no effect on the CYC-B overexpression phenotype. Alone, neither reduction of PSC levels nor PC depletion had an appreciable effect on eye development. Thus, PSC interacts both genetically and biochemically with CYC-B.

To test whether PSC regulates abundance of CYC-B in vivo, we used the *Patched* (*Ptc*) driver to direct the expression of dsRNA directed against *Psc* mRNA in a central band across the wing imaginal disc of third instar larvae. Immunostaining of CYC-B (red) and PSC (green) revealed a strong increase in CYC-B, precisely in the area of the disc where PSC was depleted (Fig. 3, A and B). CYC-B abundance was also reported to increase in cellular clones that lack both *Psc* and *Suz12*, but not in *Pc* or *dRing* mutant clones (12). The effect of PSC on CYC-B was transcription-independent because expression of *cyc-B* mRNA was not affected by PSC

Fig. 2. PSC interacts biochemically and genetically with CYC-B. (A) Interaction heatmap, based on mascot scores, depicting associated factors identified by mass spectrometry after immunoprecipitation of PSC, PC, dRING, and PH. See table S2 for details. (B) Co-IPs of PcG proteins. Associated proteins were detected by immunoblotting with antibodies against the indicated proteins. Input represents 10% of the binding reactions. (C) CDC2 and CYC-B co-IPs. (D) Cartoon summarizing the proteomics results. MR, Morula. (E) Scanning electron micrographs of fly eyes in which ectopic CYC-B expression was driven by the GMR enhancer. CYC-B overexpression was combined with RNAi-mediated depletion of PSC or PC. Genotypes are indicated.



depletion (Fig. 3C and fig. S4). Likewise, loss of PSC or LMG in S2 cells caused accumulation of CYC-B, which was even greater when both

factors were depleted (fig. S5A). However, the abundance of *cyc-B* mRNA in S2 cells was not affected by depletion of PSC or LMG (fig. S5B)

Thus, CYC-B accumulation appears to be caused by a transcription-independent mechanism, possibly involving PSC-directed ubiquitylation

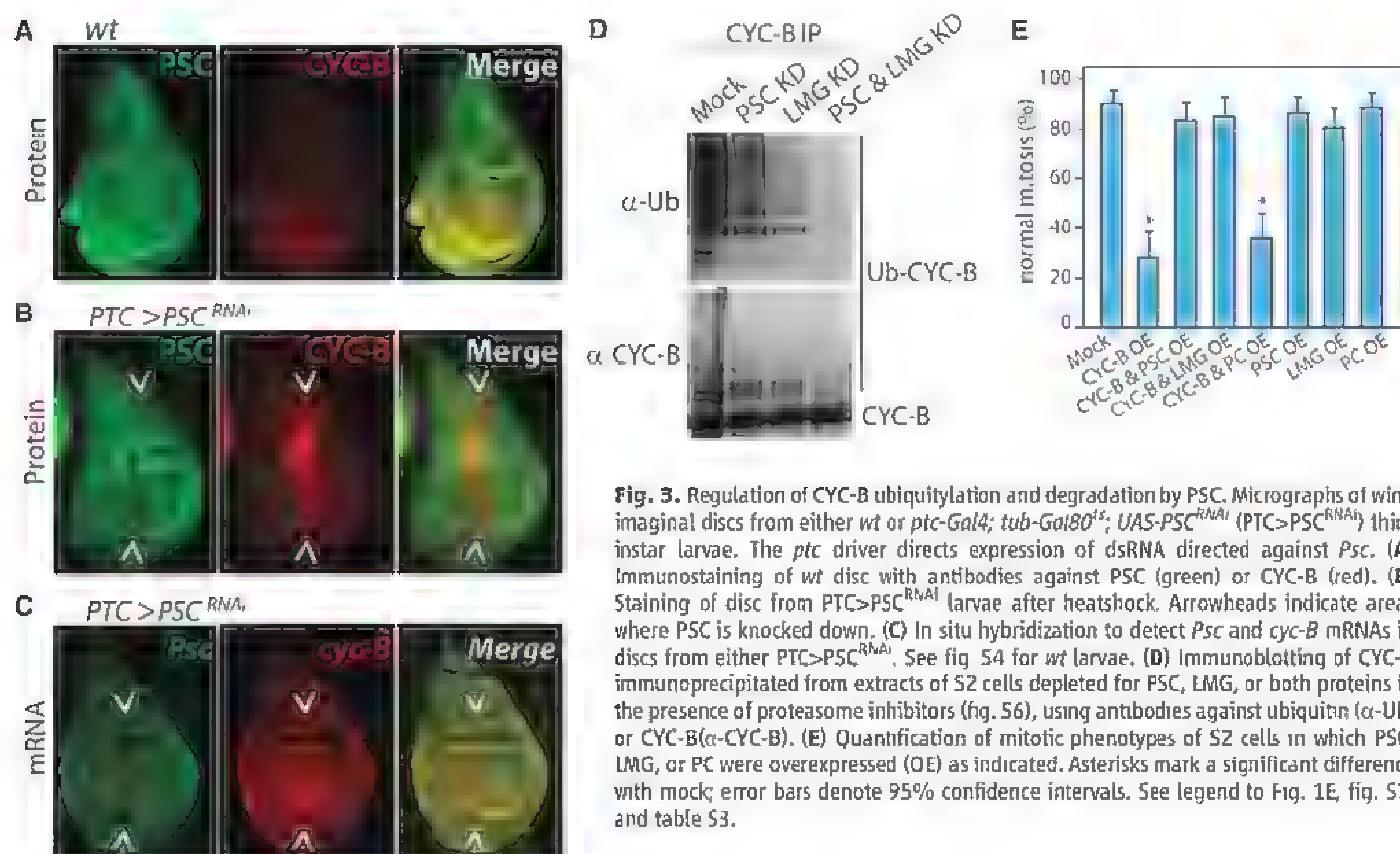
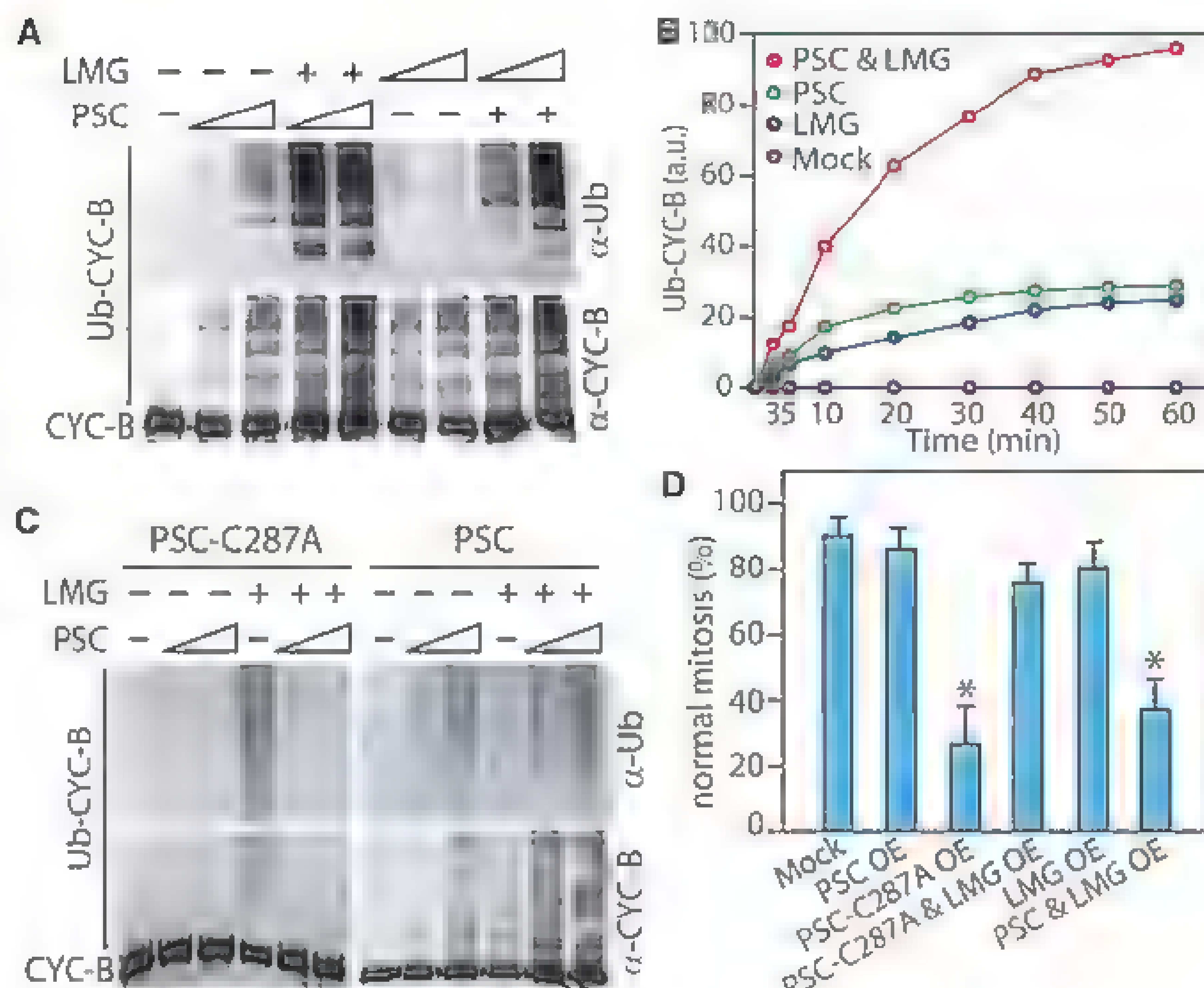


Fig. 4. Cooperation between PSC and LMG during CYC-B ubiquitylation. (A) Reconstituted CYC-B ubiquitylation by PSC and LMG, detected by immunoblotting with α -Ub or α -CYC-B. CYC-B was incubated with a buffer control or in the presence of increasing amounts (~ 20 or 80 nM) of PSC alone or in addition to ~ 20 nM LMG (+), ~ 20 nM or 80 nM of LMG alone, or in addition to ~ 20 nM PSC (+). For purified proteins, see fig. S8. (B) Quantification of CYC-B ubiquitylation by PSC, LMG, or PSC and LMG (~ 20 nM each) by lumimager fluorometry of gels (fig. S9). Ub-CYC-B was plotted as a function of the reaction time. a.u., arbitrary units. (C) Effect of PSC-C287A on CYC-B ubiquitylation. Analysis as described above. (D) Quantification of mitotic phenotypes of S2 cells in which PSC, PSC-C287A, and LMG were overexpressed as indicated. See legend to Fig. 1E, fig. S11, and table S3.



To investigate the role of PSC in CYC-B ubiquitylation, we immunopurified CYC-B from cells that were depleted of PSC or LMG and treated with proteasome inhibitors (Fig. 3D and fig. S6). Immunoblotting revealed that the loss of either PSC or LMG caused decreased levels of polyubiquitylated CYC-B (Ub-CYC-B). Almost no Ub-CYC-B was detectable in cells lacking both PSC and LMG. To test whether failed CYC-B destruction could explain the mitotic defects after the loss of PSC, we overexpressed CYC-B in S2 cells. After ectopic expression of CYC-B, ~70% of mitotic cells displayed a variety of defects (Fig. 3E, fig. S7, and table S3). Concomitant overexpression of either PSC or LMG almost completely reversed the CYC-B misexpression phenotype. In contrast, extra PC had no effect. Collectively, these results suggest that PSC-mediated CYC-B ubiquitylation is crucial for normal mitosis.

We used purified PSC, LMG, and CYC-B (fig. S8) in a reconstituted ubiquitylation system, which was dependent on E1 and E2 enzymes, to test the ability of PSC to act as a ubiquitin E3 ligase for CYC-B. Approximately equimolar amounts of either PSC or LMG could direct CYC-B ubiquitylation (Fig. 4A). But together, PSC and LMG generated higher levels of Ub-CYC-B. Determination of the CYC-B ubiquitylation rate revealed a more-than-additive effect of combining PSC and LMG, indicating that they function cooperatively (Fig. 4B and fig. S9). A substitution mutation replacing a signature cysteine residue of the RING consensus with an alanine [PSC-C287A (C287A, Cys²⁸⁷→Ala²⁸⁷)] abrogated PSC's ability to ubiquitylate CYC-B (Fig. 4C). PSC-C287A blocked ubiquitylation of CYC-B by LMG, suggesting that it acts as a dominant negative. Indeed, the C287A mutation did not affect PSC binding to LMG or CYC-B

(fig. S10). In contrast to ectopic PSC, expression of PSC-C287A caused severe mitotic defects in S2 cells (Fig. 4D and fig. S11). This mitotic phenotype was relieved by concomitant overexpression of LMG, suggesting that extra LMG squelches the dominant-negative PSC. Whereas ectopic expression of either PSC or LMG in S2 cells did not affect mitosis, overexpression of both PSC and LMG caused mitotic defects. These results suggest that PSC and LMG cooperate in the ubiquitylation of CYC-B, marking it for destruction by the proteasome.

Regulated protein destruction is fundamental to cell cycle progression. The work reported here shows that, in addition to transcriptional repression, PSC cooperates with LMG in the APC to direct CYC-B degradation. During mitosis, PSC (and its mammalian homologs) and key PRC1 subunits PH and PC dissociate from the chromatin, making a transcriptional function at that time unlikely (28, 29). Like PSC, other chromatin regulators may also target proteins that are neither involved in chromatin dynamics nor transcription.

References and Notes

1. A. A. Mills, *Nat. Rev. Cancer* **10**, 669 (2010).
2. J. Müller, P. Verrijzer, *Curr. Opin. Genet. Dev.* **19**, 150 (2009).
3. B. Schwettengruber, G. Cavallo, *Development* **136**, 3531 (2009).
4. Y. B. Schwartz, V. Pirrotta, *Curr. Opin. Cell Biol.* **20**, 266 (2008).
5. J. A. Simon, R. E. Kingston, *Nat. Rev. Mol. Cell Biol.* **10**, 697 (2009).
6. A. Lagarou et al., *Genes Dev.* **22**, 2799 (2008).
7. E. O'Dor, S. A. Beck, H. W. Brock, *Dev. Biol.* **290**, 312 (2006).
8. S. A. Beck, E. Falconer, A. Catching, J. W. Hodgson, H. W. Brock, *Dev. Biol.* **339**, 320 (2010).
9. C. Kwong et al., *PLoS Genet.* **4**, e1000178 (2008).
10. A. M. Martinez, S. Colomb, J. Déjardin, F. Bantignies, G. Cavallo, *Genes Dev.* **20**, 501 (2006).

11. N. Nègre et al., *PLoS Biol.* **4**, e170 (2006).
12. K. Oktaba et al., *Dev. Cell* **15**, 877 (2008).
13. A. W. Murray, *Cell* **116**, 221 (2004).
14. J. M. Peters, *Mol. Cell* **9**, 931 (2002).
15. M. Sullivan, D. O. Morgan, *Nat. Rev. Mol. Cell Biol.* **8**, 894 (2007).
16. B. R. Thornton, D. P. Toczyski, *Genes Dev.* **20**, 3069 (2006).
17. D. H. Parry, G. R. Hickson, P. H. O'Farrell, *Curr. Biol.* **13**, 647 (2003).
18. D. H. Parry, P. H. O'Farrell, *Curr. Biol.* **11**, 671 (2001).
19. B. R. Thornton, D. P. Toczyski, *Nat. Cell Biol.* **5**, 1090 (2003).
20. R. J. Deshaies, C. A. Joazeiro, *Annu. Rev. Biochem.* **78**, 399 (2009).
21. M. Gmachl, C. Gellers, A. V. Podtelejnikov, M. Mann, J. M. Peters, *Proc. Natl. Acad. Sci. U.S.A.* **97**, 8973 (2000).
22. J. D. Levenson et al., *Mol. Biol. Cell* **11**, 2315 (2000).
23. Z. Tang et al., *Mol. Biol. Cell* **12**, 3839 (2001).
24. G. Buchwald et al., *EMBO J.* **25**, 2465 (2006).
25. R. Cao, Y. Tsukada, Y. Zhang, *Mol. Cell* **20**, 845 (2005).
26. H. Wang et al., *Nature* **431**, 873 (2004).
27. A. H. Brand, N. Perrimon, *Development* **118**, 401 (1993).
28. P. Buchenau, J. Hodgson, H. Strutt, D. J. Arnáiz-Joven, *J. Cell Biol.* **141**, 469 (1998).
29. J. W. Voncken et al., *J. Cell Sci.* **112**, 4627 (1999).

Acknowledgments: We thank S. Bray, J. Svejstrup, and Y. Moshkin for valuable discussions. This work was supported in part by Nederlandse Organisatie voor Wetenschappelijk Onderzoek-Chemical Sciences Veni grant 700.57.406 (to A.M.-S.).

Supplementary Materials

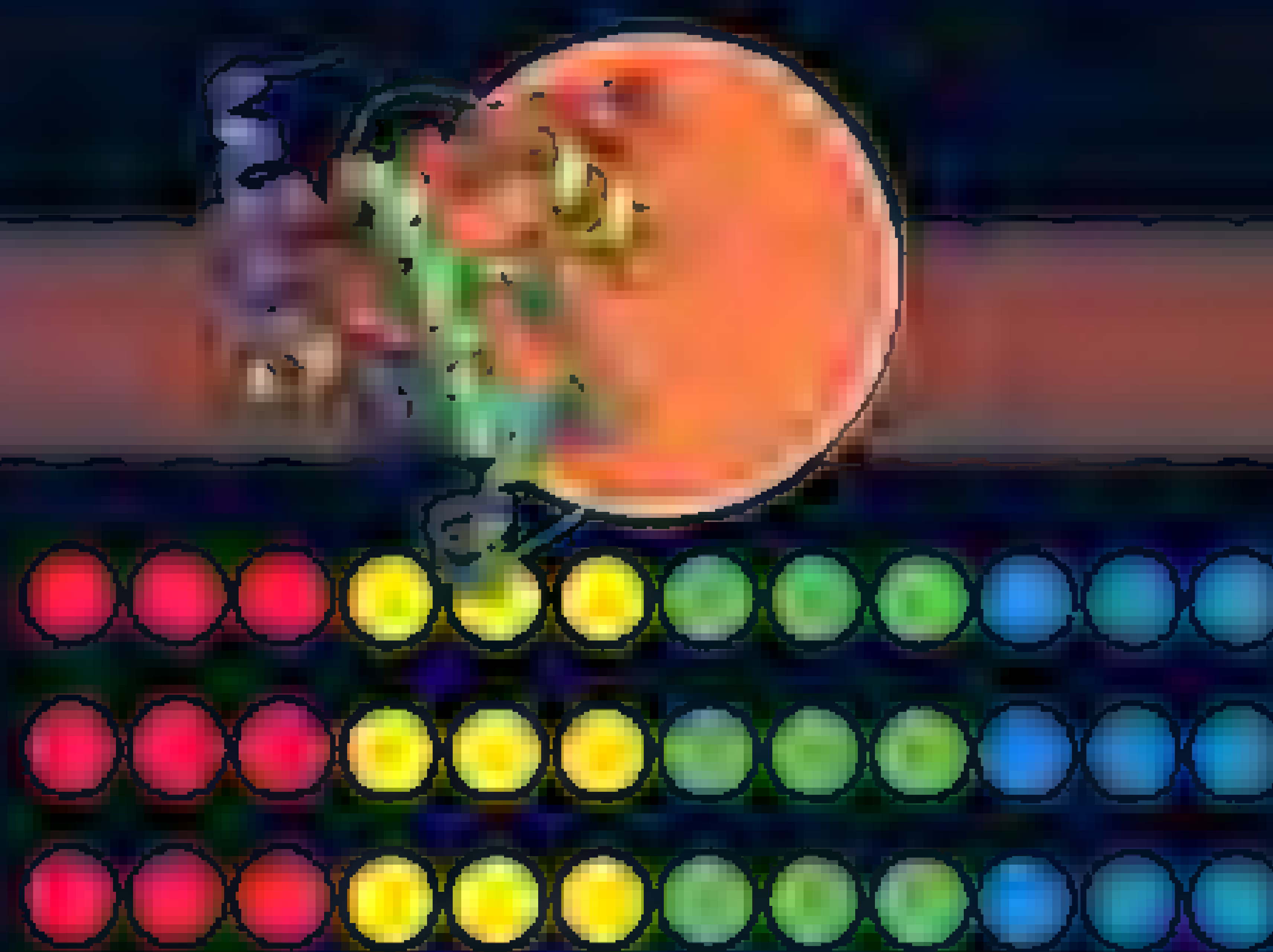
www.sciencemag.org/content/1215927/DC1
Materials and Methods
Figs. S1 to S11
Tables S1 to S3
References

28 October 2011, accepted 20 March 2012
Published online 5 April 2012,
10.1126/science.1215927

Spot-on Protein Microarrays

An Old Proteomics Tool Learns New Tricks

When it comes to omics-inspired bioscience tools, next-gen DNA sequencing is the undisputed king. The previous champ was the DNA microarray, with the protein array its logical successor. Yet while DNA arrays achieved their potential, protein arrays never really took off, owing largely to the fact that, while every DNA oligo behaves more or less identically, the same cannot be said of proteins. They're also harder to synthesize, purify, and stabilize. Still, to paraphrase Mark Twain, the rumor of protein array's death has been greatly exaggerated. Today, new array formats and strategies have made the protein microarray a viable and growing tool for biomarker discovery, interactome research, functional genomics, and more. By Jeffrey M. Perkel



"DNA is really the architectural plans [of the cell], and RNA is the blueprint. But what does the work; the bricks and mortar of the building, is protein."

To witness the power of protein microarrays, consider inflammatory breast cancer (IBC)

IBC is a relatively rare form of the disease, accounting for 1%–5% of breast cancers overall. Yet it is highly aggressive, with a five-year distant metastasis-free survival rate of only 53%, according to Fredrika Robertson, an IBC researcher at the **University of Texas MD Anderson Cancer Center**.

Robertson was using transcriptome analysis to understand the molecular underpinnings of the disease. But there's a problem with that approach. It's true that DNA encodes RNA and RNA encodes protein. But protein does the heavy lifting in the cell, and neither DNA nor RNA says much at all about how, why, or when a given protein will be activated.

"DNA is really the architectural plans [of the cell], and RNA is the blueprint," says Gordon Mills, chairman of the Department of Systems Biology at the MD Anderson Cancer Center. "But what does the work, the bricks and mortar of the building, is protein."

Protein coding mutations and translocations can easily be detected by sequencing, but not protein activity—there simply are no clues in the nucleic acid to predict the timing of posttranslational modifications of, for instance, the protein kinases that drive signaling pathways. Plus, Robertson found she simply couldn't collect enough samples to tease out the biomarker signatures she was hoping to find. So she decided to complement her RNA work with some amino acid-level pathway analysis.

Robertson teamed up with Emanuel Petricoin and Lance Liotta, co-directors of the **Center for Applied Proteomics and Molecular Medicine at George Mason University**, who profiled signal transduction pathways using so-called reverse-phase protein microarrays (RPA). Liotta and Petricoin, who first described reverse phase arrays in 1999 while at the NIH and founded **Theranostics Health** to commercialize the technology, applied RPA to a series of Robertson's patient samples, controls, and cell lines. To their surprise, Petricoin says, one particular cellular circuit, the anaplastic lymphoma kinase

(ALK) pathway, appeared amplified and dysregulated.

"Shockingly, the entire ALK signaling pathway was lit up like a string of lights in IBC cancers, and was completely shut off in non-IBC," says Petricoin.

That observation, he says, led the team to hypothesize that ALK could be a key therapeutic target for the disease. Indeed, inhibiting the pathway in IBC patient tumor cells did result in cell death, and one patient was subsequently enrolled in a clinical trial based on those findings. "This is an example of how this study allowed us to personalize therapy based on the proteomic signature of the patient's tumor," Robertson says.

Yet more to the point, the study underscores the importance of protein analysis in general—that nucleic acids are not the be-all, end-all of biology. Proteins matter.

PROTEIN MICROARRAYS 101

Protein microarrays come in two basic formats. In "forward phase" arrays, capture reagents—whether antibodies, aptamers, or other proteins—are arrayed at defined positions on a glass slide or similar substrate, which is then interrogated with any of a variety of probes, from protein lysate and enzymes to small molecules and nucleic acids.

A few such arrays are commercially available. With 380 disease-related antibodies, **Clontech's** Antibody Array 380 is most commonly used for comparing disease state protein profiles of cells, tissues, or serum samples, says Product Manager Garima Mehta. Applications of **Life Technologies' ProtoArray Human Protein Microarray**, with some 9,400 human proteins arrayed in duplicate, include antibody

UPCOMING FEATURES

Digital Imaging—June 8

Nanotechnology—July 6

Proteomics: Clinical Diagnostics—August 31

specificity characterization; detecting targets of enzymatic activity; identifying protein-protein, protein-nucleic acid, or protein-small molecule interactions, and quantifying autoimmune responses, says Product Manager Heath Balcer.

On a reverse phase array, on the other hand, such as the ones Petricoin and Liotta used, protein lysates are spotted. The arrays are then probed with antibodies to, for instance, phosphorylated signaling molecules—one antibody probing multiple samples as opposed to one sample for multiple capture reagents.

Often, protein samples are spotted at multiple dilutions, and the approach, says Muis, is like a “very high throughput ELISA.” But there’s one significant advantage: each slide requires just nanograms of material. “It’s really nanotechnology,” he says. Neil Carragher, who uses **Bayer Technology Services’** commercial Zeptosens platform in his research at **Edinburgh University**, says the platform uses so little material that he can take precious clinical biopsy samples, distribute them at multiple dilutions over 200 or so identical slides, and still have material left over. “We couldn’t do that by a Western blot, and we couldn’t do it quantitatively,” he says.

Carragher has used the Zeptosens platform to study chemotherapeutics in mice, probing some 30 animal samples for each of 180 different markers. Jens Traenkle, Zeptosens technology manager at Bayer Technology Services GmbH, has run even bigger studies, including one involving six drugs tested at five concentrations in seven cell lines—some 210 conditions in total, each tested in replicate and at different concentrations. For each condition, his lab interrogated 60 different signaling marker proteins.

In all, Traenkle says, the study was the equivalent of 12,600 Western blots, and yet was completed in under two weeks on the Zeptosens platform. “The scalability of this platform is immense,” he says.

ARRAYING STRATEGIES

Heng Zhu, associate professor of pharmacology at the **Johns Hopkins University School of Medicine**, developed one of the first practical proteome-scale protein arrays as a postdoc with **Stanford University** researcher Michael Snyder (who was at Yale at the time).

The array used a forward-phase design. Zhu and Snyder cloned, expressed, and purified all 6,000 yeast open reading frames as glutathione-S-transferase (GST) fusion proteins. Normally, purifying all the proteins for a protein array and keeping them folded properly, constitute significant hurdles in microarray development. But the GST tag provided a generic strategy that enabled the team to purify all 6,000 proteins in about a week. “Without this key technology development, we couldn’t make a protein microarray,” Zhu says. (Snyder co-founded **Protometrix** to commercialize the approach. Protometrix was subsequently acquired by Invitrogen, now Life Technologies, which still uses GST fusion proteins in its ProtoArray product line. According to Balcer, Life Technologies’ arrays differ from Snyder’s design in the surface chemistry and printing methods used.)

Zhu and his coworkers used their array to pinpoint the substrates for some 87 kinases, and he has developed assays to identify other modification substrates as well, including ubiquitin and SUMO E3 ligases, and the yeast NuA4 acetyltransferase.

At Hopkins, Zhu made additional arrays for *E. coli* K12, herpes viruses, and finally, the human proteome. That latter array contains some 17,000 human proteins, all individually expressed, purified, and spotted. At that level, Zhu says, “the cost ramps up rapidly,” though his lab can purify about 3,000 proteins per day. (Life Technologies’



Often, protein samples are spotted at multiple dilutions, and the approach is like a “very high throughput ELISA.”

website lists its ProtoArray Human Protein Microarray, with 9,400 proteins, for \$1,726 per array, compared with \$927 for its NCode Human Non-coding RNA microarray, which contains two subarrays of 105,000 probes apiece.)

Zhu’s team also made a smaller array comprising some 4,200 unique human full-length proteins, including 1,500 transcription factors but also other potential nucleic acid-binders, such as RNA-binding proteins and chromatin-associated proteins as well as mitochondrial proteins and some 300 protein kinases as controls. Their goal was to identify DNA-binding proteins that could target potential regulatory elements in the human proteome, which had been bioinformatically flagged by researchers in the ENCODE project.

They probed the array with 460 putative regulatory sequences, and observed that 41% of the transcription factors displayed sequence-specific binding—an indication that at least that many proteins were properly folded. But they also found something unexpected, says Zhu: “Many proteins that do not have any annotated DNA-binding domain, showed sequence-specific DNA-binding activities.”

Some 4.3% of protein kinases and 14.9% of mitochondrial proteins could bind specific sequences, they found, including the protein kinase MAPK1/Erk2, best known for its role in mediating growth factor signaling. As it turns out, Erk2 contains two C-terminal basic residues, separate from its kinase domain, that mediate the protein’s ability to bind the consensus sequence GAAAC. And not only in vitro; chromatin immunoprecipitation studies confirmed that Erk2 binds promoter elements upstream of genes regulated by interferon-gamma in vivo, apparently fine-tuning the expression of genes like IRF9 and OAS1.

In light of these findings, Zhu says the human genome could encode many such “unconventional DNA-binding proteins,” and his team is actively pursuing them.

FROM DNA, PROTEIN

Josh LaBaer, director of the **Virginia G. Piper Center for Personalized Diagnostics** at **Arizona State University**, uses his array of 14,000 human proteins to identify autoantibody targets of breast, ovarian, and oropharyngeal cancers. In one study his team identified a panel of 28 antigens that can apparently identify breast cancer in serum with specificities between 80% and 100%, he says.

But LaBaer doesn’t bother purifying all those proteins—pity the poor postdoc tasked with that drudgery. Instead he developed a strategy called NAPPA, or “nucleic acid programmable protein arrays,” which spots protein-coding genes rather than **continued** »

Proteomics

FEATURED PARTICIPANTS

Bayer Technology Services
www.bayertechnology.com/en/americas.html

Center for Applied Proteomics and Molecular Medicine at George Mason University
capmm.gmu.edu

Clontech
www.clontech.com

Edinburgh University
www.ed.ac.uk

Fox Chase Cancer Center
www.fccc.edu

Howard Hughes Medical Institute
www.hhmi.org

Johns Hopkins University School of Medicine
www.hopkinsmedicine.org/som

Life Technologies
www.lifetechnologies.com

Novartis
www.novartis.com

Promega
www.promega.com

Salk Institute
www.salk.edu

Scripps Research Institute
www.scripps.edu

Stanford University
www.stanford.edu

Theranostics Health
www.theranosticshealth.com

University of Texas MD Anderson Cancer Center
www.mdanderson.org

Virginia G. Piper Center for Personalized Diagnostics at Arizona State University
schoolofsustainability.asu.edu

proteins. NAPPA arrays are as cheap and easy to fabricate as other DNA microarrays, LaBaer says. To ready them for use, he simply coats the chip with an in vitro transcription/translation system (such as a **Promega** rabbit reticulocyte lysate), which cranks out the encoded proteins. Those proteins, which are fused to a GST affinity tag, are then captured on the glass.

According to LaBaer, NAPPA obviates issues of both protein purification and stability (as the proteins are synthesized immediately prior to use). That translates into cost savings. "Really what you're doing is DNA minipreps," he says. "And even though nothing is cheap when you do it 10,000 times, it's certainly cheaper than doing protein purifications."

LaBaer can easily spot 2,300 nucleic acids per array. Yet if he goes much higher, he runs into a new problem, he says. "Since we're doing transcription and then translation, there is a brief moment when the product that we're making"—RNA—"is not tethered to the surface." At high spot densities, that can muddy the results, producing a signal that drifts like smoke from a smokestack, according to **Salk Institute** and **Howard Hughes Medical Institute** Investigator Joseph Ecker, who also uses NAPPA.

LaBaer's solution is to use etched silicon surfaces to create discrete "nanowells," which can be fabricated and arrayed at very high density. "Twenty-thousand spots per slide is very manageable," he says.

Ecker hit upon an alternative strategy. Instead of a GST fusion, Ecker clones his ORFs as fusions to Promega's HaloTag, a mutated enzyme that covalently bonds to a chloroalkane substrate. If that substrate is irrevocably bound to the glass, then so too is the protein, minimizing diffusion, he says.

Ecker has some 12,000 *Arabidopsis* ORFs cloned as HaloTag

fusions, and is using the array to probe protein-protein interactions with genes that don't work in the yeast-two hybrid assay—especially transcription factors.

He envisions other applications too, such as scanning for proteins that can bind methylated DNA, or substrates for *Arabidopsis*' many E3 ubiquitin ligases. "Plants are just loaded with these E3 ligases but we have no idea what their targets are," Ecker says.

NONTRADITIONAL BIOMARKER DISCOVERY

According to Mike Snyder, the two biggest applications for protein microarrays are studying posttranslational modifications and identifying autoantibody targets. LaBaer uses his arrays for both applications.

In the case of autoantibody biomarker discovery, the idea is that long before a tumor is palpable or symptomatic, it may already be triggering an immune response. The key is to detect that response and the standard approach involves arraying normal cellular proteins and seeing which, if any, bind autoantibodies in patient sera.

But Tom Kodadek, professor of chemistry and cancer biology at the **Scripps Research Institute** in Florida, suspects that it isn't "normal" proteins that are inducing those antibodies, as they shouldn't trigger an immune response at all.

"Far more likely is that the antigens that are setting off these disease-specific antibody responses are ... chemically modified in weird ways due to the pathophysiology of the disease," he says.

Yet how does one build an array that can detect such "weird" modifications when, by definition, researchers don't know what they are? Kodadek's solution was to build an array of 4,608 wholly artificial molecules called "peptoids," and hope one of those shapes would attract an autoantibody.

Kodadek likens the approach to finding a small-molecule inhibitor for an enzyme. "Let's think about the antigen-binding site of an antibody as something we wish to 'drug,' and it ought to be possible to find an unnatural synthetic molecule that binds to that."

When he tested his peptoid array using samples from six Alzheimer's patients, six Parkinson's patients, and six normal controls, he found three peptoids that specifically bound antibodies in the Alzheimer's set—a finding that now has been "validated beautifully" in several hundred additional patients.

Now, says Kodadek, the goal is to "harden" those peptoids, making them more robust for use in the clinic. They ultimately could form the foundation for an Alzheimer's blood test, something that doesn't yet exist. If that should happen, it won't be the first protein array-based findings to make it to the clinic.

IBC researcher Robertson is collaborating with **Fox Chase Cancer Center** medical oncologist Massimo Cristofanili on an open-label trial of a **Novartis** inhibitor called LDK378 that targets ALK, the protein she linked to IBC using Petricoin and Liotta's reverse phase protein array.

Cristofanili didn't initiate the trial to study IBC—ALK dysregulation also figures in non-small-cell lung carcinoma—but thanks to Robertson's findings, he now is specifically recruiting those patients, and four are already enrolled. "This is the kind of story we hope will replay itself over and over again," Petricoin says.

Jeffrey M. Perkel is a freelance science writer based in Pocatello, Idaho.

DOI: 10.1126/science.opms.p1200065

PROTEIN QUANTITATION

The Direct Detect system offers fast, accurate protein quantitation with minimal sample preparation. The infrared (IR)-based spectrometry system and novel membrane technology accurately quantifies amide bonds intrinsic to all proteins, distinguishing proteins from interfering sample components. Because IR-based quantitation does not rely on amino acid composition, dye binding, or redox potential, this approach surpasses conventional UV-Vis spectroscopy and colorimetric assays and allows protein quantification in the presence of reducing agents and detergents. The system requires only a small sample volume (2 μ L) and can measure protein concentrations from 0.2 mg/mL to 5 mg/mL within minutes. In addition, the system's calibration standard curve needs to be generated only once, providing additional time savings and ease of use. The Direct Detect system is also capable of quantifying other biomolecules, including lipids and nucleic acids.

EMD Millipore

For info: 800-645-5476 | www.millipore.com/directdetect



RECOMBINANT PROTEIN DETECTION

Detection and purification of recombinant proteins have become even easier with conjugated anti-DDK antibodies. AMSBIO offers a family of anti-tag antibodies to optimize the detection and purification of recombinant tagged proteins. Most of AMSBIO's anti-tag antibodies are mouse monoclonal antibodies which have been screened and extensively validated for high sensitivity and specificity, in applications including Western blot, immunofluorescent staining, flow cytometry, and immunoprecipitation. The anti-DDK clone 4C5 antibody detects the DDK epitope, which is widely used as a tag in recombinant proteins and is included in the pCMV6-Entry vector that forms the backbone of the TrueORF cDNA series. It has been used to validate the expression of over 15,000 mammalian recombinant proteins, purify more than 5,000 human recombinant proteins from HEK293 cells and purify immunogens under native conditions for the development of antibodies. The new conjugated anti-DDK antibodies have been developed using the highest standards of production procedure and validation.

AMS Biotechnology

Tel: +44-(0)-1235-828200 | www.amsbio.com

IN VITRO TRANSLATION KITS

Two new kits enable the in vitro expression of full-length proteins from mRNA or DNA templates with yields of up to 750 μ g per milliliter of reaction. The expressed proteins by either the Thermo Scientific 1-Step Human Coupled IVT Kit for DNA or the 1-Step Human IVT Kit for RNA can be used to study protein interactions, to perform mutational analysis, or for structural studies. The 1-Step Human IVT Kits rely on the unique HeLa cell lysate that contains all the machinery for in vitro protein expression. While 1-Step Human Coupled IVT reactions are complete in 90 minutes, reactions can be extended for up to six hours for higher protein yields. These kits can produce proteins greater than 250 kD in size and can express functional enzymes, phosphoproteins, glycoproteins, and membrane proteins. In addition to the 1-Step Human IVT Kits, 10 new expression vectors optimized for use with these lysates are now available.

Thermo Fisher Scientific

For info: 800-874-3723 | www.thermoscientific.com/pierce

PROTEIN SENSOR CHIP

The ProteOn HTG Sensor Chip provides a robust new alternative for pharmaceutical researchers studying polyhistidine-tagged protein interactions that can reduce cost per data point by 90%. Used with Bio-Rad's ProteOn XPR36 system, the HTG Sensor Chip's innovative surface chemistry has increased binding stability and specificity for His-tagged proteins compared to chips from other surface plasmon resonance (SPR) system providers. Additionally, the HTG Sensor Chip's ability to regenerate and reuse HTG chips multiple times can significantly reduce the cost of generating data. The ProteOn HTG Sensor Chip's Tris-NTA complex contains three NTA molecules for improved binding stability and selectivity to His-tagged molecules. This results in better data quality and reduced ligand decay. Furthermore, binding via the polyhistidine tag is reversible, so the ligand can be removed from the surface and the chip can be reused 10 times or more. This increases reproducibility by eliminating chip-to-chip variability, and it decreases cost per data point.

Bio-Rad

For info: 800-424-6723 | www.biorad.com

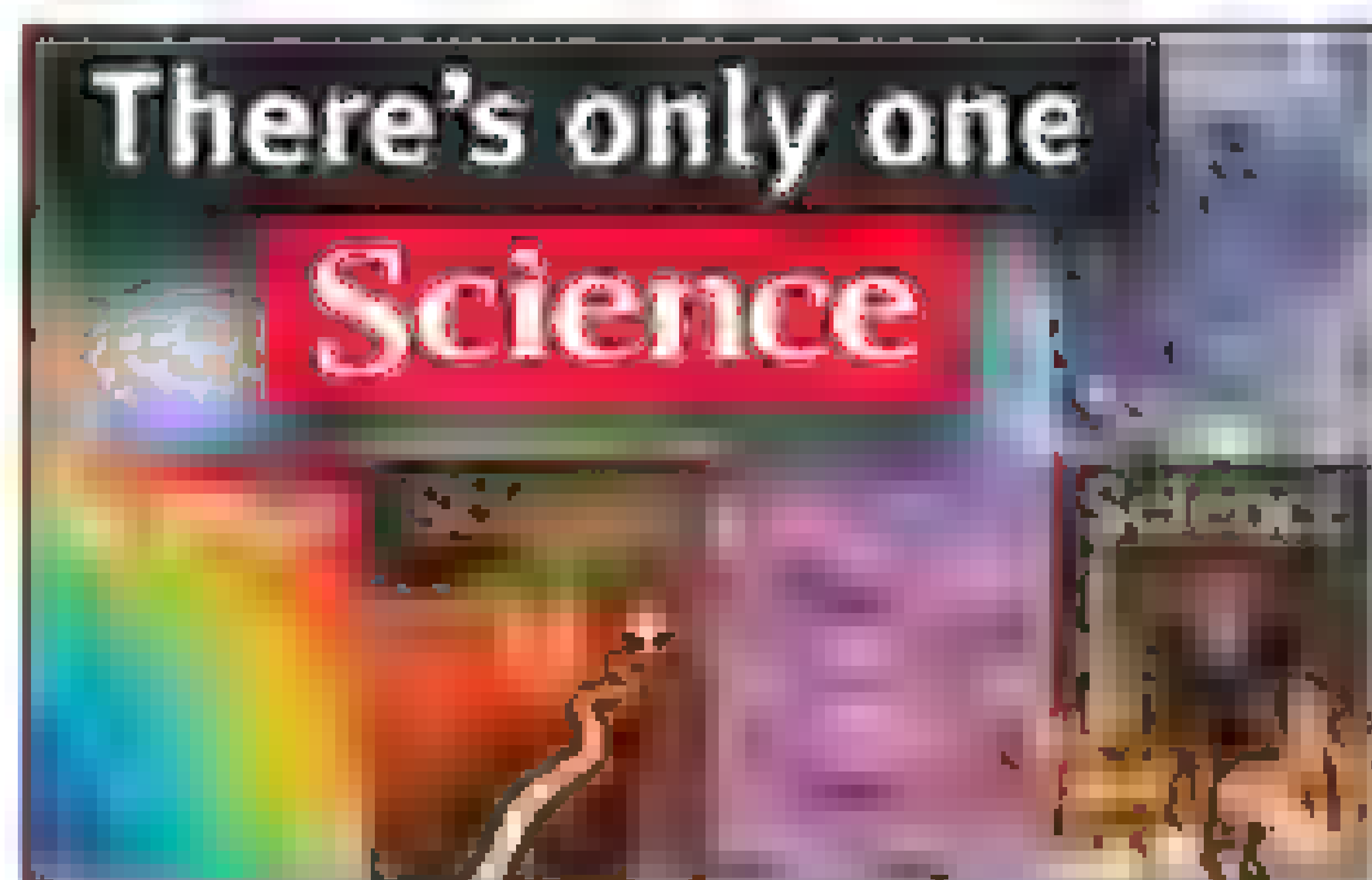
MONOCLONAL ANTIBODIES

UltraMAB Antibodies are a collection of monoclonal antibodies that are exclusively developed by OriGene for immunohistochemistry (IHC) applications and are the industry's only antibody products available on the market that have been validated with the company's 10K High Density Protein Microarray Technology. OriGene's 10K High Density Protein Microarray Platform enables the screening of candidate antibodies against greater than 10,000 human proteins to identify the most specific monoclonal antibodies for IHC applications. Each UltraMAB is validated for IHC and for immunoassay analysis, and determined to have no cross-reactivity with other human proteins other than the antibody's intended target protein as determined by OriGene's 10K High Density Protein Microarray Platform. Consequently, each UltraMAB is quality control verified, guaranteeing superior performance for IHC applications, where specificity-verification and the highest quality antibodies are critical for accurate detection.

OriGene Technologies

For info: 888-267-4436 | www.origene.com/ultramab

Electronically submit your new product description or product literature information! Go to www.sciencemag.org/products/newproducts.dtl for more information. Newly offered instrumentation, apparatus, and laboratory materials of interest to researchers in all disciplines in academic, industrial, and governmental organizations are featured in this space. Emphasis is given to purpose, chief characteristics, and availability of products and materials. Endorsement by *Science* or AAAS of any products or materials mentioned is not implied. Additional information may be obtained from the manufacturer or supplier.



Science Careers Advertising

For full advertising details, go to ScienceCareers.org and click For Employers, or call one of our representatives.

Tracy Holmes
Worldwide Associate Director
Science Careers
Phone: +44 (0) 1223 326525

UNITED STATES & CANADA

E-mail: advertise@sciencecareers.org
Fax: 202 289-6742

Tina Burks
Midwest/West Coast/
South Central/Canada
Phone: 202 326-6577

Elizabeth Early
East Coast & Corporate
Phone: 202-326-6578

Marti Gallun
Sales Administrator
Phone: 202-326-6582

Online Job Posting Questions
Phone: 202 312-6375

EUROPE & REST OF WORLD

E-mail: ads@science-int.co.uk
Fax: +44 (0) 1223 326532

Simone Jux
Phone: +44 (0)1223 326529

Lucy Nelson
Phone: +44 (0)1223 326527

Kelly Graco
Phone: +44 (0) 1223 326528

JAPAN

Yuri Kobayashi
Phone: +81-6-6627-9250
E-mail: ykobayas@aaas.org

CHINA & TAIWAN

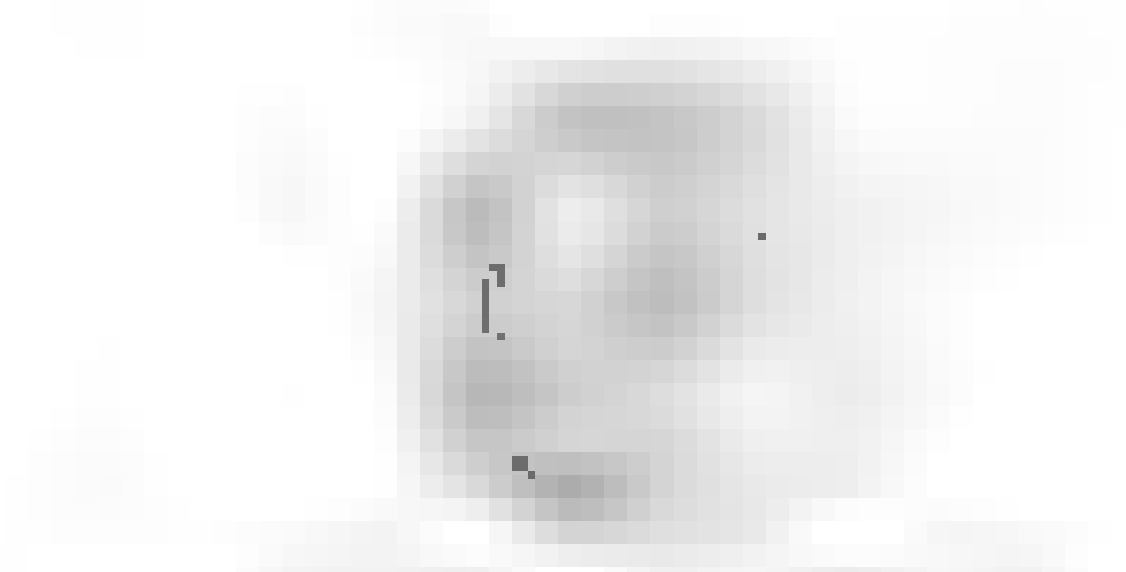
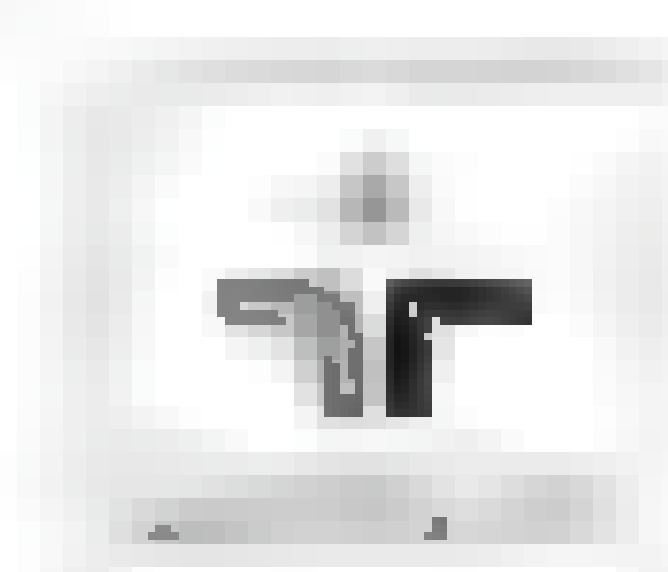
Ruolei Wu
Phone: +86-1367-1015-294
E-mail: rwl@aaas.org

All ads submitted for publication must comply with applicable U.S. and non-U.S. laws. Science reserves the right to refuse any advertisement at its sole discretion for any reason, including without limitation for offensive language or inappropriate content, and all advertising is subject to publisher approval. Science encourages our readers to alert us to any ads that they feel may be discriminatory or offensive.



Max Planck Institute of Immunobiology and Epigenetics

Max-Planck-Institut für Immunbiologie und Epigenetik



The Max Planck Institute of Immunobiology and Epigenetics in Freiburg, Germany invites applications from scientists for

Group Leader in the field of Epigenetics

One of the two major themes at the Max Planck Institute (MPI) Freiburg is dedicated to fostering an outstanding environment for cutting-edge research in the area of Epigenetics (www.ie-freiburg.mpg.de). We are now seeking to fill a group leader position, with a tenure track option, at the Institute. The successful candidate will head an independent research group, with generous funds available for positions, start-up investments and annual running costs. In addition, the group will have full access to the institutional infrastructure including mouse and Drosophila facilities as well as service units supporting mass-spectrometry, bioinformatics, deep-sequencing, live cell imaging and FACS sorting. PhD students will be enrolled through the international PhD program IMPRS-MCB (International MPI School of Molecular and Cellular Biology; www.imprs-mcb.mpg.de).

We are looking for an outstanding group leader with novel and exciting research programs that would integrate well with our present framework of the chromatin and epigenetic research. We are especially interested in candidates with a strong background in fields that complement the current research at the Institute, e.g. biochemistry, transcription, cell cycle, non-coding RNA biology, DNA methylation, chromatin remodeling, epigenetic inheritance and novel forms of memory such as prions. Informal inquiries can be made with Asifa Akhtar and Thomas Jenuwein.

The MPI of Immunobiology and Epigenetics is an international research institute with English as the working language. Salaries will be based on previous experience according to TVöD guidelines. A childcare facility is directly attached to the institute. Women are especially encouraged to apply; handicapped applicants with equal qualifications will be given preferential treatment.

Applications indicating the reference number 020412 comprising C.V., summary of scientific achievements and future research plans as well as the names of three referees should be sent directly via e-mail to Ms. Weigold at weigold@ie-freiburg.mpg.de or to the Max Planck Institute of Immunobiology and Epigenetics, Personnel Department, Stübeweg 51, 79108 Freiburg.

Applications will be accepted until June 30th 2012.

Ottawa Hospital Research Institute



Institut de recherche de l'Hôpital d'Ottawa

The Ottawa Hospital Research Institute (OHRI) and the Kidney Research Centre (KRC) are seeking outstanding candidates to fill two positions at the Scientist and Senior Scientist levels. Both positions will align with the OHRI Vascular Health research priority.

Scientist position: The candidate must be involved in the use of advanced biomolecular technologies pertaining to vascular biology, hypertension, and kidney disease, and will be expected to work at the KRC laboratory facility at the OHRI and hold an academic appointment in the Faculty of Medicine of the University of Ottawa. The successful applicant will be expected to conduct a vigorous program of independent, externally funded research, to teach at the graduate level and to attract excellent trainees, students and future researchers. Candidates must have a PhD or MD or equivalent degree and postdoctoral experience demonstrating outstanding achievement in their field and the capacity to achieve international recognition within five years.

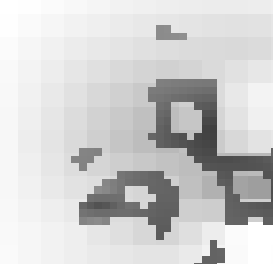
Senior Scientist position: The candidate will be appointed as the Jindal Research Chair for the Prevention of Kidney Disease. The ideal candidate will have an established research program in kidney-related research, with an interest in hypertension and vascular health. The Jindal Research Chair will hold a primary appointment in the Division of Nephrology, Department of Medicine. The successful applicant will be a Clinician Scientist, with Nephrology training and, if not Canadian, should be eligible for permanent residency and medical licensure as a Nephrologist in Canada. The ideal candidate will be an established investigator, with an excellent international reputation, including a strong track record of sustained peer reviewed funding, publications, and trainee supervision. The Chair will have a term of five (5) years, and is potentially renewable for an additional five (5) year term.

Interested Applicants are invited to submit an application consisting of the following: curriculum vitae, copies of representative reprints, statement of research interests, names of three persons able to supply letters of reference. The application package should be sent to cleroux@ohri.ca or by mail courier to

Ottawa Hospital Research Institute
c/o Carmella Leroux
725 Parkdale Avenue
Ottawa ON K1Y 4E9

Applications will be accepted until July 30, 2012. The review of applications will begin immediately and will continue until the position is filled.

Equity is OHRI and University of Ottawa policy; women, aboriginal peoples, members of visible minorities and persons with disabilities are encouraged to apply



INNOVATION AND TECHNOLOGY COMMISSION

Science Advisor

(Salary : HK\$126,500 - HK\$138,350 per month)

Entry Requirements :

Candidate are required to have :

- (a) (i) full professorship status in a relevant field^{Note}, or
(ii) a **PhD Degree** in a relevant field^{Note} and a **minimum of 10 years' relevant post-qualification experience** at a senior management level in a scientific or corporate setting;
- (b) strong research or technical background in the development, application and commercialisation of technology (preferably enjoy recognised international standing in his/her own specialist field), good scientific and/or business networks; competency in research and development and/or business and product development; and understanding of current trends in technology and market (familiarity with the research and development trend in the Mainland will be an advantage); and
- (c) strong command of both written and spoken English. Proficiency in written Chinese and spoken Cantonese and Putonghua will be an advantage

Note : A field relevant to the technology focus areas under the responsibility of ScA

Duties :

Science Advisor (ScA) is a non-civil service position responsible for providing specialist advice to the Commissioner for Innovation and Technology on matters related to innovation and technology development in designated focus areas, including supporting the Technology Committees of the Research and Development Centres and assisting them to set their technology roadmaps. The prevailing technology focus areas under the responsibility of ScA are automotive parts and accessory, communication technologies, consumer electronics, environmental technology, integrated circuit design, logistics and supply chain management enabling technologies, nanotechnology and advanced materials, and optoelectronics, textile and clothing.

He/She is required to lead a team of professional staff to provide assistance to the Innovation and Technology Commission (the Commission) in developing solicitation themes, undertaking project assessment, monitoring progress and evaluating the programmes in related fields under the Innovation and Technology Fund and other funding schemes administered by the Commission. He/She is also expected to maintain contacts with academia, research institutes, industries and other relevant bodies, liaising and supporting the activities of other government departments/organizations in relevant fields, and undertaking ad hoc activities related to the Commission's operation and strategic development in this aspect.

Terms of Appointment : The successful candidate will be appointed on non-civil service agreement terms for two years

Fringe Benefits :

- (a) An end-of-contract gratuity may be granted upon satisfactory completion of the contract. The amount of gratuity payable will be the sum, which, when added together with the Government's contribution to the Mandatory Provident Fund scheme, equals 15% of the total basic salary drawn during the contract period; and
- (b) leave passage allowance and housing benefits in the form of non-accountable cash allowance (subject to the meeting of the eligibility criteria as stipulated in the regulations relating to the provision of such benefits)

How to apply :

Candidates should apply in writing with a completed application form [G.F.340 (Rev.1/2011)] which can be downloaded from the Civil Service Bureau's website (<http://www.csb.gov.hk>) and a full C.V. giving a detailed account of employment records with description of duties and past experience in research/project administration/product development in related fields. Copies of academic qualification certificates and record of previous employment should also be provided. Applications should reach the following mailing or email address on or before the closing date for application. Candidates who are selected for interview will normally receive an invitation for interview for interview in about ten to twelve weeks after the closing date for application. Interviews are tentatively scheduled to be conducted in Hong Kong during late August 2012 (subject to change at the discretion of the Government without prior notification to applicants). Applicants should make themselves available for the interview during that period. Those who are not invited for interview may assume that their applications are unsuccessful.

Address and Enquiry:

Korn/Ferry International (HK) Limited, 15/F, St George's Building, 2 Ice House Street, Central, Hong Kong

e-Mail Address: ITC_ScA@KornFerry.com (For Science Advisor) / ITC-BD@KornFerry.com (For Biotechnology Director)

Contact Person: TT Ho

Contact Number: (852) 2971 2700

Closing date for Application : 25 May 2012

General Notes :

- (a) Non-civil service vacancies are not positions on the civil service establishment. Candidates appointed are not on civil service terms of appointment and conditions of service. Candidates appointed are not civil servants and will not be eligible for posting, promotion or transfer to any posts in the Civil Service.
- (b) Persons who are not permanent residents of the Hong Kong Special Administrative Region may also apply for the post but will be appointed only when no suitable and qualified candidates who are permanent residents are available.
- (c) Candidates with relevant experience in excess of the stipulated minimum may be granted increments.
- (d) As an Equal Opportunities Employer, the Government is committed to eliminating discrimination in employment. The vacancy advertised is open to all applicants meeting the basic entry requirement (irrespective of the disability, sex, marital status, pregnancy, age, family status, sexual orientation and race).
- (e) Where a large number of candidates meet the specified entry requirements, shortlisting criteria may be devised to select the better qualified candidates for further processing. In these circumstances, only shortlisted candidates will be invited to attend the interview.
- (f) It is Government policy to place people with a disability in appropriate jobs wherever possible. If a disabled candidate meets the entry requirements, he/she will be invited to attend the selection interview without being subject to any further shortlisting criteria.
- (g) The entry pay, terms of appointment and conditions of service to be offered are subject to the provisions prevailing at the time the offer of appointment is made.
- (h) Holders of academic qualifications other than those obtained from Hong Kong institutions/Hong Kong Examinations and Assessment Authority may also apply but their qualifications will be subject to assessments on equivalence with the required entry qualifications. They should submit copies of their official transcripts and certificates by post or email.
- (i) Non-civil service vacancy information contained in this advertisement is also available on the GovHK on the Internet at <http://www.gov.hk> and the Innovation and Technology Commission Homepage at <http://www.itc.gov.hk>

Biotechnology Director

(Salary : HK\$126,500 - HK\$138,350 per month)

Entry Requirements :

Candidates are required to have

- (a) a **PhD Degree** in the field of life science or biotechnology;
- (b) a **minimum of 10 years' relevant post-qualification experience** at a senior management level in a scientific or corporate setting;
- (c) strong research or technical background in biotechnology and related areas (preferably enjoy recognised international standing in his/her own specialist field), good scientific and/or business networks; competency in research and development and/or business and product development; and understanding of current trends in technology and market (familiarity with the development and commercial application of biotechnology in the Mainland will be an advantage); and
- (d) strong command of both written and spoken English. Proficiency in written Chinese and spoken Cantonese and Putonghua will be an advantage

Duties :

Biotechnology Director is a non-civil service position responsible for providing expert technology-related advice in biotechnology and related fields to the Commissioner for Innovation and Technology. He/She is required to lead a team of professional staff to provide assistance to the Innovation and Technology Commission (the Commission) in developing solicitation themes, undertaking project assessment, monitoring progress and evaluating the programmes in related fields under the Innovation and Technology Fund and other funding schemes administered by the Commission. He/She is also expected to maintain contacts with academia, research institutes, industries and other relevant bodies, liaising and supporting the activities of other government departments/organizations in the biotechnology field, and undertaking ad hoc activities related to the Commission's operation and strategic development in this aspect.

Terms of Appointment : The successful candidate will be appointed on non-civil service agreement terms for two years

Fringe Benefits :

- (a) An end-of-contract gratuity may be granted upon satisfactory completion of the contract. The amount of gratuity payable will be the sum, which, when added together with the Government's contribution to the Mandatory Provident Fund scheme, equals 15% of the total basic salary drawn during the contract period; and
- (b) leave passage allowance and housing benefits in the form of non-accountable cash allowance (subject to the meeting of the eligibility criteria as stipulated in the regulations relating to the provision of such benefits)

How to Apply :

Candidates should apply in writing with a completed application form [G.F.340 (Rev.1/2011)] which can be downloaded from the Civil Service Bureau's website (<http://www.csb.gov.hk>) and a full C.V. giving a detailed account of employment records with description of duties and past experience in research/project administration/product development in related fields. Copies of academic qualification certificates and record of previous employment should also be provided. Applications should reach the following mailing or email address on or before the closing date for application. Candidates who are selected for interview will normally receive an invitation for interview in about six to eight weeks after the closing date for application. Interviews are tentatively scheduled to be conducted in Hong Kong during late July 2012 (subject to change at the discretion of the Government without prior notification to applicants). Applicants should make themselves available for the interview during that period. Those who are not invited for interview may assume that their applications are unsuccessful.

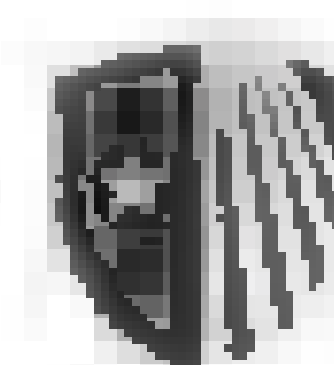
The best ideas in medicine start with the best people.

At Stony Brook Medicine, our highest calling is to put the power of ideas to work in our patients' lives. Stony Brook Medicine integrates and elevates all of Stony Brook University's health-related initiatives: education, research and patient care. It includes Stony Brook University Hospital, Long Island's premier academic medical center. With 597 beds, SBUH is the region's only tertiary care center and Level 1 Trauma Center. We are home of the Stony Brook Heart Institute, Stony Brook Cancer Center, Stony Brook Long Island Children's Hospital, Stony Brook Neurosciences Institute and Stony Brook Digestive Disorders Institute. At Stony Brook Medicine, we put the power of ideas to work. Join our team at Stony Brook Medicine—the best ideas in medicine.

Deputy Director for Research - Stony Brook Cancer Center

The Stony Brook University Cancer Center is seeking candidates and nominees for the Deputy Director for Research. The Deputy Director for Research will work with the Director to set the strategy for basic and translational science research in the Cancer Center. The Deputy Director will provide direction for associated directors and program leaders within the Cancer Center. Additional activities may include working with internal and external advisory boards, fundraising and legislative relations. Applicants for this position should have a record of accomplishments in either basic or translational science and experience in developing complex integrative programs. Candidates should also demonstrate the highest level of ethical conduct and a commitment to diversity. In addition, the applicant should have significant administrative leadership experience along with strong interpersonal and communication skills. **Required Academic and Professional Credentials:** The successful candidate will have an MD or PhD degree. Demonstrated administrative leadership experience. Must be eligible for a senior faculty appointment in accordance with the criteria established by the Stony Brook University appointment, promotion and tenure. Review of applications will continue until the position is filled.

For a full position description and/or application procedures, visit www.stonybrook.edu/jobs (Job Reference #: F-7247-12-04). Nominations and applications, to include a State employment application and curriculum vitae, should be submitted to: Kenneth R. Shroyer, MD, PhD, Chair, Department of Pathology, The Marvin Kuschner Professor Search Committee Chair, c/o Ms. Lauren Cufala, Health Sciences Tower L-4, Room 178, Stony Brook University, Stony Brook, NY 11794. Fax: (631) 444-1719.



Stony Brook
Medicine

Stony Brook University/SBUH is an equal opportunity affirmative action employer.

A Career in science is more than just science.

www.sciencecareers.org

Science Careers

From the journal Science

AAAS



NAVAL RESEARCH LABORATORY Superintendent, Materials Science and Technology Division

www.nrl.navy.mil

Senior Executive Service Career Opportunity
GS-806, 1301, or 1310: \$119,554 to \$179,700 per annum*

*Actual salary may vary depending on the scope and complexity of the position and the qualifications and current compensation of the selectee.

Become a member of an elite research and development community involved in basic and applied scientific research and advanced technological development for tomorrow's Navy and for the Nation.

- Manages, directs, and administers a recognized scientific work force conducting a broad spectrum program of highly sophisticated basic and applied research, and exploratory and advanced development of new or improved materials to be used in Naval weapon platforms and systems.
- Final technical authority for broad and demanding scientific programs of national importance, including the intrinsic behavior of metals, alloys, ceramics, glasses, and composites and their performance and reliability in Naval structures and devices.
- Principal consultant to the Navy, other agencies and nations on the science and developing applications for the research programs under his/her cognizance.
- Applicants should be recognized as national/international authorities and should have planned and executed difficult programs of national significance that show outstanding attainment in their field of research.

For information regarding this vacancy and specific instructions on how to apply, go to www.usajobs.gov, log in and enter the following announcement number NW22XXX-00-630932K9290719-S. Please carefully read the announcement and follow instructions when applying. The announcement closes 31 May 2012. Please contact Ginger Kisamore at ginger.kisamore@nrl.navy.mil for more information; E-mailed resumes cannot be accepted.

NRL is an Equal Opportunity Employer

NRL 4555 Overlook Ave SW, Washington DC 20375



The EGL Foundation invites you to apply to the Gruss Lipper Post-Doctoral Fellowship Program

Eligibility

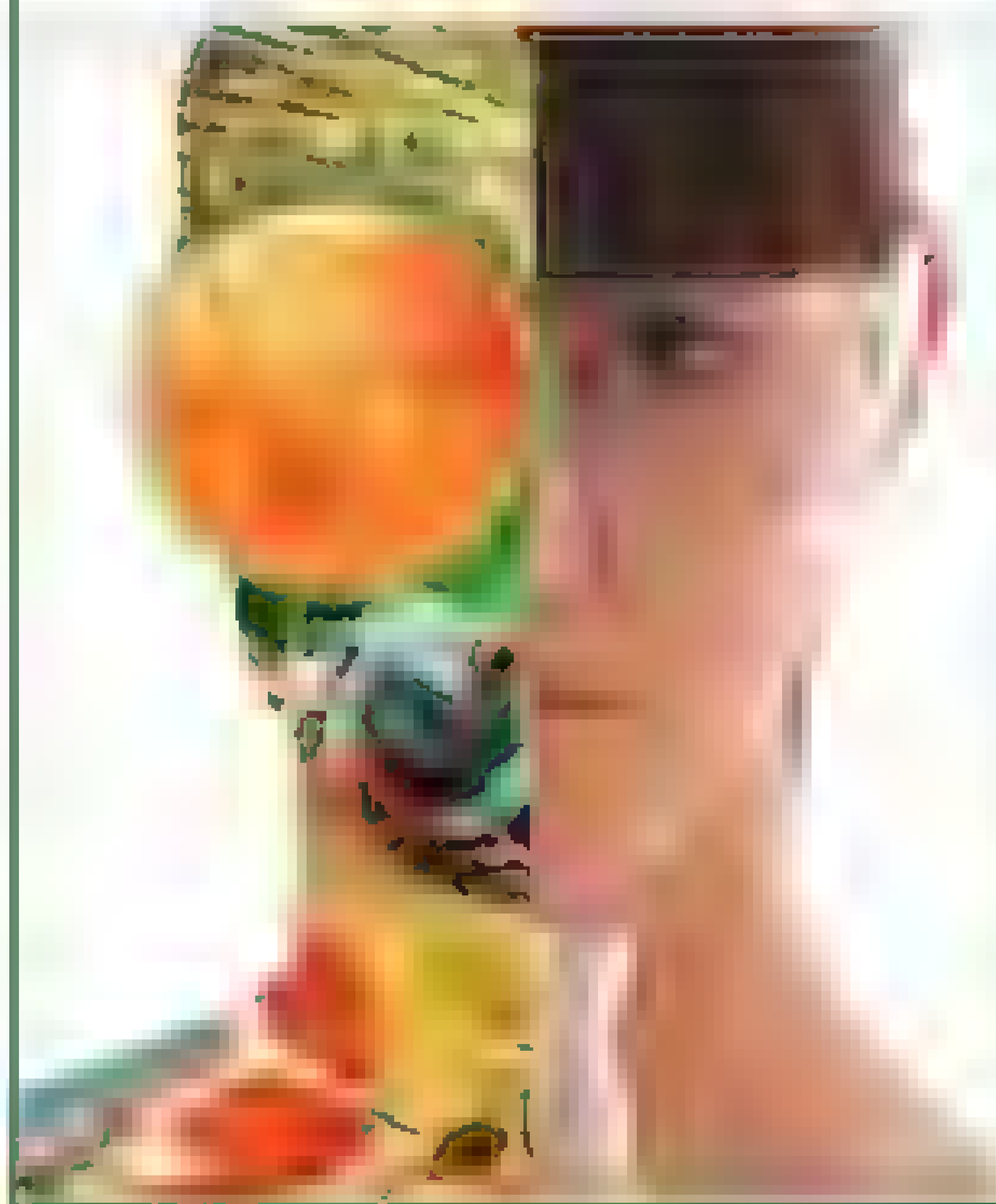
- Israeli citizenship
- Candidates must have completed PhD and/or MD/PhD degrees in the Biomedical Sciences at an accredited Israeli University/Medical School or be in their final year of study
- Candidates must have been awarded a postdoctoral position in the U.S. host research institution.

Details regarding the fellowship are available at www.eglc.org

NW22XXX00630932K9290719-S

WOMEN IN SCIENCE

forging
new pathways in
green
science



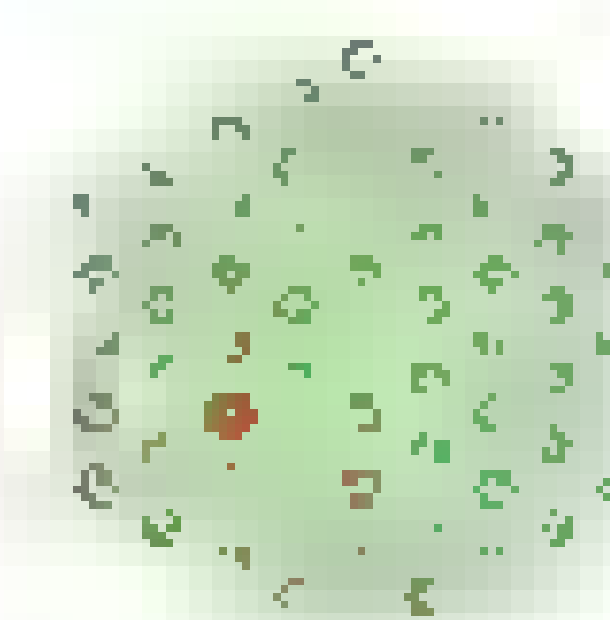
Read inspiring stories
of women working in
"Green Science"
who are blending
a unique combination of
enthusiasm for science
and concern for others
to make the world
a better place.

Download this
free booklet
ScienceCareers.org/
LOrealWiS



This booklet is brought to you by the
AAAS/Science Business Office
in partnership with the
L'Oréal Foundation

EMBL



EMBL offers a highly collaborative, uniquely international culture. It fosters top quality, interdisciplinary research by promoting a vibrant environment consisting of young, independent researchers with access to outstanding graduate students and postdoctoral fellows. EMBL is an inclusive, equal opportunity employer offering attractive conditions and benefits appropriate to an international research organisation

Team Leader – Head of Electron Microscopy Core Facility

The post holder will lead a mixed service and research team with currently eight members providing advanced electron microscopy (EM) service, including electron tomography and correlative light and electron microscopy, to EMBL and external users from EMBL's member states. Furthermore, the facility – based in Heidelberg, Germany – regularly organises courses to train scientists in EM methods and actively collaborates with industrial partners to develop new applications of EM.

It is desirable that the future Team Leader has an interest in EM methods development in order to maintain the technology at the cutting edge and extend the facility's service portfolio to enable new biological applications (e.g. new 3D EM methods, automation for high throughput EM, new correlative EM methods or new data analysis methods). Methods development could be driven by an independent interest in biological questions or by a keen interest in scientific collaborations with biological research groups at EMBL. If appropriate, a joint appointment as a research team leader in one of EMBL's biological research units is foreseen to strengthen and support these interactions.

The successful candidate should have in-depth knowledge and broad experience in EM methods, including data analysis. Excellent organisational skills, experience in EM service & training and strong skills to manage a team of technical and scientific personnel will be essential. The Team Leader should have excellent communication skills and a strong motivation to work in the multidisciplinary and collaborative environment of EMBL. Experience in collaborations with industrial partners will be an asset. Fluency in English as the working language of EMBL is required.

Please apply online through www.embl.org/jobs and include a cover letter, CV and a concise description of research interests and future research plans. Please also arrange for 3 letters of recommendation to be emailed to references@embl.de at the latest by 10 June 2012.

Interviews are planned for 11, 12 and 13 July 2012.

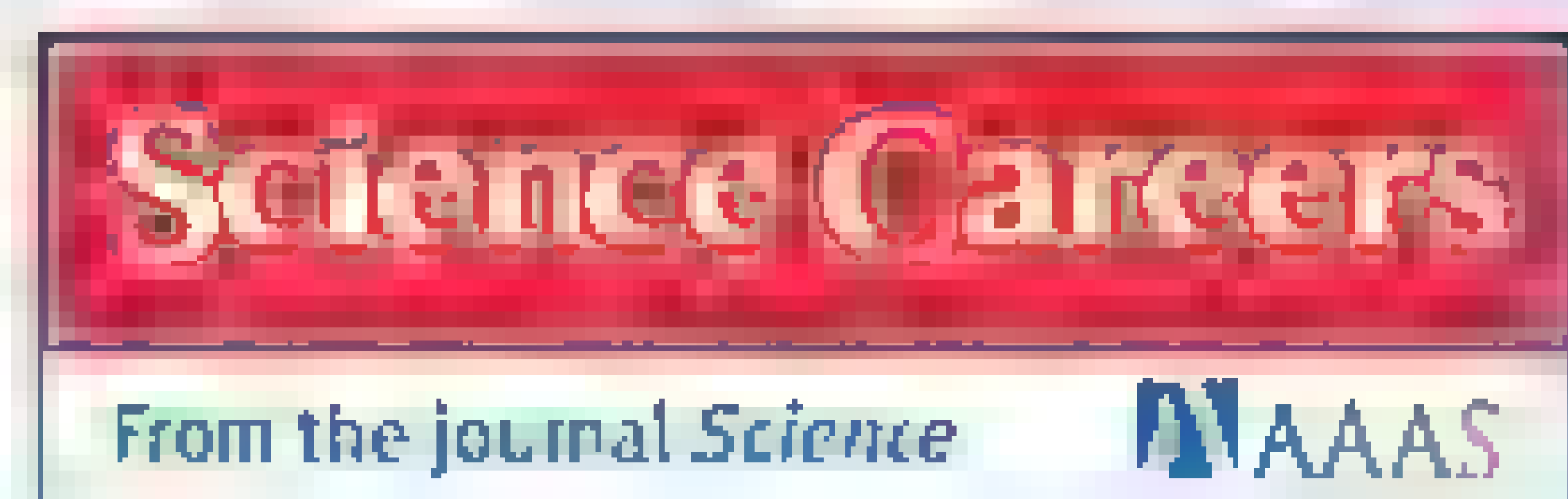
Further details on Team/Group Leader appointments can be found under www.embl.org/gi-faq

For further information about the position and about research at EMBL please visit

www.embl.org

Get a Career Plan that Works.

An exceptional career requires insightful planning and management. That's where *Science Careers* comes in. From job search to career enhancement, *Science Careers* has the tools and resources to help you achieve your goals. Get yourself on the right track today and get a real career plan that works. Visit ScienceCareers.org.



ScienceCareers.org

Find My Job

Develop My Career

Navigate

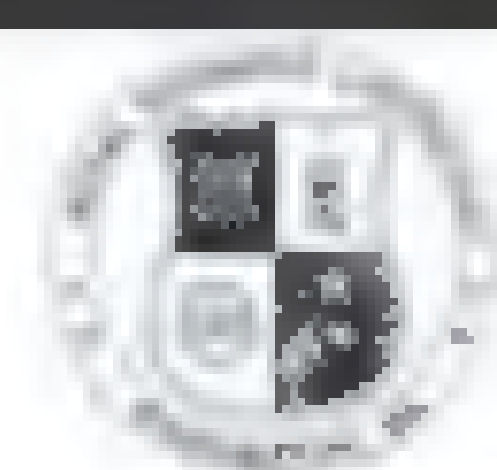
Network

Research

Search

Track





NAVAL RESEARCH LABORATORY
Superintendent, Electronics Science
and Technology Division

www.nrl.navy.mil

Senior Executive Service Career Opportunity
ES-855, 1301, or 1310: \$119,554 to \$179,700 per annum*

*Actual salary may vary depending on the scope and complexity of the position and the qualifications and current compensation of the selectee.

Become a member of an elite research and development community involved in basic and applied scientific research and advanced technological development for tomorrow's Navy and for the Nation

- Manages, directs, and administers a recognized scientific work force conducting a broad spectrum program of highly sophisticated experimental and theoretical research involving electron device technology.
- Final technical authority for broad and demanding scientific programs of national importance, including developing high performance microwave millimeter wave tubes; developing microwave integrated circuits and passive devices; investigating new semiconductors and insulator materials; the electron physics of interfaces and layered films; the reliability physics of electron devices; and the radiation hardening and vulnerability assessment of electron device, components and assemblies.
- Principal consultant to the Navy, other agencies and nations on the science and developing applications for the research programs under his/her cognizance.
- Applicants should be recognized as national/international authorities and should have planned and executed difficult programs of national significance that show outstanding attainment in their field of research.

For information regarding this vacancy and specific instructions on how to apply, go to www.usajobs.gov, log in and enter the following announcement number: NW2XXXX-00-630938K9290738-S. Please carefully read the announcement and follow instructions when applying. The announcement closes on **31 May 2012**. Please contact **Ginger Kisamore** at ginger.kisamore@nrl.navy.mil for more information. E-mailed resumes cannot be accepted.

NRL is an Equal Opportunity Employer

NRL • 4555 Overlook Ave SW, Washington DC 20375

www.abdn.ac.uk/jobs



**UNIVERSITY
OF ABERDEEN**

School of Medical Sciences



Research Fellows

(2 posts) References: YMS356R and YMS357R

We are inviting applicants to join the Aberdeen Fungal Group to study the spatial and temporal regulation of fungus-host interactions during fungal infection. This European Commission funded project (STRIFE) involves genomics, molecular genetics and infection biology, and is led by Professor Al Brown.

Salary: £30,122 per annum

Closing date: 18 May 2012.

The University of Aberdeen is a charity registered in Scotland, No SC013683.

For further information on this opportunity and to view all current vacancies at the University visit:

www.abdn.ac.uk/jobs

Promoting Diversity and Equal Opportunities throughout the University



OAW
Austrian Academy
of Sciences

Austrian Academy of Sciences

New Frontiers Groups

The Austrian Academy of Sciences (OeAW) is the leading organization in Austria performing non-university-based competitive basic research in various fields of sciences and humanities with more than 1.400 employees.

The new excellence program "New Frontiers Groups" aims at investigator-driven innovative research in order to promote promising academic careers and to further strengthen the Academy's research portfolio.

The OeAW invites applications from highly talented researchers at early stages of their careers to establish a **New Frontiers Group (NFG)**.

We are looking for candidates with records of significant scientific achievements and the ability to lead an independent research group. Applicants are invited to submit a project proposal characterized by novelty and high originality, focusing on new areas and approaches within the Academy's research portfolio. Candidates with interdisciplinary interests and experience are particularly welcome.

Applications will be evaluated by an international jury coordinated by the Austrian Science Fund (FWF).

Successful candidates will be offered a New Frontiers Group for a period of five years **at an OeAW Institute of their choice**.

The budget per New Frontiers Group ranges from € 1.2 to 4 million for five years and covers expenses for up to six research positions, for project related investments, overhead costs, etc. The cumulative amount of funding is competitive with top class start-up packages of international career development programs.

For detailed program information, including instructions on how to apply, please visit our website: <http://www.oeaw.ac.at/nfg>

With successful completion of the NFG project, the OeAW may offer tenure track positions to outstanding NFG leaders.

The OeAW values diversity and is an equal opportunity employer.

Deadline for application is July 15th, 2012.

**Download
your free copy
today.**

ScienceCareers.org/booklets



From technology specialists to patent attorneys to policy advisers, learn more about the types of careers that scientists can pursue and the skills needed in order to succeed in nonresearch careers.



POSITIONS OPEN

University of Louisville

ASSISTANT/ASSOCIATE PROFESSOR

The Institute of Molecular Cardiology at the University of Louisville is seeking qualified candidates to join the members of the Institute in work focusing on cell therapy for myocardial repair. Appointments will be at Assistant/Associate Professor level depending on qualifications. The successful candidate will have a track record of working with stem/progenitor cells in the cardiovascular system. He/she will join a productive, highly collegial, and multidisciplinary team of investigators supported by state-of-the-art facilities and considerable funds. Submit letter of application with curriculum vitae and statement of interest to: **Dr. Roberto Bolli, 550 South Jackson Street, ACB, Third Floor, Louisville, KY 40202. Affirmative Action/Equal Opportunity.**

TENURE-TRACK FACULTY POSITION Section of Anatomy

The Section of Anatomy at Southern Illinois University School of Dental Medicine (SIU-SDM) is seeking applicants for a full time (12 month) tenure-track faculty position in Gross Anatomy at the **ASSISTANT/ASSOCIATE PROFESSOR** level. Applicants must have a Ph.D. in the Anatomical Sciences or Ph.D./DMD/DDS/M.D.; additional Postdoctoral training and teaching experience in the Anatomical Sciences is desirable. Teaching duties are shared within the Section and include courses in Gross Anatomy, Neuroanatomy, Histology, and Oral Biology. The candidate is expected to direct either the Gross Anatomy or Histology course and participate in additional teaching. Candidates are also expected to possess a strong research portfolio to establish an independent research program, or to actively participate and/or collaborate in ongoing research areas supported by the School. Academic rank and salary are commensurate with experience and qualifications.

Review of applications will begin immediately and continue until the position is filled. Applicants should submit a letter of interest with brief statements of teaching experience, research experience and interests related to dental medicine, curriculum vitae, and three letters of reference to: **Dr. Bruce Rotter, Interim Dean, School of Dental Medicine, Southern Illinois University, 2800 College Avenue, Alton, Illinois 62002-4900** or electronically to e-mail: brotter@siue.edu. SIU-SDM is an Equal Employment Opportunity/Affirmative Action Employer. Women and minorities are encouraged to apply. SIUE is a state university - benefits under state sponsored plans will not be available to holders of F-1 or J-1 visas.

**Find your
future here.**



Science Careers

From the journal Science AAAS

www.ScienceCareers.org

Widely
Recognized
Original &
Guaranteed

KlenTaq1

8¢/u
Truncated
Taq DNA
Polymerase
Withstand 99°C

US Pat #5,436,149
Call: **Ab Peptides**
Fax: 314•968•8988

e-mail: abpeps@msn.com
1•800•383•3362
www.abpeps.com



Announcing Keystone Symposia 2012–2013 Conferences

Pulmonary Vascular Disease and Right Ventricular Dysfunction: Current Concepts and Future Therapies

Sep 10–15 • Portola Hotel & Spa • Monterey, California, USA

Aging and Diseases of Aging

Oct 22–27 • Sheraton Miyako Hotel Tokyo • Tokyo, Japan

Immunological Mechanisms of Vaccination

Nov 7–12 • Fairmont Château Laurier • Ottawa, Ontario, Canada

Type 2 Immunity: Initiation, Maintenance, Homeostasis and Pathology *joint with: Pathogenic Processes in Asthma and COPD*

Jan 10–15 • Santa Fe Community Convention Center • Santa Fe, New Mexico, USA

Multiple Sclerosis

Jan 11–16 • Big Sky Resort • Big Sky, Montana, USA

New Frontiers in Cardiovascular Genetics beyond GWAS

Jan 13–18 • Granlibakken Resort • Tahoe City, California, USA

Frontiers of NMR in Biology

Jan 13–18 • Snowbird Resort • Snowbird, Utah, USA

Hematopoiesis

Jan 14–19 • Sheraton Steamboat Resort • Steamboat Springs, Colorado, USA

Emerging Topics in Immune System Plasticity:

Cellular Networks, Metabolic Control and Regeneration

Jan 15–20 • Santa Fe Community Convention Center • Santa Fe, New Mexico, USA

Plant Abiotic Stress and Sustainable Agriculture:

Translating Basic Understanding to Food Production

Jan 17–22 • Sagebrush Inn and Conference Center • Taos, New Mexico, USA

Noncoding RNAs in Development and Cancer

Jan 20–25 • Fairmont Hotel Vancouver • Vancouver, British Columbia, Canada

Malaria

Jan 20–25 • JW Marriott New Orleans • New Orleans, Louisiana, USA

Metabolic Control of Inflammation and Immunity

Jan 21–26 • Beaver Run Resort • Breckenridge, Colorado, USA

Antibodies as Drugs *joint with:*

Cancer Immunology and Immunotherapy

Jan 27–Feb 1 • Fairmont Hotel Vancouver • Vancouver, British Columbia, Canada

Adipose Tissue Biology *joint with:*

Diabetes – New Insights into Mechanism of Disease and Its Treatment

Jan 27–Feb 1 • Keystone Resort • Keystone, Colorado, USA

Mitochondria, Metabolism and Myocardial Function –

Basic Advances to Translational Studies

Feb 3–8 • Keystone Resort • Keystone, Colorado, USA

Neurogenesis *joint with:*

New Frontiers in Neurodegenerative Disease Research

Feb 3–8 • Santa Fe Community Convention Center • Santa Fe, New Mexico, USA

Lung Development, Cancer and Disease

Feb 5–10 • Sagebrush Inn and Conference Center • Taos, New Mexico, USA

The Gut Microbiome: The Effector/Regulatory Immune Network

Feb 10–15 • Sagebrush Inn and Conference Center • Taos, New Mexico, USA

B Cell Development and Function *joint with: HIV Vaccines*

Feb 10–15 • Keystone Resort • Keystone, Colorado, USA

Autophagy, Inflammation and Immunity

Feb 17–22 • Fairmont The Queen Elizabeth • Montreal, Québec, Canada

Nutrition, Epigenetics and Human Disease

Feb 19–24 • Hilton Santa Fe/Historic Plaza • Santa Fe, New Mexico, USA

Myeloid Cells: Regulation and Inflammation

Feb 19–24 • Keystone Resort • Keystone, Colorado, USA

Stem Cell Regulation in Homeostasis and Disease

Feb 24–Mar 1 • Fairmont Banff Springs • Banff, Alberta, Canada

PI3-Kinase and Interplay with Other Signaling Pathways

joint with: Tumor Metabolism

Feb 24–Mar 1 • Keystone Resort • Keystone, Colorado, USA

Structural Analysis of Supramolecular Assemblies by Hybrid Methods

Mar 3–7 • Granlibakken Resort • Tahoe City, California, USA

Understanding Dendritic Cell Biology to Advance Disease Therapies

Mar 3–8 • Keystone Resort • Keystone, Colorado, USA

DNA Replication and Recombination

joint with: Genomic Instability and DNA Repair

Mar 3–8 • Fairmont Banff Springs • Banff, Alberta, Canada

Growing to Extremes: Cell Biology and Pathology of Axons

Mar 10–15 • Granlibakken Resort • Tahoe City, California, USA

Host Response in Tuberculosis *joint with:*

Tuberculosis: Understanding the Enemy

Mar 13–18 • Whistler Conference Centre • Whistler, British Columbia, Canada

Precision Genome Engineering and Synthetic Biology: Designing Genomes and Pathways

Mar 17–22 • Beaver Run Resort • Breckenridge, Colorado, USA

Neuronal Control of Appetite, Metabolism and Weight

Mar 17–22 • Fairmont Banff Springs • Banff, Alberta, Canada

RNA Silencing

Mar 19–24 • Whistler Conference Centre • Whistler, British Columbia, Canada

Epigenetic Marks and Cancer Drugs

Mar 20–25 • Eldorado Hotel & Spa • Santa Fe, New Mexico, USA

Molecular Clockworks and the Regulation of Cardio-Metabolic Function

Apr 3–7 • Snowbird Resort • Snowbird, Utah, USA

Immune Activation in HIV Infection:

Basic Mechanisms and Clinical Implications

Apr 3–8 • Beaver Run Resort • Breckenridge, Colorado, USA

Nuclear Receptors and Friends:

Roles in Energy Homeostasis and Metabolic Dysfunction

Apr 3–8 • Alpbach Congress Centrum • Alpbach, Austria

Immunopathology of Type 1 Diabetes *joint with:*

Advances in the Knowledge and Treatment of Autoimmunity

Apr 4–9 • Fairmont Chateau Whistler • Whistler, British Columbia, Canada

Cardiac Remodeling, Signaling, Matrix and Heart Function

Apr 7–12 • Snowbird Resort • Snowbird, Utah, USA

Plant Immunity: Pathways and Translation

Apr 7–12 • Big Sky Resort • Big Sky, Montana, USA

Positive Strand RNA Viruses

Apr 28–May 3 • Boston Park Plaza & Towers • Boston, Massachusetts, USA

The Innate Immune Response in the Pathogenesis of Infectious Disease

May 10–15 • Ouro Preto, Brazil

The Hippo Tumor Suppressor Network:

From Organ Size Control to Stem Cells and Cancer

May 19–23 • Hyatt Regency Monterey • Monterey, California, USA

Human Genomics and Personalized Medicine

Jun 17–21 • Clarion Hotel Sign • Stockholm, Sweden

Scholarships are available to students and postdoctoral fellows. Abstract and scholarship deadlines are four months before meetings, and early registration deadlines, saving US\$150 on later fees, precede conferences by two months. Visit www.keystonesymposia.org/2013meetings for more information.

KEYSTONE SYMPOSIA
on Molecular and Cellular Biology
Accelerating Life Science Discovery

Cancer

Development

Endocrinology

Glycobiology

Immunology

Neuroscience

Proteases

Signal Transduction

Stem Cells

R&D Systems Tools for Cell Biology Research™

StoreMags.com



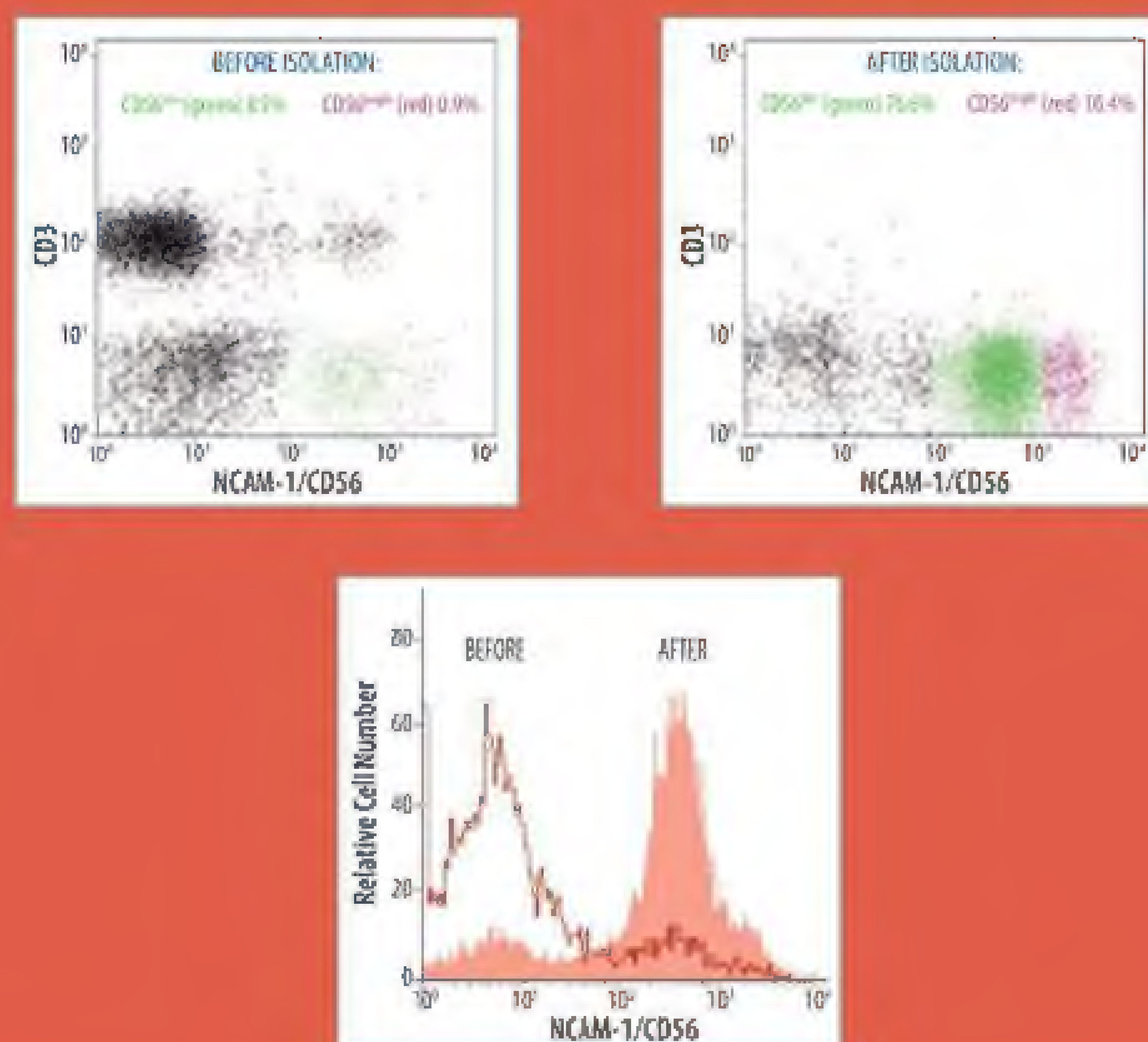
Killer Selection

R&D Systems is a leading manufacturer of products for immunology research, including an extensive collection of antibodies and antibody-based kits designed to simplify the isolation and characterization of different immune cell types. We have recently added the MagCelect™ Mouse and Human Natural Killer Cell Isolation Kits to our rapidly expanding line of cell selection products. These kits utilize negative selection and a magnetically-based separation technique to isolate natural killer cells from a heterogeneous cell population.

ADVANTAGES

- **Negative selection**- target cells remain untouched during the selection process
- **Flexible** – compatible with several magnet systems
- **Fast** – target cells can be enriched in approximately one hour
- **High purity** - typical purity for the human kit is 75-85%; for the mouse kit 80-90%

Isolation of Natural Killer Cells using the MagCelect Human NK Cell Isolation Kit



Visit our website at www.RnDSystems.com/NKCells

R&D Systems, Inc. www.RnDSystems.com

R&D Systems Europe, Ltd. www.RnDSystems.co.uk

R&D Systems China Co., Ltd. www.RnDSystemsChina.com.cn

For research use only. Not for use in diagnostic procedures.

R&D
SYSTEMS®